Published by Empress Catherine II
Saint Petersburg Mining University

SINCE 1907

ISSN 2411-3336
E-ISSN 2541-9404

JOURNAL OF MINING INSTITUTE

ZAPISKI GORNOGO INSTITUTA

SCIENTIFIC JOURNAL



Volume 280
N 4 • 2026

SCOPUS (Q1, CITESCORE – 8.8)
WEB OF SCIENCE (Q1, JIF – 2.9)
SJR 2025 – 1.222

WWW.PMI.SPMI.RU

Journal of Mining Institute
Scientific journal



Empress Catherine II Saint Petersburg Mining University

The International Competence Center for Mining Engineering Education under the auspices of **UNESCO**

The peer-reviewed scientific periodical “Journal of Mining Institute” is published since 1907 by Empress Catherine II Saint Petersburg Mining University – the first higher technical educational institution in Russia, founded in 1773 by the decree of Catherine II as the embodiment of the ideas of Peter I and M.V.Lomonosov on the training of engineers for the development of mining business.

The International Competence Center for Mining Engineering Education under the auspices of UNESCO operates on the basis of Empress Catherine II Saint Petersburg Mining University and contributes to active interaction of the Journal with the international scientific community.

The purpose of the Journal is to create an information space in which Russian and foreign scientists can present results of their theoretical and empirical research on the problems of the mining sector. The journal invites the leading specialists to publish scientific articles and promotes them in the international scientific community.

Published articles cover the issues of geology, geotechnical engineering and engineering geology, mining and petroleum engineering, mineral processing, energy, geoecology and life safety, economics of raw materials industries.

The Journal is indexed by Scopus (Q1, CiteScore – 8.8), Web of Science (JCR – Q1, JIF – 2.9), SJR 2025 – 1.222, DOAJ, RSCI, GeoRef, Islamic World Science Citation Database (ISC), Google Scholar. It is included in the White list of the Ministry of Education and Science of the Russian Federation.

The Journal is published six times a year. The average first decision time is one month.

Articles are published free of charge. Translation is provided by the author.

The cover shows an exhibit of the Mining Museum – large, tabular crystals of native antimony, tin-white in color, in a fine-grained carbonate rock stained with antimony ochres, France. Native antimony is a mineral relatively rare in nature in its pure form (the chemical element antimony). Another antimony mineral, stibnite (antimonite, “antimony glitter”), is of greatest industrial significance.

The Mining Museum is the world’s third largest natural-science exposition, it contains more than 230 thousand exhibits, including precious metals and stones, unique collections of minerals, ores, rocks, paleontological remains, meteorites, a collection of models and prototypes of mining equipment, pieces of stone-cutting and jewelry art.

JOURNAL OF MINING INSTITUTE

ZAPISKI GORNOGO INSTITUTA

PEER-REVIEWED SCIENTIFIC JOURNAL

Published since 1907

ISSN 2411-3336
e-ISSN 2541-9404

Volume 280

N 4 • 2026

ST. PETERSBURG

Journal founder: Empress Catherine II Saint Petersburg Mining University

CHIEF EDITOR
V.S.Litvinenko, Doctor of Engineering Sciences, Professor, Member of the International Academy of Higher Education, RANS, RAHS, MANEB, Rector (Empress Catherine II Saint Petersburg Mining University, Saint Petersburg, Russia)

DEPUTY CHIEF EDITOR
S.G.Skublov, Doctor of Geological and Mineralogical Sciences, Professor, Member of the Russian Mineralogical Society, Expert of the RSF and RAS (Empress Catherine II Saint Petersburg Mining University, Saint Petersburg, Russia)

EXECUTIVE SECRETARY
S.V.Sinyavina, Candidate of Engineering Sciences, Director of the Publishing House (Empress Catherine II Saint Petersburg Mining University, Saint Petersburg, Russia)

EDITORIAL BOARD

O.E.Aksyutin, Doctor of Engineering Sciences, Corresponding Member of the RAS, Deputy Chairman of the Management Board, Head of Department (PAO Gazprom, Moscow, Russia)
A.A.Baryakh, Doctor of Engineering Sciences, Professor, Academic Advisor (Mining Institute Ural Branch RAS, Perm, Russia)
V.N.Brichkin, Doctor of Engineering Sciences, Professor, Head of Department of Modern Natural Sciences (Empress Catherine II Saint Petersburg Mining University, Saint Petersburg, Russia)
S.G.Gendler, Doctor of Engineering Sciences, Professor, Member of the RANS, Head of Department of Occupational Safety (Empress Catherine II Saint Petersburg Mining University, Saint Petersburg, Russia)
O.M.Ermilov, Doctor of Engineering Sciences, Professor, Member of the RAS, RAHS, Deputy Engineer-in-Chief of Science Programmes (OOO Gazprom Development Nadym, Nadym, Russia)
V.P.Zubov, Doctor of Engineering Sciences, Professor, Head of the Department of Underground Mining (Empress Catherine II Saint Petersburg Mining University, Saint Petersburg, Russia)
A.V.Kozlov, Doctor of Geological and Mineralogical Sciences, Member of the Russian Mineralogical Society, Head of Department of Geology and Exploration of Mineral Deposits (Empress Catherine II Saint Petersburg Mining University, Saint Petersburg, Russia)
A.D.Kuranov, Candidate of Engineering Sciences, Director of Design of Technological Disciplines (Gipronickel Institute LLC, Saint Petersburg, Russia)
Yu.B.Marin, Doctor of Geological and Mineralogical Sciences, Professor, Corresponding Member of the RAS, Honorary President (Russian Mineralogical Society, Saint Petersburg, Russia)
V.A.Morenov, Candidate of Engineering Sciences, Associate Professor (Empress Catherine II Saint Petersburg Mining University, Saint Petersburg, Russia)
M.A.Pashkevich, Doctor of Engineering Sciences, Professor, Head of Department of Geoecology (Empress Catherine II Saint Petersburg Mining University, Saint Petersburg, Russia)
T.V.Ponomarenko, Doctor of Economics, Professor (Empress Catherine II Saint Petersburg Mining University, Saint Petersburg, Russia)
O.M.Prishchepa, Doctor of Geological and Mineralogical Sciences, Professor, Member of the RANS, Vice-Rector for Research (Empress Catherine II Saint Petersburg Mining University, Saint Petersburg, Russia)
A.G.Protosenya, Doctor of Engineering Sciences, Professor (Empress Catherine II Saint Petersburg Mining University, Saint Petersburg, Russia)
A.A.Tronin, Doctor of Geological and Mineralogical Sciences, Director (Saint Petersburg Scientific-Research Centre for Ecological Safety RAS, Saint Petersburg, Russia)
V.L.Trushko, Doctor of Engineering Sciences, Professor, Member of the International Higher Education Academy of Sciences, RANS, RAHS, MANEB, Head of Department of Mechanics (Empress Catherine II Saint Petersburg Mining University, Saint Petersburg, Russia)
P.S.Tsvetkov, Doctor of Economics, Associate Professor (Empress Catherine II Saint Petersburg Mining University, Saint Petersburg, Russia)
A.E.Cherepovitsyn, Doctor of Economics, Professor, Head of Department of Economics, Organization and Management (Empress Catherine II Saint Petersburg Mining University, Saint Petersburg, Russia)
Ya.E.Shklyarskii, Doctor of Engineering Sciences, Professor, Head of the Department of General Electric Engineering (Empress Catherine II Saint Petersburg Mining University, Saint Petersburg, Russia)
Oleg Antzutkin, Professor (University of Technology, Luleo, Sweden)
Gabriel Weiss, Doctor of Sciences, Professor, Pro-Rector for Science and Research (Technical University, Kosice, Slovakia)
Hal Gurgenci, Professor (School of Mining Machine-Building in University of Queensland, Brisbane, Australia)
Edwin Kroke, Doctor of Sciences, Professor (Institute of Inorganic Chemistry in Freiberg Mining Academy, Freiberg, Germany)
Zhou Fubao, Doctor of Sciences, Professor, Vice President (China University of Mining and Technology, Beijing, PR China)
Zhao Yuemin, Doctor of Sciences, Professor, Director of Academic Committee (China University of Mining and Technology, Beijing, PR China)

Sections

• Geology • Geotechnical Engineering and Engineering Geology • Economic Geology • Energy

The journal invites the leading specialists to publish scientific articles and promotes them in the international scientific community
Registration Certificate PI N FS 77-70453 dated 20 July 2017

PH License N 06517 dated 09.01.02

Editorial staff: Head of the Editorial Center V.L.Lebedev, Editors E.S.Dribinskaya, M.G.Khachirova, L.V.Nabieva, A.I.Yakovleva, E.D.Bokareva
Bibliographer A.A.Belova. Computer Design N.N.Sedykh, V.I.Kashirina, E.A.Golovinskaya

© Empress Catherine II Saint Petersburg Mining University, 2026

Publishing date 10.09.2026. Format 60 × 84/8. Academic Publishing Division 42.
Circulation: 100 copies. Order 440. Printed by RIC of Empress Catherine II Saint Petersburg Mining University. Free sale price.

Editorial and publisher address 2, 21st Line, St. Petersburg, 199106, Russia
Phone: +7 (812) 328-8416; +7 (812) 328-8216
E-mail: pmi@spmi.ru Journal website: pmi.spmi.ru

CONTENTS

Georgii I. Malov, Vera D. Strakhovenko, Ekaterina A. Ovdina, Viktor I. Malov. Assessment of carbon deposition rates by bottom sediments of small lakes in the south of Western Siberia 3

Pavel I. Alekseev, Evgenii A. Vasilev. Investigation of "Kolchedan amber" with IR spectroscopy 16

Dmitrii A. Boreiko, Nikolai D. Tskhadaya, Dmitrii Yu. Serikov, Vyacheslav A. Khlamov. Design improvement of a near-bit reaming-ejection device for enhancing rock-breaking efficiency during well construction..... 27

Vyacheslav N. Kuchin, Georgii V. Buslaev, Vladimir A. Sidorov, Olga S. Zubkova. A study of grouting mortars using chromium-containing catalyst sludge for well cementing in permafrost zones ... 37

Anastasiya R. Yusupova, Nouria G. Nourgalieva. Lithological characteristics of lacustrine sediments in lakes Bolshoye Miassovo and Maloye Miassovo (Southern Urals, Russia) 47

Ella V. Sokol, Anna S. Polovykh, Svetlana N. Kokh, Ivan S. Karputin, Olga A. Kozmenko. Isomorphic capacity of combustion metamorphic melilite solid solutions 70

Danzan B. Bembeev, Sofya I. Merenkova, Aleksei A. Samsonov, Ruslan R. Gabdullin. Mineralogical and geochemical characteristics of coals from the Mugun deposit and sediment provenance during their formation..... 85

Aleksandr K. Kozin, Sergei Yu. Stepanov, Roman S. Palamarchuk, Valeriya S. Zhdanova, Natalya S. Vlasenko. Morphological features, internal structure, and compositional signatures of native gold from the Murzinka placer group (Middle Urals): identification of lode sources and conditions of placer formation..... 104

Irina A. Kozlova, Sergei V. Biryulin, Anatolii K. Yurkov. Radon monitoring possibilities in short-term earthquake prediction 122

Aleksei V. Ivanov, Ruslan R. Gabdullin, Sofya I. Merenkova, Aleksei A. Samsonov, Alvina V. Chistyakova, Dmitrii F. Ayatskov, Mikhail A. Vinnik, Evgenii Yu. Pogozhev, Afanasii E. Telnov, Yurii A. Churikov, Nikita N. Anisimov, Natalya V. Badulina. Microfragments of the Saratov meteorite in the magnetic fraction of modern soils: search and identification 131

Mohsen Riazi, Hossein Mehrjoo, Mohammad-Saber Dabiri, Jamilyam Ismailova, Masoud Riazi. Predicting gas hydrate formation temperature using a hybrid artificial intelligence-empirical approach..... 145

Oksana V. Lunina, Aleksei S. Nizovtsev. Insights into field surveying and automated processing of digital outcrop models for fracture analysis 163

Ilya V. Rakitin, Dmitrii A. Vasilev, Aleksei V. Bolshunov, Anatolii Yu. Ozhigin. Analysis of technologies and equipment for Antarctic subglacial lake research 176

ISSN 2411-3336; e-ISSN 2541-9404

JOURNAL OF MINING INSTITUTE

Zapiski Gornogo instituta

Journal homepage: pmi.spmi.ru

Research article

Geotechnical Engineering and Engineering Geology

Assessment of carbon deposition rates by bottom sediments of small lakes in the south of Western Siberia

Georgii I. Malov, Vera D. Strakhovenko, Ekaterina A. Ovdina, Viktor I. Malov✉

V.S.Sobolev Institute of Geology and Mineralogy SB RAS, Novosibirsk, Russia

***How to cite this article*:** Malov G.I., Strakhovenko V.D., Ovdina E.A., Malov V.I. Assessment of carbon deposition rates by bottom sediments of small lakes in the south of Western Siberia. Journal of Mining Institute. 2026. Vol. 280, p. 3-15.

Abstract

The study is devoted to the quantitative assessment of organic carbon (C_{org}) deposition rates in the bottom sediments of small lakes located in the south of Western Siberia. The studied water bodies cover a wide range of landscape-climatic conditions and types of sedimentation environments. Despite their local dimensions, the small lakes of the region demonstrate exceptionally high efficiency of long-term carbon burial. It is shown that their capacity to accumulate C_{org} is comparable to or even exceeds that of such recognized carbon depots as bogs and marine shelves. The work is based on a comprehensive analysis of bottom sediments, including radiometric dating (Pb-210, Cs-137) to determine sedimentation rates and layer ages, as well as morphological, elemental (CHNS analysis), and X-ray diffraction analyses. According to the obtained data, the average C_{org} deposition rate in the studied lakes reaches 462±29 g/m^2 per year. It has been established that the majority of carbon (> 50 % in most cases) accumulates specifically in the form of organic matter, even in lakes with intensive intra-basin (authigenic) carbonate formation. The study revealed the main factors controlling carbon accumulation: productivity of aquatic communities (phytoplankton, zooplankton, macrophytes), total sedimentation rate, sediment ash content (mineral fraction proportion), and local morphometric features of the lakes (depth, basin shape). The absence of a clear dependence of carbon deposition rates on landscape zonality underscores the critical importance of considering local conditions when modeling the contribution of small lakes to the global carbon cycle. The obtained results substantially fill gaps in regional carbon assessment and prove the significance of small lakes in the south of Western Siberia as highly efficient and stable natural depots of organic carbon under conditions of continental sedimentation.

Keywords

sapropel; bottom sediments; small lakes; carbon deposition; carbonate carbon; carbonates

Funding

Work was carried out under the State assignment of IGM SB RAS FWZN-2026-0008.

Received: 16.06.2025 ***Accepted: 04.03.2026*** ***Online: 11.06.2026*** ***Published: 10.09.2026***

Introduction

Changes in the global carbon cycle are a fundamental factor of contemporary climate shifts, which necessitates a reassessment of the contribution of various natural systems to carbon sequestration [1, 2].

Continental water bodies are characterized by intensive carbon exchange with the atmosphere and significant deposition of organic matter into bottom sediments (BS), which makes them important components of the terrestrial carbon reservoir. Continental water bodies, especially small lakes and ponds, demonstrate high efficiency of organic carbon accumulation per unit area compared to large lakes and marine areas [3, 4]. Small artificial and restored ponds have particularly high carbon accumulation rates, reaching 152 g/m^{-2} per year^{-1} [5]. Larger water bodies are characterized by lower accumulation rates due to morphometric features [6]. Inland waters overall exceed oceans in terms of organic carbon burial efficiency per unit area [3]. Despite this, their contribution to global estimates

This is an open access article under the CC BY 4.0 license

of carbon burial remains insufficiently studied and, consequently, is poorly represented in climate models and scenarios of future changes.

In the global carbon balance, it is customary to speak of "land-absorbed carbon" (SLAND) – the volume of CO_2 that terrestrial ecosystems retain in response to rising CO_2 concentrations and climate change. Dynamic Global Vegetation Models (DGVM) are used to assess this absorption. Formally, the concept of SLAND includes not only forests and soils but also all continental water bodies – rivers, lakes, reservoirs, and estuaries [1]. In practice, however, models describe terrestrial processes in much greater detail than aquatic ones. Existing models hardly account for how much carbon is washed from land into rivers and lakes and how this flux has changed over time. As a result, the role of lakes and other inland waters in the global carbon cycle, although recognized as important, remains quantitatively underestimated. Models record terrestrial CO_2 absorption without tracking the subsequent pathway of carbon that is exported from terrestrial ecosystems to aquatic systems [1].

Existing studies confirm that continental water bodies can act as both sources and sinks of carbon, but estimates vary widely, especially for lakes of small dimensions. According to H.E.Chmiel [7], the increased sensitivity of small lakes to changes in temperature, hydrological regime, and input of terrigenous organic matter results in high variability of their carbon balance, which further complicates assessment and yields a spectrum of uncertainty in global carbon balance calculations.

The south of Western Siberia is a unique natural polygon that includes the boundary between forest and steppe zones, thereby providing a wide spectrum of hydrological and sedimentation conditions. Within the region, humid, arid, and nival types of sedimentogenesis are combined, while the lakes themselves vary in morphometry, degree of anthropogenic load, and sources of organic matter. However, quantitative estimates of carbon deposition rates in the lake sediments of this territory are practically absent in the scientific literature.

Despite the high forest cover, bog coverage, and lake density, Western Siberia remains a "blank spot" in global carbon assessments. Peatlands here occupy ≈ 22 % of the lowland area and accumulate ~$7 \cdot 10^{13}$ kg of carbon [8]. In the work of E.A.Golovatskaya [9] an analysis of the carbon balance in the bogs of the region confirms the enormous stocks and potential role of these ecosystems as stable carbon depots. Landsat-8 satellite data reveal > 720,000 lakes with an area > 0.5 ha (about 6 % of the territory); however, for most small water bodies, direct measurements of gas exchange and carbon stocks are lacking [10]; the global BAWLD database notes a critical deficit of CH_4 measurements for the Ob-Irtysh floodplain and lakes of the region [11].

The aim of the work is to assess the rates and spatial variability of organic carbon deposition in the bottom sediments of small lakes in the south of Western Siberia under different landscape zones.

The results will allow refining the assessment of the role of inland water bodies in the regional and global carbon balance, and can also be used to improve the parameterization of lake systems in climate models [12] and in the development of strategies for adaptation to climate change in high-latitude regions. Moreover, accounting for the specifics of carbon accumulation in Siberian lakes is critically important for improving the accuracy of carbon balance predictions in the Northern Hemisphere.

Objects and methods of research

The objects of the study are the BS of small lakes in the south of Western Siberia, which in the studied water bodies are represented by sapropels – organomineral bottom sediments of water bodies that form as a result of biochemical, microbiological, and mechanical processes from the remains of dying plant and animal organisms, authigenic minerals, and organic and mineral particles introduced into the water bodies.

The studied lakes are localized in the south of Western Siberia (Fig.1), mainly in the southeastern part of the West Siberian Platform bordering the Altai-Sayan fold region, within the Ob-Irtysh interfluve and on the territory of Gorny Altai (Ukok Plateau, Ulagan Valley).

This is an open access article under the CC BY 4.0 license

© Georgii I. Malov, Vera D. Strakhovenko, Ekaterina A. Ovdina, Viktor I. Malov, 2026

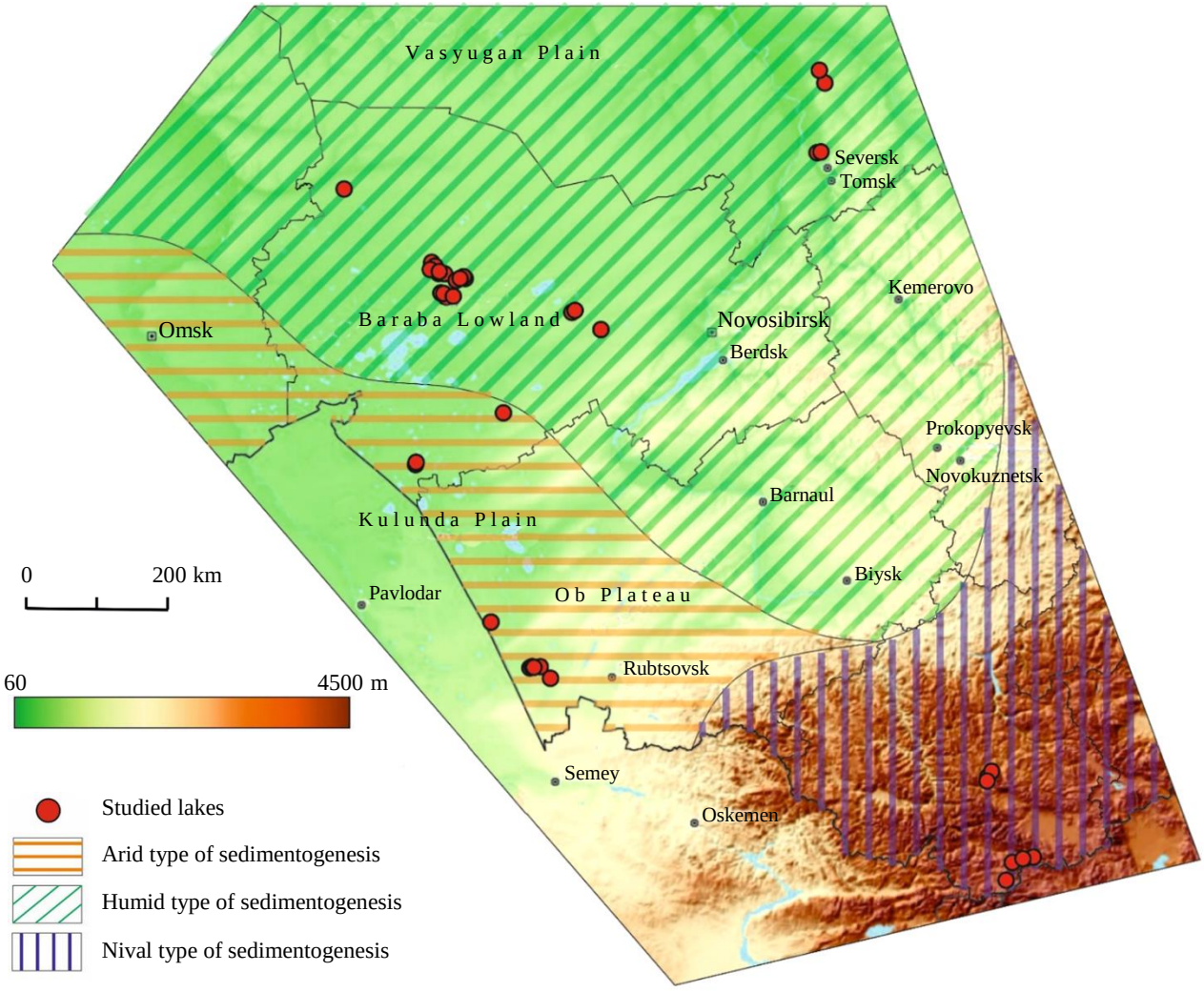


Fig.1. Location map of the studied lakes

In the plain part of the studied territory, natural-climatic zonality is manifested. From north to south, the boreal Vasyugan taiga-bog flat plain is represented, followed by the subboreal Baraba lowland forest-steppe, which transitions into the Kulunda steppe plain. In the extreme southwest of the Kulunda Steppe, the dry-steppe zone is distinguished [13]. To the southeast, with increasing elevation in the territory of Gorny Altai, latitudinal zonality is replaced by altitudinal zonality.

In parallel with the change in landscape-climatic zones, a change in sedimentation types occurs in the studied lakes (according to N.M.Strakhov [14]):

• Vasyugan Plain – humid type of sedimentogenesis;

• Barabinsk Plain and Kulunda Steppe – gradual transition from humid to arid type;

• Ulagan Valley and Ukok Plateau (Russian Altai) – nival type of sedimentogenesis in a mountain landscape.

Since the work aims at a regional assessment, the selection of study objects was carried out according to general morphometric, hydrological, hydrochemical, trophic, and other parameters corresponding to the average characteristics of the predominant lakes for the studied territories. In total, 41 lakes were studied: 10 located under arid type of sedimentogenesis, 7 under nival type, and 24 under humid type of sedimentogenesis. All studied lakes are small ($0.1 < S < 10$ km^2) with a depth of up to 10 m (average depth 3 m), permanent, closed basins (in steppe regions with arid climate, some of the studied lakes lose a significant portion of water during the low-water period). According to the degree of eutrophication, the studied lakes range from mesotrophic to eutrophic under humid type of

This is an open access article under the CC BY 4.0 license

sedimentogenesis to oligotrophic under nival type. Among the studied lakes, suffosion-subsidence basins predominate in the plain parts of the study areas (steppe, forest-steppe, and taiga landscapes), which are often inheritors of the ridge-and-hollow relief in the Baraba Lowland and Kulunda Plain. In the mountain landscape, lake basins of thermokarst and moraine-dammed types with superimposed neotectonic processes predominate.

The collected factual material is the result of comprehensive long-term studies [15-17]. Fieldwork was conducted during the summer period, after snowmelt, during the low-water stage. At the study sites, an integrated approach was used: each lake was considered as a separate lake system, with sampling of bottom sediments, water, soil, bedrock (where present), dominant vegetation, and sands from the wave-break zone of the lake. The bottom topography of the lake basin and the structure of the lake bottom sediments were surveyed using an ECHOMAP Plus 62cv echo sounder, followed by sampling at the most representative locations (maximum bottom sediment section, distance from anthropogenic objects). Bottom sediment sampling was performed using a cylindrical corer with a vacuum seal designed by Taifun Research and Production Association (diameter d = 82 mm, length L = 120 cm). Core sampling was conducted on site at 3-5 cm intervals.

Analytical studies were conducted at the Analytical Center for multi-elemental and isotope research SB RAS, Novosibirsk. The main characteristics of bottom sediments (moisture content, ash content, and pH) were determined according to State standards: GOST 26713, GOST 27980, and GOST 27979. The major- and trace element composition of the samples was determined by atomic absorption spectrometry using a Solaar M6 spectrometer (Thermo Electron, USA) and by inductively coupled plasma mass spectrometry using an ELEMENT high-resolution mass spectrometer (Finnigan MAT). The study of the morphology, mineral, phase, and chemical compositions of bottom sediments was carried out using a MIRA 3 Tescan scanning electron microscope (SEM) and by X-ray diffractometry using an ARL X'TRA diffractometer. Sedimentation rates were estimated by radiometric dating using excess atmospheric Pb-210 according to the Constant Rate of Supply (CRS) model, under the assumptions that the atmospheric input of Pb-210 into bottom sediments is constant; the sedimentation rate within the considered time interval (of a single sample) does not change, and that there is no post-depositional migration of radioactive elements [17, 18]. Verification of the dating estimates was performed using Cs-137 activities based on marker horizons. The use of the CRS model is due to the fact that small lakes are almost completely free from mixing of the upper layers of bottom sediments and, consequently, from redistribution of material, which provided the necessary assumptions and the required accuracy for the CRS model. Measurements were carried out using a well-type gamma spectrometer on a coaxial high-purity germanium (HPG) detector with a preamplifier and a low-background cryostat EGPC 192-P21/SHF 00-30A-CLF-FA (Eurisys Mesures, France). The elemental composition of the organic fraction of bottom sediments was studied by Pregl – Dumas organic elemental analysis [19, 20] using a CHNS/O PE 2400 Series II analyzer (Perkin Elmer) at the Analytical Center of the Institute of Soil Science and Agrochemistry SB RAS (Novosibirsk).

Since direct measurements of carbon deposition over large territories and within complex biocenoses are impossible in most cases (the difference between the net primary productivity of aquatic organisms and heterotrophic respiration – CO_2 emission into the atmosphere resulting from organic matter mineralization), the authors applied a method for calculating the carbon deposition rate through sediment accumulation rates. For this purpose, a stratigraphically undisturbed stratified section of bottom sediments was used: it was dated using a set of geochronological methods; the sedimentation rate was determined and multiplied by the carbon content in the sediment sample accumulated over the dated period. For deposition calculations, the average sedimentation rate over the entire interval of possible measurements (100-120 years) was taken. For 16 lakes, carbon determination was performed on stratified horizons at 3-5 cm intervals using the Pregl – Dumas CHNS analysis method. The analysis showed that the amount of organic carbon in the bottom sediments

This is an open access article under the CC BY 4.0 license

exhibits low variability and has a significant positive correlation with the amount of organic matter relative to the total sediment mass. For the remaining lakes, carbon determination was carried out on an average sample using the Pregl – Dumas CHNS analysis method and verified by the loss-on-ignition (LOI) method on stratified horizons at 3-5 cm intervals. Data on carbon content in the article are presented as mean values for the entire core. Data on deposition rates are presented for the upper parts of the core down to the dating depth (on average, up to 60 cm). Total carbon stocks were determined taking into account sediment moisture content and density using geological exploration methods, as the mean carbon content multiplied by sapropel reserves per area of 1 ha.

Sapropel reserves were determined as the product of volume and sapropel yield at 60 % moisture, followed by recalculation to dry weight. Sapropel yield was determined according to the formula:

$$P_{60\,\%} = V\,(100 - W_{nat})/(100 - W_{cond}),$$

where V is the volume of sapropel, thousand m^3; W_{nat}, W_{cond} are natural and conditional humidity of sapropel, equal to 60 %.

The calculation of buried organic carbon was performed under the assumption that the species composition of biota and/or the C/H/N ratio of the organic fraction does not change or changes only insignificantly over time, and was carried out according to the formula:

$$C_{org} = P_{dry}N/100 \cdot L/100,$$

where P_{dry} is dry sapropel reserves; N is the percentage of organic matter; L is the percentage of carbon in the organic fraction.

The calculation of carbon buried in carbonates was performed for calcite and for dolomite according to the formulas:

$$C_{min} = P_{dry}Z/100 \cdot 0.3K_{Ca}/100;$$

$$C_{min} = P_{dry}Z/100 \cdot 0.375K_{Ca,Mg}/100,$$

where P_{dry} is dry sapropel reserves; Z is ash content; K_{Ca} is the content of Ca in the dry sample in carbonates; $K_{Ca,Mg}$ is the content of Ca and Mg in the dry sample in carbonates.

Carbon deposition rates into bottom sediments were calculated as the mass of carbon buried in bottom sediments per year. The mass of sapropel accumulating per year was calculated per area of 1 ha according to the formula:

$$V = vS,$$

where v is the sedimentation rate; S = 1 ha (10,000 m^2).

Materials and discussion of results

Currently, there is no unified classification of bottom sediments in Russia or worldwide. The diversity of classifications and typological characteristics of BS is due to different goals and objectives in the research of specialists from various scientific fields: geology, geography, chemistry, biology, ecology, etc. For the classification of BS in our studies, the classification of N.V.Korde [21] with modifications by V.D.Strakhovenko [15] was used. In this classification, sapropel types are distinguished by ash content (ratio of organic and mineral parts): “Organic sapropel with ash content up to 30 %; organic-mineral sapropel with ash content 30-50 %; mineral-organic sapropel with ash content 50-70 %; mineralized sapropel with ash content 70-85 %; mineral silts with ash content above 85 %” [15]. The division of sapropel classes within each type is based on chemical composition according to the ratio of main major elements (Si, Ca, mixed), and the division into species is based on the species composition of the predominant organic part in each individual sapropel class. The BS of the studied lakes are in the predominant cases represented by sapropels of different types and classes (Fig.2). The mean ash content is 65.3 %, standard deviation 19.2 %, minimum value 15.5 %, median 66.6 %, maximum value 95 %. Figure 2 presents a diagram showing the distribution of BS of the studied lakes by classes and types.

This is an open access article under the CC BY 4.0 license

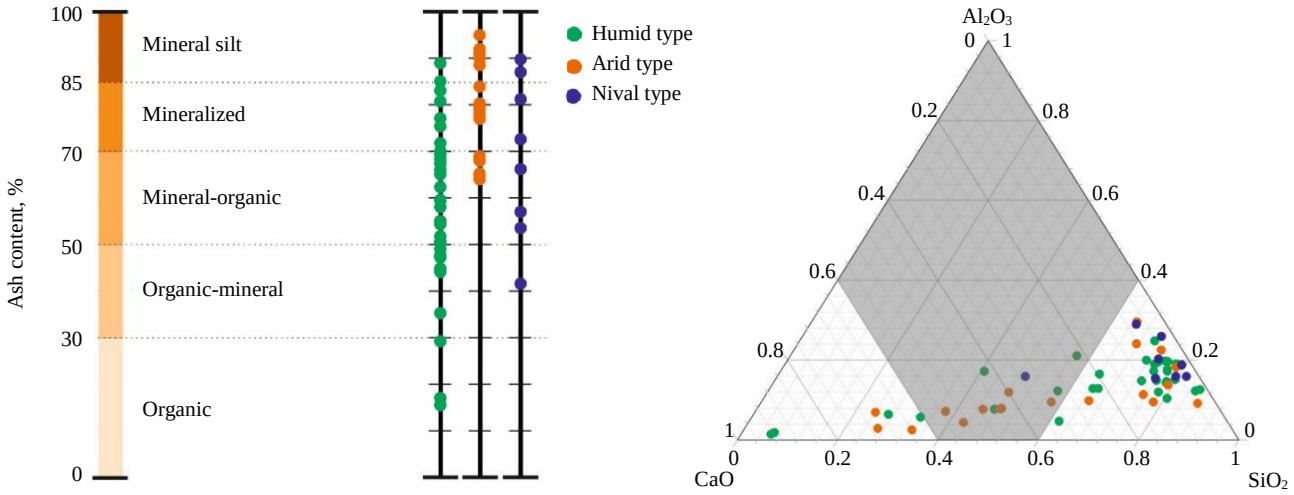


Fig.2. Diagrams of the prevalence of sapropel types and classes in lakes located under arid, nival, and humid types of sedimentogenesis

As shown by previous studies [15-17], the mineral composition of the studied lakes is represented by terrigenous, biogenic, chemogenic, and biochemogenic components. In the terrigenous fraction, quartz and feldspars predominate – albite, oligoclase, potassium feldspar, micas (muscovite), chlorites (Fe~Mg), illites (Fe~Mg). Hornblende, actinolite, epidote, and accessory minerals may be present as admixtures. The grains are well sorted, unrounded or poorly rounded, of pelitic, aleuropelitic, and more rarely psammitic (for mountainous regions) size. The biogenic fraction is represented by diatom frustules – SiO_2 (amorphous) (Fig.3), fragments of calcite and aragonite shells, and mineralized remains of macrophytes of both siliceous and carbonate compositions. Pyrite is unevenly distributed throughout the core, occasionally forming thin laminae, nest-like segregations, and in places produces an uneven dissemination among other minerals of the clastic fraction of the bottom sediment (Fig.3). Pyrite framboids are spherical aggregates of densely packed, rounded microcrystals. Carbonate formations (calcite-dolomite series, aragonite, rarely siderite, rhodochrosite, and magnesite) are also widespread, ranging from micron-sized "curdy" segregations (Fig.3) to large stromatolitic formations tens of centimeters in size (Fig.4). The genesis of carbonates is polygenetic (authigenic) – biogenic, biochemogenic, chemogenic. Determining the genesis of carbonates in each specific case is a complex, multifaceted task.

According to data obtained from hydrobiologists (IWEP SB RAS) working in the joint expedition for sample collection, the main sources of organic matter in bottom sediments are bacteria, phytoplankton, zooplankton, as well as higher plants, both aquatic and coastal [22, 23]. Biological diversity and the structure of aquatic communities vary significantly from one lake to another, which leads to considerable differences in the contribution of various organism groups to the accumulation of organic matter and, accordingly, affects the chemical composition of the bottom sediments. The highest production of organic matter is observed in lakes located under humid type of sedimentogenesis. Nevertheless, in all studied water bodies, including high-mountain oligotrophic lakes, the processes of productive accumulation of organic matter exceed the processes of its destruction [22, 23].

To assess the ratio of autochthonous to allochthonous organic matter input, the C/N ratio is used. For higher terrestrial vegetation (allochthonous organic matter), $C/N > 30$; for aquatic flowering plants and benthic algae, $C/N \approx 20$; for plankton, zoobenthos, and fish, $C/N < 10$. Thus, the C/N ratio in bottom sediments allows qualitative determination of the source of organic matter input. For the studied lakes, the average C/N ratio is 13±3, which indicates a mixed autochthonous component. For 16 lakes, not only the elemental composition but also the group composition of organic matter in the bottom sediments was investigated by sequential extraction [15]. Colleagues from the Institute

This is an open access article under the CC BY 4.0 license

© Georgii I. Malov, Vera D. Strakhovenko, Ekaterina A. Ovdina, Viktor I. Malov, 2026

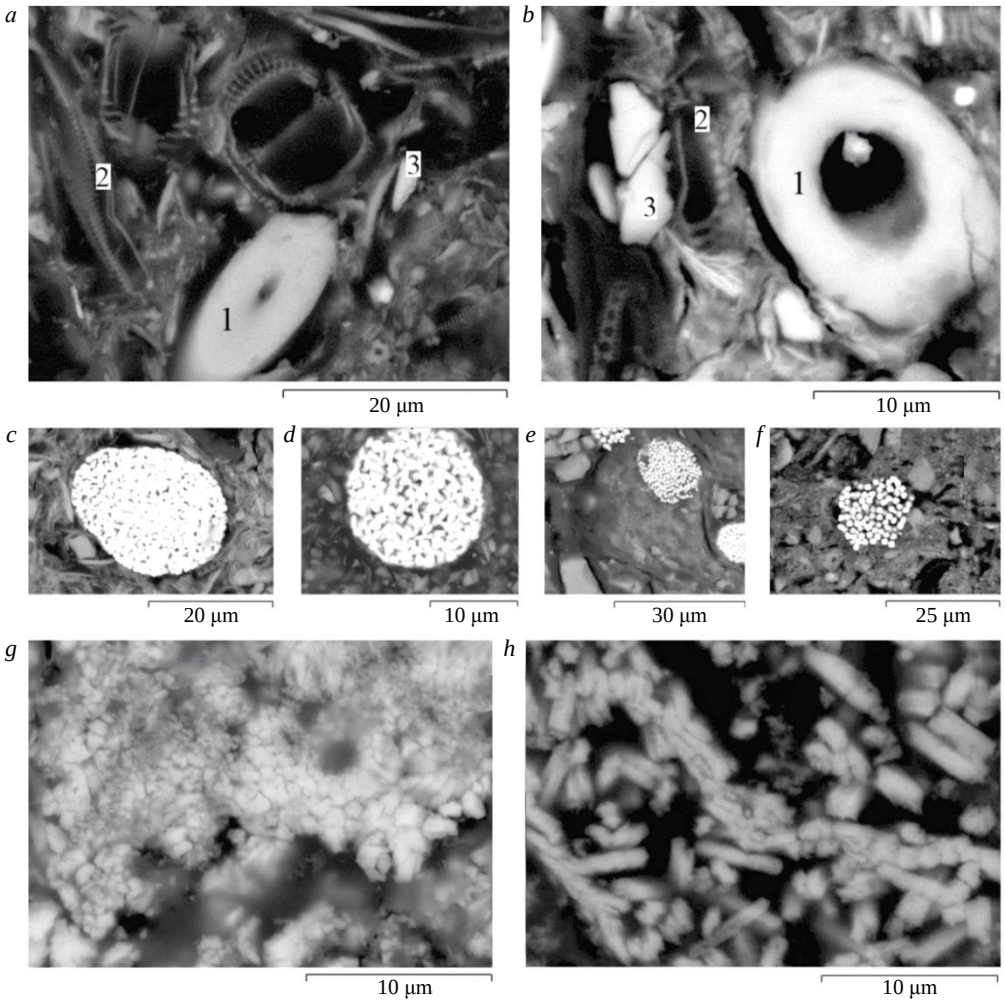


Fig.3. Mineral composition of bottom sediments: *a* – BS of Bazovoe Shchuchye Lake (humid type of sedimentogenesis); *b* – BS of Podkova Lake (nival type); *c* – pyrite framboid at the initial stage of formation in the BS of Teply Klyuch Lake under nival sedimentogenesis; *d* – pyrite framboid in Maloe Tarkhatinskoe Lake under nival sedimentogenesis; *e* – pyrite framboids in the BS of Bazovoe Shchuchye Lake under humid sedimentogenesis; *f* – pyrite framboid in the BS of Tanatar-6 Lake under arid sedimentogenesis; *g* – "curdy" aggregates of low-Mg calcite (Biryuzovoe Lake); *h* – prismatic aggregates of low-Mg calcite (Tanatar-4 Lake). Photo taken via a MIRA 3 Tescan SEM, BSE

1 – remains of macrophytes ($m SiO_2 \cdot n H_2O$); 2 – diatom frustules ($m SiO_2 \cdot n H_2O$); 3 – in association with aggregates of minerals of the terrigenous fraction

of Water and Environmental Problems SB RAS determined the biological composition of the sapropel [21, 23] using experiments with sediment traps to determine the qualitative composition of settling lake suspended matter and quantitative parameters (fluxes of material per unit area of the bottom). All studies showed that the allochthonous component makes a small contribution to the carbon budget, and the main source of organic carbon is autochthonous material.

Table 1 presents the initial data necessary for calculating carbon deposition rates in the studied lakes. In the sample of studied lakes, the ash content of bottom sediments ranges from 15.5 to 92 %, with a mean value of 61.5±18.3 %, a median of 64.9 %. The organic carbon content varies from 1.1 to 45.4 %, with a mean of 21.0±11.3 %, a median of 20.0 %. The moisture content of bottom sediments ranges from 20 to 89 % with a mean of 71.2±11.6 % and a median of 71 %.



Fig.4. Stromatolitic formations (calcite), Petukhovo Lake

This is an open access article under the CC BY 4.0 license

© Georgii I. Malov, Vera D. Strakhovenko, Ekaterina A. Ovdina, Viktor I. Malov, 2026

Table 1

Initial data for calculating carbon deposition rates

Lake	Ash content, %	C, %	Sedimentation rate, cm/year	*W*, %
Bazovoe Shchuchye	15.50	27.00	0.21	83
Layskoe-1	40.00	30.00	0.64	83
Yakovo	50.60	45.00	0.42	79
Kachkulnya	17.00	43.30	0.31	71
Nizhnee	39.53	33.40	0.30	70
Bilgen	71.70	33.98	0.30	69
Sarbalyk	47.61	30.60	0.30	76
Podkova	41.57	27.50	0.30	81
Bugristoe	49.00	26.53	0.30	76
Kukley	64.00	28.10	0.30	71
Suetok	59.55	18.89	0.40	73
Krugloe	59.50	20.25	0.41	70
Argamdzhi	53.50	24.61	0.40	70
Yargol	35.25	35.00	0.35	71
Maloe Tarkhatinskoe	57.00	21.50	0.27	74
Bolshoy Kurgan	44.09	15.97	0.30	80
Kambala	58.00	26.70	0.16	74
Kazatovo	70.00	26.64	0.30	62
Zerlyukol-Nur	72.56	9.20	0.30	81
Bolshie Kayly	67.40	20.00	0.30	63
Krasnoe	83.25	6.10	0.30	67
Maloe Minzelinskoe	44.85	45.44	0.30	89
Kayly	55.00	32.65	0.30	79
Peschanoe	50.37	19.00	0.18	79
Igistu-Kol	87.00	6.50	0.22	71
Bergul	65.00	18.00	0.23	71
Barchin	51.71	22.80	0.30	71
Kusgan	91.00	4.70	0.30	71
Petukhovo (near the vil. Severka)	79.44	15.31	0.30	59
Tanatar-6	80.30	9.85	0.34	43
Krotova Lyaga	92.00	2.30	0.30	71
Biryuzovoe	81.18	15.90	0.26	77
Tanatar-4	65.26	12.10	0.21	55
Zolotoe	69.00	15.50	0.28	73
Demkino	64.86	15.30	0.20	73
Rublevo	68.38	15.31	0.16	69
Shchuchye-L	66.63	22.50	0.30	84
Kankul	85.00	7.30	0.30	71
Itkul	83.00	7.30	0.30	71

Sedimentation rates in the lakes range from 2.1 to 4 mm/year for lakes under nival type of sedimentogenesis; from 1 to 6.4 mm/year for lakes under humid type; from 1.7 to 3.4 mm/year for lakes under arid type (Fig.5). Since the study territory was subjected to radioactive fallout from nuclear weapons tests at the Semipalatinsk test site, additional assessment of sedimentation rates was performed using Cs-137 marker horizons (Fig.6).

The study of the material composition of bottom sediments made it possible to establish that the input and burial of carbon in lakes is mainly determined by two processes – the deposition of autochthonous and allochthonous organic matter (C_{org}) and the formation of authigenic carbonates (C_{carb}) [15, 17, 21, 22].

This is an open access article under the CC BY 4.0 license

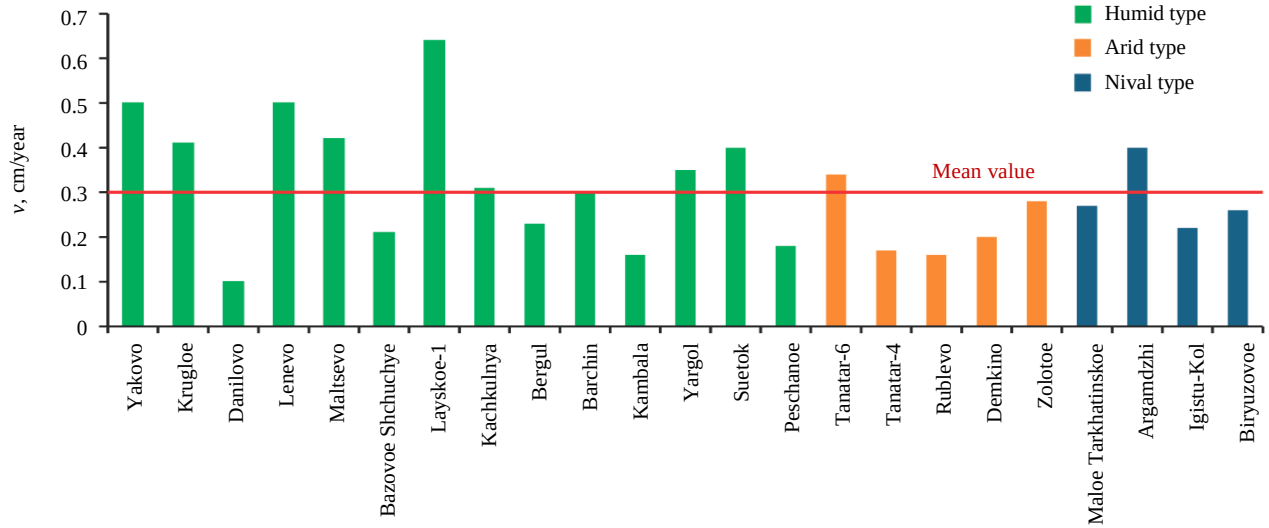


Fig.5. Diagram of sedimentation rates for the studied lakes located under nival, humid, and arid sedimentogenesis

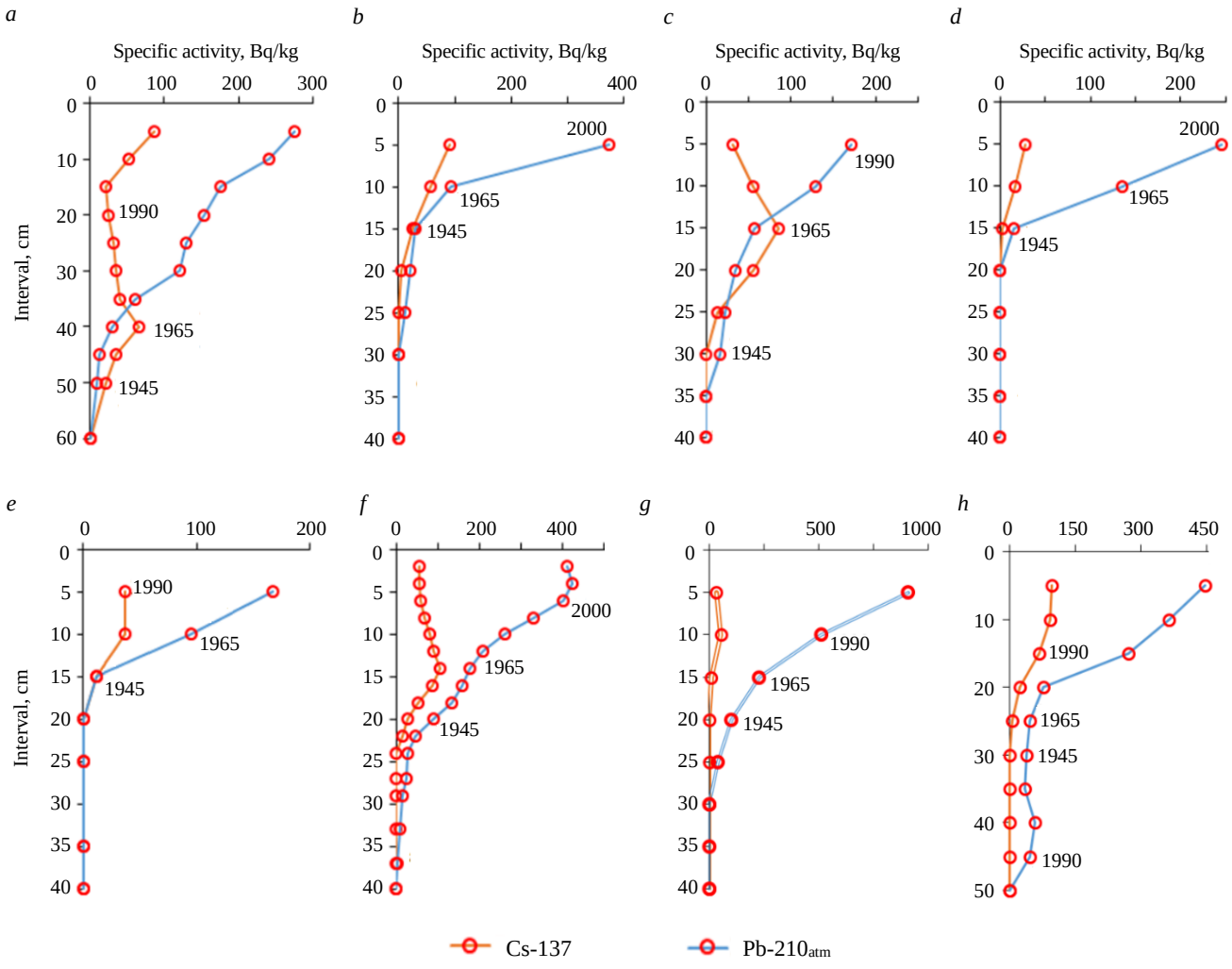


Fig.6. Graphs of Pb-210 and Cs-137 distribution for the studied lakes in different landscapes under different types of sedimentogenesis: *a* – Layskoe Lake – 5.4 mm/year, humid type, taiga; *b* – Danilovo Lake – 1.9 mm/year, humid type, taiga; *c* – Barchin Lake – 3.2 mm/year, humid type, forest-steppe; *d* – Kambala Lake – 1.6 mm/year, humid type, forest-steppe; *e* – Tanatar Lake – 1.7 mm/year, arid type, steppe; *f* – Zolotoe Lake – 2.9 mm/year, arid type, ribbon forest; *g* – Biryuzovoe Lake – 2.6 mm/year, nival type, mid-mountain area; *h* – Argamdzhi Lake – 4 mm/year, nival type, high-mountain area

This is an open access article under the CC BY 4.0 license

© Georgii I. Malov, Vera D. Strakhovenko, Ekaterina A. Ovdina, Viktor I. Malov, 2026

In all landscape zones, among the bottom sediments of small lakes, sapropels have been identified in which carbonates constitute a significant part of the bottom sediment and are capable of efficiently burying carbon. For a comparative analysis of the ratios of organic and mineral (carbonate) carbon, an assessment was carried out on 15 lakes (Table 2). As can be seen from Table 2, even for high-ash sapropels, the carbonate carbon content does not exceed 22 % of the total carbon pool in the bottom sediments. The highest values are characteristic of lakes with mineralized calcium and mixed sapropels (Rublevo, Demkino, Shchuchye-L, Kankul). No spatial landscape patterns were found; in each landscape zone under different types of sedimentogenesis, high-ash carbonate sapropels are formed, but the largest carbon pool resides in the organic fraction of the BS.

Table 2

Organic and carbonate carbon content in the BS of small lakes

Lake	Ash content, %	C_{org}, %	C_{carb}, %
Humid type of sedimentogenesis			
Kachkulnya	17	99.8	0.2
Yargol	35	99.1	0.9
Maloe Minzelinskoe	45	97.6	2.4
Peschanoe	50	92.3	7.7
Barchin	52	92.3	7.7
Kayly	55	97.4	2.6
Bergul	65	92.7	7.3
Shchuchye-L	67	82.6	17.4
Kankul	85	77.6	22.4
Arid type of sedimentogenesis			
Demkino	65	83.8	16.2
Tanatar-4	65	84.8	15.2
Rublevo	68	82.9	17.1
Zolotoe	69	84.4	15.6
Petukhovo (near the vil. Severka)	79	91.2	8.8
Nival type of sedimentogenesis			
Biryuzovoe	81	85.2	14.8
Podkova	41	99.29	0.71

The data on carbon deposition rates correlate well with the data of N.I.Yermolaeva, E.Yu.Zarubina, and G.V.Fetter on the productivity of aquatic organisms in the studied lakes [22, 23]. In terms of primary production, the highest values are characteristic of lakes located in territories with the humid type of sedimentogenesis (taiga zone, forest-steppe), while the lowest values are typical of low-productivity steppe and mid- to high-mountain lakes of the nival type of sedimentogenesis. The average carbon deposition rates for bottom sediments are 560 g/m^2 per year for lakes localized under the humid type, and 300 and 340 g/m^2 per year for lakes localized under the arid and nival types of sedimentogenesis, respectively. The average carbon deposition rates in small lakes of the south of Western Siberia are 462±29 g/m^2 per year; the minimum values refer to Krotova Lyaga Lake (steppe, arid type of sedimentogenesis) – 50 g/m^2 per year, and the maximum values correspond to Yakovo Lake (taiga zone, humid type of sedimentogenesis) – 1110 g/m^2 per year.

At the same time, in each landscape zone, lakes located under a specific type of sedimentogenesis include both lakes with quite high and quite low carbon deposition rates. Based on this, it can be stated that, in addition to regional factors, local conditions are limiting factors affecting carbon deposition rates. Examples include lakes localized in territories with the humid type of sedimentogenesis (Peschanoe, Kankul, Shchuchye-L), where either active authigenic mineral formation leads to the formation of high-ash sapropels with low organic carbon content, or low carbon deposition rates result

This is an open access article under the CC BY 4.0 license

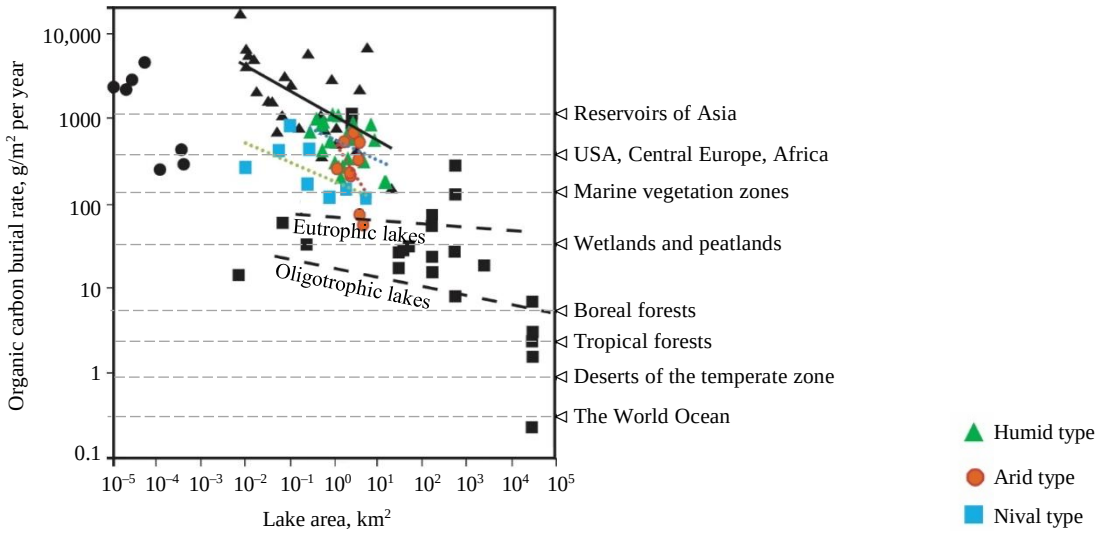


Fig.7. Graph comparing the organic carbon burial rate in sediments of lakes located under different types of sedimentogenesis (authors' data are shown as colored shapes on the graph [24]).
Arrows on the right indicate average carbon uptake levels in different ecosystem types [3, 25, 26]

in the accumulation of small amounts of organic carbon. In the sapropel deposit of Itkul Lake, despite the high biological productivity of the lake (1.1 g/m^2 per day), diatoms make a significant contribution, whose frustules consist of amorphous silica (SiO_{2bio}), resulting in the formation of high-ash sapropels (85 %), which dilutes the amount of organic matter in a given volume and, consequently, negatively affects carbon deposition rates. Under the nival and arid types of sedimentogenesis, there are lakes with quite high organic matter contents in the BS (Argamdzhi Lake – 47 % and Kukley Lake – 36 %). This is due to the exceptionally high productivity of the lakes [24], which also determines high carbon deposition rates.

A graph comparing the organic carbon burial rate in the sediments of the studied lakes with data from other researchers and with average carbon uptake levels in various ecosystem types is presented in Fig.7.

The obtained estimates for lakes in the south of Western Siberia correspond to data from other inland water bodies worldwide [27-31] and exceed the average carbon deposition rates on shelves and in bogs. The observed decrease in deposition rate with increasing water body area is consistent with known morphometric dependencies, but local conditions (bioproductivity, ash content, intensity of carbonate formation) play a decisive role. No effect of lake depth on carbon deposition was identified, because at the shallow depths of the studied lakes, nearly the entire flux of material formed during the day in the upper layers of the lake manages to reach the bottom, undergoing almost no mineralization in the water column. Further transformation of biological material occurs at the bottom as a result of the activity of bacteria and benthic organisms [32].

Since there are no data on carbon deposition rates in lakes for the territory of Western Siberia, it was decided to additionally compare the obtained values with carbon deposition rates in peats. In scientific articles by E.A.Golovatskaya and co-authors, estimates of carbon burial in bogs of the southern taiga subzone of Western Siberia are provided – the carbon deposition rate averages 0.19 t/ha per year and ranges from 0.11 to 0.26 t/ha per year [9]. According to other researchers, carbon burial rates for peats are 0.24-0.56 t/ha per year [33], and for bogs in the territory of the former USSR – 0.12-0.8 t/ha per year [34]. All these estimates are significantly lower (by a factor of 10-20) than the obtained data on carbon burial in lake bottom sediments, but are fully consistent with data from researchers in other regions of the world (Fig.7) [3, 25, 26].

This is an open access article under the CC BY 4.0 license

This can be explained by the similar amount of carbon in the organic fraction of peat and sapropel deposits – peat formation occurs at significantly lower rates. Among oligotrophic phytocenoses, the ridge-hollow complex (0.77 mm/year) and low ryam (0.63 mm/year) are characterized by the highest peat accumulation rates, while the lowest rate is found in high ryam (0.25 mm/year) [32], which is significantly lower than the sedimentation rates in lakes calculated in this study.

Conclusion

The study has shown that small lakes in the south of Western Siberia are efficient carbon accumulators, with average deposition rates of 462±29 g/m^2 per year, which is comparable to global values in other regions of the world and exceeds the analogous indicators of peatlands in the territory of Western Siberia. The total volume of carbon sequestration in the bottom sediments of small lakes in the south of Western Siberia varies both at regional and local spatial scales, does not depend on the type of sedimentogenesis, and ranges from 0.6 to 11.2 t/ha per year.

The majority of carbon is fixed in the form of organic matter, despite the widespread occurrence of carbonate minerals. No spatial landscape patterns of carbonate carbon burial were found; in each landscape zone under different types of sedimentogenesis, high-ash carbonate sapropels are formed, but the largest carbon pool resides in the organic fraction of the bottom sediments.

The main factors determining the volume of carbon sequestration are the sedimentation rate, the balance between production and destruction of organic matter, and authigenic mineral formation processes.

The obtained data highlight the necessity of including small lakes in global carbon cycle models.

REFERENCES

1. Friedlingstein P., O'Sullivan M., Jones M.W. et al. Global Carbon Budget 2024. *Earth System Science Data*. 2025. Vol. 17. Iss. 3, p. 965-1039. DOI: 10.5194/essd-17-965-2025

2. Weifeng Xu, Yaofei Cheng, Mengyuan Luo et al. Progress and Limitations in Forest Carbon Stock Estimation Using Remote Sensing Technologies: A Comprehensive Review. *Forests*. 2025. Vol. 16. Iss. 3. N 449. DOI: 10.3390/f16030449

3. Mendonça R., Müller R.A., Clow D. et al. Organic carbon burial in global lakes and reservoirs. *Nature Communications*. 2017. Vol. 8. N 1694. DOI: 10.1038/s41467-017-01789-6

4. Casas-Ruiz J.P., Bodmer P., Bona K.A. et al. Integrating terrestrial and aquatic ecosystems to constrain estimates of land-atmosphere carbon exchange. *Nature Communications*. 2023. Vol. 14. N 1571. DOI: 10.1038/s41467-023-37232-2

5. Ljung K., Lin S. Organic Carbon Burial in Constructed Ponds in Southern Sweden. *Earth Science, Systems and Society*. 2023. Vol. 3. Iss. 1. N 10061. DOI: 10.3389/esss.2023.10061

6. Cael B.B., Seekell D.A. Simple model of morphometric constraint on carbon burial in boreal lakes. *Frontiers in Environmental Science*. 2023. Vol. 11. N 1101332. DOI: 10.3389/fenvs.2023.1101332

7. Chmiel H.E., Kokic J., Denfeld B.A. et al. The role of sediments in the carbon budget of a small boreal lake. *Limnology and Oceanography*. 2016. Vol. 61. Iss. 5, p. 1814-1825. DOI: 10.1002/lno.10336

8. Beilman D.W., MacDonald G.M., Smith L.C., Reimer P.J. Carbon accumulation in peatlands of West Siberia over the last 2000 years. *Global Biogeochemical Cycles*. 2009. Vol. 23. Iss. 1. N GB1012. DOI: 10.1029/2007GB003112

9. Golovatskaya E.A., Dyukarev E.A., Veretennikova E.E. et al. Evaluation of the dynamics of the carbon balance for peatlands of the southern-taiga subzone of West Siberia (Tomsk region). *The Journal of Soils and Environment.* 2022. Vol. 5. N 4. N e194 (in Russian). DOI: 10.31251/pos.v5i4.194

10. Polishchuk Y.M., Bogdanov A.N., Polishchuk V.Y. et al. Size Distribution, Surface Coverage, Water, Carbon, and Metal Storage of Thermokarst Lakes in the Permafrost Zone of the Western Siberia Lowland. *Water*. 2017. Vol. 9. Iss. 3. N 228. DOI: 10.3390/w9030228

11. Kuhn M.A., Varner R.K., Bastviken D. et al. BAWLD-CH_4: a comprehensive dataset of methane fluxes from boreal and arctic ecosystems. *Earth System Science Data*. 2021. Vol. 13. Iss. 11, p. 5151-5189. DOI: 10.5194/essd-13-5151-2021

12. Morris J., Sokolov A., Reilly J. et al. Quantifying both socioeconomic and climate uncertainty in coupled human–Earth systems analysis. *Nature Communications*. 2025. Vol. 16. N 2703. DOI: 10.1038/s41467-025-57897-1

13. State Geological Map of the Russian Federation. Scale 1:1,000,000. Seriya Altae-Sayanskaya. List N-44 – Novosibirsk. Obyasnitelnaya zapiska. St. Petersburg: VSEGEI, 2015, p. 392 (in Russian).

14. Strakhov N.M. Fundamentals of the Lithogenesis Theory. In 3 volumes. Vol. 1. Types of Lithogenesis and Their Distribution on the Earth's Surface. Moscow: Izd-vo Akademii nauk SSSR, 1960, p. 212 (in Russian).

15. Strakhovenko V.D., Ovdina E.A., Malov G.I. et al. Genesis of Organomineral Deposits in Lakes of the Central Part of the Baraba Lowland (South of West Siberia). *Russian Geology and Geophysics.* 2019. Vol. 60. N 9, p. 978-989. DOI: 10.15372/GiG2019093

This is an open access article under the CC BY 4.0 license

16. Strakhovenko V.D., Ovdina E.A., Malikova I.N., Malov G.I. Radioactivity Assessment of Sapropel Sediments in Small Lakes in the Baraba Lowland and Kulunda Plain, West Siberia. *Geochemistry International.* 2022. Vol. 60. N 8, p. 792-807. DOI: 10.1134/S0016702922080080

17. Strahovenko V.D., Malov G.I., Ovdina E.A., Malov V.I. Mineral composition and formation conditions of bottom sediments of the small lakes of The Ukok Plateau (Altai). *Geomorfologiya i paleogeografiya.* 2023. Vol. 54. N 4, p. 207-225 (in Russian). DOI: 10.31857/S2949178923040138

18. Appleby P.G., Oldfield F. The calculation of lead-210 dates assuming a constant rate of supply of unsupported ^{210}Pb to the sediment. *Catena*. 1978. Vol. 5. Iss. 1, p. 1-8. DOI: 10.1016/S0341-8162(78)80002-2

19. Abril-Hernández J.M. ^{210}Pb-dating of sediments with models assuming a constant flux: CFCS, CRS, PLUM, and the novel χ-mapping. Review, performance tests, and guidelines. *Journal of Environmental Radioactivity*. 2023. Vol. 268-269. N 107248. DOI: 10.1016/j.jenvrad.2023.107248

20. Zauer E.A. Modern automatic CHNS/O/X organic compound analyzers. *Analitika i kontrol.* 2018. Vol. 22. N 1, p. 6-19 (in Russian). DOI: 10.15826/analitika.2018.22.1.001

21. Korde N.V. Biostratification and Typology of Russian Sapropels. Moscow: Izd-vo Akademii nauk SSSR, 1969, p. 219 (in Russian).

22. Zarubina E.Yu., Fetter G.V. To hydrological and hydrochemical characteristics of high altitude lakes in the river Multa basin (Gorny Altai). *Bulletin of the Altay Branch of the Russian Geographical Society.* 2020. Vol. 59. N 4, p. 74-82 (in Russian). DOI: 10.24411/2410-1192-2020-15908

23. Fetter G.V., Yermolaeva N.I. The influence of abiotic factors on zooplankton structure in small lakes in South of West Sibiria. *Bulletin of the Altay Branch of the Russian Geographical Society.* 2018. Vol. 49. N 2, p. 95-103 (in Russian).

24. Downing J.A. Emerging global role of small lakes and ponds: Little things mean a lot. *Limnetica*. 2010. Vol. 29 (1). P. 9-24. DOI: 10.23818/limn.29.02

25. Ivanov D.V., Osmelkin E.V., Ziganshin I.I. Spatial regularities of carbon, nitrogen and phosphorus accumulation in lake sediments of the Chuvash Republic. *Transactions of the Karelian Research Centre of the Russian Academy of Sciences.* 2021. N 4, p. 108-118 (in Russian). DOI: 10.17076/lim1402

26. Capelle D.W., Kuzyk Z.Z.A., Papakyriakou T. et al. Effect of terrestrial organic matter on ocean acidification and CO_2 flux in an Arctic shelf sea. *Progress in Oceanography*. 2020. Vol. 185. N 102319. DOI: 10.1016/j.pocean.2020.102319

27. Jones J.R., Pope-Cole K., Obrecht D.V. et al. Carbon and nutrient sequestration in small impoundments: a regional study with global implications. *Inland Waters*. 2023. Vol. 13. Iss. 3, p. 374-387. DOI: 10.1080/20442041.2023.2265799

28. Yulai Ji, Jiacong Huang, Qing Zhu et al. Small Ponds as Carbon Emission and Burial Hotspots in Lowland Agricultural Landscape. *Earth's Future*. 2025. Vol. 13. Iss. 4. N e2024EF005441. DOI: 10.1029/2024EF005441

29. Munroe J., Brencher Q. Holocene Carbon Burial in Lakes of the Uinta Mountains, Utah, USA. *Quaternary*. 2019. Vol. 2. Iss. 1. N 13. DOI: 10.3390/quat2010013

30. Skwierawski A. Carbon Sequestration Potential in the Restoration of Highly Eutrophic Shallow Lakes. *International Journal of Environmental Research and Public Health*. 2022. Vol. 19. Iss. 10. N 6308. DOI: 10.3390/ijerph19106308

31. Jeffries M.J., Gilbert P.J., Taylor S. et al. Organic carbon in British lowland ponds: estimating sediment stocks, possible practical benefits and significant unknowns. *Hydrobiologia*. 2023. Vol. 850. Iss. 15, p. 3225-3239. DOI: 10.1007/s10750-022-04972-z

32. Taran O.P., Boltenkov V.V., Ermolaeva N.I. et al. Relations between the Chemical Composition of Organic Matter in Lacustrine Ecosystems and the Genesis of Their Sapropel. *Geochemistry International*. 2018. Vol. 56. N 3, p. 256-265. DOI: 10.1134/S0016702918030096

33. Babikov B.V., Kobak K.I. Absorption of Atmospheric Carbon Dioxide by the Wetland Ecosystems of Russia in Holocene. The Problems of Paludification. *Lesnoy zhurnal.* 2016. N 1, p. 9-36 (in Russian). DOI: 10.17238/issn0536-1036.2016.1.9

34. Lapshina E.D. Vegetation of Bogs in the Southeast of Western Siberia. Khanty-Mansiisk: Yugorskii gosudarstvennyi universitet, 2010, p. 184 (in Russian).

***Authors*: Georgii I. Malov,** *Junior Researcher* (*V.S.Sobolev Institute of Geology and Mineralogy SB RAS, Novosibirsk, Russia*), *https://orcid.org/0000-0002-4150-4171*, **Vera D. Strakhovenko,** *Doctor of Geological and Mineralogical Sciences, Leading Researcher* (*V.S.Sobolev Institute of Geology and Mineralogy SB RAS, Novosibirsk, Russia*), *https://orcid.org/0000-0003-1350-2045*, **Ekaterina A. Ovdina,** *Candidate of Geological and Mineralogical Sciences, Senior Researcher* (*V.S.Sobolev Institute of Geology and Mineralogy SB RAS, Novosibirsk, Russia*), *https://orcid.org/0000-0002-4920-8860*, **Viktor I. Malov,** *Candidate of Geological and Mineralogical Sciences, Researcher* (*V.S.Sobolev Institute of Geology and Mineralogy SB RAS, Novosibirsk, Russia*), *malov@igm.nsc.ru, https://orcid.org/0000-0002-2175-3971*.

The authors declare no conflict of interests.

This is an open access article under the CC BY 4.0 license

ISSN 2411-3336; e-ISSN 2541-9404

JOURNAL OF MINING INSTITUTE

Zapiski Gornogo instituta

Journal homepage: pmi.spmi.ru

Research article *Geology*

Investigation of “Kolchedan amber” with IR spectroscopy

Pavel I. Alekseev✉, **Evgenii A. Vasilev**

Empress Catherine II Saint Petersburg Mining University, Saint Petersburg, Russia

How to cite this article: Alekseev P.I., Vasilev E.A. Investigation of “Kolchedan amber” with IR spectroscopy. Journal of Mining Institute. 2026. Vol. 280, p. 16-26.

Abstract

This work is devoted to the study of fossil resins from the collection of the Mining Museum using infrared spectroscopy (FTIR). Samples of amber from the Iset River in the Middle Urals, collected in the early 19th century and known as “Kolchedan amber”, were examined. For comparison, fossil resins from other localities in Northern Eurasia were studied: the Peschanka River on the coast of the Barents Sea, the Amderma River on the Yugorsky Peninsula, and the Khatanga River on the Taimyr Peninsula. The obtained data indicate that “Kolchedan amber” belongs to an independent and widespread type of fossil resin in Northern Eurasia, the finds of which are confined to Cretaceous deposits. Previously, this type of resin was identified as “krantzite” for the locality on the Iset River or as “retinite” for localities on the coast of the Arctic Ocean. A comparison with other mineral species of fossil resins is carried out in this work. An analysis of the absorption peaks in the IR spectrum suggests that, according to K.Anderson’s resin classification, “Kolchedan amber” belongs to Class I, which is represented by resins with a predominance of labdane-type diterpenoids. A distinctive and most characteristic feature of the IR spectrum of “Kolchedan amber” is a “comb” consisting of three approximately equal absorption peaks at 936, 909, and 888 cm^{-1}. An analysis of the systematically significant features of the IR spectrum indicates that the most likely biological source of this type of fossil resin was plants from the Pinaceae family. An additional argument supporting such a biological origin is the comparison of the diagnostic region of the IR spectrum of “Kolchedan amber” with the spectrum of amber from Axel Heiberg Island in the Canadian Arctic, which originated from the resin of the genus *Pseudolarix*.

Keywords

Mining Museum; fossil resins; IR spectra; Kolchedan amber; source of amber

Funding

None.

Received: 19.09.2025 ***Accepted: 28.04.2026*** ***Online: 17.06.2026*** ***Published: 10.09.2026***

Introduction

Due to their resistance to chemical degradation, fossil resins are preserved in sedimentary deposits for hundreds of millions of years, dating back to the Carboniferous period [1]. Currently, the most widely used methods for their study are infrared spectroscopy (FTIR) and gas chromatography (Py-MsCS), which make it possible to obtain data on the chemical composition of the resin, upon which modern classifications of fossil resins are based [2, 3]. These methods can accurately distinguish between different types of resins, allowing researchers to study their geographical and stratigraphic distribution and, prospectively, to use fossil resins as geological and paleontological markers. Once a resin is identified, it is possible to infer the age and stratigraphic position of the deposits from which it originated; furthermore, if the biological source of the resin is known, data can be obtained on the distribution of specific plant communities and paleoclimatic zonation, since different resin-producing plants grow under different climatic conditions. For paleobotanical research, fossil resins represent an alternative source of information that complements data from the analysis of spore-pollen assemblages and the study of leaf floras.

The extensive paleontological and mineralogical collections [4, 5] are housed in the Mining Museum of Empress Catherine II Saint Petersburg Mining University, serving as a basis for modern scientific

This is an open access article under the CC BY 4.0 license

research [6-8]. The museum's collections also contain fossil resin specimens, including "Kolchedan amber" – a long-known but still poorly studied mineralogical object. Occurrences of amber were discovered near the village of Kolchedan on the Iset River in the Middle Urals as early as the end of the 18th century. In 1802, the specimen was examined by the famous chemist, academician T.E.Lowitz, who concluded that this resin did not differ from Baltic amber [9]. No special mineralogical name was proposed for it, and subsequently, in the literature, it is referred to as "Kolchedan amber" – after the location of its initial collection. A report on the geological section of its locality was presented by the mining engineer, head of the Kamensky plant, captain Barozzi de Elsa [9]. Specimens of "Kolchedan amber", collected "from sandstone strata of Kolchedan settlement 18 versts from the Kamensky plant" have been stored in the Mining Museum since 1835.

In 1935, specimens from the Mining Museum were studied at the Central Geological Prospecting Institute in Leningrad – solubility analyses were performed, and the relative content of chemical elements was calculated. Based on the results of these studies, "Kolchedan amber" was assigned to the "krantzite group", which combines properties of "immature ambers" with obvious chemical transformations of the material [10].

In 1964 and 1966, specimens of this amber from the Mining Museum were taken for research by S.S.Savkevich, who was one of the first in the world to study fossil resins using infrared spectroscopy. These studies are evidenced by receipts for the specimens, which are preserved in the collections together with the labels; however, the results remained unknown, and later S.S.Savkevich classified amber from the Middle Urals as gedanite [11, рис.1.3]. Since 2020, "Kolchedan amber" has once again come into the focus of scientists [12, 13]. Specimens from the Mining Museum collection were not studied, but based on the characteristic physical properties (elasticity, softness) described earlier by Barozzi de Elsa [9], a hypothesis was proposed that they belong to krantzite – a rare type of fossil resin from Paleogene deposits of Europe [13]. Currently, data on "Kolchedan amber" are contradictory, and its botanical origin and chemical composition remain unknown. Therefore, 60 years after the research of S.S.Savkevich, specimens of "Kolchedan amber" from the Mining Museum collection were again studied using infrared spectroscopy, and a comparison was made between this amber and fossil resins from other localities.

Materials and methods

All studied specimens of fossil resins (40 specimens) are stored in the Mining Museum (Table 1).

Table 1

Studied specimens of fossil resins from the collection of the Mining Museum

Locality	Age, geological data	Numbers of specimens, collection MGS 930
Iset River, Kolchedan Village, Middle Urals	Late Cretaceous (Coniacian), Kamyshlovka Formation, shallow coastal-marine deposits	25/1, 25/2, 25/3, 25/4, 25/5, 25/6_2, 25/6_3, 25/6_4, 25/6_5, 25/6_6
Peschanka River, Arkhangelsk Region	Late Cretaceous (?), Arctic Ocean shelf	94/1, 94/2, 94/3, 94/4, 94/5, 94/6, 94/7, 94/8, 94/9
Amderma River, Yugorsky Peninsula		41/1, 41/2, 41/3
Khatanga River, Taimyr Peninsula	Late Cretaceous (Santonian), Kheta Formation, coastal-marine deposits	95/1, 95/2, 95/3, 95/4, 95/5, 95/6, 95/7, 95/8, 95/9, 95/10, 95/11, 95/12, 95/13, 95/14, 95/15, 95/16, 95/17
Yantarny settlement, Kaliningrad Region	Paleogene (Eocene), Prussian Formation, coastal-marine deposits	930/92/11

"Kolchedan amber" was collected in the 19th century on the banks of the Iset River from layers of clays and brown coal overlain by reddish sandstone [9] (Fig.1). Some recent authors indicate that the age of the deposits from which it originates is Eocene [12]; however, A.P.Karpinsky noted the occurrence of two Cretaceous horizons in the vicinity of Kolchedan Village – a lower horizon with plant remains and an upper horizon with remains of marine Cretaceous fauna [14]. Based on the location of the site, it can be established that the layers containing "Kolchedan amber" belong to

This is an open access article under the CC BY 4.0 license

Journal of Mining Institute. 2026. Vol. 280. P. 16-26
© Pavel I. Alekseev, Evgenii A. Vasilev, 2026

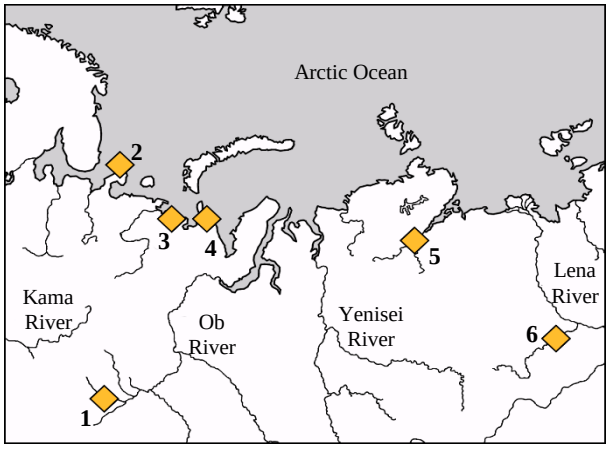


Fig.1. Localities of fossil resins with IR spectrum same with "Kolchedan amber"

1 – Kolchedan village, Iset River; 2 – Kanin Peninsula; 3 – Peschanka River, Arkhangelsk Region; 4 – Amderma River, Yugorsky Peninsula; 5 – Khatanga River, Taimyr Peninsula; 6 – Vilyuy River, Khatyryk-Khomo settlement

shallow marine deposits of the Kamyshlovka Formation of Coniacian age and are overlain by deeper marine deposits of the Fadyushkina Formation of Campanian age [15].

The locality designated on the label as "Peschanka River, Arkhangelsk Region" is presumably located on the coast of the Barents Sea. Relatively nearby, in the area of the Amderma River on the Yugorsky Peninsula, fossil resin finds are associated with reworked shelf deposits of the Arctic Ocean of Late Cretaceous age [16]. On the Taimyr Peninsula, the Kheta River, a tributary of the Khatanga, exposes several formations of Late Cretaceous age; the amber-bearing locality Yantardakh, the richest in amber, belongs to the Kheta Formation of Santonian-Campanian age [17] (Fig.1).

The fossil resin specimens were studied using FTIR (Fourier-Transform Infrared Spectroscopy) to obtain IR absorption spectra in the range of 4000-600 cm^{-1}. The work was carried out on a VERTEX 70 spectrometer (Bruker, Germany) with a Hyperion 1000 microscope at the Shared Research Center of the Mining University. Transparent particles of the specimen, taken from a fresh surface with a thickness of less than 50 μm, were placed on a KBr plate for IR spectral acquisition. Data in .dpt format were converted into graphs using Matplotlib, Pandas, and NumPy libraries in the Python 3 software environment. The parallel coordinates plot method was used for visualization of the spectral data. Each of the four spectral ratios is represented by a separate axis, and specimens are represented by thin lines connecting their values across all axes, which allows simultaneous visualization of differences between different types of fossil resins across all parameters.

Results and discussion

Physical properties and IR spectrum of "Kolchedan amber". Amber collected from the Iset River consists of roughly rounded resin pieces up to 3 cm in size, covered with an opaque weathering crust (Fig.2). The color varies from light yellow to dark orange and reddish; transparent areas of the resin are combined with the cloudy texture of "cloudy amber" – opaque white streaks. By analogy with Baltic amber, such opaque areas within the resin are not related to its chemical composition but result from water incorporation into the still-unhardened resin. "Kolchedan amber" is characterized by plasticity – the material is cut with a scalpel rather than crumbling.



Fig.2. Samples of fossil resin from the Iset River, collection of Mining Museum (MGS 930/25)

Spectroscopy results show that all specimens from the Mining Museum originating from the Iset River, from the coast of the Barents Sea, and some specimens from the Taimyr Peninsula and the Yugorsky Peninsula have an identical set of absorption bands in the IR spectrum and belong to the same type of fossil resin (Fig.3). Depending on the degree of weathering, the IR spectrum plot may be more or less smoothed, and weak absorption bands become difficult to distinguish, but this does not affect the wavenumber values and the relative height of the peaks in the plot.

This is an open access article under the CC BY 4.0 license

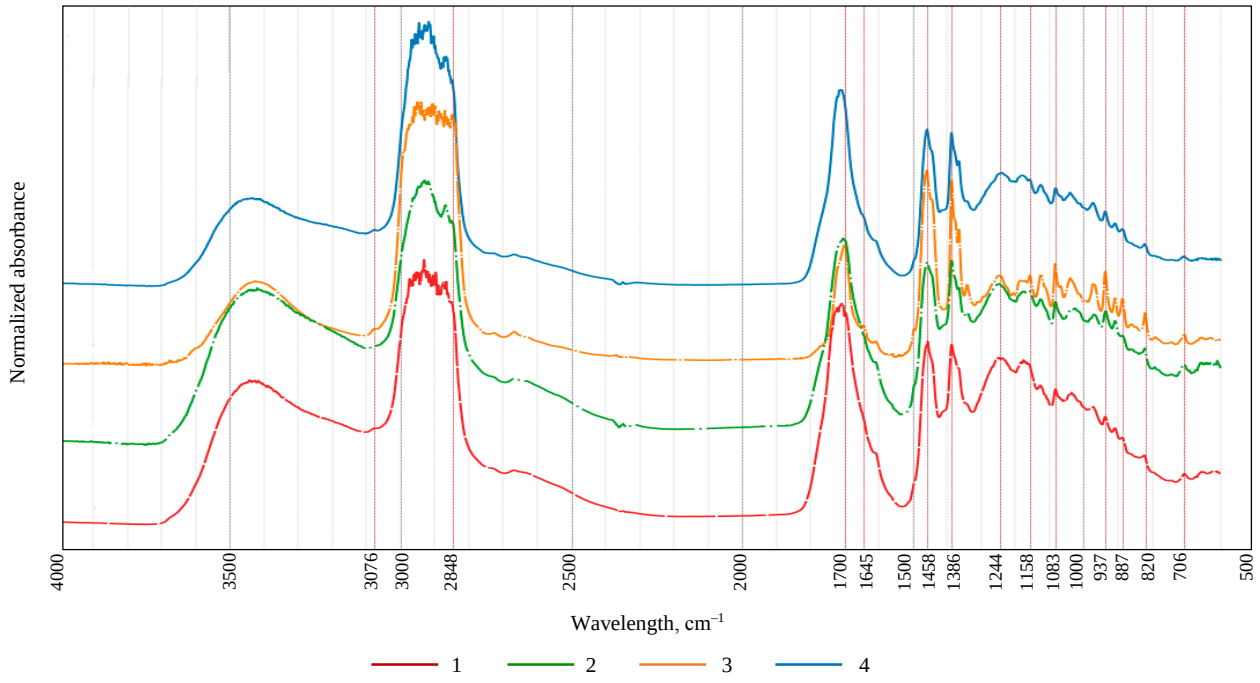


Fig.3. IR spectra of "Kolchedan amber" from different localities in range of 4000-600 cm^{-1}

1 – spec. 930/25/4, Kolchedan Village, Middle Urals; 2 – spec. 930/25/6/4, Kolchedan Village, Middle Urals; 3 – spec. 930/41/1, Amderma River, Yugorsky Peninsula; 4 – spec. 930/94/9, Peschanka River, Barents Sea

The identified absorption bands of the IR spectrum of "Kolchedan amber" are shown in Table 2; the identification of structural groups in the IR spectra was carried out based on literature data [2, 18, 19].

Table 2

Absorption bands in the IR spectrum of "Kolchedan amber"

Value, cm^{-1}	Intensity	Functional group
706	ΔΔ	Cis-configuration of double bond –CH=CH–
743	Δ	CH=CH bonds. Methyl substitution at the α-position
790	Δ	Absorption band of unsaturated bond $R_1R_2C=CHR_3$
820	ΔΔ	Cis-configuration of CH=CH–COOR group
861	Δ	Not identified
887	ΔΔ	C–H bond in exocyclic methylene group $=CH_2$
909	ΔΔ	C–O bonds in primary alcohols
937	ΔΔ	C–O bonds in primary alcohols
972	ΔΔ	OH group of carboxylic acids in solid state
1001	Δ	C–O groups in primary alcohols or phenolic hydroxyls
1039	ΔΔ	C–O bond in secondary and tertiary alcohols
1067	Δ	C–O bond in secondary and tertiary alcohols
1083	ΔΔ	C–O bond in secondary and tertiary alcohols
1125	ΔΔ	C–O bond in secondary and tertiary alcohols
1158	ΔΔ	C–O bond of esters
1245	ΔΔ	C–O bond of carboxylic acids
1293	Δ	C–O bonds
1310	Δ	C–O bonds
1365	ΔΔ	C–H bonds
1341	ΔΔ	C–H bonds

This is an open access article under the CC BY 4.0 license

End of Table 2

Value, cm^{-1}	Intensity	Functional group
1386	ΔΔΔ	C–H bond in CH_3 adjacent to carbonyl group (acids, esters)
1458	ΔΔΔ	C–H bond in CH_2 adjacent to carbonyl group (acids, esters)
1496	Δ	C–H bond
1609	Δ	Carbon–carbon bonds in aromatic compounds
1645	Δ	Exocyclic methylene group CH_2
1701	ΔΔΔ	C=O bond in unsaturated carboxylic acids
1720	ΔΔ	C=O bond in saturated carboxylic acids and esters
2667	Δ	Associated OH group of carboxyl
2727	Δ	Associated OH group of carboxyl
2900	ΔΔΔ	C–H bond in aliphatic CH_2 and CH_3 groups
3076	Δ	Secondary C–H bond in exocyclic $=CH_2$ group
3426	ΔΔ	O–H bond of water and carboxylic acids

Notes: Δ – weak, ΔΔ – medium, ΔΔΔ – strong intensity.

The IR absorption bands of "Kolchedan amber" from the Mining Museum correspond to the spectra of typical terpenoid resins [20, 21]. The most pronounced absorption bands are associated with the following functional groups: OH of alcohols and carboxylic acids (3400-3480 cm^{-1}), aliphatic CH_2 and CH_3 groups (2900 cm^{-1}, 2840 cm^{-1}), CH_2 and CH_3 groups of organic acids and esters (1370 cm^{-1}, 1458 cm^{-1}). The combined presence of absorption bands at 888, 1642, and 3076 cm^{-1} indicates the presence of compounds with exocyclic methylene groups, likely bicyclic diterpenoids of the labdane type. This suggests that "Kolchedan amber" belongs to Class I according to Anderson's classification [3, 22] – the most widespread among fossil resins – with the caveat that chromatographic studies of the chemical composition are required for a definitive conclusion. The absence of absorption peaks at 1735 cm^{-1} and 1160 cm^{-1} suggests the absence of a polymer matrix of succinic acid esters with labdane components [23]. The absorption peak of carboxyl groups at 1720-1700 cm^{-1} indicates that the material belongs to fragile fossil resins. A weak peak at approximately 1600 cm^{-1} indicates the presence of aromatic compounds; in fossil resins, their source is often abietic acid derivatives (e.g., dehydroabietic acid).

Distribution of "Kolchedan amber". Examination of IR spectra of fossil resin specimens from different localities showed that this type is frequently encountered in the subarctic region of Eurasia, predominantly in Late Cretaceous deposits. Identical IR spectra are exhibited by all studied specimens from the Peschanka River (coast of the Barents Sea). Despite minor individual spectral variations, the set of absorption peaks in these specimens is the same as that of "Kolchedan amber", and a "comb" of three distinct and approximately equal-height peaks at 936, 909, and 888 cm^{-1} is particularly characteristic of these resins (Fig.4). This type of resin is also found among specimens from the Taimyr Peninsula and the Yugorsky Peninsula.

In some specimens from the Khatanga River basin, the absorption band at 1030 cm^{-1} is strongly pronounced. According to M.A.Bogdasarov, this is characteristic of retinites: "... a feature of the IR spectra of retinites is strong absorption in the range of 980-1300 cm^{-1} with a dominant peak at 1030 cm^{-1}" [24]. However, since the remainder of the spectrum of the "retinite-like" specimens does not differ from that of typical "Kolchedan amber" and "normal" specimens from the Khatanga River, it would be incorrect to consider them a different type of fossil resin. Thus, "Kolchedan amber" is not a fossil resin type specific to the Middle Urals. Identical fossil resins are widely distributed in many localities of the Arctic Ocean basin (Fig.4) but are usually classified as other types of fossil resins, most often as retinites.

This is an open access article under the CC BY 4.0 license

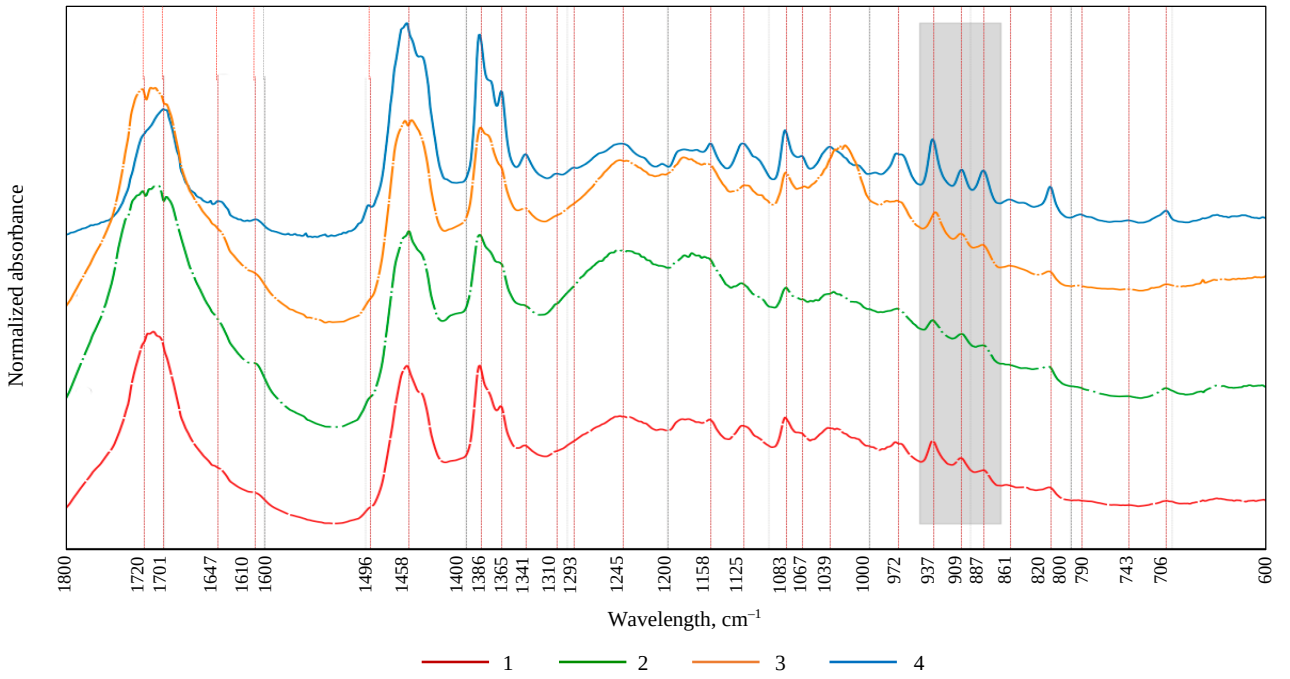


Fig.4. IR spectra of "Kolchedan amber" from different localities in the range of 1800-600 cm^{-1}.
The diagnostic "comb" region is highlighted in gray

1 – spec. 930/94/1, Peschanka River, Yugorsky Peninsula; 2 – spec. 930/25/4, Kolchedan Village, Middle Urals;
3 – spec. 930/95/3, Khatanga River, Taimyr Peninsula; 4 – spec. 930/41/1, Amderma River, Yugorsky Peninsula

IR spectra published in the literature also confirm the wide distribution of fossil resin with the "Kolchedan amber" spectrum in the Russian Subarctic. It is present in the Santonian deposits of the Kheta Formation at Yantardakh Mountain on the Taimyr Peninsula, in the Late Cretaceous deposits near the village of Khatyryk-Khomo on the Vilyuy River in Yakutia, and on the Kanin Peninsula [16, 25, 26]. However, "Kolchedan amber" is not recognized as a distinct type of fossil resin, except for the work of S.S.Savkevich [25], who notes that this type of resin "has no known analogues in terms of IR spectra" and proposes assigning it to the "retinite family". Probably the same type of resin is referred to by O.V.Martirosyan [17], who writes that "resins from the Khatanga River area are close in spectral characteristics to both retinite and gedanite".

The chemical composition of fossil resin from the Khatanga River basin was studied using pyrolysis chromatography [24, 27]; however, due to the co-occurrence of different resin types in this region and the lack of IR spectra for the studied specimens, we cannot state with certainty that the published data can be attributed specifically to "Kolchedan amber". According to K.Anderson, fossil resins from the Yantardakh locality (Khatanga River) have an atypical chemical composition – they belong to Class Ib of fossil resins and consist of a mixture of labdane-type diterpenoids (biformene) and communol derivatives, with the absence of free monomers of communic acid [27].

Position of "Kolchedan amber" in the classification of fossil resins. Amber found on the Iset River was presumed to belong to Baltic amber (succinite) or krantzite [9, 13]; however, the IR spectrum of "Kolchedan amber" (curve 1, Fig.5) differs greatly from the spectra of both fossil resin types. The IR spectrum of European krantzite from Germany [26, 28] is characterized by very strong absorption bands at 700 cm^{-1} and 750 cm^{-1} (curve 2, Fig.5) and a weak band at 921 cm^{-1}, which are not observed in "Kolchedan amber", whereas krantzite lacks absorption peaks at 909 and 937 cm^{-1}. Thus, the property of plasticity, which is observed in both fossil resin types, is not a diagnostic feature that could be used to confirm their mineral species.

Some scientists believe that krantzite has a separate oxidized form – oxykrantzite [28, 29] (Geisetal, Germany), the IR spectrum of which is characterized by weak expression of the absorption

This is an open access article under the CC BY 4.0 license

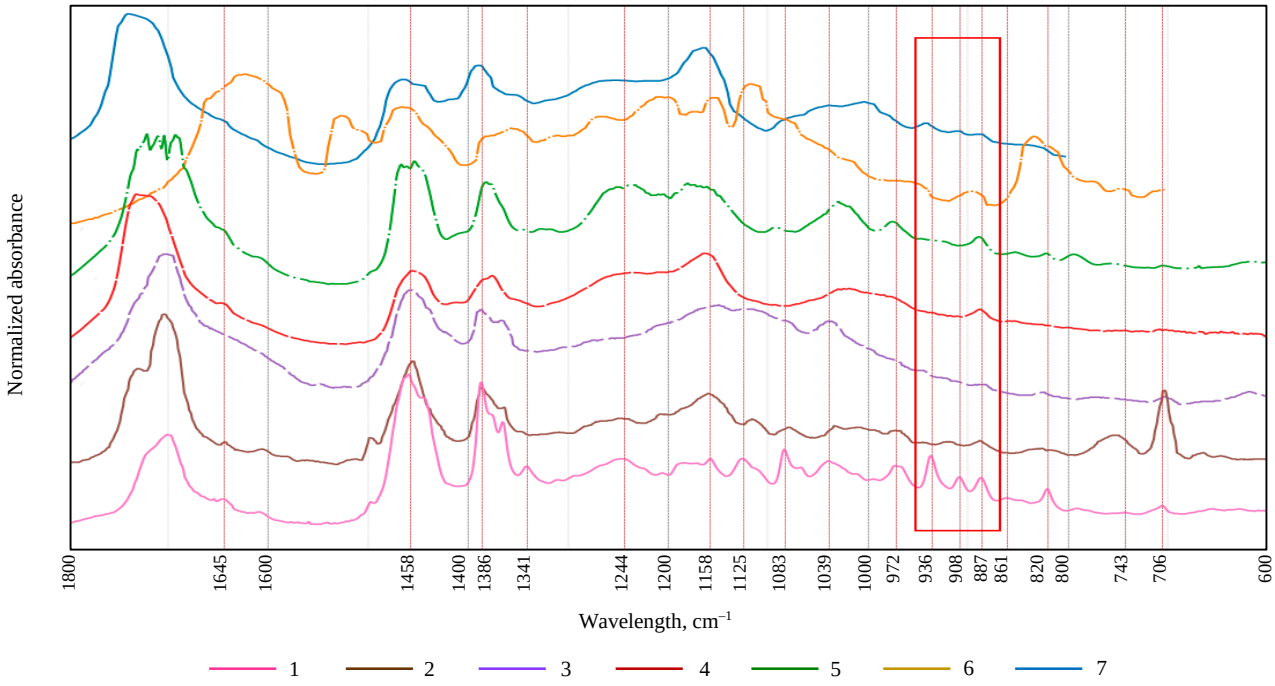


Fig.5. IR spectra of "Kolchedan amber" from different localities in the range of 1800-600 cm^{-1}.
The diagnostic "comb" region, in which "Kolchedan amber" exhibits three characteristic absorption peaks, is highlighted with a red rectangle

1 – "Kolchedan amber" (spec. 930/25/6); 2 – krantzite, Geiselthal [28]; 3 – oxykrantzite, Geiselthal (retinite) [28]; 4 – succinite, Baltic amber (spec. 930/92/11); 5 – gedanite, Khatanga River (spec. 930/95/13); 6 – retinite from Halle [29]; 7 – amber from Axel Heiberg Island (Canadian Arctic) originating from golden larch (*Pseudolarix*) resin [30]

bands at 700 and 750 cm^{-1} (curve 3, Fig.5). However, the IR spectrum of oxykrantzite is similar to that of krantzite in terms of its set of absorption bands and shows strong smoothing across the entire range, which is not observed in "Kolchedan amber", while the diagnostic bands of the latter, including 909 and 937 cm^{-1}, are absent in oxykrantzite.

The spectrum of succinite differs greatly in many features – it has a maximum of the carboxyl group band at 1735 cm^{-1} and a pronounced "Baltic shoulder" with a maximum at 1160 cm^{-1}; moreover, it lacks the absorption peaks at 907 and 937 cm^{-1} characteristic of "Kolchedan amber" (curve 4, Fig.5).

According to S.S.Savkevich, O.V.Martirosyan, and M.A.Bogdasarov, two mineral species of fossil resins occur on the coast of the Arctic Ocean – gedanite and retinite [17, 24], and it was logical to assume that "Kolchedan amber" might belong to one of them. In this work, a comparison was made with gedanite, a specimen of which originates from the Upper Cretaceous deposits of the Taimyr Peninsula, where it occurs together with "Kolchedan amber". In terms of its IR spectrum, gedanite differs sharply by the absence of absorption bands at 909, 936, and 1125 cm^{-1} and by stronger absorption bands at 887 and 975 cm^{-1} (curve 5, Fig.5).

Unlike the previous mineral species of fossil resins, retinite is often a synonym for "fragile fossil resin", and this name may encompass different types of fossil resins with different chemical compositions [10]. For example, the IR spectrum of "retinite" presented in the monograph [29] differs sharply from the spectra of any modern and fossil resins (curve 7, Fig.5). Another type of fossil resin – oxkrantzite [28] – has also historically been defined as "retinite" (curve 3, Fig.5). Some scientists deny the existence of retinite as a distinct mineral species of fossil resin [31].

Retinite as a mineral species of fossil resin and the distinctive features of its IR spectrum are discussed in publications of Russian scientists [2, 18, 32]. According to the classification of O.V.Martirosyan and M.A.Bogdasarov [2], retinite has a pimarane skeleton and consists of tricyclic labdane diterpenoids (pimaric, isopimaric, abietic acids), which do not polymerize. This corresponds to Class V of Anderson's resin classification [3]. At the same time, the only fossil resin assigned to Class V

This is an open access article under the CC BY 4.0 license

on the basis of gas pyrolysis chromatography data is Eocene London copalite [3], for which IR spectroscopy was not performed. The widespread distribution of retinite in Eurasia, according to [2], requires confirmation; it is also necessary to define a "typical" retinite whose IR spectrum could be relied upon for the identification of fossil resin species.

The IR spectrum of "Kolchedan amber" does not correspond to the spectral characteristics of retinite [2, 18, 32] – its IR spectrum has an absorption band at 824 cm^{-1}, characteristic of immature resins and absent in retinite, and a band at 1085 cm^{-1} that is more intense than that of gedanite. The band at 1030 cm^{-1}, important for the identification of retinite, is very intense in some "Kolchedan amber" specimens from the Taimyr Peninsula but is weakly expressed in specimens from other localities. The distinctive spectral bands of "Kolchedan amber" at 936 and 909 cm^{-1} are not observed in retinite. Thus, "Kolchedan amber" cannot be assigned to the recognized mineral species of fossil resins established for Northern Eurasia.

Biological origin of "Kolchedan amber". An important issue in the study of fossil resins is not only the formal determination of their mineral type but also the identification of the resin-producing plant. In this case, a particular type of fossil resin can become an indicator of the age, climate, and range that were characteristic of that resin-producing plant. Furthermore, resins accumulate in the soils of forest biological communities [3]; therefore, they themselves indicate the presence of forest landscapes in the past and can provide data on the forest-forming plants that grew on interfluves area, the remains of which rarely enter the "standard" assemblages of leaf floras from alluvial deposits.

The possibility that fossil resins preserve features by which they can be linked to modern plants is assessed differently by different authors. In the Russian literature, the dominant viewpoint is that the geochemical conditions of the surrounding environment play a key role in shaping the chemical composition of fossil resin, whereas differences in the composition of the original plant resin are secondary [24, 32, 33]. In the foreign literature, conversely, it is often argued that the chemical composition of terpenoid resins is extremely resistant to external influences, and their IR spectra retain a characteristic set of absorption bands for tens or hundreds of millions of years over a certain range [30, 34, 35]. This is supported by comparisons of IR spectra of fossil resins with established biological origins and their "analogues" from modern plants [19, 30, 36], including for localities in the Southern Hemisphere [37].

In the IR spectrum of terpenoid resins, there is a variable region in the range of 1550-650 cm^{-1}, the so-called "fingerprint region" [34], which has a unique set of absorption bands for different plant species. Theoretically, this makes it possible to distinguish some plant species from others based on a resin sample, but it does not allow the sample to be classified within botanical systematics, since the systematic significance of individual absorption bands in the IR spectrum is poorly understood [38].

According to R.Tappert [38], who studied resins from 60 species of modern conifers, IR spectroscopy allows a resin to be assigned to one of two groups – pine-type resins or cypress-type resins. Resins of the first type are produced by plants from the families Pinaceae (pine family) and Taxaceae (yew family), and those of the second type – from Cupressaceae (cypress family), Podocarpaceae (podocarp family), Araucariaceae (araucaria family), and Sciadopityaceae (umbrella pine family). To determine the resin type, R.Tappert proposed using four ratios of absorption band values: 832/791, 1460/1448, 1448/1385, and 2858/2848 [38]. The results of a comparison of the spectra of "Kolchedan amber", gedanite, and Baltic amber against a database of modern resins* are shown in Fig.6.

Based on the results of comparing the IR spectral features of fossil resins with modern resins, the following conclusions can be drawn:

• "Kolchedan amber" and gedanite are clearly separated into two distinct groups, confirming that they are different types of fossil resins, although they often occur together;

• specimens of "Kolchedan amber" are closer to pine-type resins, whereas gedanite is closer to cypress-type resins, indicating different plant sources for these resins;

* FTIR Spectral_ Database_Plant Exudates and Resins_Tappert et al 2011 IJPS. DOI: 10.13140/RG.2.1.3636.4645

This is an open access article under the CC BY 4.0 license

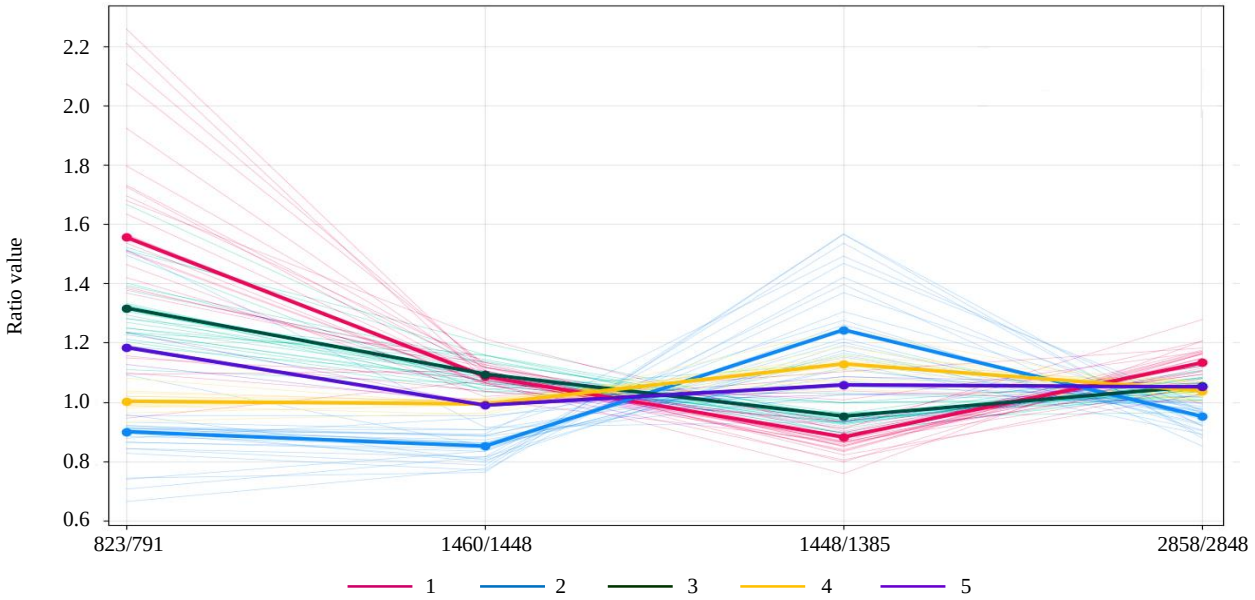


Fig.6. Parallel coordinates plot for visualizing differences in IR spectra of modern and fossil resins
1 – pine-type resin; 2 – cypress-type resin; 3 – "Kolchedan amber"; 4 – gedanite; 5 – Baltic amber

• the ratio of the absorption band values at 2858/2848 in this work is uninformative, since in this part of the spectrum the strong bands of C–H bonds create noise, against which the small peak at 2858 cm^{-1} is often lost;

• based on these spectral characteristics, Baltic amber cannot be assigned to either cypress-type or pine-type resins.

The results of this comparison also provide an argument in favor of the fact that the source of "Kolchedan amber" was some plant from the Pinaceae family (pine family), although fossil resins of pine origin are considered rarer [30].

When comparing the IR spectroscopy results of "Kolchedan amber" with other fossil resins, partial similarity was found with amber from Axel Heiberg Island in the Canadian Arctic. For the latter, the parent plant has been firmly established [39] – an extinct species of false larch, *Pseudolarix wehrii* Gooch, from the Pinaceae family. The IR spectra of fossil resin from Axel Heiberg Island [39], similarly to "Kolchedan amber", exhibit three characteristic "comb" peaks (936, 909, and 888 cm^{-1}) in the "fingerprint region" (curve 7, Fig.5). Mass spectrometry of the Canadian specimens has shown [40] that their base consists of labdane-type monomers of a non-regular but enantio-configuration (predominantly ozic acid and enantio-biformenes). The similarity of the IR spectra of fossil resin from false larch and "Kolchedan amber" provides an additional argument in favor of its origin from a pine-type resin. However, the Canadian specimens contain a large amount of bound succinic acid, and because of this, their IR spectrum is distinguished by a shift of the carboxyl group peak to 1735 cm^{-1} and the presence of a "Baltic shoulder" in the range of 1250-1160 cm^{-1}. Fresh conifer resins do not contain succinic acid, as it is a degradation product of other compounds [40]. In "Kolchedan amber", succinic acid is absent or, at least, does not form cross-links between diterpenoid molecules. Although false larch was widely distributed at high and middle latitudes of Eurasia and North America during the Late Cretaceous and Paleogene [36], including in the localities where "Kolchedan amber" is found, without finds of the latter in organic association with remains of golden larch, it cannot be asserted that this plant was its source.

Conclusion

The studies of fossil resins from the collections of the Mining Museum have shown that "Kolchedan amber" does not belong to krantzite but rather to a distinct and widely distributed type of fossil resin in Northern Eurasia. The most valuable diagnostic feature of its IR spectrum is a "comb" of three approximately equal absorption peaks at 936, 909, and 888 cm^{-1}. The presence of "Kolchedan amber" in different localities of the Russian Subarctic is confirmed both by studies of resins from the

This is an open access article under the CC BY 4.0 license

Mining Museum collection and by literature data. Most of its finds are associated with Late Cretaceous deposits, including the locality near the village of Kolchedan studied by mining engineers. The museum collections also house fossil resin specimens of this type from localities on the Peschanka River (Arkhangelsk Region), the Amderma River (Yugorsky Peninsula), and the Khatanga River (Taimyr Peninsula). Fossil resin specimens with similar IR spectra have also been recorded on the Kanin Peninsula (coast of the Barents Sea) and on the Vilyuy River (Yakutia).

The IR spectra of "Kolchedan amber" suggest that, in terms of its chemical composition, it belongs to Class I of Anderson's resin classification, which is represented by resins with a predominance of labdane-type diterpenoids. This is the most widespread class for fossil resins, comprising four subclasses. Unfortunately, the features of the IR spectrum are insufficient to determine the specific subclass to which the studied specimens belong.

Formal mineral species identification according to the system proposed by O.V.Martirosyan and M.A.Bogdasarov also proved impossible due to the lack of reference spectra for specific fossil resin species in this classification and the contradictory interpretation of the term "retinite". IR spectroscopy data indicate that "Kolchedan amber" from the Iset River in the Middle Urals and from numerous localities in the Russian Arctic belongs to a distinct type of fragile fossil resin that has not yet been discovered in localities in Europe or North America. The specific absorption bands of the IR spectrum indicate that the source of this fossil resin type was plants from the Pinaceae family. An additional argument supporting such an origin for "Kolchedan amber" is the similarity of its diagnostic IR spectral regions to those of the IR spectrum of fossil resin from false larch (Pseudolarix) from Axel Heiberg Island in the Canadian Arctic.

REFERENCES

1. Bray P.S., Anderson K.B. Identification of Carboniferous (320 Million Years Old) Class Ic Amber. *Science*. 2009. Vol. 326. N 5949, p. 132-134. DOI: 10.1126/science.1177539
2. Martirosyan O.V., Bogdasarov M.A. Fossil resins: diagnostics, classification and structural transformation under the thermal influence. *Vestnik IG Komi SC UB RAS.* 2014. N 4 (232), p. 10-15 (in Russian).
3. Seyfullah L.J., Beimforde C., Dal Corso J. et al. Production and preservation of resins – past and present. *Biological Reviews.* 2018. Vol. 93. Iss. 3, p. 1684-1714. DOI: 10.1111/brv.12414
4. Borovkova N.V., Pilipenko A.R., Yakimaha M.N. From England to Russia: Fluorite Vases from the Second Half of the 18th – Beginning of the 19th Centuries. *Vestnik of Saint Petersburg University. Arts.* 2022. Vol. 12. Iss. 2, p. 380-395 (in Russian). DOI: 10.21638/spbu15.2022.208
5. Alekseev P.I., Vasiliev E.A. Study of Rumanite and Rumanite-Like Resins from the Collections of the Mining Museum with IR Spectroscopy. *Zapiski Rossiiskogo mineralogicheskogo obshchestva.* 2025. Vol. 154. N 4, p. 113-124 (in Russian). DOI: 10.7868/S2658435225040084
6. Bazhin V.Yu., Suslov A.P., Gorshkova O.A. Examining the structure and properties of 1823 silver rouble. *Tsvetnye metally.* 2023. N 8, p. 85-92 (in Russian). DOI: 10.17580/tsm.2023.08.14
7. Sennikov A.G., Sennikova E.A., Saburov P.G. The first dinosaurs in Mining Museum of St. Petersburg Mining University. *Priroda.* 2024. N 5 (1305), p. 26-45 (in Russian). DOI: 10.7868/S0032874X24050037
8. Petrov D.A., Ryzhkova S.O., Gembitskaya I.M. Rare minerals of noble metals in the collection of the Mining Museum: new data. *Journal of Mining Institute.* 2022. Vol. 255, p. 493-500. DOI: 10.31897/PMI.2022.42
9. Mamyshev N.R. On the amber locality near the Kamensky Plant in the Yekaterinburg district. *Gornyi zhurnal.* 1836. Book 4. Part. 2, p. 180-186.
10. Orlov N.A., Uspenskii V.A. Mineralogy of Caustobiolites. Moscow; Leningrad: Izd-vo Akademii nauk SSSR, 1936, p. 198.
11. Savkevich S.S. New Developments in Amber and other Fossil Resins Mineralogical Studies. Gem Minerals. Proceedings of the XI General Meeting of IMA, 4-10 September, 1978, Novosibirsk, USSR. Leningrad: Nauka, 1980, p. 17-28.
12. Martirosyan O.V. Is there amber in the Middle Urals? *Vestnik of Geosciences.* 2020. N 6 (306), p. 27-30 (in Russian). DOI: 10.19110/geov.2020.6.5
13. Martirosyan O.V. "Immature amber" – krantzite – in the Middle Urals. *Vestnik of Geosciences.* 2022. N 3 (327), p. 25-30 (in Russian). DOI: 10.19110/geov.2022.3.3
14. Karpinskii A.P. Collected Works. In 4 volumes. Vol. 4. Geological Investigations on the Eastern Slope of the Urals. Moscow: Izd-vo Akademii nauk SSSR, 1949, p. 464.
15. Gosudarstvennaya geologicheskaya karta Rossiiskoi Federatsii. Masshtab 1:100000 (trete pokolenie). List O-41 – Ekaterinburg. Obyasnitelnaya zapiska. St.Petersburg: Kartfabrika VSEGEI, 2011, p. 492.
16. Krylov A.V., Vasiliev E.A., Trikolidi F.A. et al. The amber and jet of the Russian Arctic: the new finds and perspectives of the practice using. *Relief and quaternary deposits of the Arctic, Subarctic and North-West Russia*. 2021. Iss. 8, p. 125-135 (in Russian). DOI: 10.24412/2687-1092-2021-8-125-135
17. Martirosyan O.V. Fossil resins of the Russian Arctic: to the history of study. *Zapiski Rossiiskogo mineralogicheskogo obshchestva.* 2020. Vol. 149. N 1, p. 131-138 (in Russian). DOI: 10.31857/S0869605520010098

This is an open access article under the CC BY 4.0 license

18. Martirosyan O.V., Bogdasarov M.A. Varieties of fossil resins of South Sakhalin and their molecular composition. *Zapiski Rossiiskogo mineralogicheskogo obshchestva.* 2024. Vol. 153. N 3, p. 97-112 (in Russian). DOI: 10.31857/S0869605524030061

19. Wolfe A.P., Csank A.Z., Reyes A.V. et al. Pristine Early Eocene Wood Buried Deeply in Kimberlite from Northern Canada. *PLOS ONE*. 2012. Vol. 7(9). N e45537. DOI: 10.1371/journal.pone.0045537

20. Wolfe A.P., McKellar R.C., Tappert R. et al. Bitterfeld amber is not Baltic amber: Three geochemical tests and further constraints on the botanical affinities of succinate. *Review of Palaeobotany and Palynology*. 2016. Vol. 225, p. 21-32. DOI: 10.1016/j.revpalbo.2015.11.002

21. Seyfullah L.J., Szwedo J., Schmidt A.R., Prestianni C. Chemical and palaeoentomological evidence of a relationship between early Eocene Belgian and Oise (France) ambers. *Scientific Reports*. 2024. Vol. 14. N 13705. DOI: 10.1038/s41598-024-64286-z

22. Anderson K.B., Winans R.E., Botto R.E. The nature and fate of natural resins in the geosphere–II. Identification, classification and nomenclature of resinites. *Organic Geochemistry*. 1992. Vol. 18. Iss. 6, p. 829-841. DOI: 10.1016/0146-6380(92)90051-X

23. Poulin J., Helwig K. Inside amber: New insights into the macromolecular structure of Class Ib resinite. *Organic Geochemistry*. 2015. Vol. 86, p. 94-106. DOI: 10.1016/j.orggeochem.2015.05.009

24. Bogdasarov M.A. Mesozoic fossil resins of Northern Eurasia. *Vestnik IG Komi SC UB RAS.* 2017. N 7, p. 3-11 (in Russian). DOI: 10.19110/2221-1381-2017-7-3-11

25. Savkevich S.S., Popkova T.N. New Data on the "Amber" from the Right Bank of the Kheta and Khatanga Rivers. *Doklady Akademii nauk SSSR*. 1973. Vol. 208. N 2, p. 427-429.

26. Kosmowska-Ceranowicz B. Infrared spectra atlas of fossil resins, subfossil resing and selected imitations of amber. Infrared Spectra of the World's Resins. Holotype Characteristics. Atlas. Warszawa: Polska Akademia Nauk Muzeum Ziemi w Warszawie, 2015, p. 4-214.

27. Anderson K.B. The nature and fate of natural resins in the geosphere–IV. Middle and Upper Cretaceous amber from the Taimyr Peninsula, Siberia–evidence for a new form of polylabdanoid of resinite and revision of the classification of Class I resinites. *Organic Geochemistry*. 1994. Vol. 21. Iss. 2, p. 209-212. DOI: 10.1016/0146-6380(94)90155-4

28. Wimmer R., Galle H., Wagner-Wysiecka E. Retinit im mittleren Geiseltal und in Nordwestsachsen. *Mauritiana (Altenburg)*. 2019. Band 37. S. 32-41 (in German).

29. Shaks I.A., Faizullina E.M. Infrared Spectra of Fossil Organic Matter. Leningrad: Nedra, 1974, p. 131.

30. Wolfe A.P., Tappert R., Muehlenbachs K. et al. A new proposal concerning the botanical origin of Baltic amber. *Proceedings of Royal Society B. Biological Sciences*. 2009. Vol. 276. Iss. 1672, p. 3403-3412. DOI: 10.1098/rspb.2009.0806

31. Vavra N. Mineral names used for fossil resins, subfossil resins and similar materials. Infrared Spectra of the World's Resins. Holotype Characteristics. Atlas. Warszawa: Polska Akademia Nauk Muzeum Ziemi w Warszawie, 2015, p. 215-280.

32. Martirosyan O.V., Bogdasarov M.A. Varieties of cretaceous fossil resins of the Caucasus and features of their molecular structure. *Zapiski Rossiiskogo mineralogicheskogo obshchestva.* 2022. Vol. 151. N 1, p. 92-104 (in Russian). DOI: 10.31857/S0869605521060058

33. Bogdasarov M.A., Rudko G.I. The Geological-Evolutional Concept of Resin Genesis. *Journal of Geological Resource and Engineering*. 2018. Vol. 6. Iss. 3, p. 112-123. DOI: 10.17265/2328-2193/2018.03.003

34. Beck C.W. Spectroscopic investigations of Amber. *Applied Spectroscopy Reviews*. 1986. Vol. 22. Iss. 1, p. 57-110. DOI: 10.1080/05704928608060438

35. Tappert R., McKellar R.C., Wolfe A.P. et al. Stable carbon isotopes of C3 plant resins and ambers record changes in atmospheric oxygen since the Triassic. *Geochimica et Cosmochimica Acta*. 2013. Vol. 121, p. 240-262. DOI: 10.1016/j.gca.2013.07.011

36. Anderson K.B., LePage B.A. Analysis of Fossil Resins from Axel Heiberg Island, Canadian Arctic. Amber, Resinite, and Fossil Resins. American Chemical Society, 1995, p. 170-192. DOI: 10.1021/bk-1995-0617.ch009

37. Mays C., Coward A.J., O'Dell L.A., Tappert R. The botanical provenance and taphonomy of Late Cretaceous Chatham amber, Chatham Islands, New Zealand. *Review of Palaeobotany and Palynology*. 2019. Vol. 260, p. 16-26. DOI: 10.1016/j.revpalbo.2018.08.004

38. Tappert R., Wolfe A.P., McKellar R.C. et al. Characterizing Modern and Fossil Gymnosperm Exudates Using Micro-Fourier Transform Infrared Spectroscopy. *International Journal of Plant Sciences*. 2011. Vol. 172. N 1, p. 120-138. DOI: 10.1086/657277

39. Poulin J., Helwig K. Class Id resinite from Canada: A new sub-class containing succinic acid. *Organic Geochemistry*. 2012. Vol. 44, p. 37-44. DOI: 10.1016/j.orggeochem.2011.11.012

40. Poulin J., Helwig K. Inside Amber: The Structural Role of Succinic Acid in Class Ia and Class Id Resinite. *Analytical Chemistry*. 2014. Vol. 86. Iss. 15, p. 7428-7435. DOI: 10.1021/ac501073k

***Authors*: Pavel I. Alekseev,** *Candidate of Biological Sciences, Senior Researcher* (*Empress Catherine II Saint Petersburg Mining University, Saint Petersburg, Russia*), *Alexeev_PI@spmi.pers.ru, https://orcid.org/0000-0002-3741-355X*, **Evgenii A. Vasilev,** *Doctor of Geological and Mineralogical Sciences, Leading Researcher* (*Empress Catherine II Saint Petersburg Mining University, Saint Petersburg, Russia*), *https://orcid.org/0000-0003-2216-0956*.

The authors declare no conflict of interests.

This is an open access article under the CC BY 4.0 license

ISSN 2411-3336; e-ISSN 2541-9404

JOURNAL OF MINING INSTITUTE
Zapiski Gornogo instituta
Journal homepage: pmi.spmi.ru

Research article
Geotechnical Engineering and Engineering Geology

Design improvement of a near-bit reaming-ejection device for enhancing rock-breaking efficiency during well construction

Dmitrii A. Boreiko[1]✉, **Nikolai D. Tskhadaya**[1], **Dmitrii Yu. Serikov**[2], **Vyacheslav A. Khlamov**[3]
[1] *Empress Catherine II Saint Petersburg Mining University, Saint Petersburg, Russia*
[2] *National University of Oil and Gas "Gubkin Unversity", Moscow, Russia*
[3] *Ukhta State Technical University, Ukhta, Komi Republic, Russia*

How to cite this article: Boreiko D.A., Tskhadaya N.D., Serikov D.Yu., Khlamov V.A. Design improvement of a near-bit reaming-ejection device for enhancing rock-breaking efficiency during well construction. Journal of Mining Institute. 2026. Vol. 280, p. 27-36.

Abstract
This research investigates the operational performance of ejection systems integrated into drilling rock-breaking assemblies. The object of the study is a near-bit reaming-ejection device (RED), which is installed in the bottom hole assembly (BHA) and is intended to improve bottom hole cleaning efficiency during drilling through the operation of integrated ejection systems that ensure effective entrainment of drilling fluid jets from the near-bit region enriched with drilled cuttings and fragmented rock. The subject of the study is the flow of drilling fluid through ejection nozzles with different cross-sectional geometries, which determine the hydrodynamic characteristics of the fluid flow. The design of the near-bit RED combines two systems – a drilling reamer and ejection devices – which makes it possible to reduce the space occupied within the BHA, improve borehole diameter stabilization, and enhance bottom hole cleaning efficiency simultaneously. Computational fluid dynamics simulations of ejection nozzles with various cross-sectional geometries (circle, triangle, square, pentagon, regular hexagon, and specially oriented hexagon) showed that the increase in the velocity of the fluid-flow core issuing from the nozzle model with a specially oriented hexagonal cross-section amounted to approximately 4.5 % compared with the baseline design (circular cross-section) and approximately 5.5 % compared with the remaining models. It was found that the nozzle design with a specially oriented hexagonal cross-section enables the fluid flow to be directed at an angle toward the borehole wall. The results of additional computational fluid dynamic simulations made it possible to establish a relationship between the angle of deviation of the drilling fluid flow from the vertical and the value of the control angle of the specially oriented hexagonal cross-section of the ejection nozzle. This relationship provides an opportunity for purposeful control of the drilling fluid trajectory through modification of the nozzle geometry. This capability may be used for additional sealing of borehole walls without significant deviation from the designed borehole diameter.

Keywords
reaming-ejection device; ejection system; computational fluid dynamics; ejection nozzle; drilling efficiency; well drilling; cross-sectional geometry; bottom hole cleaning; drilling fluid

Funding
None.

Received: 26.02.2026 ***Accepted: 28.04.2026*** ***Online: 22.06.2026*** ***Published: 10.09.2026***

Introduction

A key factor in improving the productivity and service life of drilling tools is the development of rational designs, engineering solutions, and methods for their reinforcement [1, 2]. However, regardless of the type of drilling tool used and the characteristics of the drilling equipment employed, bottom hole cleaning is of particular importance during drilling operations. This technological process is a key factor in the successful execution of drilling operations, since it performs a number of

This is an open access article under the CC BY 4.0 license

essential functions, including the prevention of drilling-related complications (bottom hole cuttings accumulation, tool wear, increased material and financial costs, etc.) [3-5]. At the same time, the efficiency of drilling tools largely depends on the successful operation of the circulation system, which plays one of the key roles in the well drilling process [6, 7]. Under modern conditions, characterized by a tendency toward increasing well depths and more complex geological conditions, a properly designed circulation system becomes critically important. It not only improves drilling efficiency but also significantly minimizes the likelihood of technological problems associated with the formation of stagnant zones and deterioration of reservoir parameters [8, 9]. Imperfections in the design of circulation units contribute to increased wear [10, 11], thereby affecting the rate of penetration of drilling tools, resulting in greater deviations from the designed wellbore diameter and potentially having a negative impact on the stress-strain state of the drill string.

The drilling process is influenced by numerous factors, including geological conditions (rock and reservoir properties), equipment and tools (drill bits, circulation systems), technological parameters (rotational speed, drilling fluid flow rate, etc.), physicochemical properties of the drilling fluid, and other factors (human factors, weather conditions, etc.) [12, 13]. Since geological features of the formation cannot be controlled, adaptability and innovation in rock-breaking tool designs, as well as in annular space cleaning technologies, become key factors for increasing drilling efficiency [14]. In this regard, more advanced designs of rock-breaking tools and bottom hole cleaning systems make it possible to optimize drilling and cleaning processes while maintaining high well productivity.

A key component of a roller-cone drill bit is the circulation system, the operability and durability of which critically affect the efficiency of the entire rock-breaking process during well drilling [15, 16]. Conventional bottom hole cleaning schemes for roller-cone bits have long been known and are classified into three types: side cleaning, central cleaning, and combined cleaning [17, 18]. Modern trends in drilling-tool design are aimed at improving these systems, further emphasizing their importance in enhancing drilling performance [7, 19, 20]. A wide range of specialized cleaning-system designs for roller-cone bits has been developed to increase their efficiency and optimize the transportation of drilled cuttings from the bottom hole area to the near-bit region and subsequently to the wellhead [21, 22]. All of these innovations are intended to ensure more efficient distribution and utilization of the kinetic energy of the drilling fluid.

Existing circulation systems of roller-cone drill bits are characterized by several design shortcomings that negatively affect bottom hole cleaning quality and the efficiency of drilled-cuttings removal from the operating zone, thereby increasing tool wear. The main disadvantages are as follows [13, 20, 23]:

• circulation-system designs that are unsuitable for specific drilling conditions and well characteristics, such as improper distribution, orientation, or shape of nozzles that fail to provide efficient direction of drilling fluid flow;

• drilling fluid velocities inside the nozzle exceeding recommended values, which may lead to erosive damage of circulation channels and roller-cone-bit components;

• insufficient efficiency of drilled-cuttings removal from the operating zone of the roller cones into the near-bit annular space.

Considering the evolution of drilling-tool designs and the experience gained from implementing various innovative solutions, these problems can only be solved through a comprehensive approach that includes both optimization of cleaning-system operation and improvement of its functionality (for example, the use of asymmetric circulation schemes, application of the ejection principle, installation of vortex chambers in drill bits, implementation of pulse-cleaning systems, and other methods) [24, 25].

This is an open access article under the CC BY 4.0 license

To reduce the negative impact of shielding effects created by high-velocity jets during drilling, methods involving modifications to drill-bit designs are widely used [26, 27]. These modifications include the creation of openings in the bit legs for efficient removal of drilled cuttings from the contact zone between the roller-cone teeth, the bottom hole, and the borehole wall. In particular, the bit legs located directly above the bearings are equipped with channels connecting the area near the bit-bottom hole contact zone with the near-bit annular space. However, according to scientific studies, this approach allows the removal of only up to 11 % of the drilled cuttings through these openings [17, 28], indicating limited efficiency and suggesting that the remaining cuttings may undergo secondary grinding by the drilling tool.

Thus, the development and improvement of equipment intended to enhance bottom hole cleaning efficiency is an important task that contributes to increasing the efficiency of rock destruction during the construction of oil and gas wells.

Previous studies have demonstrated the potential and effectiveness of integrating an ejector pump into a drilling reaming device to improve rock-breaking efficiency and wellbore cleaning [29]. The reaming-ejection device (RED) is capable of simultaneously reaming the borehole wall and creating an ejection effect that entrains drilling fluid containing drilled cuttings into the near-bit region. The device is integrated into the body of a standard blade-type reamer of modified design, allowing redistribution of drilling fluid flows and directing them upward through the annular space [30] (Fig.1).

The near-bit RED consists of a hollow cylindrical body equipped with a system of reaming blades of different lengths. All blades are reinforced with carbide elements, while the shorter blades contain special openings of two configurations (horizontal and vertical) into which special nozzles are installed. The pressure-distribution system operates due to a throttling nozzle located in the lower part of the internal circulation channel. An important parameter is the ratio between the area of the throttling nozzle and the total area of all ejection nozzles, which prevents insufficient cooling of the drilling tool.

The operation of the device begins when the drill string rotates together with the drill bit 11. During operation, the rotating roller cones interact with the bottom hole, their cutting structure 15 destroys the rock, and the reinforced inserts of the reamer stabilize the borehole wall. Bottom hole cleaning is achieved through circulation of drilling fluid through the drill pipes, the internal channels of the RED 8, and the drilling tool 10, thereby ensuring removal of cuttings from the rock-destruction zone. The fluid passing through channel 8 encounters resistance from the throttling nozzle 9, which creates the pressure required within the system and directs the flow into the ejection channels. The operating principle of the RED is based on the Bernoulli effect, according to which an increase in fluid-flow velocity results in a decrease in static pressure within the

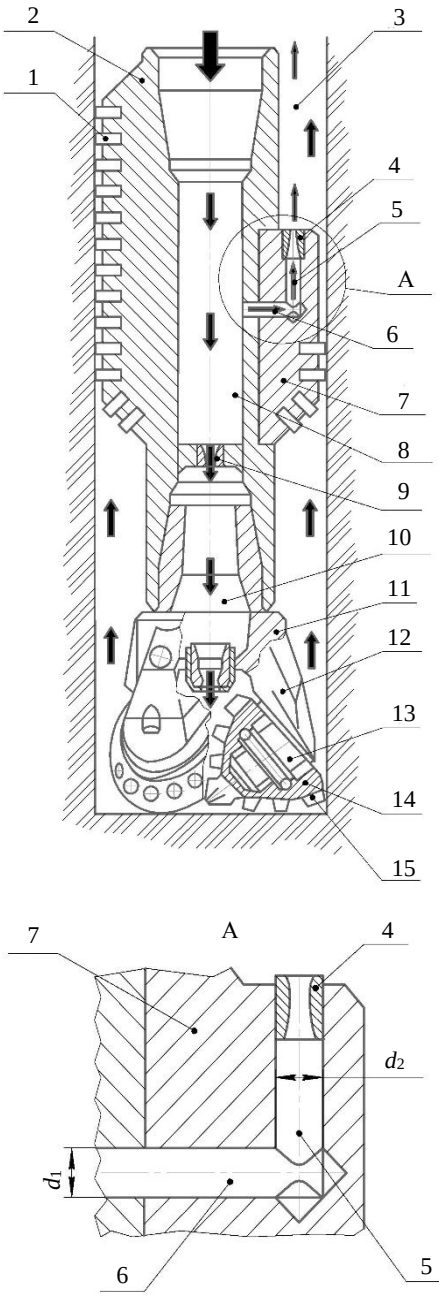


Fig.1. Design and operating principle of the drilling reaming-ejection device [30]

1 – carbide-reinforced wear-resistant inserts; 2 – body; 3 – ejection chamber; 4 – ejection nozzle; 5, 6 – flow channels; 7 – ejection blade; 8 – central drilling fluid circulation channel; 9 – throttling nozzle; 10 – rock-breaking tool; 11 – roller-cone drill bit; 12 – bit legs; 13 – journals; 14 – roller cones; 15 – teeths

This is an open access article under the CC BY 4.0 license

mixing zone. The drilling fluid enters through the ejection nozzle 4 into a specially formed chamber bounded by the borehole wall, the reamer body, and two adjacent long blades that are part of the RED body. In this zone, high-velocity fluid jets from nozzles 4 mix with slower upward flows containing rock particles and drilled cuttings transported from the bottom hole through the spaces between the blades into the ejection chamber 3. Interaction of these flows leads to the formation of an integrated ejected flow characterized by significantly higher velocity and lifting capacity compared with the original flow. At the same time, a low-pressure zone is formed in the near-bottom hole region, creating favorable conditions for efficient rock destruction. This effect is achieved through a reduction in the differential pressure acting on the bottom hole, which significantly facilitates the drilling process. These processes reduce the probability of secondary grinding of drilled rock and decrease the wear intensity of drilling tools.

It is well known that increasing the contact area between the drilling fluid jet and the side surface of the nozzle can improve the removal of drilled cuttings to the surface and increase the performance of nozzles used in rock-breaking tools. This is because a larger contact area can improve the efficiency of energy transfer from the jet to the drilled rock by increasing the jet velocity. Analysis of the calculated data confirms the evident advantage of a hexagonal nozzle profile in the process of drilling fluid jet formation. The design feature of this type of nozzle is that it generates a fluid flow with a significantly larger contact area with the working medium in the near-bottom hole zone compared with conventional circular nozzles. Such a design provides more effective interaction between the drilling fluid flow and the hydraulic environment of the bottom hole [9, 28].

This design solution ensures a more efficient involvement of large volumes of bottom hole hydraulic medium containing drilled cuttings in the circulation process. Consequently, the quality of cleaning of both the drilling tool and the entire near-bottom hole zone is improved. Therefore, the correct selection of nozzle type 4 and cross-sectional geometry directly affects the density and velocity of the emerging jet, which ultimately determine the operating efficiency of the RED.

Methods

To ensure a rational and well-founded selection of the optimal design of the RED ejection nozzles, this study proposes an investigation and comparison of cross-sections of different geometries (circular, triangular, square, pentagonal, regular hexagonal, and specially oriented hexagonal) using Computational Fluid Dynamics (CFD) simulation, which is one of the most accurate methods and has been validated in a sufficient number of similar applied studies [22, 31, 32]. For a detailed investigation of this issue, the design parameters of ejection nozzles with cross-sections of different geometric shapes were analyzed: circle, triangle, square, pentagon, regular hexagon, and specially oriented hexagon. The main initial condition of the simulation was the equality of the nozzle cross-sectional areas at the inlet and outlet, as well as equal nozzle height and outer cylinder diameter.

For numerical simulation of hydrodynamic processes in the CFD software package, the following initial system parameters were specified: working volume 0.017 m^3; distance between the outlet nozzle and the boundary of the computational domain 0.4 m; fluid flow rate at the nozzle inlet 0.03 m^3/s; process medium – liquid phase with a density of 1200 kg/m^3; outlet pressure 0.2 MPa.

The computational domain used for the simulation is shown in Fig.2, *a*, while the geometric shapes of the modeled cross-sections are presented in Fig.2, *b*. The dimensions of the computational domain correspond to the overall dimensions of the ejection chamber formed by the borehole wall and the adjacent long blades of the RED body. The lower plane of the computational domain coincides with the nozzle inlet cross-section.

A submerged vertical jet of liquid with a density of 1200 kg/m^3 issuing from the nozzle was simulated. An ejection nozzle with a circular cross-section was selected as the reference case for analysis

This is an open access article under the CC BY 4.0 license

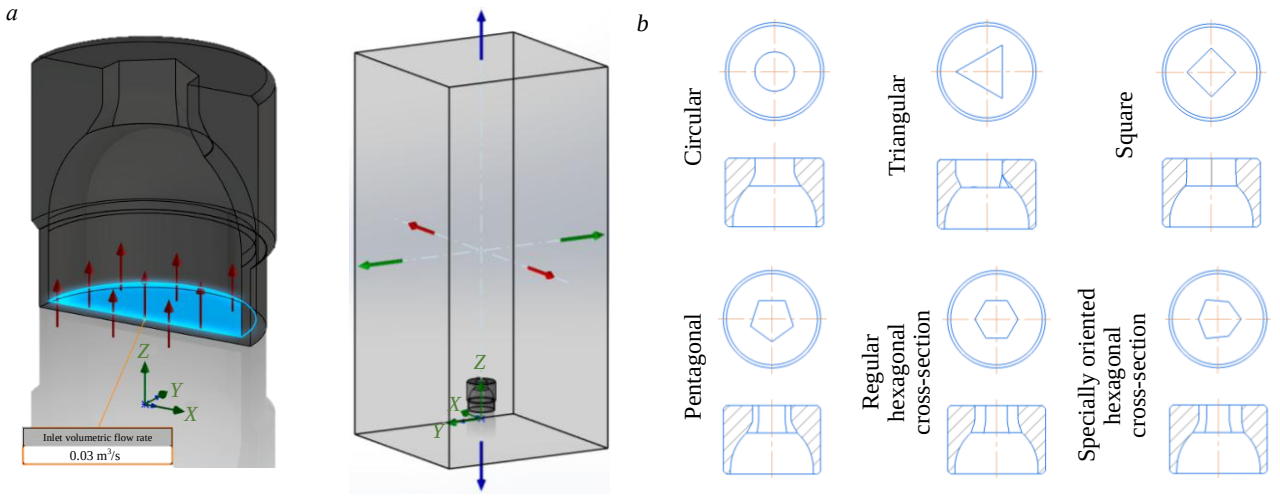


Fig.2. Input data for the simulation of fluid flow through an ejection nozzle:
a – computational model and simulation domain; *b* – geometries of the modeled nozzle cross-sections

because the prototype of the RED ejection nozzles is the hydraulic monitor nozzle of drilling rock-breaking tools, which predetermines their future interchangeability.

It is important to note the following limitations of the model:

• the model does not account for drill-string rotation effects and the associated dynamic loads;

• idealized boundary conditions were adopted;

• dynamic changes in the rheological properties of the drilling fluid during actual drilling operations were not considered;

• the results were obtained for steady-state conditions, whereas real drilling is characterized by an inherently unsteady process.

These limitations should be taken into account when interpreting the results and applying them in practice. Additional studies are recommended to refine the obtained relationships under actual drilling conditions.

The geometric feature of the specially oriented hexagonal cross-section is that it consists of three angles of one size ($\beta_1 = \beta_2 = \beta_3$) and three angles of another, smaller, size ($\alpha_1 = \alpha_2 = \alpha_3$) (Fig.3). In the design of the drilling RED, the ejection nozzle with this cross-section is fixed against rotation relative to the ejection blade. One of the vertices formed by the smaller angles is oriented toward the RED axis, while the second is directed toward the leading face of one adjacent long blade. The third vertex formed by the smaller angles is directed toward the trailing face of the other adjacent long blade [30].

Discussion of the results

The main indicators characterizing the efficiency of ejection nozzles are the velocity and height of the core of the drilling fluid jet issuing from the nozzle. Among these parameters, flow velocity is the most important, since it directly affects the occurrence and intensity of the ejection (suction) effect, which draws fluid from the operating zone of the drilling tool into the near-bit region and subsequently accelerates it upward through the annular space, thereby improving cleaning efficiency [15, 17]. The simulation results are presented in Fig.4 as a comparative analysis of the velocity and height of the jet core for nozzles with the investigated cross-sectional geometries.

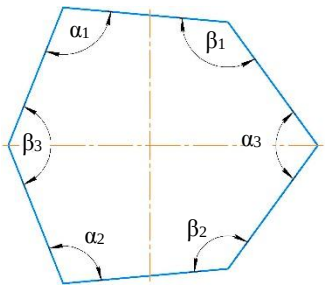


Fig.3. Geometric parameters of specially oriented hexagonal cross-section

This is an open access article under the CC BY 4.0 license

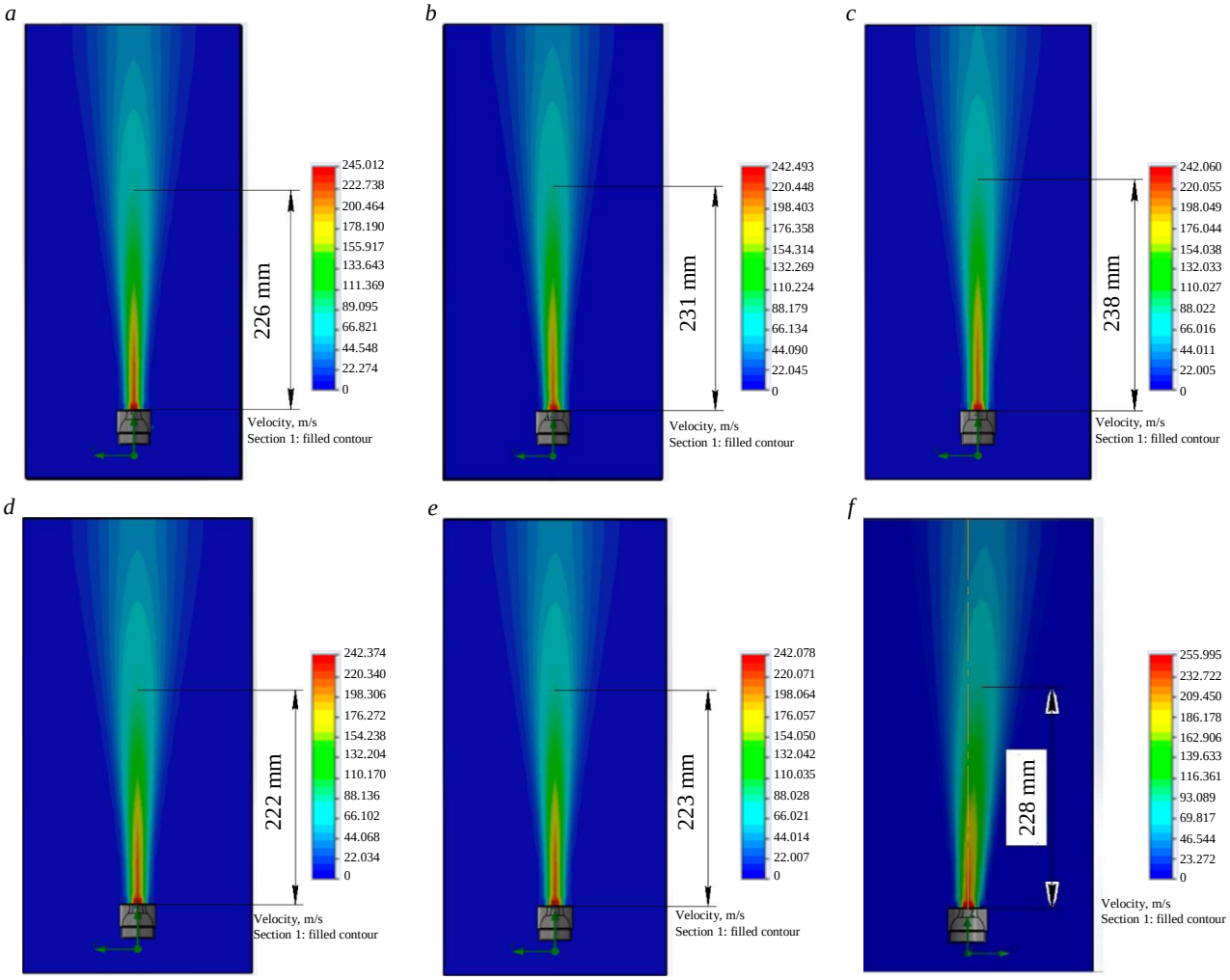


Fig.4. Results of CFD simulation of drilling fluid flow through ejection nozzles with different cross-sectional geometries (jet-core velocity at the end of the potential core, m/s / maximum height of the main flow, mm): *a* – circular (111/226); *b* – triangular (110/231); *c* – square (110/238); *d* – pentagonal (110/222); *e* – regular hexagonal (110/223); *f* – specially oriented hexagonal (116/228)

All nozzles with different cross-sectional geometries, except for the specially oriented hexagonal nozzle, exhibited the same flow velocity. The increase in the velocity of the fluid-flow core issuing from the nozzle model with a specially oriented hexagonal cross-section amounted to approximately 4.5 % compared with the baseline design (circular cross-section) and approximately 5.5 % compared with the remaining models. This contributes to an increase in the velocity of the integrated mixed flow and improves the efficiency of drilled-cuttings removal from the bit operating zone, which in turn enhances bit reliability by reducing the probability of secondary rock grinding. Therefore, it can be concluded that the drilling RED equipped with ejection nozzles having a specially oriented hexagonal cross-section will operate more efficiently than the baseline circular nozzle and the other investigated designs.

As a result of the simulations, it was established that the nozzle with a specially oriented hexagonal cross-section deflected the fluid flow from the vertical by 2° (Fig.4, *f*). A detailed analysis showed that this deviation occurred toward one of the three smaller angles, α_3, whose value was 105°50′. This observation prompted an additional investigation in which nozzles with different values of α_3 (85°, 95°, 115°, and 125°) were modeled while maintaining the principal simulation condition, namely, equality of the inlet and outlet cross-sectional areas. The jet-deflection angle from the vertical was designated as β. The simulation results for fluid flow through asymmetric hexagonal cross-sections with different α_3 values are presented in Fig.5.

This is an open access article under the CC BY 4.0 license

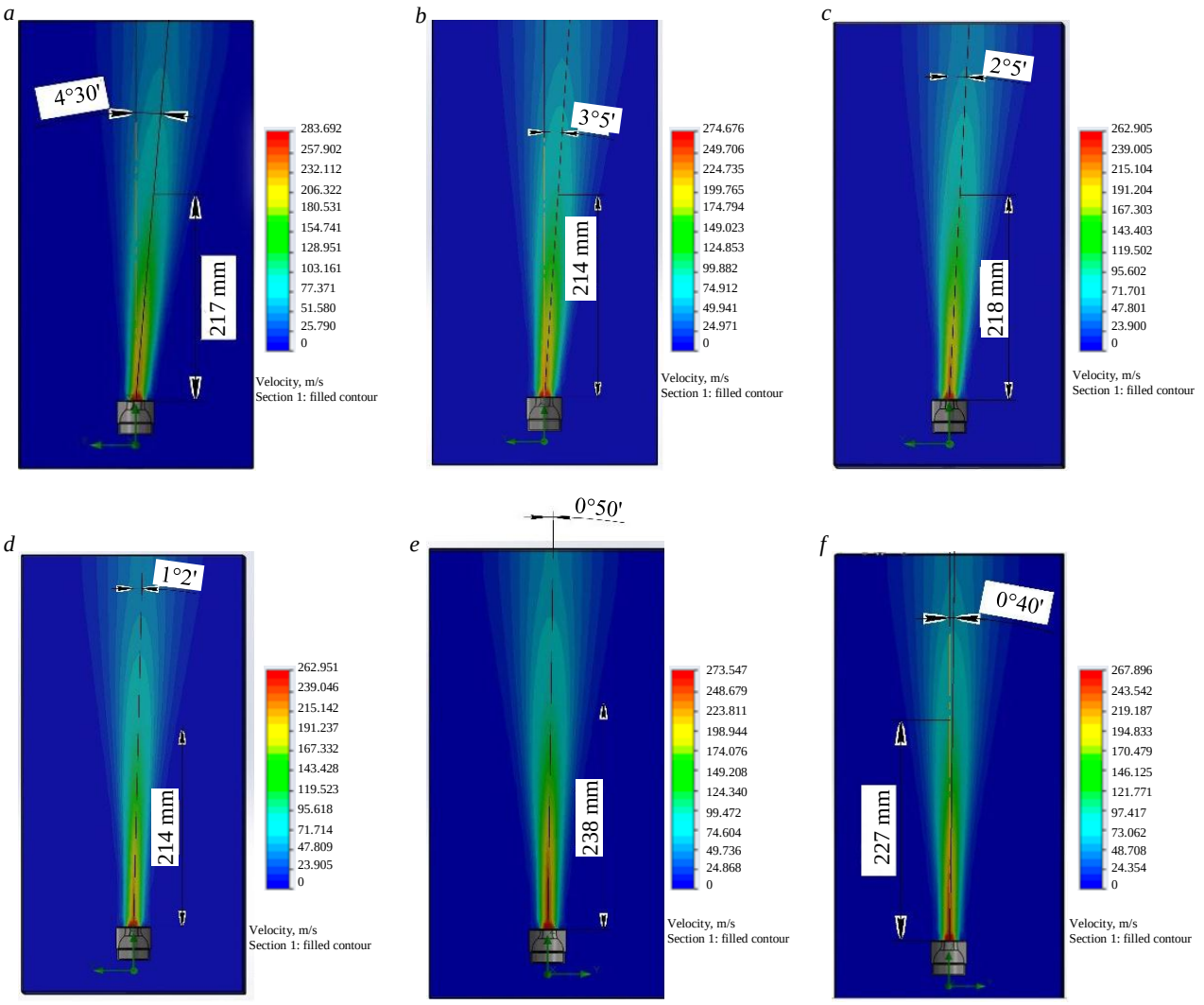


Fig.5. Results of drilling fluid flow simulation through an ejection nozzle with a specially oriented hexagonal cross-section at different values of α_3: *a* – 85°; *b* – 95°; *c* – 100°; *d* – 110°; *e* – 115°; *f* – 125°

Based on the additional data obtained, a graph was constructed showing the relationship between the deviation angle β of the drilling fluid flow from the vertical and the angle α_3 of the specially oriented hexagonal ejection nozzle (Fig.6). The following relationship was established between the

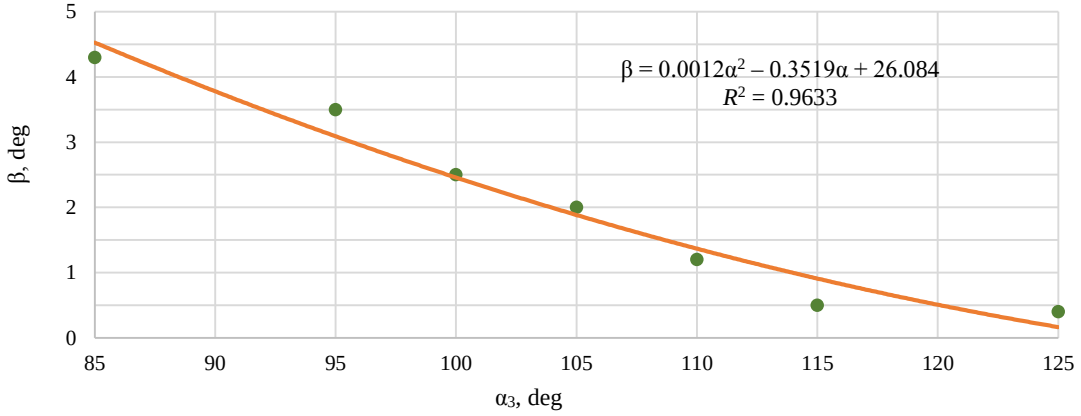


Fig.6. Dependence of the drilling fluid flow deviation angle β from the vertical on the control angle α_3 of the specially oriented hexagonal cross-section of the ejection nozzle

This is an open access article under the CC BY 4.0 license

deviation angle β of the drilling fluid flow and the control angle α_3 of the specially oriented hexagonal cross-section: $\beta = 0.0012\alpha_3^2 - 0.3519\alpha_3 + 26.084$. This relationship indicates that as the angle α_3 increases, the deviation angle β also increases, confirming the possibility of purposeful control of the drilling fluid flow direction through modification of nozzle geometry. The coefficient of determination $R^2 = 0.9633$ indicates a high degree of reliability of the established relationship. The obtained coefficient of determination falls within the range typical of precise engineering measurements, demonstrating the high reliability of the relationship and the possibility of its practical application.

The physical meaning of this phenomenon can be explained as follows. When the nozzle geometry changes (through variation of the control angle α_3), the flow pattern of the fluid also changes. This leads to a redistribution of flow velocities, changes in the pressure distribution within the system, and the emergence of lateral forces that deflect the flow. The quadratic relationship indicates that the influence of the control angle on flow deviation is nonlinear: at small values of α_3, its effect on β is relatively weak, whereas with increasing α_3 the deflection effect increases nonlinearly. Thus, for different drilling conditions, optimal angle ranges can be identified in which maximum flow deflection is achieved.

Conclusion

Based on the conducted studies, it was established that the increase in the velocity of the drilling fluid flow core issuing from the nozzle model with a specially oriented hexagonal cross-section amounted to approximately 4.5 % compared with the baseline design (circular cross-section) and approximately 5.5 % compared with the remaining models. In addition, it was found that the nozzle design with a specially oriented hexagonal cross-section also makes it possible to direct the fluid flow at an angle toward the borehole wall.

The results of the additional numerical simulations made it possible to establish a relationship between the deviation angle of the drilling fluid flow from the vertical and the control angle of the specially oriented hexagonal cross-section of the ejection nozzle: $\beta = 0.0012\alpha_3^2 - 0.3519\alpha_3 + 26.084$. This relationship provides an opportunity for purposeful control of the drilling fluid trajectory through modification of nozzle geometry. In practice, this capability may be used for additional sealing of borehole walls without significant deviation from the designed borehole diameter. However, to increase the efficiency of this process, it is necessary to additionally employ modern innovative drilling fluids, such as those described in [33, 34].

As a result of the conducted study, relationships governing the influence of ejection-nozzle geometry on the hydrodynamic characteristics of drilling fluid flow, as well as on the possibility of influencing the flow trajectory in a controlled manner, were established. These findings expand the scientific understanding of ejection processes in rock-breaking drilling tools.

The obtained results create prerequisites for further research aimed at optimizing the design parameters of ejection nozzles (including hydraulic monitor nozzles of drill bits), investigating the influence of new geometric parameters on the efficiency of circulation systems as a whole, and developing methodologies for selecting optimal parameters for specific drilling conditions. In the future, these developments may be of considerable importance for the advancement of well drilling technologies and may be applied in the design of modern drilling tools to improve rock-breaking efficiency and the quality of bottom hole cleaning.

REFERENCES

1. Alieva L., Zhukov I.A. Upgrading rotary-percussion drilling of high-strength rocks by improving the structure of a rock-crushing blade-free tool. *Sustainable Development of Mountain Territories.* 2024. Vol. 16. N 4 (62), p. 1681-1694 (in Russian). DOI: 10.21177/1998-4502-2024-16-4-1681-1694

2. Afanasev A., Simisinov D., Zubov V. Modeling of gear production in loose-abrasive machining technique. *Materials Today: Proceedings*. 2019. Vol. 19. Part 5, p. 2358-2360. DOI: 10.1016/j.matpr.2019.07.693

This is an open access article under the CC BY 4.0 license

3. Xiaohua Zhu, Keyu Shen, Bo Li. Investigation: Cutting Transport Mechanism in Inclined Well Section under Pulsed Drilling Fluid Action. *Energies*. 2021. Vol. 14. Iss. 8. N 2141. DOI: 10.3390/en14082141

4. Al-Rubaii M., Al-Shargabi M., Al-Shehri D. A Novel Automated Model for Evaluation of the Efficiency of Hole Cleaning Conditions during Drilling Operations. *Applied Sciences*. 2023. Vol. 13. Iss. 11. N 6464. DOI: 10.3390/app13116464

5. Rastvorova I.I., Dvoynikov V.M. Analysis of Mathematical Models for Developing a Methodology to Measure Energy and Spatial Characteristics of Axial Impact During Well Drilling. *WSEAS Transactions on Applied and Theoretical Mechanics*. 2025. Vol. 20, p. 130-137. DOI: 10.37394/232011.2025.20.15

6. Xiaohua Zhu, Keyu Shen, Bo Li, Yanxin Lv. Cuttings Transport Using Pulsed Drilling Fluid in the Horizontal Section of the Slim-Hole: An Experimental and Numerical Simulation Study. *Energies*. 2019. Vol. 12. Iss. 20. N 3939. DOI: 10.3390/en12203939

7. Povalikhin A.S., Bliznyukov V.Yu. Drilling technology features and the preparation of vertical borehole to the running of casing of large diameter. *Inzhener-neftyanik*. 2017. N 1, p. 5-12 (in Russian).

8. Xiaoming Li, Yuyue Fan, Jiahua Li et al. Research on the Influence of a Cuttings Bed on Drill String Friction Torque in Horizontal Well Sections. *Processes*. 2022. Vol. 10. Iss. 10. N 2061. DOI: 10.3390/pr10102061

9. Kunshin A.A., Buslaev G.V., Reich M. et al. Numerical Simulation of Nonlinear Processes in the "Thruster–Downhole Motor–Bit" System While Extended Reach Well Drilling. *Energies*. 2023. Vol. 16. Iss. 9. N 3759. DOI: 10.3390/en16093759

10. Šporin J., Balaško T., Mrvar P. et al. Change of the Properties of Steel Material of the Roller Cone Bit Due to the Influence of the Drilling Operational Parameters and Rock Properties. *Energies*. 2020. Vol. 13. Iss. 22. N 5949. DOI: 10.3390/en13225949

11. Ovchinnikov V.P., Ryabukha A.V., Rozhkova O.V., Listak M.V. Causes and types of accidents with rock-cutting tools (by the example of well N 307 of the Kopan field). *Bulletin of the Association of Drilling Contractors*. 2022. N 3, p. 18-22 (in Russian).

12. Boreiko D.A., Lutoev A.A., Serikov D.Yu. Theoretical studies on the nature and conditions of interaction of heel and peripheral nose cones of offset roller cone bits with a bottom hole. *Mining Science and Technology*. 2022. Vol. 7. N 3, p. 231-239. DOI: 10.17073/2500-0632-2022-3-231-239

13. Litvinenko V.S., Dvoinikov M.V. Methodology for determining the parameters of drilling mode for directional straight sections of well using screw downhole motors. *Journal of Mining Institute*. 2020. Vol. 241, p. 105-112. DOI: 10.31897/PMI.2020.1.105

14. Tretyak A.Ya., Popov V.V., Grossu A.N., Borisov K.A. Innovative approaches to designing highly efficient rock-breaking tool. *Mining Informational and Analytical Bulletin*. 2017. N 8, p. 225-230 (in Russian). DOI: 10.25018/0236-1493-2017-8-0-225-230

15. Rawal R., Karmakar N.C., Sharma S.K. Optimization of Fluid Flushing Rate: A Study on Laboratory Drilling Setup. *Journal of the Institution of Engineers (India): Series C*. 2022. Vol. 103. Iss. 4, p. 985-990. DOI: 10.1007/s40032-022-00809-9

16. Toshniyozov L.G., Toshov J.B. Theoretical and experimental research into process of packing in drilling. *Mining Informational and Analytical Bulletin*. 2019. N 11, p. 139-151 (in Russian). DOI: 10.25018/0236-1493-2019-11-0-139-151

17. Bogomolov R.M., Panin N.M. Improvement of Components of Roller-Cone Drill Bit Circulation Systems. *Sfera. Neft i Gaz*. 2021. N 3 (82), p. 52-57 (in Russian).

18. Serikov D.Yu., Blinkov O.G., Panin N.M., Shigin A.O. Improvement of central washing of a rolling drilling tool. *Equipment and technologies for oil and gas complex*. 2019. N 3 (111), p. 23-27 (in Russian). DOI: 10.33285/1999-6934-2019-3(111)-23-27

19. Povalikhin A.S., Bliznyukov V.Yu. Selective control of a drill-pipe casing string when drilling a horizontal well. *Construction of oil and gas wells on land and sea*. 2019. N 5, p. 5-10 (in Russian). DOI: 10.30713/0130-3872-2019-5-5-10

20. Shigin A.O., Gilev A.V., Shigina A.A. Stresses and stability of rolling cutter bits in complex-structure rock masses. *Mining Informational and Analytical Bulletin*. 2013. N 4, p. 325-333 (in Russian).

21. Tungusov S.A. Pulsed flow and its generation for borehole flushing. *Proceedings of higher educational establishments. Geology and Exploration*. 2024. Vol. 66. N 1, p. 109-115 (in Russian). DOI: 10.32454/0016-7762-2024-66-1-109-115

22. Kun Bo, Fangzhou Ji, Zhiqiang Zhao et al. Optimum Design of Large-Diameter Reverse Circulation Drill Bit for Drilling Rescue Wells Using Orthogonal Experimental Method and CFD Simulation. *Energies*. 2023. Vol. 16. Iss. 9. N 3913. DOI: 10.3390/en16093913

23. Leusheva E., Alikhanov N., Tabatabaee Moradi S.S. Experimental Evaluation of Influence of Physico-chemical Properties of Surfactants on Drilling Process in Pay-zones. *International Journal of Engineering, Transactions A: Basics*. 2025. Vol. 38. Iss. 4, p. 819-829. DOI: 10.5829/ije.2025.38.04a.13

24. Xinda Qi, Weishan Chen, Yingxiang Liu et al. A Novel Well Drill Assisted with High-Frequency Vibration Using the Bending Mode. *Sensors*. 2018. Vol. 18. Iss. 4. N 1167. DOI: 10.3390/s18041167

25. Jalakani R., Tabatabaee Moradi S.S., Morenov V. Reliability Analysis of a Drilling Bit Penetration Model in Oil and Gas Wells: A Case Study. *International Journal of Engineering, Transactions B: Applications*. 2024. Vol. 37. Iss. 11, p. 2213-2222. DOI: 10.5829/ije.2024.37.11b.08

26. Elovyh P.F., Neskoromnyh V.V., Elovyh V.F. Determination of the coefficient side of the milling abilities of the deflection system in the drilling of a directional wellbore. *Inzhener-neftyanik*. 2018. N 1, p. 11-14 (in Russian).

27. Djuraev R.U., Merkulov M.V., Khatamova D.N., Asanov A.T. Engineering solutions for sludging prevention at bottomhole. *Mining Informational and Analytical Bulletin*. 2025. N 7, p. 102-114 (in Russian). DOI: 10.25018/0236_1493_2025_7_0_102

28. Shigin A.O., Boreyko D.A., Tskhadaya N.D., Serikov D.Yu. Comparative Analysis of Roller Drill Bit Performance. *SOCAR Proceedings*. 2021. N S2, p. 7 (in Russian). DOI: 10.5510/OGP2021SI200536

29. Serikov D.Yu., Myagkov K.A., Vasiliev A.A. Improvement of the design of the supra-bit rectilinear calibrator-ejector. *Construction of oil and gas wells on land and sea*. 2019. N 10, p. 21-26 (in Russian). DOI: 10.30713/0130-3872-2019-10-21-26

30. Serikov D.Yu., Borejko D.A., Muradov A.V. Patent N 2799295 RF. Downhole calibrator. Publ. 04.07.2023. Bul. N 19 (in Russian).

31. Buslaev G.V., Konoplyannikov A.V. Mathematical Modeling of a Hydro-mechanical System with a Positive Displacement Motor and Hydraulic Thruster to Optimize the Drilling Process for Extended-reach Drilling Wells. *International Journal of Engineering*. 2026. Vol. 39. Iss. 5, p. 1077-1087. DOI: 10.5829/ije.2026.39.05b.03

This is an open access article under the CC BY 4.0 license

32. Ganiev R.I., Deboer L., Agliullin A.Kh., Ismakov R.A. CIRCUL+ self-activated circulation translator: modeling, bench validation and field tests. *Bulletin of the Association of Drilling Contractors.* 2025. N 4, p. 31-39 (in Russian).

33. Litvinenko V.S., Nikolaev N.I. Technological fluids for increasing effectivity of construction and exploitation oil and gas wells. *Journal of Mining Institute.* 2011. Vol. 194, p. 84-90 (in Russian).

34. Shishov A.M., Ulyasheva N.M. On the possibility of regulating the formation of the bottom hole zone of the well by controlling the composition of the drilling mud. *Inzhener-neftyanik*. 2023. N 4, p. 67-71 (in Russian).

***Authors*: Dmitrii A. Boreiko,** *Candidate of Engineering Sciences, Associate Professor* (*Empress Catherine II Saint Petersburg Mining University, Saint Petersburg, Russia*), *Boreyko_DA@pers.spmi.ru*, *https://orcid.org/0000-0002-0248-4526*, **Nikolai D. Tskhadaya,** *Doctor of Engineering Sciences, Special Representative of the Rector* (*Empress Catherine II Saint Petersburg Mining University, Saint Petersburg, Russia*), *https://orcid.org/0000-0003-2332-1117*, **Dmitrii Yu. Serikov,** *Doctor of Engineering Sciences, Professor* (*National University of Oil and Gas "Gubkin Unversity", Moscow, Russia*), *https://orcid.org/0000-0003-3256-580X*, **Vyacheslav A. Khlamov,** *Assistant Lecturer* (*Ukhta State Technical University, Ukhta, Komi Republic, Russia*), *https://orcid.org/0009-0003-1950-652X*.

The authors declare no conflict of interests.

This is an open access article under the CC BY 4.0 license

ISSN 2411-3336; e-ISSN 2541-9404

JOURNAL OF MINING INSTITUTE
Zapiski Gornogo instituta
Journal homepage: pmi.spmi.ru

Research article
Geotechnical Engineering and Engineering Geology

A study of grouting mortars using chromium-containing catalyst sludge for well cementing in permafrost zones

Vyacheslav N. Kuchin✉, Georgii V. Buslaev, Vladimir A. Sidorov, Olga S. Zubkova
Empress Catherine II Saint Petersburg Mining University, Saint Petersburg, Russia

How to cite this article: Kuchin V.N., Buslaev G.V., Sidorov V.A., Zubkova O.S. A study of grouting mortars using chromium-containing catalyst sludge for well cementing in permafrost zones. Journal of Mining Institute. 2026. Vol. 280, p. 37-46.

Abstract
This article presents an experimental study of the effect of chromium (III) oxide, recovered from chromium-containing catalyst sludge, on the properties of grouting mortars used for well cementing in permafrost zones. The necessity of modifying grouting mortars to increase the strength of the cement stone for intervals in permafrost formations is justified. A method for reducing Cr(VI) to the stable form Cr(III) has been developed, and Cr_2O_3 has been obtained for use as an active mineral additive. Four grouting mixture compositions are considered: a base mixture, commonly used at sites, based on Portland cement with a setting accelerator; a mixture based on Portland cement; a mixture based on Portland cement with the addition of chromium (III) oxide; and a mixture based on Portland cement with calcium chloride and the addition of chromium (III) oxide. The experiments include testing of the four compositions at two water-to-solid ratios (W/S = 0.4 and 0.5) with an assessment of flowability, compressive and flexural strength, microstructure (microtomography, SEM) and phase composition (XRD) at normal and sub-zero temperatures, including cyclic temperature changes. The data obtained show that at W/S = 0.5, the addition of Cr_2O_3 increases the compressive and flexural strength of the cement stone; a reduction in the content of free $Ca(OH)_2$ is observed, the proportion of calcium silicate hydrates (CSH) increases, and a more homogeneous and dense microstructure is evident. This modification increases the flowability of the grout, which facilitates better replacement of the drilling fluid. The use of Cr_2O_3 to improve the durability and watertightness of support structures in cryolithozone conditions is clearly advisable.

Keywords
permafrost; well cementing; grouting mortar; strength; chromium-containing catalyst sludge; industrial waste disposal

Funding
None.

Received: 28.11.2025 ***Accepted: 28.04.2026*** ***Online: 24.06.2026*** ***Published: 10.09.2026***

Introduction

Modern oil and gas field development increasingly involves the exploitation of areas located in geotechnically complex regions, including zones of permafrost – the cryolithozone [1, 2]. Carrying out construction work on a well under such conditions presents a number of serious challenges: sharp temperature fluctuations, the presence of meltwater and frozen rock, and a high probability of cracking and loss of cement ring integrity. One of the most critical problems remains inter-casing flow, caused by a breach in the integrity of the cement stone or its poor adhesion to the casing string and the wellbore wall [3-5].

Conventional cement slurry compositions do not provide the required durability in permafrost conditions and are susceptible to degradation under the influence of freezing, thawing and the migration of aggressive fluids [6]. When testing cements for northern regions, a temperature regime based on the temperature conditions during well drilling may be used [7].

When drilling wells in permafrost using a water-based clay slurry, the temperature of the slurry is artificially maintained between 5 and 7 °C. Consequently, the temperature of the mortar used

This is an open access article under the CC BY 4.0 license

under these conditions must be the same. This is dictated by the need to equalize the temperature of the grouting mortar pumped into the well and emerging at the wellhead with the temperature inside the well [8, 9]. After the cementing process is complete, this temperature is maintained for some time or decreases slightly. Subsequently, the grouting mortar cools under the influence of the cold from the frozen rock mass or heats up due to the exothermic nature of the hydration process [10, 11].

Cementing of casing strings in a frozen rock interval (FR) involves the formation of cement stone and its behaviour under cyclic, alternating temperature stresses [12]. As a result of the changing boundary aggregate state of the residual fluid (after the hydration process in the grouting slurry has been fully completed) remaining in the closed porosity of the cement stone, at temperatures ranging from +5 to –5 °C, a cyclic volumetric effect occurs, leading to a disruption of the integrity of its structure [13, 14].

The aim of this study is to experimentally demonstrate the effectiveness of using catalyst sludge containing aluminium oxide and chromium (III) oxide as an active mineral additive to grouting cement for use in cryolitezones.

The idea behind the work is to increase the strength of the cement stone by introducing the additive in question into the composition of the grouting mortar; this additive promotes the formation of a denser and more stable cement stone structure and acts as an antioxidant, which in this case is chromium (III) oxide in a quantity of 10-14 % relative to the application medium.

Main research objectives:

• analysis of the operating conditions of cement stone in permafrost zones and identification of the main factors contributing to its deterioration;

• investigation of the effect of chromium (III) oxide admixture on the strength characteristics of cement stone at various water-to-solid ratios;

• assessment of the structure and microporosity of the resulting cement stone;

• determination of the optimal admixture content to enhance resistance to external influences.

The article examines the influence of temperature on the formation of water crystals within the cement stone during freeze-thaw cycles upon hydration. An approach is proposed for the utilization of industrial waste by re-incorporating it into the technological processes of well construction.

The practical significance of the work lies in the development of an effective formulation for a modified grouting mortar, ensuring enhanced sealing and long-term durability of well casings in permafrost regions. The results obtained can be utilized in the design of oil and gas well construction works in Arctic and sub-Arctic regions.

Literature review and research framework

Characteristics of cementing in permafrost zones. Permafrost constitutes a complex system comprising a mineral matrix, water in various phases, and gases. The temperature at which they occur varies from 0 to –15 °C and below. Upon contact with drilling and grouting mortars at above-freezing temperatures, local thawing of the rock occurs, accompanied by deformation, the formation of cracks and changes in filtration properties [15-17]. The main requirement for grouting materials under such conditions is the maintenance of the cement ring's integrity and resistance to repeated freeze-thaw cycles. At the same time, it is necessary to ensure minimal heat transfer to the rock so as not to disrupt the thermal balance of the frozen mass [18, 19].

When the temperature drops below 0 °C, the rate of cement hydration falls sharply, leading to a shortfall in strength and the formation of a porous structure [20, 21]. When water freezes before setting begins, ice inclusions and microcracks form, which subsequently act as channels for fluid filtration. Thus, even minor temperature fluctuations can lead to a breach in the integrity of the cement stone [22, 23].

Problems with traditional grouting cements. Pure Portland cements used for well grouting are not designed to withstand sub-zero temperatures. They are characterized by excessive shrinkage, the

This is an open access article under the CC BY 4.0 license

formation of free $Ca(OH)_2$, low resistance to leaching, and cracking during freezing [24, 25]. When the water-cement mixture freezes, volumetric expansion of up to 5 % occurs, which causes internal stresses and reduces flexural strength to 10-15 % of standard values [26, 27].

Various additives are used to compensate for these effects: calcium chloride to accelerate hydration, microsilica and fly ash to densify the structure, as well as polymer and latex modifiers to increase the elasticity of the cement stone [28]. However, these methods do not always ensure stability under prolonged exposure to sub-zero temperatures and aggressive formation fluids [29, 30].

The use of industrial waste as active additives. Traditionally, secondary industrial products have been widely used in drilling; these possess an active mineral structure and are capable of improving the physical and mechanical properties of cement stones [31-33]. Such materials include fly ash, slurries from sulphuric acid and petrochemical production, metallurgical slags, red slurries, and catalyst wastes [34, 35].

Chromium-containing catalyst sludges are a by-product of the chemical industry, containing oxides of chromium, iron, aluminium and silicon [36, 37]. Once the sludges have been reduced to a stable state with a Cr^{3+} content, they can be used as active mineral additives [38, 39]. Their use not only improves the performance properties of the cement stone but also addresses the challenge of the environmentally safe disposal of hazardous waste [40, 41].

Methods

Method for the preparation of reduced chromium (III) oxide. Chromium is a transition metal with pronounced redox properties and is capable of existing in various oxidation states, the most stable of which are Cr(III) and Cr(VI). Hexavalent chromium compounds are highly toxic and must be neutralized, whereas trivalent forms are chemically stable and can be used as active mineral additives. According to the patented method (Patent RU 2796659 C1), the conversion of Cr(VI) into the safe form Cr(III) is carried out by reduction with sodium metabisulphite in a suspension of catalytic sludge at 70-85 °C and a reducer-to-slurry ratio of 0.005:1, which ensures up to 99 % process efficiency. The resulting precipitate – chromium (III) hydroxide – can be used as a source of chromium (III) oxide in grouting solutions after filtration and drying.

Cr_2O_3 compounds improve the structure of the cement stone, increasing its density, frost resistance and chemical resistance, which makes them promising for use in well cementing in permafrost zones [42, 43].

Reduction with sodium metabisulphite (Table 1) proceeds via the following reaction:

$$4CrO_{4(l)}^{2-} + 3S_2O_{5(l)}^{2-} + 7H_2O \rightarrow 3Cr(OH)_{3(s)} + 6SO_{4(l)}^{2-} + 2OH_{(l)}^{-}.$$

Table 1

Material balance of the reduction process [42]

Input	Amount, kg	Output	Amount, kg
Catalyst sludge pulp	359	Recovered catalyst sludge pulp	361.52
Liquid phase	180	Liquid phase	180
Solid phase	179	Solid phase	181.52
Sodium metabisulphite	2.52		
Total	361.52	Total	361.52

Research Methodology. Four grouting mixtures are examined: a base mixture commonly used for cementing wells in MMP intervals, based on PCT with a setting accelerator (N 1); a mixture based on PCT (N 2); based on PCT with the addition of chromium (III) oxide (N 3); based on PCT with calcium chloride and the addition of chromium (III) oxide (N 4). The characteristics of the

This is an open access article under the CC BY 4.0 license

© Vyacheslav N. Kuchin, Georgii V. Buslaev, Vladimir A. Sidorov, Olga S. Zubkova, 2026

base mixture are required as initial data and for comparison with the characteristics of the alternative mixtures.

Each composition was prepared with two water-to-solid ratios (W/S) of 0.4 and 0.5, except for composition N 4.2, as the study revealed that Cr_2O_3 performs better at a higher water-to-solid ratio.

Formulations of grouting mixtures with the main binder PTS-I-50: N 1 – base, 2 % $CaCl_2$; N 2 – pure; N 3 – 4 % Cr_2O_3; N 4.1 – 4 % Cr_2O_3 and 2 % $CaCl_2$; N 4.2 – 2 % Cr_2O_3 and 2 % $CaCl_2$. Purpose of additives: Cr_2O_3 – to improve strength characteristics; $CaCl_2$ – to increase the rate of hydration, reduce the setting time of the grouting mortar, and accelerate strength development.

The required mass of the cement sample for mixing the mortar is calculated using the formula

$$m_{\text{mix}} = \frac{m_{\text{w}}}{\text{W/S}},$$

where m_{w} – mass of water, kg.

The components of the mixture are weighed on an A&D DX-500 bench-top laboratory balance with an accuracy of ±0.02 g. An IKA Eurostar power control-visc 6000 top-drive mixer is used to prepare the grouting mortars. Mixing is carried out by adding the components of the dry grouting mixture to the mixer beaker containing deionized water and stirring for 180±5 s at a speed of 1500±100 rpm.

The KR-1 spread cone (AzNII) is used to determine the spreadability of grouting mortar, whilst the CONTROLS Digimax 3 testing press is used to measure the compressive and flexural strength characteristics of cement samples.

The density of the grouting mortar is determined using a FANN 140 lever balance. The structure of the grouted rock is examined using a TESCAN VEGA3 scanning electron microscope fitted with an elemental analysis attachment.

A SkyScan 1173 microtomograph is used to study the internal structure of the cement stone. In addition to determining the total open porosity and the shape of the pore space within the sample volume, the instrument allows the identification of physical and chemical changes, including filtration effects arising from acid treatments, and the assessment of the mineral composition and distribution of mineral aggregates.

A cryostat with a climatic chamber [43] was used to age cement stone samples at sub-zero temperatures and to simulate cyclic changes; a Shimadzu XRD-7000 X-ray powder diffractometer was used to determine the phase composition of the cement stone.

Discussion

The aim of the experiments is to demonstrate that the proposed grouting mortar, with the addition of chromium (III) oxide, offers superior strength and frost resistance compared to the base mixture (N 1).

Objectives of the experiments: to determine the composition and water-to-solid ratio of the grouting mixture that will achieve optimum compressive and flexural strength, as well as frost resistance; to test the strength of grouting mixtures that have hardened under normal conditions (20 °C) and at sub-zero temperatures (–5 °C); to test the strength of grouted stones subjected to cyclic temperature changes during the hardening process.

Table 2

Results of compressive and flexural strength measurements of mixtures cured at 20 °C for 2 days

Number mixture	W/S	Compressive strength, MPa	Flexural strength, MPa
1	0.4	23.22	4.36
	0.5	17.16	3.61
2	0.4	21.77	7.69
	0.5	11.75	4.05
3	0.4	18.28	6.33
	0.5	12.45	5.25
4.1	0.4	18.14	4.71
	0.5	16.55	4.36
4.2	0.5	12.05	4.95

Table 2 presents the results of compressive and flexural strength measurements for all mixtures.

As can be seen from Table 2, mixtures N 3, N 4.1 and N 4.2 with the addition of Cr_2O_3 exhibit lower compressive strength values, but have higher flexural strength values. Flexural strength is a more important indicator than compressive

This is an open access article under the CC BY 4.0 license

strength, as in the cryolithzone the cement stone is subjected to internal tensile stresses due to the freezing of water. A stone with high compressive strength but low flexural strength will crack under such stresses.

The next stage of the experiment involves testing the strength of cement stones that have been stored for 7 days at a temperature of –5 °C.

The samples were placed in the freezer in accordance with GOST 30744-2001. The moisture content of the samples in the freezer was maintained without contact with the air by means of airtight packaging on the samples, as during the hardening of grout in a confined space they do not dry out, and the effect of moisture on strength is significant.

Curing of the grouting samples under normal conditions at a liquid temperature of 20 °C was carried out in a water bath.

Table 3

Compressive strength of mixtures cured for 7 days at −5 °C

Number mixture	W/S	Compressive strength, MPa
1	0.4	13.69
	0.5	12.82
2	0.4	7.67
	0.5	5.53
3	0.4	7.05
	0.5	5.98
4.1	0.4	19.94
	0.5	12.56
4.2	0.5	13.11

Table 3 presents the results of the compressive strength test for mixtures that had been in the freezer for 7 days at a temperature of –5 °C (Fig.1). It should be noted that the addition of Cr_2O_3 reduces the compressive strength at W/S = 0.4, but increases it at W/S = 0.5. After fracture, distinct inclusions of Cr_2O_3 were visible in the samples.

Figure 1 shows that samples of all compositions have cracks, demonstrating the negative effect of low temperature on the grout.

The next stage involves testing the samples for strength following cyclic temperature changes. The samples were placed in a freezer, where the temperature varied according to the schedule (Fig.2). The temperature of the cement stone was measured using a contact method with a Testo 905-T2 temperature logger, which is listed in the State Register of Measuring Instruments and holds a valid calibration certificate C-SP/28-11-2025/484519722.

Table 4 shows the results of the compressive strength tests for mixtures N 2 and N 3, which were subjected to cyclic temperature changes over a period of 3 days. The addition of Cr_2O_3 slightly reduces the compressive strength at W/S = 0.4, but significantly increases this value at W/S = 0.5.

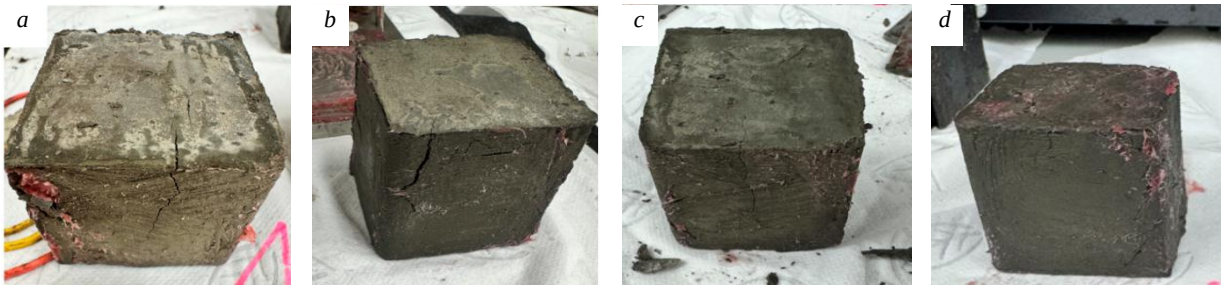


Fig.1. Cement cubes cured at −5 °C for 7 days:
a – mixture N 1; *b* – mixture N 2; *c* – mixture N 3; *d* – mixture N 4.1

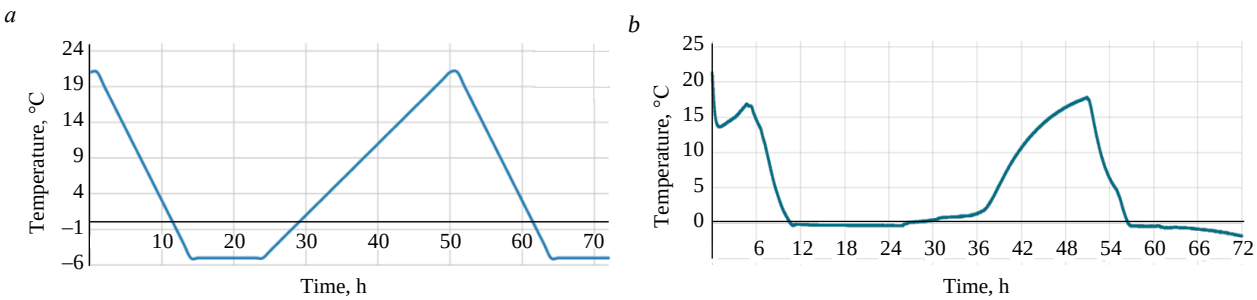


Fig.2. Change in temperature in the freezer compartment (*a*)
and in the temperature of the cement block in the freezer compartment (*b*)

This is an open access article under the CC BY 4.0 license

© Vyacheslav N. Kuchin, Georgii V. Buslaev, Vladimir A. Sidorov, Olga S. Zubkova, 2026

Table 4

Compressive strength of mixtures N 2 and N 3 cured for 3 days

Number mixture	W/S	Compressive strength, MPa
2	0.4	13.460
	0.5	6.09
3	0.4	12.735
	0.5	10.395

Table 5

Compressive strength of mixtures cured for 2 days at −5 °C

Number mixture	W/S	Compressive strength, MPa
1	0.4	3.78
	0.5	0.72
2	0.5	0.1
3	0.5	0.8
4.1	0.4	3.56
	0.5	2.15
4.2	0.5	2.14

Table 5 presents the results of compressive strength tests on samples that had been stored in a freezer for 2 days at a temperature of –5 °C (Fig.3). The addition of Cr_2O_3 reduces the compressive strength at a W/S ratio of 0.4, but increases these values at a W/S ratio of 0.5. A 2 % Cr_2O_3 content yields better results compared to a 4 % content in specimens with a W/S ratio of 0.5. This is due to more favourable conditions for the dispersion of the additive and the progression of hydration processes. At a W/S ratio of 0.4, the effect of the additive on strength is negligible.

Based on the research results (Table 4, 5), it can be concluded that the addition of Cr_2O_3 is advisable at a W/S ratio of 0.5; this value for the water-solid ratio is specified in the technical data sheet for PCT-I-50.

It can be observed that the sample containing chromium sludge and calcium chloride did not disintegrate after testing in the chamber (composition N 4.1).

The next stage of the study was to determine the spreadability of the grouting mortar: composition N 4.1 – 230 mm, composition N 1 – 170 mm. Low rheological characteristics allow for an increase in the upward flow rate of the grouting mortar, as it will exert less stress on the rock. As the upward flow rate of the grouting mortar increases, the quality of cementation improves due to better replacement of the drilling fluid by the grout.

Next, the phase composition of the cement stone was determined (Fig.4).

Chromium (III) and (VI) can replace aluminium Al^{3+} in the structure of cementitious minerals, forming new stable compounds. Chromium oxides can interact with silicates and calcium aluminates, altering the phase composition and density of the cement stone. Such interaction promotes the formation of a more homogeneous structure and increases the material's resistance to environmental influences.

X-ray diffraction analysis of the additive shows that the crystalline phases present in the sample include a mixture of alpha and delta aluminium oxide, as well as coarse-grained crystallites of a Cr_2O_3-Al_2O_3 solid solution (chromium-aluminium oxide). The X-ray diffraction data indicate that a high proportion of the amorphous phase is present. The chemical composition of the solid phase of the catalyst sludge remains unchanged before and after boiling. The bulk of the solid phase of the catalyst sludge consists of aluminium oxide, silicon oxide, chromium-containing compounds and impurity elements (iron, potassium, calcium, manganese, and zirconium), the total amount of which, expressed as oxides, does not exceed 4.1 wt.%. When the additive in question is incorporated into the cement system, chromium-containing hydrates and complex silicates may form, which enhance the strength, frost resistance, and chemical resistance of the cement stone. A reduction in the

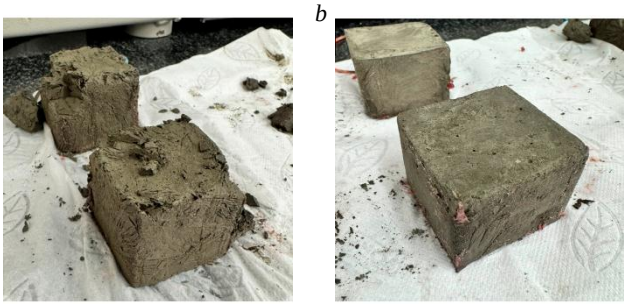


Fig.3. Samples of cement stone that have been kept in a freezer for 2 days at –5 °C:
a – mixture N 2; *b* – mixture N 4.1

This is an open access article under the CC BY 4.0 license

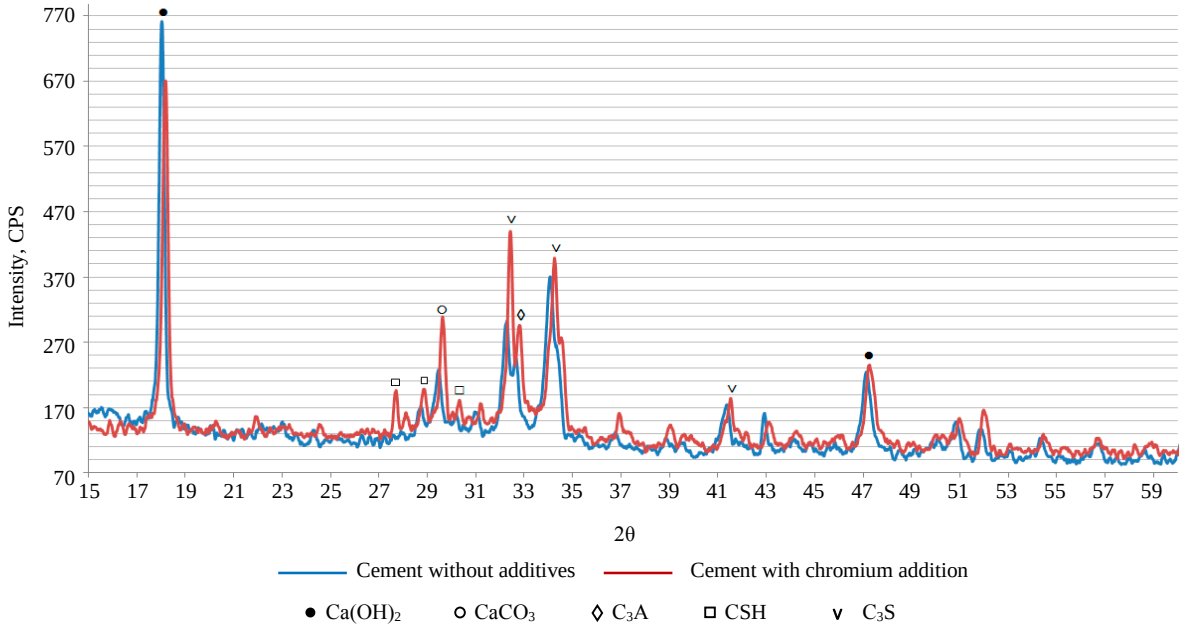


Fig.4. Results of X-ray phase analysis of mixtures N 2 and N 3

content of unstable compounds, such as free calcium oxide, lowers the likelihood of cracking during cyclic temperature changes, which is particularly important for use in permafrost conditions.

X-ray phase analysis showed that the addition of chromium to the cement mixture resulted in changes to the phase composition of the cement stone (Fig.4):

• The intensity of the peaks corresponding to $Ca(OH)_2$ is lower in the mixture containing chromium than in pure cement. Free portlandite ($Ca(OH)_2$) is a weak phase susceptible to leaching and degradation under the influence of aggressive water. A lower $Ca(OH)_2$ content increases durability and resistance to aggressive environments, which is critical for permafrost conditions.

• Figure 4 shows an increase in the intensity of the peaks corresponding to CSH upon the addition of Cr_2O_3; CSH (calcium silicate hydrate) is the main binding phase of the cement stone, ensuring its strength and density. The greater the proportion of the CSH phase, the stronger and more stable the structure of the cement stone. The addition of chromium oxide promotes the formation of a denser and stronger structure capable of withstanding mechanical loads and thermal fluctuations in permafrost zones.

Following X-ray phase analysis, the cement stone was scanned on a SkyScan 1173 microtomograph to determine its internal structure. The results of the study of compositions N 2 and N 3, which underwent testing in a chamber with cyclic temperature changes, are presented in Fig.5.

Composition N 3 has a denser structure with fewer channels compared to composition N 2 following the cyclic temperature change test over a period of 3 days. This is an important indicator, as fluid can migrate through the channels formed, leading to intercolumn flow.

Following microtomography scanning, compositions N 2 and N 3 were examined using a TESCAN VEGA3 electron microscope. The results are shown in Fig.6.

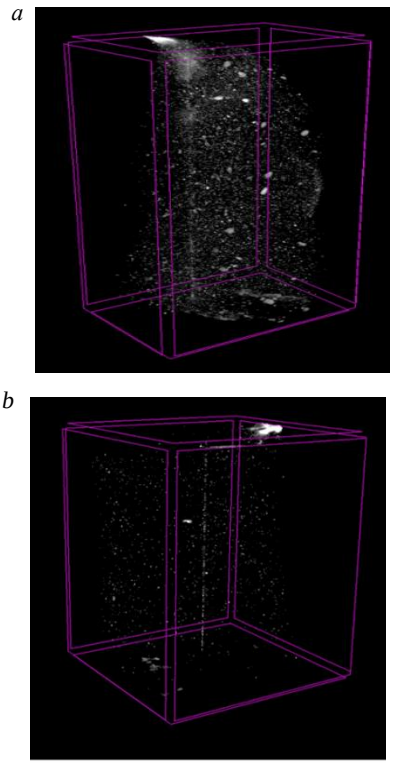


Fig.5. Internal structure of compositions N 2 (*a*) and N 3 (*b*) with W/S = 0.5 after testing in a freezer

This is an open access article under the CC BY 4.0 license

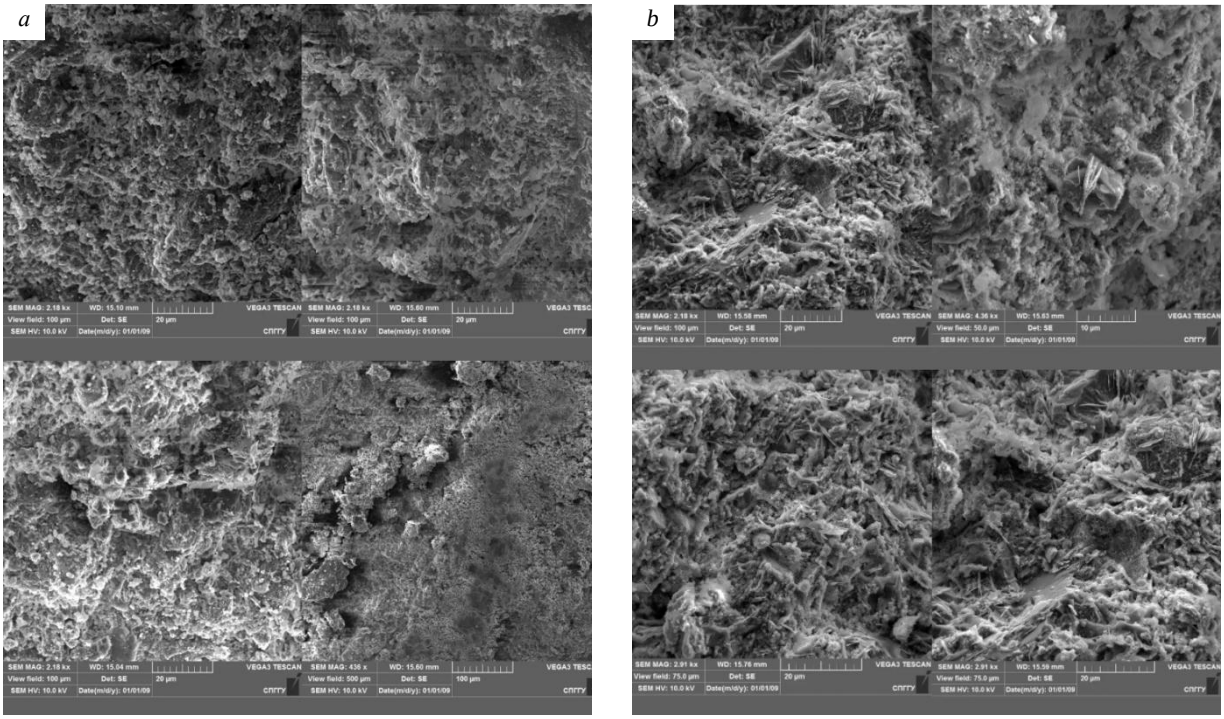


Fig.6. Scanning results for samples N 2 (*a*) and N 3 (*b*)

The dense microstructure reduces the number of micropores, improving compressive and flexural strength. A lower content of free $Ca(OH)_2$ and the presence of chromium-containing phases result in a denser cement stone, which reduces water permeability and prevents leaching.

Conclusion

It has been established that the use of chromium oxide (Cr_2O_3) in the composition of the grouting mortar has a positive effect on its properties at a water-to-solid ratio of 0.5. This composition ensures the formation of a more durable cement stone, which is particularly important for cryolithzone conditions, where the presence of microcracks and pores can lead to inter-pillar flow and a reduction in the integrity of the support.

The results of microtomographic analysis showed that the structure of the cement stone with the addition of chromium becomes more homogeneous, with fewer internal channels and pores. Although the overall density of the cement stone remained unchanged (due to the equivalent replacement of 24 g of cement powder with 24 g of chromium oxide), an improvement in the internal structure is observed, indicating a reduction in permeability and a potential increase in the material's durability.

The observed reduction in the number of internal channels and the more homogeneous structure of the samples with chromium (III) oxide additive may indicate a potential reduction in the permeability of the cement stone.

X-ray phase analysis confirmed that the presence of chromium oxide reduces the $Ca(OH)_2$ content, indicating a more complete course of hydration processes. At the same time, an increase in the intensity of the peaks corresponding to calcium hydrosilicates (CSH) as well as aluminate and silicate phases (C_3A and C_2S) is observed, which is directly linked to the improvement in the material's strength characteristics. Stable chromium compounds slow down the degradation processes of the cement stone, extending the well's service life.

The use of chromium oxide helps to increase the flowability of the grout, significantly facilitates its injection and improves the quality of the annular space filling. Low rheological properties allow for an increase in the upward flow rate of the grouting mortar, as it exerts less pressure on the wellbore walls and surrounding rock. The increased flow rate facilitates a more effective replacement of the drilling fluid with the grouting mortar, which directly improves the quality of the cementing.

This is an open access article under the CC BY 4.0 license

Reduced water absorption and the dense structure of the cement stone minimize the risk of damage during freezing and thawing. Promising avenues for further research include optimizing the composition of grout containing chromium additives under various climatic conditions, investigating the effect of the additive on the rheology of the grout at extremely low temperatures, and conducting field tests on actual wells in permafrost formations.

The issue of cement stone durability is particularly relevant for wells operated in permafrost conditions. The main potential problems are associated with the destruction of the cement stone during repeated freeze-thaw cycles. The addition of chromium sludge helps to minimize this problem by reducing the capillary moisture content. Furthermore, chromium-containing compounds can enhance the chemical resistance of the cement stone, preventing its degradation under the influence of groundwater (cement leaching).

Thus, the addition of Cr_2O_3 improves the internal structure of the cement stone, enhances its strength and technical properties, whilst maintaining its density. This makes the additive an effective solution for cementing wells in permafrost zones.

REFERENCES

1. Blinov P.A., Sadykov M.I., Gorelikov V.G., Nikishin V.V. Development and research of backfill compounds with improved elastic and strength properties for oil and gas well lining. *Journal of Mining Institute.* 2024. Vol. 268, p. 588-598.

2. Dvoynikov M., Kutuzov P. Identification of Critical and Post-Critical States of a Drill String Under Dynamic Conditions During the Deepening of Directional Wells. *Eng.* 2025. Vol. 6. Iss. 11. N 306. DOI: 10.3390/eng6110306

3. Yang Li, Yuanfang Cheng, Chuanliang Yan et al. Mechanical study on the wellbore stability of horizontal wells in natural gas hydrate reservoirs. *Journal of Natural Gas Science and Engineering*. 2020. Vol. 79. N 103359. DOI: 10.1016/j.jngse.2020.103359

4. Litvinenko V. The Role of Hydrocarbons in the Global Energy Agenda: The Focus on Liquefied Natural Gas. *Resources*. 2020. Vol. 9. Iss. 5. N 59. DOI: 10.3390/resources9050059

5. Zaitsev V.I., Karpikov A.V. Analysis of production well construction features in permafrost conditions. *Earth Sciences and Subsoil Use.* 2024. Vol. 47. N 3, p. 302-315 (in Russian). DOI: 10.21285/2686-9993-2024-47-3-302-315

6. Xuerui Wanga, Baojiang Sun, Zhiyuan Wang et al. Coupled heat and mass transfer model of gas migration during well cementing through a hydrate layer in deep-water regions. *Applied Thermal Engineering*. 2019. Vol. 163. N 114383. DOI: 10.1016/j.applthermaleng.2019.114383

7. Zhen-quan Lu, Chu-guo Wu, Neng-you Wu et al. Change trend of natural gas hydrates in permafrost on the Qinghai-Xizang Plateau (1960-2050) under the background of global warming and their impacts on carbon emissions. *China Geology*. 2022. Vol. 5. Iss. 3, p. 475-509. DOI: 10.31035/cg2022034

8. Kuchin V.N., Sidorov V.A., Kopteva A.I. Well cementing and formation of isolation in intervals containing permafrost: scientific and methodological principles. *Neftegaz.RU*. 2025. N 7 (163), p. 37-41 (in Russian).

9. Gizatullin R., Dvoynikov M., Romanova N., Nikitin V. Drilling in Gas Hydrates: Managing Gas Appearance Risks. *Energies*. 2023. Vol. 16. Iss. 5. N 2387. DOI: 10.3390/en16052387

10. Xuerui Wang, Zhenhao Li, Baojiang Sun et al. Coupling mechanisms between cement hydration and permafrost during well construction in the Arctic region. *Geoenergy Science and Engineering*. 2023. Vol. 222. N 211429. DOI: 10.1016/j.geoen.2023.211429

11. Yucheng Xue, Chengwen, Wang Jingping Liu et al. A cement hydration kinetics model and its application in designing cement formulation for natural gas hydrate well. *Cement and Concrete Research*. 2024. Vol. 179. N 107483. DOI: 10.1016/j.cemconres.2024.107483

12. Kuznetsov V.G., Shcherbich N.E., Gerasimov D.S. et al. Fundamental requirements for properties of cement slurry and stone for low-temperature wells. *Oil and Gas Studies.* 2019. N 5 (137), p. 57-63 (in Russian). DOI: 10.31660/0445-0108-2019-5-57-63

13. Yershiev K.T., Akhmetov D.A., Aitkulov Y.K. et al. Summary on the application of the gravitational method to eliminate intercasing pressure. *Kazakhstan journal for oil & gas industry.* 2021. Vol. 3. N 3 (8), p. 43-51 (in Russian). DOI: 10.54859/kjogi88919

14. Rybakov D.A., Dorokhin E.G., Andreev K.V., Straupnik I.A. Flushing Fluid Dynamics in a Flowing Piston with Confusor Transition Modelling. *International Journal of Engineering, Transactions A: Basics*. 2025. Vol. 38. Iss. 4, p. 937-944. DOI: 10.5829/ije.2025.38.04a.21

15. Zhenyu Wu, Liang Xu, Bing Li et al. Hydrothermal coupling model between wellbore and permafrost for drilling in arctic cold regions. *International Journal of Heat and Mass Transfer*. 2024. Vol. 235. N 126236. DOI: 10.1016/j.ijheatmasstransfer.2024.126236

16. Ghosal Mainak, Chakraborty A.K. Engineering the properties of nanomaterials for its use in cement concrete. *Materials Today: Proceedings*. 2021. Vol. 46. Part 17, p. 7502-7506. DOI: 10.1016/j.matpr.2021.01.206

17. Sheng Wang, Liming Jian, Zhihong Shu et al. Preparation, properties and hydration process of low temperature nano-composite cement slurry. *Construction and Building Materials*. 2019. Vol. 205, p. 434-442. DOI: 10.1016/j.conbuildmat.2019.02.049

18. Fang Jin, Feng Huang, Guobiao Zhang et al. Feasibility assessment of enhancing permeability and stability in marine hydrate reservoirs with dual-enhanced stimulation: Slurry-sediment cementation characteristics. *Applied Ocean Research*. 2025. Vol. 158. N 104545. DOI: 10.1016/j.apor.2025.104545

19. Xuerui Wang, Baojiang Sun, Songyan Li et al. Numerical modeling of hydration performance for well cement exposed to a wide range of temperature and pressure. *Construction and Building Materials.* 2020. Vol. 261. N 119929. DOI: 10.1016/j.conbuildmat.2020.119929

This is an open access article under the CC BY 4.0 license

20. Xuerui Wang, Baojiang Sun, Yonghai Gao et al. Numerical simulation of the stability of hydrate layer during well cementing in deep-water region. *Journal of Petroleum Science and Engineering*. 2019. Vol. 176, p. 893-905. DOI: 10.1016/j.petrol.2019.02.003

21. Yuhuan Bu, Rui Ma, Huajie Liu et al. Low hydration exothermic well cement system: The application of energy storage microspheres prepared by high-strength hollow microspheres carrying phase change materials. *Cement and Concrete Composites*. 2021. Vol. 117. N 103907. DOI: 10.1016/j.cemconcomp.2020.103907

22. Nikolaev N.I., Lu Tianli. The modern technology of drilling and casing of well during the exploration of gas hydrates. *Journal of Mining Institute.* 2016. Vol. 218, p. 206-214 (in Russian).

23. Yuhuan Bu, Zilong Lu, Chang Lu et al. Synthesis and performance evaluation of hydrate dissociation inhibitors suitable for cementing hydrate formations. *Fuel.* 2025. Vol. 386. N 134197. DOI: 10.1016/j.fuel.2024.134197

24. Changliang Fang, Mingming Zheng, Hongzhi Lu et al. A simplified method for predicting the penetration distance of cementing slurry in gas hydrate reservoirs around wellbore. *Journal of Natural Gas Science and Engineering*. 2018. Vol. 52, p. 348-355. DOI: 10.1016/j.jngse.2018.01.042

25. Ivanov V.N., Parfenova S.N. A study of the bond strength of cement grouts used for well cementing in intervals containing permafrost. Ashirovskie chteniya: Sbornik trudov Vserossiiskoi nauchno-prakticheskoi konferentsii, 21 noyabrya 2024, Cheboksary, Rossiya. V 2 tomakh. Samara: Samarskii gosudarstvennyi tekhnicheskii universitet, 2024. Vol. 2, p. 98-102 (in Russian).

26. Buslaev G.V., Lavrik A.Yu., Islamov R.R., Muslimov B.S. Review of modern research on gas hydrates and hydrate formation inhibitors for use in well development. *Scientific Journal of the Russian Gas Society.* 2024. № 2 (44), p. 16-25 (in Russian).

27. Samoilovich A.V., Medvedev Yu.V. An effective solution for securing wells in permafrost intervals. *Burenie i neft.* 2025. N 3, p. 40-41 (in Russian). DOI: 10.62994/2072-4799.2025.43.36.007

28. Mozaffari S., Rahmani O., Piroozian A. et al. Oil-well lightweight cement slurry for improving compressive strength and hydration rate in low-temperature conditions. *Construction and Building Materials.* 2022. Vol. 357. N 129301. DOI: 10.1016/j.conbuildmat.2022.129301

29. Xueyu Pang, Lijun Sun, Min Chen et al. Influence of curing temperature on the hydration and strength development of Class G Portland cement. *Cement and Concrete Research*. 2022. Vol. 156. N 106776. DOI: 10.1016/j.cemconres.2022.106776

30. Lijun Sun, Xueyu Pang, Haibing Yan. Hydration kinetics of oil well cement in the temperature range between 5 and 30 °C. *Frontiers in Materials*. 2022. Vol. 9. N 985332. DOI: 10.3389/fmats.2022.985332

31. Nassan T.H., Kirch M., Freese C. et al. Experimental investigation of wellbore integrity during geological carbon sequestration: Thermal- and pressure-cycling experiments. *Gas Science and Engineering*. 2024. Vol. 124. N 205253. DOI: 10.1016/j.jgsce.2024.205253

32. Merzlyakov M.Y., Straupnik I.A., Serbin D.V. Study of water-containing ability of gas-liquid cement mixtures. Topical Issues of Rational Use of Natural Resources. In 2 volumes. CRC Press, 2019. Vol. 2, p. 851-859. DOI: 10.1201/9781003014638-48

33. Ivanchev I. Investigation with Non-Destructive and Destructive Methods for Assessment of Concrete Compressive Strength. *Applied Sciences*. 2022. Vol. 12. Iss. 23. N 12172. DOI: 10.3390/app122312172

34. Chernyshov S.E., Galkin V.I., Ulyanova Z.V., Macdonald D.I.M. Development of mathematical models to control the technological properties of cement slurries. *Journal of Mining Institute.* 2020. Vol. 242, p. 179-190. DOI: 10.31897/PMI.2020.2.179

35. Adjei S., Elkatatny S. Overview of the lightweight oil-well cement mechanical properties for shallow wells. *Journal of Petroleum Science and Engineering*. 2021. Vol. 198. N 108201. DOI: 10.1016/j.petrol.2020.108201

36. Davoodi S., Al-Shargabi M., Wood D.A., Rukavishnikov V.S. Recent advances in polymers as additives for wellbore cementing applications: A review. *Fuel*. 2024. Vol. 357. Part A. N 129692. DOI: 10.1016/j.fuel.2023.129692

37. Leusheva E., Morenov V. Effect of Temperature Conditions in Arctic Offshore Oil Fields on the Rheological Properties of Various Based Drilling Muds. *Energies*. 2022. Vol. 15. Iss. 15. N 5750. DOI: 10.3390/en15155750

38. Buslaev G., Lavrik A. Comparative Study of Efficiency of Hydrate Inhibitors Based on Ammonium Salts and Polyvinylpyrrolidone. *International Journal of Engineering: Transactions A: Basics*. 2026. Vol. 39. Iss. 4, p. 898-905. DOI: 10.5829/ije.2026.39.04a.08

39. Sotoudeh S., Ndeh-Ngwa A., Akbari S. et al. Optimization of Primary Cementing for Heavy Oil Wells: A Simulation-Based Case Study. 44th International Conference on Ocean, Offshore and Arctic Engineering, 22-27 June 2025, Vancouver, British Columbia, Canada. ASME, 2025. N OMAE2025-155064. DOI: 10.1115/OMAE2025-155064

40. Al Dhaif M., Al Qatari M., Toktabolat Z. Enhancing Well Integrity with Managed Pressure Drilling and Cementing in Challenging Zones with Significant Fluid Losses. Middle East Oil, Gas and Geosciences Show, 16-18 September 2025, Manama, Bahrain. OnePetro, 2025. N SPE-227083-MS. DOI: 10.2118/227083-MS

41. Pyagay I., Zubkova O., Zubakina M., Sizyakov V. Method for Decontamination of Toxic Aluminochrome Catalyst Sludge by Reduction of Hexavalent Chromium. *Inorganics*. 2023. Vol. 11. Iss. 7. N 284. DOI: 10.3390/inorganics11070284

42. Piagai I.N., Zubkova O.S., Zubakina M.A. Patent N 2796659 RF. Method for recovery of hexavalent chromium from process waste. Publ. 29.05.2023. Bul. N 16 (in Russian).

43. Yurtaev S.L., Gromov D.A., Ozhigin A.Yu., Kopteva A.I. Patent N 2828105 RF. Climatic chamber for studying process of thermosetting of cement mortar samples at negative temperatures. Publ. 07.10.2024. Bul. N 28 (in Russian).

***Authors*: Vyacheslav N. Kuchin,** *Candidate of Engineering Sciences, Head of Laboratory* (*Empress Catherine II Saint Petersburg Mining University, Saint Petersburg, Russia*), *kuchin_vn@pers.spmi.ru*, *https://orcid.org/0000-0003-3719-3873*, **Georgii V. Buslaev,** *Candidate of Engineering Sciences, Scientific Supervisor of Laboratory* (*Empress Catherine II Saint Petersburg Mining University, Saint Petersburg, Russia*), *https://orcid.org/0000-0002-4987-8645*, **Vladimir A. Sidorov,** *Postgraduate Student* (*Empress Catherine II Saint Petersburg Mining University, Saint Petersburg, Russia*), *https://orcid.org/0009-0002-2312-4746*, **Olga S. Zubkova,** *Candidate of Engineering Sciences, Senior Researcher* (*Empress Catherine II Saint Petersburg Mining University, Saint Petersburg, Russia*), *https://orcid.org/0000-0002-5833-528X*.

The authors declare no conflict of interests.

This is an open access article under the CC BY 4.0 license

ISSN 2411-3336; e-ISSN 2541-9404

JOURNAL OF MINING INSTITUTE

Zapiski Gornogo instituta

Journal homepage: pmi.spmi.ru

Research article

Geology

Lithological characteristics of lacustrine sediments in lakes Bolshoye Miassovo and Maloye Miassovo (Southern Urals, Russia)

Anastasiya R. Yusupova✉, Nouria G. Nourgalieva

Kazan Federal University, Kazan, Republic of Tatarstan, Russia

How to cite this article: Yusupova A.R., Nourgalieva N.G. Lithological characteristics of lacustrine sediments in lakes Bolshoye Miassovo and Maloye Miassovo (Southern Urals, Russia). Journal of Mining Institute. 2026. Vol. 280, p. 47-69.

Abstract

Climate is one of the key factors controlling sediment accumulation in lacustrine ecosystems. Integrated studies of continuous lake-sediment cores, including radiocarbon dating, grain-size analysis, mineralogical and chemical characterization, and measurements of magnetic properties, enable reconstructions of sedimentation conditions during the Late Quaternary. Such studies are particularly relevant for lakes of the Southern Urals, which are located near a climatic divide and for which episodes of increasing/decreasing moisture have been interpreted inconsistently. This paper presents data on the age, material composition, and genetic features of bottom sediments from lakes Bolshoye Miassovo and Maloye Miassovo. The results show that, based on grain-size distribution, mineral composition, and inorganic geochemistry, the studied lacustrine sediments exhibit a pattern typical of freshwater lakes – the predominance of allothigenic silt-sized particles. This is supported by the structure of allothigenic-input factor F1 derived from factor analysis. Quaternary deposits represented by eluvial, slopewash, colluvial, and alluvial facies were identified as the main source of allothigenic material for the investigated basins. The ICV index and the A-CN-K diagram indicate that the sediments formed predominantly from stable allothigenic minerals of the primary sedimentation cycle, sourced mainly from Quaternary deposits and exposed pre-Quaternary rocks. The transport pathways of allothigenic material are linked to the directions of slope flows and channel networks visible on the Quaternary-deposit map. The integrated analysis allowed us to identify the most informative proxies and to correlate them with global and regional climatic stages and events, including the Bølling warming (~14,700 cal. yr BP), the ~8200 cal. yr BP cooling event, aridization in the Southern Urals (~2000 cal. yr BP), and Bond Event 1 (~1500 cal. yr BP). Additional climate-arid events were identified at ~11,430, ~6100, ~4250, ~3537, and ~1065 cal. yr BP.

Keywords

modern lake sediments; radiocarbon dating; grain-size analysis; geochemistry; mineral composition; factor analysis; paleoclimate; Holocene; Late Pleistocene

Funding

This work was funded by the subsidy allocated to Kazan Federal University for the State assignment in the sphere of scientific activities (project N FZSM-2023-0023).

Received: 14.08.2025 ***Accepted: 24.12.2025*** ***Online: 01.07.2026*** ***Published: 10.09.2026***

Introduction

At present, because of the high probability of climate-related hazards and the need to adapt to ongoing climate change, understanding modern environmental and climatic change has become a pressing issue. Studying the causes of climate change in past epochs is an important part of climate-evolution research and is of fundamental interest [1-3]. Bottom sediments of modern lakes are geochemical and mineralogical archives. Their study is useful for understanding regional and global climate change [1]. At the same time, the geochemistry of lake sediments can reflect the complexity of processes occurring not only within the lake itself but also within its catchment [4]. Climate affects the

This is an open access article under the CC BY 4.0 license

distribution of chemical elements in modern lake sediments because temperature and moisture largely govern the intensity of near-surface weathering, soil formation, and sedimentation through interactions among the atmosphere, hydrosphere, biosphere, and lithosphere [5]. Different ratios of mobile and immobile elements therefore record changes in the direction and intensity of these processes [5]. The chemical composition of lake sediments, in turn, determines their mineral composition. The mineral assemblage reflects the relative contributions of detrital, chemogenic, and biogenic material, which vary with climate. Climate controls allothigenic input, lake-level fluctuations, and lake productivity [6]. Allothigenic material is typically represented by mature minerals and is related to the composition of the source province and (or) the catchment area. Authigenic minerals are usually represented by carbonates, sulfates, chlorides, and sulfides [6].

The Southern Urals, owing to their geographic position, complex geological structure, and climate sensitivity, have attracted increasing research interest [6-8]. Among the representative lakes of the Southern Urals with thick sediment sequences are lakes Bolshoye Miassovo and Maloye Miassovo [7-9]. To date, these lakes have been studied in several respects.

The increase in lake-water mineralization in the Southern Urals over the last 100 years has been linked to climate warming in this area. For sediment cores from lakes Bolshoye Miassovo and Maloye Miassovo spanning the Late Pleistocene – Holocene, preliminary data on chemical and mineral composition have been reported [9]. A diatom analysis of sediments from Bolshoye Miassovo Lake [8] characterized the main stages of lake evolution during the Late Quaternary. A spore-pollen analysis [7] reconstructed vegetation cover within the lake catchment and the regional climatic conditions over the last 13,400 cal. yr BP.

The aim of this study is to identify the structure and material-composition features formed under climatic change during the Late Pleistocene and Holocene using long sediment cores from lakes Bolshoye Miassovo and Maloye Miassovo. For the first time in the Southern Urals, we compare sedimentary sequences from two nearby lakes using an integrated set of material proxies-grain-size, mineralogical and geochemical analyses, and magnetic parameters. This approach advances our understanding of Late Quaternary climate change.

Geographical setting and geological characteristics of the study area

Lakes Bolshoye Miassovo (55°09'59.89" N; 60°20'51.82" E) and Maloye Miassovo (55°10'04" N; 60°21'08" E) are located in the Southern Urals. They are situated within the Ural mountain-ridge zone and within the contact zone between an erosional-abrasional platform (the Trans-Ural peneplain) and the West Siberian Lowland [10].

According to the geological map of pre-Quaternary bedrock, the western margin of the studied lake group is composed mainly of rocks of the Yelanchikov formation (PR_1el), represented by plagiogneisses and migmatites (Fig.1, *a*). The plagiogneisses include biotite, amphibole-biotite, garnet-biotite, and sillimanite-garnet-biotite varieties. Migmatites are characterized by the predominance of plagioclase over K-feldspar. Compared with rocks of the Ilmenogorsk formation, both felsic and mafic rocks of the Yelanchikov formation show somewhat higher Al_2O_3 contents, lower Fe contents, and higher Ca contents. The southern and southeastern margin of the lake group is composed of rocks of the Uvildy-Kisegach monzodiorite-granosyenite-granite complex, the Kagan complex of metamorphosed ultramafic rocks and gabbroids, and rocks of the Kyshtym formation. The northern margin is composed of pre-Quaternary rocks of the following complexes and suites: the Yelanchikov formation, the Baik complex of metamorphosed ultramafics and gabbroids, the Verkhnesait and Igish suites, and the Urazbaev complex. These rocks are represented by biotite gneisses, enstatite-olivine rocks, graphite-bearing quartzites, garnet and pyroxene amphibolites, biotite plagiogneisses, staurolite-garnet-biotite rocks, micaceous quartzites, and marble.

This is an open access article under the CC BY 4.0 license

Journal of Mining Institute. 2026. Vol. 280. P. 47-69
© Anastasiya R. Yusupova, Nouria G. Nourgalieva, 2026

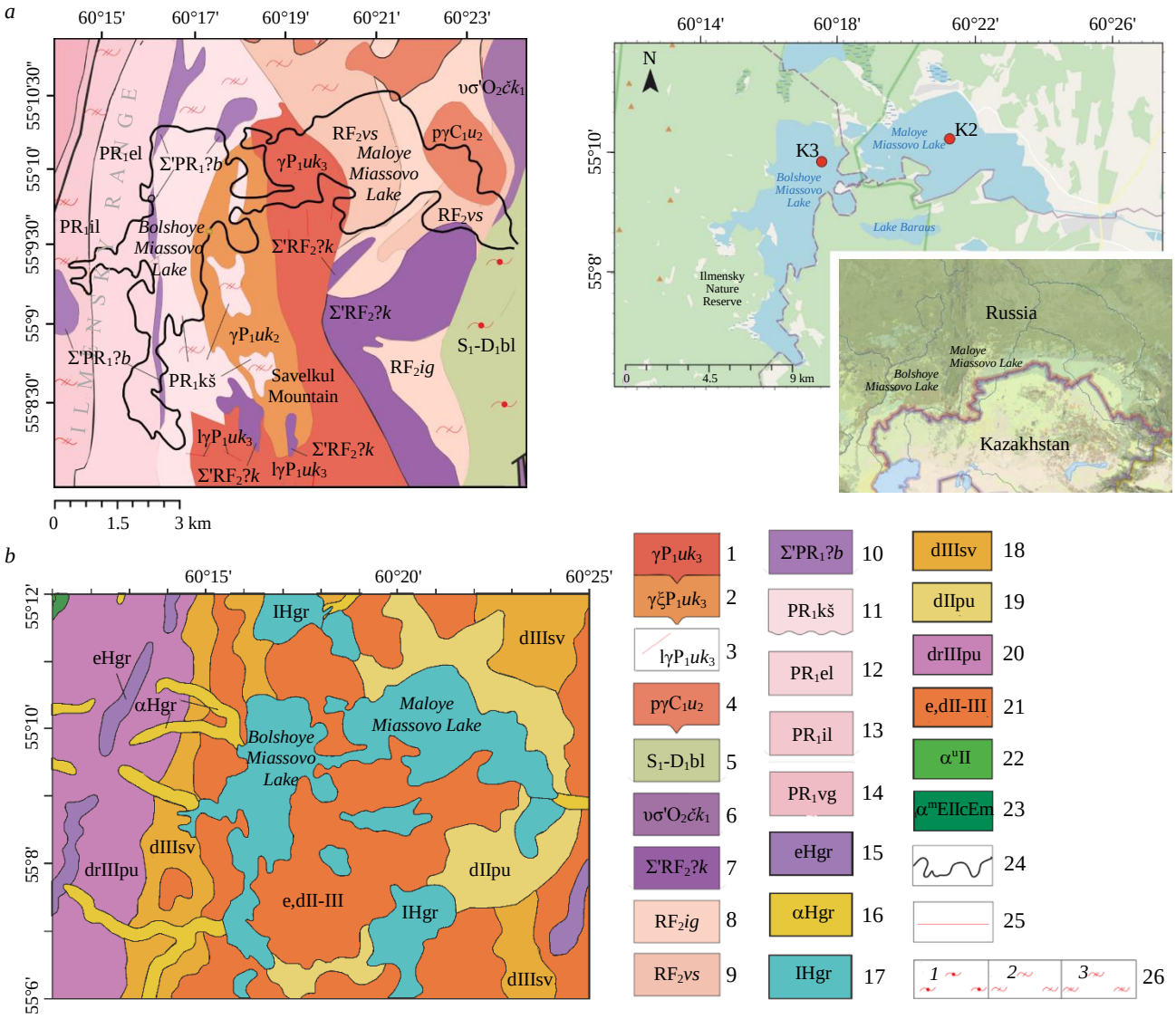


Fig.1. Schematic geological maps of the area of lakes Bolshoye Miassovo and Maloye Miassovo: *a* – pre-Quaternary bedrock; *b* – Quaternary deposits (based on the State geological map of the Russian Federation, scale 1:200,000, sheet N-41-VII)

1 – Uvildy-Kisegach monzodiorite-granosyenite-granite complex; 2, 3 – phases (2 – second phase: granosyenites, porphyritic granites, 3 – third phase: biotite granites, leucogranites, leucogranite, pegmatite dikes); 4 – Urazbaev tonalite-plagiogranite complex (plagiogranites); 5 – Bulatov formation (carbonaceous-siliceous schists, quartzites, metabasalt, and metatuff (≥ 900 m); 6 – Chebarkul-Kazbaev complex of serpentinized rocks (after dunites, harzburgites, and gabbro); first phase (serpentinites after dunites and harzburgites, less commonly after pyroxenites, antigorite serpentinites, talc-carbonate rocks); 7 – Kagan complex of metamorphosed ultramafic and gabbroic rocks (antigorite serpentinites, olivine-antigorite, olivine-talc, enstatite-talc-anthophyllite, and tremolite rocks, rarely clinopyroxenites and gabbroic rocks, talcites); 8, 9 – suites: 8 – Igish Suite (graphite-bearing quartzites, phosphate-bearing quartzites, interbeds of garnet-biotite and staurolite-garnet-biotite plagioclase schists (400-500 m), 9 – Verkhnesait Suite (amphibole plagioclase schists, garnet-biotite-amphibole schists, amphibole-biotite, biotite, and garnet-biotite schists, interbeds of graphite-bearing and phosphate-bearing quartzites (560 m); 10-14 – Ilmenogorsky Uplift: 10 – Baik complex of metamorphosed ultramafic and gabbroic rocks: enstatite-olivine rocks and related serpentinites, olivine-amphibole-enstatite rocks, anthophyllite rocks, tremolite rocks, tremolite-talc-anthophyllite rocks, talc-carbonate rocks, metagabbro; 11-14 – formations: 11 – Kyshtym formation: amphibolites, including garnet-bearing, biotite, garnet-biotite, and two-mica gneisses, mica-quartz schists, quartzites, interbeds of marble (900 m), 12 – Yelanchikov formation: biotite gneisses, less commonly garnet-biotite and amphibole-biotite gneisses, amphibolites; interbeds of graphite-bearing quartzites (1300 m), 13 – Ilmenogorsk formation: amphibolites, including biotite-, garnet-, and pyroxene-bearing, biotite and amphibole-biotite plagiogneisses, garnet-biotite plagiogneisses with sillimanite, garnet-biotite and graphite-bearing quartzites, pyroxene-plagioclase crystalline schists (600-1110 m), 14 – Vishnevogorsk formation: biotite plagiogneisses, garnet-biotite plagiogneisses with graphite and sillimanite, amphibolites, including garnet- and pyroxene-bearing, diopside-plagioclase crystalline schists, calc-silicate rocks, marbles (500-1800 m); 15-17 – Holocene: 15 – eluvial deposits: blocky-gravelly bedrock debris (up to 1.5 m), GU zone, 16 – alluvial deposits of floodplain terraces and channels: polymictic sands with gravel, silty and peaty clays, pebbles and boulders (up to 10 m), 17 – lacustrine deposits: sands, silt, and silty clays (up to 2 m); 18-23 – Pleistocene: 18-21 – Neopleistocene, Middle-Upper units (18 – Severouralsky superhorizon: slopewash deposits, brown loams with grus, crushed stone, and rare gravel of local rocks (up to 6 m), 19 – Polyarnouralsky horizon: slopewash deposits, clays with rare crushed stone of underlying rocks and rare gravel (up to 5 m), MU zone, 20 – Polyarnouralsky horizon: colluvial deposits, blocks, crushed stone, sandy clays with crushed stone (up to 5 m), GU zone, 21 – eluvial and slope-wash deposits: weathered crushed stone of underlying rocks with a loamy matrix; grus and rare pebbles (up to 2 m); 22, 23 – Eopleistocene, Upper unit: 22 – alluvial deposits of the Ufa terrace: loams, polymictic sands, interbeds of gravel with pebbles (up to 20 m), GU zone, 23 – Chumlyak horizon: alluvial deposits of the Miass terrace, polymictic sands with an admixture of gravel, loams with buried soils, gravel and pebbles (up to 20 m), GU zone; 24 – shorelines of lakes Bolshoye Miassovo and Maloye Miassovo; 25 – faults; 26 – metamorphic facies: *1* – greenschist, *2* – epidote-amphibolite, *3* – amphibolite. K2, K3 – sediment-core sampling sites

This is an open access article under the CC BY 4.0 license

The Quaternary-deposit map shows that the shores of lakes Bolshoye Miassovo and Maloye Miassovo are bordered by eluvial and slopewash deposits (e,dII-III). These deposits are represented by gravel and grus of weathered rocks with rare quartz pebbles, cemented by brown clays [11] (Fig.1, *b*). On the western and northern shores of Bolshoye Miassovo Lake, slopewash deposits of the Severouralsky superhorizon (Neopleistocene) are present (Fig.1, *b*). On the western shore of Bolshoye Miassovo Lake, Holocene alluvial deposits of floodplain terraces and channels are also present; they consist of polymictic sands with gravel, silty clays, pebbles, and boulders (Fig.1, *b*). The northern, eastern, and southeastern shores of Maloye Miassovo Lake are composed of slopewash deposits of the Polyarnouralsky horizon (Neopleistocene), represented by clays with rare gravel of the underlying rocks and rare gravel-sized material [11] (Fig.1, *b*). The thickness of Quaternary deposits rarely exceeds 10 m. Smaller thicknesses are observed in the west compared with the rest of the framing of the studied lakes.

Materials and methods

Material was collected during a scientific expedition in 2018. Detailed investigations were carried out for sediment core N 3 (55°09'51.1" N; 60°17'21.9" E) from Bolshoye Miassovo Lake (depth of 24 m) and sediment core N 2 (55°10'13.6" N; 60°21'04.6" E) from Maloye Miassovo Lake (depth of 7 m) (points K3, K2, Fig.1, *a*). The cores were selected based on preliminary seismo-acoustic surveys and rapid measurements of magnetic susceptibility. Samples were taken at 2-centimeter intervals.

Based on the primary lithological description conducted in the field, the sediment sequence of Bolshoye Miassovo Lake consists of dark-green, dense mud with abundant plant remains (interval 526-2 cm, thickness 526 cm). The upper part of the Maloye Miassovo Lake core (interval 422-2 cm, thickness 422 cm) is also composed of dark-green, dense mud with abundant plant remains. The lower part of this core (interval 512-422 cm, thickness 92 cm) consists of dense gray clayey mud. The samples were packed in plastic bags and delivered to the Laboratory of paleoclimatology, paleoecology, and paleomagnetism of Institute of Geology and Petroleum Technologies of Kazan Federal University, for subsequent comprehensive laboratory analyses.

Preliminary magnetic-property data and the primary lithological description were used to select samples for radiocarbon dating (nine samples from each site). Prepared samples were sent to NTUAMS Lab of National Taiwan University. Measurements were performed using a 1.0 MV HVE accelerator mass spectrometer. Sample ages were calibrated using OxCal 4.2.4 [12] and the IntCal20 calibration curve. Detailed procedures for sample preparation and measurements are described in [13]. Radiocarbon-dating results and the age model for Bolshoye Miassovo Lake sediments are presented in [7].

Lithological types of the studied deposits were determined by laser grain-size analysis. Initial sample pretreatment included digestion with 10 % HCl and 30 % H_2O_2 to remove carbonate and organic matter. Measurements were performed with an LS 13 320 XR particle-size analyzer (Beckman Coulter, USA) equipped with a universal liquid module. The analyzer was calibrated and internal quality control was performed using reference materials. Blanks (distilled water) were measured to control the background signal. Background was checked before each measurement; if an unacceptable background level (> 10 %) was obtained, the cuvette was washed. A background signal < 10 % was accounted for by the software when calculating the particle-size distribution. The resulting histograms show the distribution of size fractions. We also calculated the median grain size (Md), which reflects the energy of the hydrodynamic environment and lacustrine accommodation. Lithological types were classified using the classification of unlithified sediments proposed by N.V.Logvinenko.

Changes in the ratio of allothigenic and authigenic minerals are known to be informative for reconstructing depositional conditions, including climatic conditions [6, 9]. Mineral composition was determined using a D2 PHASER X-ray diffractometer. The measurement settings were as follows:

This is an open access article under the CC BY 4.0 license

X-ray tube voltage 30 kV; current 10 mA; step size 0.02°; scan speed 1°/min; Bragg – Brentano geometry; 2θ range 3-40°. Data were interpreted using DIFFRACplus Evaluation Package – EVA, Search/Match (Bruker, Germany) to perform qualitative and quantitative analyses. Analytical accuracy was ±0.02° across the entire range. The obtained diffractograms were compared with reference patterns in a computerized database. Principal d-spacings were determined and assigned to specific mineral phases. The PDF-2 international powder diffraction database was used. Quantitative analysis was performed in Topas program (Bruker, Germany) using full-profile Rietveld refinement. To investigate the morphology and elemental composition of mineral particles in the bottom sediments of the studied lakes, and to identify allothigenic/authigenic minerals, samples were examined by scanning electron microscopy. Analyses were carried out using a Merlin field-emission scanning electron microscope (Carl Zeiss, Germany) at the Interdisciplinary Center "Analytical Microscopy" of Kazan Federal University. The instrument is equipped with an Aztec X-MAX energy dispersive spectroscopy detector, energy resolution is 127 eV. Measurement accuracy is 0.01-1 %, depending on the state of the analyzed object. Surface morphology was imaged at an accelerating voltage of 5 keV to increase depth of field. Elemental analysis was performed at 20 keV and a working distance of 9 mm, which minimized analytical errors. The interaction depth was less than 1 μm.

Major and trace element contents were determined using a Bruker S8 Tiger X-ray fluorescence (XRF) spectrometer. Sample preparation included grinding the material to a particle size of 40-50 μm and pressing it with boric acid in a 20-ton press to produce a pellet with a flat surface. The pellet was then placed in the instrument for analysis. Instrument calibration was performed using standard reference materials. The matrix in the standards was SiO_2, which allows matrix effects to be taken into account when analyzing all other elements. Loss on ignition (LOI) was determined as follows. Aliquots of the studied samples (~ 0.5 g) were placed into ceramic crucibles and covered with 10 % HCl for 24 h. This treatment removed carbon contained in the sediment. The crucibles were then ignited in an SNOL1100 muffle furnace at 900 °C for 4 h. After cooling, the residue was weighed and LOI values were calculated.

Statistical processing was performed using Statistica software package. For the entire geochemical dataset from lakes Bolshoye Miassovo and Maloye Miassovo, correlation analysis was carried out using Spearman's nonparametric coefficient R at a significance level of $p < 0.05$. To better resolve the genetic characteristics of the studied objects, the geochemical datasets were tested for normality. Factor analysis was then performed using principal component analysis with "Varimax normalized" rotation. We also calculated the index of compositional variability as ICV = [(Fe_2O_3 + K_2O + Na_2O + + CaO + MgO + MnO + TiO_2) / Al_2O_3]. Values of ICV < 1 indicate weathering/maturity, and values of ICV > 1 indicate the opposite [14].

For all samples from the studied sediment cores from lakes Maloye Miassovo and Bolshoye Miassovo, normal remanent magnetization curves were obtained during a continuous increase in the external magnetic field up to 1.5 T. Measurements were performed using a J_meter coercivity spectrometer [15]. The magnetic moment sensitivity of the J_r channel (remanent magnetization) is ~$1 \cdot 10^{-8}$ A·m^2, and that of the J_i (induced magnetization) is ~$1 \cdot 10^{-6}$ A·m^2. The maximum induction of the magnetizing field is 1500 mT. Sample preparation for magnetic measurements included drying, grinding in a non-magnetic agate mortar, and packing into specialized paper containers. Each sample was weighed before measurement because sample mass is accounted for during the measurements. As a result, complete hysteresis loops were obtained simultaneously for remanent and induced magnetization. Based on the normal magnetization curves, the contributions of different components to the magnetic signal of the sediment were determined – ferromagnetic (k_ferro), dia-/paramagnetic (k_para), and superparamagnetic (k_super), following the procedure described in [16]. In general, the paramagnetic component reflects the influx of allothigenic material into the depositional basin.

This is an open access article under the CC BY 4.0 license

Ferromagnetic material has a mixed origin (allothigenic and biogenic). Superparamagnetic minerals may also be of either biogenic or allothigenic origin; superparamagnetic grains may be represented by hematite or by biogenically induced iron oxides or sulfides [16]. To perform correlation analysis between magnetic parameters and the factor-analysis results, the resulting dataset was tested for normality.

Results

Radiocarbon dating. In study [7] it was established that sedimentation in Bolshoye Miassovo Lake began no later than ~13,400 cal. yr BP. Table 1 presents the results of radiocarbon dating of sediments from Maloye Miassovo Lake; according to these data, sedimentation in the lake began no later than ~20,100 cal. yr BP. The mean sediment-accumulation rate was ~0.32 mm/year (Fig.2, *a*).

Table 1

Radiocarbon dating results for bottom sediments from Maloye Miassovo Lake*

Laboratory ID	Sample number	Depth, cm	Dated material	AMS ^{14}C age, ^{14}C yr BP	Calibrated ^{14}C age, cal. yr BP
NTUAMS-5023-1	116	30	Lake sediment	123±78	80±80
NTUAMS-5024-1	147	92		1987±82	1920±205
NTUAMS-5025-1	193	184		3396±82	3650±200
NTUAMS-5026-1	236	270		4823±87	5585±150
NTUAMS-5027-1	265	328		6814±87	7700±140
NTUAMS-8498-1	287	374		8216±83	9175±165
NTUAMS-50281	306	410		9496±85	10,840±275
NTUAMS-5029-1	323	444		11,443±95	13,330±165
NTUAMS-5031	355	508		16,462±233	19,915±545

* Radiocarbon ages are reported in years before present with the associated statistical uncertainty; "present" is defined as AD 1950.

Grain-size composition. According to the data obtained, the silt fraction predominates in sediments of both lakes (Table 2, Fig.2, *b*). Sand and clay fractions are less abundant (Table 2, Fig.2, *b*). The sediment core from Bolshoye Miassovo Lake consists mainly of interbedded light silty loam and silty sandy loam (Fig.2, *b*). The lower part of the core is represented by sandy loam (Fig.2, *b*).

Table 2

Grain-size composition of sediments from lakes Bolshoye Miassovo and Maloye Miassovo, %

Lake	Silt	Sand	Clay	Md, mm
Bolshoye Miassovo	43.33-79.07 67.48	10.00-49.10 21.73	7.29-16.93 10.79	0.01-0.05 0.02
Maloye Miassovo	47.23-74.12 64.92	13.22-40.67 23.70	5.58-19.60 11.37	0.02-0.04 0.02

Note. The numerator shows the minimum and maximum values, and the denominator shows the mean value.

In the Late Pleistocene (interval 522-502 cm, ~13,400-13,220 cal. yr BP), the sediment is represented by sandy loam, and Md is ~ 0.046 mm. Upsection (interval 502-346 cm, ~13,220-7500 cal. yr BP), Md values decrease sharply (Fig.2, *b*), with a mean of ~0.021 mm. This interval is characterized by alternation of silty sandy loam and light silty loam. A distinct event is recorded at a depth of 322 cm (~6760 cal. yr BP), where Md increases to ~0.033 mm, corresponding to the Holocene thermal maximum. The interval 322-142 cm (~6760-2600 cal. yr BP) is characterized by alternation of light silty loam and silty sandy loam; mean Md is ~0.024 mm. In the interval 142-8 cm (Subatlantic stage, ~2600-790 cal. yr BP), silt fraction predominates (Fig.2, *b*), and light silty loam is dominant. Md values are minimal, mean value is ~ 0.017 mm.

This is an open access article under the CC BY 4.0 license

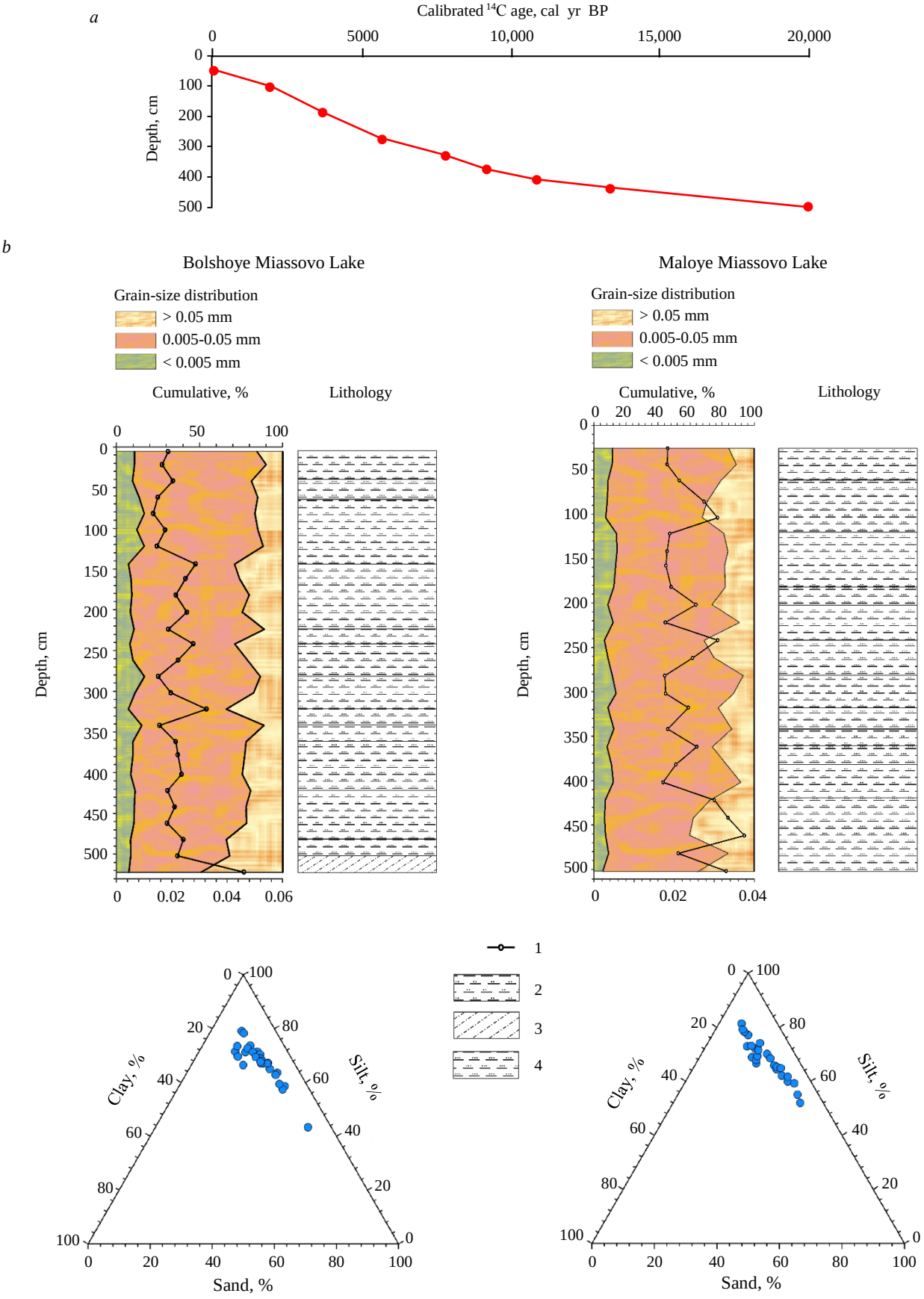


Fig.2. Age-depth model for sediments of Maloye Miassovo Lake (*a*);
results of grain-size analysis for lakes Bolshoye Miassovo and Maloye Miassovo (*b*)

1 – Md, mm; 2 – light silty loam; 3 – sandy loam; 4 – silty sandy loam

This is an open access article under the CC BY 4.0 license

The sediment sequence of Maloye Miassovo Lake is characterized by interbedding of light silty loam and silty sandy loam (Fig.2, *b*). The Pleistocene part of the Maloye Miassovo Lake core (interval 502-422 cm) is characterized by a substantial presence of the psammitic (sand) fraction (up to 40.67 %). Lithologically, the Late Pleistocene sediments are represented by silty sandy loam. The mean Md during this period is 0.03 mm. The interval 422-402 cm (beginning of the Holocene, Preboreal stage to the beginning of the Boreal stage) is characterized by a noticeable increase in the silt fraction and a marked decrease in Md to 0.015 mm. The sediments are represented by light silty loam. In the interval 402-382 cm (end of the Boreal stage), the content of the psammitic fraction increases, and Md also increases to 0.026 mm. The sediment is represented by silty sandy loam. In the interval 382-282 cm (Atlantic stage), interbedding of light silty loam and silty sandy loam is typical. Md varies within 0.018-0.024 mm. The highest Md value corresponds to the middle of the Atlantic stage (depth 318 cm, ~7200 cal. yr BP), which coincides with the Holocene thermal maximum. Sediments of the Subboreal stage are represented by interbedding of light silty loam and silty sandy loam. In the interval 262-142 cm (Subboreal stage), a pronounced increase in Md to 0.031 mm is observed (depth 242 cm, ~4900 cal. yr BP). A small increase in Md during the Subboreal stage is also recorded at 202 cm (~4000 cal. yr BP). For the Subatlantic stage (122-26 cm), an increase in Md to 0.031 mm is observed at 104 cm (~2100 cal. yr BP).

Mineral composition. X-ray diffraction analysis showed that sediments from the studied lakes are characterized by the predominance of allothigenic minerals (Table 3).

Table 3

Mineral composition of sediments from lakes Bolshoye Miassovo and Maloye Miassovo, %

Lake	Allothigenic minerals	Opal + + cristobalite + + tridymite	Pyrite	Gypsum	Calcite
Bolshoye Miassovo	49-80 63	6-36 24	1-9 4	2-26 7	2-19 9
Maloye Miassovo	20-84 71	9-26 15	1-5 2	2-77 14	3-20 7

Note. The numerator shows the minimum and maximum values, and the denominator shows the mean value.

In sediments of Bolshoye Miassovo Lake, allothigenic minerals are represented by quartz, microcline, albite, mica, chlorite, and amphiboles. In sediments of Maloye Miassovo Lake, in addition to the minerals listed above, talc and mixed-layer clay minerals were identified (Fig. 3, *a*). Biogenic silica was recorded in sediments from both lakes (Fig.4, image 3, Fig.5, images 1, 6). Its abundance was assessed from the content of opal + cristobalite + tridymite (see Fig.3, *a*), which are associated with an X-ray amorphous biogenic component. This component includes material derived from diverse diatom frustules and stomatocysts (see Fig.4, image 3) [17]. Scanning electron microscopy showed that stomatocysts are spherical and mostly have smooth surfaces, with sizes of 5-10 μm (see Fig.4, image 3, Fig.5, images 1, 6) [18]. Authigenic pyrite was identified using scanning electron microscopy (see Fig.4, image 10, Fig.5, images 3, 11). Carbonate minerals were also detected in sediments from the studied lakes, including calcite (see Fig.3, *b*, Fig.4, images 1, 11, Fig.5, image 9), aragonite (see Fig.4, images 4, 6, 7, 9, Fig.5, image 4) and dolomite (see Fig.4, image 5, Fig.5, images 8, 10). Sulfates in sediments of lakes Maloye Miassovo and Bolshoye Miassovo are represented by gypsum (see Fig.3, Fig.4, image 8, Fig.5, images 2, 5, 7) and barite (see Fig.4, image 2). Iron oxides were also recorded in sediments of Bolshoye Miassovo Lake (see Fig.4, image 12).

This is an open access article under the CC BY 4.0 license

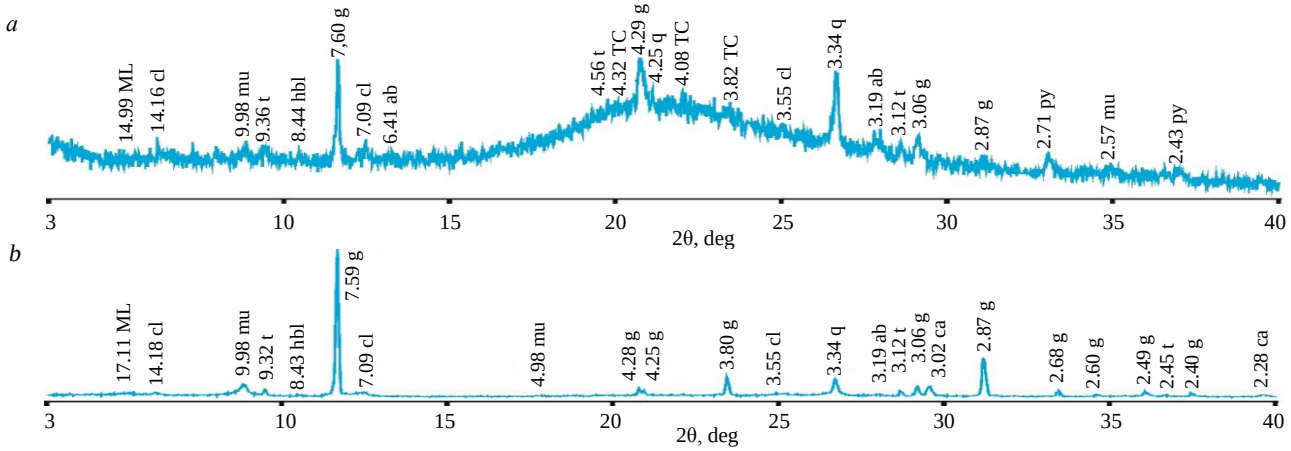


Fig.3. X-ray diffraction patterns from depths 20 cm (*a*) and 500 cm (*b*)
ML – mixed-layer clay minerals; TC – tridymite-cristobalite phase; cl – chlorite; mu – muscovite; t – talc; hbl – hornblende; g – gypsum; ab – albite; q – quartz; py – pyrite; ca – calcite

Chemical composition of sediments based on XRF data. Table 4 presents data on the contents of major chemical elements in sediments from lakes Bolshoye Miassovo and Maloye Miassovo. Among trace components in the sediments, the presence of Cl, BaO, SrO, Br, V_2O_5, ZnO, NiO, Cr_2O_3, CuO, MoO_3, ZrO_2, Rb_2O, CoO was identified, with mean contents, wt.%: 0.05; 0.0238; 0.019; 0.0135; 0.0126; 0.0095; 0.0078; 0.0075; 0.0058; 0.0041; 0.0040; 0.0033; 0.0012. In addition, along the sediment core from Bolshoye Miassovo Lake, UO_2 was detected in six samples (mean content 0.0056 wt.%), Nb_2O_5 was detected in two samples (mean content 0.0012 wt.%) and Y_2O_3 was detected in one sample (mean content 0.0012 wt.%). In sediments from Maloye Miassovo Lake, the presence of Cl, BaO, SrO, Br, NiO, Cr_2O_3, V_2O_5, ZnO, was recorded, with mean contents, wt.%: 0.051; 0.025; 0.018; 0.010; 0.015; 0.015; 0.013; 0.01. Less common trace components in sediments of Maloye Miassovo Lake include CuO, PbO, ZrO_2, Y_2O_3, Rb_2O, Ga_2O_3, As_2O_3, CoO, with mean contents, wt.%: 0.007; 0.005; 0.005; 0.004; 0.003; 0.002; 0.002; 0.0015.

Table 4

Descriptive statistics for major-element contents in sediments of lakes Bolshoye Miassovo and Maloye Miassovo, wt.%

Component	Minimum	Maximum	Mean	Standard deviation	Number of samples
Bolshoye Miassovo Lake					
SiO_2	19.0	40.1	30.6	5.1	53
TiO_2	0.1	0.7	0.2	0.1	53
Al_2O_3	1.6	9.9	3.6	2.1	53
Fe_2O_3	2.0	7.3	3.6	1.1	53
MnO	0.1	0.6	0.2	0.1	53
MgO	0.5	4.3	1.3	0.9	53
CaO	0.7	20.5	4.4	6.0	53
Na_2O	0.0	0.7	0.3	0.2	53
K_2O	0.3	2.3	0.7	0.5	53
P_2O_5	0.3	0.7	0.5	0.1	53
SO_3	3.01	18.7	6.2	3.5	53
LOI	22.6	58.6	48.2	10.2	53
Maloye Miassovo Lake					
SiO_2	8.0	47.9	18.5	6.5	52
TiO_2	0.1	0.9	0.3	0.1	52
Al_2O_3	2.1	17.6	5.2	2.7	52
Fe_2O_3	1.0	8.1	3.5	1.4	52
MnO	0.0	0.5	0.1	0.1	52
MgO	1.0	4.5	2.1	0.8	52
CaO	1.2	29.5	5.5	7.8	52
Na_2O	0.2	0.7	0.3	0.1	49
K_2O	0.3	2.6	0.8	0.5	52
P_2O_5	0.3	0.8	0.4	0.1	52
SO_3	1.1	30.7	7.2	6.2	52
LOI	22.5	75.9	56.8	15.6	52

This is an open access article under the CC BY 4.0 license

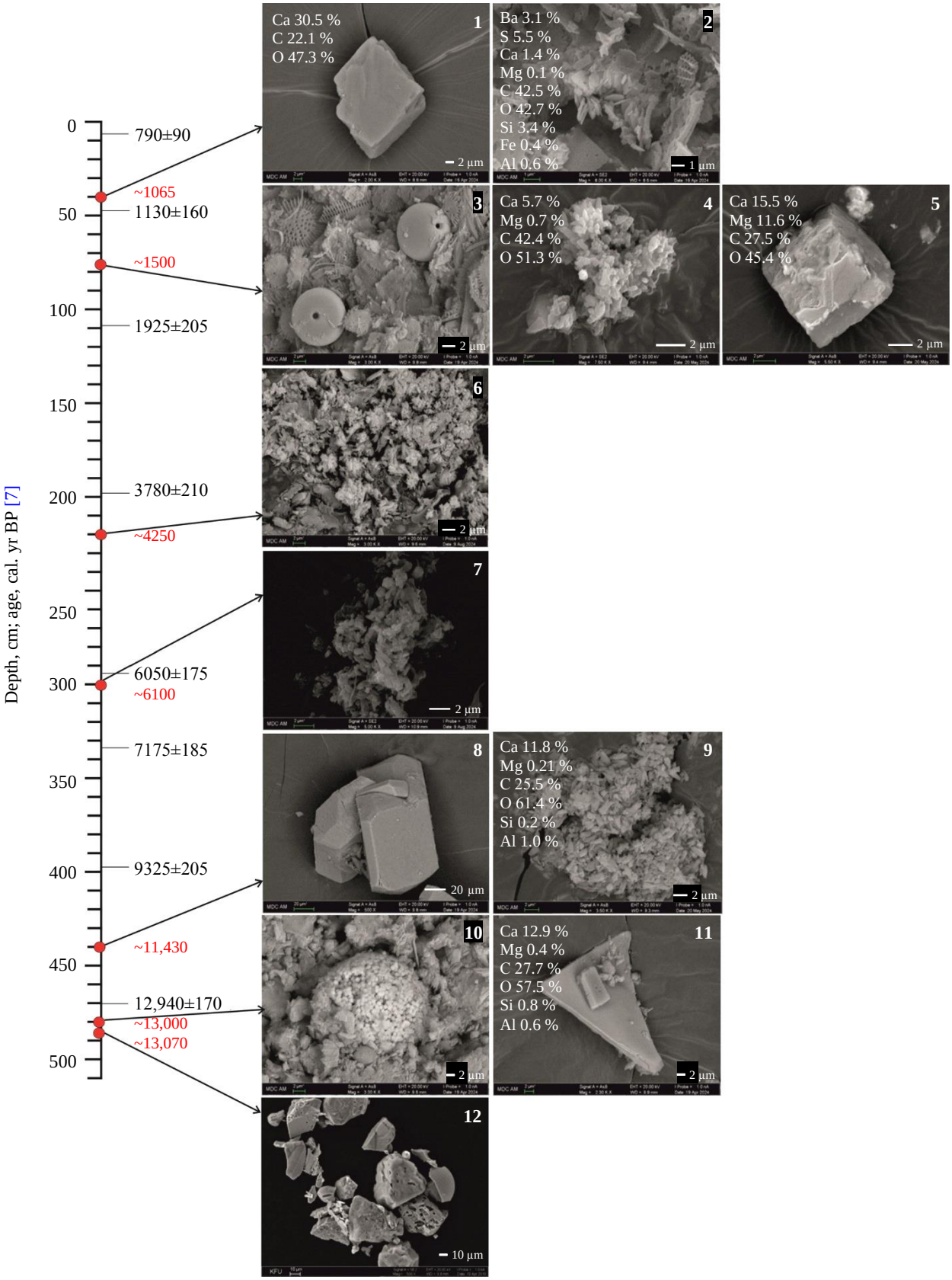


Fig.4. Scanning electron microscope images of studied samples

1, 11 – calcite; 2 – barite; 3 – biogenic silica; 4, 6, 7, 9 – aragonite; 5 – dolomite; 8 – gypsum; 10 – pyrite; 12 – iron oxides

This is an open access article under the CC BY 4.0 license

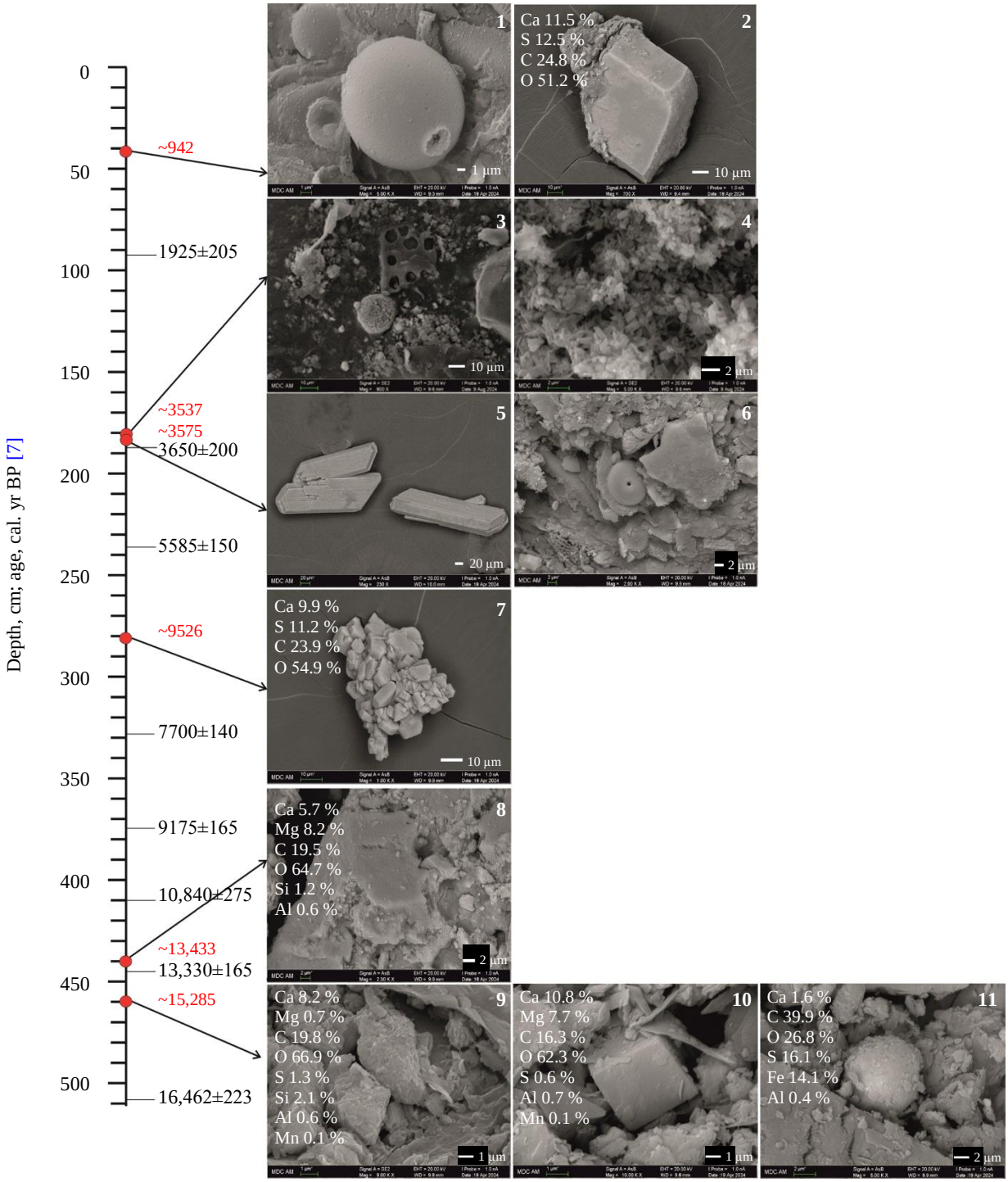


Fig.5. Scanning electron microscope images of studied samples

1, 6 – biogenic silica; 2, 5, 7 – gypsum; 3, 11 – pyrite; 4 – aragonite; 8, 10 – dolomite; 9 – calcite

Figure 6 shows the chemical compositions of the studied sediments compared with the compositions of other lakes and rocks forming the surroundings of the lakes.

Values of the ICV, which reflects the effects of recycling and sorting of sedimentary material, were calculated. Sediments from lakes Bolshoye Miassovo and Maloye Miassovo show high ICV values (> 1). This allowed us to conclude that the studied deposits represent products of primary allothigenic input [19, 20].

This is an open access article under the CC BY 4.0 license

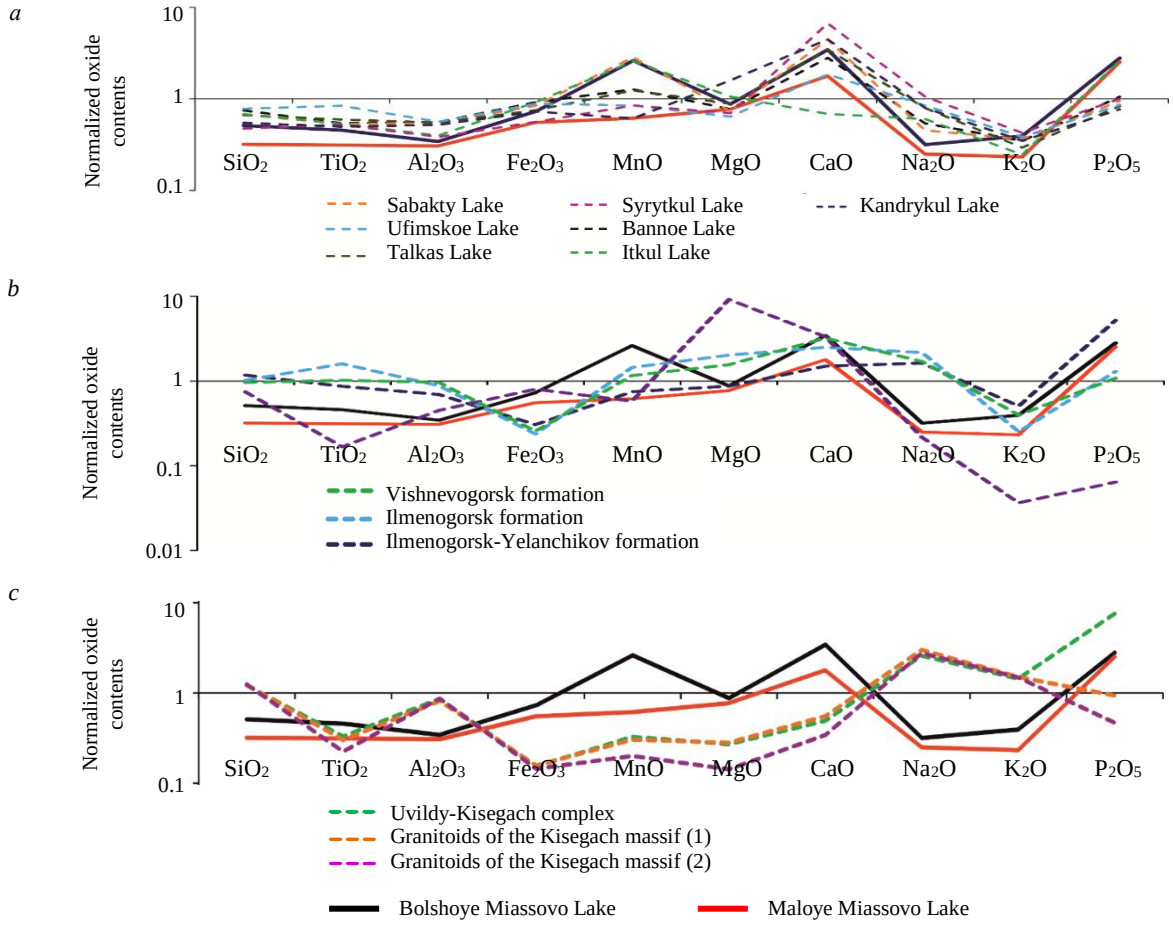


Fig.6. Comparison of the major-element compositions of sediments from lakes Bolshoye Miassovo and Maloye Miassovo with published datasets from [6, 17, 21, 22] (*a*), chemical compositions of rocks of the Vishnevogorsk and Ilmenogorsk-Yelanchikov formations, and the Baik complex after [11], and chemical composition of rocks of the Ilmenogorsk formation after [23] (*b*), chemical compositions of rocks of the Uvildy-Kisegach complex after [11], granitoids of the Kisegach massif (1) after [24], and granitoids of the Kisegach massif (2) after [23] (*c*). Normalization was performed after [20]

The results of correlation analysis for the entire dataset from Bolshoye Miassovo Lake (Table 5) and Maloye Miassovo Lake (Table 6) are presented. Spearman's rank correlation coefficients were used, pairwise deletion was applied, correlations highlighted in red are significant at $p < 0.05$ (Tables 5, 6).

Table 5

Correlation matrix (Bolshoye Miassovo Lake)

	LOI	Na_2O	MgO	Al_2O_3	SiO_2	P_2O_5	SO_3	Cl	K_2O	CaO	TiO_2	MnO	Fe_2O_3	NiO	CuO	ZnO	Rb_2O	SrO	ZrO_2
LOI	**1.00**																		
Na_2O	–0.46	**1.00**																	
MgO	–0.48	0.86	**1.00**																
Al_2O_3	–0.34	0.66	0.82	**1.00**															
SiO_2	–0.32	–0.38	–0.43	–0.55	**1.00**														
P_2O_5	–0.17	0.44	0.53	0.30	0.03	**1.00**													
SO_3	0.27	0.16	0.20	0.35	–0.77	–0.25	**1.00**												
Cl	0.27	–0.10	–0.13	–0.37	0.21	0.28	–0.06	**1.00**											
K_2O	–0.47	0.81	0.96	0.88	–0.41	0.49	0.19	–0.20	**1.00**										
CaO	–0.61	0.80	0.80	0.48	–0.18	0.43	–0.06	–0.01	0.73	**1.00**									
TiO_2	–0.49	0.78	0.94	0.88	–0.40	0.47	0.19	–0.23	0.98	0.71	**1.00**								
MnO	–0.56	0.25	0.31	0.15	0.10	0.34	–0.13	0.04	0.22	0.45	0.25	**1.00**							
Fe_2O_3	0.05	0.20	0.31	0.63	–0.62	0.08	0.47	–0.42	0.36	–0.11	0.38	0.13	**1.00**						
NiO	–0.42	0.70	0.84	0.85	–0.38	0.51	0.23	–0.23	0.87	0.52	0.89	0.30	0.53	**1.00**					
CuO	–0.35	0.53	0.69	0.80	–0.40	0.23	0.25	–0.54	0.75	0.36	0.76	0.12	0.58	0.75	**1.00**				
ZnO	–0.05	0.22	0.34	0.36	–0.03	0.56	–0.13	0.06	0.37	0.10	0.37	0.16	0.31	0.44	0.34	**1.00**			
Rb_2O	–0.48	0.68	0.80	0.74	–0.34	0.35	0.12	–0.22	0.81	0.70	0.83	0.32	0.34	0.75	0.66	0.26	**1.00**		
SrO	–0.65	0.81	0.83	0.52	–0.16	0.47	–0.05	0.00	0.77	0.98	0.75	0.47	–0.07	0.59	0.40	0.14	0.73	**1.00**	
ZrO_2	–0.48	0.78	0.90	0.82	–0.40	0.50	0.22	–0.19	0.95	0.71	0.94	0.25	0.37	0.83	0.74	0.35	0.80	0.75	**1.00**

This is an open access article under the CC BY 4.0 license

Table 6

Correlation matrix (Maloye Miassovo Lake)

	LOI	Na_2O	MgO	Al_2O_3	SiO_2	P_2O_5	SO_3	K_2O	CaO	TiO_2	Cr_2O_3	MnO	Fe_2O_3	NiO	CuO	ZnO	Rb_2O	SrO	ZrO_2
LOI	**1.00**																		
Na_2O	–0.66	**1.00**																	
MgO	–0.78	0.73	**1.00**																
Al_2O_3	–0.85	0.68	0.93	**1.00**															
SiO_2	–0.54	0.51	0.74	0.73	**1.00**														
P_2O_5	–0.48	0.59	0.78	0.73	0.73	**1.00**													
SO_3	–0.38	0.19	0.24	0.22	–0.25	0.02	**1.00**												
K_2O	–0.84	0.70	0.93	0.99	0.72	0.73	0.23	**1.00**											
CaO	–0.81	0.62	0.60	0.63	0.16	0.35	0.58	0.64	**1.00**										
TiO_2	–0.75	0.69	0.95	0.97	0.82	0.81	0.10	0.97	0.51	**1.00**									
Cr_2O_3	–0.57	0.56	0.84	0.76	0.78	0.85	0.03	0.73	0.32	0.83	**1.00**								
MnO	–0.91	0.67	0.75	0.82	0.34	0.50	0.53	0.82	0.93	0.70	0.49	**1.00**							
Fe_2O_3	–0.58	0.65	0.88	0.84	0.80	0.88	0.02	0.83	0.34	0.92	0.84	0.54	**1.00**						
NiO	–0.59	0.64	0.91	0.84	0.82	0.90	0.04	0.83	0.37	0.92	0.90	0.56	0.94	**1.00**					
CuO	–0.69	0.60	0.81	0.86	0.70	0.75	0.10	0.87	0.47	0.88	0.75	0.67	0.82	0.84	**1.00**				
ZnO	–0.58	0.61	0.87	0.84	0.73	0.90	0.10	0.84	0.42	0.89	0.86	0.61	0.89	0.94	0.87	**1.00**			
Rb_2O	–0.78	0.73	0.89	0.87	0.70	0.74	0.21	0.85	0.61	0.87	0.78	0.74	0.83	0.83	0.77	0.85	**1.00**		
SrO	–0.86	0.60	0.66	0.71	0.22	0.34	0.59	0.71	0.95	0.58	0.37	0.93	0.40	0.43	0.52	0.49	0.71	**1.00**	
ZrO_2	–0.77	0.70	0.92	0.94	0.66	0.71	0.27	0.95	0.66	0.93	0.71	0.79	0.83	0.82	0.80	0.85	0.90	0.75	**1.00**

Factor analysis. As a result of factor analysis of the geochemical dataset for Bolshoye Miassovo Lake sediments (for the retained variables), five factors (F1-F5) were identified. Each factor includes variables with significant loadings of at least 0.7 (Table 7).

From Table 7 it can be seen that, for Bolshoye Miassovo Lake, factor F1 explains the largest share of the total variance (0.33) and is associated with increased contents of Ti, K, Mg, Ni, and Zr. Biogenic-chemogenic particles are represented by biogenic silica, carbonates, sulfates, and sulfides (see Fig.4, 5). Their contribution is reflected in the structure of factors F2-F5 (Table 7). For Bolshoye Miassovo Lake, these factors indicate pyrite crystallization (F2), carbonate formation (F3), Br accumulation (F4) as an indicator of Holocene warming [25], and Cl accumulation (F5) – chlorine may originate from rocks containing small inclusions of chloride salts in pores and fractures (Table 7). Factor F2 accounts for 0.19 of the total variance and has a bipolar structure. On one pole it reflects increasing Fe and S contents, and on the other pole it reflects decreasing Si. Factor F3 accounts for 0.13 of the total variance and is associated with increased Ca and Sr contents. Factor F4 (0.09 of the total variance) and factor F5 (0.08 of the total variance) are the bromine and chlorine factors, respectively.

For sediments of Lake Maloye Miassovo, the largest share of the total variance (0.48) is explained by factor F1 (Table 7). Factor F1 has a bipolar structure: on one pole it correlates with increasing contents of allothigenic elements Si, Ti, Al, Cr, K, Ni, Mg, Cu, Zn, Fe, Rb, and Zr, and on the other pole it reflects decreasing organic-matter content (LOI). Factor F2, which explains 0.21 of the total variance, reflects increasing Ca, Sr, and S contents. Factor F3 (0.06 of the total variance) correlates with increasing Cl contents. Factor F4 is associated with increasing Br contents (0.06 of the total variance). These factors are analogous to factors F5 and F4 for Bolshoye Miassovo Lake. Factor F5 (0.06 of the total variance) reflects increasing phosphorus contents.

Coercivity spectrometry. For Bolshoye Miassovo Lake, total magnetic susceptibility (k_full) ranges within $(2.16\text{-}52.16)\cdot10^{-5}$, k_para ranges within $(1.81\text{-}8.33)\cdot10^{-5}$, k_ferro ranges from $0.24\cdot10^{-5}$ to $42.61\cdot10^{-5}$ and k_super ranges from $0.001\cdot10^{-5}$ to $1.35\cdot10^{-5}$. For Maloye Miassovo Lake, k_full ranges from $(1.31\text{-}22.31)\cdot10^{-5}$, k_para ranges from $(0.29\text{-}8.78)\cdot10^{-5}$, k_ferro ranges from $0.03\cdot10^{-5}$ to $15.41\cdot10^{-5}$ and k_super ranges within $0.001\cdot10^{-5}$ to $0.41\cdot10^{-5}$. A strong positive relationship between k_para and factor F1 was found for both lakes (correlation coefficient 0.65 for Bolshoye Miassovo Lake sediments and 0.79 for Maloye Miassovo Lake sediments).

Late Pleistocene sediments of Bolshoye Miassovo Lake (depth interval 528-480 cm, ~13,400-13,000 cal. yr BP), represented by sandy loam and silty sandy loam, show reduced k_para values. The end of the Late Pleistocene (depth interval 480-448 cm, ~13,000-11,700 cal. yr BP) is characterized

This is an open access article under the CC BY 4.0 license

by increased k_para values. During the interval 480-304 cm (~11,700-6200 cal. yr BP), k_para varies within (2.02-4.95)·10^{-5}. During the Subboreal stage, k_para and factor F1 decrease sharply, whereas Md increases at 242 cm (~ 4752 cal. yr BP).

Table 7

Results of factor analysis of sediments of lakes Bolshoye Miassovo and Maloye Miassovo

Component	F1	F2	F3	F4	F5
Bolshoye Miassovo Lake					
Mg	0.83	0.18	0.33	0.21	0.15
Si	–0.21	–0.5	–0.07	–0.11	–0.02
P	0.46	0.05	0.23	0.22	0.12
Cl	0.12	–0.05	0.26	0.09	0.95
K	0.91	0.17	0.21	0.18	0.10
Ti	0.94	0.19	0.13	0.13	0.05
Ni	0.79	0.31	0.02	0.01	0.00
Fe	0.20	0.83	–0.38	–0.16	–0.18
Br	0.32	0.07	0.30	0.87	0.11
Rb	0.59	0.07	0.28	0.08	0.14
Sr	0.40	–0.22	0.73	0.30	0.29
Zr	0.75	0.19	0.18	0.33	0.11
S	0.20	0.95	–0.11	0.11	0.02
Ca	0.29	–0.24	0.83	0.21	0.27
Total variance	4.64	2.67	1.89	1.20	1.17
Share of total variance	0.33	0.19	0.13	0.09	0.08
Maloye Miassovo Lake					
LOI	–0.88	–0.36	–0.06	–0.09	–0.16
Na	0.32	0.31	0.05	0.15	0.13
Mg	0.82	0.46	0.14	0.16	0.11
Al	0.89	0.34	0.11	0.11	0.16
Si	0.85	–0.06	–0.11	0.13	0.08
P	0.45	0.16	0.22	0.07	0.83
Cl	0.11	0.36	0.91	0.02	0.17
K	0.87	0.38	0.11	0.11	0.17
Ca	0.26	0.87	0.16	0.01	0.24
Ti	0.90	0.32	0.05	0.14	0.17
Cr	0.85	0.20	0.13	0.09	0.25
Mn	0.64	0.65	0.16	–0.14	0.22
Fe	0.85	0.31	0.04	0.10	0.20
Ni	0.82	0.37	0.19	0.15	0.26
Zn	0.73	0.25	0.30	0.11	0.18
Br	0.25	0.00	0.02	0.96	0.05
Rb	0.75	0.49	0.10	0.24	0.01
Sr	0.47	0.80	0.21	0.19	–0.04
Zr	0.75	0.56	0.08	0.22	–0.01
S	0.25	0.82	0.28	–0.13	0.05
Cu	0.74	0.00	0.30	0.15	0.18
Total variance	9.98	4.33	1.36	1.30	1.21
Share of total variance	0.48	0.21	0.06	0.06	0.06

Late Pleistocene sediments of Maloye Miassovo Lake (depth interval 512-454 cm, ~ 20,100-14,700 cal. yr BP) are characterized by low k_para values. The subsequent warm Bølling stage 454-448 cm, ~14,700-14,100 cal. yr BP) is accompanied by a sharp increase in k_para; values then vary within a narrow range from 5.59·10^{-5} to 6.92·10^{-5} until the beginning of the Holocene. The Preboreal and Boreal stages (depth interval 422-398 cm, ~11,700-10,200 cal. yr BP) show a decreasing trend in k_para, indicating reduced input of allothigenic material. At the same time, LOI increases, indicating higher organic-matter content in the sediment. The beginning of the Atlantic stage (depth interval 354-346 cm, ~ 8500-8200 cal. yr BP) is marked by a sharp increase in k_para and factor F1, together with a sharp decrease in LOI. In addition to the events described above, the Subatlantic stage is characterized by a sharp decrease in k_para and factor F1, and by a sharp increase in Md and in the proportion of the psammitic fraction at 104 cm (~ 2100 cal. yr BP). This depth is also characterized by increased LOI and increased biogenic-silica content.

This is an open access article under the CC BY 4.0 license

Discussion

Based on grain-size data and mineralogical and chemical composition, the studied lacustrine sediments show a pattern typical of freshwater lakes: the predominance of allothigenic particles in the silt-size range.

Comparison of the geochemical composition of sediments from the studied lakes with that of the other lakes of the Southern Urals shows the expected regional similarity (Fig.6, *a*). Distinctive features include higher MnO and CaO contents in sediments of Bolshoye Miassovo Lake. These values reflect a substantial presence of authigenic carbonates and evaporites in the sediment (see Fig.4). In contrast, sediments of Maloye Miassovo Lake have higher P_2O_5 contents, which is linked to the occurrence of phosphorite-bearing rocks within the lake basin (see Fig.1).

Analysis of geological maps of pre-Quaternary bedrock and Quaternary deposits (see Fig.1) indicates that the main source of allothigenic material for the studied lakes is Quaternary deposits. These deposits are represented by eluvial, slopewash, colluvial, and alluvial facies. As expected, they consist of clasts of mature mineral components such as quartz, feldspars, clay minerals, and iron oxides. In the west, Quaternary deposits are only a few meters thick, whereas around the rest of the lakes their thickness can reach up to 20 m. Therefore, when deep channel incisions develop from the west, material may enter the lake as a result of erosion not only of Quaternary deposits but also of pre-Quaternary bedrock. In the western sector, erosion may primarily affect the Ilmenogorsk formation, the Yelanchikov formation, and the Baik complex (see Fig.1). Figure 6, *b* compares the chemical composition of rocks from these formations with that of the lake sediments.

On the western shore of Bolshoye Miassovo Lake, amphibolites of the Ilmenogorsk formation crop out. Compared with amphibolites of the Kyshtym formation, which occur farther east, these amphibolites are characterized by lower Na contents and slightly lower Ca and Fe contents. The low Na_2O contents in sediments of the studied lakes (Fig.6, *b*) are likely related to leaching of amphibolites of the Ilmenogorsk formation, as well as leaching of mafic and ultramafic rocks of the Ilmenogorsk complex and igneous rocks of the Ilmensky Mountains [26].

The eastern shore of Bolshoye Miassovo Lake is composed of granitoids of the Kisegach massif. A comparative plot of major elements for lakes Bolshoye Miassovo and Maloye Miassovo and the chemical composition of rocks of the Kisegach massif is shown in Fig.6, *c* [24]. Rocks of the Kisegach massif are represented mainly by leucogranites, which locally contain small xenoliths of granosyenites, granodiorites, and adamellites. The comparative plots (Fig.6) show that the chemical composition of sediments from the studied lakes is less similar to the composition of rocks of the Uvildy-Kisegach complex and to granitoids of the Kisegach massif (Fig.6, *c*). This suggests that allothigenic material was supplied not directly from the Uvildy-Kisegach complex and the Kisegach massif, but from the Quaternary deposits that overlie them. On the eastern side of the lakes, these Quaternary deposits are thicker than on the western side (see Fig.1).

Based on ICV values and A-CN-K diagrams [19, 20], the sediments of the studied lakes formed predominantly from stable allothigenic minerals of the primary sedimentation cycle, sourced mainly from Quaternary deposits and exposed pre-Quaternary rocks. The transport pathways of allothigenic material are linked to the directions of slope flows and channel networks visible on the Quaternary-deposit map (see Fig.1).

Based on correlation matrix for Bolshoye Miassovo Lake, Si, among the major elements, shows a pronounced negative correlation with Al, Fe, and S (see Table 5). At the same time, Si shows no correlation with Ti, Mg, K, or Na. This pattern suggests that a substantial fraction of Si is hosted in quartz grains, while another substantial fraction is associated with biogenic silica. This interpretation is generally supported by scanning electron microscopy (see Fig.4, image 3). Al shows positive correlations with K, Ti, Fe, Ni, Cu, Rb, Sr, and Zr. This allows us to infer the presence of feldspars, montmorillonite, rutile, anatase, iron oxides, nickel sulfides, and zircons. Indeed, aluminosilicate minerals such as feldspars and montmorillonite clays show a positive relationship between Al and K, as well as with other cations, for example Ti [27]. In titanium oxides (rutile and anatase), Ti can be

This is an open access article under the CC BY 4.0 license

substituted by Al in the crystal lattice. Hematite and magnetite are Fe-bearing minerals in which Fe can be isomorphically substituted by Al [28]. In nickel sulfides, the association of Ni and Fe with Al can reflect their common magmatic source. In zircons, a positive correlation between Zr and Al may occur due to structural substitutions [29]. Rb belongs to the alkali-element group and can substitute for K in the structures of feldspars or montmorillonite. A positive correlation of Rb with Al has been reported for alkaline silicate rocks [30].

The mineralogical inferences based on chemistry are supported by X-ray diffraction data (XRD) (see Table 3, Fig.3), which revealed feldspars, mixed-layer clays, and other clay minerals in substantial amounts. Other minerals (hematite, magnetite, nickel sulfides, zircons) are not detected by XRD because their contents are below 2 % and they occur as accessory phases. A positive correlation of Na with Mg, K, Ca, and Ti is typical for a number of mineral groups. For example, in nepheline-bearing silicates, Na content is closely related to the presence of K, Ca, and Mg [31]. In Na-Mg silicates, Na often substitutes for K or Mg in structural sites [32]. In leucoxenes or rutile, Ti content can correlate with Na [33]. In sodium-calcium carbonates, Na content is linked to Ca through exchange processes [34]. Positive relationships of Mg with K, Ca, Ti, and P may indicate the presence of magnesian carbonates and phosphates [35]. For example, magnesium hydrogen phosphate (magnesium phosphate) contains substantial Mg associated with the phosphate group. In Ti- and K-rich pegmatites, minerals with elevated Mg contents are often found. [36]. In olivines, Mg content is related to Ca and sometimes to K in cases of structural substitution [37]. In natural olivines, Mg often correlates with Ti due to inclusions or substitutions in the structure [38]. LOI shows a negative correlation with Ca, Mn, and Sr. This indicates an inverse relationship between carbonate material and organic matter. Organic matter in sediments decomposes upon heating and causes substantial mass loss. Therefore, higher organic-matter content results in higher LOI. In clay-rich sedimentary deposits, organic matter is associated with humic substances, organic remains, or hydrated compounds. In carbonate deposits, mass loss is also related to the decomposition of $CaCO_3$, while the proportion of organic matter decreases [39]. The pattern of correlations for Maloye Miassovo Lake (see Table 6) may be controlled by several mineral groups: the (Si, Al, Ti, Zr, K, Mg, Fe) association may reflect silicate minerals (quartz, opal, clay minerals); the (Al, Si, K, Mg, Fe) association may reflect clay minerals (kaolinite, illite, smectite); the P-Ca association may reflect phosphate minerals (apatite); the (Fe, S, Cu) association may reflect sulfates and sulfides; Fe alone may reflect hematite and magnetite; the (Zr, Si) association may reflect zircons; and the (Mg, Ca) association may reflect magnesite and dolomite [40, 41]. The negative correlation of LOI with all elements indicates that, as in Bolshoye Miassovo Lake, LOI is associated with hydrated and/or organic components that readily decompose upon heating.

According to the factor analysis for Bolshoye Miassovo Lake (Table 7), factor F1 explains the largest share of the total variance and is associated with increased Ti, K, Mg, Ni, and Zr contents. The most likely candidates responsible for a simultaneous increase in Ti, K, Mg, Ni, and Zr-either as trace admixtures or through isomorphism are K-feldspars (minerals derived from sedimentary rocks); garnets and zircon (igneous minerals); titanomagnetite (a magnetic mineral formed during metasomatism); hornblende, and sulfides of hydrothermal ores [40]. The influence of factor F2 can be explained as follows. In lacustrine bottom sediments, decreasing Eh-among other reasons due to decomposition of organic matteroften activates bacterial sulfate reduction. This process reduces Fe(III) to Fe(II), which is readily precipitated as hydrogenic hydrates or sulfides (e.g., pyrite). In lake sediments, Si is largely represented by diatom remains (silica), which precipitate actively under favorable conditions. Under acidic or alkaline conditions, diatom skeletons may dissolve or decompose due to bacterial activity. When Eh decreases, silica dissolution can intensify due to the formation of soluble Si species. Thus, increasing Fe and S may be related to post-sedimentary formation of hydrogenic sulfides, whereas decreasing Si may reflect dissolution of diatom remains under changed environmental conditions [40, 41]. Factor F3 is associated with increased Ca and Sr contents. Calcium and strontium have similar chemical properties because both are alkaline-earth elements and form analogous compounds, for example carbonates ($CaCO_3$ and $SrCO_3$). Strontium often enters Ca-bearing

This is an open access article under the CC BY 4.0 license

minerals such as calcite ($CaCO_3$), which promotes their joint supply and accumulation in sediments. Inputs of Ca and Sr from surrounding rocks affect their concentrations in lake water. For example, weathering of limestones or dolomites increases the concentrations of these elements in the lake. In regions where limestones and dolomites are common, Ca and Sr levels increase in water and, consequently, in bottom sediments.

Climate change can influence the chemical balance of lakes. Higher humidity promotes leaching of elements from soils and rocks, whereas temperature changes affect biological activity and sedimentation rates. This can lead to a simultaneous increase in Ca and Sr concentrations [21]. Factors F4 and F5 are the bromine and chlorine factors, respectively. In freshwater lakes, exchange with the surrounding environment can lead to accumulation of Cl and Br through infiltration of water from surrounding soils and rocks. Decomposition of organic matter and biogeochemical cycles can contribute to the mobilization and redistribution of Br and Cl within the lake [42].

For Maloye Miassovo Lake, the factor analysis (Table 7), shows that factor F1 is associated with increased contents of allothigenic elements Si, Ti, Al, Cr, K, Ni, Mg, Cu, Zn, Fe, Rb, and Zr, and with decreased organic-matter content (LOI). This pattern reflects an increase in stable minerals (hematite, quartz, feldspars, zircon, kaolinite, chlorite, and hornblende) and a decrease in hydrated clays and organic matter [40, 41]. Factor F2 reflects increasing Ca, Sr, and S contents and is similar to factor F3 for Bolshoye Miassovo Lake (the coupled increase in Ca and Sr). The difference for Maloye Miassovo Lake is the additional element S. This structure can be explained by the simultaneous formation of carbonate and sulfate minerals in Maloye Miassovo Lake sediments. Factors F3 and F4 are analogous to factors F5 and F4, respectively, for Bolshoye Miassovo Lake. Factor F5 reflects increasing phosphorus contents, which may indicate changes in the ecological state of the lake, intensified eutrophication, or changes in input sources.

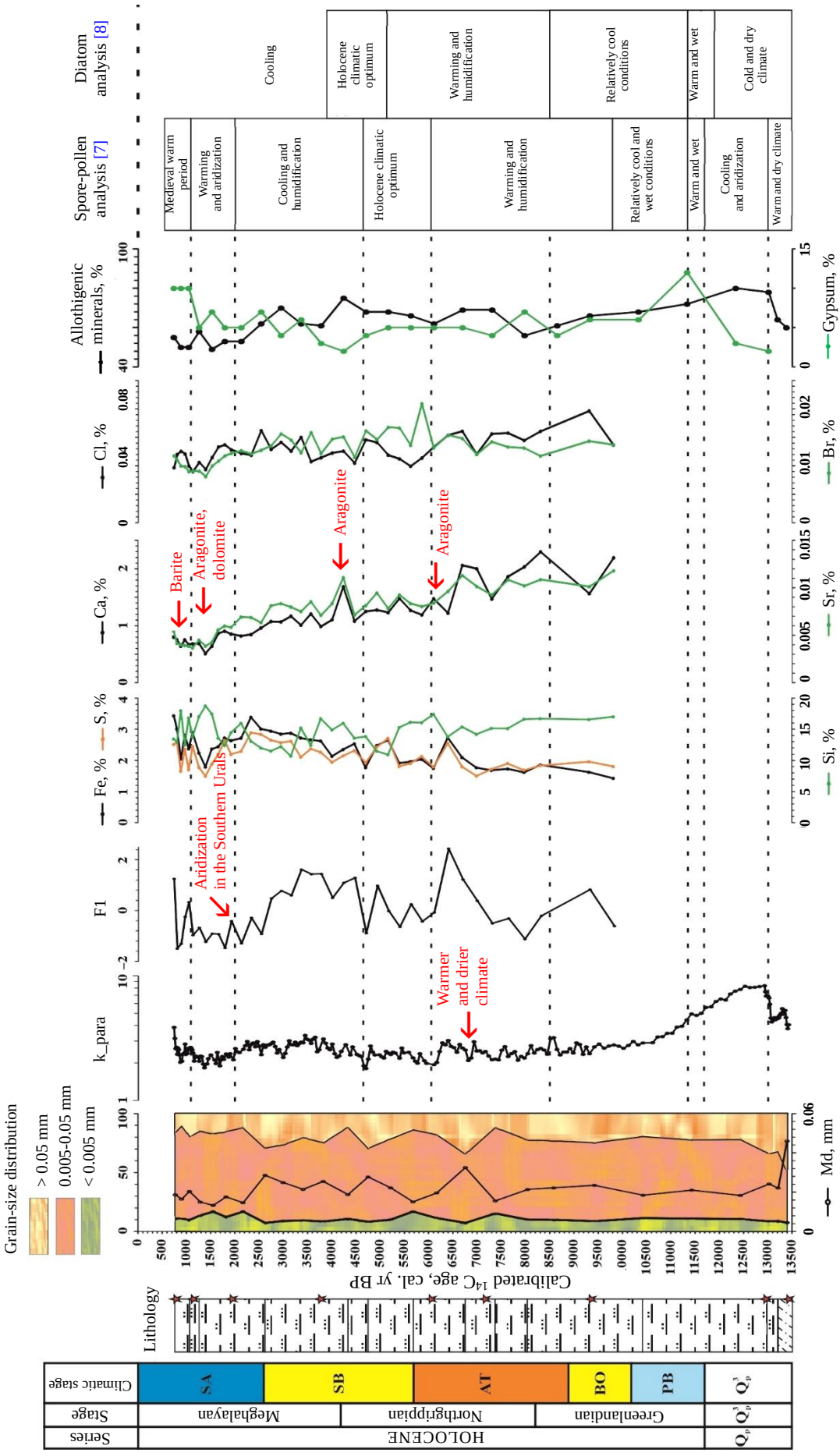
The main sources of phosphorus are organic and inorganic substances delivered by water masses through weathering of bedrock, river runoff, agricultural and industrial waste, and atmospheric deposition. In aquatic environments, phosphorus is readily bound to suspended particles and to the biomass of microorganisms, plants, and animals. After their death and decomposition, phosphorus becomes incorporated into bottom sediments. Under low dissolved-oxygen conditions, phosphate minerals precipitate (e.g., apatite, $Ca_5(PO_4)_3(OH, F, Cl)$. The hydrogen parameter also affects phosphate solubility: under neutral to alkaline conditions, phosphates tend to precipitate. Concentrations of Fe(III) and Al(III) are also important because, upon oxidation, they bind phosphate ions and form insoluble compounds [43]. Given the consistent relationship between factor F1 and k_para in both lakes, k_para can be treated as an indicator of allothigenic material supply to the lacustrine basin, as has also been shown for other lakes [17, 21].

Grain-size, mineralogical, and chemical data are presented as variations of the main indicators and are compared with global and regional climatic stages and events (Fig.7).

Late Pleistocene. The Last Glacial Maximum represents the period of maximum cooling during the last glaciation. During this interval (between ~27,000 and ~19,000 cal. yr BP), global ice sheets reached their maximum integrated volume [44, 45]. In Fig.7, *b*, this episode is represented by a small number of observations. These points mark the beginning of a coherent trend of decreasing k_para and decreasing allothigenic-mineral content that continues through the Early Dryas to ~16,000 cal. yr BP. This trend indicates reduced delivery of allothigenic material to the sedimentation basin, likely associated with the cold and dry conditions of the last glaciation. At the same time, gypsum contents are high and appear to be largely diagenetic. The warming that followed the last glaciation occurred at ~14,700 cal. yr BP and marked the onset of the Bølling climatic stage [43]. Warming and increased moisture were accompanied by higher k_para values, indicating enhanced delivery of allothigenic material to the sedimentation basin of Maloye Miassovo Lake (Fig.7, *b*). During ~13,000-11,700 cal. yr BP, sediments of both lakes Bolshoye Miassovo and Maloye Miassovo show increased k_para values and higher allothigenic-mineral contents. This reflects enhanced allothigenic

This is an open access article under the CC BY 4.0 license

Journal of Mining Institute. 2026. Vol. 280. P. 47-69
© Anastasiya R. Yusupova, Nouria G. Nourgalieva, 2026



a

This is an open access article under the CC BY 4.0 license

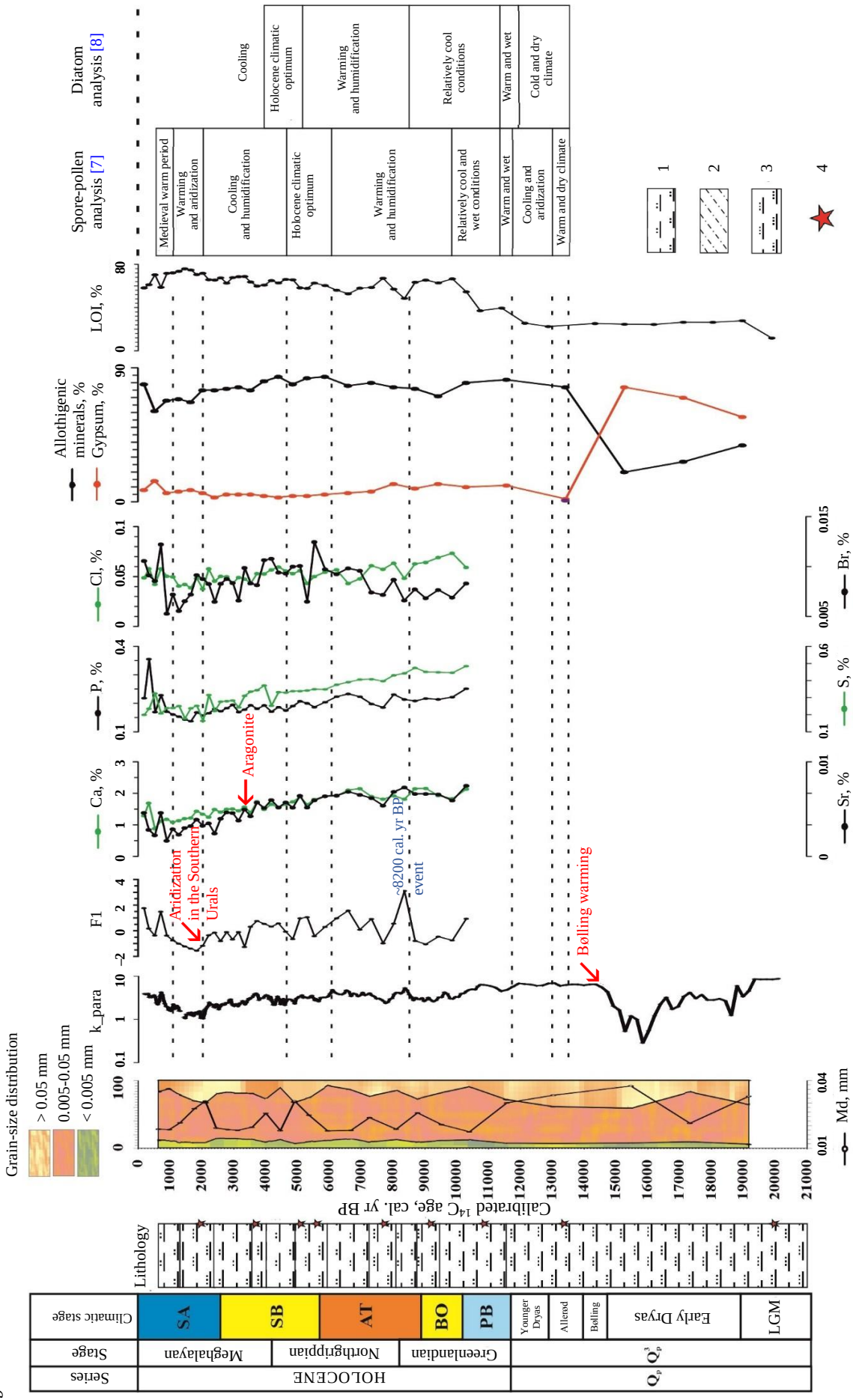


Fig.7. Results of integrated analysis of sediments from lakes Bolshoye Miassovo (*a*) and Maloye Miassovo (*b*)

1 – light silty loam; 2 – sandy loam; 3 – silty sandy loam; 4 – dated samples

This is an open access article under the CC BY 4.0 license

input (products of erosion of rocks of the Ilmenogorsk and Yelanchikov formations and the Baik complex). The dominance of the allothigenic component together with low organic-matter contents (mean LOI ~ 23.85 %, Fig.7, *b*), indicates low productivity of the lake ecosystem under cold climatic conditions, according to [46]. Consistently, study [7] showed that during the Late Glacial (~13,200-11,700 cal. yr BP) Bolshoye Miassovo Lake was a deep-water basin with a stable water level and an extensive shallow-water zone overgrown with macrophytes under cool climatic conditions.

Holocene. With the onset of the Holocene (~11,700-8500 cal. yr BP), organic-matter content in the sediment increases sharply. This increase is likely related to the shift from the cold Pleistocene climate to the warmer Holocene climate. This interval is also characterized by increasing Br and Cl trends. At ~11,430 cal. yr BP, aragonite was identified in Bolshoye Miassovo Lake sediments (see Fig.4, image 9). This suggests that the lake was shallow and more mineralized during this time due to climate aridization, possibly including the global Bond Event 8 (~11,100 cal. yr BP) [47]. Maloye Miassovo Lake also shows a decreasing trend in k_para and allothigenic-mineral contents, while LOI increases. A similar trend is reported for Sabakty Lake (Southern Urals) [46], where early Holocene organic-matter accumulation and reduced allothigenic input were explained by increased lake productivity and/or soil formation in the catchment under continuing climate warming.

According to diatom analysis [8], during ~ 8500-4600 cal. yr BP Bolshoye Miassovo Lake was deep-water. This likely reflects a longer and warmer growing season, which led to complete melting of the Ural glaciers. Our results show that at ~8500 cal. yr BP the sediment-core record from Bolshoye Miassovo Lake exhibits a sharp change in k_para, factor F1, LOI, and Ca and Sr contents. This change is likely related to the global cooling event at ~8200 cal. yr BP [46]. The ~8200 cal. yr BP cooling event is reflected in numerous paleorecords from lacustrine and marine sediments and from cave speleothems in both the Northern and Southern hemispheres [48, 49]. The temperature decline is commonly attributed to the influx of large volumes of freshwater into the North Atlantic due to ice-sheet collapse and glacier melting. In Maloye Miassovo Lake, this event is accompanied by a sharp increase in k_para and factor F1 and a sharp decrease in LOI. Study [46] reports a sharp decrease in electrical conductivity in sediments of Sabakty Lake during ~8200-7700 cal. yr BP, which also corresponds to the ~8200 cal. yr BP event.

Subsequently, until ~ 7000 cal. yr BP, k_para, factor F1, and Md decrease, whereas LOI increases. This pattern may indicate subsidence of the pelagic zone due to neotectonic processes. During the same period, Maloye Miassovo Lake also shows decreases in k_para, factor F1, and in the contents of Ca, Sr, P, S, and Cl. Two events characterized by abrupt changes in k_para are distinguished. The first occurred at ~ 6760 cal. yr BP and is accompanied by an increase in Md to ~ 0.033 mm as well as increased Ca and Sr contents in the sediment. The second occurred at ~ 6100 cal. yr BP, when Ca and Sr contents increased and the presence of aragonite was recorded (see Fig.4). These events are most likely related to climatic warming and reduced humidity. For example, accumulation of laminated sapropel in Sabakty Lake during ~ 7900-6000 cal. yr BP, with high organic-matter and carbonate contents and low concentrations of allothigenic elements, indicates enhanced lake productivity, likely in response to warming [46]. For Bolshoye Miassovo Lake sediments during ~ 7000-6000 cal. yr BP, factor F1, Cl, Fe, and Md increase sharply, indicating enhanced allothigenic input to the sedimentation basin. At the same time, Ca, Sr, Si, and LOI decrease sharply. During the same interval, Maloye Miassovo Lake also shows higher values of indicators of allothigenic input, reflecting increased delivery of allothigenic material to the sedimentation basin. Notably, at ~ 6100 cal. yr BP in Bolshoye Miassovo Lake sediments, Ca and Sr increase sharply, while the indicators of allothigenic input decrease (Fig.7, *a*). This pattern likely reflects climate aridization, which is supported by the occurrence of aragonite in the sediments (see Fig.4, 5).

This is an open access article under the CC BY 4.0 license

Elevated LOI and Br values characterize the interval ~ 6000-4700 cal. yr BP in Bolshoye Miassovo Lake sediments. This most likely reflects warm climatic conditions consistent with the Holocene climatic optimum identified in [7]. Maloye Miassovo Lake sediments during this interval are characterized by elevated Ca, Sr, and Br contents.

The interval ~ 4700-2000 cal. yr BP is characterized by increasing k_para and factor F1 values, which can be explained by increased climatic humidity and is consistent with [7]. However, the same study [7] indicates climate cooling during this period, which is supported by a decreasing trend in Ca and Sr contents in the sediments. At the same time, scanning electron microscopy identified aragonite in Bolshoye Miassovo Lake sediments at ~ 4250 cal. yr BP (see Fig.4, image 6), and sediments of Bannoe Lake (Southern Urals) show an increase in $\delta^{18}O$ [17]. In addition, aragonite was also identified in Maloye Miassovo Lake sediments at ~ 3540 cal. yr BP, consistent with data from lakes Sabakty and Talkas [6, 21]. Thus, this interval requires additional investigation.

According to [7], during ~ 2500 to ~ 800 cal. yr BP, against a background of decreasing temperature, Bolshoye Miassovo Lake ultimately formed as a deep-water basin with low-mineralized water and with boggy shallow-water zones where acidification processes occurred. Our data show that at ~2000 cal. yr BP Bolshoye Miassovo Lake sediments exhibit a sharp decrease in k_para, factor F1, Fe, Cl, and in the content of allothigenic minerals. This pattern is most likely related to climate aridization, which has been reported in multiple studies of lakes sediments in the Southern Urals [6, 7, 21]. In addition, aragonite and dolomite were identified in a Bolshoye Miassovo Lake sample at ~1500 cal. yr BP (see Fig.4, images 4, 5). This occurrence is linked to the global Bond Event 1, which manifested as aridization in the Southern Urals. Maloye Miassovo Lake sediments also show a sharp decrease in indicators of allothigenic input and in Cl and P contents, indicating reduced delivery of allothigenic material to the sedimentation basin.

Conclusion

Based on radiocarbon dating and grain-size, mineralogical, and geochemical analyses of bottom sediments from lakes Bolshoye Miassovo and Maloye Miassovo, we identified key features of the material composition of the studied lacustrine sediments and reconstructed lacustrine sedimentation conditions during the Late Quaternary.

The sediment core from Bolshoye Miassovo Lake consists predominantly of interbedded light silty loam and silty sandy loam. The lower part of the core is represented by sandy loam. The sediment sequence of Maloye Miassovo Lake is represented by interbedded light silty loam and silty sandy loam.

X-ray diffraction analysis showed that sediments from the studied lakes are characterized by a predominance of allothigenic minerals. Biogenic-chemogenic particles are represented by biogenic silica, carbonates, sulfates, and sulfides.

We obtained data on the contents of major and trace elements in bottom sediments of the studied lakes. Comparative plots of major-element contents for the lake sediments of the Southern Urals show that deposits from Bolshoye Miassovo Lake are characterized by higher MnO and CaO contents, which is explained by a substantial presence of authigenic carbonates and evaporites in the sediment. In sediments of Maloye Miassovo Lake, P_2O_5 contents are higher, which is linked to the occurrence of phosphorite-bearing rocks within the lake basin.

Variations in the most informative indicators identified from grain-size, mineralogical, and geochemical data (factor analysis) were compared with global and regional climatic stages and events. Based on the sediment records from lakes Bolshoye Miassovo and Maloye Miassovo, we identify the Bølling warming, the ~ 8200 cal. yr BP event (cooling), aridization in the Southern Urals (~ 2000 cal. yr BP), and Bond Event 1 (~1500 cal. yr BP). In addition, aragonite – an indicator of reduced climatic humidity – was recorded at ~11,430, ~6100, ~4250, and ~3540 cal. yr BP. The presence of barite at ~1065 cal. yr BP also supports the inference of climate aridization.

This is an open access article under the CC BY 4.0 license

REFERENCES

1. Ekoa Bessa A.Z., Richards K., Egbe A.M., Ambo F.B. A geochemical and palynological study of lake sediments at Mboandong, Cameroon: Chemical weathering and vegetation linked to Holocene palaeoclimate. *Journal of African Earth Sciences*. 2025. Vol. 223. N 105512. DOI: 10.1016/j.jafrearsci.2024.105512

2. Subetto D.A., Rybalko A.E., Naumenko M.A. et al. The Geology, Geomorphology, and History of Lake Ladoga: A Review. *Doklady Earth Sciences*. 2024. Vol. 519. Suppl. 1, p. S91-S109. DOI: 10.1134/S1028334X24604735

3. Rybalko A.E., Repkina T.Yu., Starovoitov A.V. et al. The Main Stages in Studying Quaternary Deposits of the White Sea and Controversial Problems of Its Late Pleistocene and Holocene Paleogeography. *Izvestiya Rossiiskoi akademii nauk. Seriya Geograficheskaya.* 2022. Vol. 86. N 6, p. 848-869 (in Russian). DOI: 10.31857/S2587556622060152

4. Hongpan Xue, Xin Zhou, Luyao Tu et al. Climate-vegetation-erosion interactions revealed by the sediments of Huguangyan Maar Lake, southern China. *Catena*. 2023. Vol. 231. N 107276. DOI: 10.1016/j.catena.2023.107276

5. Shuguang Lu, Li Wu, Chunmei Ma et al. Shifting sediment sources track environmental changes since the last glacial period: Evidence from sediment records in Chaohu Lake, eastern China. *Quaternary Science Reviews*. 2025. Vol. 365. N 109472. DOI: 10.1016/j.quascirev.2025.109472

6. Maslennikova A.V., Udachin V.N., Deryagin V.V. Paleoecology and geochemistry of the lake sedimentation of the Urals. Ekaterinburg: RIO UrO RAN, 2014, p. 136 (in Russian).

7. Nigamatzyanova G.R., Frolova L.A., Nigmatullin N.M. et al. Vegetation and climate changes in the Southern Urals in the Late Glacial and Holocene derived from pollen record of Lake Bolshoe Miassovo. *Geomorfologiya i paleogeografiya.* 2023. Vol. 54. N 4, p. 179-194 (in Russian). DOI: 10.31857/S2949178923040060

8. Valieva E.A., Frolova L.A., Palagushkina O.V. et al. Late Glacial and Holocene history of Lake Bolshoe Miassovo (Southern Urals) based on diatom analysis of bottom sediments. *Geomorfologiya i paleogeografiya.* 2023. Vol. 54. N 4, p. 195-206 (in Russian). DOI: 10.31857/S2949178923040151

9. Yusupova A.R., Kuzina D.M., Kosareva L.R. et al. Geochemistry and mineralogy of sediments of lakes in the Southern Urals. Mineraly: stroenie, svoistva, metody issledovaniya: Materialy X Vserossiiskoi molodezhnoi nauchnoi konferentsii, 27-31 May 2019, Ekaterinburg, Rossiya. Ekaterinburg: Institut geologii i geokhimii Uralskogo otdeleniya RAN, 2019. 2019, p. 292-293 (in Russian).

10. Sigov A.P., Shub V.S. Geomorphological regionalization of the Urals. Materialy po geomorfologii i noveishei tektonike Urala i Povolzhya. Ufa: Akademiya nauk SSSR, Bashkirskii filial, Institut geologii, 1972. N 3, p. 44-51 (in Russian).

11. State Geological Map of the Russian Federation. Scale 1:200,000. 2nd ed. Southern Ural series. Sheet N-41-VII. Explanatory note. Moscow: Moskovskii filial VSEGEI, 2015 (in Russian).

12. Bronk Ramsey C., Lee S. Recent and Planned Developments of the Program OxCal. *Radiocarbon*. 2013. Vol. 55. Iss. 2: Proceedings of the 21st International Radiocarbon Conference (Part 1 of 2), p. 720-730. DOI: 10.1017/S0033822200057878

13. Kuzina D.M., Shcherbakov V.P., Salnaia N.V. et al. Relative Paleointensity of Geomagnetic Field over the Past 9000 Years Estimated by the Pseudo-Thellier Method from the Bottom Sediments of Lake Shira, Northern Khakassia. *Izvestiya, Physics of the Solid Earth.* 2024. Vol. 60. N 4, p. 663-680. DOI: 10.1134/S1069351324700587

14. Cox R., Lowe D.R., Cullers R.L. The influence of sediment recycling and basement composition on evolution of mudrock chemistry in the southwestern United States. *Geochimica et Cosmochimica Acta*. 1995. Vol. 59. Iss. 14, p. 2919-2940. DOI: 10.1016/0016-7037(95)00185-9

15. Nurgaliev D.K., Yasonov P.G. Utility model patent RU 81805: Coercivity spectrometer. Publ. 27.03.2009. Bull. N 7 (in Russian).

16. Kosareva L.R., Nourgaliev D.K., Kuzina D.M. et al. Ferromagnetic, dia-/paramagnetic and superparamagnetic components of Aral Sea sediments: significance for paleoenvironmental reconstruction. *ARPN Journal of Earth Sciences*. 2015. Vol. 4. N 1, p. 1-6.

17. Yusupova A.R., Nurgalieva N.G., Kuzina D.M. et al. Lithological features of Lake Bannoe sediments (Southern Urals) as an indicator of environmental and climate changes in the Holocene. *Lithosphere.* 2024. Vol. 24. N 1, p. 173-194 (in Russian). DOI: 10.24930/1681-9004-2024-24-1-173-194

18. Leusova N.Yu. Stability and preservation of biogenic forms of silica in coals. *Advances in current natural sciences.* 2020. N 12, p. 117-123 (in Russian). DOI: 10.17513/use.37547

19. Xiugen Fu, Jian Wang, Chunyan Song et al. The Permian-Triassic transition in ocean island setting: Environmental disturbances and new high-resolution carbon-isotope record from the Qiangtang Basin, NW China. *Palaeogeography, Palaeoclimatology, Palaeoecology*. 2019. Vol. 522, p. 40-51. DOI: 10.1016/j.palaeo.2019.03.012

20. Rudnick R.L., Gao S. Composition of the Continental Crust. Treatise on Geochemistry. Elsevier, 2003. Vol. 3, p. 1-64. DOI: 10.1016/B0-08-043751-6/03016-4

21. Yusupova A.R., Nurgalieva N.G., Kuzina D.M. et al. Composition characteristics of Sabakty Lake lacustrine sediments (Southern Urals). *Advances in current natural sciences.* 2023. N 7, p. 72-81 (in Russian). DOI: 10.17513/use.38074

22. Yusupova A.R., Nourgalieva N.G., Kuzina D.M., H.-Ch. Li. The Composition of Lacustrine Sediments of Lake Kandrykul (Republic of Bashkortostan) Based on Mineralogical, Geochemical Data and Climatic Changes in the Holocene. *Georesursy.* 2025. Vol. 27. N 2, p. 281-296 (in Russian). DOI: 10.18599/grs.2025.2.21

23. Ecology of Lake Bolshoye Miassovo. Ed. by A.G.Rogozin, V.A.Tkachev. Miass: Ilmenskii gosudarstvennyi zapovednik im. V.I.Lenina UrO RAN, 2000, p. 318 (in Russian).

24. Snachev V.I., Snachev A.V., Rykus M.V. Physical and chemical conditions of generation and formation belonging to Kisegachsky granitoid massiv (South Ural). *Petroleum Engineering.* 2020. Vol. 18. N 5, p. 6-14 (in Russian). DOI: 10.17122/ngdelo-2020-5-6-14

25. Kalugin I., Daryin A., Smolyaninova L. et al. 800-yr-long records of annual air temperature and precipitation over southern Siberia inferred from Teletskoye Lake sediments. *Quaternary Research*. 2007. Vol. 67. Iss. 3, p. 400-410. DOI: 10.1016/j.yqres.2007.01.007

26. Korinevsky V.G., Korinevsky E.V. Results of geological-petrographic study of 1998-2018 of the Ilmenogorsky complex, South Urals. *Mineralogy.* 2020. Vol. 6. Iss. 2, p. 67-99 (in Russian). DOI: 10.35597/2313-545X-2020-6-2-6

This is an open access article under the CC BY 4.0 license

27. Smith J.V., Brown W.L. Feldspar Minerals. Vol. 1. Crystal Structures, Physical, Chemical, and Microtextural Properties. Springer-Verlag, 1988, p. 846. DOI: 10.1007/978-3-642-72594-4

28. Popov N., Marijan S., Pavić L. et al. Influence of Al^{3+} ions on the direct hydrothermal formation and properties of hematite (α-Fe_2O_3) nanorods. *Journal of Alloys and Compounds*. 2025. Vol. 1018. N 179223. DOI: 10.1016/j.jallcom.2025.179223

29. Cherniak D.J. Aluminum diffusion in zircon. *Chemical Geology*. 2021. Vol. 584. N 120510. DOI: 10.1016/j.chemgeo.2021.120510

30. Lange I.M., Reynolds R.C., Lyons J.B. KRb ratios in coexisting K-feldspars and biotites from some New England granites and metasediments. *Chemical Geology*. 1966. Vol. 1, p. 317-322. DOI: 10.1016/0009-2541(66)90027-1

31. Igneous Rocks: A classification and glossary of terms. Recommendations of the International Union of Geological Sciences Subcommission on the Systematics of Igneous Rocks. Ed. by R.W. Le Maitre. Cambridge University Press, 2002, p. 252. DOI: 10.1017/CBO9780511535581

32. Rhodes J.M. On the chemistry of potassium feldspars in granitic rocks. *Chemical Geology*. 1969. Vol. 4. Iss. 3-4, p. 373-392. DOI: 10.1016/0009-2541(69)90004-7

33. Usui H., Domi Y., Sakaguchi H. Rutile TiO2 Creates Advanced Na-Storage Materials. *ACS Applied Energy Materials*. 2023. Vol. 6. Iss. 8, p. 4089-4102. DOI: 10.1021/acsaem.3c00266

34. Rashchenko S., Shatskiy A., Litasov K. High-Pressure Na-Ca Carbonates in the Deep Carbon Cycle. *Carbon in Earth's Interior*. Wiley, 2020, p. 127-136. DOI: 10.1002/9781119508229.ch13

35. Bernard E., Yio M., Rentsch D. et al. Insights on the effects of carbonates and phosphates on the hydration of magnesia (alumino-)silicate cements. *Applied Geochemistry*. 2024. Vol. 167. N 106001. DOI: 10.1016/j.apgeochem.2024.106001

36. Baijot M., Hatert F., Philippo S. Mineralogy and geochemistry of phosphates and silicates in the Sapucaia pegmatite, Minas Gerais, Brazil: genetic implications. *The Canadian Mineralogist*. 2012. Vol. 50. N 6, p. 1531-1554. DOI: 10.3749/canmin.50.6.1531

37. Zaccarini F., Garuti G., Moser R. et al. Mineral Chemistry of Olivine, Oxy-Spinel, and Clinopyroxene in Lavas and Xenoliths from the Canary, Azores, and Cape Verde Islands (Macaronesia, North Atlantic Ocean): New Data and Comparisons with the Literature. *Minerals*. 2024. Vol. 14. Iss. 2. N 161. DOI: 10.3390/min14020161

38. Hermann J., O'Neill H.S.C., Berry A.J. Titanium solubility in olivine in the system TiO_2-MgO-SiO_2: no evidence for an ultra-deep origin of Ti-bearing olivine. *Contributions to Mineralogy and Petrology*. 2005. Vol. 148. Iss. 6, p. 746-760. DOI: 10.1007/s00410-004-0637-4

39. Santisteban J.I., Mediavilla R., López-Pamo E. et al. Loss on ignition: a qualitative or quantitative method for organic matter and carbonate mineral content in sediments? *Journal of Paleolimnology*. 2004. Vol. 32. Iss. 3, p. 287-299. DOI: 10.1023/B:JOPL.0000042999.30131.5b

40. Yudovich Ya.E., Ketris M.P. Geochemical Indicators of Lithogenesis. Syktyvkar: Geoprint, 2011, p. 742 (in Russian).

41. Yudovich Ya.E., Ketris M.P. Mineral Indicators of Lithogenesis. Syktyvkar: Geoprint, 2008, p. 564 (in Russian).

42. Qing Sun, Daryin A., Jiayu Zhao et al. High-Resolution Elemental Record from the Holocene Sediments of an Alpine Lake in the Central Altai Mountains: Implications for Arctic Sea-Ice Variations. *Earth and Space Science*. 2021. Vol. 8. Iss. 8. N e2021EA001810. DOI: 10.1029/2021EA001810

43. Ziwei Long, Zehua Ji, Yuansheng Pei. Characteristics and distribution of phosphorus in surface sediments of a shallow lake. *Journal of Environmental Sciences*. 2023. Vol. 124, p. 50-60. DOI: 10.1016/j.jes.2021.10.012

44. DoĞan M., Ünlü Y., Gürboğa Ş. et al. Climate variability in West Anatolia from Last Glacial Maximum to present based on the µXRF data from Buldan Yayla Lake (Denizli). *Journal of Quaternary Science*. 2025. Vol. 40. Iss. 1, p. 86-105. DOI: 10.1002/jqs.3658

45. López-Sáez J.A., Carrasco R.M., Turu V. et al. Late Glacial-early holocene vegetation and environmental changes in the western Iberian Central System inferred from a key site: The Navamuño record, Béjar range (Spain). *Quaternary Science Reviews*. 2020. Vol. 230. N 106167. DOI: 10.1016/j.quascirev.2020.106167

46. Maslennikova A.V., Artemiev D.A., Zazovskaia E.P. et al. Geochemical record of Lake Sabakty: Electrical conductivity and reconstruction of the Lateglacial and Holocene environments in the Southern Urals (Russia) steppe. *Lithosphere.* 2023. Vol. 23. N 3, p. 410-429 (in Russian). DOI: 10.24930/1681-9004-2023-23-3-410-429

47. Qimei Guo, Baohua Li, Yue Cai. Intermediate water circulation in the mid-latitude Northeast Atlantic over the past 13,000 years: Multi-proxy evidence from IODP Site U1391. *Palaeogeography, Palaeoclimatology, Palaeoecology*. 2024. Vol. 654. N 112428. DOI: 10.1016/j.palaeo.2024.112428

48. Walker M., Head M.J., Berkelhammer M. et al. Formal ratification of the subdivision of the Holocene Series/Epoch (Quaternary System/Period): two new Global Boundary Stratotype Sections and Points (GSSPs) and three new stages/subseries. *Episodes*. 2018. Vol. 41. N 4, p. 213-223. DOI: 10.18814/epiiugs/2018/018016

49. Walker M.J.C., Berkelhammer M., Björck S. et al. Formal subdivision of the Holocene Series/Epoch: a Discussion Paper by a Working Group of INTIMATE (Integration of ice-core, marine and terrestrial records) and the Subcommission on Quaternary Stratigraphy (International Commission on Stratigraphy). *Journal of Quaternary Science*. 2012. Vol. 27. Iss. 7, p. 649-659. DOI: 10.1002/jqs.2565

***Authors*: Anastasiya R. Yusupova,** *Candidate of Geological and Mineralogical Sciences, Senior Researcher* (*Kazan Federal University, Kazan, Republic of Tatarstan, Russia*), *i@ajusupova.ru, https://orcid.org/0000-0001-8732-3053*, **Nouria G. Nourgalieva,** *Doctor of Geological and Mineralogical Sciences, Professor* (*Kazan Federal University, Kazan, Republic of Tatarstan, Russia*), *https://orcid.org/0000-0003-4372-9777*.

The authors declare no conflicts of interests.

This is an open access article under the CC BY 4.0 license

ISSN 2411-3336; e-ISSN 2541-9404

JOURNAL OF MINING INSTITUTE
Zapiski Gornogo instituta
Journal homepage: pmi.spmi.ru

Research article Geology

Isomorphic capacity of combustion metamorphic melilite solid solutions

Ella V. Sokol, **Anna S. Polovykh**✉, **Svetlana N. Kokh**, **Ivan S. Karputin**, **Olga A. Kozmenko**
V.S.Sobolev Institute of Geology and Mineralogy SB RAS, Novosibirsk, Russia

***How to cite this article*:** Sokol E.V., Polovykh A.S., Kokh S.N., Karputin I.S., Kozmenko O.A. Isomorphic capacity of combustion metamorphic melilite solid solutions. Journal of Mining Institute. 2026. Vol. 280, p. 70-84.

Abstract
Partitioning of trace elements between minerals crystallized from Ca-rich Si-undersaturated melts is constrained for the first time in samples of coarse combustion metamorphic (CM) melt rocks (paralavas) from the Hatrurim Formation. The partition coefficients of trace elements (including REE) in wollastonite, rankinite, cuspidine, Ti-andradite, melilite solid solutions, kalsilite, and fluorapatite are calculated on the basis of their contents determined by laser ablation inductively coupled plasma mass spectrometry (LA-ICP-MS). Most of REE are hosted by fluorapatite (≤ 900 ppm ΣREE), garnet (≤ 600 ppm), and cuspidine (≤ 300 ppm), while other phases contain < 100 ppm of total REE. Sr is found in all minerals except garnet, with its contents reaching 7500 ppm in melilite, 5500 ppm in fluorapatite, 4500 ppm in rankinite, 2150 ppm in wollastonite, 2000 ppm in cuspidine, and 800 ppm in kalsilite. High-field strength elements (HFSE) occur in cuspidine (up to 2100 ppm U, 1600 ppm Zr, 1300 ppm Ti, and 200 ppm Nb) and garnet (up to 3000 ppm Zr, 600 ppm Y, 350 ppm HREE and Sc, and 130 ppm Nb). Melilite is the principal host of Zn (≤ 17,000 ppm), Ni (≤ 2100), Cu (≤ 1200), Mn (≤ 750), Co (≤ 100), and Ga (≤ 65). It also bears Ba (up to 5500 ppm), while the amount of Ba reaches 8500 ppm in kalsilite, along with ≤ 1350 Rb. The partition coefficients of trace elements for all listed minerals were calculated. Isomorphic substitutions in melilite are controlled by structural positions at three sites (Ca, T1, and T2) which can accommodate Na, Sr, and Ba (Ca); Zn, Co, Ni, Cu (T1); Fe^{3+}, and Ga (T2). Melilite crystallized from CM melts lacks significant amounts of REE and HFSE. The obtained partition coefficients of trace elements in CM melilite are consistent with the available estimates for minerals from igneous alkaline complexes and thus have implications for trace element partitioning in Ca-rich Si-undersaturated melts. The partitioning patterns of trace elements during the crystallization of CM melts mainly depend on the crystal chemistry of minerals.

Keywords
melilite; garnet; cuspidine; kalsilite; LA-ICP-MS; trace elements; partition coefficients; paralavas; Hatrurim Formation

Funding
The study was supported by the Russian Science Foundation grant N 24-77-00014, https://www.rscf.ru/project/24-77-00014/.

Received: 23.12.2025 ***Accepted: 28.04.2026*** ***Online: 21.07.2026*** ***Published: 10.09.2026***

Introduction

Recent progress in microanalytical tools, such as mass spectrometry with secondary ions (SIMS) or laser ablation inductively coupled plasma mass spectrometry (LA-ICP-MS), allows using trace element patterns in rock-forming and accessory minerals as informative petrogenetic proxies for meteoritic material [1, 2], igneous [3-5], and metamorphic [6] rocks.

Minerals of the melilite group have been a focus of interest for igneous petrology, meteorite studies, and experimental work due to their large *P-T* stability field and high isomorphic capacity. These features facilitate isomorphic substitutions making the melilite-group minerals highly adaptive to changing conditions. The structure of melilite can accommodate more than twenty elements in considerable amounts. Melilite belongs to space group $P4\bar{2}_1m$; with the general formula

This is an open access article under the CC BY 4.0 license

*X*T1(T2)$_2$O$_7$), where *X* stands for Ca, Na, Sr, Ba, Pb, Y, and REE, while T1 and T2 correspond to Mg, Al, Mn, Fe^{2+}, Fe^{3+}, Zn, Co, Cu, Cd (T1) and Si, Al, Fe^{3+}, Ti, B, Be, Ga, Ge (T2). The structural type is used as a framework to synthesize compounds involving Be, B, Ga, Ge, Co, Ni, Cd, Zn, Sr, Ba, and REE, which impart valuable technological properties to ferrimagnetic, ferroelectric, and ferroelastic materials. The melilite structure is strongly anisotropic (till divergent lattice distortion along *a* and *c* directions), which reduces thermal expansion of melilite-based ceramic and composite materials and substituted derivatives [7].

Most of petrological research commonly deals with melilite from igneous rocks, such as ultramafic alkaline nephelinite [4, 5, 8], melilitite [8-10], and carbonatite [11-13]) complexes, or from primitive chondrite [14-16]. Meanwhile, petrogenetic reconstructions for such rocks are difficult because magmatic melilite is compositionally complex ($Ca_2MgSi_2O_7$–$NaCaAlSi_2O_7$ solid solutions with variable contents of the $Ca_2Fe^{2+}Si_2O_7$ and $Ca_2Al_2SiO_7$ endmembers) and can be involved in peritectic reactions. Only few studies have addressed the fractionation of trace elements during the crystallization of melilite-bearing igneous rocks. Those studies have revealed considerable difference in the partitioning patterns of impurities between coexisting silicates, as well as between melilite and melt in the case of early crystallization of perovskite, apatite, titanite, loparite, and other hosts of Sr, Zr, Hf, Nb, Ta, Th, U, and REE [3, 17, 18]. Melilite was mainly investigated in high-temperature skarn [19, 20], contact metamorphic [21-23], and combustion metamorphic rocks from the Hatrurim Formation [24-26], as well as in coal-fire buchites from the Buffalo complex (Wyoming) [27], paralavas from the Central Apennines (Italy) [28], and the Khamaryn-Khural-Khiid complex (Mongolia) [29]. As evidenced by the cited publications, melilite solid solutions growing from the cooling melt become progressively enriched in Na and Fe but depleted in Al and/or Mg [3, 17, 23].

In addition to the limitations of microanalytical facilities, the concentrations of trace elements in melilite can be hard to measure because they are low, especially in melilite coexisting with perovskite, apatite, titanite, loparite, etc., while the crystals are too small and contain abundant inclusions. Correspondingly, the scanty geochemical data are insufficient to highlight the fractionation trends in Ca-rich alkaline melts. The partition coefficients (K_d) of trace elements between melt and melilite solid solutions remain poorly constrained as well [5, 17, 30].

This study focuses on the chemical evolution of melilite solid solutions during crystallization of high-temperature Si-undersaturated combustion metamorphic (CM) melts rich in Ca and K, for the case of the Hatrurim Formation paralavas. The kalsilite-rankinite-wollastonite paralavas crystallized from the CM melts bear coarse crystals, including zoned melilites. The chosen natural CM system of the Hatrurim Formation is advantageous as the duration of crystallization far exceeded that in experimental systems and was long enough to equilibrate the mineral assemblages.

Methods

Two selected fresh paralava samples h-07-Gr-1 and h-07-51-3 were analyzed by several methods at the Analytical Center for Multielement and Isotope Research of the V.S.Sobolev Institute of Geology and Mineralogy (IGM, Novosibirsk, Russia). Electron probe microanalysis (EPMA) and laser ablation inductively coupled plasma mass spectrometry (LA-ICP-MS) were applied to characterize the compositions of seven coexisting minerals. The average element contents in bulk rock and separate minerals were then used to calculate the respective partition coefficients as a ratio of element concentrations in minerals to those in rocks: $K_d = [El_{mineral}]/[El_{rock}]$.

Scanning electron microscopy was used to identify the mineral species and study the morphology of crystals and mineral chemistry. The measurements were performed on a Tescan MIRA 3 MLU scanning electron microscope equipped with an AZtec Energy XMax-50+ microana-lysis system (Oxford Instruments NanoAnalysis Ltd.). The operating conditions were: 20 kV accelerating voltage, 1 nA beam current, 3 to 10 μm beam diameter, and 20 s count time. The mineral chemistry of melilite

This is an open access article under the CC BY 4.0 license

and garnet was additionally analyzed on a Jeol JXA-8230 electron probe microanalyzer at an accelerating voltage of 20 keV, a beam current of 20 nA, a count time of 10 s for each analytical line, and a probe diameter of 2 μm, at a chamber vacuum of ≤ 0.001 Pa. The data quality was checked against the reference materials of standard minerals and synthetic compounds: wollastonite for Ca, garnet O-145 for Si, Al, Fe, Mg, garnet IGEM for Mn, orthoclase O-359-1 for K, albite for Na, and glass Gl-10 for Sr, as well as $BaTiSi_3O_9$ for Ba and Ti, $NiFe_2O_4$ for Ni, Cu_2O for Cu, and $ZnFe_2O_4$ for Zn. The detection limits (3σ criterion) were 0.01 wt.% for K_2O, 0.02 wt.% for CaO, MnO, and TiO_2, 0.03 wt.% for FeO, 0.04 wt.% for Al_2O_3, NiO, and CuO, 0.05 wt.% for SrO and ZnO, 0.06 wt.% for Na_2O, SiO_2, and BaO, and 0.10 wt.% for MgO.

Trace element abundances were determined by LA-ICP-MS on a Thermo Scientific iCAP Qc quadrupole inductively coupled plasma mass spectrometer with an Elemental Scientific NewWaveResearch 213 laser ablation platform (Nd:YAG laser, 213 nm wavelength, 10 Hz frequency, ~5 J/cm^2 fluence, and 50 μm beam diameter). The quality of determination was checked against the reference materials of NIST 612 glass standard and in-house standards of CaO concentrations (in apatite, rankinite, wollastonite, cuspidine, melilite, and garnet) and SiO_2 (in kalsilite). The instrument drift was monitored using the NIST 610 glass standard as an unknown sample. The duration of analysis was 90 s at each ablation spot, including 30 s for background measurements. The analyses were applied to flat polished sections and mineral grains extracted from monofractions. Trace elements were measured in 10-20 mg aliquots following the common method. The mineral names are abbreviated according to [31]: Aak – alumoakermanite ($NaCaAlSi_2O_7$), Ak – akermanite ($Ca_2MgSi_2O_7$), Ap – apatite, Brt – barite, Csp – cuspidine, CSH – Ca hydrosilicates, Fe^{2+}-Ak – ferroakermanite ($Ca_2Fe^{2+}Si_2O_7$), Fe^{3+}-Gh – ferrigehlenite ($Ca_2Fe^{3+}{}_2SiO_7$), Gh – gehlenite ($Ca_2Al_2SiO_7$), Grt – garnet, Hdy – hardystonite ($Ca_2ZnSi_2O_7$), Kls – kalsilite, Mag – magnetite, Mll – melilite, Rnk – rankinite, and Wo – wollastonite.

Garnet-melilite-wollastonite paralava from CM complexes of the Hatrurim Formation

The Hatrurim Basin (Israel) is the largest complex of CM rocks in the western side of the Dead Sea. Combustion metamorphism in the area involved the Maastrichtian Gareb Formation bioproductive marly limestone of the shelf facies during tectonic reactivation in the zone of the Dead Sea transform between 7 and 0.5 Ma. The Hatrurim Formation CM complex comprises garnet paralava (granitite), which is an exceptional group of Ca-rich melt rocks, along with high-temperature marbles and hornfels [24, 32, 33].

Veins of coarse paralava rich in Ti-garnet and melilite are occasionally found among high-temperature hornfels in the southwestern flank of the Gurim anticline within the Hatrurim Basin. The veins are commonly 1-3 cm thick, rarely reaching 5-10 cm (sample h-07-51-3). They are exposed on the surface and penetrate no more than 2-3 cm deep into fine-grained hornfels. The hornfels-paralava contacts are sharp and are delineated by quench zones that record rapid cooling of the CM melts.

The samples we studied represent Si-undersaturated Ca-rich rocks containing comparable moderate amounts of Fe_2O_3 and Al_2O_3, with K enrichment over Na. They have relatively high contents of phosphorus and fluorine due to the presence of phosphorite in the sedimentary protolith. The paralava samples selected for analyses (Fig.1, *a*, *b*) are compositionally similar though coming from the central parts of different veins, wt.%: 33.95-35.18 – SiO_2, 1.41-1.66 – TiO_2, 7.63-8.26 – Al_2O_3, 7.61-8.82 – Fe_2O_3, 0.54-0.60 – MgO, 40.76-41.41 – CaO, 0.35-0.40 – Na_2O, 0.41-1.12 – K_2O, 1.78-1.81 – P_2O_5, 0.09-0.18 – SO_3, and 0.42-0.48 – F. The samples differ slightly in the degree of secondary carbonation (0.89-1.42 wt.% CO_2) and hydration (1.54-3.08 wt.% H_2O), as well as in the percentages of retrograde minerals (CSH, zeolites, gypsum, thaumasite, and calcite).

The sedimentary protolith of the Hatrurim Formation paralavas was originally depleted in Mg, Mn, Rb, and Pb but enriched in such elements as P, S, Fe, V, Cr, Ni, Zn, Cu, Mo, Cd, and U, which are typical of bioproductive carbonate sediments deposited in anoxic marine environments [33]. The paralavas derived from this protolith bear the respective geochemical fingerprints (Table 1), with high contents

This is an open access article under the CC BY 4.0 license

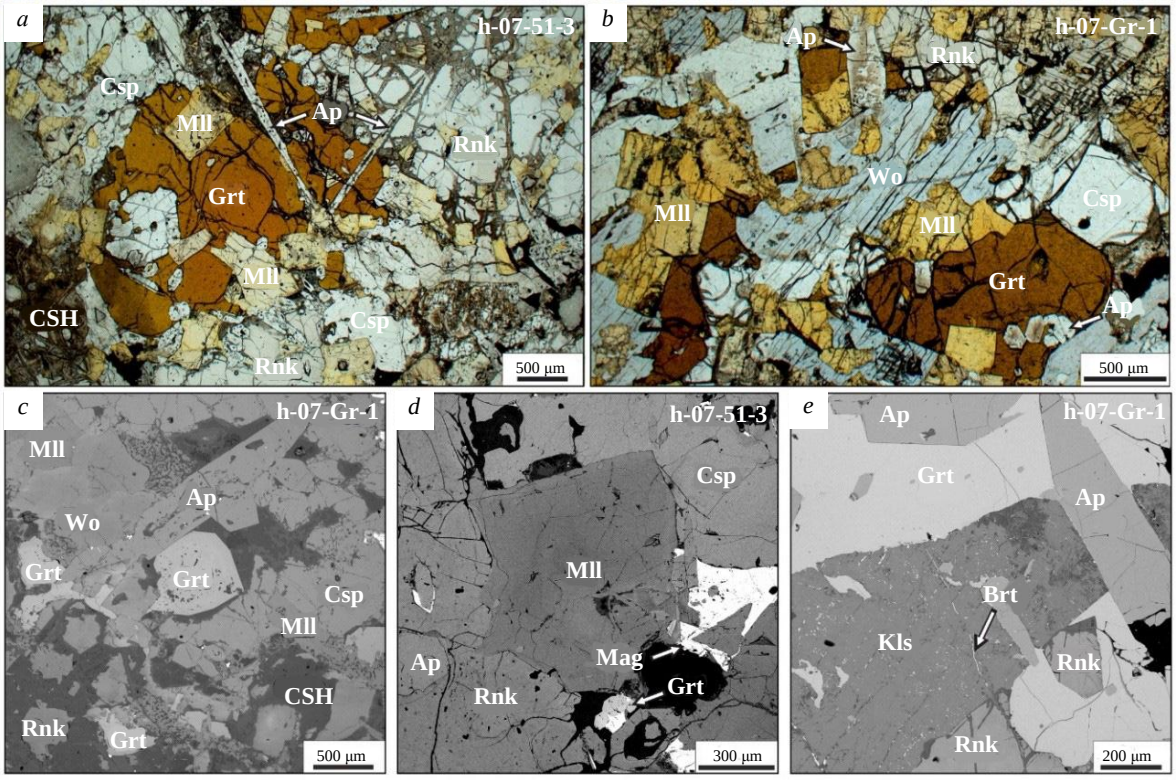


Fig.1. Morphology and spatial relations of rock-forming and accessory minerals in Hatrurim Formation high-Ca paralavas: *a-c* – general view of garnet paralava samples with anhedral wollastonites, rankinites, and cuspidines occupying up to 2/3 of the rock volume, as well as large poikilitic crystals of fluorapatite, grains and crystals of Ti-garnet and melilite; *d* – large zoned melilite crystal coexisting with rankinite, cuspidine, garnet, and fluorapatite; *e* – large anhedral grain of kalsilite with ingrown barite. Panels *a* and *b* are optical photographs; *c-e* are BSE images

of V, Cr, Ni, Cu, and Zn (hundreds of ppm), as well as Mo and U (tens of ppm). Furthermore, the high concentrations of Sr (1500 to 2400 ppm) and Ba (400 to 3200 ppm) in the paralavas likewise record the features of parent carbonate sediments that bear authigenic barite. According to an earlier detailed description [34], the representative paralava samples share similarity in trace-element chemistry.

Table 1

Average trace-element compositions of Ca-rich combustion metamorphic rocks, Hatrurim Formation (LA-ICP-MS data), ppm

Element	Sample							
	h-07-51-3				h-07-Gr-1			
	Mean, *n* = 5	*SD*	Min	Max	Mean, *n* = 5	*SD*	Min	Max
Sc	31.5	1.16	30.2	32.9	32.6	1.35	31.0	34.7
V	281	17.6	264	305	493	25.9	459	531
Cr	628	61.5	580	697	454	84.0	309	528
Mn	142	6.38	136	151	243	27.4	214	286
Co	13.9	0.51	13.1	14.5	22.0	1.05	20.7	23.3
Ni	504	37.9	452	539	802	53.5	726	868
Cu	297	46.7	241	360	705	265	487	1133
Zn	1369	108	1247	1544	2763	205	2613	3116
Ga	10.3	0.69	9.30	11.0	27.6	1.21	26.5	29.6
Rb	12.3	1.45	9.94	13.9	52.8	2.67	49.4	55.3
Sr	1655	118	1515	1802	2766	88.2	2639	2868

This is an open access article under the CC BY 4.0 license

End of Table 1

Element	Sample							
	h-07-51-3				h-07-Gr-1			
	Mean, *n* = 5	*SD*	Min	Max	Mean, *n* = 5	*SD*	Min	Max
Y	72.2	3.87	67.7	76.7	90.3	3.38	87.4	95.2
Zr	200	11.3	185	213	272	16.3	250	292
Nb	20.9	0.83	19.9	21.9	42.0	2.27	38.8	45.1
Cd	7.59	2.57	5.13	10.3	25.3	10.4	13.0	40.1
Cs	0.11	0.02	0.09	0.15	0.42	0.05	0.38	0.50
Ba	466	14.0	451	483	3640	189	3435	3934
La	36.1	1.49	33.7	37.7	60.0	3.40	57.4	65.7
Ce	51.3	2.21	48.1	54.1	78.3	5.38	72.4	84.0
Pr	6.88	0.25	6.48	7.11	11.1	0.39	10.5	11.5
Nd	28.0	1.67	25.3	29.4	38.4	1.55	37.0	41.0
Sm	5.46	0.73	4.89	6.38	7.60	0.46	7.05	8.12
Eu	1.51	0.15	1.37	1.75	2.00	0.12	1.89	2.20
Gd	6.68	0.44	6.04	7.26	8.67	0.33	8.24	9.00
Tb	1.09	0.09	1.00	1.23	1.43	0.05	1.37	1.51
Dy	7.00	0.27	6.64	7.26	8.88	0.26	8.47	9.07
Ho	1.60	0.06	1.52	1.68	2.06	0.12	1.92	2.22
Er	5.11	0.17	4.95	5.35	6.42	0.32	6.06	6.79
Tm	0.73	0.04	0.68	0.78	0.85	0.05	0.78	0.92
Yb	5.32	0.37	5.00	5.95	6.07	0.29	5.72	6.42
Lu	0.79	0.04	0.72	0.82	0.95	0.07	0.87	1.06
Hf	5.45	0.20	5.14	5.64	6.29	0.21	5.96	6.51
Ta	1.40	0.09	1.33	1.56	2.37	0.10	2.22	2.49
Pb	8.55	0.32	8.05	8.92	24.0	1.49	22.3	25.7
Th	6.24	0.33	5.78	6.70	9.45	0.53	8.88	10.2
U	65.3	4.85	58.4	71.8	119	7.05	113	131

Note. n – number of analyses; *SD* – standard deviation; Min – minimum value; Max – maximum value.

The mineralogy of garnet paralava consists of wollastonite, rankinite, melilite solid solutions, Ti-andradite, fluorapatite, kalsilite, cuspidine (±flamite), and accessory carriers of Ba, V, Fe, Ni, and Cu. The crystallization sequence began with fluorapatite enclosing micrometer grains of K-Fe-Ni-Cu sulfides, phases of the zadovite-aradite solid solution series $BaCa_6((SiO_4)(PO_4))(PO_4)_2F$-$BaCa_6((SiO_4)(VO_4))(VO_4)_2F$, gurimite $Ba_3(VO_4)_2$, and barite (Fig.1, *a*, *c*; Fig.2). The following crystallized phases were Ca silicates (wollastonite and rankinite) and Ca fluorosilicate (cuspidine). Fresh wollastonite occurs as ≤ 2 mm subhedral

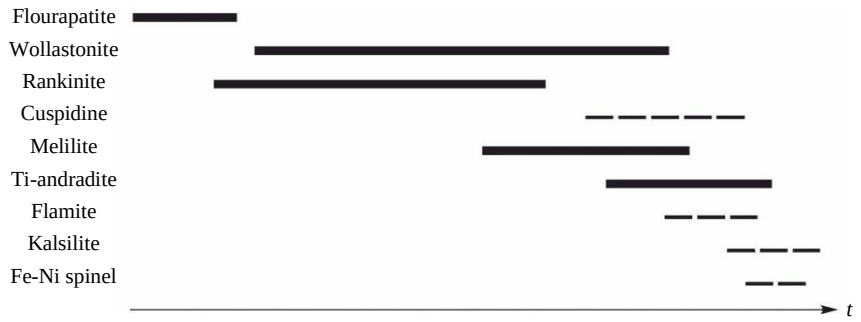


Fig.2. Crystallization sequence of minerals in the analyzed Hatrurim Formation high-Ca paralava samples. The solid line is the established crystallization sequence, the dotted line is the proposed sequence

This is an open access article under the CC BY 4.0 license

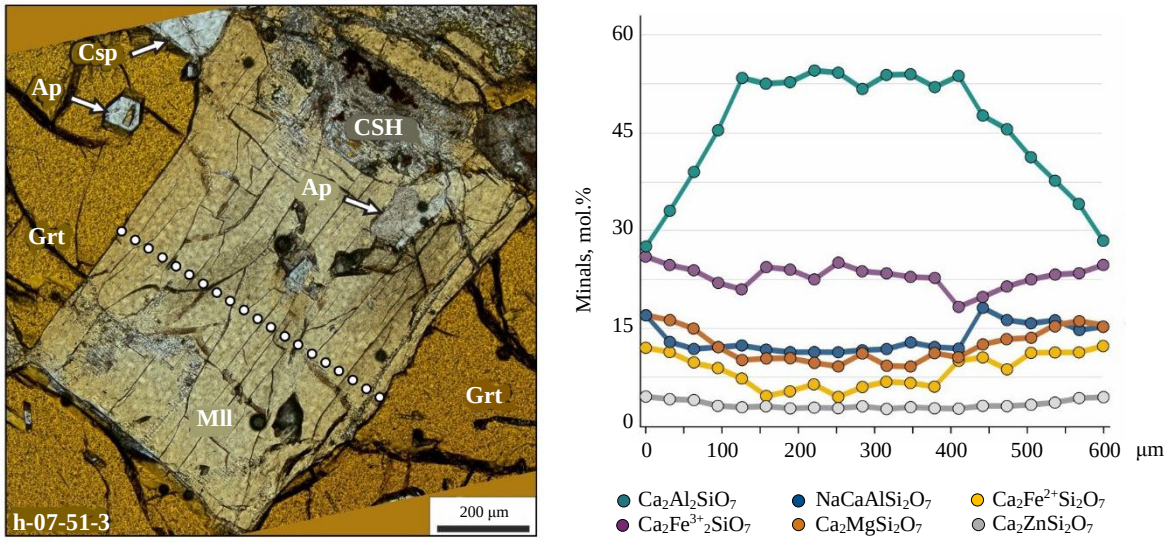


Fig.3. Profile of a zoned melilite crystal (endmembers in molar percentages) coexisting with garnet, cuspidine, and fluorapatite (optical photograph) from the Hatrurim Formation
High-Ca paralavas based on EPMA data

grains with fluorapatite inclusions (up to 0.2-0.4 mm). Rankinite forms anhedral grains (also ≤ 2 mm), often cracked and partly replaced by CSH (see Fig.1, *a-c*). The rankinite grains are mostly free from mineral inclusions (except for fluorapatite) but abound in melt inclusions. Cuspidine is found as anhedral grains (≤ 1 mm) or grain clusters (0.3-0.4 mm) and bears numerous fluorapatite inclusions (see Fig.1, *a-d*).

Melilite, which crystallized after or partly concurrently with Ca silicates, occurs as ≤ 1-2 mm zoned crystals or grains with sporadic inclusions of earlier fluorapatite and flamite (see Fig.1, *a, b, d*; Fig.3). The mineral is relatively stable against replacement, which makes it suitable for LA-ICP-MS analysis of trace elements and crystal zonation. Ti-andradite, a late phase in the crystallization sequence, not prone to replacement, exists as coarse zoned or sectorial crystals with inclusions of fluorapatite, wollastonite, Al-rich melilite, and ingrown flamite (see Fig.1, *a-c*). Kalsilite, crystallized the latest from CM melts, forms ≤ 1-2 mm anhedral grains, often fills the interstitial space, and contains multiple microinclusions, mostly barite; in some cases, the mineral is partly altered (see Fig.1, *e*). Fe-Ni spinel microcrysts is present sporadically. The lack of interstitial glass, along with the scarcity of melt inclusions in melilite, indicates that the rapidly cooling CaO-rich Si-undersaturated low-viscosity CM melts crystallized completely, like slags. The crystallization trends in the temperature range between 1500 and 1100 °C were reconstructed with reference to thermobarometry of melt inclusions, the $CaO–SiO_2–Al_2O_3$ phase diagram, and evidence from melting experiments [32].

Results

Major- and trace-element chemistry of minerals in paralavas. Fluorapatite contains on average, wt.%: 5.0 SiO_2, 3.9 SO_3, ≤ 1.4 SrO, ≤ 0.7 V_2O_3, and occasionally ≤ 1.1 FeO. Its average formula is $(Ca_{4.9}Sr_{\leq 0.1})_{\sum 5.0}(P_{2.4}Si_{0.4}S_{0.2}V_{\leq 0.1})_{\sum 3.0}O_{12.0}F_{0.9}(OH)_{0.1}$ (n = 21). The mineral bears 400-900 ppm of total REE, including 390-770 ppm ΣLREE, at ≤ 85.0 ppm Th and 144 ppm U. Fluorapatite from sample h-07-51-3 also contains 24.6 ppm of Pb on average (Tables 2, 3, Supplements 1, 2).

Wollastonite has an average composition of $Ca_{1.0}Si_{1.0}O_{3.0}$ (n = 22), with minor amounts of FeO (≤ 0.5 wt.%) and TiO_2 (≤ 0.4 wt.%) in a few grains. Trace elements have quite low uniform contents, with common Sr (650-1200 ppm). The concentrations of Ba are an order of magnitude lower (9.00 to 90.0 ppm). The REE total is 30.0-80.0 ppm; ≤ 800 ppm Ti (Table 3, Supplement 1).

This is an open access article under the CC BY 4.0 license

Table 2

Average contents of REE and Y in rock-forming and minor minerals from Ca-rich combustion metamorphic rocks, Hatrurim Formation (LA-ICP-MS data), ppm

Element	Y	La	Ce	Pr	Nd	Sm	Eu	Gd	Tb	Dy	Ho	Er	Tm	Yb	Lu
Fluorapatite, h-07-51-3 (n = 3)															
Mean	65.4	207	277	27.6	80.0	12.0	2.85	12.4	1.44	7.88	1.60	4.84	0.59	3.46	0.46
SD	12.3	46.6	101	3.35	3.48	2.09	0.93	4.32	0.55	2.69	0.54	2.48	0.32	2.09	0.25
Min	57.2	163	214	24.7	76.1	10.4	2.28	9.44	1.06	6.19	1.21	3.12	0.39	2.25	0.32
Max	79.6	255	394	31.3	82.8	14.3	3.93	17.3	2.07	11.0	2.21	7.68	0.96	5.87	0.75
K_d	0.91	5.74	5.14	4.00	2.86	2.19	1.88	1.85	1.31	1.12	1.00	0.95	0.81	0.65	0.59
Wollastonite, h-07-51-3 (n = 4)															
Mean	21.3	16.6	20.6	3.97	14.5	3.35	1.17	3.84	0.78	3.15	0.96	1.91	0.48	1.43	0.47
SD	12.9	6.07	12.6	2.02	7.33	2.39	1.20	2.91	0.85	2.49	1.00	1.51	0.68	1.30	0.71
Min	4.26	10.9	9.66	1.85	5.56	0.91	0.20	0.55	0.10	0.48	0.10	0.29	0.05	0.24	0.06
Max	31.4	24.9	38.5	6.67	22.8	6.47	2.90	7.46	2.02	6.28	2.39	3.76	1.50	3.12	1.53
K_d	0.30	0.46	0.40	0.58	0.52	0.61	0.77	0.58	0.72	0.45	0.60	0.37	0.66	0.27	0.60
Rankinite, h-07-51-3 (n = 3)															
Mean	36.6	20.0	20.8	4.14	14.7	2.69	0.74	3.51	0.54	3.52	0.80	2.32	0.33	2.01	0.33
SD	11.1	15.4	21.3	2.12	6.75	0.40	0.03	0.35	0.14	1.17	0.26	0.72	0.09	0.38	0.08
Min	23.9	10.4	812	2.85	9.43	2.25	0.71	3.17	0.38	2.21	0.49	1.49	0.22	1.59	0.24
Max	44.3	37.7	45.4	6.59	22.3	3.02	0.77	3.88	0.63	4.43	0.97	2.76	0.39	2.32	0.40
K_d	0.51	0.55	0.41	0.60	0.53	0.49	0.49	0.52	0.50	0.50	0.50	0.45	0.45	0.38	0.42
Cuspidine, h-07-Gr-1 (n = 10)															
Mean	100	28.0	97.7	6.90	26.4	6.13	1.67	7.59	1.35	9.74	2.57	8.70	1.36	10.7	1.65
SD	18.5	5.99	10.5	0.82	2.58	0.75	0.25	1.18	0.22	1.54	0.48	1.71	0.26	2.65	0.31
Min	75.5	20.8	79.1	5.67	24.3	5.31	1.29	5.89	0.96	7.34	1.85	6.08	1.01	7.48	1.28
Max	139	39.8	111	8.12	32.0	7.69	2.18	9.67	1.76	13.1	3.49	11.7	1.96	16.8	2.42
K_d	1.11	0.47	1.25	0.62	0.69	0.81	0.84	0.88	0.94	1.10	1.25	1.35	1.59	1.76	1.73
Garnet – low-Ti cores, h-07-51-3 (n = 2)															
Mean	103	20.1	76.0	12.5	55.8	12.7	3.44	13.0	1.88	12.0	2.48	8.32	1.21	8.79	1.51
SD	8.01	4.00	2.52	2.21	7.46	1.80	0.21	1.11	0.15	0.22	0.32	0.78	0.01	0.40	0.09
Min	97.2	17.3	74.3	10.9	50.5	11.4	3.29	12.2	1.77	11.8	2.26	7.76	1.20	8.50	1.45
Max	109	23.0	77.8	14.0	61.0	13.9	3.59	13.8	1.99	12.1	2.71	8.87	1.22	9.07	1.58
K_d	1.42	0.56	1.48	1.81	1.99	2.32	2.27	1.94	1.72	1.71	1.55	1.63	1.66	1.65	1.93
Garnet – high-Ti rims, h-07-51-3 (n = 6)															
Mean	401	13.0	79.5	9.54	59.3	19.9	6.32	31.2	5.34	40.0	9.65	32.2	4.81	36.0	5.98
SD	88.5	3.87	28.0	2.71	14.3	4.57	1.40	6.36	1.36	10.1	2.73	9.27	1.36	10.1	1.48
Min	326	8.50	43.0	5.96	42.2	14.2	4.51	25.7	3.97	32.0	7.88	26.6	3.79	29.2	4.69
Max	573	17.2	112	12.6	76.8	24.4	8.22	42.3	7.81	59.2	15.0	50.5	7.43	56.0	8.77
K_d	5.55	0.36	1.55	1.39	2.12	3.65	4.17	4.66	4.88	5.72	6.03	6.30	6.62	6.78	7.61
Melilite – low-Fe cores, h-07-51-3 (n = 5)															
Mean	1.53	1.85	1.94	0.41	1.59	0.31	0.09	0.32	0.04	0.21	0.04	0.11	0.01	0.07	0.01
SD	0.16	0.10	0.16	0.03	0.18	0.06	0.01	0.04	0.01	0.03	0.00	0.03	0.00	0.02	0.00
Min	1.32	1.71	1.76	0.37	1.39	0.23	0.08	0.25	0.03	0.17	0.03	0.08	0.01	0.04	0.01
Max	1.71	1.95	2.18	0.44	1.83	0.37	0.09	0.36	0.05	0.25	0.04	0.14	0.02	0.10	0.01
K_d	0.02	0.05	0.04	0.06	0.06	0.06	0.06	0.05	0.04	0.03	0.02	0.02	0.02	0.01	0.01
Melilite – high-Fe rims, h-07-51-3 (n = 11)															
Mean	0.67	4.67	4.86	0.74	2.44	0.28	0.09	0.23	0.02	0.11	0.02	0.05	0.01	0.04	0.01
SD	0.35	1.17	1.17	0.11	0.54	0.12	0.03	0.12	0.02	0.08	0.02	0.04	0.01	0.05	0.01
Min	0.10	3.05	2.78	0.58	1.43	0.11	0.04	0.05	0.00	0.01	0.00	0.01	0.00	0.00	0.00
Max	1.29	6.88	6.78	0.89	3.60	0.54	0.14	0.51	0.06	0.33	0.07	0.14	0.02	0.16	0.02
K_d	0.01	0.13	0.09	0.11	0.09	0.05	0.06	0.03	0.02	0.02	0.01	0.01	0.01	0.01	0.01
Kalsilite, h-07-Gr-1 (n = 21)															
Mean	1.55	3.97	5.57	0.59	1.80	0.31	0.12	0.25	0.04	0.21	0.04	0.14	0.02	0.15	0.03
SD	0.72	2.20	2.62	0.32	0.87	0.15	0.07	0.12	0.02	0.09	0.02	0.08	0.01	0.06	0.04
Min	0.66	1.43	2.25	0.21	0.61	0.12	0.03	0.08	0.01	0.07	0.01	0.05	0.00	0.06	0.00
Max	2.94	9.18	9.86	1.15	3.30	0.60	0.27	0.51	0.08	0.37	0.09	0.32	0.05	0.25	0.19
K_d	0.02	0.07	0.07	0.05	0.05	0.04	0.06	0.03	0.03	0.02	0.02	0.02	0.03	0.02	0.03

This is an open access article under the CC BY 4.0 license

© Ella V. Sokol, Anna S. Polovykh, Svetlana N. Kokh, Ivan S. Karputin, Olga A. Kozmenko, 2026

Table 3

Average trace-element compositions of rock-forming and minor minerals from Ca-rich combustion metamorphic rocks, Hatrurim Formation (LA-ICP-MS data), ppm

Element	Sc	Ti	V	Cr	Mn	Co	Ni	Cu	Zn	Ga	Rb	Sr	Zr	Nb	Ba	Hf	Ta	Th	U
Flourapatite, h-07-51-3 (n = 3)																			
Mean	2.38	578	1662	61.3	137	8.82	103	572	723	7.39	4.60	3296	10.9	1.39	1128	0.15	0.02	25.1	37.8
SD	0.35	370	1129	76.1	153	14.0	114	204	1035	4.38	5.72	1427	8.87	1.14	873	0.15	0.004	3.46	14.5
Min	1.99	215	531	13.9	19.1	0.55	6.11	427	69.9	2.76	0.56	1665	5.20	0.59	127	0.05	0.02	22.3	21.1
Max	2.67	954	2788	149	310	25.0	229	716	1916	11.5	8.65	4312	21.1	2.70	1729	0.32	0.03	29.0	47.2
K_d	0.08	0.07	5.91	0.10	0.96	0.63	0.20	1.92	0.53	0.72	0.38	1.99	0.05	0.31	2.42	0.03	0.02	4.03	0.58
Wollastonite, h-07-51-3 (n = 4)																			
Mean	7.24	485	19.3	3.41	26.1	0.94	7.38	0.25	7.02	0.49	0.75	836	2.43	0.36	12.6	0.28	0.37	0.67	0.37
SD	0.88	152	6.79	0.48	11.8	0.56	1.70	0.001	3.36	0.23	0.18	147	3.28	0.64	4.57	0.51	0.51	0.76	0.11
Min	6.05	247	13.0	3.07	17.7	0.57	6.18	0.25	4.65	0.32	0.63	662	0.17	0.01	9.00	0.01	0.01	0.14	0.24
Max	8.10	680	26.5	3.75	34.4	1.58	8.58	0.25	9.40	0.65	0.88	1011	7.13	1.31	17.7	1.05	0.73	1.54	0.46
K_d	0.23	0.06	0.07	0.01	0.18	0.07	0.01	0.01	0.01	0.05	0.06	0.50	0.01	0.02	0.03	0.05	0.26	0.11	0.01
Rankinite, h-07-51-3 (n = 3)																			
Mean	6.00	139	16.8	11.7	25.5	0.91	4.78	100	35.9	0.21	bdl	793	0.14	0.02	10.0	bdl	bdl	0.12	0.07
SD	0.34	10.4	13.5	10.3	1.25	0.28	0.12	88.8	5.72	0.12	–	7.48	0.07	0.01	1.03	–	–	0.09	0.04
Min	5.73	130	8.85	0.09	24.7	0.62	4.70	1.24	29.6	0.12	bdl	787	0.07	0.01	9.31	bdl	bdl	0.07	0.03
Max	6.39	150	32.4	19.8	26.4	1.18	4.87	173	40.7	0.34	bdl	798	0.20	0.03	10.8	bdl	bdl	0.22	0.11
K_d	0.19	0.02	0.06	0.02	0.18	0.07	0.01	0.34	0.03	0.02	–	0.48	0.01	0.01	0.02	–	–	0.02	0.01
Cuspidine, h-07-Gr-1 (n = 10)																			
Mean	15.8	909	31.4	21.2	33.4	0.37	1.79	3.25	6.70	0.59	1.82	1434	1112	164	53.4	21.5	9.90	24.3	1347
SD	2.40	160	12.3	19.2	6.14	0.12	0.99	2.60	3.74	0.35	1.51	264	262	32.2	30.0	5.52	3.20	4.63	492
Min	12.8	702	17.1	7.61	26.2	0.19	0.85	0.12	1.75	0.16	0.14	984	637	86.9	23.1	12.9	2.42	17.4	547
Max	21.7	1257	54.9	34.7	42.4	0.61	3.38	8.47	10.8	1.38	4.30	1971	1590	197	95.0	34.0	14.0	33.1	2059
K_d	0.48	0.07	0.06	0.05	0.14	0.02	0.01	0.01	0.01	0.02	0.03	0.52	4.08	3.92	0.01	3.41	4.18	2.57	11.35
Garnet – low-Ti cores, h-07-51-3 (n = 2)																			
Mean	27.1	28498	882	29.3	37.6	1.93	71.2	1.31	20.9	5.39	0.82	51.4	231	80.4	0.28	3.98	6.97	20.8	113
SD	3.09	6576	6.56	5.14	11.8	0.62	16.1	0.09	3.00	0.78	0.01	4.65	22.7	6.08	0.17	0.37	0.77	3.44	17.6
Min	24.9	23848	817	25.7	29.3	1.49	59.8	1.25	18.8	4.84	0.81	48.1	215	76.1	0.15	3.72	6.42	18.4	101
Max	29.3	33148	827	32.9	45.9	2.37	82.6	1.38	23.0	5.94	0.83	54.7	247	84.8	0.40	4.24	7.51	23.3	126
K_d	0.86	3.38	2.92	0.05	0.26	0.14	0.14	0.01	0.02	0.52	0.07	0.03	1.16	3.85	0.01	0.73	4.98	3.34	1.73
Garnet – high-Ti rims, h-07-51-3 (n = 6)																			
Mean	202	63013	245	4581	48.9	1.37	82.8	306	213	5.60	bdl	35.7	2190	38.4	0.30	51.9	7.29	16.6	24.1
SD	66.3	9036	95.4	3536	14.2	0.40	23.7	648	366	1.15	–	8.94	516	11.9	0.33	15.6	1.45	5.41	7.86
Min	159	54631	141	1584	31.5	0.85	50.8	4.22	37.8	3.91	bdl	23.9	1669	24.3	0.03	38.5	5.73	11.8	16.6
Max	336	79402	339	10609	61.6	1.86	104	1621	959	6.97	bdl	43.7	2873	51.2	0.73	82.0	9.67	24.0	33.6
K_d	6.43	7.47	0.87	7.30	0.34	0.10	0.16	1.03	0.16	0.54	–	0.02	10.95	1.84	0.01	9.51	5.21	2.65	0.37
Melilite – low-Fe cores, h-07-51-3 (n = 5)																			
Mean	4.38	122	1.35	5.21	30.2	20.0	297	281	1655	25.5	2.40	1387	1.29	0.03	26.3	bdl	bdl	0.02	0.02
SD	0.52	11.0	0.83	1.12	4.47	2.90	29.8	327	121	1.27	1.89	245	2.72	0.03	8.56	–	–	0.02	0.02
Min	3.46	109	0.52	4.09	23.4	16.9	227	92.5	1475	24.3	0.79	1014	0.07	0.01	17.3	bdl	bdl	0.01	0.01
Max	4.72	133	2.53	6.39	35.8	22.8	301	857	1798	27.5	4.97	1636	6.16	0.09	36.4	bdl	bdl	0.05	0.05
K_d	0.14	0.01	0.01	0.01	0.21	1.43	0.55	0.94	1.21	2.47	0.20	0.84	0.01	0.01	0.06	–	–	0.01	0.01
Melilite – high-Fe rims, h-07-51-3 (n = 11)																			
Mean	5.65	184	18.0	10.9	283	46.6	790	515	7547	25.8	0.73	4021	0.11	0.07	806	bdl	bdl	0.07	0.23
SD	0.49	30.3	22.3	13.4	199	13.7	219	377	1980	2.38	0.56	1809	0.13	0.12	996	–	–	0.09	0.10
Min	4.97	130	0.60	1.85	54.2	31.3	459	76.3	2574	21.2	0.01	2047	0.01	0.01	39.7	bdl	bdl	0.01	0.11
Max	6.49	231	59.3	45.3	729	69.3	1154	1136	10355	29.7	1.73	6469	0.48	0.38	3019	bdl	bdl	0.28	0.37
K_d	0.18	0.02	0.06	0.02	1.99	3.34	1.57	1.73	5.51	2.50	0.06	2.43	0.01	0.01	1.73	–	–	0.01	0.01
Kalsilite, h-07-Gr-1 (n = 21)																			
Mean	9.17	216	51.1	55.4	27.5	0.56	2.82	62.6	68.7	14.8	348	317	55.8	8.72	2032	1.26	0.26	0.56	1.87
SD	3.88	96.5	86.5	75.6	12.1	0.38	2.65	73.4	77.0	12.0	314	149	25.1	3.65	2528	0.61	0.12	0.25	1.04
Min	4.22	86.2	2.47	2.46	11.2	0.11	0.68	2.30	1.71	3.19	33.9	103	25.0	4.04	273	0.52	0.10	0.25	0.46
Max	14.7	347	389	281	48.9	1.67	13.5	230	310	42.5	1351	806	96.2	14.9	8563	2.36	0.43	0.98	4.12
K_d	0.28	0.02	0.10	0.12	0.11	0.03	0.01	0.09	0.02	0.53	6.59	0.11	0.20	0.21	0.56	0.20	0.11	0.06	0.02

Notes: bdl – below detection limit; flourapatite contains 2.31 ppm Cd (K_d = 0.31) and 24.6 ppm Pb (K_d = 2.87); high-Ti garnet rims contain 1.75 ppm Cd (K_d = 0.23); high-Fe melilite rims contain 1.97 ppm Cd (K_d = 0.26); kalsilite contains 2.68 ppm Cs (K_d = 6.32) and 8.45 ppm Pb (K_d = 0.35); cuspidine contains 1.59 ppm Pb (K_d = 0.07).

This is an open access article under the CC BY 4.0 license

Rankinite having an average composition of $Ca_{3.0}Si_{2.0}O_{7.0}$ (n = 17) contains only FeO (≤ 0.7 wt.%) and Sr (750-1300 ppm) impurities. The total content of REE is 40.0 to 130 ppm; Ti is ≤ 250 ppm (see Table 3, Supplement 1).

The composition of cuspidine fits the theoretical formula $Ca_{4.0}Si_{2.0}O_{7.0}F_{2.0}$ (n = 12). It stores a moderate amount of Sr (950-2000 ppm), low Ba (23.0-95.0 ppm), high concentrations of high-field strength elements, HFSE (700-1300 ppm Ti, 630-1600 ppm Zr, and 86.0-200 ppm Nb), and up to 2100 ppm U; ΣREE is quite low (≤ 260 ppm), with ≤ 35.0 ppm Th, ≤ 34.0 ppm Hf, and ≤ 14.0 ppm Ta (Tables 2, 3, Supplements 1, 2).

Melilites changed considerably its major-element chemistry while growing (Fig.3, 4), which is evident in the profile of a zoned crystal and tabulated data (Table 4, Supplement 3). The composition of melilite in two paralava samples was determined in 80 analyses of core and 65 analyses of rim zones. The trend is from relatively high Al_2O_3 (23.7 wt.% on average) and moderate contents of FeO (6.7 wt.%) and MgO (1.9 wt.%) at low Na_2O (0.7 wt.%) and K_2O (0.4 wt.%) in the core to lower Al_2O_3 (10.8 wt.%) but higher FeO (8.9 wt.%) and MgO (5.0 wt.%) in the rim. Sodium, which is minor in the rock (0.4 wt.% Na_2O), became a major element in melilite having reached an average of 1.9 wt.% at the final growth stage. Note that the amounts of potassium and zinc are minor in the rock (0.4-1.1 K_2O wt.% and 1250-3120 ppm Zn) but comparable in late melilite (0.8 wt.% K_2O and 1.2 wt.% ZnO on average).

Melilite in garnet paralava is the principal carrier of Zn (up to 7000 ppm in the core and 17,000 ppm in the rim), Co (up to 90.0 ppm), and Ga (up to 63.0 ppm) and shows Sr enrichment of 1000-7500 ppm. The contents of these elements are systematically higher in the rim, where the contents of Cu, Ni, and Mn are high as well: up to 4016 ppm Cu, 2060 ppm Ni, and 729 ppm Mn (see Table 3, Supplement 1).

The formulas corresponding to the average core and rim compositions of melilite crystals in the Hatrurim garnet paralava are, respectively, $Gh_{53}Fe^{3+}$-$Gh_{22}Ak_{15}Fe^{2+}$-$Ak_6Hdy_2Aak_2$ and Gh_2Fe^{3+}-$Gh_{34}Ak_{36}Fe^{2+}$-$Ak_1Hdy_6Aak_{21}$. The core is dominated by the gehlenite and ferrigehlenite endmembers ($Gh_{53}Fe^{3+}$-Gh_{22}), while the akermanite and ferroakermanite total is 21 mol.% ($Ak_{15}Fe^{2+}$-Ak_6); the contributions of the Na and Zn endmembers are modest (Hdy_2Aak_2). The amounts of the akermanite (Ak_{36}) and ferrigehlenite (Gh_2Fe^{3+}-Gh_{34}) endmembers in the rim are similar, while the molar percentages of the Na and Zn minals increase to 21 mol.% (Na-bearing alumoakermanite Aak_{21}) and 6 mol.% (Zn-bearing Hdy_6). The total of REE does not exceed 20 ppm.

Garnet, one of late phases, occurs as ≤ 2-3 mm zoned crystals with inclusions of fluorapatite, wollastonite, melilite, and ingrown flamite (see Fig.1, *a*-*c*). The core composition is similar to andradite,

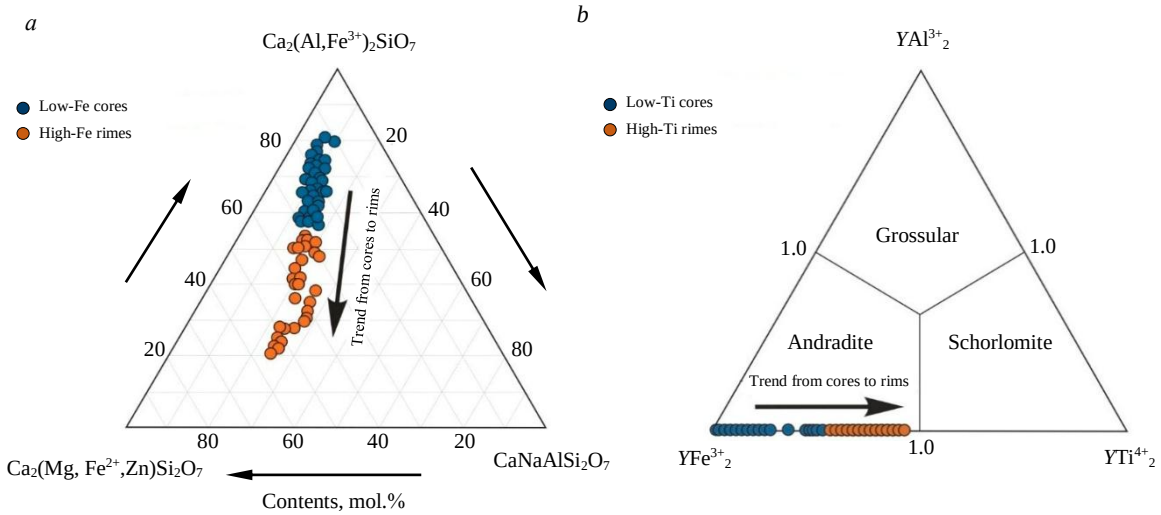


Fig.4. Melilite (*a*) and garnet (*b*) from the Hatrurim Formation high-Ca paralava in ternary diagrams:
a – melilite composition in the $Ca_2(Mg,Fe^{2+},Zn)Si_2O_7$–$Ca_2(Al,Fe^{3+})_2SiO_7$–$CaNaAlSi_2O_7$ diagram, mol.%;
b – garnet composition in the YFe^{3+}_2–YAl^{3+}_2–YTi^{4+}_2 diagram (formula based on 8 cations).
Plotted for *Y* occupancy proceeding from the general formula of garnet-group minerals $X_3Y_2Z_3O_{12}$, according to the nomenclature from [35]

This is an open access article under the CC BY 4.0 license

with 5.3 wt.% TiO_2 and 820-3350 ppm V on average (n = 15), and corresponds to the formula $Ca_{3.0}(Fe^{3+}_{1.6}Ti_{0.3}V_{\leq 0.01})_{\sum 2.0}(Si_{2.6}Al_{0.2}Fe^{3+}_{0.2})_{\sum 3.0}O_{12.0}$. The rim is enriched in TiO_2 (11.3 wt.% on average) and contains 1000 to 10,000 ppm Cr, 150 to 2990 ppm Zr, 80.0 to 600 ppm Y, 15.0 to 340 ppm Sc, 24.0 to 125 ppm Nb, ≤ 82.0 ppm Hf, and ≤ 11.0 ppm Ta. The formula of the average rim composition is $Ca_{3.0}(Fe^{3+}_{1.2}Ti_{0.7}Cr_{0.04}Sc_{\leq 0.01}Fe^{2+}_{\leq 0.01})_{\sum 2.0}(Si_{2.2}Fe^{3+}_{0.5}Al_{0,3})_{\sum 3.0}O_{12.0}$ (n = 60) (Supplement 4). Garnets store Th (≤ 30.0 ppm) and U (≤ 130 ppm) at ΣREE reaching 570 ppm (see Tables 2, 3, Supplements 1, 2).

Table 4

Representative analyses of melilite from Ca-rich combustion metamorphic rocks, Hatrurim Formation (EPMA data), wt.%

Component	1	2	3	4	5	6	7	8	9	10	11	12
SiO_2	25.31	26.29	27.04	27.19	27.85	28.75	29.14	30.27	31.41	31.71	32.73	34.32
Al_2O_3	24.17	23.62	22.94	22.79	20.94	19.23	18.33	17.31	16.53	14.59	12.89	11.94
FeO*	0.00	0.00	0.00	0.15	0.00	0.53	0.86	0.45	0.00	0.00	0.33	0.00
Fe_2O_3*	7.29	7.73	7.40	7.93	7.82	7.95	8.68	9.94	8.35	9.29	10.31	10.07
MgO	1.84	2.06	2.16	1.86	2.27	2.54	2.62	2.77	3.05	3.10	3.63	3.88
CaO	39.49	39.23	39.44	38.07	38.41	37.89	37.48	37.55	37.16	36.23	36.55	36.21
Na_2O	0.40	0.47	0.49	0.80	0.63	0.77	1.02	0.92	1.23	1.67	1.54	1.71
K_2O	0.17	0.25	0.30	0.42	0.42	0.53	0.43	0.60	0.67	0.54	0.63	0.80
ZnO	0.46	0.70	0.41	0.49	0.68	0.83	0.92	1.13	0.85	1.47	1.61	1.02
Total	99.13	100.35	100.18	99.70	99.02	99.02	99.48	100.94	99.25	99.01	100.22	99.95
Coefficients calculated for 7 oxygen atoms												
Si^{4+}	1.227	1.267	1.311	1.325	1.193	1.317	1.438	1.543	1.314	1.384	1.502	1.505
Al^{3+}	1.301	1.267	1.214	1.170	1.343	1.167	0.951	0.757	1.141	1.024	0.815	0.788
Fe^{2+}	0.000	0.000	0.000	0.006	0.000	0.021	0.034	0.018	0.000	0.000	0.013	0.000
Fe^{3+}	0.257	0.271	0.260	0.283	0.278	0.283	0.310	0.358	0.299	0.331	0.367	0.363
Mg^{2+}	0.143	0.151	0.155	0.176	0.129	0.160	0.208	0.238	0.186	0.181	0.219	0.232
Ca^{2+}	1.963	1.981	1.939	1.946	1.995	1.946	1.892	1.825	1.955	1.903	1.839	1.888
Na^+	0.057	0.045	0.061	0.071	0.037	0.058	0.107	0.161	0.054	0.104	0.153	0.120
K^+	0.018	0.018	0.024	0.020	0.010	0.025	0.031	0.040	0.018	0.032	0.033	0.044
Zn^{2+}	0.019	0.014	0.020	0.027	0.016	0.024	0.030	0.039	0.032	0.041	0.051	0.051
Minals, mol.%												
$Ca_2Al_2SiO_7$	49.69	47.58	45.32	41.99	51.29	41.61	26.47	11.83	39.71	29.12	14.48	14.89
$Ca_2Fe^{3+}{}_2SiO_7$	26.88	28.20	27.08	29.15	28.99	29.12	31.93	37.57	30.76	34.44	37.95	38.25
$Ca_2MgSi_2O_7$	15.79	14.88	16.88	16.99	13.45	16.46	21.42	24.97	19.14	18.83	22.65	24.45
$NaCaAlSi_2O_7$	6.16	7.36	8.53	8.68	4.60	8.18	13.60	19.65	7.10	13.34	18.30	15.98
$Ca_2Fe^{2+}Si_2O_7$	0.00	0.00	0.00	0.62	0.00	2.16	3.50	1.89	0.00	0.00	1.34	0.00
$Ca_2ZnSi_2O_7$	1.46	1.98	2.19	2.57	1.67	2.47	3.09	4.09	3.29	4.27	5.27	6.43

* Contents of FeO and Fe_2O_3 were calculated based on the stoichiometric composition.

Kalsilite has an average composition of $(K_{0.9}Na_{0.1})_{\sum 1.0}(Al_{0.9}Fe_{0.1})_{\sum 1.0}Si_{1.0}O_{4.0}$ (n = 11) and commonly contains notable amounts of FeO (3.0-3.9 wt.%) and Na_2O (0.3-1.0 wt.%). The mineral is the main host of Ba (≤ 8500 ppm) and the only carrier of Rb (≤ 1350 ppm), while its Sr contents are moderate (100 to 800 ppm). The total of REE is as low as 5 to 26 ppm (see Table 3, Supplement 1).

Discussion

Crystallization sequence of minerals in paralavas and element partitioning trend. The crystallization scenario of Si-undersaturated CM melts, with originally high contents of Ca at moderate Fe and K, consisted in successive growth of silicates with a progressively decreasing Ca/Si ratio [32, 34]. The trend lacks peritectic reactions which typically appear in the phase diagrams describing the crystallization of alkaline Si-undersaturated magmas and obscure the patterns of element fractionation in the presence of melilite solid solutions [17, 36, 37]. This feature of the Hatrurim paralava allows estimating K_d of trace elements between melilite solid solutions and the coexisting silicates and fluorapatite.

This is an open access article under the CC BY 4.0 license

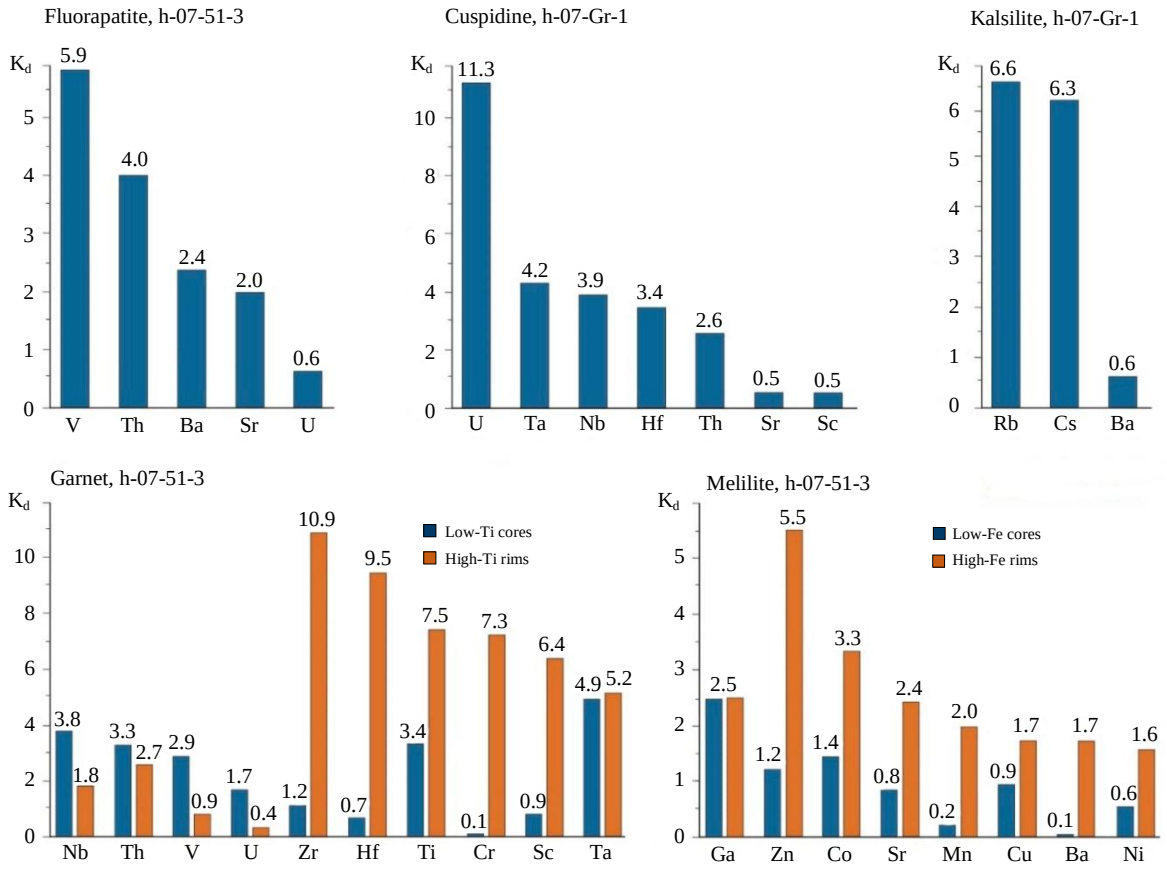


Fig.5. Partition coefficients of typical trace elements in rock-forming minerals from the Hatrurim Formation high-Ca paralavas

Fluorapatite begins the crystallization of CM melts and is the main storage of V (K_d = 2.7-5.9), LREE, MREE (K_d = 1.1-5.7), and Th (K_d = 4.0-5.2). It is always enriched in Sr (K_d = 1.3-2.0) and stores notable amounts of U (up to 144 ppm, at K_d = 0.4-0.6) (see Tables 2, 3, Supplements 1, 2; Fig.5, 6). The ubiquitous presence of SiO_2 and very low Na_2O contents (< 0.2 wt.%) provide evidence for the $Ca^{2+} + P^{5+} \rightarrow REE^{3+} + Si^{4+}$ isomorphic substitution.

The crystallization of fluorapatite is followed by Ca silicates (wollastonite and rankinite) which occupy up to 2/3 of the rock volume in total and have low contents of minor and trace elements. As a result, most of impurities in the residual melt increase dramatically. At this stage, only Ba, V, and LREE become partly immobilized in fluorapatite and in accessory Ba-V phases. Wollastonite and rankinite show notable enrichment only in Sr ($K_d \leq 0.5$) (see Table 3, Supplement 1). This crystallization scenario of CM melts influences greatly the major-element chemistry of melilite solid solutions and the trace-element composition of cuspidine. The final cooling stage also produces Ti-andradite rich in HFSE and REE and kalsilite as a major carrier of Rb.

The composition of melilite, which crystallized after Ca silicates, evolves from high Al contents at high temperatures to enrichment in Mg, Fe, Na, and Zn (see Fig.4), when the temperature decreases. Analysis of core and rim, which was possible in large zoned crystals, revealed distinct correlation between the partition coefficients of trace elements and the composition of melilite solid solutions (see Table 3, Supplement 1; Fig.5). Out of the four above-mentioned elements in the rim, only iron reached a major-element level in rock/melt (7.6-8.8 wt.% Fe_2O_3). The others, including Mg and Na, should be considered as impurities. Melilite solid solutions can accumulate chalcophile elements (Zn, Co, and Ni), as well as Ga, a geochemical equivalent of Al, at all growth stages. The respective partition coefficients increase as the composition of the growing mineral evolves from high Al toward higher Na, Fe^{3+}, Mg, and Zn contents. A notable amount of Cu is found in late melilite only. The

This is an open access article under the CC BY 4.0 license

maximum Sr, Ba, and Mn concentrations are likewise common to the rim of melilite crystals with low gehlenite but high percentages of the alumoakermanite (Aak_{11-28}) and akermanite (+ferroakermanite) ($Ak+Fe^{2+}$-Ak_{21-42}) endmembers. The partition coefficients of Co, Zn, and Ni vary from 0.5 to 2.5 in the core and reach 5.5 in the rim (see Fig.5), whereas the content of Ga is proportional to the share of the gehlenite endmember. Zn and Ga enrichment ($K_d > 1$) was reported earlier for magmatic melilite as well. Therefore, these elements become incorporated into the structure of the host mineral by the (Mg, Fe^{2+}) → Zn^{2+} and $Al^{3+} \rightarrow Ga^{3+}$ substitutions. In general, the composition trend of CM melilite results from the uptake of Al in the early generation (crystal core) and respective enrichment of the residual melt in the major elements of Mg, Fe, and Na, minor iron-group elements (Co, Ni, Mn), and such elements as Zn and Cu, as well as Ga, Sr, Ba and Mn.

The structural affinity of melilite to chalcophile elements is known from directed synthesis technologies and is used in the production of the respective composite materials [7]. Meanwhile, melilite from the Hatrurim paralava owes its prominent enrichment in these elements not only to the protolith chemistry [33], but also to unusual oxidizing conditions during the crystallization of CM melts in a zone of free oxygen access near the ground surface [34]. In these conditions, the commonly predominant oxide and/or sulfide hosts of Fe, Co, Ni, Mn, and Zn give way to Fe^{3+}-bearing silicates (Ti-andradite and melilite).

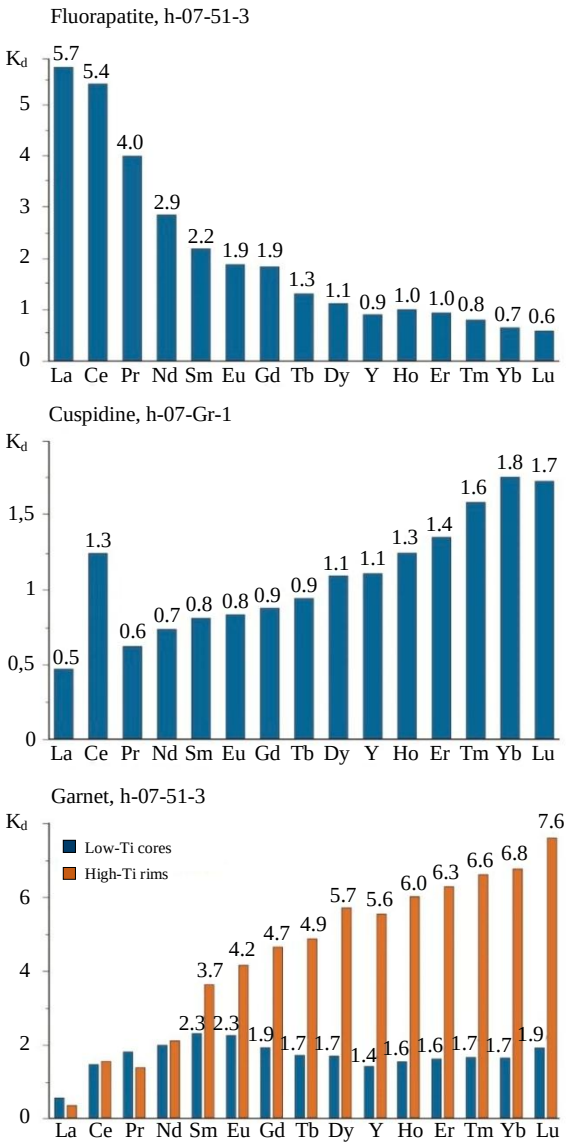


Fig.6. Partition coefficients of REE and Y in fluorapatite, cuspidine, and garnet from the Hatrurim Formation high-Ca paralava

As for large ion lithophile elements, the Hatrurim melilites store only Sr (K_d = 0.8-2.4) while Ba is mainly restricted to the rim (K_d = 0.3-1.7) at only $K_d < 0.1$ in the core. Sr can incorporate into the melilite structure also in igneous rocks from alkaline complexes. Most of Ba in these rocks resides in feldspar, though K_d of Ba exceeds 1 in a few analyses of melilite (Fig.7). The melilite structure is generally favorable for accommodating Ba at large cation sites, along with Fe, Co, Cu, and Mn at the T1 sites. At the time being, numerous Ba-analogs of akermanite ($BaMe^{2+}Si_2O_7$, where Me^{2+} = Mg, Co, Cu, Mn) have been synthesized [7]. The recent discovery of a natural Ba-bearing analog of melilite (bennesherite $Ba_2Fe^{2+}Si_2O_7$) was reported particularly from the Hatrurim Formation rocks [26].

The partition coefficients of REE we estimated for the melilite solid solutions from the Hatrurim paralava samples are below 0.1 and generally fit the ranges for melilite from igneous rocks (Fig.7). The K_d values for MREE and HREE decrease steadily till 0.01, while those for Y, HREE, as well as Zr and Hf, in melilite from paralava are likewise within the known values for magmatic melilite varying from 0.001 to 0.01 (Fig.7).

Garnets in the Hatrurim paralava store most of Ti, V, Cr, Zr, Hf, Nb, Ta, REE, Y, and Th. Andraditic cores contain more V, Nb, and Th than the high-Ti rims which show enrichment in HREE and Y, as well as in other HFSE (Sc, Zr, Hf, Ta) and Cr. The K_d coefficients approach 7 for Cr and

This is an open access article under the CC BY 4.0 license

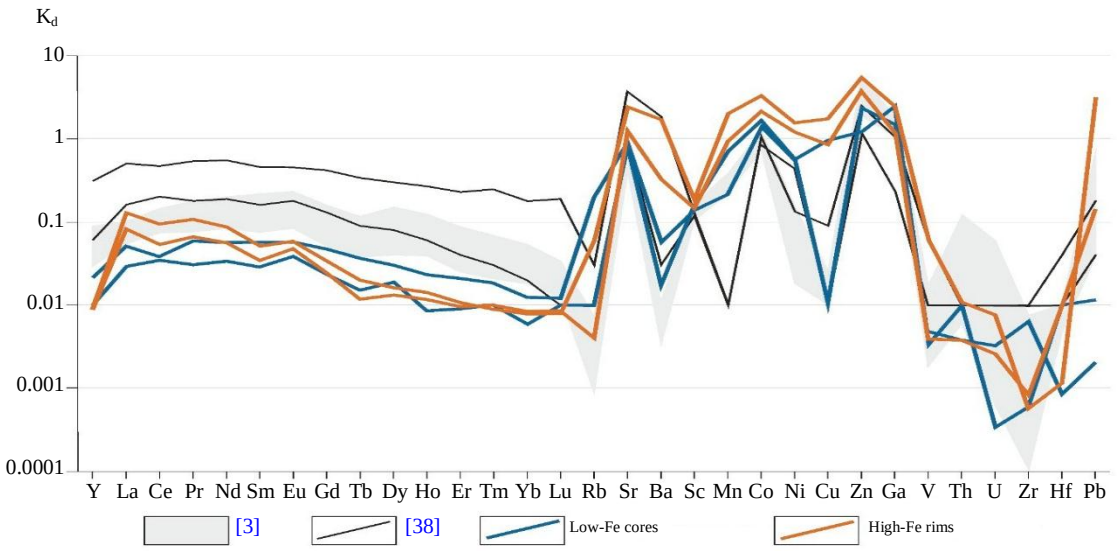


Fig.7. Partition coefficients of trace elements (including REE and Y) in melilite from the Hatrurim Formation high-Ca paralava, compared to published estimates [3, 38]. The curves represent K_d of specific analyzed paralava samples

Hf, 6 for Zr, 5 for Ti and Lu, 4 for other HREE, Sc, Ta, and Y, whereas those for U in garnet are as low as 0.1-0.35 (see Tables 2, 3, Supplements 1, 2).

High contents of uranium in the analyzed paralava samples (58.4 to 131 ppm) motivated the search for separate U phases. We found no Ca uranates, which are common to other Hatrurim CM rocks [33], but revealed extremely high concentrations of 2000 ppm U (K_d = 11.4) in large pure cuspidine grains ($Ca_4Si_2O_7F_2$). Cuspidine also competes with garnet in the accumulation of other HFSE (K_d from 2.5 to 4.0) and HREE (K_d up to 1.8) (see Tables 2, 3, Supplements 1, 2; Fig.5, 6). Cuspidine is enriched in HFSE apparently because these elements can easily form fluorine complexes [39]. The available data on the trace-element chemistry of cuspidine is very limited, but it is known to have structural affinity to Zr, Ce, La, Y, and Sr [40].

Conclusion

The patterns of element partitioning in main minerals of alkaline ultramafic rocks correspond to the trends of REE, Sr, Y, Zr, Hf, Nb, and Ta enrichment in the latest phases while the K_d values of these elements are far below 1 in the earliest phases of the crystallization sequence. This pattern was observed, for instance, in samples from the Khibiny alkaline ultramafic complex, with systematically high Nb, Ta, REE, Sr, and Y contents in all products of melts' differentiation [5]. We revealed a similar pattern in Ca-rich K-bearing Si-undersaturated combustion metamorphic melts. The contents of these elements are low ($K_d \leq 0.02$) in main rock-forming minerals from the Hatrurim Formation paralava samples (wollastonite, rankinite, and melilite solid solutions) which crystallized early from the CM melt, except for Sr and Ba stored in melilite.

As a result, the silicates that crystallized late from the Si-undersaturated and Ca-K-rich CM melts acquired times greater concentrations of K, Rb, Cs, Cr, V, Zr, Hf, Nb, Ta, Th, U, REE, and F, in the absence of the common hosts of incompatible elements (but for accessory fluorapatite). Such melts are compositionally favorable for crystallization of three rare minerals that can store the largest amounts of these elements: kalsilite, cuspidine, and Ti-andradite. Kalsilite becomes enriched in K (K_d = 24.5), Rb (K_d = 6.6), and Ba (K_d = 0.6), cuspidine hosts F (K_d = 20.8-23.8), Zr, Hf, Nb, Ta, U, Th, and HREE, while Ti-andradite accumulates Ti, V, Cr, Zr, Hf, Nb, Ta, REE, Y, and Th.

Melilite from the Hatrurim paralava samples bears signatures of isomorphic substitutions at all structural sites. Its late generations are especially prone to the formation of complex solid solutions. Melilites store Na (K_d = 6.6-7.3), Sr, and some Ba at the Ca site, Zn, Co, Ni, and Cu at the T1 site,

This is an open access article under the CC BY 4.0 license

while Fe^{3+} and Ga occupy T2 (the assignment is by analogy with synthetic compounds). Although it is possible to synthesize REE-bearing compounds with a melilite-type structure, REE and other incompatible elements are reluctant to incorporate into melilite crystallized from natural CM melts. The K_d estimates of minor and trace elements in the Hatrurim melilites are consistent with earlier determinations for minerals from igneous alkaline complexes (Fig.7). These estimates can be used for quantitative reconstructions of element fractionation trends in Ca-rich alkaline melts.

The partitioning of elements between phases crystallized *in situ* from small batches of low-viscosity CM melts is mainly controlled by crystal chemistry of Ca silicates, aluminosilicates, and phosphates. The case we studied provides an idea of fractionation patterns for a large scope of trace elements during the crystallization of Si-undersaturated melts in the absence of phases that commonly host incompatible elements in igneous alkaline rocks.

Access to data

Additional materials are available at the following links:
Supplement 1, https://pmi.spmi.ru/pmi/article/download/16876/16670.
Supplement 2, https://pmi.spmi.ru/pmi/article/download/16876/16671.
Supplement 3, https://pmi.spmi.ru/pmi/article/download/16876/16672.
Supplement 4, https://pmi.spmi.ru/pmi/article/download/16876/16673.

We greatly appreciate the analytical support to this study by the Candidates of Geological and Mineralogical Sciences A.Ragozin, N.Karmanov, E.Nigmatulina; V.Danilovskaya and M.Khlestov from the Analytical Center for Multielement and Isotope Research at the V.S.Sobolev Institute of Geology and Mineralogy.

REFERENCES

1. Sukhanova K.G. Trace elements in the silicate minerals of the Borodino Meteorite (H5). *Journal of Mining Institute.* 2024. Vol. 265, p. 16-33.
2. Sukhanova K.G, Galankina O.L. Trace element composition of silicate minerals from Kunashak Meteorite (L6). *Journal of Mining Institute.* 2024. Vol. 270, p. 877-892.
3. Stoppa F., Jones A.P., Sharygin V. Nyerereite from carbonatite rocks at Vulture volcano: implications for mantle metasomatism and petrogenesis of alkali carbonate melts Research Article. *Central European Journal of Geosciences*. 2009. Vol. 1. Iss. 2, p. 131-151. DOI: 10.2478/v10085-009-0012-9
4. Arzamastsev A.A., Fedotov Zh.A., Arzamastseva L.V. Dike Magmatism in the Northeastern Fennoscandian Shield. St. Petersburg: Nauka, 2009, p. 383.
5. Arzamastsev A.A., Arzamastseva L.V. Geochemical Indicators of the Evolution of the Ultrabasic–Alkaline Series of Paleozoic Massifs of the Fennoscandian Shield. *Petrology*. 2013. Vol. 21. N 3, p. 249-279. DOI: 10.1134/S0869591113020021
6. Gusev N.I., Romanova L.Yu. Paleoproterozoic Saltakh Pluton, Anabar Shield: mineralogical composition, age and a geodynamic setting. *Journal of Mining Institute*. 2025. Vol. 272, p. 16-39.
7. Brooks K. Minerals explained 61: Melilites. *Geology Today*. 2021. Vol. 38. Iss. 1, p. 32-36. DOI: 10.1111/gto.12380
8. Fedorenko V., Czamanske G., Zenko T. et al. Field and Geochemical Studies of the Melilite-Bearing Arydzhangsky Suite, and an Overall Perspective on the Siberian Alkaline-Ultramafic Flood-Volcanic Rocks. *International Geology Review*. 2000. Vol. 42. Iss. 9, p. 769-804. DOI: 10.1080/00206810009465111
9. Wilkinson J.F.G., Stolz A.J. Low-pressure fractionation of strongly undersaturated alkaline ultrabasic magma: the olivine-melilite-nephelinite at Moiliili, Oahu, Hawaii. *Contributions to Mineralogy and Petrology*. 1983. Vol. 83. Iss. 3-4, p. 363-374. DOI: 10.1007/BF00371205
10. Cundari A., Ferguson A.K. Petrogenetic relationships between melilitite and lamproite. In the Roman Comagmatic Region: the lavas of S. Venanzo and Cupaello. *Contributions to Mineralogy and Petrology*. 1991. Vol. 107. Iss. 3, p. 343-357. DOI: 10.1007/BF00325103
11. Wiedenmann D., Keller J., Zaitsev A.N. Melilite-group minerals at Oldoinyo Lengai, Tanzania. *Lithos*. 2010. Vol. 118. Iss. 1-2, p. 112-118. DOI: 10.1016/j.lithos.2010.04.002
12. Melluso L., Srivastava R.K., Guarino V. et al. Mineral compositions and petrogenetic evolution of the ultramafic-alkaline – carbonatitic complex of Sung Valley, northeastern India. *The Canadian Mineralogist*. 2010. Vol. 48. N 1, p. 205-229. DOI: 10.3749/canmin.48.1.205
13. Ogorodova L.P., Gritsenko Y.D., Vigasina M.F. et al. Thermodynamic properties of natural melilites. *American Mineralogist*. 2018. Vol. 103. N 12, p. 1945-1952. DOI: 10.2138/am-2018-6475

This is an open access article under the CC BY 4.0 license

14. MacPherson G.J. Calcium–Aluminum-rich Inclusions in Chondritic Meteorites. Treatise on Geochemistry. Elsevier, 2005. Vol. 1. Meteorites, Comets, and Planets, p. 201-246. DOI: 10.1016/B0-08-043751-6/01065-3

15. Ivanova M.A. Ca–Al-rich inclusions in carbonaceous chondrites: the oldest solar system objects. *Geochemistry International*. 2016. Vol. 54. N 5, p. 387-402. DOI: 10.1134/S0016702916050037

16. Rubin A.E., Chi Ma. Meteoritic minerals and their origins. *Geochemistry*. 2017. Vol. 77. Iss. 3, p. 325-385. DOI: 10.1016/j.chemer.2017.01.005

17. Asavin A.M. Partitioning of Trace Elements in the System 'Melt-Olivine-Ca Pyroxene' of Alkaline Melts: Evidence from Experiments and Field Data. Avtoref. dis. … kand. geol.-mineral. nauk. Irkutsk: Institut zemnoi kory SO RAN, 2016, p. 18.

18. Molendijk S.M., Namur O., Mason P.R.D. et al. Trace element partitioning in silica-undersaturated alkaline magmatic systems. *Geochimica et Cosmochimica Acta*. 2023. Vol. 346, p. 29-53. DOI: 10.1016/j.gca.2023.01.025

19. Pascal M.-L., Fonteilles M., Verkaeren J. et al. The melilite-bearing high-temperature skarns of the Apuseni Mountains, Carpathians, Romania. *The Canadian Mineralogist*. 2001. Vol. 39. N 5, p. 1405-1434. DOI: 10.2113/gscanmin.39.5.1405

20. Marincea Ş., Dumitraş D.-G., Ghineţ C. et al. Gehlenite from three occurrences of high-temperature skarns, Romania: new mineralogical data. *The Canadian Mineralogist*. 2011. Vol. 49. N 4, p. 1001-1014. DOI: 10.3749/canmin.49.4.1001

21. Pertsev N.N. High-Temperature Metamorphism and Metasomatism of Carbonate Rocks. Moscow: Nauka, 1977, p. 256.

22. Reverdatto V.V., Pertsev N.N., Korolyuk V.N. P_{CO_2}-*T*-Evolution and origin of zoning in melilite during the regressive stage of contact metamorphism in carbonate-bearing rocks. *Contributions to Mineralogy and Petrology*. 1979. Vol. 70. Iss. 2, p. 203-208. DOI: 10.1007/BF00374449

23. Sokol E.V., Kokh S.N., Polovykh A.S. et al. The Anakit contact aureole: spurrite–merwinite metamorphism and retrograde processes. *Russian Geology and Geophysics*. 2025. Vol. 66. N 11, p. 1446-1466. DOI: 10.2113/RGG20254887

24. Gross S. The Mineralogy of the Hatrurim Formation, Israel. Geological Survey of Israel, 1977. Bulletin 70, p. 80.

25. Grapes R. Pyrometamorphism. Springer, 2011, p. 376. DOI: 10.1007/978-3-642-15588-8

26. Krzątała A., Krüger B., Galuskina I. et al. Bennesherite, $Ba_2Fe^{2+}Si_2O_7$: A new melilite group mineral from the Hatrurim Basin, Negev Desert, Israel. *American Mineralogist*. 2022. Vol. 107. N 1, p. 138-146. DOI: 10.2138/am-2021-7747

27. Foit F.F., Hooper R.L., Rosenberg P.E. An unusual pyroxene, melilite, and iron oxide mineral assemblage in a coal-fire buchite from Buffalo, Wyoming. *American Mineralogist*. 1987. Vol. 72. N 1-2, p. 137-147.

28. Melluso L., Conticelli S., D'Antonio M. et al. Petrology and mineralogy of wollastonite- and melilite-bearing paralavas from the Central Apennines, Italy. *American Mineralogist*. 2003. Vol. 88. N 8-9, p. 1287-1299. DOI: 10.2138/am-2003-8-911

29. Peretyazhko I.S., Savina E.A. Melting Processes of Pelitic Rocks in Combustion Metamorphic Complexes of Mongolia: Mineral Chemistry, Raman Spectroscopy, Formation Conditions of Mullite, Silicate Spinel, Silica Polymorphs, and Cordierite-Group Minerals. *Geosciences*. 2023. Vol. 13. Iss. 12. N 377. DOI: 10.3390/geosciences13120377

30. Beckett J.R., Stolper E. The partitioning of Na between melilite and liquid: part I. the role of crystal chemistry and liquid composition. *Geochimica et Cosmochimica Acta*. 2000. Vol. 64. Iss. 14, p. 2509-2517. DOI: 10.1016/S0016-7037(00)00360-4

31. Warr L.N. IMA–CNMNC approved mineral symbols. *Mineralogical Magazine*. 2021. Vol. 85. Iss. 3, p. 291-320. DOI: 10.1180/mgm.2021.43

32. Seryotkin Yu.V., Sokol E.V., Kokh S.N. Natural pseudowollastonite: Crystal structure, associated minerals, and geological context. *Lithos*. 2012. Vol. 134-135, p. 75-90. DOI: 10.1016/j.lithos.2011.12.010

33. Sokol E.V., Kokh S.N., Sharygin V.V. et al. Mineralogical Diversity of Ca_2SiO_4-Bearing Combustion Metamorphic Rocks in the Hatrurim Basin: Implications for Storage and Partitioning of Elements in Oil Shale Clinkering. *Minerals*. 2019. Vol. 9. Iss. 8. N 465. DOI: 10.3390/min9080465

34. Sokol E., Novikov I., Zateeva S. et al. Combustion metamorphism in the Nabi Musa dome: new implications for a mud volcanic origin of the Mottled Zone, Dead Sea area. *Basin Research*. 2010. Vol. 22. Iss. 4, p. 414-438. DOI: 10.1111/j.1365-2117.2010.00462.x

35. Grew E.S., Locock A.J., Mills S.J. et al. Nomenclature of the garnet supergroup. *American Mineralogist*. 2013. Vol. 98. N 4, p. 785-811. DOI: 10.2138/am.2013.4201

36. Gee L.L., Sack R.O. Experimental Petrology of Melilite Nephelinites. *Journal of Petrology*. 1988. Vol. 29. Iss. 6, p. 1233-1255. DOI: 10.1093/petrology/29.6.1233

37. The Evolution of the Igneous Rocks. Fiftieth Anniversary Perspectives / Ed. by H.Yoder. Moscow: Mir, 1983, p. 528 (in Russian).

38. Arzamastsev A.A., Arzamastseva L.V., Bea F., Montero P. Trace Elements in Minerals as Indicators of the Evolution of Alkaline Ultrabasic Dike Series: LA-ICP-MS Data for the Magmatic Provinces of Northeastern Fennoscandia and Germany. *Petrology*. 2009. Vol. 17. N 1, p. 46-72. DOI: 10.1134/S0869591109010032

39. Gramaccioli C.M., Diella V., Demartin F. The formation of scandium minerals as an example of the role of complexes in the geochemistry of rare earths and HFS elements. *European Journal of Mineralogy*. 2000. Vol. 12. N 4, p. 795-808. DOI: 10.1127/ejm/12/4/0795

40. Bellezza M., Merlino S., Perchiazzi N. Chemical and structural study of the Zr, Ti-disilicates in the venanzite from Pian di Celle, Umbria, Italy. *European Journal of Mineralogy*. 2004. Vol. 16. N 6, p. 957-969. DOI: 10.1127/0935-1221/2004/0016-0957

***Authors*: Ella V. Sokol,** *Doctor of Geological and Mineralogical Sciences, Chief Researcher* (*V.S.Sobolev Institute of Geology and Mineralogy SB RAS, Novosibirsk, Russia*), *https://orcid.org/0000-0002-1130-6609*, **Anna S. Polovykh,** *Candidate of Geological and Mineralogical Sciences, Researcher* (*V.S.Sobolev Institute of Geology and Mineralogy SB RAS, Novosibirsk, Russia*), *devyatiyarova@igm.nsc.ru, https://orcid.org/0000-0003-0298-9185*, **Svetlana N. Kokh,** *Doctor of Geological and Mineralogical Sciences, Senior Researcher* (*V.S.Sobolev Institute of Geology and Mineralogy SB RAS, Novosibirsk, Russia*), *https://orcid.org/0000-0002-0264-7639*, **Ivan S. Karputin,** *Postgraduate Student, Research Engineer* (*V.S.Sobolev Institute of Geology and Mineralogy SB RAS, Novosibirsk, Russia*), *https://orcid.org/0009-0006-4651-1166*, **Olga A. Kozmenko,** *Lead Engineer* (*V.S.Sobolev Institute of Geology and Mineralogy SB RAS, Novosibirsk, Russia*), *https://orcid.org/0000-0003-4365-6483*.

The authors declare no conflict of interests.

This is an open access article under the CC BY 4.0 license

ISSN 2411-3336; e-ISSN 2541-9404

JOURNAL OF MINING INSTITUTE
Zapiski Gornogo instituta
Journal homepage: pmi.spmi.ru

Research article Geology

Mineralogical and geochemical characteristics of coals from the Mugun deposit and sediment provenance during their formation

Danzan B. Bembeev[1]✉, **Sofya I. Merenkova**[2,3], **Aleksei A. Samsonov**[1], **Ruslan R. Gabdullin**[1,4]
[1] *Lomonosov Moscow State University, Moscow, Russia*
[2] *Shirshov Institute of Oceanology of RAS, Moscow, Russia*
[3] *Schmidt Institute of Physics of the Earth of the RAS, Moscow, Russia*
[4] *Vernadsky Institute of Geochemistry and Analytical Chemistry of the RAS, Moscow, Russia*

***How to cite this article*:** Bembeev D.B., Merenkova S.I., Samsonov A.A., Gabdullin R.R. Mineralogical and geochemical characteristics of coals from the Mugun deposit and sediment provenance during their formation. Journal of Mining Institute. 2026. Vol. 280, p. 85-103.

Abstract
This study presents a comprehensive mineralogical and geochemical investigation of lignites from the Mugun deposit within the Irkutsk Coal Basin. The relevance of the research is determined by the need for the rational utilization of coal resources amid growing interest in the recovery of valuable and potentially valuable trace elements, including Ge, Ga, Sc, REE, U, and others, from coal and coal combustion products. The study aims to identify the distribution patterns of trace elements in coals and host rocks, determine their modes of occurrence, and reconstruct the provenance of the sedimentary material that formed the coal-bearing sequence. The research employed a combination of analytical methods, including X-ray fluorescence analysis, mass spectrometry, and scanning electron microscopy, together with statistical approaches such as correlation analysis and principal component analysis. It was established that trace-element enrichment in the coals resulted from clastic, biogenic, diagenetic, and epigenetic processes. The principal trace-element-bearing phases include clay minerals, particularly kaolinite, as well as sulfides, phosphates, and organic matter. Discriminant analysis of the composition of terrigenous rock interlayers, represented by siltstones and mudstones occurring between the coal seams, made it possible to reconstruct the sediment sources. These included granitoids and felsic and subalkaline volcanic rocks exposed in the foothills of the Eastern Sayan. The results provide a basis for proposing a highly plausible model of the coal-forming conditions and for predicting the distribution of trace elements in the coals and host rocks.

Keywords
Mugun deposit; lignite; geochemistry; trace elements; ash yield; mineralogy; principal component analysis; sediment provenance

Funding
The study was conducted within the framework of the State assignment of Lomonosov Moscow State University and was partially funded under the State assignment of Shirshov Institute of Oceanology of RAS (FMWE-2024-0020), as well as the State assignments of Vernadsky Institute of Geochemistry and Analytical Chemistry of the RAS, and Schmidt Institute of Physics of the Earth of the RAS.

Received: 06.10.2025 ***Accepted: 28.04.2026*** ***Online: 24.07.2026*** ***Published: 10.09.2026***

Introduction

The relevance of studying the geochemistry of lignite is determined by several factors. In recent years, the integrated processing of coal resources has become increasingly important. This approach involves not only utilizing the energy potential of coal itself, but also recovering critical elements, such as Ge, Ga, REE, and others, from coal and coal combustion wastes. Anomalous concentrations of several valuable rare and non-ferrous metals, including Ti, Zr, V, W, Y, Co, Ga, Ge, Nb, and Be, have been reported in deposits of the Kuznetsk Basin. These concentrations are most commonly associated with zones of tectonic disruption within coal seams, particularly where the seams occur near intrusive bodies [1, 2]. The successful recovery of REE from coal ash may improve the economic efficiency of the thermal power industry by creating additional sources of revenue [3, 4]. The environmental implications are also of particular importance. Large-scale coal mining and combustion

This is an open access article under the CC BY 4.0 license

result in the accumulation of ash and slag wastes, which, in the absence of proper disposal or utilization, may become a source of particulate emissions into the biosphere. Accordingly, studies of the mineralogical and elemental composition of coals, ashes, and slags are essential for developing approaches to reducing anthropogenic impacts and improving the efficiency of coal-resource utilization. In addition to their practical importance, investigations into the accumulation patterns of trace elements in coal are of fundamental scientific interest because they contribute to the reconstruction of coal accumulation and coal-forming conditions in the region under consideration [5].

The Mugun lignite deposit forms part of the Irkutsk Coal Basin, a major coal-bearing region that has served as one of the sources of fuel and energy resources for Eastern Siberia for many decades. Over recent decades, understanding of the geochemical and mineralogical characteristics of coals from the Mugun deposit has expanded considerably. Previous studies [6-8] have shown that, in addition to their energy potential, the local lignites contain rare mineral inclusions and coal-affinitive elements, whereas the ash and slag wastes produced during combustion are enriched in certain strategically important metals. However, the principal concentrators and modes of occurrence of valuable elements remain insufficiently characterized, and a comprehensive assessment of their recovery efficiency is still lacking. Addressing these issues may contribute to improving the economic viability of the Mugun deposit and to more complete utilization of the region's resource potential.

Brief geological setting and study materials

The Mugun lignite deposit is located in the Tulun District of Irkutsk Region, 40 km southwest of the town of Tulun, on the gently sloping watershed between the Kurzanka and Manut rivers, tributaries of the larger Iya River (Fig.1). The deposit lies within the southern part of the Siberian Platform and is characterized by a relatively simple geological structure. Lower Paleozoic deposits occur here in nearly horizontal or gently undulating attitudes and are intruded by lens-shaped sill-like bodies. Nearly horizontal, unconsolidated Jurassic freshwater sedimentary rocks overlie the eroded surface of this basement. Post-Jurassic erosion deeply dissected the sedimentary succession, particularly the Jurassic deposits. The latter have been preserved either on watersheds or within depressions in the surface of the Paleozoic basement, which have highly irregular outlines. Depending on the depth of erosion, different stratigraphic units are exposed at the present-day surface [9].

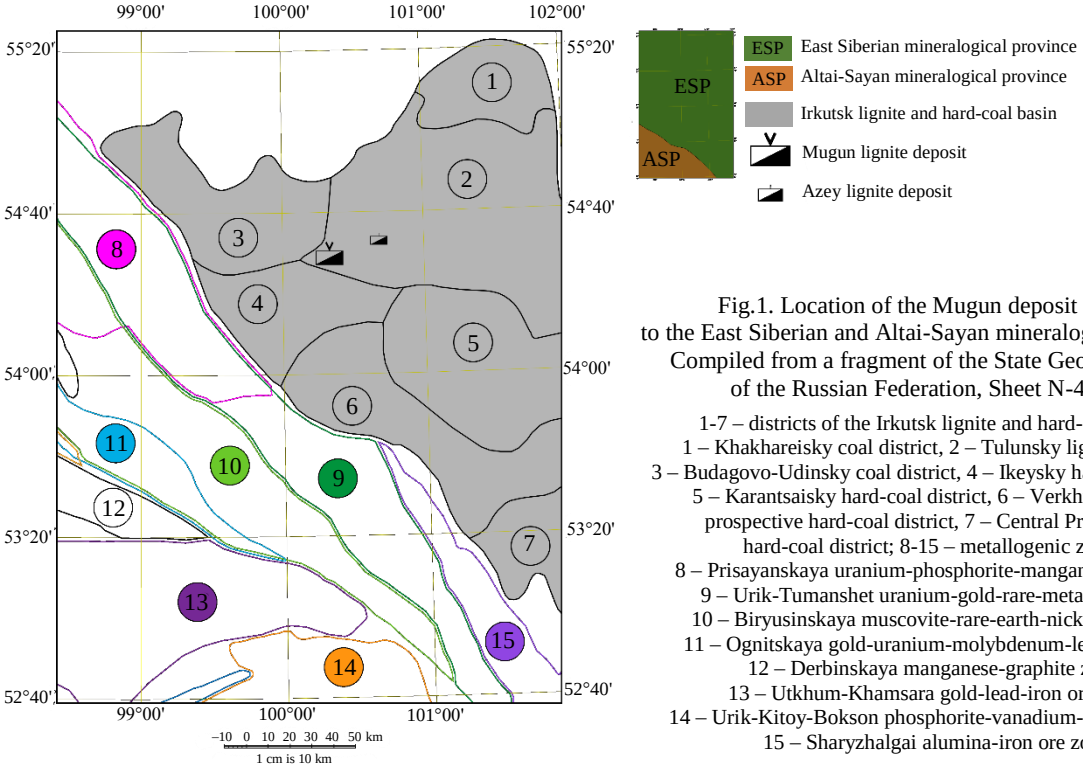


Fig.1. Location of the Mugun deposit relative to the East Siberian and Altai-Sayan mineralogical provinces. Compiled from a fragment of the State Geological Map of the Russian Federation, Sheet N-47 [10]

1-7 – districts of the Irkutsk lignite and hard-coal basin:
1 – Khakhareisky coal district, 2 – Tulunsky lignite district,
3 – Budagovo-Udinsky coal district, 4 – Ikeysky hard-coal district,
5 – Karantsaisky hard-coal district, 6 – Verkhneziminsky prospective hard-coal district, 7 – Central Prisayanskii hard-coal district; 8-15 – metallogenic zones:
8 – Prisayanskaya uranium-phosphorite-manganese ore zone,
9 – Urik-Tumanshet uranium-gold-rare-metal ore zone,
10 – Biryusinskaya muscovite-rare-earth-nickel ore zone,
11 – Ognitskaya gold-uranium-molybdenum-lead ore zone,
12 – Derbinskaya manganese-graphite zone,
13 – Utkhum-Khamsara gold-lead-iron ore zone,
14 – Urik-Kitoy-Bokson phosphorite-vanadium-gold ore zone,
15 – Sharyzhalgai alumina-iron ore zone

This is an open access article under the CC BY 4.0 license

Structurally, the area may be divided into two zones: the platform zone proper and the foreland-depression zone. The platform zone occupies the northeastern part of the area. It is characterized by a relatively limited thickness of coal-bearing Jurassic deposits, which were preserved from erosion within depressions in the comparatively stable Paleozoic basement. The Jurassic succession reaches a thickness of up to 150 m in this zone. The southern boundary of the platform zone may conventionally be traced along the southern boundary of the Mugun deposit [11]. To the southwest, the platform zone gradually passes into the foreland-depression zone, which is bordered to the south by the folded region of the Eastern Sayan. The immediate proximity of the folded belt promoted mobility of the pre-Jurassic basement during deposition of the Jurassic succession. As a result, the thickness of the coal-bearing deposits increases in the central part of the zone and reaches 200-300 m in some parts of the foreland depression. The geological succession of the area and the deposit comprises Paleozoic and Mesozoic sedimentary units overlain by Quaternary deposits [11]:

• the Paleozoic complex, composed mainly of Ordovician sandstones, siltstones, mudstones, and trap intrusions, forms an irregularly dissected pre-Jurassic basement;

• the Mesozoic complex is represented by Middle Jurassic deposits of the Zalarinskaya, Cheremkhovskaya, and Prisajanskaya formations, with coal-bearing seams occurring in erosional-tectonic depressions; the productive, or Cheremkhovskaya, Formation contains several principal mineable lignite seams;

• Quaternary deposits, represented by alluvial and eluvial-deluvial sediments, continuously cover the sedimentary sequence; they are relatively thin on watersheds and become thicker in valleys.

The Jurassic deposits of the Mugun deposit occur within an erosional-tectonic depression in the Paleozoic basement and comprise three formations: the Zalarinskaya (J_1zl), Cheremkhovskaya ($J_{1\text{-}2}cr$), and Prisajanskaya (J_2ps). The barren Zalarinskaya Formation, 0-53 m thick, consists of quartz sandstones, siltstones, and less commonly conglomerates, and contains no commercially significant coal seams. The Prisajanskaya Formation, 0-20 m thick, likewise contains no mineable coal seams, although it may include isolated thin coal lenses.

According to P.P.Timofeev [12], the Cheremkhovskaya coal-bearing formation accumulated in a continental freshwater basin dominated by swampy plains alternating with lacustrine-alluvial systems. These conditions favored the formation of thick coal seams interbedded with terrigenous deposits represented mainly by siltstones and mudstones. In some cases, transitional varieties of terrigenous rocks compositionally similar to clay-rich rocks occur. Hereafter, these are conventionally referred to as terrigenous interlayers.

The Cheremkhovskaya Formation, 60-85 m thick, is of primary importance for the commercial coal potential of the deposit and is divided into three horizons:

• the lower, non-commercial horizon, composed of polymictic sandstones with rare thin coal lenses;

• the productive-seam horizon, comprising sandstones, siltstones, mudstones, and coal seams of mineable thickness;

• the upper, non-commercial horizon, dominated by sandstones with occasional lenses of carbonaceous rocks.

Thus, all commercially significant coal reserves of the Mugun deposit are confined to the productive-seam horizon of the Cheremkhovskaya Formation, specifically Seams I and II. Coal sampling was carried out within the Mugun deposit, where the Southern, Western, and Central blocks, as well as the boundary trench of the Central Block, were being mined at the time of the study. Seams I, II, and IIa were under development. Sampling locations were selected with due consideration of the current mining and technical conditions. During sampling, a considerable part of the section was inaccessible because drainage ditches were flooded and some areas were characterized by an increased risk of rock collapse. Navigation was performed using built-in smartphone GPS modules and the SpotLens and GPS Camera applications; coordinates were recorded in the UTM WGS84 coordinate system.

This is an open access article under the CC BY 4.0 license

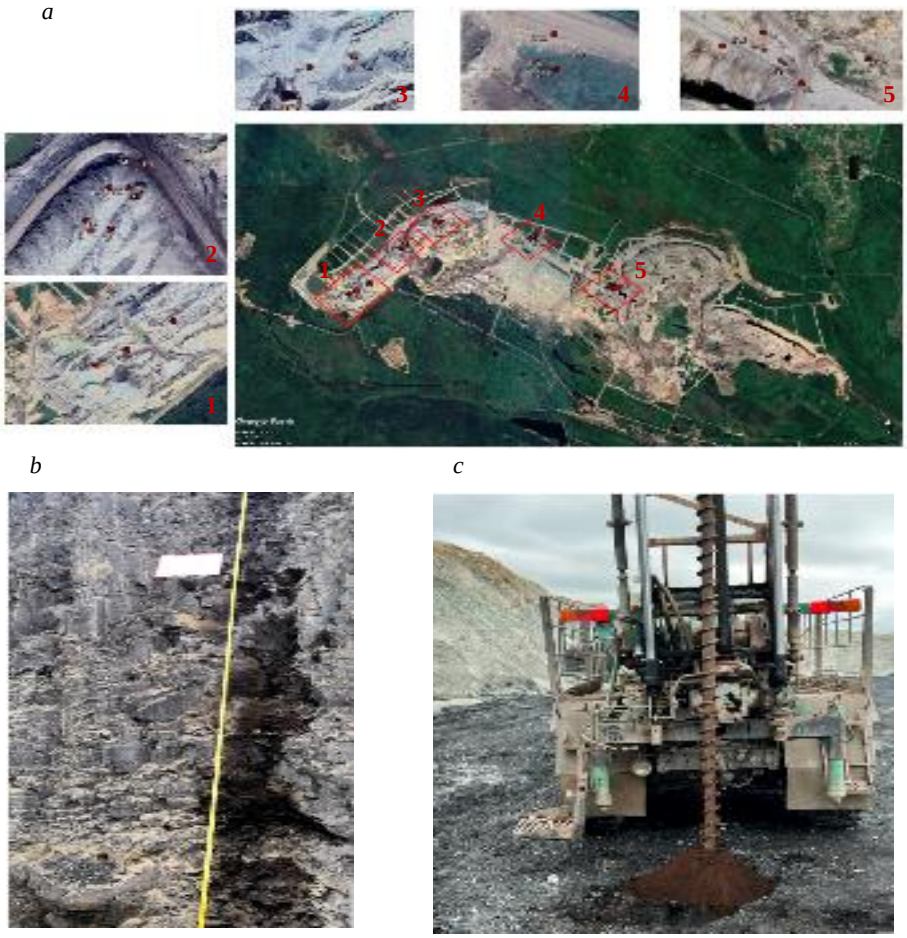


Fig.2. Map showing the locations of the sampling sites (*a*) and sampling methods at the Mugun deposit: *b* – manual; *c* – drilling

Sampling was conducted at five sites, numbered 1-5 (Fig.2, *a*), located within the Southern, Western, and Central blocks of the Mugun deposit. Sites 1 and 2 were situated within the Southern Block: Site 1 was located in its southern part and included three sampling points, whereas Site 2 was located in its northern part and included eight sampling points. Sites 3-5 were located within the Western and Central blocks: Site 3 was situated in the western part of the Western Block near the boundary with the Southern Block and included three sampling points, Site 4 was located in the central part of the Western Block and included four points, and Site 5 was situated in the western part of the Central Block near the boundary with the Western Block and included six points.

Samples were collected along the active mining front with due regard for the prevailing mining and technical conditions. Each sampling record included information on seam thickness, the characteristics of individual benches, the lithological composition of the sampled material, and the sample type, either differential or production. Differential samples were collected for subsequent investigation of element distribution within individual benches. In some cases, samples were also taken from the seam roof, floor, and thick interbeds for comparison with the main coal body.

Sampling was performed both manually and by drilling. Manual sampling employed the channel-sampling method, in which the geometric dimensions of the channel, approximately 10 cm in both width and depth, were used as a guide to ensure uniform coverage of the sampled interval (Fig.2, *b*). The material was collected on a tarpaulin placed beneath the sampling point and then packed into bags containing identification sheets. The samples were subsequently transported to the technical quality-control department, where they were crushed to a particle size of less than 3 mm, reduced, and packed into airtight zip-lock bags. Auger drilling was used for drill sampling; the samples were also reduced

This is an open access article under the CC BY 4.0 license

on site and packed into similar bags (Fig.2, *c*). After crushing and reduction, the average mass of a laboratory sample was approximately 600 g.

Photographic documentation of the actual sampling location was prepared at each sampling point (Fig.2, *b*, *c*). Figure 2, *b* shows a transverse channel approximately 3.7 m long, 10 cm wide, and 10 cm deep, from which a manual sample was collected by channel sampling. Figure 2, *c* illustrates drill sampling: an auger drill was advanced into the coal seam to a depth of up to 4.5 m, after which the recovered core material was used to prepare a sample of comparable mass.

A total of 89 samples were collected from 24 sampling points within the Mugun deposit (Fig.2, *a*). In the Southern Block, 41 samples were collected from 11 points, including nine manually collected samples from Seam I at two points, five manually collected samples from Seam II at one point, and 27 drill samples from eight points.

In the Western Block, 29 samples were collected from seven points, including 25 drill samples from Seam I at six points and four manually collected samples from Seam II at one point.

In the Central Block, 19 samples were collected from six points, including nine manually collected samples from Seam I at three points and 10 drill samples from three points. No sampling was conducted within the boundary trench of the Central Block because no accessible exposed sections were available. Sampling-point and sample numbers are listed in Table 1.

Table 1

Sampling locations and sample numbers from the Mugun deposit

Sampling location	Sample	Sampling location	Sample	Sampling location	Sample	Sampling location	Sample
Mu1	Mu-D-1-1-1	B3	Mu-D-B3-2-1	M3	M-D-3-1-1	B12	M-D-B12-1-1
	Mu-D-1-1-2		Mu-D-B3-2-2		M-D-3-1-2		M-D-B12-1-2
	Mu-D-1-1-3		Mu-D-B3-2-3		M-D-3-1-3		M-D-B12-1-3
	Mu-D-1-1-4	B4	Mu-D-B4-2-1	M4	M-D-4-1-1		M-D-B12-1-4
	Mu-D-1-1-5		Mu-D-B4-2-2		M-D-4-1-2	B13	M-D-B13-1-1
Mu2	Mu-D-2-1-1		Mu-D-B4-2-3		M-D-4-1-3		M-D-B13-1-2
	Mu-D-2-1-2	B5	Mu-D-B5-2-1	M5	M-D-5-2-1		M-D-B13-1-3
	Mu-D-2-1-3		Mu-D-B5-2-2		M-D-5-2-2		M-D-B13-1-4
	Mu-D-2-1-4		Mu-D-B5-2-3		M-D-5-2-3	B14	M-D-B14-1-1
Mu3	Mu-D-3-2-1	B6	Mu-D-B6-2-1		M-D-5-2-4		M-D-B14-1-2
	Mu-D-3-2-2		Mu-D-B6-2-2	B9	M-D-B9-1-1		M-D-B14-1-3
	Mu-D-3-2-3		Mu-D-B6-2-3		M-D-B9-1-2		M-D-B14-1-4
	Mu-D-3-2-4	B7	Mu-D-B7-2-1		M-D-B9-1-3	B15	M-D-B15-1-1
	Mu-D-3-2-5		Mu-D-B7-2-2		M-D-B9-1-4		M-D-B15-1-2
B1	Mu-D-B1-2-1		Mu-D-B7-2-3		M-D-B9-1-5		M-D-B15-1-3
	Mu-D-B1-2-2		Mu-D-B7-2-4	B10	M-D-B10-1-1	B16	M-D-B16-1-1
	Mu-D-B1-2-3	B8	Mu-D-B8-2-1		M-D-B10-1-2		M-D-B16-1-2
	Mu-D-B1-2-4		Mu-D-B8-2-2		M-D-B10-1-3		M-D-B16-1-3
B2	Mu-D-B2-2-1		Mu-D-B8-2-3		M-D-B10-1-4		M-D-B16-1-4
	Mu-D-B2-2-2		Mu-D-B8-2-4	B11	M-D-B11-1-1	B17	M-D-B17-1-1
	Mu-D-B2-2-3	M2	M-D-2-1-1		M-D-B11-1-2		M-D-B17-1-2
			M-D-2-1-2		M-D-B11-1-3		M-D-B17-1-3
			M-D-2-1-3		M-D-B11-1-4		

This is an open access article under the CC BY 4.0 license

Research methods

X-ray fluorescence (XRF) analysis was performed using a PANalytical Axios mAX wavelength-dispersive spectrometer operated under vacuum. The method is based on excitation of atoms in the analyzed sample by X-rays and measurement of the characteristic fluorescent radiation emitted by the constituent elements. The spectrometer was equipped with a 4 kW X-ray tube with an Rh anode, with a maximum accelerating voltage of 60 kV and a maximum anode current of 160 mA. The analyses were carried out using procedures approved by the Federal Scientific and Methodological Centre for Laboratory Research and Certification of Mineral Raw Materials "VIMS". The results correspond to accuracy category III for quantitative analysis in accordance with OST RF 41-08-205-04.

Inductively coupled plasma mass spectrometry (ICP-MS) following acid digestion was performed using an Agilent MS7900 quadrupole mass spectrometer. The samples were digested in a mixture of nitric and hydrochloric acids (aqua regia), after which the elements in the resulting solutions were determined by high-sensitivity ICP-MS analysis.

Photomicrographs and X-ray spectral microanalysis were obtained at the Shared Research Facilities Centre of Schmidt Institute of Physics of the Earth of the RAS, using a TESCAN MIRA LMS scanning electron microscope (SEM) equipped with an Ultim Max 65 energy-dispersive X-ray (EDX) spectrometer and integrated AZtecLive Automated software (Oxford Instruments). The analyses were conducted at an accelerating voltage of 20 KeV and a working distance of 15 mm.

Principal component analysis (PCA) was applied to the trace-element concentration data to identify correlations among the elements. PCA is a widely used statistical technique that transforms interrelated variables into a set of independent, orthogonal components. When applied to geochemical data, PCA simplifies the analysis of multidimensional datasets, reveals latent patterns in element distribution, and assists in interpreting the factors controlling their accumulation.

The ash yield of the coal samples was determined by the slow-ashing reference method in accordance with GOST R 55661-2013. The method involves combustion of a weighed fuel sample under free access of air, followed by ignition of the ash residue to constant mass at 815±10 °C. The analysis was performed on air-dried samples. The ash yield of each analytical sample was calculated using the standard formula and expressed as a percentage; the reported value was taken as the arithmetic mean of two parallel determinations.

Results

The XRF and ICP-MS data were summarized using the principal descriptive statistical parameters, which made it possible to characterize variations in element concentrations and identify their distribution patterns within the Mugun deposit. The summary statistics are presented in Tables 2-4. Table 2 includes 89 samples, Table 3 includes 74 samples, and Table 4 includes 15 samples. Trace-element concentrations in the coals were determined from the chemical-analysis results. To assess the degree of element enrichment, the measured concentrations were compared with world coal Clarke values (C) [13], which represent average element concentrations in coals. Sulfur is an exception because its coal Clarke value cannot be determined empirically.

Table 2

Statistical characteristics of trace-element concentrations in coal and host-rock samples

Element	Min	Max	Mean	Median	σ*	CV**
Ash yield, %	3.8	86.9	22.4	13.9	20.0	89.0
Li, ppm	2.4	153.4	37.4	24.4	33.1	89.0
Be, ppm	0.6	3.9	1.7	1.4	0.8	48.0
B, ppm	40.4	243.6	147.2	148.7	40.4	27.0
Sc, ppm	0.9	47.4	8.4	4.5	9.5	113.0

This is an open access article under the CC BY 4.0 license

End of Table 2

Element	Min	Max	Mean	Median	σ*	CV**
Ti, %	0.005	0.6	0.1	0.1	0.1	126.0
V, ppm	14.5	315.9	70.0	54.2	51.5	74.0
Cr, ppm	3.6	118.3	32.5	21.8	27.8	85.0
Mn, ppm	29.3	366.3	107.9	89.4	64.1	59.0
Fe, %	0.2	4.0	0.9	0.6	0.7	79.0
Ni, ppm	6.5	81.2	18.1	13.5	12.6	69.0
Cu, ppm	8.8	499.5	50.1	30.4	70.7	141.0
Zn, ppm	1.2	158.6	37.7	21.2	39.2	104.0
Ga, ppm	1.0	24.4	7.7	5.3	6.0	78.0
Ge, ppm	0.3	35.2	3.1	1.0	6.2	199.0
As, ppm	0.2	87.1	5.3	2.8	10.3	193.0
Rb, ppm	0.1	99.4	13.6	2.5	23.3	171.0
Sr, ppm	3.6	283.7	87.4	91.4	48.4	55.0
Y, ppm	1.3	50.1	18.2	16.7	10.0	55.0
Zr, ppm	3.9	192.8	52.3	36.7	43.1	83.0
Nb, ppm	0.1	19.9	4.4	2.9	4.4	99.0
Mo, ppm	0.4	5.2	1.3	1.0	0.9	68.0
Ag, ppm	0.015	0.297	0.075	0.047	0.08	101.0
Cd, ppm	0.015	1.644	0.295	0.221	0.28	94.0
Sn, ppm	0.015	3.839	1.241	0.969	0.97	78.0
Sb, ppm	0.015	1.697	0.332	0.288	0.25	75.0
Cs, ppm	0.015	6.238	0.899	0.199	1.49	165.0
Ba, ppm	18.7	648.0	82.8	45.6	110.6	134.0
Hf, ppm	0.039	5.703	1.595	1.248	1.20	75.0
Ta, ppm	0.015	1.460	0.351	0.248	0.33	93.0
Pb, ppm	0.5	24.6	7.2	5.9	5.2	72.0
Th, ppm	0.4	16.4	4.8	3.4	3.9	80.0
U, ppm	0.2	7.9	2.3	2.0	1.4	62.0
W, ppm	2.8	169.9	19.5	11.7	24.4	125.0
P, %	0.001	0.093	0.01	0.005	0.01	133.0
S, %	0.2	5.4	1.7	0.9	1.4	83.0
Cl, %	0.004	0.009	0.005	0.005	0.002	30.0
F, %	0.005	0.064	0.016	0.01	0.02	96.0

* σ – standard deviation.
** CV – coefficient of variation, %.

Table 3

Statistical characteristics of trace-element concentrations in coal samples

Element	Min	Max	Mean	Median	σ	CV
Ash yield, %	3.8	37.8	14.1	12.2	6.6	47.0
Li, ppm	2.4	72.7	25.3	21.5	14.2	56.2
Be, ppm	0.6	3.9	1.5	1.3	0.6	44.2
B, ppm	93.1	243.6	158.9	155.4	30.7	19.3
Sc, ppm	0.9	36.9	5.7	3.7	6.6	115.4
Ti, %	0.005	0.199	0.057	0.035	0.048	84.5

This is an open access article under the CC BY 4.0 license

End of Table 3

Element	Min	Max	Mean	Median	σ	CV
V, ppm	14.5	216.2	58.0	49.0	41.0	71.0
Cr, ppm	3.6	64.2	21.8	18.4	14.0	64.3
Mn, ppm	29.3	366.3	99.9	87.5	63.6	63.6
Fe, %	0.2	4.0	0.7	0.6	0.5	67.9
Ni, ppm	6.5	81.2	14.7	12.2	9.9	67.5
Cu, ppm	8.8	499.5	48.6	26.3	75.4	155.1
Zn, ppm	1.2	158.6	28.8	18.5	33.3	115.6
Ga, ppm	1.0	14.7	5.5	4.7	3.0	55.5
Ge, ppm	0.3	33.1	2.2	0.8	4.8	223.1
As, ppm	0.2	87.1	4.4	2.1	10.8	245.3
Rb, ppm	0.1	32.2	4.5	2.1	6.0	134.4
Sr, ppm	3.6	283.7	90.9	94.1	49.6	54.6
Y, ppm	1.3	50.1	16.2	14.0	9.0	55.4
Zr, ppm	3.9	90.2	36.7	33.3	19.6	53.4
Nb, ppm	0.1	7.8	2.8	2.5	1.6	57.2
Mo, ppm	0.6	4.3	1.2	1.0	0.7	57.9
Ag, ppm	0.015	0.162	0.047	0.015	0.042	89.6
Cd, ppm	0.015	1.644	0.282	0.201	0.295	104.8
Sn, ppm	0.015	3.839	0.974	0.772	0.762	78.2
Sb, ppm	0.015	1.270	0.286	0.227	0.194	67.8
Cs, ppm	0.015	3.549	0.349	0.129	0.580	166.3
Ba, ppm	18.7	109.3	43.3	42.9	16.9	38.9
Hf, ppm	0.039	2.806	1.180	1.091	0.607	51.4
Ta, ppm	0.015	0.731	0.241	0.206	0.162	67.4
Pb, ppm	0.5	14.2	5.6	5.2	3.1	55.8
Th, ppm	0.4	14.1	3.7	2.9	2.9	77.5
U, ppm	0.2	7.9	2.0	1.8	1.3	64.9
W, ppm	2.8	69.6	14.6	11.1	13.3	91.3
P, %	0.001	0.046	0.007	0.005	0.008	117.3
S, %	0.6	5.4	1.7	0.9	1.4	82.6
Cl, %	0.004	0.008	0.005	0.005	0.001	17.1
F, %	0.005	0.033	0.010	0.005	0.008	74.0

Table 4

Statistical characteristics of trace-element concentrations in host-rock samples

Element	Min	Max	Mean	Median	σ	CV
Ash yield, %	39.5	86.9	63.1	61.3	12.2	19.3
Li, ppm	25.9	153.4	97.3	102.6	35.1	36.1
Be, ppm	0.9	3.9	2.6	2.7	0.8	31.1
B, ppm	40.4	148.7	89.4	88.1	32.4	36.2
Sc, ppm	11.0	47.4	21.5	19.7	10.7	49.4
Ti, %	0.194	0.587	0.395	0.379	0.125	31.7
V, ppm	73.6	315.9	129.5	113.7	57.2	44.2
Cr, ppm	65.4	118.3	84.9	84.5	16.5	19.4
Mn, ppm	55.0	239.0	147.3	138.5	52.5	35.7
Fe, %	0.6	3.9	1.9	1.9	0.8	42.3

This is an open access article under the CC BY 4.0 license

End of Table 4

Element	Min	Max	Mean	Median	σ	CV
Ni, ppm	14.9	54.5	35.2	35.9	10.3	29.1
Cu, ppm	9.3	188.4	57.5	48.9	41.3	71.8
Zn, ppm	18.9	141.2	81.8	86.5	37.5	45.8
Ga, ppm	8.9	24.4	18.6	19.9	4.8	26.0
Ge, ppm	1.3	35.2	7.8	3.6	9.6	122.8
As, ppm	1.4	21.2	10.0	9.8	5.6	55.6
Rb, ppm	11.2	99.4	58.8	58.7	24.6	41.8
Sr, ppm	16.7	136.0	70.3	76.6	38.3	54.4
Y, ppm	14.0	45.8	28.2	28.8	8.9	31.6
Zr, ppm	57.5	192.8	129.3	140.6	45.4	35.1
Nb, ppm	2.8	19.9	12.4	12.3	5.0	40.7
Mo, ppm	0.4	5.2	2.0	1.6	1.4	71.1
Ag, ppm	0.115	0.297	0.211	0.214	0.048	22.5
Cd, ppm	0.104	0.794	0.363	0.306	0.164	45.3
Sn, ppm	0.833	3.610	2.561	2.758	0.829	32.4
Sb, ppm	0.180	1.697	0.558	0.510	0.352	63.2
Cs, ppm	0.574	6.238	3.613	3.846	1.618	44.8
Ba, ppm	72.6	648.0	277.8	239.5	162.6	58.5
Hf, ppm	1.452	5.703	3.643	4.015	1.290	35.4
Ta, ppm	0.204	1.460	0.896	0.917	0.383	42.7
Pb, ppm	5.3	24.6	15.2	15.2	5.8	38.5
Th, ppm	4.5	16.4	10.3	9.3	3.6	34.9
U, ppm	1.1	4.8	3.7	4.1	1.1	29.3
W, ppm	4.6	169.9	43.8	26.2	45.3	103.5
P, %	0.012	0.093	0.029	0.021	0.021	73.5
S, %	0.2	4.0	1.6	0.7	1.4	86.0
Cl, %	0.007	0.009	0.008	0.008	0.001	7.4
F, %	0.012	0.064	0.043	0.045	0.014	32.7

Based on comparison of the analytical data with the Clarke values, concentration coefficients (Cc) were calculated to characterize the degree of enrichment or depletion of the coals relative to the global background. The mean Cc was defined as the ratio of the arithmetic mean concentration of an element in the entire sample set to its world coal Clarke value and was used to assess the overall level of element accumulation in the coals of the deposit.

A geochemical spectrum of coals from the Mugun deposit was constructed from the calculated concentration coefficients (Fig.3). For interpretation, the elements were grouped according to their Cc values. The geochemical spectrum showed that the mean concentrations of Li, B, V, Cr, Cu, and Er exceeded the corresponding world coal Clarke values by factors of 2.5-3.2, whereas W exceeded its Clarke value by a factor of 12.2. These elements may therefore be regarded as potentially significant targets for further investigation of their modes of occurrence and distribution.

Mineralogical characteristics. SEM observations identified the following mineral inclusions in coals from the Mugun deposit. The most common phases are kaolinite (Fig.4, *a*), which probably formed through alteration of feldspars, as indicated by shapes inherited from the original grains, as well as pyrite and quartz (Fig.4, *b*). In addition to quartz, the allogenic components include zircon containing Hf and rutile (Fig.4, *c*, *f*). Fractures contain magnetite with Zn and Al impurities (Fig.4, *d*), oxidized galena (possibly anglesite) with chalcopyrite inclusions (Fig.4, *e*), calcite (Fig.4, *g*), apatite

This is an open access article under the CC BY 4.0 license

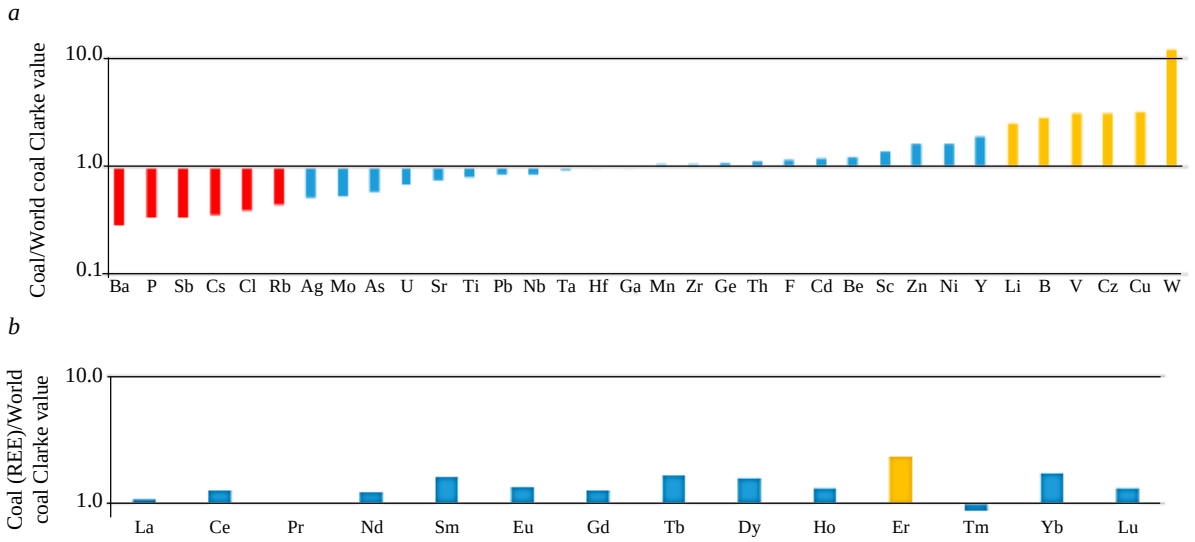


Fig.3. Element concentrations in coals from the Mugun deposit normalized to the world coal Clarke values [13]: *a* – trace elements, arranged in order of enrichment; *b* – rare-earth elements. Element groups are colour-coded according to their Cc: red – depleted (Cc < 0.5), blue – comparable (0.5 ≤ Cc ≤ 2), and yellow – enriched to the world coal Clarke values (Cc > 2)

containing up to 7 % F and approximately 2 % Sr (Fig.4, *h*), sphalerite containing Fe (Fig.4, *i*), galena with chalcopyrite inclusions (Fig.4, *k*), and aggregates of barite containing Sr and Ca together with pyrite (Fig.4, *j*).

Previous SEM studies [8] identified relatively large kaolinite particles, quartz grains, isolated grains of zircon, barite, and sphalerite, pyrite framboids, ilmenite with the composition $(Fe_{0.98}(Mg, Co)_{0.04})_{1.02}TiO_3$ [14], and monazite [7] in coals from the Mugun deposit. Plagioclase, micas, and hematite were identified in the coal ashes [8].

Principal component analysis. PCA was performed to identify the main factors controlling the distribution of trace elements in the coals and host rocks. This statistical method reduces the dimensionality of multivariate data and reveals the principal trends in their variation. The analysis was carried out in two stages. The first stage included both coals and terrigenous interlayers, represented by 74 and 15 samples, respectively (Fig.5, *a*, *b*). The second stage included only coal samples analyzed for an extended suite of elements, including REE, and comprised 11 samples (Fig.5, *c*). On the loading plot for the first and second principal components, which account for 55.62 and 9.03 % of the total variance, respectively, elements positively loaded on the first principal component are separated and correlate with total ash yield A. The vector of total ash yield and the associated elements is directed toward the field of terrigenous rock interlayers (Fig.5, *b*), because their concentrations increase in these samples. The strongest correlations with total ash yield, at $p < 0.0001$, are observed for Ti 0.95; Cl 0.95; Rb 0.94; Cr 0.93; Nb 0.91; Ga 0.90; Ag 0.90; Cs 0.90; Zr 0.90; Hf 0.89; Li 0.87; Ba 0.85; Ta 0.85; Pb 0.82 and F 0.88. This suggests, on the one hand, a clastic origin for these elements and, on the other, a probable commonality of the epigenetic transformations affecting the coals and terrigenous rock interlayers.

Be, P, Sc, V, Fe, Ni, Zn, Y, Sn, Th, and U have correlation coefficients greater than 0.56 with total ash yield at $p < 0.0001$. B has a pronounced negative loading on the first principal component, whereas Sr and S show weak negative or positive loadings. The vectors of these elements, by contrast, are directed toward the field of low-ash coals and are probably associated with the organic fraction. Cu and Cd have high positive loadings on the second principal component, whereas S and B show pronounced negative loadings. The loadings on the second principal component of elements strongly correlated with total ash yield are close to zero. Notably, B has a clear negative loading on both principal components considered.

This is an open access article under the CC BY 4.0 license

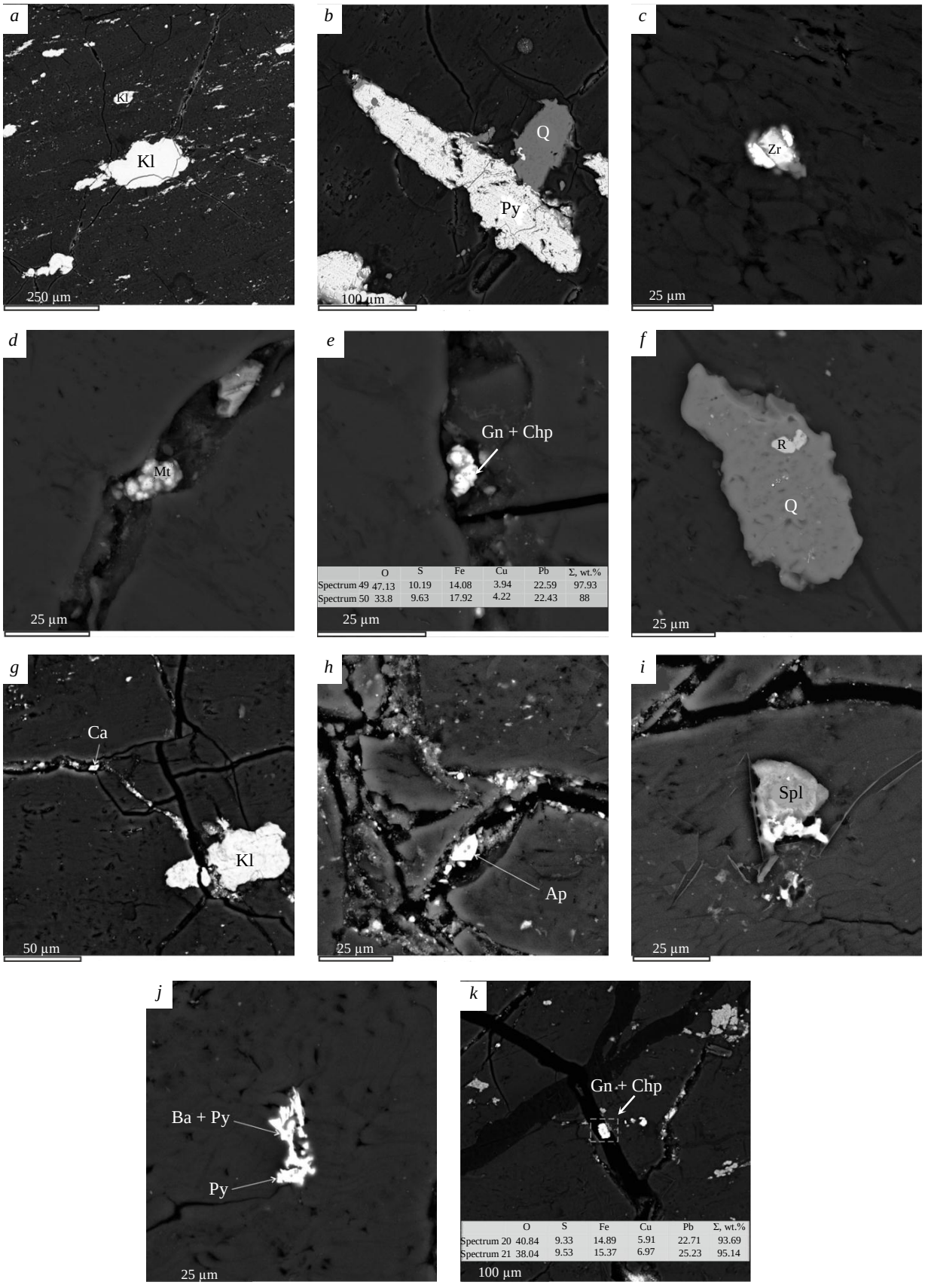


Fig.4. Allogenic and authigenic minerals in coals from the Mugun deposit: *a* – kaolinite; *b* – quartz and pyrite; *c* – zircon; *d* – magnetite; *e* – oxidized galena (anglesite?) containing chalcopyrite inclusions; *f* – quartz containing a rutile inclusion; *g* – calcite and kaolinite; *h* – apatite; *i* – sphalerite; *j* – barite-pyrite aggregate; *k* – galena containing chalcopyrite inclusions. Samples: *a*, *g-k* – Mu-D-B5-2-2 (Seam I); *b* – Mu-D-B2-2-2 (Seam II); *c-f* – Mu-D-B3-2-1 (Seam II)

This is an open access article under the CC BY 4.0 license

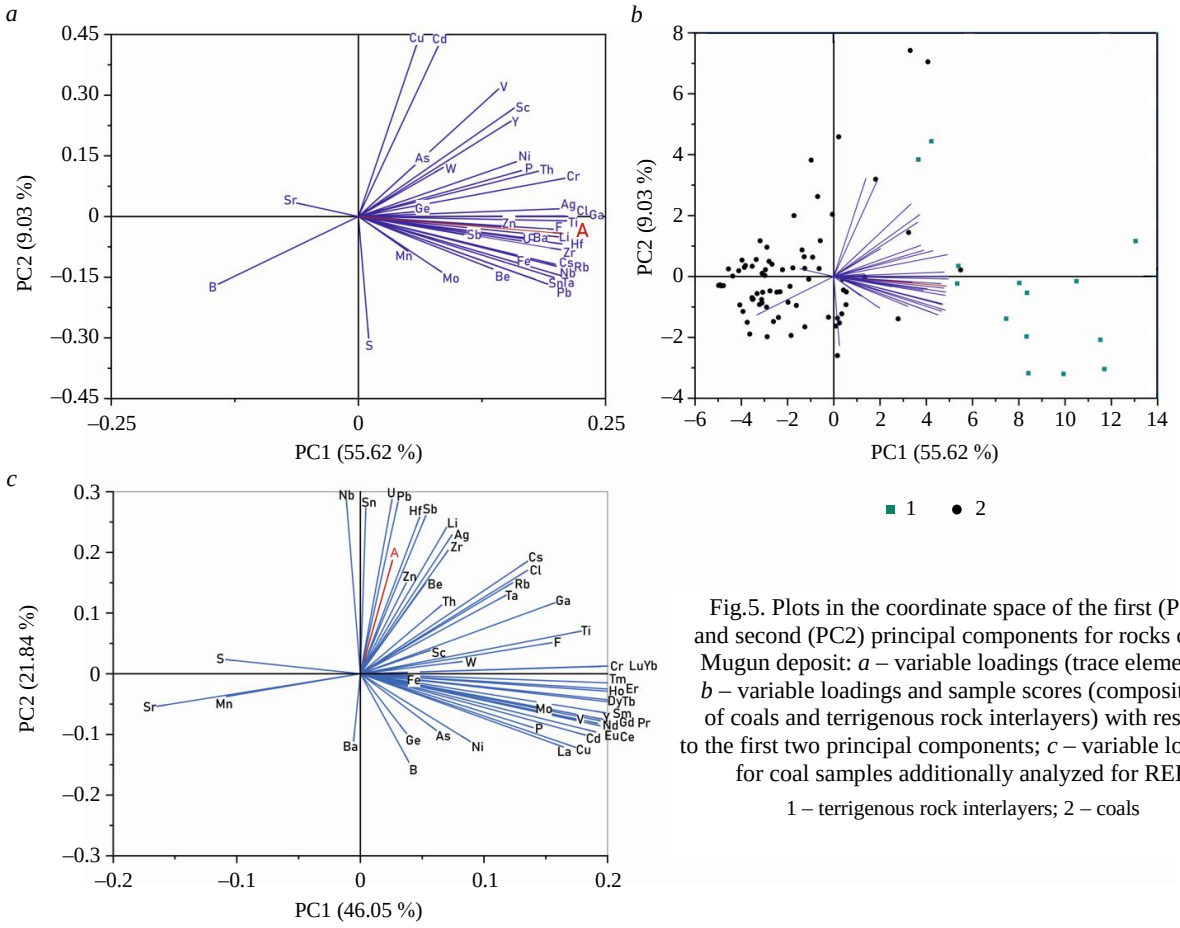


Fig.5. Plots in the coordinate space of the first (PC1) and second (PC2) principal components for rocks of the Mugun deposit: *a* – variable loadings (trace elements); *b* – variable loadings and sample scores (compositions of coals and terrigenous rock interlayers) with respect to the first two principal components; *c* – variable loadings for coal samples additionally analyzed for REE

1 – terrigenous rock interlayers; 2 – coals

The PCA plot constructed for coal samples only, with the REE dataset included, is shown in Fig.5, *c*. Elements strongly correlated with total ash yield have low loadings on the first principal component, which accounts for 46.05 % of the total variance. The highest loadings are shown by the REE, as well as by P, Cu, Cd, Mo, V, Cr, Cs, Cl, Rb, Ta, Ga, Ti, and F. Sr, Mn, and S have distinct negative loadings on the first principal component. On the second principal component, which explains 21.84 % of the variance, the highest positive loadings are shown by Li, Be, Zn, Zr, Nb, Ag, Sn, Sb, Hf, Pb, and U. Negative loadings are observed for B, P, Ni, Cu, Ge, As, Cd, Ba, and the light REE.

Discussion

Modes of occurrence of chemical elements. When coals and terrigenous rock interlayers are analyzed jointly (Fig.5, *a*, *b*), the first principal component clearly separates elements associated with total ash yield and tending toward the host-rock compositions from B on the opposite side. Along the second principal component, B likewise has a strong negative loading, unlike the other variables considered, together with S, which shows a weak positive loading on the first component. Cu and Cd display high positive loadings on the second principal component.

Coal-affinitive elements form stable chemical compounds with organic matter. In general, trace-element enrichment in coal may be represented by the following theoretical models: enrichment by terrigenous clastic material, enrichment by pyroclastic material, enrichment associated with infiltration and groundwater, and fluid-related enrichment (exudation enrichment) caused by the upward migration of fluids of various origins [15]. For elements associated with total ash yield, the composition of the ash should be considered in greater detail. The principal carriers of coal-affinitive elements in coal are sorption ash (Be, Ge, Ba, Sr, Mo), clastogenic ash (Mn, Ga, V, Cr, Ti, Zr), and biogenic ash, in which B predominates and Cu, Mn, Zn, Co, and Mo may also occur; diagenetic and epigenetic ashes are characterized by variable impurity contents [16]. Empirical models of rare-element distribution in

This is an open access article under the CC BY 4.0 license

ash reported in the literature [16] suggest that the group of elements with positive loadings on the first principal component is dominated by clastogenic carriers, with some contribution from diluting ash. Such diluting ash may also contain these elements, but in substantially lower amounts. Apparently, clastogenic, diagenetic, and epigenetic ash components, including authigenic minerals developed in rock fractures, all contribute to total ash yield. Sulfur occurs both in the carbonaceous matter itself and in authigenic minerals and therefore has a loading close to zero. The interpretation of the positive loading on the second principal component is less straightforward, particularly because this component accounts for less than 10 % of the total variance.

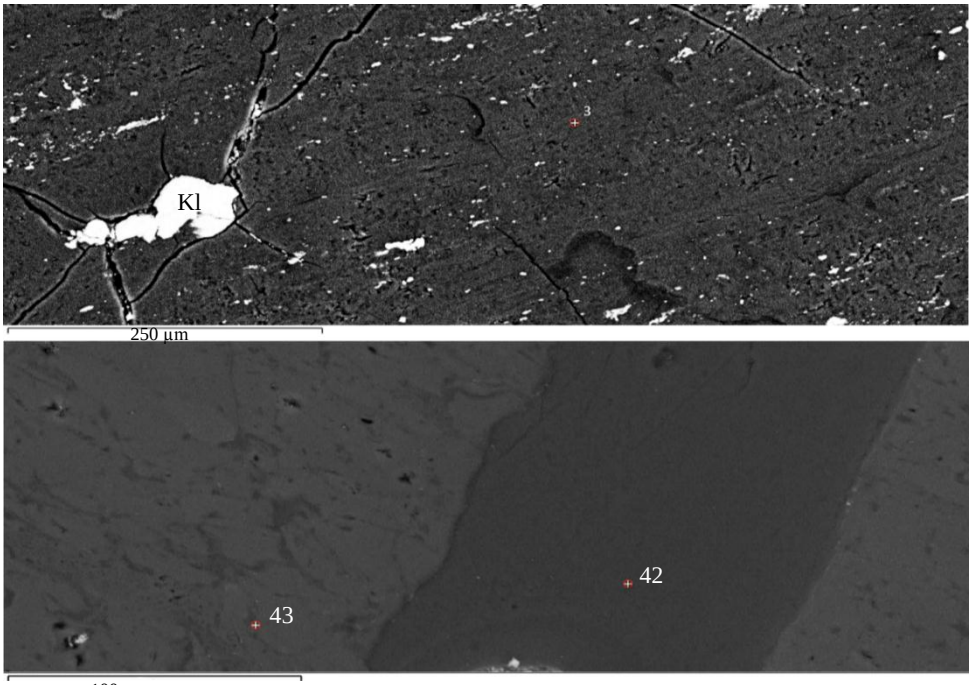
The PCA results for coal samples alone (Fig.5, *c*) should now be considered. The correlation with P and the pronounced positive loading on the first principal component indicate that phosphates are the principal carriers of light REE. Apatite was identified both in the present study and in earlier work, and monazite has also been reported. Laboratory model experiments have shown that peat, lignite, and their organomineral constituents have a high capacity to remove all lanthanides from aqueous solutions, while REE sorption by organic-matter components proceeds through physical sorption, ion-exchange reactions involving carboxyl and hydroxyl groups, and complex formation [17]. It may therefore be assumed that some of the REE in the coals of the Mugun deposit are associated with organic matter.

Other elements with pronounced positive loadings on the first principal component and their probable carriers include: Cs – clay minerals, feldspars, and micas; Cl – apatite and compounds associated with organic matter; Rb – clay minerals and micas; Ta – oxides; Ga – clay minerals, compounds associated with organic matter, and sulfides; Ti – oxides (particularly rutile), clay minerals, and compounds associated with organic matter; F – apatite, clay minerals, micas, and compounds associated with organic matter; Cr – clay minerals, magnetite, and rutile; V – clay minerals, magnetite, rutile, and sulfides; and Mo – sulfides and compounds associated with organic matter. Thus, the strong positive loading on the first principal component appears to reflect several factors operating simultaneously: phosphates, clay minerals, in this case primarily kaolinite, and, to some extent, compounds associated with organic matter. The latter interpretation is indirectly supported by the low but positive loading of B on the first principal component. Some trace elements, for example Cu, are probably supplied to the coals of the Mugun deposit predominantly through carbonaceous matter [18].

Negative loadings on the first principal component are observed for S, Sr, and Mn. Sulfur shows relatively high correlation coefficients with Sr 0.65, and Mn 0.50. This may indicate that the negative loading reflects the occurrence of these elements in sulfates; Ba also has a weak negative loading. Alternatively, Sr and Mn may occur in organic matter as biophile elements. The influx of sulfates from waters circulating through anhydrite-bearing underlying rocks of the Moty Formation into the peat-forming environment was previously discussed for the deposits under study [7]. According to those data, sulfide sulfur predominates in coals from the Mugun deposit and occurs mainly in pyrite and marcasite, with rarer sphalerite, galena, and chalcopyrite inclusions. Sulfates are represented by anhydrite and, less commonly, barite, whereas organic sulfur averages 0.84 %. According to our SEM data, sulfur concentrations in carbonaceous matter range from 1.74 to 5.3 % in sample Mu-D-B5-2-2 from Seam I and reach 0.93 % in sample Mu-D-B3-2-1 from Seam II (Fig.6). This suggests that organic sulfur may play a substantial role in individual samples from Seams I and II. However, local sulfur concentrations of up to 5.3 % in carbonaceous matter obtained by SEM-EDX require cautious interpretation. They probably reflect not only organically bound sulfur, but also the presence of submicron sulfide inclusions that cannot be resolved by SEM.

The highest loadings on the second principal component, exceeding even that of total ash yield, are shown by typical clastophile elements, which may occur, for example, in zircon, including Nb, Sn, Hf, Be, U, and Zr, as well as by elements characteristic of sulfides such as sphalerite and galena. Sulfur has a weak positive loading because it occurs both in the carbonaceous matter itself and in sulfates. Pronounced negative loadings on the second principal component are shown by B, P, Ni, Cu, Ge, As, Cd, Ba, and some light REE. For these elements, several carrier phases may therefore be inferred, with a dominant contribution from their occurrence in carbonaceous matter.

This is an open access article under the CC BY 4.0 license



	O	S	Cl	Ca	Σ, wt.%
Spectrum 3	6.73	5.3		0.88	12.91
Spectrum 42	1.92		0.25		2.17
Spectrum 43	5.09	0.93		0.77	6.79

Fig.6. Coal-affinitive trace elements in carbonaceous matter.
Images were acquired using an LE-BSE detector

Sediment provenance inferred from geochemical data. A synthesis of published data makes it possible to identify the principal factors controlling the input and accumulation of trace elements in coal-bearing sequences [19].

Composition of the source-rock assemblage. The geochemical specialization of coal largely reflects the composition of bedrock in the source area. Where felsic igneous and metamorphic complexes predominate, elements characteristic of these rocks become more important, whereas carbonate- or mafic-dominated source areas produce different elemental associations. Geochemical zonation may occur within a single basin as a result of spatial and temporal changes in sediment sources [20, 21].

Weathering crusts. The maturity of terrigenous material and the intensity of weathering of source rocks determine the chemical composition of detritus entering the peat-forming environment. Mature quartz-kaolinite material is generally depleted in many trace elements, whereas weathering crusts developed on rocks with anomalous geochemical backgrounds may act as independent sources of elevated concentrations of particular elements [16, 22, 23].

Volcanic ash input. Explosive volcanism and episodes of ash fall into peat-forming environments represent an important source of tuff-affinitive elements such as Zr, Hf, REE, Nb, Ta, etc. Repeated ash input may lead to the formation of metal-bearing coals enriched in rare and high-field-strength lithophile elements, while the composition of tonsteins can be used to identify the type of volcanic source [24].

Mineralized waters. Groundwater and surface water draining mineralized areas may transport dissolved components, particularly U, W, and other elements, and generate local anomalies within peatlands. The influence of water-borne input is most pronounced in discharge zones and topographic depressions [19].

Paleogeographic distance and facies conditions of peat accumulation. The distance from the source area, hydrological regime, and type of peatland control both the total terrigenous influx and the degree of geochemical differentiation. In marginal parts of a basin, the contribution of terrigenous

This is an open access article under the CC BY 4.0 license

material and the concentrations of several elements generally increase, whereas farther from the source area the material becomes more mature and chemically depleted. Such facies-related changes may be expressed both laterally and vertically through the succession [19].

Overall, studies of coals from different regions confirm the key role of terrigenous, including volcanogenic, material in enriching coal seams in rare and dispersed elements [11, 25-27]. The nature of the resulting elemental associations and their concentration levels are controlled by the source type, including the composition of the source-rock assemblage and volcanic ash input [28-30], the intensity of weathering, the magnitude of terrigenous influx, and, in some cases, the influence of external solutions [31, 32].

Russian studies likewise demonstrate the importance of source-area composition. At the Azey deposit of the Irkutsk Coal Basin, anomalous concentrations of several trace elements in coal seams are interpreted mainly in terms of the composition of rocks in the source area. According to published studies [33, 34], possible sources of clastic material for the Azey coals included Riphean and Karelian granitoids of the Proterozoic basement and the weathering crusts developed upon them. These ancient weathered rocks are thought to have supplied REE, Y, U, Th, Ta, and Sn to the coals of the area. Triassic traps, including gabbro-dolerites and dolerites, together with their weathering crusts, also played an important role. These rocks are widespread both on the Angara-Lena Plateau and near the Azey deposit. According to previous authors, these basaltic rocks may have been the principal source of Sc in the Azey coals. Altered volcanogenic pyroclastic interlayers, or tonsteins, have also been identified in the Azey succession [35]. Isotopic and geochemical data indicate that their original material consisted of felsic tuffs [36], which were subsequently altered in the aggressive environment of a peat swamp [37]. This example confirms that, even within a single region, the composition of terrigenous material may vary substantially, from granitic to basaltic rocks and volcanic ash, thereby controlling the geochemical specialization of the coals.

These global patterns make it possible to identify key indicators for diagnosing sediment provenance. For the Mugun deposit, particular attention was therefore paid to elemental ratios indicative of specific source-rock assemblages. To determine the probable sources of sediment during formation of the coal-bearing sequence of the Mugun deposit in the Irkutsk Basin, the geochemical characteristics of terrigenous rock interlayers, represented by siltstones and mudstones occurring between the coal seams, were examined. Because REE in the Mugun coals are concentrated mainly in phosphate minerals, particularly apatite, REE patterns and anomalies are difficult to use for provenance analysis. Instead, relatively immobile lithophile high-field-strength elements associated with clastic material were selected, including Zr, Ti, Nb, Sc, Th, and Y. Their concentrations and ratios in the clastogenic interlayers make it possible to reconstruct the composition and type of source rocks.

On the Zr/Sc – Th/Sc diagram (Fig.7, *a*), the data points representing the terrigenous interlayers of the Mugun succession plot outside the field of repeated sedimentary recycling. In other words, the Th/Sc and Zr/Sc ratios do not indicate a substantial contribution from reworked sedimentary rocks. Instead, the values are consistent with first-cycle sedimentation, in which clastic material was supplied directly from primary bedrock without a prolonged prior history of sedimentary reworking. The geochemical data may therefore be interpreted as reflecting direct erosion and transport of igneous and metamorphic rocks into the depositional basin rather than recycling of pre-existing sedimentary sequences.

On the Nb/Y – Zr/TiO_2 diagram (Fig.7, *b*), which is commonly used to evaluate the petrogenetic character of source rocks, most samples from the rock interlayers plot within the field of intermediate-composition rocks, namely andesites and diorites. This suggests that the principal source rocks were probably volcanic or plutonic rocks of andesitic composition. Some samples, however, are shifted toward the field of felsic rocks, including rhyodacites, dacites, and granodiorites. These include the siltstone from the roof of Seam I, sample M-D-2-1-1, and the carbonaceous siltstone from the floor of Seam I in the central part of the deposit, sample M-D-B16-1-4. This indicates an episodic contribution

This is an open access article under the CC BY 4.0 license

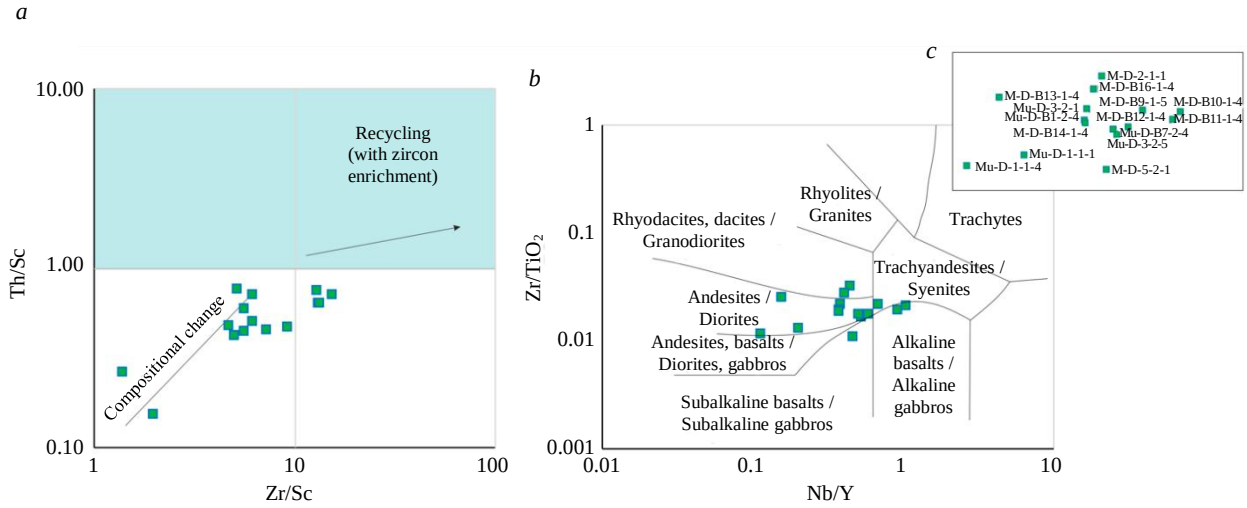


Fig.7. Compositions of the host rocks from the Mugun deposit plotted on: *a* – the Zr/Sc – Th/Sc diagram [15]; *b* – the Nb/Y – Zr/TiO_2 diagram [38]; *c* – inset showing the data-point numbers in Fig. *b*

of more felsic material. Several other samples display elevated Nb/Y ratios and lower Zr/TiO_2 values and plot in the fields of alkaline and subalkaline basalts and their gabbroic equivalents. These include the siltstone from the roof of Seam II, sample M-D-5-2-1, and the siltstones from the floor of Seam I, samples M-D-B10-1-4 and M-D-B11-1-4. Some of these points also tend toward the trachydacite – trachyandesite and syenite fields (for example, M-D-B10-1-4, M-D-B11-1-4, and M-D-B9-1-5 lie near the boundary between the basaltic and trachytic fields). Thus, the geochemical diagram indicates a mixed provenance: rocks of intermediate, mainly andesitic, composition were dominant, but felsic material and basaltic rocks, including alkaline varieties, also contributed.

It should be noted that the siltstone samples designated as the “roof” and “floor” of coal seams, including M-D-2-1-1 and M-D-5-2-1, etc. represent independent lithological units of the host-rock sequence adjacent to the coal benches and are not part of the coal seams in the strict stratigraphic sense. Accordingly, these samples are hereafter treated as host siltstones reflecting depositional conditions distinct from those under which the coals themselves formed.

The potential source-rock types identified from the geochemical data are in good agreement with the geological structure of the areas surrounding the Mugun deposit. Igneous complexes ranging in age from the Paleozoic to the Mesozoic are widely developed in the foothills of the Eastern Sayan in southern Cisbaikalia, which surround the basin. Late Paleozoic-Triassic volcano-plutonic belts occur in southwestern Irkutsk Region and adjacent areas and include orogenic andesites and diorites. More evolved felsic plutons are also known in the region, including granitoids, rhyodacites, dacites, and granodiorites, commonly associated with local domal structures such as the Sayan granitoid massif. These rocks correspond to the felsic component of the source province. In addition, lava flows and intrusions of the Late Permian-Triassic trap complex are present in the adjacent region and consist of subalkaline basalts and gabbrodolerites. They are associated with rift structures and plateaus, including the Angara-Lena Plateau, and correspond to the basaltic component inferred from the geochemical data. Rare occurrences of Late Paleozoic – Mesozoic trachyte-trachyandesite-syenite intrusive complexes, including nepheline syenites and other alkaline varieties, are also known within various blocks of the Eastern Sayan foothills. Their presence is consistent with the trachytic, alkaline component identified in the clastic material of the Mugun deposit. Thus, the full range of rock types indicated by the Nb/Y – Zr/TiO_2 diagram has geological counterparts among the regional igneous complexes, supporting the reliability of the geochemical provenance reconstruction.

This is an open access article under the CC BY 4.0 license

Conclusions

The complex multidimensional system describing the carrier phases of rare elements in coal is difficult to represent adequately by deliberately projecting a data cloud into a low-dimensional space with only two coordinate axes. Consequently, several factors may contribute simultaneously to a given principal component. Ash yield itself is the sum of heterogeneous components. Elements associated with the organic fraction of coal are concentrated most strongly in the ash, whereas elements occurring exclusively in the inorganic fraction are not enriched in ash relative to the host rocks and may even be depleted [17]. As established previously [6], the ash and slag produced from Mugun coal are enriched relative to the coal most strongly in Cu (up to 40 times), Fe (6-40 times), Ba (12-48 times), as well as Nb (3-8 times), Sr (4-12 times), As (up to 4 times), Pb (2-16 times), Zn (4-21 times), Cr (3-9 times), V (up to 6 times), Ti (4-10 times), U (up to 9 times), and Th (up to 13 times).

Based on the evidence considered above, the following assumptions may be proposed:

• Li, Be, Zn, Zr, Nb, Ag, Sn, Sb, Hf, Pb, and U occur in the clastic fraction and in sulfides;

• F, Cl, Ti, Ga, Rb, Cs, Ta, and Th are associated with clay minerals, compounds bound to organic matter, and sulfides;

• P, V, Cr, Cu, Mo, Cd, and REE are associated with phosphates and compounds bound to organic matter;

• B, S, Mn, Ni, Ge, As, Sr, and Ba are associated with sulfates and compounds bound to organic matter, with a possible minor contribution from sulfides.

On the Nb/Y – Zr/TiO_2 diagram (Fig.7, *b*), the silty varieties of the host-rock sequence adjacent to the coal seams of the Mugun deposit display a broader compositional range than the coals. Some samples plot within the field of intermediate-composition rocks, namely andesites and diorites, whereas others tend toward felsic rhyodacite-dacite compositions or, conversely, toward more alkaline, including subalkaline, basaltic varieties. This suggests differentiation of the sources of clastic material between different parts or stratigraphic levels of the succession:

• Samples M-D-2-1-1 (a host-rock siltstone adjacent to the roof of Seam I), and M-D-B16-1-4 (a carbonaceous siltstone from the floor of Seam I) plot in the rhyodacite-dacite field, close to granitoid compositions. The probable sediment source was erosion of granitoid, including granodioritic and dacitic, massifs in the foothills of the Eastern Sayan, formed during Paleozoic-Mesozoic orogenic stages. Given the location of the deposit, the most likely influence was from granitoids of the Sayan complex, exposures of which are known in the central and southwestern parts of the region.

• Samples M-D-5-2-1 (a host-rock siltstone adjacent to the roof of Seam II) and M-D-B10-1-4 and M-D-B11-1-4 (siltstones from the floor of Seam I) plot within the alkaline and subalkaline basalt/gabbro fields (samples M-D-B10-1-4 and M-D-B11-1-4 show a transition toward trachyandesites and syenites). These geochemical characteristics may indicate a contribution from rocks related to subalkaline basaltic and syenitic magmatism. In the region, such igneous formations are associated particularly with Late Paleozoic and Mesozoic magmatic phases and with local alkaline massifs, including the Ziminsky and Ognitsky complexes. Such material could have been supplied through erosion of gabbroic intrusions and/or volcanic flows developed along the periphery of the Eastern Sayan.

• Sample M-D-B9-1-5 is similarly displaced toward the trachyandesite and syenite fields, likewise indicating an alkaline or subalkaline character of the source province.

Thus, the host rocks of the productive seams at the Mugun deposit contain multicomponent clastic material and collectively indicate a polygenetic source of the sandy-silty detritus. This material was supplied from the west and southwest from granitoid domes and batholiths of the Sayan orogenic belt, represented by the granodiorite-dacite association, and from the east and northeast from local alkaline and subalkaline massifs in the foothills of the Eastern Sayan, including the Ziminsky and Ognitsky complexes. The following principal conclusions can therefore be drawn:

• The mineralogical and geochemical characteristics of the Mugun coals are controlled by a combination of allogenic and authigenic phases, including kaolinite, zircon, rutile, pyrite, sphalerite, apatite, barite, and other minerals identified by scanning electron microscopy and energy-dispersive X-ray analysis.

This is an open access article under the CC BY 4.0 license

• Trace elements in the coals occur in several types of carriers: clastogenic, phosphate, sulfide, and organic. The most important carrier phases include clay minerals (especially kaolinite), phosphates (apatite and monazite), sulfides (pyrite, galena, and sphalerite), and organic matter.

• Principal component analysis identified statistically significant groups of elements correlated with total ash yield, making it possible to distinguish elements according to their origin and accumulation conditions: clastogenic elements are associated mainly with terrigenous rocks, whereas organophilic elements tend toward low-ash coals.

• Discriminant geochemical analysis using the Nb/Y – Zr/TiO_2 and Zr/Sc – Th/Sc diagrams showed that the sources of sediment supplied to the coal-bearing succession of the Cheremkhovskaya Formation were polygenetic and included granitoids, felsic volcanic rocks, and subalkaline volcanic rocks from the foothills of the Eastern Sayan.

The authors thank the staff of EN+ COAL LLC for their assistance in collecting the study material and for supporting the research. The authors also express their sincere gratitude to Ya.E.Yudovich for his valuable advice and consultations.

REFERENCES

1. Krasnov O.S., Salikhov V.A. Prospects of producing scarce non-ferrous and less-common metals from coal wastes in Kuzbass. *Tsvetnye metally.* 2007. N 8, p. 8-11 (in Russian).

2. Arbuzov S.I., Ershov V.V., Potzeluyev A.A., Rikhvanov L.P. Rare elements in Kuznetsk basin coals. Kemerovo: Kemerovskii poligrafkombinat, 2000, p. 248 (in Russian).

3. Krasnov O.S., Salikhov V.A. Economical valuation of coal fields useful coproducts. *Journal of Mining Institute.* 2013. Vol. 201, p. 196-200 (in Russian).

4. Jaiswal H., Singh A.K. Coal as a non-conventional resource of rare earth elements (REEs) and trace elements: Benefits and impacts on environment and human health – A review. *Results in Earth Sciences.* 2025. Vol. 3. N 100064. DOI: 10.1016/j.rines.2025.100064

5. Pogrebitskii E.O. Some regularities of germanium distribution in coals of the Donets Basin. *Journal of Mining Institute.* 1959. Vol. 35. Iss. 2, p. 87-103 (in Russian).

6. Bembeev D.B., Samsonov A.A. Geochemical characterization of ash and slag from coals of the Mugun deposit (Irkutsk region). *Nedropolzovanie XXI vek.* 2024. N 2 (103), p. 28-35 (in Russian).

7. Dzhumayan N.R. Formation conditions and qualitative composition of lignite from the Mugun deposit (Irkutsk coal basin): Avtoref. dis. … kand. geol.-mineral. nauk. Rostov-na-Donu: Yuzhnyi federalnyi universitet, 2022, p. 26.

8. Dzhumayan N.R., Shumilova T.G., Svetov S.A. Impurity Elements in Coals from the Mugunsk Deposit (Irkutsk Coal Basin). *Solid Fuel Chem.* 2021. Vol. 55. N 6, p. 407-413. DOI: 10.3103/S0361521921060045

9. Coal Resources of Russia. In 6 volumes. Vol. III. Coal Basins and Deposits of Eastern Siberia. Southern Part (Krasnoyarsk Territory, Kansk-Achinsk Basin; Republic of Khakassia, Minusinsk Basin; Republic of Tuva, Ulug-Khem Basin and other deposits; Irkutsk Region, Irkutsk Basin and coal deposits of the Cis-Baikal region) / Editor-in-Chief V.F.Cherepovskii. Moscow: Geoinformtsentr, 2002, p. 488.

10. Gosudarstvennaya geologicheskaya karta Rossiiskoi Federatsii. Masshtab 1:1,000,000 (trete pokolenie). Seriya Angaro-Eniseiskaya. List N-47 – Nizhneudinsk. Obyasnitelnaya zapiska. St. Petersburg: Kartograficheskaya fabrika VSEGEI, 2012, p. 652.

11. Ziyi Ye, Baoqing Li, Jialiang Cao. Enrichment characteristics and genesis mechanism of critical elements (Nb-Ta-Zr-Hf-REE-Y) in coals: a case study of Late Permian coalfield in Northeastern Guizhou, China. *Frontiers in Earth Science*. 2024. Vol. 12. N 1520502. DOI: 10.3389/feart.2024.1520502

12. Timofeev P.P. Jurassic coal measures in Southern Siberia and conditions of its formation. Moscow: Nauka, 1970, p. 207 (in Russian).

13. Yudovich Ya.E., Ketris M.P. Valuable Trace Elements in Coal. Ekaterinburg: Ural Division of the Russian Academy of Sciences, 2006, p. 538 (in Russian).

14. Dzhumayan N.R., Nastavkin A.V. Scanning Electron Microscopy of Pyrite from Brown Coal (Mugun Coal Deposit, Irkutsk Basin). Minerals: Structure, Properties, Methods of Investigation. Springer, 2020, p. 29-34. DOI: 10.1007/978-3-030-00925-0_5

15. McLennan S.M., Taylor S.R., McCulloch M.T., Maynard J.B. Geochemical and Nd–Sr isotopic composition of deep-sea turbidites: Crustal evolution and plate tectonic associations. *Geochimica et Cosmochimica Acta*. 1990. Vol. 54. Iss. 7, p. 2015-2050. DOI: 10.1016/0016-7037(90)90269-Q

16. Yudovich Ya.E. Geochemistry of fossil coals. Leningrad: Nauka, 1978, p. 262.

17. Pavlova L.M., Shumilova L.P., Radomskaya V.I. et al. Sorption of Rare Earth Elements by Organic Matter from Aqueous Solutions according to Experimental Data. *Doklady Earth Sciences.* 2023. Vol. 512. Iss. 2, p. 946-952. DOI: 10.1134/S1028334X23601207

18. Dzhumayan N.R., Silaev V.I., Vasiliev E.A. et al. Mineralogical and geochemical properties of coals of the Mugun deposit (Irkutsk coal basin). *Vestnik of Geosciences.* 2022. N 2 (326), p. 19-36 (in Russian). DOI: 10.19110/geov.2022.2.3

19. Yudovich Ya.E., Ketris M.P. Inorganic matter of coal. Ekaterinburg: Ural Division of the Russian Academy of Sciences, 2002, p. 424 (in Russian).

20. Foscolos A.E., Goodarzi F., Koukouzas C.N., Hatziyannis G. Reconnaissance study of mineral matter and trace elements in Greek lignites. *Chemical Geology*. 1989. Vol. 76. Iss. 1-2, p. 107-130. DOI: 10.1016/0009-2541(89)90131-9

21. van der Flier-Keller E., Goodarzi F. Geological controls on major and trace element characteristics. Cretaceous coals of Vancouver Island, Canada. *Bulletin de la Société Géologique de France*. 1991. Vol. 162. N 2, p. 255-265.

This is an open access article under the CC BY 4.0 license

22. Arbuzov S.I., Levitskii V.M. Radiogeochemical correlation of granites of Sayansky and Taraksky complex at the south-west boundary of the Siberian platform. Radioaktivnost i radioaktivnye elementy v srede obitaniya cheloveka: Materialy mezhdunarodnoi konferentsii, posvyashchennoi stoletiyu so dnya otkrytiya yavleniya radioaktivnosti i stoletiyu Tomskogo politekhnicheskogo universiteta, 22-24 maya 1996, Tomsk, Rossiya. Tomsk: Natsionalnyi issledovatelskii Tomskii politekhnicheskii universitet, 1996, p. 86-89 (in Russian).

23. Likhachev V.V. Rare-metal mineralization of the bauxite-bearing weathering crust of the Middle Timan. Syktyvkar: Komi nauchnyi tsentr UrO RAN, 1993, p. 224.

24. Seredin V.V., Finkelman R.B. Metalliferous coals: A review of the main genetic and geochemical types. *International Journal of Coal Geology*. 2008. Vol. 76. Iss. 4, p. 253-289. DOI: 10.1016/j.coal.2008.07.016

25. Biswas S., Moroeng O.M., Wagner N.J. Mineralogy and geochemical controls on the distribution of REY-Ga-Se-Nb enrichment in the No. 6 Coal Seam, Soutpansberg Coalfield, South Africa. *Ore Geology Reviews*. 2024. Vol. 174. N 106310. DOI: 10.1016/j.oregeorev.2024.106310

26. Zhanming Guo, Beilei Sun, Chao Liu et al. Geochemistry of tonsteins and its implications for Li-Zr (Hf)-Nb (Ta) enrichments in Cisuralian coal seams, Shanxi Province, North China. *International Journal of Coal Geology*. 2025. Vol. 300. N 104697. DOI: 10.1016/j.coal.2025.104697

27. Qiuchan Han, Jingjing Liu, Niande Shang et al. Mineralogy and geochemistry of the Middle Jurassic coal in the southern Ordos Basin, China: Responses of element geochemical behavior to climatic changes. *Palaeogeography, Palaeoclimatology, Palaeoecology*. 2024. Vol. 648. N 112284. DOI: 10.1016/j.palaeo.2024.112284

28. Bo Jiu, Wenhui Huang, Nana Mu. Mineralogy and elemental geochemistry of Permo-Carboniferous Li-enriched coal in the southern Ordos Basin, China: Implications for modes of occurrence, controlling factors and sources of Li in coal. *Ore Geology Reviews*. 2022. Vol. 141. N 104686. DOI: 10.1016/j.oregeorev.2021.104686

29. Yang Lin, Jing Li, Xuanphu Nguyen et al. Enrichment of rubidium and cesium in upper Triassic coals from the Cam Pha coalfield, NE Vietnam: Implications on sediment source and hydrothermal influence. *Ore Geology Reviews*. 2025. Vol. 178. N 106484. DOI: 10.1016/j.oregeorev.2025.106484

30. Jidun Sha, Jian Chen, Bofei Zhang et al. Geochemistry of source rock–controlled Late Triassic coal: An example from the Dabaoding Coal Mine in Panzhihua, Sichuan Province, southwestern China. *International Journal of Coal Geology*. 2020. Vol. 221. N 103431. DOI: 10.1016/j.coal.2020.103431

31. Niande Shang, Jingjing Liu, Qiuchan Han et al. Mineralogy and geochemistry of the Middle Jurassic coal from the Hexi Mine, Shenfu Mining Area, Ordos Basin: With an emphasis on genetic indications of siderite. *International Journal of Coal Geology*. 2023. Vol. 279. N 104384. DOI: 10.1016/j.coal.2023.104384

32. Yang Wang, Manli Huang, Yanming Zhu et al. Mineralogy, geochemistry and enrichment mechanism of critical elements (Li and Zr-Nb-Hf-Ta-REY) in the coals from western Guizhou Province, China: Source and sedimentary environment. *Ore Geology Reviews*. 2025. Vol. 176. N 106402. DOI: 10.1016/j.oregeorev.2024.106402

33. Ilenok S.S., Arbuzov S.I. Metalliferous coals of the Azeyskoe deposit of Irkutsk coal basin. *Bulletin of the Tomsk Polytechnic University. Geo Assets Engineering.* 2018. Vol. 329. N 8, p. 132-144 (in Russian).

34. Ilenok S.S., Arbuzov S.I. Mineral modes of rare elements in coals and ashes of coals of Azey deposit in Irkutsk coal basin. *Bulletin of the Tomsk Polytechnic University. Geo Assets Engineering.* 2016. Vol. 327. N 2, p. 6-20 (in Russian).

35. Admakin L.A., Portnov A.G. Tonsteins of the Irkutsk basin. *Lithology and Mineral Resources.* 1987. N 3, p. 88-98 (in Russian).

36. Arbuzov S.I., Mezhibor A.M., Spears D.A. et al. Nature of tonsteins in the Azeisk deposit of the Irkutsk Coal Basin (Siberia, Russia). *International Journal of Coal Geology*. 2016. Vol. 153, p. 99-111. DOI: 10.1016/j.coal.2015.12.001

37. Arbuzov S.I., Volostnov A.V., Ilenok S.S., Rybalko V.I. Nature of tonsteins from the Azey deposit of the Irkutsk coal basin. *Izvestiya Tomskogo politekhnicheskogo universiteta*. 2012. Vol. 321. N 1, p. 89-97.

38. Winchester J.A., Floyd P.A. Geochemical discrimination of different magma series and their differentiation products using immobile elements. *Chemical Geology*. 1977. Vol. 20, p. 325-343. DOI: 10.1016/0009-2541(77)90057-2

***Authors*: Danzan B. Bembeev,** *Postgraduate Student* (*Lomonosov Moscow State University*, *Moscow*, *Russia*), *bembeev.danzan@yandex.ru*, *https://orcid.org/0009-0001-3275-7329*, **Sofya I. Merenkova,** *Candidate of Geological and Mineralogical Sciences*, *Researcher* (*Shirshov Institute of Oceanology of RAS*, *Moscow*, *Russia*), *Junior Researcher* (*Schmidt Institute of Physics of the Earth of the RAS*, *Moscow*, *Russia*), *https://orcid.org/0000-0003-3204-4393*, **Aleksei A. Samsonov,** *Candidate of Geological and Mineralogical Sciences*, *Senior Researcher* (*Lomonosov Moscow State University*, *Moscow*, *Russia*), *https://orcid.org/0009-0007-4637-0399*, **Ruslan R. Gabdullin,** *Doctor of Geological and Mineralogical Sciences*, *Professor* (*Lomonosov Moscow State University*, *Moscow*, *Russia*), *Leading Researcher* (*Vernadsky Institute of Geochemistry and Analytical Chemistry of the RAS*, *Moscow*, *Russia*), *https://orcid.org/0000-0001-8296-7191*.

The authors declare no conflict of interests.

This is an open access article under the CC BY 4.0 license

ISSN 2411-3336; e-ISSN 2541-9404

JOURNAL OF MINING INSTITUTE
Zapiski Gornogo instituta
Journal homepage: pmi.spmi.ru

Research article Geology

Morphological features, internal structure, and compositional signatures of native gold from the Murzinka placer group (Middle Urals): identification of lode sources and conditions of placer formation

Aleksandr K. Kozin[1]✉, **Sergei Yu. Stepanov**[1], **Roman S. Palamarchuk**[1], **Valeriya S. Zhdanova**[1], **Natalya S. Vlasenko**[2]
[1] *South Ural Scientific Centre Mineralogy and Environmental Geology of the Ural branch RAS, Miass, Russia*
[2] *Saint Petersburg State University, Saint Petersburg, Russia*

***How to cite this article*:** Kozin A.K., Stepanov S.Yu., Palamarchuk R.S., Zhdanova V.S., Vlasenko N.S. Morphological features, internal structure, and compositional signatures of native gold from the Murzinka placer group (Middle Urals): identification of lode sources and conditions of placer formation. Journal of Mining Institute. 2026. Vol. 280, p. 104-121.

Abstract
The paper presents the results of a complex study of native gold from nine placers of the Murzinka group in the Middle Urals. Morphological features, chemical composition, and internal structure of native gold, as well as mineral inclusions within it, are described in detail. Based on the analysis of morphological characteristics and the gold particles rounding degree, the proximity of lode gold sources is inferred ranging from several hundred meters to the first few kilometers. Three types of native gold were identified according to the chemical composition and mineral inclusions. Type I (the predominant type) is characterized by high fineness with Ag and Hg admixture and inclusions of pyrite, chalcopyrite, galena, molybdenite, and petzite. The variation in admixture content within this type allows the definition of subtypes; their distribution in placers reflects the zoning of lode quartz gold mineralization. Type II is distinguished by elevated copper contents and bornite inclusions; Type III is defined by high Ag contents. Lode sources for the different gold types have been identified: for Type I, a quartz gold lode deposits; for Type II, precious metal mineralization in the gabbroids of the Pavdinsky massif. Application of the electron backscatter diffraction (EBSD) technique enabled a detailed characterization of the internal structure of gold particles. The observed high fineness intergranular veins and intergrowths of gold with minerals of the rhabdophane group suggest that native gold was located in the supergene zone during the period of active weathering crust development in the Upper Mesozoic and Palaeogene. It is established that the placer system in the Murzinka River basin formed during the Neogene-Quaternary period, primarily due to lode quartz gold mineralization. The obtained data allow the localization of prospective areas for the exploration of lode gold deposits and expand the understanding of the region's metallogenic potential.

Keywords
native gold; copper-bearing gold; placer gold; placer; weathering crust; rhabdophane; internal structure; EBSD; Middle Urals

Funding
The study conducted under research topic of the SUSC MEG UbRAS N FUUR-2025-0007.

Received: 11.09.2025 ***Accepted: 28.04.2026*** ***Online: 27.07.2026*** ***Published: 10.09.2026***

Introduction

The history of placer gold mining in the Urals spans two centuries. Placer gold reserves have been largely depleted over this period, making prospecting for new deposits increasingly important. Goal of expanding and revitalizing the mineral resource base is a key priority of the government policy [1]. Detailed study of gold placers of unknown sources is considered one of possible approaches to achieving this goal when it comes to precious metals.

Placer gold is a traditional subject of mineralogical studies aimed at determining types and localization of lode precious-metal mineralization. Detrital gold from unconsolidated sediments becomes highly informative for prospecting and exploration in areas with limited outcrops. The studies

This is an open access article under the CC BY 4.0 license

of the morphological characteristics and chemical composition of native gold, as well as associations of mineral inclusions, have made it possible to reliably establish the link between placers and certain geological complexes for many placer regions around the world [2-5]. Use of the mineralogical signatures of placer gold to predict lode mineralization has been demonstrated in numerous studies [6, 7].

Local artisanal and small-scale mining began in the 1850s and continued sporadically until the middle of the 20th century, when the volume of production increased significantly due to the use of dredging technologies. According to historical records, over the entire period of mining, approximately 1.5 t of gold were extracted from alluvial and alluvial-deluvial deposits in the valleys of the Murzinka River and its tributaries. Despite the abundance of detrital gold, which can be found to a varying degree in all watercourses of the Murzinka River basin, there is virtually no data on primary sources of gold. There are only brief records of some lode occurrences of gold; no lode gold deposits of industrial significance are known in the area.

This study seeks to identify types of lode sources and genesis conditions of placers within the Murzinka group. The analysis is based on the morphological features, internal structure, and chemical composition of detrital gold recovered from alluvial and alluvial-deluvial sediments. The relevance of this study is determined by the possible use of the obtained data to assess the mineral resource potential of the area. In recent years, there has been an increase in the number of exploration projects within the geological complexes of the Tagil megazone in the Middle and Northern Urals, driven by depletion of reserves at known deposits and discovery of new gold-bearing deposits, such as the Peschernoye deposit [8]. Typically, acid leaching method is used to study internal structure of native gold [9]. The use of the electron backscatter diffraction (EBSD) method in this study has made it possible to investigate the internal structures of native gold from the Murzinka group placers at a completely new level.

Methods

Trial pits with a depth of 2.5-3.5 m were excavated to study the stratigraphic sections of placer deposits in the valleys of the Murzinka, Talaya, Matyushenka, Malaya Nyasma, Maksimovka, Kamenka, Bolshaya Velichka, Kholodnaya, and Ozhegovka rivers. Samples were taken from the walls of the test pits exposing alluvial deposits. The average volume of a standard sample was 40 l, and that of a large sample was 1000 l. A total of 79 samples were collected from 11 test pits. Each sample was processed by panning to recover heavy mineral concentrates; bulk samples were washed using a sluice box.

The morphological features and size of detrital gold were studied using an optical microscope and a scanning electron microscope (SEM). A total of 208 gold particles were examined using the SEM. To investigate the assemblages of mineral inclusions using a TESCAN VEGA 3 SEM (Shared-Use Centre of SUSC MEG UbRAS, Miass, analyst M.A.Rassomakhin), the gold particles were embedded in epoxy resin discs and polished. Data on the chemical composition of the native gold were obtained using electron probe microanalysers with wavelength dispersive spectrometers Cameca SX100 ("Geoanalitik" Shared-Use Centre of the A.N.Zavaritsky Institute of Geology and Geochemistry of the Ural Branch of the RAS, Ekaterinburg, analyst V.A.Bulatov) and JEOL JXA-733 (Shared-Use Centre of SUSC MEG UbRAS, Miass, analyst V.A.Kotlyarov). A total of 130 analyses were obtained from core parts of the gold particles. The analysis was carried out at an accelerating voltage of 15-20 kV and an electron probe current of 40 nA. The pulse accumulation time at the peak maximum was 10 s. During the measurements, $CuFeS_2$ (for analyzing Fe and Cu content), HgTe (Hg, Te) and HgCl (Hg), as well as Au, Ag and Pd, were used as standards. The analysis was carried out on the following lines: Kα (Cu, Fe), Lα (Au, Ag, Te, Hg) and Mα (Hg, Au). The detection limits for the elements determined in native gold were, wt.%: Au – 0.068; Ag – 0.064; Hg – 0.080; Cu – 0.075.

Polished planar sections of gold particles were etched using an argon plasma beam on an Oxford IonFab 300 system ("Nanophotonica" Resource Centre, SPbSU, Saint Petersburg, M.S.Lozhkin). Etching conditions: exposure time 10 min, accelerating voltage 500 V, current 200 mA, angle 45°. The distribution of crystal lattice orientations in native gold was investigated using backscattered

This is an open access article under the CC BY 4.0 license

electron diffraction on a TESCAN MIRA scanning electron microscope equipped with an Oxford Nordlys Nano EBSD detector ("Geoanalitik" Shared-Use Centre of the A.N.Zavaritsky Institute of Geology and Geochemistry of the Ural Branch of the RAS, analyst N.S.Chebykin) and Hitachi S-3400N with an Oxford Instruments X-Max 20 energy-dispersive spectrometer ("Geomodel" Resource Centre, SPbSU, Saint Petersburg, analyst N.S.Vlasenko). Data acquisition conditions: accelerating voltage 30 kV, beam current 3 nA. Using the EBSD method, nine images of the distribution of crystal lattice orientations in the gold particles were obtained.

Geological setting of the area and placer deposits structure

Geological setting of the area. The Murzinka placer group is located on the eastern slope of the Urals within the Tagil megazone (Fig.1, *a*) [10]. The structure of the area comprises various complexes of intrusive rocks and volcanic rock sequences (Fig.1, *c*), formed during the development of the Tagil island arc. The oldest unit in the area is the Late Ordovician Mariinsky metamorphic complex, dominated by amphibolites and amphibolised dolerites. The rocks of the complex host Late Ordovician gabbroids of the Pavdinsky polyformational massif, which forms part of the Ural Platinum Belt (UPB) [11]. East of the intrusion, a large area is occupied by the volcanic rocks of the Kabanskaya formation, which span the Late Ordovician to Early Silurian. The formation comprises volcanic rocks of a contrasting bimodal association (mafic-felsic), with basalts and andesite-basalts markedly predominating over rhyodacites. The Kabanskaya formation hosts numerous copper-zinc VMS type occurrences [12], typical of the bimodal volcanic association in the Tagil megazone. To the east, the Kabanskaya formation is verlain by the younger Pavdinskaya formation comprising basalts, andesite-basalts, and rhyolites. In the northern part of the area, hosting the Murzinka group placers, lies the Kamensky massif, composed of diorites and gabbro-diorites of the Petropavlovsk complex. This intrusive complex is comagmatic with the volcanic rocks of the Pavdinskaya formation. Small granite stocks of the Late Silurian Severorudnichny complex intrude the rocks of the Kamensky intrusion.

Located in the axial part of Middle Urals, the Murzinka placer group belongs to the Cenozoic placer belt and lies within the prospective Isovskaya gold-ore zone [11]. Two quartz-gold occurrences are known locally, but no substantial data available.

Geomorphology and structure of placer deposits. Large-scale geomorphological and palaeoclimatic studies carried out by the team of researchers under the leadership of A.P.Sigov between 1960 and 1980 [13], distinguished six key tectonic-climate stages in the history of the relief development of the eastern slope of the Middle Urals: the Eo-Mesozoic (I), Lower Mesozoic (II), Upper Mesozoic (III), Upper Palaeogene (IV), Miocene (V), and Pliocene-Quaternary (VI). The Murzinka placer group is characterized by a wide distribution of sediments and peneplain surfaces corresponding to stages III, V, and VI. During the Upper Mesozoic stage, a stable tectonic regime combined with a predominantly humid climate caused the widespread formation of weathering crusts. Subsequently, the upper eluvial horizons of the Mesozoic peneplain were partially eroded. In the present day structure of the area, these Mesozoic weathering crusts constitute a basal surface (bedrock) that underlies younger placer deposits. The Miocene stage was marked by declining tectonic activity and a semi-arid climate, which reduced the rates of erosion and denudation. In the absence of permanent watercourses, ravine networks developed and accumulated sediments of deluvial and proluvial genesis. Unconsolidated sediments of this stage are locally exposed in the upper reaches of the Talaya and Malaya Nyasma rivers. Tectonic reactivation during the Pliocene-Quaternary period, expressed through episodic uplift of the territory, together with a shift to a moderately cold and wetter climate, significantly intensified denudation. This combination of factors caused relief dissection and established the modern drainage network. These processes were accompanied by the accumulation of the major volume of gold-bearing alluvial-deluvial and alluvial deposits [13].

This is an open access article under the CC BY 4.0 license

© Aleksandr K. Kozin, Sergei Yu. Stepanov, Roman S. Palamarchuk, Valeriya S. Zhdanova, Natalya S. Vlasenko, 2026

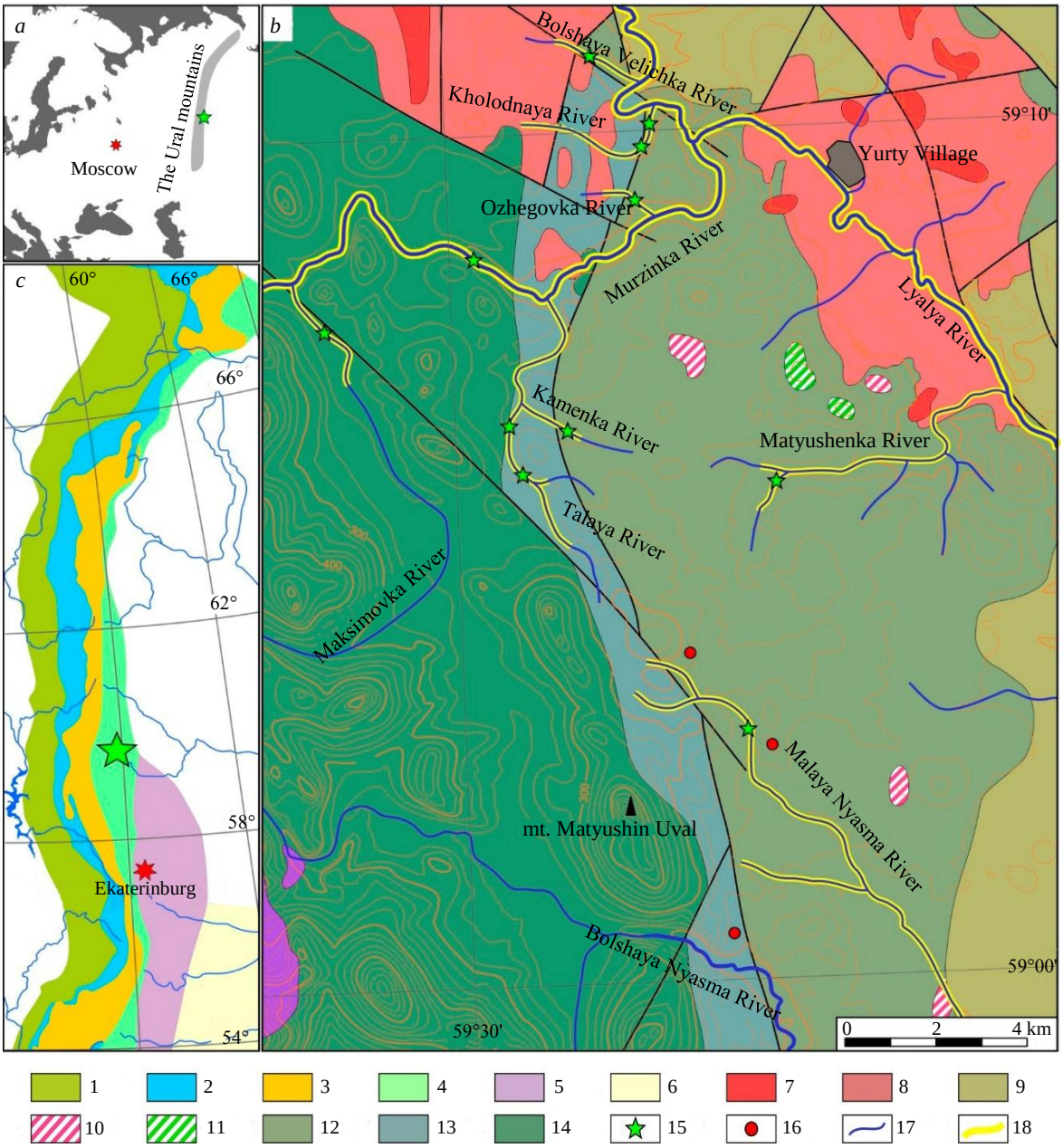


Fig.1. Location (*a*), geological structure (*b*) and tectonic setting (*c*) of the Murzinska placer group area (compiled using the following materials [10, 11])

1 – Preuralian foredeep; 2-6 – zones: 2 – West Uralian, 3 – Central Uralian, 4 – Tagilo-Magnitogorskaya, 5 – East Uralian, 6 – Transuralian; 7 – Late Silurian granites; 8 – Early Silurian diorites and gabbrodiorites of the Kamensky massif; 9 – Early Silurian volcanic rocks of the Pavdinskaya formation from basalts to rhyolites; 10 – Kaban subvolcanic formations, gabbro-dolerite stocks; 11 – Kaban subvolcanic formations, rhyodacite stocks; 12 – Late Ordovician-Early Silurian volcanic rocks of the Kabanskaya formation from basalts to rhyolites; 13 – Late Ordovician amphibolites and amphibolised dolerites of the Mariinsky metamorphic complex; 14 – Late Ordovician gabbroids of the Pavdinsky massif; 15 – sampling points; 16 – gold occurrences; 17 – watercourses; 18 – gold placers

All studied placer deposits are characterized by a similar structure and lithological composition (Fig.2). They belong to the alluvial and alluvial-deluvial (ravine) types. At the base of the placer sections lie Mesozoic weathering crusts developed over volcanic rocks; these act as a basal surface for the placers and are represented by grus-rubble, grus-clayey, and clayey varieties. Overlying these are Upper Pleistocene alluvial-deluvial deposits of the Kustanai formation, predominantly composed of loams with slightly rounded pebbles of volcanic rocks. These are overlain with an erosional contact by Middle Pleistocene hillslope and ravine sediments of clayey and sandy-clayey composition. The upper part of the section consists of clayey deluvium of the Upper Pleistocene and modern channel

This is an open access article under the CC BY 4.0 license

Journal of Mining Institute. 2026. Vol. 280. P. 104-121
© Aleksandr K. Kozin, Sergei Yu. Stepanov, Roman S. Palamarchuk, Valeriya S. Zhdanova, Natalya S. Vlasenko, 2026

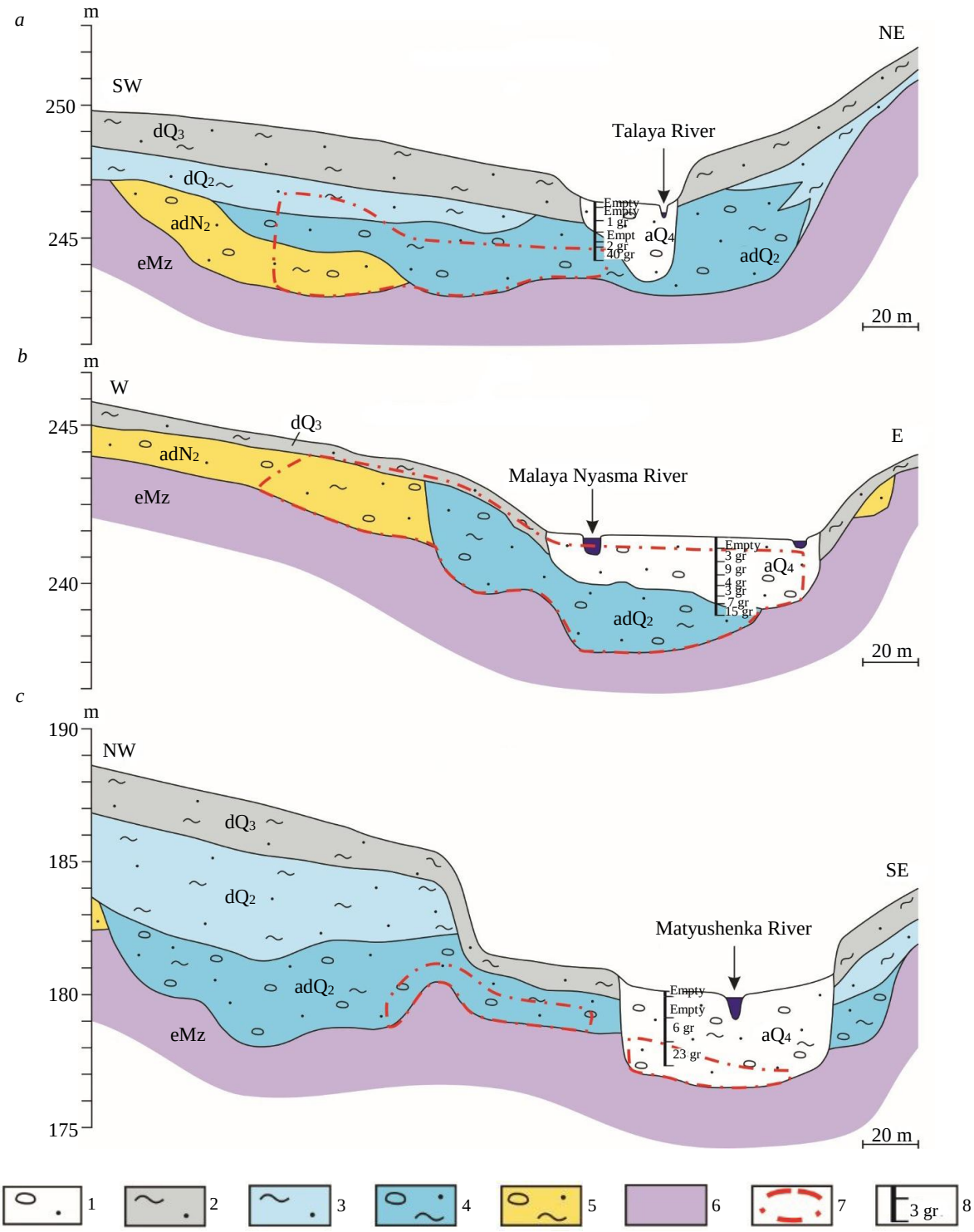


Fig.2. Representative cross-sections of alluvial and alluvial-deluvial placers of the Murzinka group of rivers: Talaya (*a*), Malaya Nyasma (*b*) и Matyushenka (*c*)

1 – Holocene channel alluvium (aQ_4); 2 – Upper Pleistocene deluvial deposits (dQ_3); 3 – Middle Pleistocene deluvial deposits (dQ_2); 4 – Middle Pleistocene alluvial-deluvial deposits (adQ_2); 5 – Upper Pliocene alluvial-deluvial deposits (adN_2); 6 – Mesozoic weathering crusts developed on volcanic rocks (eMz); 7 – outlines of placer gold grades exceeding 0.1 g/m^3; 8 – sampling intervals in pits and the number of gold grains in the samples, Empty – placer gold was not detected. The cross-sections were compiled based on the authors' field observations with reference to archival reports (A.P.Nizovoy, 1970; N.D.Shchur, 2007)

alluvium, represented by sandy loams containing a large amount of gravel and pebble material. Gold mineralization has been identified in all deposits of alluvial and alluvial-deluvial genesis, ranging from the Upper Pliocene to the Holocene. Native gold is distributed very heterogeneously throughout the sediments. The highest concentrations, satisfying current industrial cut-off grades, are preferentially located in the basal zone adjacent to the bedrock surface.

This is an open access article under the CC BY 4.0 license

Results

Size and morphological features of placer gold. The grain-size distribution of native gold in the various placers of the Murzinka group exhibits only minor variations (Table 1). The predominant size fractions comprise relatively coarse particles in the 0.25-0.5 mm and 0.5-1.0 mm classes, which are present in approximately equal proportions within the samples and collectively account for 70 % of the gold particles. The 0.1-0.25 mm fraction ranks third in terms of frequency of occurrence and constitutes 20-30 % of the particles. Particles belonging to the coarser 1.0-2.0 mm size class are significantly less abundant, typically representing only a few percent of the total grain population. An exception to this pattern is observed in the placers of the Talaya River and its tributary, the Kamenka River, where the share of this fraction reaches up to 10 %. Notably, samples recovered from the alluvial deposits of the Talaya River contain the largest gold particles identified in the study, with maximum sizes attaining 7 mm.

Table 1

Native gold from placers of Murzinka group

Placers of the rivers	Number of particles *n*	Grain-size distribution, %						Flattening coefficient
		Gold particles size, mm						
		< 0.1	0.1-0.25	0.25-0.5	0.5-1.0	1.0-2.0	> 2	
Talaya	107	–	22.43	33.64	31.78	10.28	1.87	2.48
Kamenka	76	–	21.05	31.58	39.47	7.89	–	2.98
Matyushenka	29	–	27.59	31.03	41.38	–	–	2.34
Malaya Nyasma	41	2.44	24.39	41.46	29.27	2.44	–	2.53

The morphological features of native gold are highly diverse. Gold particles frequently exhibit a slightly flattened form, with flattening coefficient values being fairly consistent across all placers and ranging within 2-3 units (Table 1). The flattening of gold particles is not related to deformation processes and represents a primary morphological feature, as it is observed in both rounded and angular particles. particles with an elongated or lumpy shape are less common.

The majority of gold particles show a moderate degree of roundness (Fig.3). The surfaces of the particles are hummocky and show multiple signs of mechanical reworking: cavities, scratches, and smoothing of protruding parts. Traces of the initial morphology remain evident in the general grain outline and isolated surface segments. Native gold individual grains and aggregates of a primary rough morphology occur much less frequently. They are characterised by intricate shapes with stepped surfaces indicative of simultaneous growth with gangue minerals. Only a few particles of this variety were identified within the Talaya River placer.

Internal structure of placer gold. Study of the internal structures using electron backscatter diffraction reveals that the majority of gold particles are granular aggregates. These consist of misoriented polygonal grains with straight or slightly curved boundaries. A correlation has been observed between the grain size and the overall size of the aggregates they compose. Aggregates ranging from 100 to 300 μm in size incorporate grains of 30-100 μm; in larger native gold particles (2-5 mm), the grain size increases to 500-1000 μm. Monocrystals are extremely rare, and their size does not exceed 250 μm. Numerous mechanical deformations are manifested in the internal structure of native gold as zones of lattice misorientation.

Images acquired with a scanning electron microscope in BSE mode demonstrate a chemically homogeneous internal structure of the placer gold, with high-fineness rims developed along the periphery. The thickness of these rims amounts to the first tens of micrometers; their boundary with the core parts of the gold particles is sharp and sinuous. Another distinctive feature of the internal structure is the presence of high-fineness veinlets developed along the boundaries of the grains composing the native gold aggregates. The thickness of these intergranular veinlets is 5-10 μm.

This is an open access article under the CC BY 4.0 license

Journal of Mining Institute. 2026. Vol. 280. P. 104-121
© Aleksandr K. Kozin, Sergei Yu. Stepanov, Roman S. Palamarchuk, Valeriya S. Zhdanova, Natalya S. Vlasenko, 2026

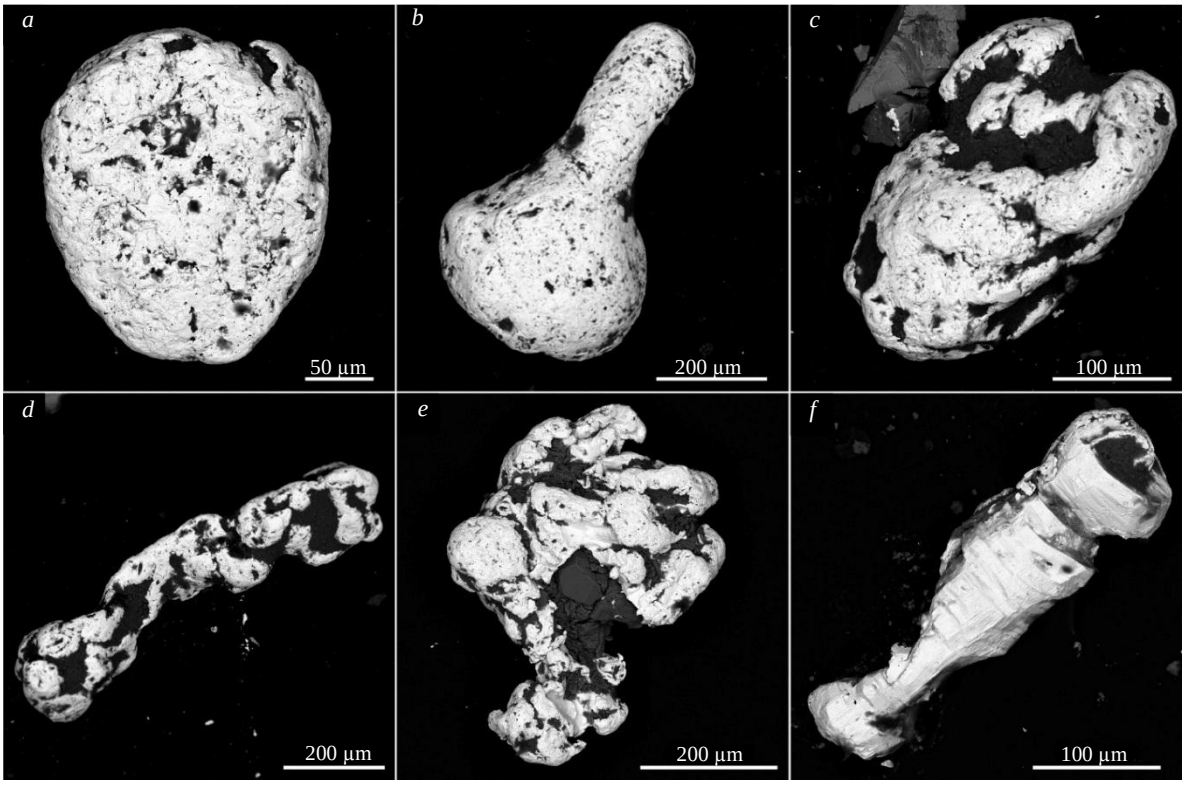


Fig.3. Morphology of native gold from the placers of the Murzinka group of rivers Malaya Nyasma (*a*), Ozhegovka (*b*), Matyushenka (*c*), Bolshaya Velichka (*d*), Kholodnaya (*e*), Talaya (*f*). BSE image

Chemical composition of placer gold. The characteristics of the chemical composition allow three types of native gold to be distinguished in the placers of the Murzinka group (Table 2, 3). Type I is the most widespread and is characterized by the presence of Ag and Hg admixture in the native gold. Variations in the admixture content allow to divide this type into four subtypes: a – the Maksimovka River placer; b – the placers of the Bolshaya Velichka, Malaya Nyasma and Murzinka rivers; c – the alluvial deposits of the Talaya and Kholodnaya rivers; d – the alluvial deposits of the Matyushenka, Kamenka, and Ozhegovka rivers. Placers grouped according to these gold subtypes exhibit very similar fineness values and concentrations of silver and mercury impurities.

Table 2

Average chemical composition of Type I placer gold, wt.%

Placers of the rivers	Number of particles *n*	Subtype	Hg			Ag			Au		
			Median	Min	Max	Median	Min	Max	Median	Min	Max
Maksimovka	17	a	0.99	–	3.01	16.76	3.39	26.15	82.68	73.74	97.36
Bolshaya Velichka	15	b	1.23	–	3.24	13.50	4.02	23.42	86.20	74.98	96.66
Malaya Nyasma	17		0.38	–	4.40	13.01	1.42	23.85	86.63	76.68	99.97
Murzinka	13		1.24	–	4.28	13.40	1.02	19.90	84.68	79.81	97.31
Talaya	18	c	0.43	–	4.96	10.03	0.57	23.11	90.26	74.60	99.99
Kholodnaya	14		–	–	0.83	7.00	0.74	23.43	92.83	75.73	100.00
Matyushenka	11	d	–	–	0.50	7.32	–	11.00	93.54	89.68	98.88
Kamenka	13		–	–	1.68	8.68	–	14.82	91.28	83.40	100.00
Ozhegovka	5		–	–	–	7.66	6.53	14.12	92.48	86.33	94.73

Type II gold is considerably less abundant; single particles were found only in the placer deposits of three watercourses: the Bolshaya Velichka, Maksimovka, and Malaya Nyasma rivers. A distinctive signature of this type is the presence of copper, the content of which varies widely

This is an open access article under the CC BY 4.0 license

(0.21-23.22 wt.%), coupled with low silver levels (0.25-5.46 wt.%). Mercury is present at concentrations up to 1.15 wt.%. The fineness of this gold type ranges from 767 to 974 ‰. Owing to the limited amount of Type II gold particles, a robust assessment of compositional variability and mean admixture concentrations is not possible

Type III native gold is provisionally defined, based on two particles collected from the Matyushenka River placer. These particles display a composition fundamentally distinct from Types I and II, with silver as the only detectable admixture at levels of 44.53 and 49.78 wt.%.

Table 3

Average chemical composition of Types II and III placer gold, wt.%

Placers of the rivers	Type	Cu	Hg	Ag	Au
Bolshaya Velichka	II	0.21	0.82	2.51	96.65
		1.62	–	1.41	97.36
Maksimovka	II	3.83	1.15	5.46	89.74
		0.82	–	3.60	95.99
Malaya Nyasma	II	23.22	–	0.25	76.74
Matyushenka	III	–	–	44.53	56.72
		–	–	49.78	50.95

Gold-rich rims, which often form along the periphery of native gold particles in alluvial deposits, have also been studied in terms of their chemical composition. They are characterized by a sharp decrease in the content of all impurities. The degree of refinement of the high-purity rims does not appear to depend on the initial composition of the gold nuggets, and the total impurity content does not exceed a few percent.

Mineral inclusions assemblages. Detrital gold contains a substantial number of ore mineral inclusions (Table 4). Pyrite is the predominant inclusion, occurring as grains with irregular shapes as well as those displaying elements of crystallographic faceting (Fig.4, *a*); the grain size ranges from 5 to 20 μm. Sporadic occurrences of pyrrhotite (Py), chalcopyrite (Chp), petzite (Ptz), galena (Gn), and molybdenite (Mol) are present as single grains (Fig.4, *a*, *c*). A single bornite inclusion, 4 μm in size, was identified in Cu-bearing Type II native gold from the Bolshaya Velichka River placer deposit.

Table 4

Mineral inclusions in native gold

Placers of the rivers	Gold type	Py	Pyh	Chp	Bn	Gn	Mol	Ptz
Talaya	I	4	1	1	–	1	–	–
Kamenka	I	10	–	1	–	1	1	–
Matyushenka	I	3	1	–	–	–	–	–
Malaya Nyasma	I	3	–	–	–	–	–	2
Maksimovka	I	1	–	–	–	–	–	–
Bolshaya Velichka	II	–	–	–	1	–	–	–

Gangue minerals are commonly observed as inclusions within native gold. Quartz, albite, and epidote are the most widespread phases, whereas calcite and apatite occur less frequently. Abundant inclusions of a hydrated REE phosphate, presumably rhabdophane, have been identified in the gold particles from Talaya River placer deposit (Fig.4, *b*). These inclusions exhibit intricate worm-like morphology and range in size from 1 to 10 μm. It is noteworthy that rhabdophane inclusions occur only in the marginal parts of the gold particle, which is characterized by a higher gold fineness relative to the core parts and the virtual absence of admixtures.

This is an open access article under the CC BY 4.0 license

© Aleksandr K. Kozin, Sergei Yu. Stepanov, Roman S. Palamarchuk, Valeriya S. Zhdanova, Natalya S. Vlasenko, 2026

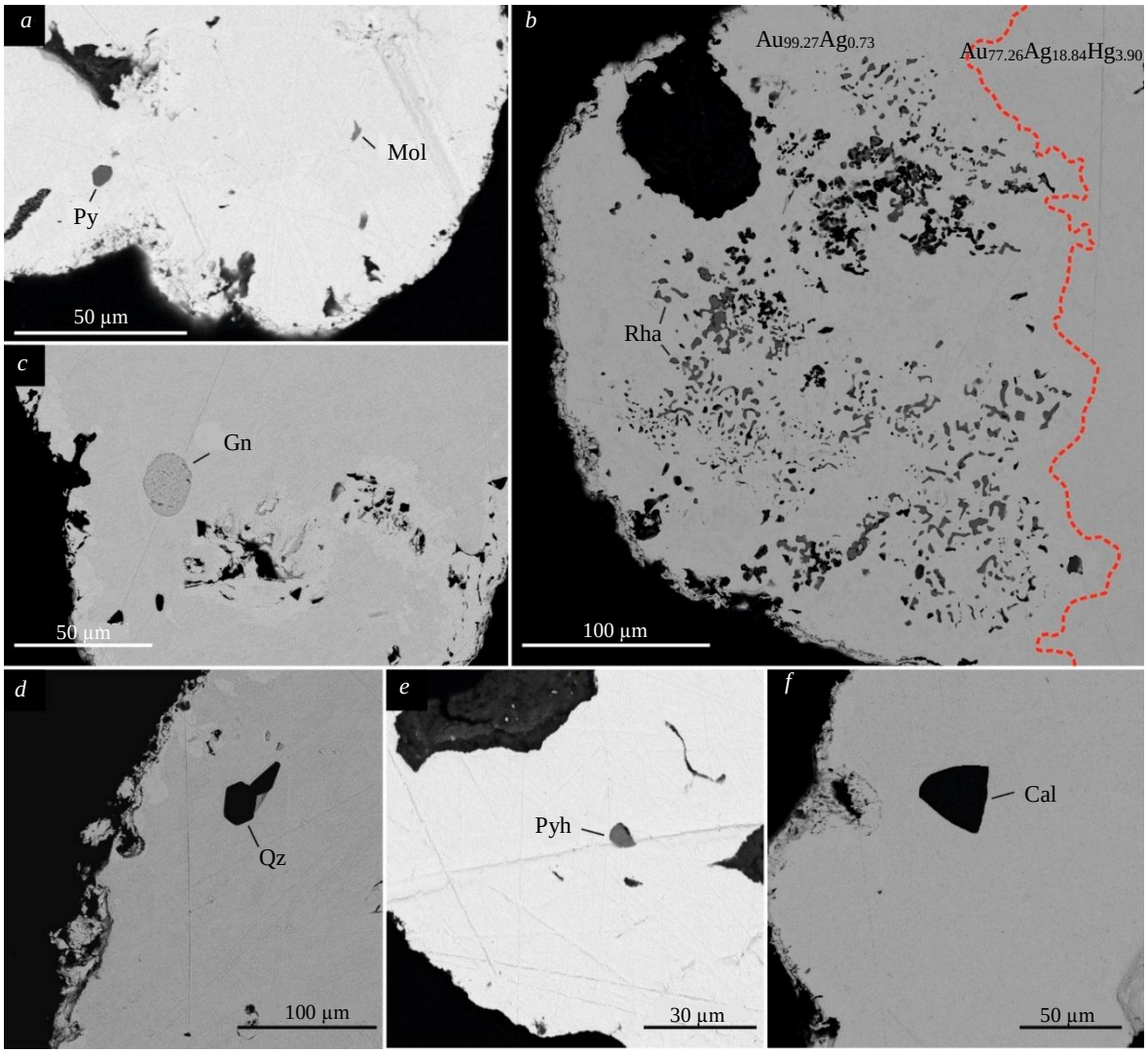


Fig.4. Inclusions in native gold from the placers of the Murzinka group

Gn – galena; Mol – molybdenite; Py – pyrite; Rha – rhabdophane; Qz – quartz; Pyh – pyrrhotite; Cal – calcite. The red dashed line marks the boundary of the high-fineness zone of the native gold

Discussion

The Murzinka River placer system, including its tributaries, constitute a significant part of the gold resource base in the Middle Urals. Approximately 1.5 t of native gold have been extracted from these placer deposits. The accumulation of such a substantial volume of gold reflects the combined influence of several key factors. The principal controls include high productivity of the lode sources and the succession of climatic and geomorphological conditions that facilitated accumulation of gold-bearing alluvium. The typomorphic features of native gold make it possible to evaluate the conditions of placer formation and identify types of lode sources.

Distance of transport from lode sources. Observation of the morphological characteristics of detrital gold from the Murzinka group placers has established the distance to the lode sources. During fluvial transport, as the distance increases and the number of mechanical deformations rises, gold particles experience consequent morphological changes, primarily manifesting as rounding and flattening [14]. Rounding, smoothing of protruding parts and grain surfaces occur during the early stages of transport, as demonstrated by studies of placers in the Klondike region (British Columbia) [15]. The degree of rounding reaches a maximum at approximately 5 km from the source and remains essentially constant with further transport. Mechanical flattening of gold particles

This is an open access article under the CC BY 4.0 license

becomes evident at distances exceeding 3 km and develops in a near linear fashion with increasing distance. The native gold from the studied placers is characterized by a predominance of moderate rounding and a shagreen surface, typical of gold transported in aqueous flows [6, 15]. The presence of slightly flattened and lumpy particles suggests preservation of primary morphologies and indicates a lack of substantial mechanical flattening. This implies that native gold in the Murzinka group placers derived from proximal lode sources, with transport distances limited to the first few kilometers. In contrast, single primary rough gold particles recovered from the Talaya River alluvial deposits retain intricate shapes with fine elements of surface, pointing to an additional local contribution from a nearby source located within the first few hundred meters.

Supergene transformation of native gold. The internal structure of native gold preserves evidence of supergene alteration. A distinctive feature is the occurrence of high-fineness veinlets developed along grain boundaries in gold aggregates. These features are common in both placer and lode gold occurrences, yet their genesis is not established. According to widely accepted interpretations [9, 16], such veins form in oxidation zones through the filling of intergranular voids that were produced during diffusion. An alternative hypothesis links these structures to metamorphically induced granulation of gold and silver redistribution [17]. Additionally, it has been proposed [18] that gold-rich intergranular veins may crystallize during the late stages of hydrothermal ore-forming processes. Taking into account the geological history of the region, the most likely cause of such structures is supergene transformation of gold within the weathering crusts developed during the Upper Mesozoic climatic stage.

Particular significance attaches to the intricate intergrowths of native gold with hydrated REE phosphates. The sinuous, worm-like structures of rhabdophane group minerals within the high-fineness marginal parts of the gold aggregates provide evidence of co-crystallization. Within the gold rich parts, abundant silver-enriched fragments of gold are observed; their chemical composition corresponds to that of the core zones. The crystallographic orientation of these fragments commonly aligns with that of larger primary native gold particles in the immediate vicinity (Fig.5). This observation suggests these fragments are relict domains of primary gold that have been partially replaced by aggregate of high-fineness gold. The internal structure of the gold rich marginal zones is characterized by smaller constituent grains. Moreover, numerous elongated twinning structures are present within these grains. Fine-grained textures are commonly reported in gold-rich rims of placer gold particles [19]. Their formation attributed to complete recrystallization of mechanically deformed zones coupled with the removal of impurities from the gold [5]. According to the morphological principles of isometricity and minimum boundary length [20], complete recrystallization produces aggregates consisting of isometric polyhedral. Development of twins and elongated individual grains is not expected under such conditions. Therefore, the microstructures observed in the gold-rich parts of the particles cannot be the result of recrystallization.

There are two possible explanations for the observed twin structures – free growth of individual crystals (growth twins) and twinning resulting from a change in the orientation of the crystal lattice due to mechanical deformations (mechanical twins). The results of backscattered electron diffraction revealed identical crystal lattice orientation within each individual grain. There are virtually no zones of local misorientation, which indicates the absence of mechanical deformations in the gold-rich parts. Thus, the twinning structures, which are common in high-fineness zones of gold particles, are interpreted as growth twins.

The REE redeposition during the formation of supergene mineralization, including rhabdophane, was documented in weathering crusts developed on granites [21, 22] and in volcanic sedimentary sequences hosting polymetallic mineralization [23]. Researchers emphasize the significance of sulfide minerals oxidation, which results in the generation of sulfate solutions. These solutions promote the decomposition of primary minerals, the liberation of REE [23], and their migration along the

This is an open access article under the CC BY 4.0 license

© Aleksandr K. Kozin, Sergei Yu. Stepanov, Roman S. Palamarchuk, Valeriya S. Zhdanova, Natalya S. Vlasenko, 2026

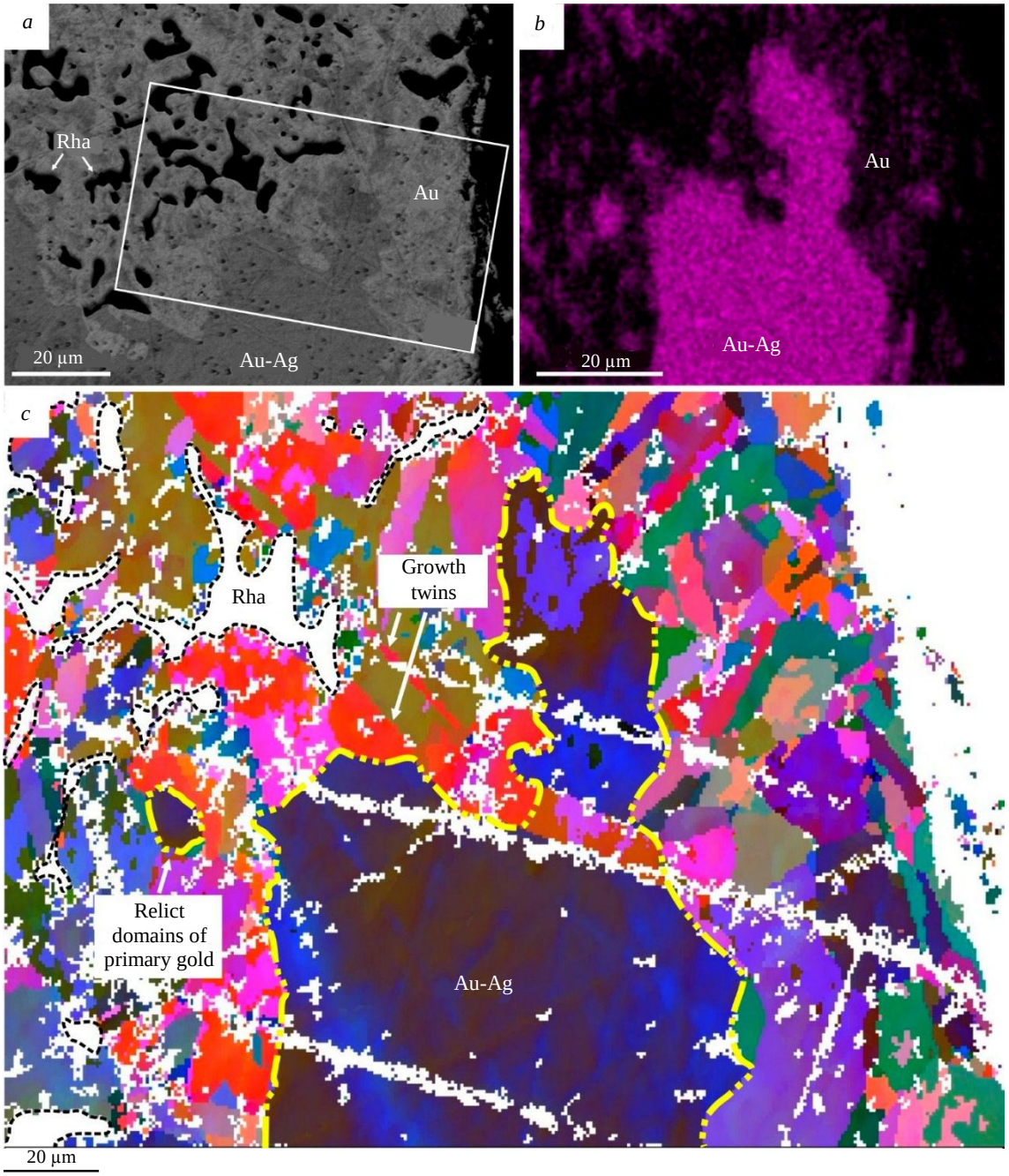


Fig.5. Internal structure of native gold with rhabdophane inclusions. BSE image (*a*); Au leves map (*b*); crystal lattice orientation map in Euler colors, obtained by EBSD, step size 0.25 μm (*c*). The white outline in Fig. *a* marks the gold grain area shown in Fig. *b* and *c*

oxidation zone profile [21]. The oxidation of sulfides (predominantly pyrite) and plagioclase is a key factor in thiosulfate formation. Thiosulfates enable the remobilization, transport, and subsequent redeposition of native gold, leading to the development of high fineness gold aggregates within weathering crusts [24, 25]. Studies of the weathering crust at the Suzdal deposit provided evidence for the formation of high fineness gold via dissolution and redeposition under oxidation zone conditions [26]. The migration of gold caused by pyrite decomposition in the oxidation zone of gold-sulfide deposits has been described in detail by a research team led by V.M.Kreiter [27]. Considering the observed internal structure of native gold, the purification mechanism can be explained by the model of self-electrorefining of gold during dissolution and instantaneous subsequent deposition, as proposed by J.Groen and co-authors [19]. Thus, conditions favorable for the co-crystallization of native gold and rhabdophane may exist within the oxidation zone due to the

This is an open access article under the CC BY 4.0 license

breakdown of sulfides minerals and plagioclase, as well as the introduction of phosphorus by groundwater. During redeposition, native gold is purified from admixtures and attains a higher fineness. The complex morphologies of hydrous REE minerals and high fineness gold intergrowths provide direct evidence for the development of gold-rich zones under conditions of weathering crust.

The internal structure of native gold preserves evidence of mechanical deformations sustained during its transport from lode sources to placer deposits. Electron backscatter diffraction reveals numerous domains of crystal lattice misorientation, formed as a result of collisions between gold particles and rock fragments. The most significant deformations took place in the marginal zones of the native gold particles, leading to the accumulation of stresses within the particles. The abundance of gold-rich rims can be explained by processes of gold purification from admixtures resulting from the recrystallization of the deformed zones [5, 28, 29]. During the development of Quaternary alluvial deposits, older Pleistocene and Neogene gold-bearing alluvial and alluvial-deluvial units underwent partial erosion. This is clearly evident in the stratigraphic sections of the modern watercourse network. The erosional process probably was accompanied by the redeposition of some placer gold. Such redeposition may have intensified the deformation of gold particles and promoted the formation of high-fineness gold-rich rims. A similar conception of native gold redeposition from intermediate Pliocene-Pleistocene reservoirs into Quaternary placers has been described for the Vagran gold bearing placer cluster in the Northern Urals [30], located approximately 100 km north of the Murzinka placer group.

Lode sources of native gold. The identification of native gold with markedly distinct compositional characteristics indicates the contribution of lode sources of multiple types to the formation of the studied placers. The similarity in the composition of native gold containing silver and mercury admixtures (Type I) across all the studied placer deposits points to a single type of the lode sources of this type of gold. Similar compositional signatures of detrital gold have been documented in placers in diverse geological settings. Numerous studies of placer clusters associated with orogenic gold deposits demonstrate a prevalent compositional variability in alluvial gold, with respect to silver content and up to a few percent of mercury [2-5, 31]. Analyses of gold from Witwatersrand conglomerates report fineness values of 809-929 ‰, silver concentrations of 6.0-17.6 wt.%, and mercury contents of 0.6-5.8 wt.% [32]. Research on the Northern Salair placers has established that metasomatic rocks related to intrusive systems can act as source for gold bearing silver and mercury impurities [33, 34]. Analogous compositional ranges (fineness of 800-995 ‰ and mercury up to 4.68 wt.%) have been determined for placer gold derived from the upper levels of the Bystrinsky skarn-porphyry Au-Cu-Fe deposit. High fineness native gold (892-899 ‰) with substantial mercury admixtures (1.72-2.16 wt.%) has been reported in watercourses of the Unya Bomsk ore-placer complex [35]. Consequently, the chemical composition of native gold does not allow the lode sources to be unequivocally attributed to a specific type. The insufficiency of compositional data for resolving the question of placer sources is corroborated by studies of detrital gold from districts where lode mineralisation of different types is combined [31].

Grain size could be an additional criterion in identifying lode sources of detrital gold in the Murzinka placer group. The predominance of the coarse gold particles (0.5-1.0 mm) and historical records of gold nuggets up to 725 g recovered during artisanal mining supports the hypothesis that Type I placer gold originated from gold quartz type sources. Such size characteristics are typical of gold derived from gold quartz veins, which are known to host big gold aggregates [36] and nuggets [9]. This interpretation is consistent with compositional data on gold from gold quartz

This is an open access article under the CC BY 4.0 license

deposits [37] and with the regional geological setting. In the upper reaches of the Malaya Nyasma River, the Malonyasmenskoe lode occurrence of the gold quartz type is documented; the erosion and mechanical breakdown of such occurrences likely supplied the material for the placers. Additionally, exploratory drilling in the Talaya River valley identified a gold bearing quartz vein at the Talovskoye ore occurrence [11].

The mineral inclusion assemblage in Type I placer gold is dominated by pyrite, pyrrhotite, galena, chalcopyrite, molybdenite, and petzite are less abundant. Such mineral inclusions can be critically important for establishing a genetic link between placer gold and bedrock precious metal mineralization. Studies of inclusion assemblages in native gold from placers hosted in areas with multiple genetic types of mineralization indicate that the aforementioned minerals are most commonly observed as inclusions in placer gold associated with plutogenic hydrothermal systems [38]. Inclusions of molybdenite and tellurides provide an evidence of a connection between the lode sources and magmatic processes [39]. Therefore, quartz veins related to the intrusion of diorites of the Kamensky massif may represent the lode source of Type I native gold in the Murzinka group placers.

Histograms of native gold fineness and cumulative curves of silver content (Fig.6) reveal a systematic compositional trend within Type I gold, progressing from subtype a to subtype d. Subtype a (Maksimovka River placer) is characterized by the highest silver contents (median 16.76 wt.%) and elevated mercury levels (up to 3.01 wt.%). In subtype b (placers of the Bolshaya Velichka, Malaya Nyasma, and Murzinka rivers), median silver contents decrease to 13.01-13.40 wt.%, while mercury admixture remain high (up to 4.40 wt.%). Subtype d (placers of the Matyushenka, Kamenka, and Ozhegovka rivers) exhibits the lowest silver contents (median 7.32-8.66 wt.%), with mercury largely undetectable in most particles. Subtype c (Talaya and Kholodnaya rivers) displays a bimodal fineness distribution (Fig.6, *c*) and occupies an intermediate position in terms of impurities content. Maximum silver and mercury values (up to 23.43 wt.% Ag and 4.96 wt.% Hg) align this gold with Type Ib, whereas the median silver contents (10.03 and 7.00 wt.%) are closer to those of Type Id (placers of the Matyushenka, Kamenka, and Ozhegovka rivers). The transitional character of Type Ic native gold from the placer deposits of the Talaya and Kholodnaya rivers is clearly reflected in the cumulative silver content curves (Fig.6, *e*). Thus, the population gold particles in the Talaya and Kholodnaya placers results from the mixing of Type I subtypes b and d.

A distinct spatial pattern is evident in the distribution of placers hosting Type I native gold (Fig.7). Placer deposits containing gold of subtype d, characterized by minimal admixture content, occur in close spatial association along the Kamenka, Matyushenka, and Ozhegovka rivers, within the volcanic rocks of the Kabanskaya formation. Placers with Type Ib and Ic gold form two elongated belts within the Mariinsky metamorphic complex and the gabbroids of the Pavdinsky massif. The westernmost occurrence is the Maximovka River placer, which hosts subtype a gold marked by the highest admixture levels. Considering the limited transport distance of the gold, the observed distribution of Type I subtypes across the Murzinka group placers reflects a zonation of lode gold quartz mineralization. This zonation is expressed as a progressive decrease in fineness and a concurrent increase in Ag and Hg content from east to west.

The observed zonation pattern can be attributed to variations in the distance of quartz vein formation from the Kamensky intrusion, which acted as the source of hydrothermal fluids. With increasing distance from the intrusion (either vertically or laterally), a decline in temperature and a shift in fluid composition likely occurred. These changes would have resulted in the deposition of native gold of lower fineness and with higher Ag and Hg contents. An additional control on gold composition is the nature of the host rocks. Placer deposits situated within the volcanogenic sedimentary strata of

This is an open access article under the CC BY 4.0 license

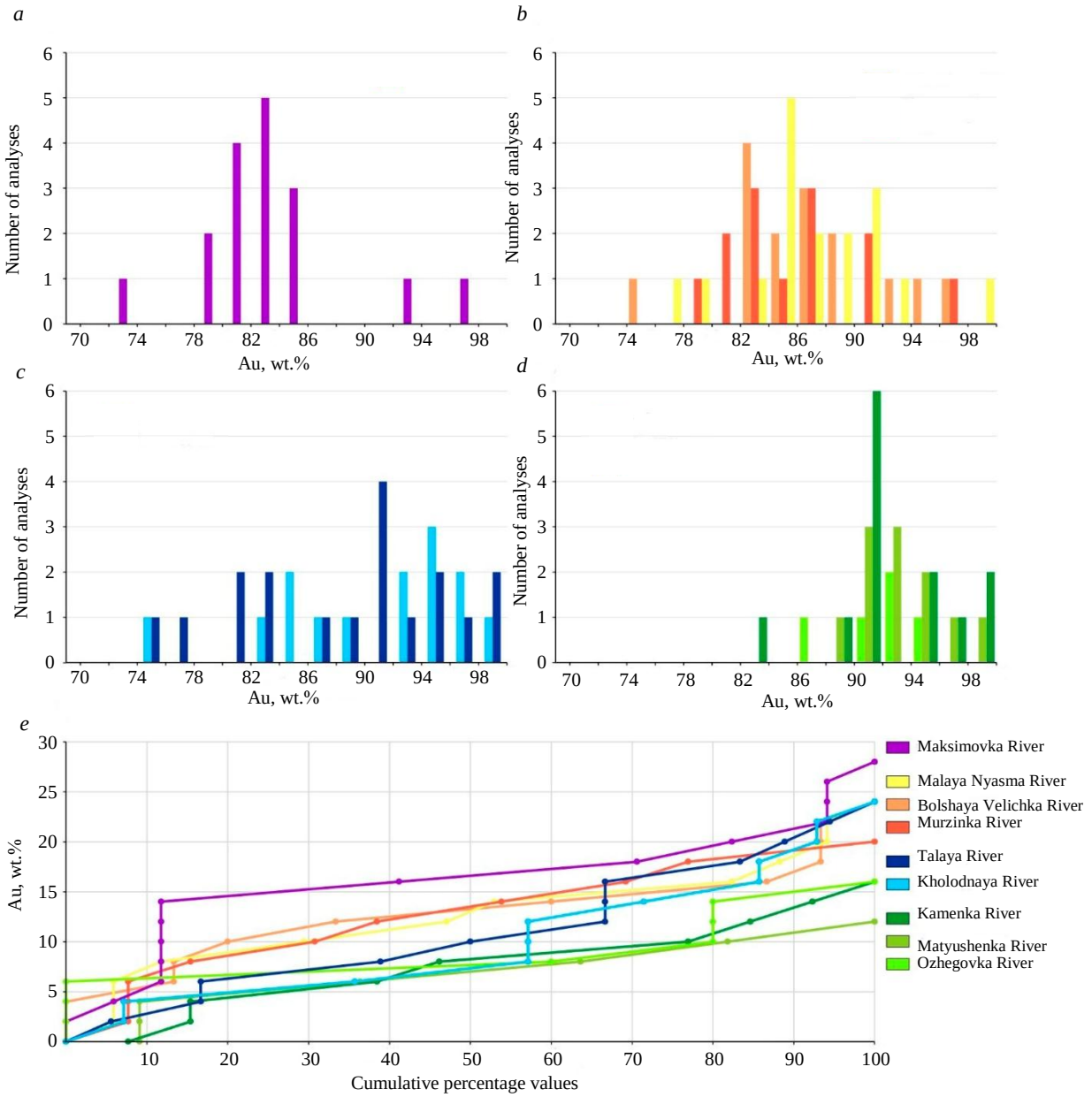


Fig.6. Distribution of Type I native gold by fineness (*a*-*d*) and cumulative curves of Ag content (*e*)
The histograms were plotted with a 2 wt.% interval

the Kabanskaya formation contain gold of higher fineness compared to that found in placers hosted within the gabbroids of the Pavdinsky Massif. This suggests that host rock chemistry contributed to the local variation in gold fineness in gold-bearing veins.

The main distinctive feature of Type II native gold is the presence of copper in its composition, coupled with lower silver and mercury levels relative to Type I gold. All finds of copper-bearing gold within the Murzinka placer group (Malaya Nyasma, Maksimovka, and Bolshaya Velichka rivers) are restricted to its western part. In this area, detrital material was transported into the river valleys from hillslopes underlain by mafic rocks of the Pavdinsky Complex. Copper enrichment in native gold is a significant feature of precious metal mineralization hosted in the gabbroid parts of the UPB massifs [40-42]. Considering the chemical signature of Type II gold, its spatial distribution within the Murzinka group placers, and the regional geology, the gabbroids of the Pavdinsky massif are inferred to represent the lode source of this gold variety. The absence of palladium admixture, which is also typical of native gold from the UPB massifs, may be attributed to the limited sample size of the analyzed gold particles.

This is an open access article under the CC BY 4.0 license

Journal of Mining Institute. 2026. Vol. 280. P. 104-121
© Aleksandr K. Kozin, Sergei Yu. Stepanov, Roman S. Palamarchuk, Valeriya S. Zhdanova, Natalya S. Vlasenko, 2026

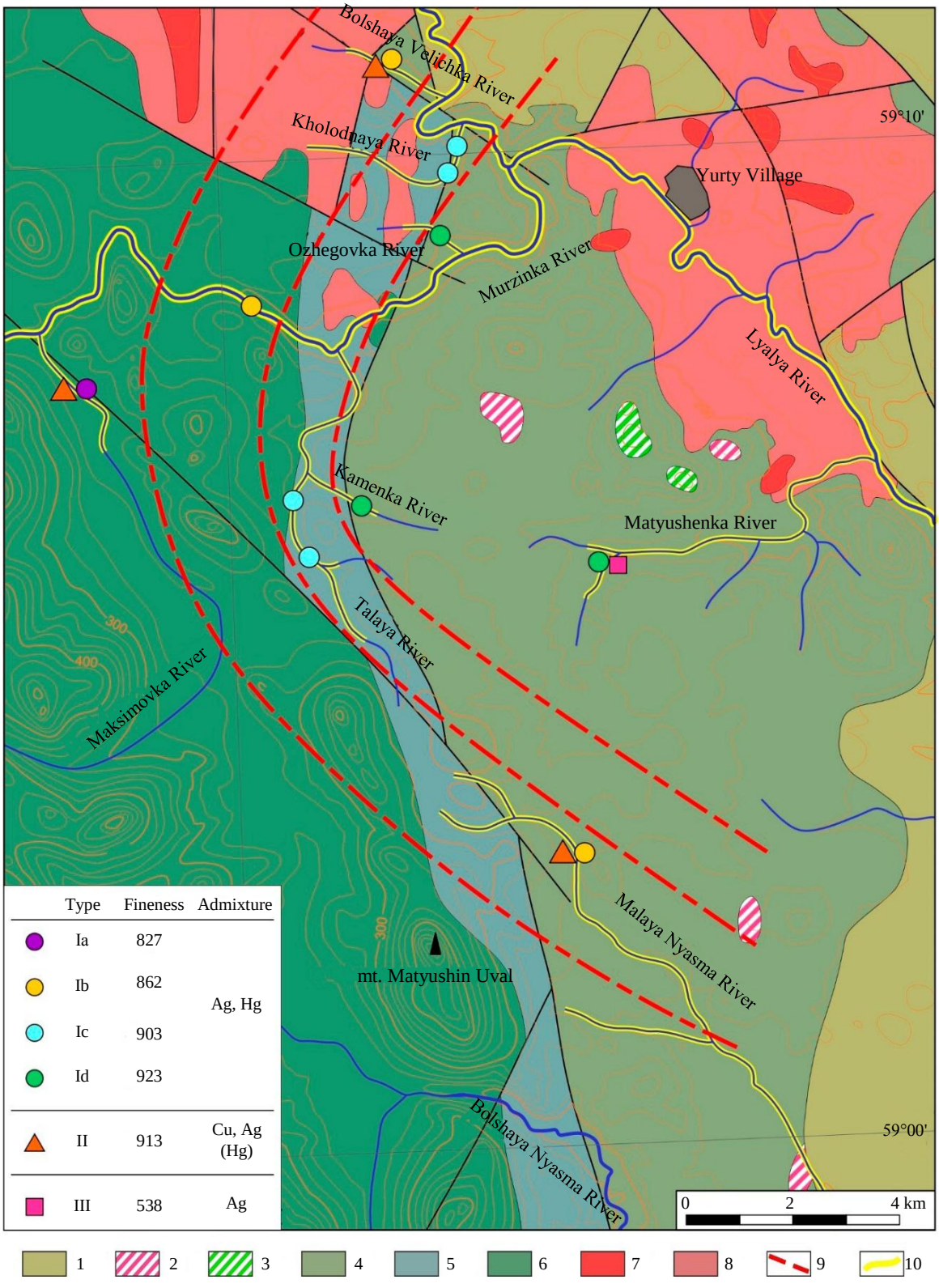


Fig.7. Distribution of native gold of different types in the placers of the Murzinskaya group

1 – Late Ordovician-Early Silurian volcanic rocks of the Kabanskaya formation from basalts to rhyolites; 2 – Kaban subvolcanic formations, gabbrodolerite stocks; 3 – Kaban subvolcanic formations, rhyodacite stocks; 4 – Early Silurian volcanic rocks of the Pavdinskaya formation from basalts to rhyolites; 5 – Late Ordovician amphibolites and amphibolised dolerites of the Mariinsky metamorphic complex; 6 – Late Ordovician gabbroids of the Pavdinsky massif; 7 – Late Silurian granites; 8 – Early Silurian diorites and gabbrodiorites of the Kamensky massif; 9 – inferred zonation pattern of Type I gold-quartz lode mineralization; 10 – gold placers

This is an open access article under the CC BY 4.0 license

The marked differences between Types I and II of native detrital gold are also reflected in the assemblages of mineral inclusions. Bornite is the only opaque mineral forming inclusions in copper-bearing gold. Mineralogical and geochemical research of gabbro from the Serebryansky Kamen massif (a part of the Kytlym pluton within the UPB) reveal that the highest precious metal grades occur in mineralized zones characterized by a chalcopyrite-chalcocite-bornite association of copper sulphide minerals [43]. These observations support the inference that Type II native gold is genetically linked to copper-precious metal mineralization hosted in gabbro.

The origin of Type III native gold, which is characterized by low fineness, remains poorly constrained due to its restricted abundance and the insufficient sample size for a statistically robust assessment of its chemical composition. Consequently, any hypotheses regarding its genesis are necessarily speculative. Lower formation depths of the quartz veins, which are the source of Type I gold, likely accounts for the presence of low-grade native gold in the Murzinka placer deposits.

Based on the integrated analysis of the studied properties of native gold, it can be concluded with a high degree of confidence that the primary source for the placers is represented by lode gold quartz veins. Zones of copper-sulphide mineralization within the gabbro of the Pavdinsky massif, which host associated precious metal mineralization, play a secondary role in the formation of the placer gold deposits of the Murzinka River and its tributaries.

Conclusion

As a result of the conducted research, the morphological features, chemical composition, and internal structure of native gold from nine placers in the Murzinka group have been characterized in detail. Analysis of grain morphology and the rounding degree indicates that the lode gold sources are located in close proximity to the placers, at distances ranging from several hundred meters to the few kilometers.

The observed internal structure patterns of gold can be attributed to the tectono-climatic and geomorphological evolution of the region. High fineness intergranular veinlets and intergrowths of gold and rhabdophane group mineral indicate that native gold resided within the oxidation zone during the period of active weathering crust development in the Upper Cretaceous and Palaeogene. Subsequent erosion and redeposition of weathering crust material, which contributed to placer formation, are recorded in the mechanical deformations of gold particles sustained during transport. Following accumulation of gold particles in alluvial and alluvial deluvial deposits, recrystallization of the most deformed marginal zones of gold particles occurred, resulting in admixture depletion and the gold-rich rims formation.

Analysis of chemical composition and mineral inclusion assemblages enabled the identification of three types of native gold in the placers and revealed their genetic links to distinct lode sources. Type I gold, characterised by high fineness and Ag and Hg admixture, is dominant in the placer deposits. This type is interpreted to originate from bedrock gold quartz mineralization, which is widely represented the study area. The variation in impurity content within Type I gold allows the recognition of subtypes. Their spatial distribution in the placers reflects the zonation pattern of the lode gold quartz mineralization.

Type II native gold, distinguished by elevated copper contents, is linked to precious metal mineralisation hosted in the gabbroids of the Pavdinsky massif. This finding represents the first reliably documented instance of native gold derived from mafic intrusives being concentrated in placers within the Ural fold belt. It confirms the potential for placer accumulation of the previously described gravity concentratable native gold from UPB gabbro.

Type III native gold, characterized by low fineness, was encountered only as a few particles, which limits the ability to confidently identify its lode source. One plausible explanation for the reduced fineness is a decrease in the formation depth of the quartz veins that served as the source for Type I gold.

The large placer system in the Murzinka River basin formed predominantly from gold quartz type sources. This, combined with the limited transport distance indicated by grain morphology,

This is an open access article under the CC BY 4.0 license

allows the prospective areas for lode gold quartz mineralization to be effectively localized. An additional contribution to the placers derives from the zones of precious metal mineralization in the mafic rocks of the Pavdinsky massif. This finding notably expands the understanding of the metallogenic and placer forming potential of gabbro within the Ural Platinum Belt.

The authors are grateful to E.V.Belogub, Director for research at the South Ural Scientific Centre Mineralogy and Environmental Geology of the Ural branch RAS (SUSC MEG UbRAS), Doctor of Geological and Mineralogical Sciences, whose constructive criticism helped improve the manuscript.

REFERENCES

1. Litvinenko V.S., Petrov E.I., Vasilevskaya D.V. et al. Assessment of the role of the state in the management of mineral resources. *Journal of Mining Institute.* 2023. Vol. 259, p. 95-111. DOI: 10.31897/PMI.2022.100
2. Chapman R.J., Mortensen J.K., Crawford E.C., Lebarge W.P. Microchemical Studies of Placer and Lode Gold in the Klondike District, Yukon, Canada: 2. Constraints on the Nature and Location of Regional Lode Sources. *Economic Geology*. 2010. Vol. 105. N 8, p. 1393-1410. DOI: 10.2113/econgeo.105.8.1393
3. Chapman R.J., Mortensen J.K., LeBarge W.P. Styles of lode gold mineralization contributing to the placers of the Indian River and Black Hills Creek, Yukon Territory, Canada as deduced from microchemical characterization of placer gold grains. *Mineralium Deposita*. 2011. Vol. 46. Iss. 8, p. 881-903. DOI: 10.1007/s00126-011-0356-5
4. Zaykov V.V., Melekestseva I.Yu., Zaykova E.V. et al. Gold and platinum group minerals in placers of the South Urals: Composition, microinclusions of ore minerals and primary sources. *Ore Geology Reviews.* 2017. Vol. 85, p. 299-320. DOI: 10.1016/j.oregeorev.2016.10.001
5. Kozin A.K., Stepanov S.Yu., Palamarchuk R.S. et al. Mineral Associations of Concentrates from Gold-Bearing Placers of the Miass Placer Zone (South Urals) and Possible Primary Sources of Gold. *Russian Geology and Geophysics.* 2023. Vol. 64. N 9, p. 1015-1030. DOI: 10.2113/rgg20234543
6. Nikiforova Z.S., Kalinin Yu.A., Makarov V.A. Evolution of Native Gold under Exogenous Conditions. *Russian Geology and Geophysics.* 2020. Vol. 61. N 11, p. 1244-1259. DOI: 10.15372/rgg2020109
7. Lalomov A.V., Naumov V.A., Grigorieva A.V. et al. Evolution of the Vagran Gold-Bearing Placer Cluster (Northern Urals) and Prospects for Revealing Bedrock Mineralization. *Geology of Ore Deposits.* 2020. Vol. 62. N 5, p. 407-418. DOI: 10.1134/S1075701520050049
8. Kuznetsov D.V., Stepanov S.Yu., Butnyakov A.V., Igosheva V.S. Lamprophyres of the Peshchernoe gold deposit, their geological position, material composition, and metasomatic alterations (Northern Urals). *Journal of Mining Institute.* 2025. Vol. 271, p. 22-41.
9. Petrovskaya N.V. Native gold: general characteristics, typomorphism, questions of genesis. Moscow: Nauka, 1973, p. 347 (in Russian).
10. Puchkov V.N. Paleogeodynamics of the Southern and Middle Urals. Ufa: Gilem, 2000, p. 146 (in Russian).
11. Gosudarstvennaya geologicheskaya karta Rossiiskoi Federatsii. Masshtab 1:200000. Izdanie vtoroe. Seriya Yuzhno-Uralskaya. List N-41-VII. Obyasnitelnaya zapiska. Moscow: Moskovskii filial VSEGEI, 2015, p. 167.
12. Desiatnichenko L.I., Fadeicheva I.F., Smirnov V.N. et al. Late Ordovician-Silurian volcanic rocks associations of Tagil zone (Eastern slope of Middle Urals): Composition of the rocks, age, amplified scheme of division. *Litosfera.* 2005. N 2, p. 68-96 (in Russian).
13. Sigov A.P. The metallogeny of the Mesozoic and Cenozoic of the Urals. Moscow: Nedra, 1969, p. 296 (in Russian).
14. Nikiforova Z. Criteria for Determining the Genesis of Placers and Their Different Sources Based on the Morphological Features of Placer Gold. *Minerals*. 2021. Vol. 11. Iss. 4. N 381. DOI: 10.3390/min11040381
15. Knight J.B., Mortensen J.K., Morison S.R. Lode and placer gold composition in the Klondike District, Yukon Territory, Canada; implications for the nature and genesis of Klondike placer and lode gold deposits. *Economic Geology*. 1999. Vol. 94. N 5, p. 649-664. DOI: 10.2113/gsecongeo.94.5.649
16. Gerasimov B.B. Internal Structures of Placer Gold Grains As Prospecting Indicators of Primary Gold Sources in the Northeast of the Siberian Platform. *Geology of Ore Deposits.* 2023. Vol. 65. N 8, p. 857-874. DOI: 10.1134/S1075701523080056
17. Nikolaeva L.A. Genetic features of native gold as criteria in the search and evaluation of ores and placers. Moscow: Nedra, 1978, p. 101 (in Russian).
18. Savva N.E., Preis V.K. Atlas of native gold of the Northeast of the USSR Moscow: Nauka, 1990, p. 292 (in Russian).
19. Groen J.C., Craig J.R., Rimstidt J.D. Gold-rich rim formation on electrum grains in placers. *The Canadian Mineralogist*. 1990. Vol. 28. N 2, p. 207-228.
20. Popov V.A. Practical genetic mineralogy. Ekaterinburg: UrO RAN, 2011, p. 167 (in Russian).
21. Berger A., Janots E., Gnos E. et al. Rare earth element mineralogy and geochemistry in a laterite profile from Madagascar. *Applied Geochemistry*. 2014. Vol. 41, p. 218-228. DOI: 10.1016/j.apgeochem.2013.12.013
22. Ichimura K., Sanematsu K., Kon Y. et al. REE redistributions during granite weathering: Implications for Ce anomaly as a proxy for paleoredox states. *American Mineralogist*. 2020. Vol. 105. N 6, p. 848-859. DOI: 10.2138/am-2020-7148
23. Belogub E.V., Shilovskikh V.V., Novoselov K.A. et al. Authigenic rhabdophane from brown iron ore of the oxidation zone of the Babaryk massive sulfide occurrence (South Urals): scanning electron microscope (SEM) and electron backscattered diffraction (EBSD) study. *European Journal of Mineralogy*. 2021. Vol. 33. Iss. 5, p. 605-620. DOI: 10.5194/ejm-33-605-2021
24. Craw D., Kerr G. Geochemistry and mineralogy of contrasting supergene gold alteration zones, southern New Zealand. *Applied Geochemistry*. 2017. Vol. 85. Part A, p. 19-34. DOI: 10.1016/j.apgeochem.2017.08.005

This is an open access article under the CC BY 4.0 license

25. Craw D., Lilly K. Gold nugget morphology and geochemical environments of nugget formation, southern New Zealand. *Ore Geology Reviews*. 2016. Vol. 79, p. 301-315. DOI: 10.1016/j.oregeorev.2016.06.001

26. Kalinin Y.A., Palyanova G.A., Naumov E.A. et al. Supergene remobilization of Au in Au-bearing regolith related to orogenic deposits: A case study from Kazakhstan. *Ore Geology Reviews*. 2019. Vol. 109, p. 358-369. DOI: 10.1016/j.oregeorev.2019.04.019

27. Kreiter V.M., Aristov V.V., Volynskii I.S. et al. Behavior of gold in the oxidation zone of gold-sulfide deposits. Moscow: Gosgeoltekhizdat, 1958, p. 268 (in Russian).

28. Palmer M., Ritchie T., Craw D. Contrasting evolution of beach gold on two sides of an active orogen, Southern Alps, New Zealand. *New Zealand Journal of Geology and Geophysics*. 2024. Vol. 68. Iss. 2, p. 260-281. DOI: 10.1080/00288306.2024.2314468

29. Stewart J., Kerr G., Prior D. et al. Low temperature recrystallisation of alluvial gold in paleoplacer deposits. *Ore Geology Reviews*. 2017. Vol. 88, p. 43-56. DOI: 10.1016/j.oregeorev.2017.04.020

30. Lalomov A.V., Chefranov R.M., Naumov V.A. et al. Typomorphic features of placer gold of Vagran cluster (the Northern Urals) and search indicators for primary bedrock gold deposits. *Ore Geology Reviews*. 2017. Vol. 85, p. 321-335. DOI: 10.1016/j.oregeorev.2016.06.018

31. Chapman R., Mortensen J.K., Murphy R. Compositional Signatures of Gold from Different Deposit Types in British Columbia, Canada. *Minerals*. 2023. Vol. 13. Iss. 8. N 1072. DOI: 10.3390/min13081072

32. Frimmel H.E., Gartz V.H. Witwatersrand gold particle chemistry matches model of metamorphosed, hydrothermally altered placer deposits. *Mineralium Deposita*. 1997. Vol. 32. Iss. 6, p. 523-530. DOI: 10.1007/s001260050119

33. Nevolko P.A., Kolpakov V.V., Nesterenko G.V., Fominykh P.A. Alluvial-Placer Gold of Northwestern Salair: Composition, Types, and Mineral Microinclusions. *Russian Geology and Geophysics.* 2019. Vol. 60. N 1, p. 67-85. DOI: 10.15372/RGG2019005

34. Fominykh P.A., Nevolko P.A., Svetlitskaya T.V., Kolpakov V.V. Native gold from the Kamenka-Barabanovsky and Kharuzovka alluvial placers (Northwest Salair Ridge, Western Siberia, Russia): Typomorphic features and possible bedrock sources. *Ore Geology Reviews*. 2020. Vol. 126. N 103781. DOI: 10.1016/j.oregeorev.2020.103781

35. Stepanov V.A., Melnikov A.V. Unja-Bomsky ore-placer node of Amur gold province. *Izvestiya Vysshikh Uchebnykh Zavedeniy. Geologiya i razvedka*. 2014. N 6, p. 26-31 (in Russian).

36. Nikolaeva L.A., Gavrilov A.M., Nekrasova A.N. et al. Native gold of ore and placer deposits of Russia: Atlas. Moscow: Akvarel, 2015, p. 200 (in Russian).

37. Nikiforova Z.S., Tolstov A.V. Gold-Bearing Placer Assemblages in the East of the Siberian Platform: Origin and Prospects. *Geology of Ore Deposits.* 2022. Vol. 64. N 1-2, p. 1-25. DOI: 10.1134/S1075701522020027

38. Chapman R.J., Mortensen J.K., Allan M.M. et al. A New Approach to Characterizing Deposit Type Using Mineral Inclusion Assemblages in Gold Particles. *Economic Geology*. 2022. Vol. 117. N 2, p. 361-381. DOI: 10.5382/econgeo.4863

39. Afifi A.M., Kelly W.C., Essene E.J. Phase relations among tellurides, sulfides, and oxides; Pt. II. Applications to telluride-bearing ore deposits. *Economic Geology*. 1988. Vol. 83. N 2, p. 395-404. DOI: 10.2113/gsecongeo.83.2.395

40. Anikina E.V., Alekseev A.V. Mineral-geochemical characteristic of gold-palladium mineralization in the Volkov gabbro massif (Platiniferous Urals Belt). *Litosfera.* 2010. N 5, p. 75-100 (in Russian).

41. Murzin V.V., Palyanova G.A., Anikina E.V., Moloshag V.P. Mineralogy of noble metals (Au, Ag, Pd, Pt) in Volkovskoe Cu-Fe-Ti-V deposit (Middle Urals, Russia). *Lithosphere.* 2021. Vol. 21. N 5, p. 643-659 (in Russian). DOI: 10.24930/1681-9004-2021-21-5-643-659

42. Stepanov S.Yu., Palamarchuk R.S., Puchkov V.N., Petrov S.V. Features of the Chemical Composition of Gold Minerals from Gabbro Massifs in the Uralian Platinum Belt, Russia. *Doklady Earth Sciences.* 2022. Vol. 507. Iss. 2, p. 1057-1063. DOI: 10.1134/S1028334X22600979

43. Mikhailov V.V., Stepanov S.Yu., Kozlov A.V. et al. New Copper–Precious Metal Occurrence in Gabbro of the Serebryansky Kamen Massif, Ural Platinum Belt, Northern Urals. *Geology of Ore Deposits.* 2021. Vol. 63. N 6, p. 528-555. DOI: 10.1134/S1075701521060040

***Authors*: Aleksandr K. Kozin,** *Junior Researcher* (*South Ural Scientific Centre Mineralogy and Environmental Geology of the Ural branch RAS, Miass, Russia*), *kozin@mineralogy.ru, https://orcid.org/0009-0004-8197-4284*, **Sergei Yu. Stepanov,** *Candidate of Geological and Mineralogical Sciences, Senior Researcher* (*South Ural Scientific Centre Mineralogy and Environmental Geology of the Ural branch RAS, Miass, Russia*), **Roman S. Palamarchuk,** *Candidate of Geological and Mineralogical Sciences, Researcher* (*South Ural Scientific Centre Mineralogy and Environmental Geology of the Ural branch RAS, Miass, Russia*), *https://orcid.org/0000-0001-5422-2627*, **Valeriya S. Zhdanova,** *Junior Researcher* (*South Ural Scientific Centre Mineralogy and Environmental Geology of the Ural branch RAS, Miass, Russia*), *https://orcid.org/0009-0000-6895-6170*, **Natalya S. Vlasenko,** *Engineer* (*Saint Petersburg State University, Saint Petersburg, Russia*), *https://orcid.org/0000-0002-5548-9478*.

The authors declare no conflict of interests.

This is an open access article under the CC BY 4.0 license

ISSN 2411-3336; e-ISSN 2541-9404

JOURNAL OF MINING INSTITUTE
Zapiski Gornogo instituta
Journal homepage: pmi.spmi.ru

Research article Geology

Radon monitoring possibilities in short-term earthquake prediction

Irina A. Kozlova✉, Sergei V. Biryulin, Anatolii K. Yurkov
Institute of Geophysics, Ural Branch of the RAS, Yekaterinburg, Russia

***How to cite this article*:** Kozlova I.A., Biryulin S.V., Yurkov A.K. Radon monitoring possibilities in short-term earthquake prediction. Journal of Mining Institute. 2026. Vol. 280, p. 122-130.

Abstract
Analysis of the results of thirteen-year radon studies in the Southern Kuril Islands allowed us to establish a reliable relationship between tectonic events and anomalous concentrations of observed radon (VRA) extracted from the near-surface layer. Radon anomalies were compared with earthquakes of magnitude higher than 4 from the United States Geological Survey (USGS) catalog, which occurred within a radius of 500 km from the observation point. It was possible to divide the epicenters of tectonic events into groups that differ in distance relative to the monitoring point. Earthquakes always occur after the maximum of the preceding radon anomaly. Events of the first group belong to the near zone and are located within a radius of less than 130 km from the radon monitoring point. Events of the second group belong to the far zone and are located at a distance of more than 180 km from the radon monitoring point. The proposed method for determining the time and place of a tectonic event is the result of research. The proposed method is based on measuring the concentration of soil radon at four spatially separated points in the corners of a square with a distance between neighboring points of 180 km, which corresponds to the distance of the far zone. If an abnormal concentration of volume radon activity is detected at one of the observation stations, the presence of radon anomalies at other points is checked. If a radon anomaly is detected at least at one of the other observation points, a tectonic event is expected within six days from the moment of the maximum radon anomaly in the spatial boundaries limited to 130 km relative to the observation point where the first VRA anomaly was recorded. The proposed method is applicable for protecting specific objects in conditions of increased seismic activity. The effectiveness of the method is determined by the fulfillment of the provisions of the developed measurement methodology.

Keywords
monitoring; radon; earthquake; precursors; short-term prediction

Funding
The work was carried out according to the State assignment of IGF UB RAS № 125032604464-7.

Received: 24.02.2026 ***Accepted: 25.06.2026*** ***Online: 02.09.2026*** ***Published: 10.09.2026***

Introduction

Currently, there is a tendency to abandon the prediction of earthquakes, since only the exact location (meters), time (minutes), and magnitude (points) can be considered a prediction. In some cases, the researchers did not completely abandon the prediction, but displaced their focus to estimating the probability of an event [1, 2]. In Russia, there is a trend in the development of seismic safety, including seismic zoning, the introduction of innovative technologies for earthquake-resistant construction and early warning systems.

Nevertheless, scientific interest in predicting and searching for earthquake precursors remains relevant [3-5]. Today, a particularly important task is the short-term prediction [6-8], which allows us to take prompt response measures to reduce human and economic losses.

Changes in the stress-strain state of rocks during earthquake preparation are among the most realistic physical mechanisms that can be used for short-term prediction [9-11]. The underground

This is an open access article under the CC BY 4.0 license

atmosphere and hydrosphere are subject to changes in the stress-strain state of the geological environment.

The state of the underground atmosphere in a rock mass can be controlled by radon isotopes. They have a continuous source of generation, are fairly easy to register, and do not have a cumulative effect, which increases the sensitivity of measurements. It is preferable to use the isotope Rn-222, because it has a source of generation contained in almost all rocks.

Many researchers point to possible important relationships between changes in radon concentrations in soil, groundwater, atmosphere and earthquakes [12-14]. Many studies have been conducted on measuring radon before earthquakes in soil [15-17], air [18-20], and water [21-23].

S.Okabe conducted the first studies of radon gas and seismic activity in 1956 [24]. He found a positive relationship between changes in atmospheric radon concentrations near the Earth's surface and regional seismic activity in Japan. Thus, he pointed to radon as a new indicator of earthquakes.

In the work performed by V.I.Ulomov [25], significant changes in the radon concentration in borehole water were noted before the Tashkent earthquake of April 26, 1966. This is the first time that radon anomalies in borehole waters can serve as an indicator of earthquakes.

A number of studies have shown that the concentration of radon in soil, water, and atmosphere varies depending on movements in the Earth's crust. For example, in the Gulf of Corinth (Greece), the level of radon in the atmosphere sharply decreased before the earthquake [26]. In the case of the Izu-Oshima-Kinkai earthquake (January 14, 1978), the concentration of radon in groundwater began to decline three months before the event and plummeted five days before it. On the contrary, before the Kobe earthquake (1995), the concentration of radon in underground waters increased and peaked nine days before the disaster [27].

Scientists from Irkutsk analyzed the observed variations in subsurface radon and time variations in atmospheric pressure. Measurements were carried out in loose sediments at three stations in the Baikal Region [28]. During the observation period, three significant earthquakes were recorded. The conducted emanation monitoring made it possible to determine the effect of changes in atmospheric pressure on the release of subsurface radon [28].

From 1997 to 2016, subsurface radon measurements were performed on the Kamchatka Peninsula and its probable relationships with tectonic events were identified [29]. Researchers have identified medium-term signs of preparation for a strong earthquake in the Kamchatka seismogenic zone [30].

Monitoring measurements in the underground atmosphere and hydrosphere, in particular soil radon, make a significant contribution to understanding the physical processes associated with earthquake preparation.

The aim of the study is to develop a new method for determining the time and location of an earthquake based on tracking changes in the stress-strain state of rocks based on measurements of soil radon in the underground atmosphere. To achieve this goal, the following tasks were performed: development of a measurement methodology; development of a method for detecting anomalies of volume radon activity (VRA); comparison of VRA anomalies with subsequent earthquakes; study of the behavior of VRA at various epicentral distances from the monitoring station.

Methods

In 2011-2024, radon monitoring was carried out on Kunashir Island in the mode of forced delivery (forced convection [31]) of soil air to the detector. Geodynamically, the selected area for research belongs to the subduction zone. From the point of view of plate tectonics, it is located in the junction zone of the Pacific plate and Okhotsk Sea plate. The rate of subduction of the Pacific plate under the Okhotsk Sea plate is about 8 cm per year. The monitoring station is located 150-200 km west of the ocean trough. This circumstance limits the registration of weak earthquakes in variations in the volume radon activity, which simplifies the identification of anomalies and events. Geologically, the

This is an open access article under the CC BY 4.0 license

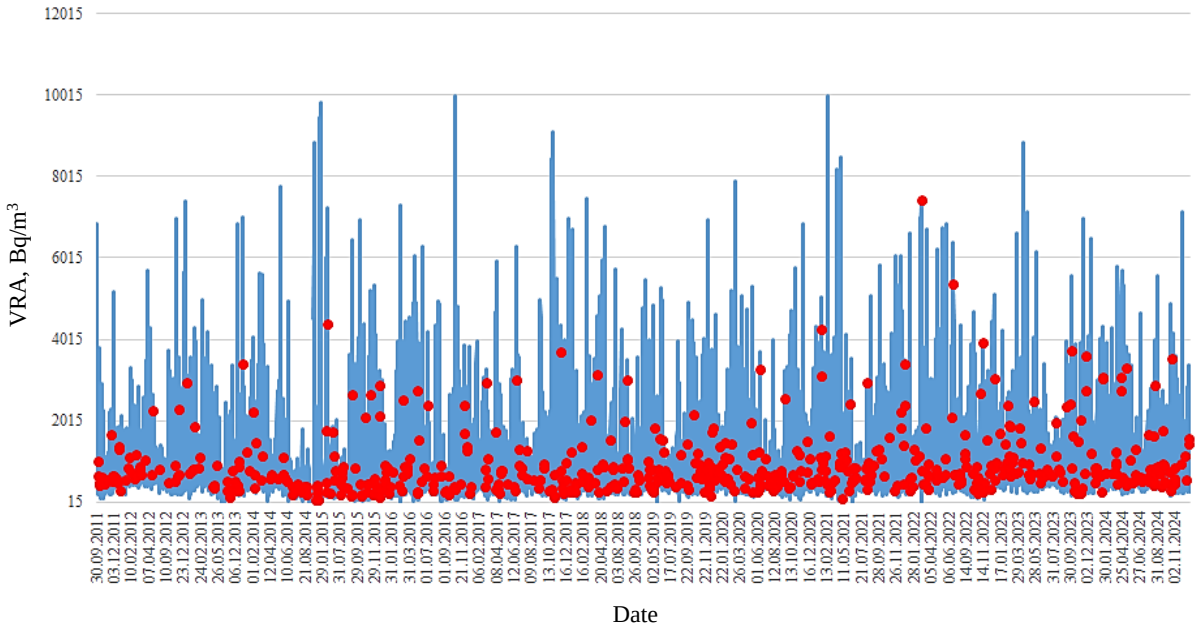


Fig.1. Variations in volume radon activity and seismic events for 2011-2024

station is located on an ancient lava flow of andesite-basalt composition, formed after one of the eruptions of the Mendeleev volcano. Rocks of this composition have elastic properties, which is a condition for obtaining informative data on variations in the volume radon activity. Measurements at this station are optimal based on the number of observed earthquakes. If a small number of earthquakes occur in the observation region, it is impossible to obtain statistically reliable patterns. Too many numbers make it difficult to compare anomalies and events. The measured velocities of satellite positioning reference points changed after the Simushir earthquakes of 2006-2007. The middle islands of the Kuril Ridge move at a rate of 1.4 cm per year, the southern ones up to 3.3 cm. This situation may indicate that there is no plate engagement in the middle part of the ridge, and stresses are accumulating in the southern part, which may lead to earthquakes. Moreover, there have been no events with a magnitude greater than 8 in the Southern Kuril Islands region for more than 30 years, and the average interval between earthquakes with a magnitude greater than 8 is about 10 years [32].

In Fig.1 presents a multi-year series of volume radon activity and seismic events from from the United States Geological Survey (USGS) catalog. As can be seen from Fig.1, the data is not suitable for processing, analysis and interpretation according to the method developed by the authors. At this scale, it is impossible to identify anomalies and compare them with subsequent earthquakes. The authors developed a method for identifying anomalies of radon volume activity and comparing them with earthquake-causing ones [31].

I.P.Dobrovolsky proposed a deformation model for the manifestation of tectonic earthquake precursors [33]. This model is used to estimate the precursors occurrence zone for the Southern Kuril Islands. The ratio of the earthquake magnitude M to the logarithm of the distance from the monitoring station to the epicenter of the tectonic event $R \geq 2.5$ was used. The ratio is applicable to the assessment of the manifestation zone of precursor effects associated with variations in porosity and permeability of the geological environment. The ratio of the earthquake magnitude to the logarithm of the distance from the monitoring station to the event is conventionally called a geodynamic criterion. During the observation period, the maximum magnitude was 7. This value was used to calculate the radius of occurrence of precursor effects, which was 500 km (the distance from the monitoring point on Kunashir Island to the epicenters of tectonic events) [31]. Retrospective analysis of earthquakes with a magnitude greater than 4 with a geodynamic criterion K higher than 2,5 was conducted (Fig.2, 3).

This is an open access article under the CC BY 4.0 license

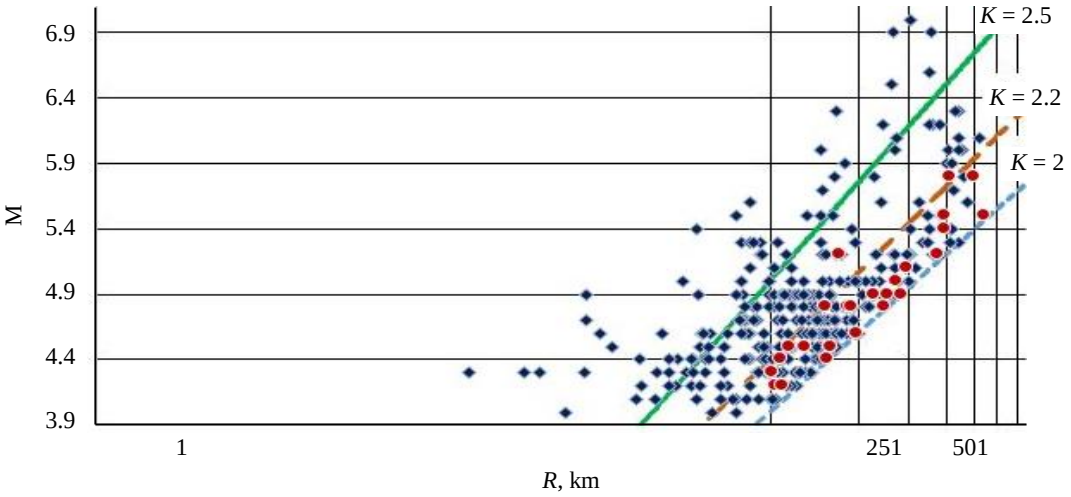


Fig.2. Earthquakes in the VRA field from 2011 to 2024. Rhombuses indicate events that were preceded by an VRA anomaly, circles indicate events that were not reflected in the VRA anomaly curves. The lines correspond to different M/log*R* ratios

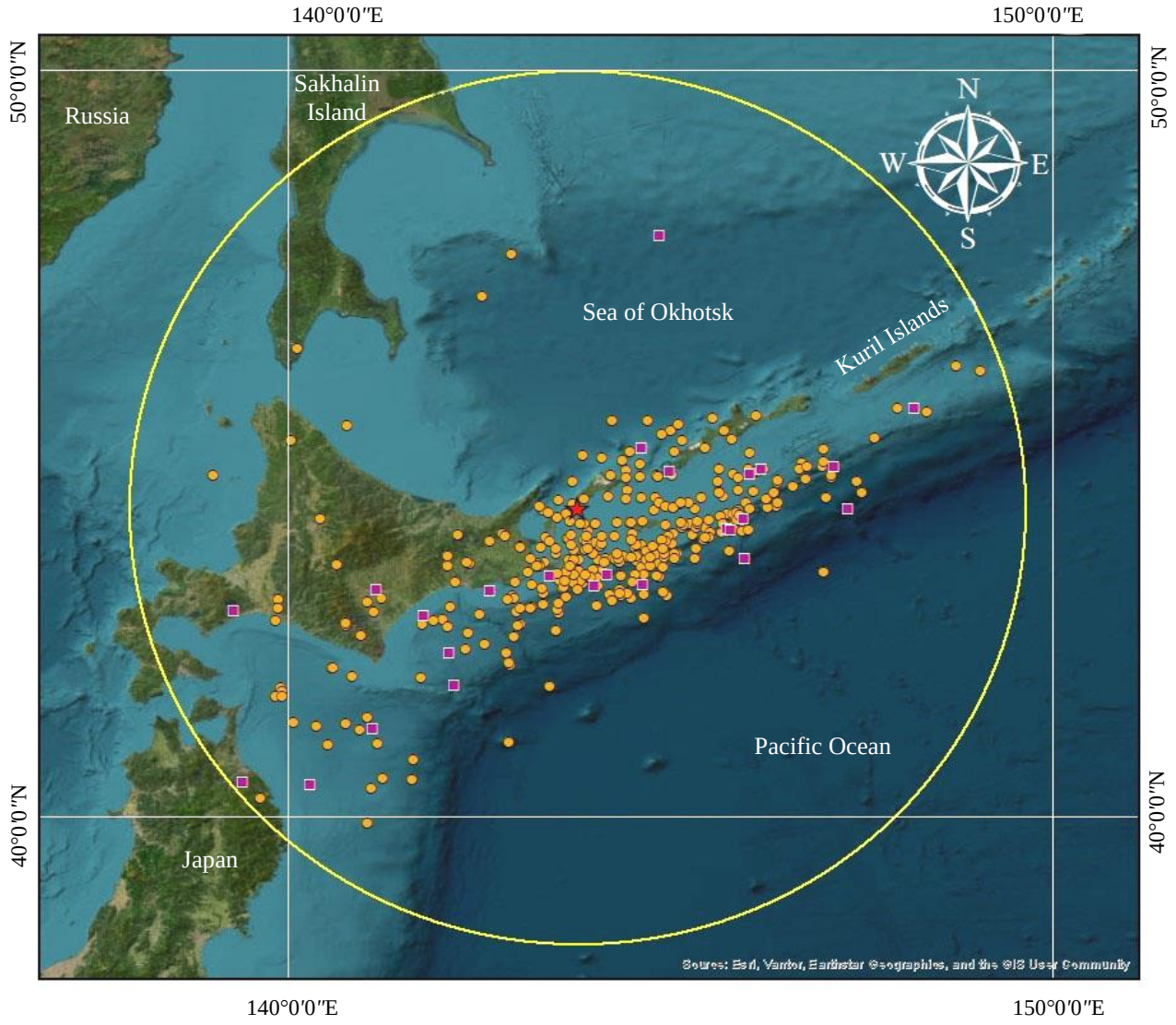


Fig.3. Map of earthquakes in the VRA field for the observation period from 2011 to 2024. The star indicates the observation station. Orange circles indicate events that were preceded by an VRA anomaly; purple squares indicate events that were not reflected in the VRA anomaly curves. The circle corresponds to a radius of 500 km from the monitoring station

This is an open access article under the CC BY 4.0 license

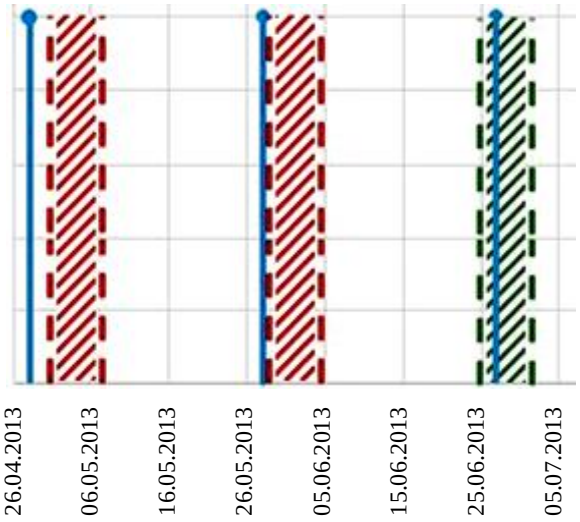


Fig.4. Example of a comparison of randomly generated earthquakes and seven-day windows of soil radon anomalies. A line with a dot at the top shows the generated moment of the earthquake, a shaded column shows the generated time interval during which the anomaly lasted

A large number of earthquakes did not correspond to $K \geq 2.5$, but were reflected in the in the field of volume radon activity. To take into account all anomalies of soil radon and considered tectonic events, it was decided to apply a geodynamic criterion higher than 2 for the geological and tectonic conditions of the Southern Kuril Islands. A total of 344 earthquakes with a magnitude higher than 4 occurred during this period, and 319 of them were reflected in the VRA curves (Fig.2, 3).

An important issue is to check whether there is a causal relationship between the precursor and the earthquake. For this purpose, statistical processing of the selected VRA anomalies and subsequent earthquakes was performed.

Random sequences of earthquakes were generated over a nine-year period, corresponding to the Poisson distribution law. The real parameters of successive earthquakes (mathematical expectation) from the catalog for the same period are taken as a basis. All generated seismic events were located within a radius of 500 km from the monitoring station and their magnitude was assumed to be greater than or equal to 4. Earthquake sequences with $K \geq 2$ and $K \geq 2.2$ were considered.

Random sequences of anomalies are also generated according to the Poisson distribution law. The mathematical expectation of the intervals between the selected VRA anomalies over a nine-year period is taken as a basis. The anomaly window is taken as the average value among all selected values between the anomaly maximum and its end – 7 days (Fig.4). Sequences of anomalies identified before earthquakes with criteria $K \geq 2$ and $K \geq 2.2$ were considered.

The generated random sequences of earthquakes and anomalies were compared. If the earthquake fell within the seven-day anomaly window, it was assumed that it was preceded by an anomaly of soil radon.

As a result of calculations, the experimental probability for earthquakes with $K \geq 2$ is 0.89, while the theoretical probability is 0.35. For earthquakes with $K \geq 2.2$, the experimental probability is 0.98, while the theoretical probability is 0.20. For both $K \geq 2$ and $K \geq 2.2$, the theoretical probability does not correspond to the experimentally obtained values. For earthquakes with $K \geq 2$ and $K \geq 2.2$ and radon anomalies, the theoretical probability is 3 and 5 times less than the experimental probability, respectively. This may indicate a causal relationship between anomalies in radon volume activity and earthquakes.

Results and discussion

It is established that seismic events occur after the maximum anomaly of the volume radon activity, and near and far earthquakes (relative to the observation point) are reflected in different parts of the VRA curve. In the time interval from the radon anomaly maximum to six days, tectonic earthquakes of the far zone are manifested. For the geological and tectonic conditions of the South Kuril geodynamic polygon, the radius of the far zone (extension zone) was more than 180 km. In the time interval from the radon anomaly end to 28 days near zone events appear. Near zone events are reflected in the VRA curve after the anomaly reaches the background level in the time interval up to 28 days. For the conditions of the South Kuril geodynamic polygon (subduction zone), the radius of the near zone (compression zone) was less than 130 km [34].

The behavior of the crack-pore space when the stress state of the massif changes directly at the monitoring point is the physical basis for reflecting the earthquake preparation process in the behavior of soil radon, taking into account that the observed radon anomalies are short and high-amplitude [35].

This is an open access article under the CC BY 4.0 license

In the near zone, radon anomalies are formed due to compression, in which, due to a decrease in the volume of free space, radon is squeezed out until cracks and pores are completely closed, up to the occurrence of a main break. A different mechanism of formation is proposed for far zone anomalies. The geological environment returns to its original state after the beginning of destruction at the epicenter of the event, cracks and pores narrow, as a result of which radon is partially released.

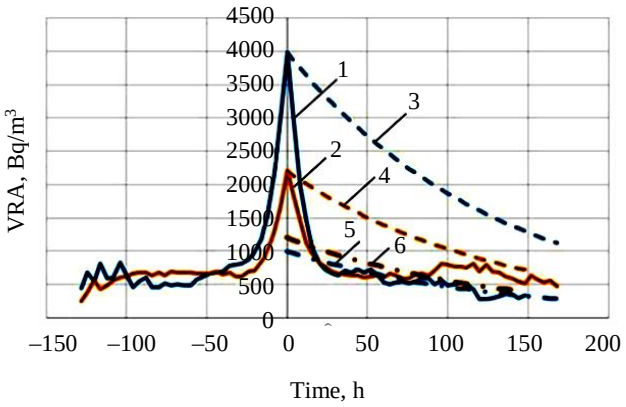


Fig.5. Averaged VRA anomalies in the compression and extension zones and radon decay curves. Solid lines – averaged values of VRA anomalies before the events of the near (1) and far (2) zones; dashed lines – radon decay curves for the maximum of the near (3) and far (4) zones; dash-dotted lines – approximation of VRA values after the completion of the anomaly, radon decay curve for the near (5) and far (6) zones

In Fig.5 shows the average anomalies of volume radon activity for the measurement period 2011-2024. When studying the decay of Rn, a regularity is observed between the initial and final amounts of the initial substance, which is approximated by the exponential law. Proportional coupling is the basis of the law of radioactive decay. The average maximum of the radon anomaly for each zone is taken as the starting point. For each measurement point, the average value for all anomalies was calculated separately for anomalies preceding near zone earthquakes (line 1, Fig.5) and far zone earthquakes (line 2, Fig.5). The average anomalies of volume soil radon activity for the near and far zones are plotted with radon decay curves (curves 3, 4, Fig.5). Curves 5 and 6 in Fig.5 is an approximation of the VRA curves after the end of the radon decay curve anomaly.

Reduction of the anomalous value of volume radon activity as for the near zone (line 1, Fig.5), and for the far zone (line 2, Fig.5) occurs not only due to the decay of radon, which was released. The flow of soil radon from the pore space is stopped. In both the first and second cases, the radon curve (lines 1, 2, Fig.5) does not agree with the law of radioactive decay, starting from the maximum value of radon concentration (curves 3, 4, Fig.5). In the case of the near zone, the VRA curve is approximated by the radon decay curve (curve 5, Fig.5) after the end of the radon anomaly at the output to the background values. In the case of the far zone, the VRA curve after the end of the anomaly returns to the initial values before the increase and is not approximated by the decay curve (curve 6, Fig.5). This is due to the fact that radon continues to be squeezed out of the pores and cracks. Thus, the described mechanism of formation of radon anomalies is justified.

Based on the described mechanism of radon anomalies formation, a method for short-term prediction of the earthquakes time and location is formulated. The key component of the proposed method is the change in the porosity and permeability of rocks under the influence of tensile and compressive stresses. Stretching in one area leads to compression in another. Accordingly, the removal of compressive stresses during destructive processes in the source at the time of an earthquake or shortly before it will cause the removal (for some time) of tensile stresses outside the source (in the far zone). This will lead to the restoration of permeability to the previous level, i.e. the pore volume will decrease and radon will be displaced to the adjacent areas of the pore space. When monitoring in the far zone (extension zone), a tectonic event is reflected on the VRA curve in the time interval after the anomaly maximum of up to six days. The radon anomaly that occurred in the far zone is caused by the process of destruction in the earthquake source. Monitoring of radon variations in the far zone, taking into account that the destructive process in the focus of a tectonic event leads to the appearance of an anomaly, will allow predicting an earthquake after the maximum of the radon anomaly [36].

This is an open access article under the CC BY 4.0 license

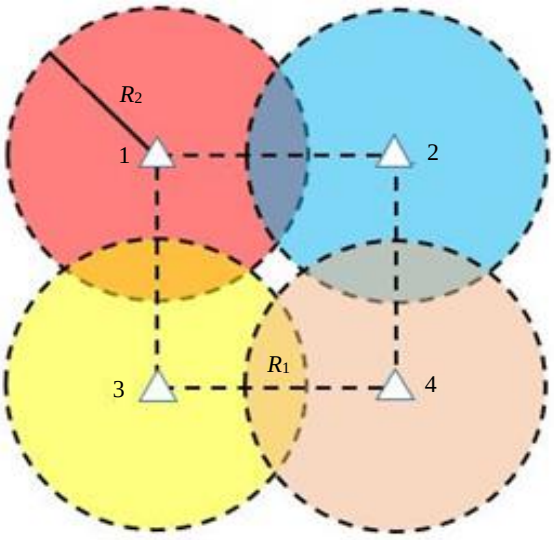


Fig.6. Layout of volume radon activity observation points

The proposed method consists in monitoring the volume soil radon activity in the mode of forced delivery of soil air to the detector, at least in four monitoring points in the vicinity of the controlled object, with a distance between neighboring points equal to the radius of the far zone R_1 (Fig.6). If an anomaly is detected at one of the observation points, anomalies are monitored at the other stations. If a radon anomaly is detected at least at one of the other observation points, a tectonic event is expected within six days from the moment of the radon anomaly maximum in the spatial borders limited by the radius of the near zone R_2 relative to the observation point where the first VRA anomaly was recorded [36].

For the practical implementation of the proposed method, it is necessary to create a network of observation points for monitoring soil radon in seismically active areas, for example, in the North Caucasus and in the Crimea. These regions are of great economic importance and have a high population density. Currently, radon monitoring sites are located in different regions with different geodynamic activity – the Kuril Islands, Sakhalin Island, Eastern Sayan (Republic of Tyva), the Urals, the Republic of Kazakhstan, and the Kyrgyz Republic. The monitoring results confirm the patterns of earthquake reflection in the radon field obtained for the subduction zone. The conducted studies show that in order to obtain standard data, it is necessary to strictly observe the mode of measuring soil radon, taking into account geological and tectonic conditions.

Conclusion

Despite the skeptical attitude towards predicting tectonic events, each new catastrophic earthquake again makes the problem relevant. To study the process of earthquake preparation, new approaches are needed based on methods that have a real physical justification. Monitoring of soil radon meets this condition and makes it possible to obtain statistically significant observation series. The proposed method for determining the time and location of an earthquake allows us to estimate the quantitative characteristics of the expected earthquake time relative to the characteristic zones of manifestation on the radon curve and determine the position of the tectonic event epicenter in space. After successful application in real conditions, the proposed method is highly likely to prevent tectonic events at controlled objects in regions with increased seismic hazard.

REFERENCES

1. Neely J.S., Salditch L., Spencer B.D., Stein S. A More Realistic Earthquake Probability Model Using Long-Term Fault Memory. *Bulletin of the Seismological Society of America*. 2023. Vol. 113. N 2, p. 843-855. DOI: 10.1785/0120220083
2. Zhonghu Jiao, Xinjian Shan. A Bayesian Approach for Forecasting the Probability of Large Earthquakes Using Thermal Anomalies from Satellite Observations. *Remote Sensing*. 2024. Vol. 16. Iss. 9. N 1542. DOI: 10.3390/rs16091542
3. Szakács A. Precursor-Based Earthquake Prediction Research: Proposal for a Paradigm-Shifting Strategy. *Frontiers in Earth Science*. 2021. Vol. 8. N 548398. DOI: 10.3389/feart.2020.548398
4. Smits G. Review of *Predicting Disasters: Earthquakes, Scientists, and Uncertainty in Modern Japan*, by Kerry Smith. *Monumenta Nipponica*. 2024. Vol. 79. N 2, p. 310-315. DOI: 10.1353/mni.2024.a952790
5. Singh R., Roy B. Scalable earthquake magnitude prediction using spatio-temporal data and model versioning. *Scientific Reports*. 2025. Vol. 15. N 19265. DOI: 10.1038/s41598-025-00804-x

This is an open access article under the CC BY 4.0 license

6. Nandan S., Kamer Y., Ouillon G. et al. Global models for short-term earthquake forecasting and predictive skill assessment. *The European Physical Journal Special Topics*. 2021. Vol. 230. Iss. 1, p. 425-449. DOI: 10.1140/epjst/e2020-000259-3

7. Fujinawa Y., Noda Y., Miyagawa M. et al. A Practical Method for Short-term Earthquake Prediction Using Multiple High-frequency Tremor Events. *Asian Journal of Physical and Chemical Sciences*. 2022. Vol. 10. Iss. 3, p. 15-24. DOI: 10.9734/ajopacs/2022/v10i3182

8. Huaizhong Yu, Rui Yan, Shiguang Deng et al. Improved medium-to-short-term earthquake predictions in China in 2022. *Geomatics, Natural Hazards and Risk*. 2024. Vol. 15. Iss. 1. N 2350482. DOI: 10.1080/19475705.2024.2350482

9. Verma U.P., Sinha M.N., Dutta P.K., Mullick S. Stress-Strain Relationship: Postulated Concept to Understand Genetic Mechanism Associated with a Seismic Event. Computational Optimization Techniques and Applications. IntechOpen, 2021. DOI: 10.5772/intechopen.97377

10. Guofu Luo, Fenghe Ding, Yingcai Xu et al. Strain fields of *Ms* > 6.0 earthquakes in Menyuan, Qinghai, China. *Frontiers in Earth Science*. 2023. Vol. 11. N 1152348. DOI: 10.3389/feart.2023.1152348

11. Orlecka-Sikora B., Ciechowska H., Zhenyu Zhang, Zhiming Liang. Seismic Strain Metrics for Tracking Fault Damage Evolution and Rupture Potential in Anthropogenic Seismicity. *Rock Mechanics and Rock Engineering*. 2025. Vol. 58. Iss. 9, p. 11061-11082. DOI: 10.1007/s00603-025-04688-1

12. Tarakçi M., Harmanşah C., Saç M.M., İçhedef M. Investigation of the relationships between seismic activities and radon level in Western Turkey. *Applied Radiation and Isotopes*. 2014. Vol. 83. Part A, p. 12-17. DOI: 10.1016/j.apradiso.2013.10.008

13. Petraki E., Nikolopoulos D., Panagiotaras D. et al. Radon-222: A Potential Short-Term Earthquake Precursor. *Journal of Earth Science & Climatic Change*. 2015. Vol. 6. Iss. 6. N 282. DOI: 10.4172/2157-7617.1000282

14. Khan M.A., Khattak N.U., Hanif M. Radon emission along faults: a case study from district Karak, Sub-Himalayas, Pakistan. *Journal of Radioanalytical and Nuclear Chemistry*. 2022. Vol. 331. Iss. 5, p. 1995-2003. DOI: 10.1007/s10967-022-08283-4

15. Ghosh D., Deb A., Sengupta R. Anomalous radon emission as precursor of earthquake. *Journal of Applied Geophysics*. 2009. Vol. 69. Iss. 2, p. 67-81. DOI: 10.1016/j.jappgeo.2009.06.001

16. Stoulos S., Papadimitriou E., Karakostas V. et al. Radon signals in soil gas associated with earthquake occurrence in Greece: review and perspective. *Journal of Radioanalytical and Nuclear Chemistry*. 2024. Vol. 333. Iss. 12, p. 6107-6120. DOI: 10.1007/s10967-024-09710-4

17. İçhedef M., Günay O., Yalçın C. et al. Assessment of soil gas radon variations in terms of seismicity in Yalova, Türkiye. *Journal of Radioanalytical and Nuclear Chemistry*. 2025. Vol. 334. Iss. 9, p. 6829-6836. DOI: 10.1007/s10967-025-10169-0

18. Kim J.W., Joo H.Y., Kim R., Moon J.H. Investigation of the relationship between earthquakes and indoor radon concentrations at a building in Gyeongju, Korea. *Nuclear Engineering and Technology*. 2018. Vol. 50. Iss. 3, p. 512-518. DOI: 10.1016/j.net.2017.12.010

19. Tsuchiya M., Nagahama H., Muto J. et al. Detection of atmospheric radon concentration anomalies and their potential for earthquake prediction using Random Forest analysis. *Scientific Reports*. 2024. Vol. 14. N 11626. DOI: 10.1038/s41598-024-61887-6

20. Sahoo B.K., Sapra B.K., Khan A. et al. A persistent radon anomaly signal preceding the destructive 7.7 M_w earthquake in Myanmar on March 28, 2025. *Scientific Reports*. 2025. Vol. 15. N 25447. DOI: 10.1038/s41598-025-10632-8

21. Tsunomori F., Tanaka H. Anomalous change of groundwater radon concentration monitored at Nakaizu well in 2011. *Radiation Measurements*. 2014. Vol. 60, p. 35-41. DOI: 10.1016/j.radmeas.2013.11.006

22. Abbas S.Q., Khan J., Riaz M.T. et al. Radon concentration in spring water as an indicator of seismic activity: a case study of the Muzaffarabad Fault in Pakistan. *Environmental Monitoring and Assessment*. 2024. Vol. 196. Iss. 1. N 41. DOI: 10.1007/s10661-023-12235-0

23. Kim J., Kim H., Kaown D, Lee K.-K. Thoron, radon and microbial community as supportive indicators of seismic activity in groundwater. *Scientific Reports*. 2024. Vol. 14. N 25955. DOI: 10.1038/s41598-024-77011-7

24. Okabe S. Time variation of the atmospheric Radon-content near the ground surface with relation to some geophysical phenomena. *Memoirs of the College of Science, University of Kyoto, Series A*. 1956. Vol. 28. N 2, p. 99-115.

25. Ulomov V.I. On the way to earthquakes prediction. *Zemlya i Vselennaya*. 1968. N 3, p. 23-30 (in Russian).

26. Karastathis V.K., Eleftheriou G., Kafatos M. et al. Observations on the stress related variations of soil radon concentration in the Gulf of Corinth, Greece. *Scientific Reports*. 2022. Vol. 12. N 5442. DOI: 10.1038/s41598-022-09441-0

27. Wakita H., Nakamura Y., Notsu K. et al. Radon Anomaly: A Possible Precursor of the 1978 Izu-Oshima-kinkai Earthquake. *Science*. 1980. Vol. 207. Iss. 4433, p. 882-883. DOI: 10.1126/science.207.4433.882

28. Seminsky K.Z., Bobrov A.A. Irregularities in the Relationship of Variations in the Radon Volume Activity and Atmospheric Pressure during Seismic Activation (by the Example of the Baikal Region). *Doklady Earth Sciences.* 2023. Vol. 510. N 1, p. 312-316. DOI: 10.1134/S1028334X23600160

29. Firstov P.P., Makarov E.O., Glukhova I.P. et al. Search for predictive anomalies of strong earthquakes according to monitoring of subsoil gases at Petropavlovsk-Kamchatsky geodynamic test site. *Geosystems of Transition Zones.* 2018. Vol. 2. N 1, p. 16-32 (in Russian). DOI: 10.30730/2541-8912.2018.2.1.016-032

30. Firstov P.P., Kopylova G.N., Solomatin A.Yu., Serafimova Yu.K. Strong earthquake forecast near the Kamchatka peninsula. *Bulletin of Kamchatka Regional Association* "*Educational-Scientific Center*". *Earth Sciences.* 2016. Iss. 32. N 4, p. 106-114 (in Russian).

31. Kozlova I.A., Biryulin S.V., Yurkov A.K. Occurrence of anomalies in soil radon volume activity before tectonic earthquakes. *Lithosphere.* 2021. Vol. 21. N 5, p. 724-733 (in Russian). DOI: 10.24930/1681-9004-2021-21-5-724-733

32. Prytkov A.S., Vasilenko N.F., Frolov D.I. Recent Geodynamics of the Kuril Subduction Zone. *Russian Journal of Pacific Geology.* 2017. Vol. 11, N 1, p. 19-24. DOI: 10.1134/S1819714017010067

33. Dobrovolskii I.P. Mathematical theory of preparation and prediction of tectonic earthquakes. Moscow: Fizmatlit, 2009, p. 240 (in Russian).

This is an open access article under the CC BY 4.0 license

34. Kozlova I.A., Yurkov A.K., Biryulin S.V. Feasibility of application of soil radon activity concentration variations in studying geodynamic processes. *Russian Geology and Geophysics.* 2025. Vol. 66. N 6, p. 703-711. DOI: 10.2113/RGG20244805

35. Outkin V.I. Radon and the problem of tectonic earthquakes. *Soros Educational Journal.* 2000. Vol. 6. N 12, p. 64-70 (in Russian).

36. Kozlova I.A., Biryulin S.V., Yurkov A.K. Patent N 2839307 RF. Method of determining time and place of earthquake. Publ. 26.05.2025. Bul. N 15 (in Russian).

Authors: **Irina A. Kozlova,** *Candidate of Geological and Mineralogical Sciences, Director* (*Institute of Geophysics, Ural Branch of the RAS, Yekaterinburg, Russia*), *ikozlova75@mail.ru*, *https://orcid.org/0000-0002-0281-9218*, **Sergei V. Biryulin,** *Candidate of Geological and Mineralogical Sciences, Senior Researcher* (*Institute of Geophysics, Ural Branch of the RAS, Yekaterinburg, Russia*), *https://orcid.org/0000-0003-4811-9185*, **Anatolii K. Yurkov,** *Candidate of Geological and Mineralogical Sciences, Leading Researcher* (*Institute of Geophysics, Ural Branch of the RAS, Yekaterinburg, Russia*), *https://orcid.org/0000-0002-6790-0340*.

The authors declare no conflict of interests.

This is an open access article under the CC BY 4.0 license

ISSN 2411-3336; e-ISSN 2541-9404

JOURNAL OF MINING INSTITUTE

Zapiski Gornogo instituta

Journal homepage: pmi.spmi.ru

Research article Geology

Microfragments of the Saratov meteorite in the magnetic fraction of modern soils: search and identification

Aleksei V. Ivanov[1,2,3], **Ruslan R. Gabdullin**[1,4], **Sofya I. Merenkova**[5,6]✉, **Aleksei A. Samsonov**[1], **Alvina V. Chistyakova**[6], **Dmitrii F. Ayatskov**[7], **Mikhail A. Vinnik**[1], **Evgenii Yu. Pogozhev**[1], **Afanasii E. Telnov**[1], **Yurii A. Churikov**[1], **Nikita N. Anisimov**[1], **Natalya V. Badulina**[1]

[1] *Lomonosov Moscow State University, Moscow, Russia*
[2] *Institute of Geography, RAS, Moscow, Russia*
[3] *Tambov State Technical University, Tambov, Russia*
[4] *Vernadsky Institute of Geochemistry and Analytical Chemistry of the RAS, Moscow, Russia*
[5] *Shirshov Institute of Oceanology of RAS, Moscow, Russia*
[6] *Schmidt Institute of Physics of the Earth of the RAS, Moscow, Russia*
[7] *Center for the Development of the Saratov Agglomeration and Industrial Parks, Saratov, Russia*

***How to cite this article*:** Ivanov A.V., Gabdullin R.R., Merenkova S.I., Samsonov A.A., Chistyakova A.V., Ayatskov D.F., Vinnik M.A., Pogozhev E.Yu., Telnov A.E., Churikov Yu.A., Anisimov N.N., Badulina N.V. Microfragments of the Saratov meteorite in the magnetic fraction of modern soils: search and identification. Journal of Mining Institute. 2026. Vol. 280, p. 131-144.

Abstract

The paper addresses the problem of identifying microscopic traces of meteoritic material in soils more than 100 years after a fall. The area of the Saratov meteorite shower of October 6, 1918 was selected as the study site. In 2024, soil samples were collected along the historical flight trajectory, and the magnetic fraction was separated using the heavy-mineral concentration (panning) method. A combination of techniques – optical microscopy, scanning electron microscopy with energy-dispersive X-ray analysis (SEM-EDX), and Raman spectroscopy – was used to study the morphology and composition of the separated particles. It is shown that the bulk of the magnetic spherules are likely technogenic in origin. However, microfragments of rock containing fayalite and olivine with Ni and Cr admixtures, as well as plagioclase with reduced crystallinity, were detected in the samples. Their composition and morphology are consistent with published data on the Saratov meteorite. The obtained results demonstrate the fundamental feasibility of detecting microfragments of meteoritic material in modern soils and illustrate the effectiveness of an integrated mineralogical-geochemical approach for reconstructing the strewn fields of meteorite showers.

Keywords

Saratov meteorite; spherules; magnetic separation; microprobe analysis; Raman spectroscopy

Funding

Fieldwork and sampling were carried out with financial support from the state assignments of the Earth Science Museum of Lomonosov MSU AAAA-A16-116042010089-2 and AAAA-A16-116042710030-7 within the framework of the State assignment of the IG RAS FMWS-2026-0005. The material for the study was obtained during the scientific and educational expedition “Flotilla of Floating Universities”. SEM-EDX and Raman spectroscopy analyses were performed at the SRF of the IPE RAS with support from the IPE RAS State assignment. Partial funding was provided by the State assignment of the IO RAS (theme N FMWE-2024-0020). Sample preparation and interpretation of analytical data were carried out with financial support from the State assignment of the GEOKHI RAS and within the framework of the State assignment of Lomonosov MSU N AAAA-A16-116033010119-4.

Received: 20.01.2026 ***Accepted: 28.04.2026*** ***Online: 01.09.2026*** ***Published: 10.09.2026***

Introduction

The study of cosmic material in soils and rocks has long been an actively developing field. However, the transformation and preservation of meteoritic microfragments over long time intervals, the possibility of their identification in deposits and soils along the meteorite's flight path, and the discrimination of cosmogenic micromaterial from technogenic “counterparts” (especially in modern soils) remain relevant and promising challenges.

This is an open access article under the CC BY 4.0 license

Journal of Mining Institute. 2026. Vol. 280. P. 131-144
© Aleksei V. Ivanov, Ruslan R. Gabdullin, Sofya I. Merenkova, Aleksei A. Samsonov, Alvina V. Chistyakova, Dmitrii F. Ayatskov, Mikhail A. Vinnik, Evgenii Yu. Pogozhev, Afanasii E. Telnov, Yurii A. Churikov, Nikita N. Anisimov, Natalya V. Badulina, 2026

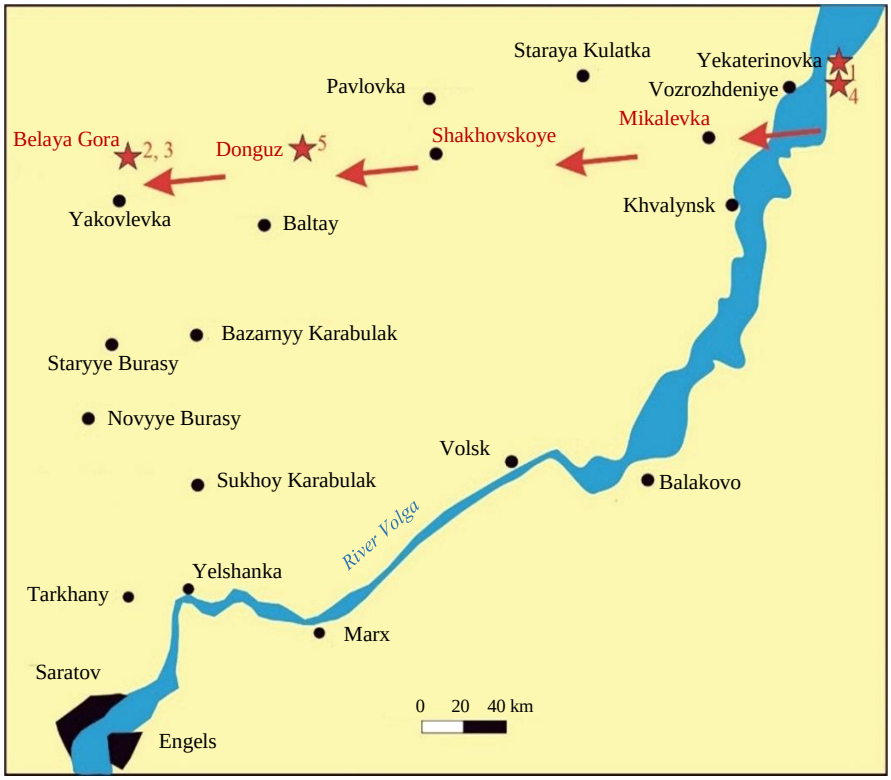


Fig.1. Schematic distribution of the main known collection sites for macrofragments of the Saratov meteorite and sampling points

Red arrows – flight trajectory of the Saratov meteorite;
names in red – settlements where known Saratov meteorite finds were recovered;
red stars – sampling sites and their numbers

The Saratov meteorite shower of October 6, 1918, located in the northern right-bank part of the Saratov Volga region, was selected as the model study area (Fig.1). The material of the Saratov meteorite was collected by local residents during the fall, and later by a special expedition led by L.A.Kulik with the active assistance of the population, especially local history and scientific-educational communities [1, 2]. The mass of fragments found at several locations along the flight axis (Fig.1), is now distributed among various museums in Russia (the Earth Science Museum of MSU, the Earth Science Museum of Saratov University, etc.). During the 20th century, the meteoritic material was studied by many researchers, including its geochemical and mineralogical characteristics [3-5], physical properties [5, 6], structural features, spectral reflectance of the material [7], etc. The Saratov meteorite continues to attract interest from modern researchers in the 21st century [8-10]. Special attention to this topic, from the very moment of the cosmic event, was paid by representatives of V.I.Vernadsky's school working at Saratov University – P.P.Pilipenko and his student V.S.Vasiliev [5, 11].

The aim of this work is to test the hypothesis of identifying meteoritic material in the magnetic fraction of modern soils as a tool for studying the area of a meteorite shower.

The research objectives included:

- collection of heavy-mineral soil samples along the flight trajectory of the Saratov meteorite;
- washing and examination of the heavy-mineral concentrates using a combination of methods;
- interpretation of the integrated dataset.

During fragmentation of a meteorite, unablated meteoroids, partially melted cosmic spherules, and meteoric fragments are formed, which settle under gravity according to their sizes [12]. During ablation, ablated metal atoms oxidize to form various compounds (oxides, hydroxides, and carbonates), which then condense to form meteoric smoke particles (MSP) [12, 13]. Due to their significantly

This is an open access article under the CC BY 4.0 license

© Aleksei V. Ivanov, Ruslan R. Gabdullin, Sofya I. Merenkova, Aleksei A. Samsonov, Alvina V. Chistyakova, Dmitrii F. Ayatskov, Mikhail A. Vinnik, Evgenii Yu. Pogozhev, Afanasii E. Telnov, Yurii A. Churikov, Nikita N. Anisimov, Natalya V. Badulina, 2026

smaller size, MSP particles do not settle as quickly under gravity and circulate in the atmosphere for up to several years [12, 14, 15]. Our study is focused on the search for microfragments resulting from fragmentation, which largely preserve the composition of the "parent" body, as well as ablation spherules with characteristic cosmogenic features.

The expected characteristics of the primary heavy-mineral material were determined, in particular, by observations of previous researchers. Alterations of the meteoritic material were identified and described within a year after the fall. P.N.Chirvinskii wrote about the studied material: "Other pieces have turned somewhat brown, as they lay in the field through the winter" [5, p. 103]. As V.S.Vasiliev noted, "the chondrules in the Belaya Gora sample are 1-2 mm and rarely 10 mm in diameter. The bulk mass is fragile; with some effort it can be ground into an ash-like powder in the palm, separating chondrules and iron inclusions" [5, p. 112]. In such a case, after 100 years, the heavy concentrate would most likely contain "rusted" individual chondrules or their fragments.

Various models exist for the atmospheric disruption and deceleration phase of bodies ~10-100 m in diameter: the Pancake Model (expanding perpendicular to the trajectory under aerodynamic pressure); the Debris Cloud Model (the body continuously fragments, and the cloud of small debris expands at a constant velocity proportional to the flight speed); and the Chain Reaction Model (the body progressively breaks into increasingly smaller and stronger fragments, with the expansion rate depending on the current strength of the fragments) [16]. According to researchers, to accurately predict the strewn field of a particular body, it is necessary to narrow the range of its initial physical parameters as much as possible, since these affect the outcome more strongly than the differences between the models themselves. Large and strong fragments have a higher mass-to-cross-sectional area ratio (greater ballistic resistance) and can travel farther along the trajectory, forming the "head" part of the ellipse with the largest meteorites, while dust-sized particles and the least strong fragments decelerate and are lost by ablation in the atmosphere earlier, forming the tail part.

It has been established that ordinary chondrites have an average strewn field width of 3.8 km, most being around 2-4 km [17]. At the same time, the term "strewn ellipse" itself is criticized by some researchers: according to modeling and observations, the main contribution to the shape, size, and location of the strewn field is made by atmospheric winds (if fragment shape and orientation were decisive, the effect of wind drift would not be so evident). The most typical form is a long, narrow, curved zone rather than a symmetric ellipse, where the curvature is caused by changes in wind direction with altitude [17]. For several meteorites, it has been shown that atmospheric fragmentation is often incomplete and the main body survives as the largest fragment, while the mass distribution of recovered fragments strongly depends on the completeness of the collection, especially the inclusion of the largest fragments, and is skewed due to rare finds of small fragments [18, 19]. The Saratov meteorite was used in these works as physical material for experimentation. In our study, to overcome the need for model calculations, material was collected near settlements where known large fragments of the Saratov meteorite were recovered (Fig.1).

In the area of the Saratov meteorite shower, Paleocene terrigenous rocks crop out (glauconite-quartz sands-sandstones and siltstones-siltites of the Syzran and Saratov formations). In the easternmost part, Lower Cretaceous deposits are observed: the Aptian Stage (sands, sandstones, clays with levels of ferruginization and siderite concretions of the Verkhazovskaya Formation) and the Albian Stage (sands, sandstones, clays of the Paramonovskaya Formation). Upper Cretaceous deposits are also present: Cenomanian, Turonian, Coniacian, Santonian, Campanian, and Maastrichtian Stages (chalk-marl and sandy-clayey sequences of the Melovatka, Bannovka, Sengilei, and Radishchevo formations). Quaternary deposits are represented by various genetic types, dominated by locally developed colluvium and proluvium. Moraine and fluvioglacial deposits, from which fragments of crystalline rocks containing olivine may potentially be derived, are developed mainly to the west, in the areas of Rtishchevo and Atkarsk.

This is an open access article under the CC BY 4.0 license

© Aleksei V. Ivanov, Ruslan R. Gabdullin, Sofya I. Merenkova, Aleksei A. Samsonov, Alvina V. Chistyakova, Dmitrii F. Ayatskov, Mikhail A. Vinnik, Evgenii Yu. Pogozhev, Afanasii E. Telnov, Yurii A. Churikov, Nikita N. Anisimov, Natalya V. Badulina, 2026

Materials and methods

Point heavy-mineral samples were collected along the flight axis of the Saratov meteorite during the work of a special team of the scientific-educational expedition "Flotilla of Floating Universities" in 2024 [20]. The sampling procedure followed instructions* for searching for meteoritic material, which recommend taking 10 cm of soil from 1 m^2, washing it, and then extracting the remaining fraction with a magnet. This method is most suitable for detecting mini-fragments of a celestial body, including known meteoritic spherules. For each specific sample, the "envelope" method was used, involving partial material collection at several locations within a single site, followed by combining into a single container. The interval cut was within the upper 10 cm of the soil layer, which clearly corresponds to the intensity of natural soil-forming processes in this area. Structural features of the layer were monitored to exclude possible changes over the last 100 years – erosion, washout, etc.

During field work (Fig.1) five samples of about 50 kg each were collected along the meteorite's flight axis – the villages of Yekaterinovka (left bank of the Volga River, two samples), Donguz, and Belaya Gora (two samples). In these locations (except for Yekaterinovka), macrofragments of the Saratov meteorite were recovered in the first years after its fall.

Washing of the heavy concentrates was performed at the Department of Geology, Geochemistry, and Economic Minerals, Faculty of Geology, Lomonosov Moscow State University. Particles presumably of cosmogenic origin were separated by dividing the sample of the upper soil horizon into non-magnetic and magnetic fractions. From the magnetic fraction, spherules and magnetite aggregates with other minerals were then selected using an optical microscope. The magnetic fraction was separated on an electromagnetic separator UEM-1 at 0.5 A. The fraction was further purified with a permanent magnet.

Microphotographs and X-ray spectral microanalysis were performed at the Shared Research Facility of the IPE RAS [21] using a TESCAN MIRA LMS scanning electron microscope (SEM) equipped with an Ultim Max 65 energy-dispersive X-ray (EDX) spectrometer with integrated AZtecLive Automated software (Oxford Instruments). The analyses were carried out at an accelerating voltage of 20 kV and a working distance of 15 mm. For SEM analysis, grains from the magnetic fraction were arranged in rows, then embedded in epoxy resin; the mounts for microprobe analysis were then ground and polished.

Additional mineral identification was carried out at the Shared Research Facility of the IPE RAS using Raman spectroscopy (Raman scattering spectroscopy) with an EnSpectr R532 spectrometer coupled to an Olympus BX53 M optical microscope. Key technical specifications of the EnSpectr R532 Raman spectrometer: laser wavelength – 532 nm, grating – 1800 grooves/mm, entrance slit – 20 μm, focal length – 75 mm. Spectra were recorded using a 50-fold objective lens (total magnification ×500) at a laser power of 2.2 mW, with spectrum accumulation in averaging mode of 20-50 measurements with 0.5-2 s exposure.

Results

Composition of the magnetic fraction. In all heavy concentrates, ferromagnetic fractions of similar order were separated – weighing from 2.2 to 10 g. The fraction is represented by spherules (predominantly magnetite), angular magnetite fragments coated with hematite oxides, and moderately rounded magnetite fragments. The contents of these components are given in Table.1, Fig.2. Certain trends in the compositional variation of the material along the meteorite's flight trajectory were identified, requiring further confirmation. A trend was established toward an increase in the concentration of spherules (from 0.5-1 to 5 %) and their average sizes (from 50 to 300 μm) toward the head part of the dispersion swarm, corresponding to the Belaya Gora area. A similar trend is characteristic of the concentration of angular magnetite grains. For all samples, an exceptionally wide size range of

* Vasiliev N.V. Instructions for the Study of Meteorite Craters. Siberian Commission on Meteorites and Cosmic Dust, Siberian Branch of the USSR Academy of Sciences. Fond 1718. Inventory 1. File 83 (in Russian).

This is an open access article under the CC BY 4.0 license

© Aleksei V. Ivanov, Ruslan R. Gabdullin, Sofya I. Merenkova, Aleksei A. Samsonov, Alvina V. Chistyakova, Dmitrii F. Ayatskov, Mikhail A. Vinnik, Evgenii Yu. Pogozhev, Afanasii E. Telnov, Yurii A. Churikov, Nikita N. Anisimov, Natalya V. Badulina, 2026

magnetite particles is observed – up to one to two orders of magnitude within a single sample (e.g., Yekaterinovka – from 50 μm to 5 mm). The origin of these particles remains unclear, since the underlying soils at the sampling sites differ. The distribution of rounded magnetite grains along the axis is relatively uniform. Possibly, their formation is related to technogenic processes.

Table 1

Distribution of ferromagnetic fraction components along the meteorite flight axis

Type	Village Yekaterinovka (concentrate 1)	Village Belaya Gora (concentrate 2)	Village Belaya Gora (concentrate 3)	Village Yekaterinovka (concentrate 4)	Village Donguz (concentrate 5)
Spherules	Up to 50 μm / 1 %	50-300 μm / 2 %	50-150 μm / 5 %	Up to 50 μm / 0.5 %	50 μm / 2 %
Magnetite (angular)	200-1000 μm	200-1000 μm	50-200 μm	Up to 50 μm, single up to до 5 mm	20-100 μm, single up to 2 mm
Magnetite (rounded)	50-100 μm	5-100 μm	5-100 μm	20-100 μm	20-100 μm

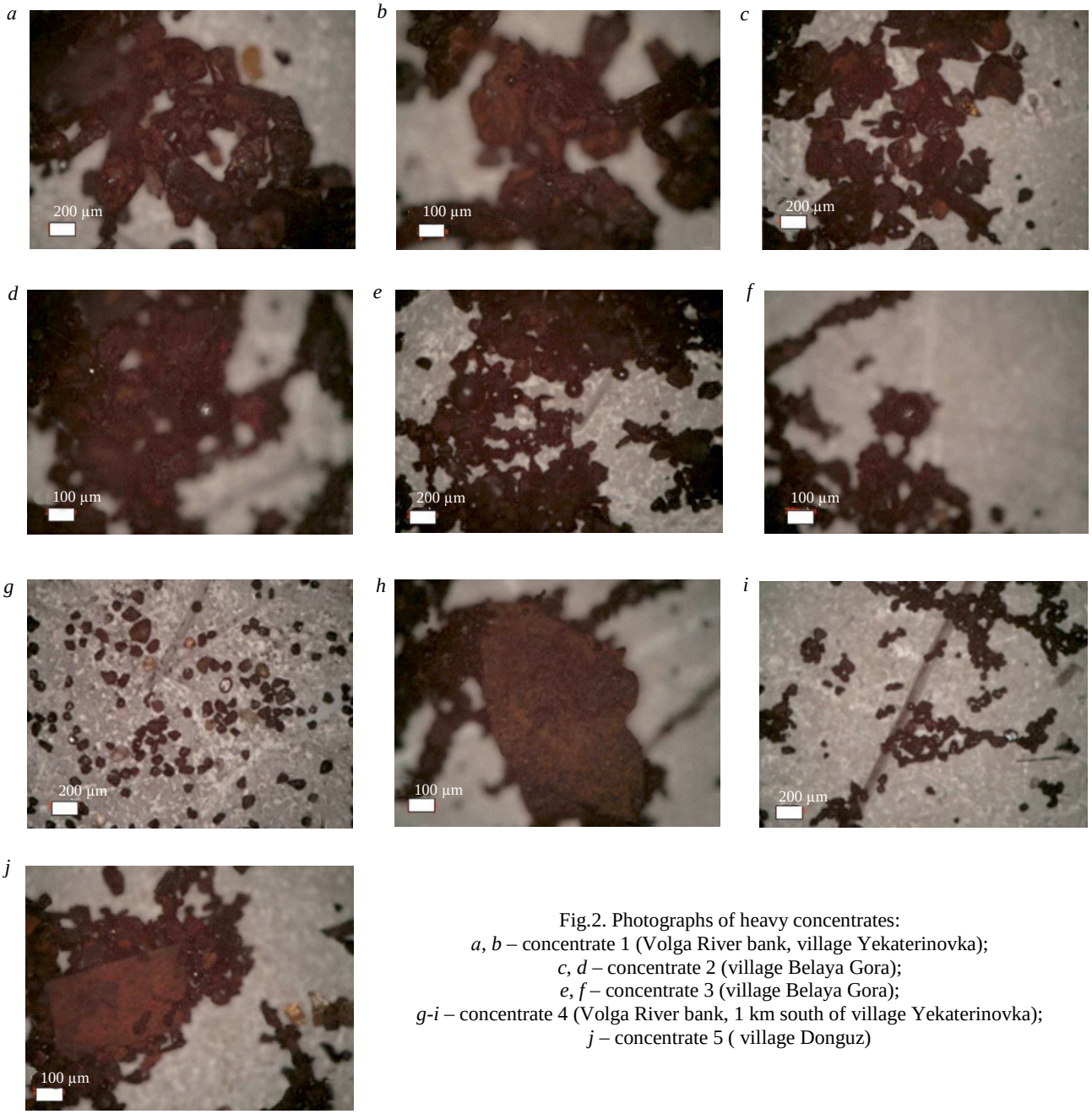


Fig.2. Photographs of heavy concentrates:
a, *b* – concentrate 1 (Volga River bank, village Yekaterinovka);
c, *d* – concentrate 2 (village Belaya Gora);
e, *f* – concentrate 3 (village Belaya Gora);
g-*i* – concentrate 4 (Volga River bank, 1 km south of village Yekaterinovka);
j – concentrate 5 (village Donguz)

This is an open access article under the CC BY 4.0 license

© Aleksei V. Ivanov, Ruslan R. Gabdullin, Sofya I. Merenkova, Aleksei A. Samsonov, Alvina V. Chistyakova, Dmitrii F. Ayatskov, Mikhail A. Vinnik, Evgenii Yu. Pogozhev, Afanasii E. Telnov, Yurii A. Churikov, Nikita N. Anisimov, Natalya V. Badulina, 2026

The non-magnetic fraction consists of quartz, K-feldspar, and amphiboles. The ferromagnetic fraction is mainly represented by magnetite of angular (200-1000 μm) and moderately rounded (50-100 μm) morphology. The angular grains are coated with hematite. The oxide color is brown or red. The magnetite color is iron-black with a weak metallic luster. Under an optical microscope, magnetite spherules with no signs of oxidation are clearly distinguishable, differing in luster (from bright metallic to black iron). The content of such spherules in the magnetic fraction is about 5 %.

Electron microscopy data revealed the presence in the magnetic fraction of chromite, titanomagnetite, fragments of native iron, and likely chromferride. Also distinguishable are rock fragments/aggregates of non-magnetic and weakly magnetic minerals with magnetite. The spherules found in the concentrates were examined in more detail for their morphology and chemical composition.

***Morphology and composition of spherules*.** The selected spherules consist of magnetite or wüstite with admixtures of Mn, Cr, or Ti. Between the magnetite crystals, compounds with admixtures of silicon, titanium, and calcium grow as dendrites, probably reflecting the widespread process of sphene-formation (sphenitization) of magnetite. Most spherules are hollow inside, but several were found to have an iron core (Fig.3, *d*). As a rule, the composition of the spherules is heterogeneous. Table 2 presents average concentrations for the main magnetite mass and separately for the veinlets.

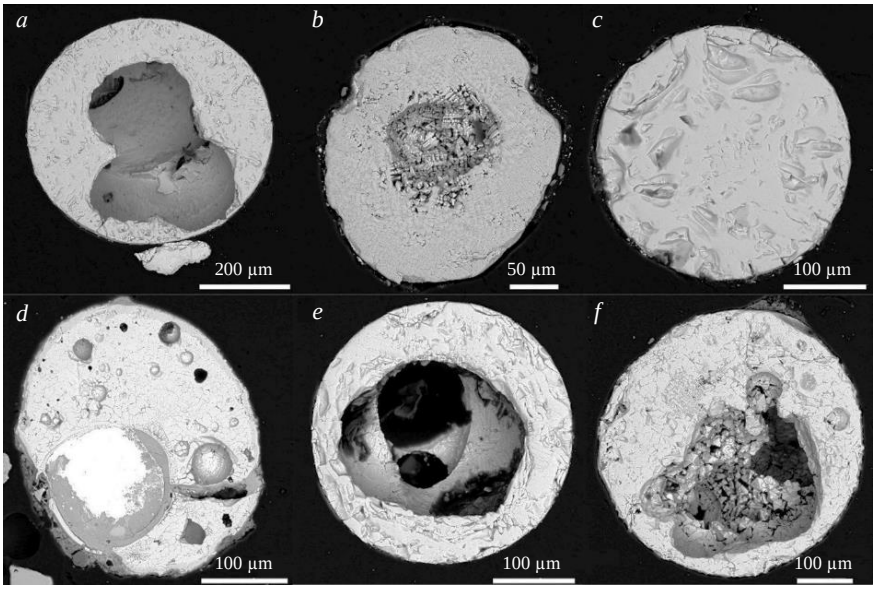


Fig.3. Magnetite spherules from village Belaya Gora concentrates (SEM BSE): *a-c* – concentrate 2, *d-f* – concentrate 3

Table 2

Composition of magnetite spherules, wt.%

Spectrum label	Magnetite			Veinlets		
	n = 16			*n* = 13		
	Min	Max	Median	Min	Max	Median
O	17.06	28.81	22.93	19.64	34.87	28.04
Mg	0	0.72	–	bdl	bdl	bdl
Al	0.31	1.8	1.12	0.28	0.74	0.44
Si	bdl	bdl	bdl	1.17	14.64	8.72
K	bdl	bdl	bdl	0.34	0.49	0.41
Ca	bdl	bdl	bdl	0.36	16.58	4.55
Ti	0.81	7.56	3.12	8.05	9.67	8.82
Cr	0.24	0.39	0.33	bdl	bdl	bdl
Mn	0.39	2.55	0.96	0.33	2.47	1.37
Fe	56.3	76.13	70.48	31.05	72.11	49.00

Note. Dash – Mg reliably determined in only one sample; bdl – below detection limit.

This is an open access article under the CC BY 4.0 license

© Aleksei V. Ivanov, Ruslan R. Gabdullin, Sofya I. Merenkova, Aleksei A. Samsonov, Alvina V. Chistyakova, Dmitrii F. Ayatskov, Mikhail A. Vinnik, Evgenii Yu. Pogozhev, Afanasii E. Telnov, Yurii A. Churikov, Nikita N. Anisimov, Natalya V. Badulina, 2026

Rock fragments. The largest number of rock fragments/aggregates of non-magnetic and weakly magnetic minerals with magnetite was found in concentrate 2. We describe the composition of the most representative ones. In the first fragment (Fig.4), magnetite, quartz, and barite forming small veinlets are clearly identified. To more accurately determine the mineral constituting the bulk of the fragment, Raman spectroscopy was performed. Its elemental composition and Raman spectra correspond to the clinopyroxene group, probably aegirine.

The second fragment (Table 3, 4, Fig.5) is composed of fayalite (Fa 81) with Mg and Mn admixtures (EDX spectrum 92), magnetite (spectra 24, 30, 31), and plagioclase (EDX spectra 26-29) with reduced crystallinity (poorly crystallized), expressed as broadening of Raman peaks. Olivine and plagioclase spectra were compared with literature data [22-24].

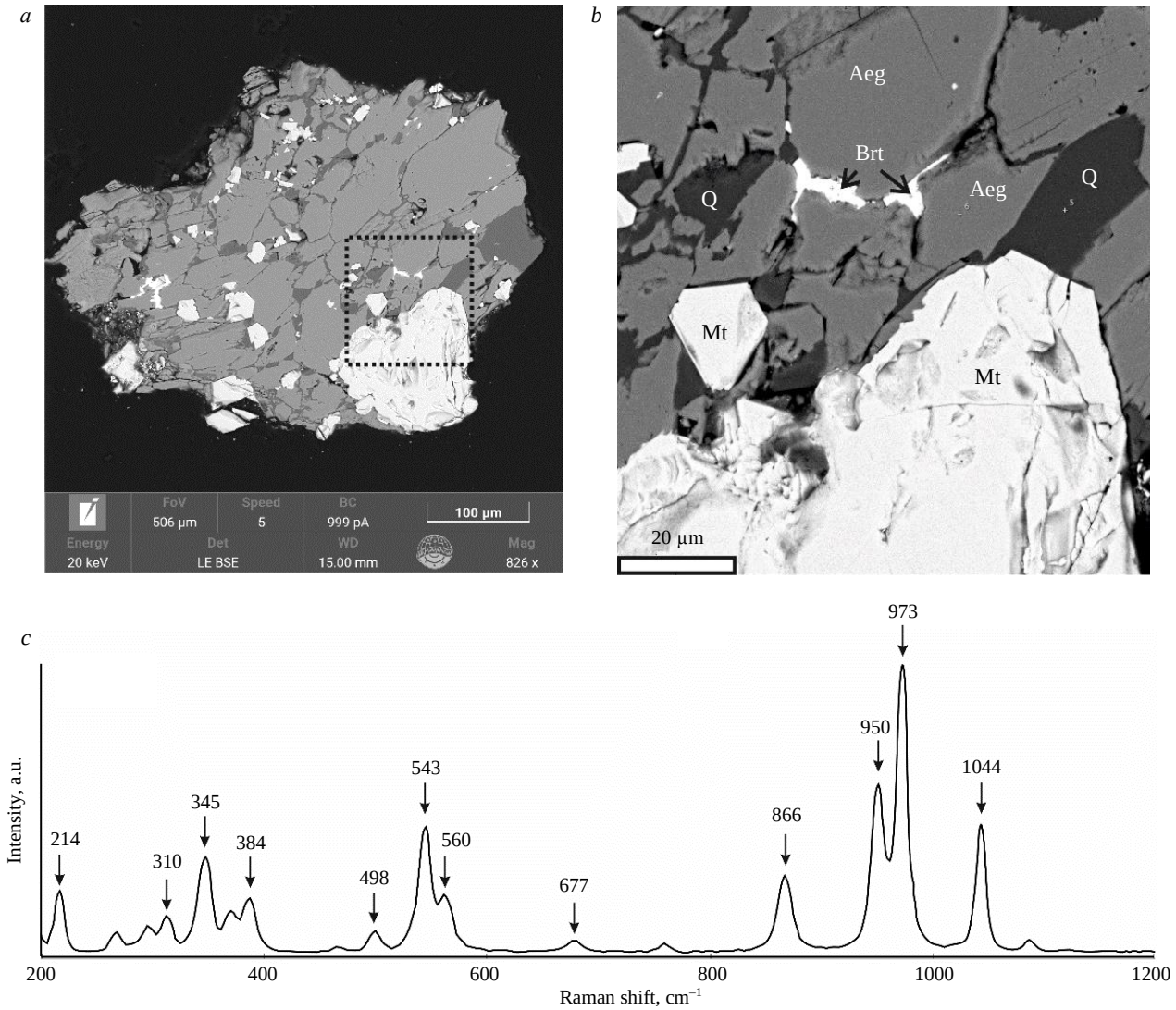


Fig.4. General view of the first fragment (SEM BSE) (*a*); mineral phases constituting it (*b*) and Raman spectrum of aegirine from the fragment (*c*)
Mt – magnetite; Aeg – aegirine; Brt – barite. Dashed contour – area of the studied fragment

Table 3

Content of major oxides in plagioclases, wt.%

Spectrum label	SiO_2	Al_2O_3	Fe_2O_3	MnO	CaO	MgO	P_2O_5	∑
Spectrum 28	38.11	3.42	28.51	1.92	20.63	0.6	6.82	100
Spectrum 29	39.05	3.16	29.27	2.12	19.72	0.5	6.18	100

This is an open access article under the CC BY 4.0 license

Journal of Mining Institute. 2026. Vol. 280. P. 131-144
© Aleksei V. Ivanov, Ruslan R. Gabdullin, Sofya I. Merenkova, Aleksei A. Samsonov, Alvina V. Chistyakova, Dmitrii F. Ayatskov, Mikhail A. Vinnik, Evgenii Yu. Pogozhev, Afanasii E. Telnov, Yurii A. Churikov, Nikita N. Anisimov, Natalya V. Badulina, 2026

Table 4

Composition of major phases constituting the second fragment, wt.%

Spectrum label	Spectrum 92	Spectrum 24	Spectrum 25	Spectrum 26	Spectrum 27	Spectrum 28	Spectrum 29	Spectrum 30	Spectrum 31
O	31.5	20.67	29.07	43.27	42.65	40.32	39.93	21.46	20.24
Na	bdl	bdl	bdl	0.81	0.56	bdl	bdl	bdl	bdl
Mg	4.52	0.4	0.62	bdl	bdl	0.36	0.3	bdl	bdl
Al	bdl	2.25	1.6	13.16	12.09	1.81	1.66	2.59	1.94
Si	15.45	0.95	15.55	23.06	24.21	17.87	18.15	2.29	bdl
P	bdl	bdl	3.7	bdl	bdl	2.99	2.68	bdl	bdl
K	bdl	bdl	bdl	3.09	6.15	bdl	bdl	bdl	bdl
Ca	0.92	0.21	17.19	6.27	1.91	14.79	14.01	1.2	bdl
Ti	bdl	0.42	bdl	bdl	bdl	bdl	bdl	0.45	0.3
Mn	3.4	0.77	1.26	bdl	bdl	1.49	1.63	0.66	0.61
Fe	43.65	67.56	19.31	2.36	1.46	20.69	21.05	63.74	69.12
Sr	bdl	bdl	bdl	2.43	2.49	bdl	bdl	bdl	bdl
Ba	bdl	bdl	bdl	4.6	9.4	bdl	bdl	bdl	bdl
∑	99.44	93.24	88.31	99.05	100.92	100.33	99.41	92.38	92.21

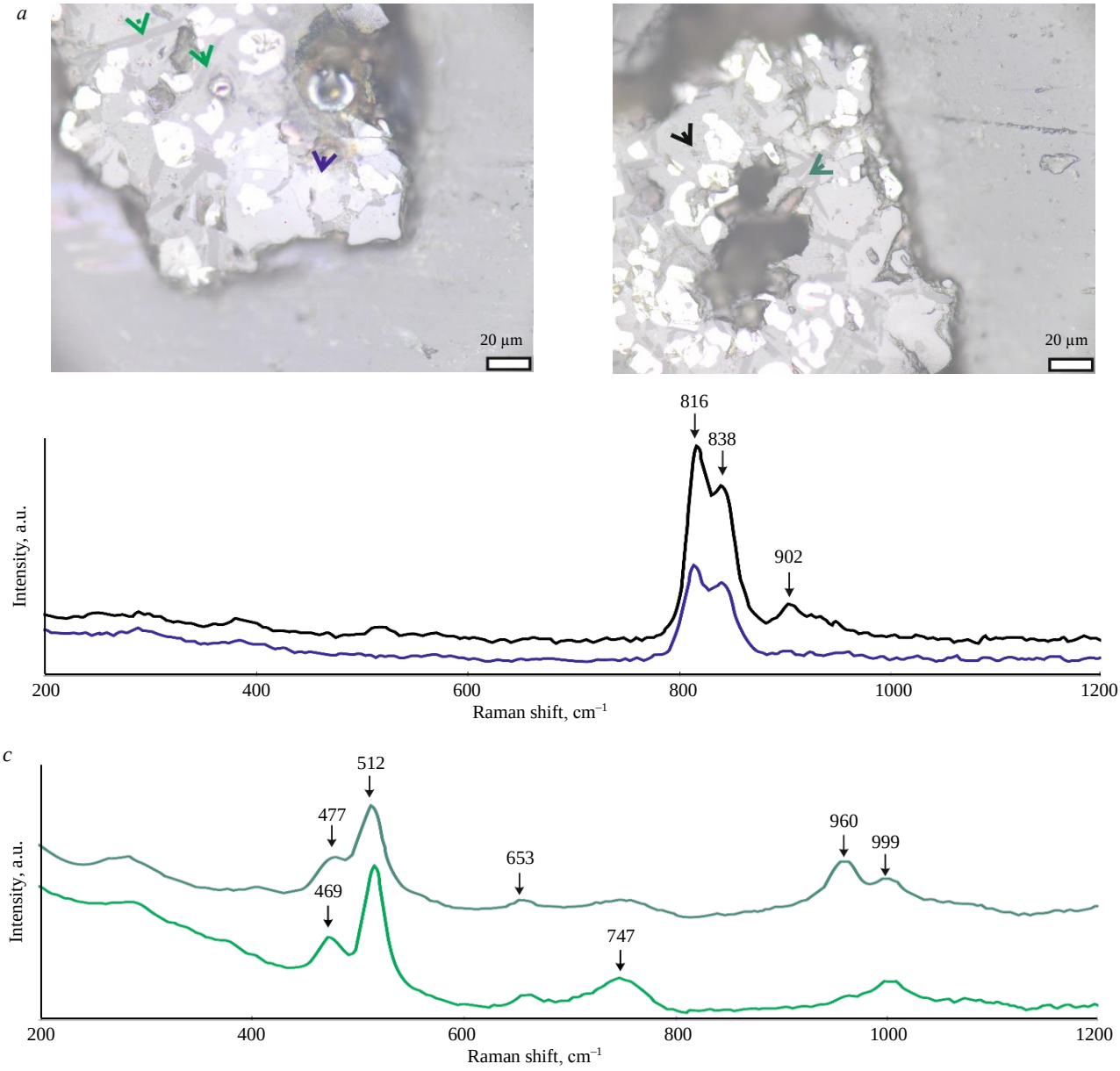


Fig.5. General view of the second fragment (*a*), Raman spectra for olivines (*b*) and plagioclases (*c*). Colored arrows mark analyzed spots corresponding to the color of the spectra

This is an open access article under the CC BY 4.0 license

© Aleksei V. Ivanov, Ruslan R. Gabdullin, Sofya I. Merenkova, Aleksei A. Samsonov, Alvina V. Chistyakova, Dmitrii F. Ayatskov, Mikhail A. Vinnik, Evgenii Yu. Pogozhev, Afanasii E. Telnov, Yurii A. Churikov, Nikita N. Anisimov, Natalya V. Badulina, 2026

The elemental map (Fig.6) clearly demonstrates the mutual arrangement of the phases. Prismatic plagioclase crystals ("rods") are distinguishable.

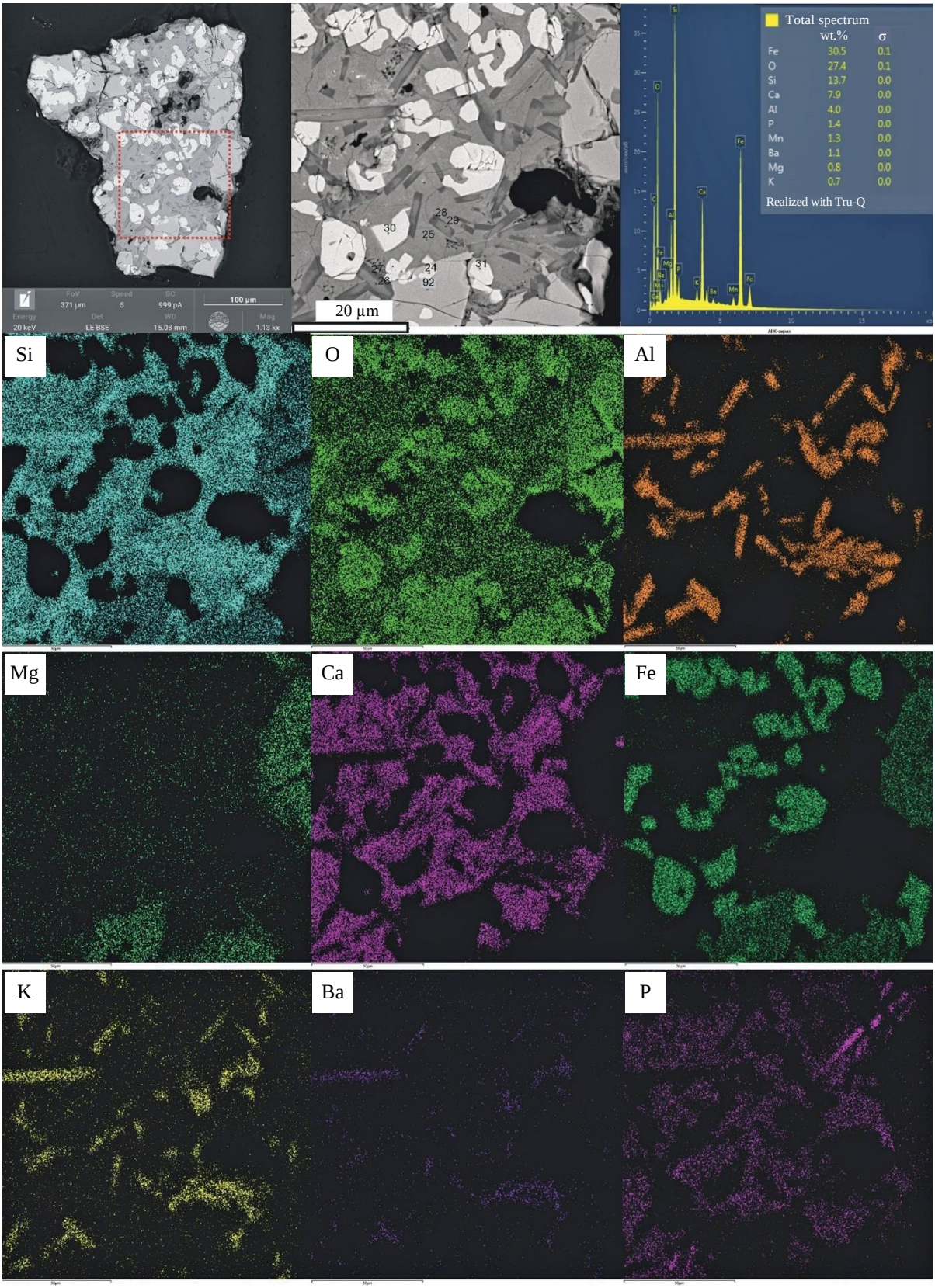


Fig.6. Elemental maps for the second fragment (dashed contour).
Dots indicate microprobe analysis spots and corresponding spectrum numbers from Table 4

This is an open access article under the CC BY 4.0 license

Journal of Mining Institute. 2026. Vol. 280. P. 131-144
© Aleksei V. Ivanov, Ruslan R. Gabdullin, Sofya I. Merenkova, Aleksei A. Samsonov, Alvina V. Chistyakova, Dmitrii F. Ayatskov, Mikhail A. Vinnik, Evgenii Yu. Pogozhev, Afanasii E. Telnov, Yurii A. Churikov, Nikita N. Anisimov, Natalya V. Badulina, 2026

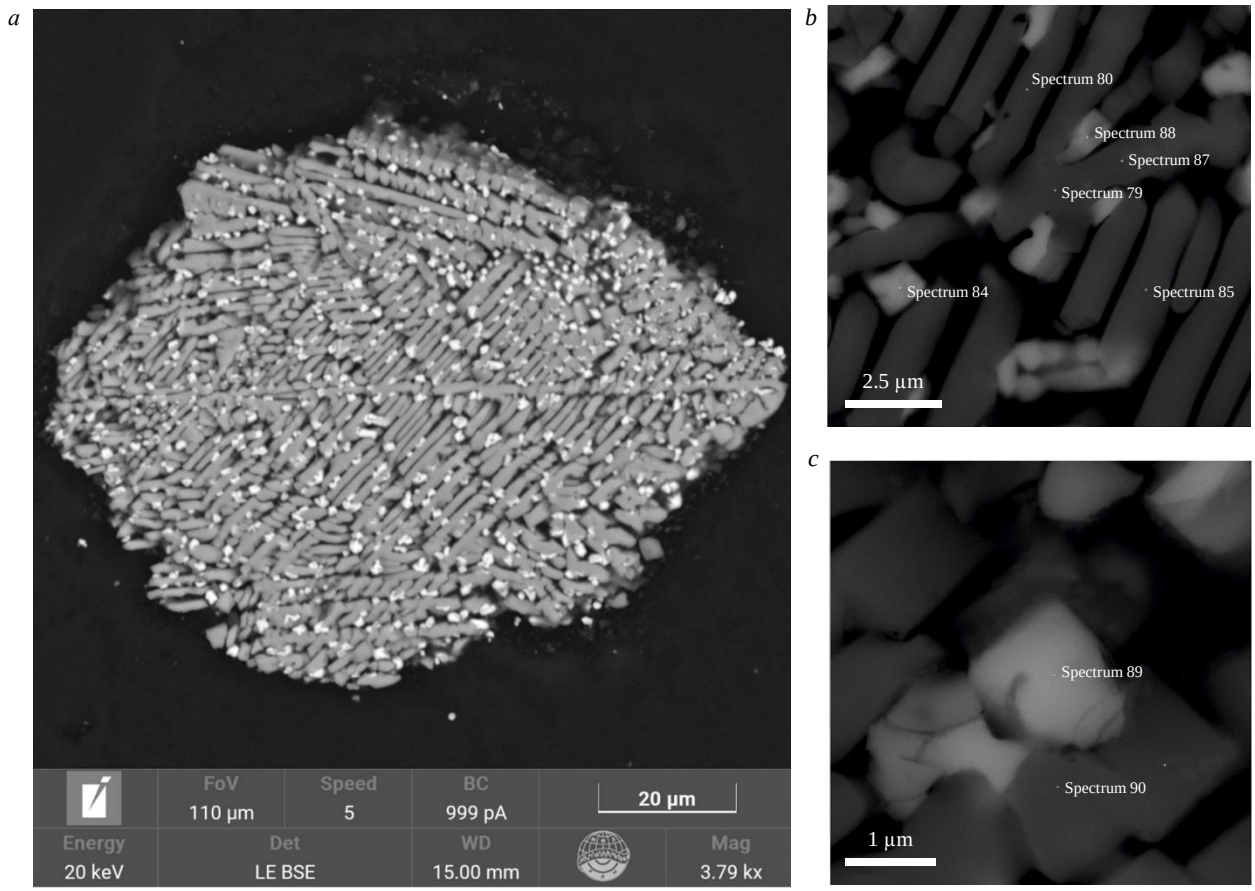


Fig.7. Third fragment (SEM BSE) (*a*) and microprobe analysis spots (*b*, *c*)

The most interesting is the third fragment with specific morphology (Fig.7). It is a spherical grain, not exceeding 80 µm along the long axis, composed of olivine with Cr and Ni admixtures (Table 5). Its composition is heterogeneous. Some crystals have forsterite Fo 62-73, while the inclusion in spectrum 89 has Fo 37 (for similar spots in another area (spectra 84 and 88) Fo 65-71).

Table 5

Composition of olivine in the third fragment, wt.%

Spectrum label	O	Mg	Al	Si	Ca	Cr	Mn	Fe	Co	Ni	∑
Spectrum 79	41.6	21.34	0.36	16.5	0.18	0.42	0.24	20.15	bdl	1.49	102.27
Spectrum 80	38.97	18.55	0.43	13.69	0.14	0.68	0.24	26.08	bdl	1.3	100.1
Spectrum 84	37.4	18.07	0.47	13.74	0.12	0.56	0.17	22.74	bdl	1.42	94.69
Spectrum 85	37.79	18.93	0.22	15.53	0.16	0.29	0.21	17.91	bdl	1.25	92.3
Spectrum 87	39.97	20.5	bdl	16.81	0.18	0.31	0.23	17.45	bdl	1.41	96.84
Spectrum 88	38.6	19.33	0.2	16.04	0.16	0.28	0.26	17.76	bdl	1.33	93.96
Spectrum 89	33.45	10.92	1.33	6.5	0.08	1.43	0.19	43.03	0.49	1.22	98.64
Spectrum 90	36.88	15.53	0.51	10.81	0.11	0.74	0.25	33.97	0.4	1.21	100.41

Note. Deficiency in totals is due to sample topography.

Discussion

Identification of meteoritic material. When studying spherules of potentially cosmogenic origin, possible genetic types should be considered. These may be micrometeorites, ablation spherules, or impact-melt spherules. Micrometeorites contribute significantly to the flux of extraterrestrial material reaching the Earth and are more common in the sedimentary record (including modern deep-sea sediments) than fragments of large meteorites [25-27], and also carry important information about past paleogeographic conditions [28-30]. Let us consider the criteria for identifying micrometeorites [31] –

This is an open access article under the CC BY 4.0 license

© Aleksei V. Ivanov, Ruslan R. Gabdullin, Sofya I. Merenkova, Aleksei A. Samsonov, Alvina V. Chistyakova, Dmitrii F. Ayatskov, Mikhail A. Vinnik, Evgenii Yu. Pogozhev, Afanasii E. Telnov, Yurii A. Churikov, Nikita N. Anisimov, Natalya V. Badulina, 2026

the presence of a partial or complete magnetite shell around micrometeorites [32, 33]; native nickeliron; chemical composition close to chondritic [34]. Secondary features include olivine with high CaO and Cr_2O_3 and very low FeO, which is uncharacteristic of terrestrial rocks [35]; evidence of surface heating (due to atmospheric entry); spherical particle morphology. The spherules we discuss from the magnetic fraction could theoretically correspond in morphology and composition to type I micrometeorites [31]. In micrometeorites of this type, FeO predominates with a small admixture of other oxides (mainly MgO and SiO_2); mineralogically they are composed of wüstite and magnetite, sometimes with a core of nickel-iron or platinum-group elements [31]. Type I spherules are often devoid of such a core and may be hollow.

There are meteoritic ablation spheres formed during atmospheric entry of larger bodies [36], and microtektites condensed from vapour plumes [37] or detached from impact melt produced by collision of cosmic bodies with the Earth [38]. Ablation spherules are formed by surface heating, melting, evaporation, oxidation of the material, and blow-off of the melt by the incoming atmospheric flow [39].

Technogenic spherules, impact spherules, and ablation spherules can have similar morphology, and industrial magnetite spherules are mineralogically indistinguishable from some melted micrometeorites [31]. Moreover, "terrestrial" spherules are highly diverse [34]. The absence of Ni in iron oxide particles is generally considered evidence of a "terrestrial" or technogenic origin of magnetite spherules [40]. In the studied spherules, Ni is either absent or below the detection limit of the method, which does not allow an unambiguous interpretation of their origin. Although spherules with an iron core similar to Fig.3, *d*, but enriched in Co and Ni, have been described as micrometeorites in works [28, 41], the studied magnetite spherules are most likely technogenic formations.

When discussing the composition of the magnetic fraction, it is worth mentioning that Fe-Ni minerals, even under arid desert weathering of ordinary chondrites, oxidize to paramagnetic iron oxyhydroxides (akaganeite), and at later stages form small amounts of ferromagnetic oxides (magnetite/maghemite) [42]. It can be assumed that the abundantly represented iron oxides and oxyhydroxides in the heavy concentrates are partly products of weathering of meteoritic fragments. In this regard, much more attention should be paid to rock fragments. Quartz and barite are not found in unaltered meteorites, but their alternative origin is possible as a result of alteration under terrestrial conditions or on parent bodies [43]. At the same time, distinguishing coesite and stishovite – shock-induced minerals in meteorites – from quartz is not possible. The genesis of the first fragment remains controversial.

The geochemical features of olivine from the Saratov meteorite were previously presented in the work of K.G.Sukhanova and co-authors [8]. According to these researchers, the olivine composition corresponds to forsterite and is rather heterogeneous (Fo 73-77), but no differences between chondrule and matrix olivine in terms of major element composition were found. In the fragments we studied, olivine corresponds to fayalite (Fa 81), although it has Mg admixtures. At the same time, fayalite and olivines $(Mg, Fe)_2(SiO_4)$ occur in many types of meteorites [43]. Plagioclases with reduced crystallinity are probably "poorly crystallized mesostasis of oligoclase-labradorite composition" [8]. The second fragment can be assumed to belong to the Saratov meteorite or its alteration products.

The third fragment, by its composition (Ni admixtures) and morphology, is probably a non-porphyritic chondrule (barred/dendritic olivine chondrules according to [44]). The composition of the olivine constituting the third fragment is heterogeneous, but at individual points Fo 71-73 is determined (spectra 79, 85, 87, 88). Thus, in the magnetic fraction of modern soils at the Saratov meteorite fall site, individual microfragments and/or their alteration products can be identified.

D.M.Pechersky and co-authors [45] showed that meteorites (of the types they studied) have identical compositions of primary magnetic minerals (kamacite, taenite, schreibersite) and differ only in concentration. Kamacite from meteorites is fully compositionally equivalent to kamacite from cosmic dust in terrestrial sediments, indicating their common origin from the cores of parent planets. Based on thermomagnetic and microprobe analyses of Quaternary deposits of the Darhad Basin (Northern

This is an open access article under the CC BY 4.0 license

Mongolia), they established no correlation with magnetite and pyrite contents, and a negative correlation with sedimentation rate, which, together with data from other regions of Eurasia and the Atlantic, indicates a predominantly cosmic origin of native iron particles in sediments [46]. It has been established that in meteorites, pure iron, kamacite, and taenite form three distinct groups with gaps in Ni content. This is explained by the specific crystallization and decomposition of Fe-Ni alloys in space [47]. Native iron without nickel in terrestrial rocks (mantle xenoliths, traps, basalts) and in meteorites has a common nature, and its global distribution in sediments is related to cosmic interplanetary dust from the asteroid belt [48]. Fragments of native iron (96-97 % Fe with Mn and Cr admixtures < 1 % and Si 2.4 %) were found in the magnetic fraction of the studied soil heavy-mineral samples, but the absence of nickel in the composition and reasonable skepticism do not allow their genesis to be determined as cosmogenic.

Geochemistry of meteoritic material and biogenic functions. According to data [4] n the chemical composition of the Saratov meteorite, the magnetic fraction (in the form soluble in hot aqua regia) contains, %: Fe 67.74-71.26; Ni 7.79-9.16; Co 0.2-0.43; SiO_2 0.38-3.38; CaO 0.72-1.54; MgO 3.71-7.73; MnO 0.06-0.07; P_2O_5 0.17-0.18; S_{total} 0.29-1.77; TiO_2 and Al_2O_3 – traces. For the same magnetic fraction, but in the form insoluble in hot aqua regia, the following are noted, %: FeO 1.03-2.03; SiO_2 7.23-8.85; Al_2O_3 0.46-0.58; Cr_2O_3 0.3-0.31; CaO 0.48-0.87; MgO 1.93-2.22; MnO 0.04; P_2O_5 0.01.

A fundamental property of soil as a bio-inert system is its ability to accumulate in the solid phase the products of its own functioning, which leads to the formation of stable pedogenic features and a restructuring of its morphological appearance. As noted by V.O.Targulian and M.A.Bronnikova, it is the accumulation and distribution of solid-phase products that constitute the essence of elementary soil-forming processes and form the "memory" of the soil [49]. The products of meteoritic material breakdown in soil are variously subjected to processes of accumulation and migration of the chemical elements composing them. As a rule, cobalt, chromium, and nickel are markers of the cosmogenic petrogenic background. At the same time, an excess of these heavy metals is toxic to plants. In this regard, further study of soils and plants within the meteoritic material dispersion area, and specifically at the points of heavy-mineral sampling of the magnetic fraction where Ni- and Cr-bearing minerals (chromite, chromferride, some olivines) were identified in our study, appears promising.

Conclusion

In the soil sample from the Belaya Gora area, a grain of fayalite was found, which with a high degree of probability can be considered a fragment of a chondrule-bearing formation of a chondrite meteorite (the Saratov meteorite belongs to this type). In several grains, unique feldspar structures were found (morphologically described in the mid-20th century in the Saratov meteorite by Professor V.S.Vasiliev of Saratov University).

Traces of the Saratov meteorite can be detected 100 years after the fall of the cosmic body at the level of microfragments. Even in the absence of detailed spatial referencing of many previous fragments and macro-finds, it is possible to effectively study the features of a meteorite shower by combining geochemical, mineralogical, and soil-science methods. In the future, it is planned to apply more extensively the integrated method of soil studies in the area of the celestial body's fall, to delineate the strewn field of fragments and dust fallout, which will allow assessment of the event's characteristics and parameters of one of the world's largest meteorite showers.

REFERENCES

1. Kulik L.A. To the fall of the meteorite in Saratov province in September 1918. *Mirovedenie*. 1921. N 1 (40), p. 71 (in Russian).

2. Kulik L.A. Report of the Meteorite Expedition on the work carried out from May 19, 1921 to November 29, 1922. *Bulletin de l'Academie des Sciences de Russie*. 1922. Vol. 16, p. 391-410 (in Russian).

3. Kupletsky B.M., Ostrovsky I.A. Materials on the Microscopical study of the Meteorites of the USSR. 6. The Saratov Stone Meteorite. *Meteoritica*. 1941. Iss. II, p. 77-81 (in Russian).

This is an open access article under the CC BY 4.0 license

4. Selivanov L.S. Chemical analysis of the "Saratov" meteorite. *Doklady Akademii nauk SSSR*. 1940. Vol. 26. N 4, p. 397-400 (in Russian).
5. Chirvinskii P.N. Chemical-mineralogical composition and microstructure of the Saratov stone meteorite. *Meteoritica*. 1951. Iss. 9, p. 102-116 (in Russian).
6. Volarovitch M.P., Leontieva A.A. A Study of the Viscosity of Meteorites. *Meteoritica.* 1941. Iss. I, p. 33-41 (in Russian).
7. Krinov E.L. Spectral reflectance of sample N 308 of the "Saratov" meteorite of 1918. *Astronomicheskii zhurnal*. 1937. Vol. 14. N 4, p. 356-363 (in Russian).
8. Sukhanova K.G., Kuznetsov A.B., Galankina O.L. Features of olivine crystallization in ordinary chondrites (Saratov meteorite): geochemistry of trace and rare earth elements. *Journal of Mining Institute.* 2022. Vol. 254, p. 149-157. DOI: 10.31897/PMI.2022.39
9. Sukhanova K.G., Skublov S.G., Galankina O.L. et al. Geochemistry of Trace Elements in Minerals of Porphyritic and Nonporphyritic Chondrules from Equilibrated Ordinary Chondrites. *Geochemistry International.* 2023. Vol. 61. N 5, p. 468-483. DOI: 10.1134/S0016702923050075
10. Bezaeva N.S., Badjukov D.D., Rochette P. et al. Experimental shock metamorphism of the L4 ordinary chondrite Saratov induced by spherical shock waves up to 400 GPa. *Meteoritics & Planetary Science*. 2010. Vol. 45. Iss. 6, p. 1007-1020. DOI: 10.1111/j.1945-5100.2010.01069.x
11. Ivanov A.V. Role of V.I. Vernadsky's students and followers in the development of the geoscientific school of a region (on the example of the Saratov Volga region). *Life of the Earth.* 2023. Vol. 45. N 1, p. 138-152 (in Russian). DOI: 10.29003/m3159.0514-7468.2023_45_1/138-151
12. James A.D., Pace F., Sikora S.N.F. et al. The importance of acid-processed meteoric smoke relative to meteoric fragments for crystal nucleation in polar stratospheric clouds. *Atmospheric Chemistry and Physics*. 2023. Vol. 23. Iss. 3, p. 2215-2233. DOI: 10.5194/acp-23-2215-2023
13. Plane J.M.C., Wuhu Feng, Dawkins E.C.M. The Mesosphere and Metals: Chemistry and Changes. *Chemical Reviews*. 2015. Vol. 115. Iss. 10, p. 4497-4541. DOI: 10.1021/cr500501m
14. Brooke J.S.A., Wuhu Feng, Carrillo-Sánchez J.D. et al. Meteoric Smoke Deposition in the Polar Regions: A Comparison of Measurements With Global Atmospheric Models. *Journal of Geophysical Research: Atmospheres*. 2017. Vol. 122. Iss. 20, p. 11112-11130. DOI: 10.1002/2017JD027143
15. Dhomse S.S., Saunders R.W., Tian W. et al. Plutonium-238 observations as a test of modeled transport and surface deposition of meteoric smoke particles. *Geophysical Research Letters*. 2013. Vol. 40. Iss. 16, p. 4454-4458. DOI: 10.1002/grl.50840
16. McMullan S., Collins G.S. Uncertainty quantification in continuous fragmentation airburst models. *Icarus*. 2019. Vol. 327, p. 19-35. DOI: 10.1016/j.icarus.2019.02.013
17. Moilanen J., Gritsevich M., Lyytinen E. Determination of strewn fields for meteorite falls. *Monthly Notices of the Royal Astronomical Society*. 2021. Vol. 503. Iss. 3, p. 3337-3350. DOI: 10.1093/mnras/stab586
18. Brykina I.G., Egorova L.A. Describing the fragment mass distribution in meteorite showers. *Planetary and Space Science.* 2024. Vol. 241. N 105838. DOI: 10.1016/j.pss.2024.105838
19. Brykina I.G., Egorova L.A. On the Power Index in Description of Mass Distributions of Fragments of Disrupted Meteoroids and Asteroids. *Moscow University Mechanics Bulletin.* 2025. Vol. 80. N 4, p. 152-160. DOI: 10.3103/S0027133025700244
20. Ivanov A.V., Yashkov I.A., Smurov A.V. et al. Organization of complex expeditions in the Volga region: the tenth season of the "Flotilla of Floating Universities". *Life of the Earth.* 2025. Vol. 47. N 2, p. 266-278 (in Russian). DOI: 10.29003/m4694.0514-7468.2020_47_2/266-278
21. Veselovskiy R.V., Dubinya N.V., Ponomarev A.V. et al. Shared Research Facilities "Petrophysics, Geomechanics and Paleomagnetism" of the Schmidt Institute of Physics of the Earth RAS. *Geodynamics & Tectonophysics.* 2022. Vol. 13. N 2. N 0579 (in Russian). DOI: 10.5800/GT-2022-13-2-0579
22. Kuebler K.E., Jolliff B.L., Wang A., Haskin L.A. Extracting olivine (Fo–Fa) compositions from Raman spectral peak positions. *Geochimica et Cosmochimica Acta*. 2006. Vol. 70. Iss. 24, p. 6201-6222. DOI: 10.1016/j.gca.2006.07.035
23. Freeman J.J., Wang A., Kuebler K.E. et al. Characterization of natural feldspars by Raman spectroscopy for future planetary exploration. *The Canadian Mineralogist*. 2008. Vol. 46. N 6, p. 1477-1500. DOI: 10.3749/canmin.46.6.1477
24. Mouri T., Enami M. Raman spectroscopic study of olivine-group minerals. *Journal of Mineralogical and Petrological Sciences*. 2008. Vol. 103. Iss. 2, p. 100-104. DOI: 10.2465/jmps.071015
25. Rojas J., Duprat J., Engrand C. et al. The micrometeorite flux at Dome C (Antarctica), monitoring the accretion of extraterrestrial dust on Earth. *Earth and Planetary Science Letters*. 2021. Vol. 560. N 116794. DOI: 10.1016/j.epsl.2021.116794
26. Pandey M., Rudraswami N.G., Singh V.P., Viegas A. Geochemical evaluation of cosmic spherules collected from the Central Indian Ocean Basin. *Deep Sea Research Part I: Oceanographic Research Papers*. 2023. Vol. 200. N 104153. DOI: 10.1016/j.dsr.2023.104153
27. Singh V.P., Rudraswami N.G. Spatial variation of micrometeorite abundance in global ocean. *Deep Sea Research Part I: Oceanographic Research Papers*. 2025. Vol. 222. N 104533. DOI: 10.1016/j.dsr.2025.104533
28. Suttle M.D., Campanale F., Folco L. et al. Fossil micrometeorites from Monte dei Corvi: Searching for dust from the Veritas asteroid family and the utility of micrometeorites as a palaeoclimate proxy. *Geochimica et Cosmochimica Acta*. 2023. Vol. 355, p. 75-88. DOI: 10.1016/j.gca.2023.06.027
29. Gabdullin R.R., Badulina N.V., Ivanov A.V. Astroclimatic benchmarks of stratigraphic correlation for Neogene-Quaternary deposits. *Moscow University Bulletin. Series 4. Geology.* 2024. N 6, p. 61-71 (in Russian). DOI: 10.55959/MSU0579-9406-4-2024-63-6-61-71
30. Ruggiu L.K., Villeneuve J., Da Silva A.-C. et al. Diversity among fossil micrometeorites in the late Devonian. *Geochimica et Cosmochimica Acta*. 2025. Vol. 405, p. 114-131. DOI: 10.1016/j.gca.2025.07.016
31. Genge M.J., Engrand C., Gounelle M., Taylor S. The classification of micrometeorites. *Meteoritics & Planetary Science*. 2008. Vol. 43. Iss. 3, p. 497-515. DOI: 10.1111/j.1945-5100.2008.tb00668.x

This is an open access article under the CC BY 4.0 license

32. Toppani A., Libourel G., Engrand C., Maurette M. Experimental simulation of atmospheric entry of micrometeorites. *Meteoritics & Planetary Science*. 2001. Vol. 36. Iss. 10, p. 1377-1396. DOI: 10.1111/j.1945-5100.2001.tb01831.x

33. Toppani A., Libourel G. Factors controlling compositions of cosmic spinels: application to atmospheric entry conditions of meteoritic materials. *Geochimica et Cosmochimica Acta*. 2003. Vol. 67. Iss. 23, p. 4621-4638. DOI: 10.1016/S0016-7037(03)00383-1

34. Wozniakiewicz P.J., Alesbrook L.S., Bradley J.P. et al. Atmospheric collection of extraterrestrial dust at the Earth's surface in the mid-Pacific. *Meteoritics & Planetary Science*. 2024. Vol. 59. Iss. 10, p. 2789-2817. DOI: 10.1111/maps.14251

35. Brearley A.J., Jones R.H. Chondritic Meteorites. *Reviews in Mineralogy*. Mineralogical Society of America, 1998. Vol. 36, p. 3-001-3-398.

36. Genge M.J., Alesbrook L., Almeida N.V. et al. The fusion crust of the Winchcombe meteorite: A preserved record of atmospheric entry processes. *Meteoritics & Planetary Science*. 2024. Vol. 59. Iss. 5, p. 948-972. DOI: 10.1111/maps.13937

37. Velázquez V.-F., Gomes C.B., Mansueto M. et al. Morphological aspects, textural features and chemical composition of spherules from the Colônia impact crater, São Paulo, Brazil. *Solid Earth Sciences*. 2021. Vol. 6. Iss. 1, p. 27-36. DOI: 10.1016/j.sesci.2020.12.004

38. Genge M.J., Davies B., Suttle M.D. et al. The mineralogy and petrology of I-type cosmic spherules: Implications for their sources, origins and identification in sedimentary rocks. *Geochimica et Cosmochimica Acta*. 2017. Vol. 218, p. 167-200. DOI: 10.1016/j.gca.2017.09.004

39. Stulov V.P., Mirskii V.N., Vislyi A.I. Aerodynamics of bolides. Moscow: Nauka. Fizmatlit, 1995, p. 240 (in Russian).

40. Badyukov D.D., Raitala J. Ablation Spherules in the Sikhote Alin Meteorite and Their Genesis. *Petrology.* 2012. Vol. 20. N 6, p. 520-528. DOI: 10.1134/S086959111206001X

41. Savelyev D.P., Savelyeva O.L., Moskaleva S.V., Rashidov V.A. Composition of Cosmic Spherules from Ferromanganese Crusts of the Magellan Seamounts. *Geochemistry International.* 2022. Vol. 60. N 5, p. 411-420. DOI: 10.1134/S0016702922050081

42. Kuzina D., Gattacceca J., Gouilloux H. et al. The effect of terrestrial weathering on the magnetic properties of meteorites from the Atacama Desert. *Uchenye Zapiski Kazanskogo Universiteta. Seriya Estestvennye Nauki.* 2025. Vol. 167. N 2, p. 353-366. DOI: 10.26907/2542-064X.2025.2.353-366

43. Ivanov A.V., Yaroshevskiy A.A., Ivanova M.A. Meteorite Minerals. *Geochemistry International.* 2019. Vol. 57. N 8, p. 931-939. DOI: 10.1134/S0016702919080056

44. Jones R.H., Villeneuve J., Libourel G. Thermal Histories of Chondrules. Petrologic Observations and Experimental Constraints. Chondrules: Records of Protoplanetary Disk Processes. Cambridge University Press, 2018, p. 57-90. DOI: 10.1017/9781108284073.003

45. Pechersky D.M., Markov G.P., Tselmovich V.A., Sharonova Z.V. Extraterrestrial Magnetic Minerals. *Izvestiya, Physics of the Solid Earth.* 2012. Vol. 48. N 7-8, p. 653-669. DOI: 10.1134/s1069351312070051

46. Pechersky D.M., Gilmanova D.M., Kazansky A.Yu. et al. Native iron in Quaternary deposits of the Darhad Basin (*northern Mongolia*). *Russian Geology and Geophysics.* 2013. Vol. 54. N 12, p. 1499-1514. DOI: 10.1016/j.rgg.2013.10.017

47. Pechersky D.M., Markov G.P., Tselmovich V.A. Pure Iron and Other Magnetic Minerals in Meteorites. *Solar System Research.* 2015. Vol. 49. N 1, p. 61-71. DOI: 10.1134/S0038094614060070

48. Pechersky D.M., Kuzina D.M., Nurgaliev D.K., Tselmovich V.A. The common nature of native iron in terrestrial rocks and meteorites: Microprobe and thermomagnetic data. *Izvestiya, Physics of the Solid Earth.* 2015. Vol. 51. N 5, p. 748-763. DOI: 10.1134/S1069351315050109

49. Targulian V.O., Bronnikova M.A. Soil Memory: Theoretical Basics of the Concept, Its Current State, and Prospects for Development. *Eurasian Soil Science.* 2019. Vol. 52. N 3, p. 229-243. DOI: 10.1134/S1064229319030116

***Authors*: Aleksei V. Ivanov,** *Candidate of Geological and Mineralogical Sciences*, *Leading Researcher* (*Lomonosov Moscow State University*, *Moscow*, *Russia*), *Senior Researcher* (*Institute of Geography*, *RAS*, *Moscow*, *Russia*), *Associate Professor* (*Tambov State Technical University*, *Tambov*, *Russia*), *http://orcid.org/0000-0003-2788-0215*, **Ruslan R. Gabdullin,** *Doctor of Geological and Mineralogical Sciences*, *Professor* (*Lomonosov Moscow State University*, *Moscow*, *Russia*), *Leading Researcher* (*Vernadsky Institute of Geochemistry and Analytical Chemistry of the RAS*, *Moscow*, *Russia*), *https://orcid.org/0000-0001-8296-7191*, **Sofya I. Merenkova,** *Candidate of Geological and Mineralogical Sciences*, *Researcher* (*Shirshov Institute of Oceanology of RAS*, *Moscow*, *Russia*), *Junior Researcher* (*Schmidt Institute of Physics of the Earth of the RAS*, *Moscow*, *Russia*), *koshelevasof@mail.ru*, *https://orcid.org/0000-0003-3204-4393*, **Aleksei A. Samsonov,** *Candidate of Geological and Mineralogical Sciences*, *Senior Researcher* (*Lomonosov Moscow State University*, *Moscow*, *Russia*), *https://orcid.org/0009-0007-4637-0399*, **Alvina V. Chistyakova,** *Researcher* (*Schmidt Institute of Physics of the Earth of the RAS*, *Moscow*, *Russia*), *https://orcid.org/0000-0001-5959-9327*, **Dmitrii F. Ayatskov,** *Doctor of History*, *Professor* (*Center for the Development of the Saratov Agglomeration and Industrial Parks*, *Saratov*, *Russia*), *https://orcid.org/0009-0007-6829-6820*, **Mikhail A. Vinnik,** *Doctor of Pedagogical Sciences*, *Leading Researcher* (*Lomonosov Moscow State University*, *Moscow*, *Russia*), *https://orcid.org/0009-0006-6970-7567*, **Evgenii Yu. Pogozhev,** *Candidate of Biological Sciences*, *Senior Researcher* (*Lomonosov Moscow State University*, *Moscow*, *Russia*), *https://orcid.org/0009-0003-3018-930X*, **Afanasii E. Telnov,** *Postgraduate Student* (*Lomonosov Moscow State University*, *Moscow*, *Russia*), *https://orcid.org/0009-0002-7428-8097*, **Yurii A. Churikov,** *Postgraduate Student* (*Lomonosov Moscow State University*, *Moscow*, *Russia*), *https://orcid.org/0009-0001-2402-7414*, **Nikita N. Anisimov,** *Postgraduate Student* (*Lomonosov Moscow State University*, *Moscow*, *Russia*), *https://orcid.org/0009-0007-9881-1969*, **Natalya V. Badulina,** *Candidate of Geological and Mineralogical Sciences*, *Senior Researcher* (*Lomonosov Moscow State University*, *Moscow*, *Russia*), *https://orcid.org/0000-0002-1465-2996*.

The authors declare no conflict of interests.

This is an open access article under the CC BY 4.0 license

ISSN 2411-3336; e-ISSN 2541-9404

JOURNAL OF MINING INSTITUTE
Zapiski Gornogo instituta
Journal homepage: pmi.spmi.ru

Research article
Geotechnical Engineering and Engineering Geology

Predicting gas hydrate formation temperature using a hybrid artificial intelligence-empirical approach

Mohsen Riazi[1], **Hossein Mehrjoo**[1], **Mohammad-Saber Dabiri**[1], **Jamilyam Ismailova**[2], **Masoud Riazi**[3]✉
[1] *Shahid Bahonar University of Kerman, Kerman, Iran*
[2] *Satbayev University, Almaty, Republic of Kazakhstan*
[3] *Nazarbayev University, Astana, Republic of Kazakhstan*

***How to cite this article*:** Riazi M., Mehrjoo H., Dabiri M.-S., Ismailova J., Riazi M. Predicting gas hydrate formation temperature using a hybrid artificial intelligence-empirical approach. Journal of Mining Institute. 2026. Vol. 280, p. 145-162.

Abstract
Accurate prediction of gas hydrate formation temperature is essential for ensuring flow assurance during natural gas production and subsea transportation. In this study, 459 experimental data points collected from the literature, covering a wide pressure range of 330-68,600 kPa and gas specific gravity range of 0.552-1.03, were utilized to develop reliable predictive tools using only two practical input variables: pressure and gas specific gravity. Two complementary modeling approaches were implemented. First, a systematic comparative analysis of several advanced machine learning technique, including Multilayer Perceptron (MLP) trained with Levenberg – Marquardt (LM), Bayesian Regularization (BR), and Scaled Conjugate Gradient (SCG) algorithms; Radial Basis Function (RBF); CatBoost; XGBoost; and Least-Squares Support Vector Machine (LSSVM), was conducted. Second, an optimized empirical correlation was formulated, with its coefficients determined using the Generalized Reduced Gradient (GRG) nonlinear optimization algorithm to minimize overall prediction error across the entire experimental dataset. Among the machine learning models, CatBoost demonstrated superior predictive performance, achieving an AAPRE of 0.094 % and an R^2 value of 0.996 on the testing dataset. The developed GRG-based correlation also exhibited strong agreement with experimental data while providing a transparent and computationally efficient alternative suitable for rapid engineering calculations. Sensitivity and leverage analyses confirmed the robustness, statistical reliability, and broad applicability of the proposed models within the investigate domain.

Keywords
gas hydrate temperature; least-squares support vector machine; machine learning; multilayer perceptron; radial basis function; generalized reduced gradient

Funding
None.

Received: 09.02.2025 ***Accepted: 25.06.2026*** ***Online: 28.08.2026*** ***Published: 10.09.2026***

Introduction

In recent years, natural gas has emerged as an abundant, valuable, and environmentally friendly energy source [1-4]. Substantial efforts are being made to promote and expand its utilization across various sectors, driven not only by its technical and economic advantages but also by its low greenhouse gas emissions [2, 5]. Nevertheless, natural gas production often occurs under unconventional conditions, presenting numerous operational challenges. Extraction, together with associated field operations such as deep-water drilling, pipeline transportation, storage, and separation, faces significant flow assurance issues [6-9]. Among these, hydrate formation is recognized as the most critical, as it can cause severe consequences, including blockages in pipelines and blowout preventers, as well as operational instability and potential safety and integrity failures in field

This is an open access article under the CC BY 4.0 license

installations [10-13]. Gas hydrates are crystalline solids with a clathrate structure, formed when small gas molecules, referred to as "guests," including hydrogen sulfide, carbon dioxide, methane, ethane, propane, and nitrogen, become encaged within cavities created by water molecules, known as the "host." These hydrates generally form under high-pressure and low-temperature conditions [14-19]. The formation of hydrates is frequently observed due to the continuous presence of water during gas production or as a result of improper pipeline design and construction.

In multiphase transfer pipelines, surface facilities, and wellheads, hydrates present a major flow assurance challenge. The effective and timely implementation of hydrate prevention strategies is critical, as blockages caused by hydrate formation can halt production for days or even months. Such disruptions may result in substantial economic losses, potentially amounting to millions of dollars in gas gathering systems or high-pressure natural gas transmission pipelines. E.Hammerschmidt et al. [20] first reported hydrate plugging in pipelines in 1934. Since then, the deposition of hydrates during the transportation and production of natural gas has become a prominent area of investigation. Considerable advancements in hydrate research have drawn significant attention, emphasizing the importance of understanding hydrate formation, identifying its key parameters, and developing effective mitigation strategies for both academic research and industrial practice [17, 21-26]. Given the multidisciplinary relevance of hydrate formation, there has been increasing interest in accurately determining its formation conditions [27]. Among these, the hydrate formation temperature is one of the most critical parameters [28, 29]. While experimental methods provide reliable predictions of hydrate formation temperature, they are often costly and time-consuming. As a result, researchers have pursued more cost-effective predictive approaches, including empirical correlations, chart-based techniques, and theoretical models based on various equations of state [27-29].

Although the earliest model for predicting hydrate formation temperature, the correlation introduced by E.Hammerschmidt in 1934 [20], elated hydrate formation temperature solely to pressure, subsequent and more advanced correlations have incorporated both pressure and gas composition as key input parameters [30-35]. Building on these developments, several researchers have also employed machine learning techniques to predict gas hydrate formation temperature, offering enhanced predictive accuracy and efficiency compared to traditional methods.

A.A.Elgibaly and A.M.Elkamel [36] developed a sophisticated artificial neural network (ANN) model to predict hydrate formation conditions for various pure gases, gas mixtures, and different inhibitors. Their study examined multiple neural network architectures to identify the most accurate configuration. According to their findings, a network with a single hidden layer containing 25 neurons provided reasonably precise results for the gravity-based model. For compositional models, networks with 40 or 50 neurons in the hidden layer yielded the lowest prediction errors. In addition, they introduced a novel ANN model based on gas gravity, incorporating updated experimental data on hydrate formation conditions. This model demonstrated superior accuracy compared with conventional gravity-graphic methods and empirical correlations. However, for gas gravities between 0.8 and 1.0, its applicability was limited due to the scarcity of experimental data. For gravities exceeding 1.0, the model produced ambiguous results, likely as a consequence of insufficient data and the limitations of relying solely on gas gravity as an input parameter.

G.Zahedi et al. [37] employed an ANN-based approach to predict hydrate formation temperature and reported outstanding predictive performance. Their results showed that the ANN model achieved higher accuracy compared with conventional prediction methods.

This is an open access article under the CC BY 4.0 license

S.H.Riazi et al. [38], using experimental data from E.D.Sloan and C.A.Koh [15], developed a new correlation through MATLAB curve-fitting techniques. The correlation was further optimized using the Genetic Algorithm (GA), Particle Swarm Optimization (PSO), and the Imperialist Competitive Algorithm (ICA) to enhance its accuracy. Compared with previous models, the proposed correlation exhibited the lowest error and the highest overall accuracy.

S.M.Hesami et al. [39] introduced two advanced ANN-based techniques optimized using ICA to predict gas hydrate formation conditions. The ICA-ANN model was developed using empirical data from the literature and evaluated against a conventional ANN model as well as a rigorous thermodynamic model under various operating conditions. Unexpectedly, the ICA-ANN model underperformed relative to the conventional ANN approach.

M.N.Amar [40] proposed a reliable and user-friendly correlation to estimate hydrate formation temperature for various types of natural gas, including sour, acidic, and sweet gases. This correlation was developed using Gene Expression Programming (GEP), an explicit machine learning technique. The results indicated that the GEP-based model predicted hydrate formation temperature with high accuracy, achieving an average absolute relative error (AAPRE) of only 0.1397 %.

M.Mesbah et al. [41] developed a universal and user-friendly correlation based on a hybrid Group Method of Data Handling (GMDH) approach to predict hydrate formation temperature for a wide range of natural gas mixtures, including both sweet and sour gases. Compared with traditional correlations, this model demonstrated superior statistical performance. Notably, it showed promising results for sour gases with high H_2S concentrations, outperforming existing thermodynamic models and empirical correlations. A leverage statistical method was applied to identify questionable data points and assess model reliability. The analysis confirmed that nearly all data points fell within the valid applicability range, supporting the statistical robustness of the proposed hybrid GMDH model.

To predict methane hydrate formation temperature over a broad range of brine concentrations, M.Hosseini and Yu.Leonenko [42] proposed machine learning-based models. Their findings indicated that extremely randomized trees achieved strong predictive performance, with a testing root mean square error (RMSE) of 0.6248.

In 2024, M.Karaköse and Ö.Yücel [43] developed advanced machine learning regression models to estimate hydrate formation temperature based on the chemical composition of sweet gas mixtures. The applied techniques included linear regression, decision tree regression (DT), random forest regression (RF), generalized additive models, and ANN. Ensemble methods, particularly random forest, demonstrated superior performance, achieving an R^2 and adjusted R^2 of 0.998. These results highlight the potential of ensemble learning approaches to improve the safety and efficiency of gas transportation and processing systems.

N.Khan et al. [44] evaluated three machine learning algorithms – Support Vector Regression (SVR), ANN, and DT – for predicting hydrate formation temperature. Their results showed R^2/RMSE values of (0.9999; 0.0631), (0.9986; 0.5011), and (0.9278; 3.5606) for SVR, ANN, and DT, respectively. Based on these findings, SVR exhibited the highest predictive accuracy, followed by ANN, while DT showed comparatively lower performance.

W.Aleem et al. [45] presented a comprehensive and novel comparative analysis of nine distinct machine learning (ML) models for the accurate prediction of methane hydrate formation temperatures in the presence of brines. The investigations applied major ML algorithms, including Multiple Linear Regression (MLR), Long Short-Term Memory (LSTM), Radial Basis Function (RBF), Support Vector Machine (SVM), ANN, Gradient Possess Regression (GPR), Random Forest (RF) and K-Nearest Neighbors (KNN). Model accuracy was validated against a large dataset comprising 1000 data points

This is an open access article under the CC BY 4.0 license

with a diverse range of salt concentrations. The experimental results exhibited the KNN algorithm as fast-converging, accurate, and consistent across the entire range of data points, achieving and R^2 score of 0.975 and an AAPRE of 0.385 %.

M.Khafaie et al. [46] in their study developed an evaluation of two ML models including ANN and hybrid Particle Swarm Optimization-ANN (PSO-ANN). The approach centered on predicting hydrate formation temperature using key input parameters, namely the mole fraction of gas components and system pressure. A dataset comparing 1841 experimental samples was utilized. The ANN model achieved a Mean Squared Error (MSE) of 0.0003533 and R^2 of 0.9976. The PSO-ANN model yielded an MSE of 0.0003298 and R^2 of 0.9899. Both models demonstrated high predictive accuracy, with the PSO-ANN exhibiting a slight advantage in MSE. This research highlighted the efficacy of a streamlined, optimized ML approach for accurate and generalizable gas hydrate temperature.

M.R.Atta et al. [47] conducted a systematic review following PRISMA guidelines and bibliometric mapping to analyze studies on Artificial Intelligence and ML for predicting gas hydrate thermodynamic conditions published between 2016 and 2025. The analysis indicated a predominant focus on binary water – gas system (87.5 %) and a strong reliance on experimental literature-derived datasets (73.9 %). ANN, SVR and RF models were the most prevalent algorithms, with R^2 and RMSE as primary evaluation metrics. A significant limitation identified was the lack of uncertainly quantification and the under-representation of field-derived datasets. The review highlighted opportunities for future work in evaluating model robustness expanding model outputs to include hydrate kinetics and morphology. Although extensive experimental and numerical investigations have been conducted on hydrate formation temperature, there remains a need for comprehensive studies that simultaneously develop accurate, robust, and practically applicable machine learning models and simplified correlations.

In this study, a comprehensive dataset comprising 459 data points was used to develop advanced predictive models for estimating gas hydrate formation temperature. In the first approach, several robust ML techniques – including CatBoost, XGBoost, Least-Squares Support Vector Machine (LSSVM), RBF network, and Multilayer Perceptron (MLP) – were implemented. The models were trained using the Levenberg – Marquardt (LM), Bayesian Regularization (BR), and Scaled Conjugate Gradient (SCG) algorithms. In the second approach, an empirical correlation was developed using the Generalized Reduced Gradient (GRG) optimization technique, accounting for variations in pressure and gas specific gravity. The objective was to derive a novel correlation capable of achieving superior accuracy and performance compared with existing models. A relevancy factor analysis was conducted to assess the influence of input parameters on gas hydrate formation temperature. Furthermore, the leverage method was applied for statistical analysis to identify potential outliers and determine the domain of applicability of the developed models.

Data

The generalizability and reliability of the developed models are strongly influenced by the diversity and quantity of the input data used during model development. In this study, a comprehensive databank comprising of 459 experimental data points, covering a wide range of operating conditions, was compiled to develop accurate predictive models for gas hydrate formation temperature [48-55]. presents a statistical summary of the input variables, including the gas specific gravity and pressure, as well as the output variable (the experimental temperature). The complete dataset used in this study is provided in Supplement https://pmi.spmi.ru/pmi/article/download/16663/16705.

This is an open access article under the CC BY 4.0 license

Table 1

Statistical description of the employed database [48-56]

Features	Gas specific gravity	Pressure, kPa	Experimental temperature, K
Maximum	1.03	68600	304.483
Minimum	0.552	330	272.04
Skewness	1.555	3.474	0.265
Kurtosis	2.338	14.396	–0.809
Mode	0.629	20684.272	283.15
Median	0.651	3164.999	284.349
Mean	0.685	6722.435	284.956
Standard deviation	0.097	10136.045	7.52

As shown in Table 1, the gas specific gravity ranges from 0.552 to 1.03. The pressure varies between 330 and 68600 kPa, with an average value of 6722.435 kPa. The experimental temperatures in the databank range from 272.04 to 304.483 K, with an average of 284.956 K.

Methods

In this study, several machine learning methods were employed to predict gas hydrate formation temperature.

Least-Squares Support Vector Machine (LSSVM). The LSSVM algorithm is widely used for regression analysis, pattern recognition, and data classification tasks. LSSVM retains the main characteristics of the traditional SVM while offering a simplified formulation that reduces computational complexity and training time. Detailed information on SVM theory can be found in the literature [57]. The LSSVM model was first introduced by J.A.K.Suykens and J.Vandewalle [58, 59]. The cost function of this method is similar to that of SVM and expressed as follows:

$$g(y) = O^T \varphi(y_i) + bi,$$

where bi – biased terms; O^T – transposed output layer vector; $\varphi(y_i)$ – kernel function; y_i – input vector of the function.

The input matrix has dimensions $M \times m$, where m and M represent the number of input parameters and the total number of data points, respectively. By minimizing the cost function, the bias term and the output layer vector can be determined [60]:

$$\mathrm{CF} = \frac{1}{2} O^T O + \frac{1}{2} \gamma \sum_{i=1}^{num} s_i^2.$$

The cost function [60]:

$$x_i = O^T \varphi(y_i) + bi + s_i^2, \quad i = 1, 2, 3, ..., M,$$

where s_i – regression error; γ – regularization (adjustable) parameter in LSSVM.

The Lagrangian form of the problem [60]:

$$K(O, s, q, bi) = \frac{1}{2} O^T O + \frac{1}{2} \gamma \sum_{i=1}^{num} s_i^2 - \sum_{i=1}^{num} q_i \left(O^T \varphi(y_i) + bi + s_i - x_k \right),$$

where q_i – Lagrange multiplier.

By taking the partial derivatives of the Lagrangian with respect to bi, q_i, s_i, and O, the unknown parameters can be obtained [60]:

This is an open access article under the CC BY 4.0 license

© Mohsen Riazi, Hossein Mehrjoo, Mohammad-Saber Dabiri, Jamilyam Ismailova, Masoud Riazi, 2026

$$\begin{cases} \dfrac{\partial K}{\partial O} = 0 \to O = \sum\limits_{i=1}^{num} q_i \varphi(y_i); \\ \dfrac{\partial K}{\partial bi} = 0 \to \sum\limits_{i=1}^{num} q_i = 0; \\ \dfrac{\partial K}{\partial s_i} = 0 \to q_i = \gamma s_i, \ \ i = 1,2,3,...,M; \\ \dfrac{\partial K}{\partial q_i} = 0 \to O^T \varphi(y_i) + bi + s_i - x_k = 0, \ \ i = 1,2,3,...,M. \end{cases}$$

Solving this system of equations yields the required variables in the LSSVM framework. The following equations present three commonly used kernel functions:

- radial basis function kernel – $\varphi(y, y_i) = \exp\left(\dfrac{-\|y_i - y\|^2}{\sigma^2}\right)$;
- linear kernel – $\varphi(y, y_i) = y_i^T y$;
- polynomal kernel – $\varphi(y, y_i) = \left(\tau + y_i^T y\right)^n$.

In LSSVM, σ^2 is an adjustable parameter that can be optimized by minimizing an objective function, such as the mean squared error. Consequently, by using the following equations, the difference between the predicted outputs of the developed model and the corresponding experimental values is minimized as follows:

$$\text{MSE} = \frac{\sum\limits_{j=1}^{m}\left(R_{exp_j} - R_{\text{rep/pred}_j}\right)^2}{m}.$$

Radial Basis Function (RBF). The RBF network is a well-established type of feedforward artificial neural network and is widely used as a robust modeling approach for solving complex problems [61, 62]. An RBF neural network typically consists of three layers: an input layer, a hidden layer, and an output layer. In the hidden layer, each neuron is associated with a center and a predefined radius, defining a specific region in the input space. Within each neuron, the distance between the input vector and the corresponding center is calculated [63]. For this purpose, various activation functions, such as thin-plate spline, Gaussian, cubic, logistic, and quadratic functions, are commonly employed [64]. The Euclidean distance between the input vector and the center of each neuron is calculated using [65]

$$r_i = \left[\sum_{j=1}^{l}\left(y_i - Ce_{ji}\right)^2\right]^{0.5}, \ \ i = 1, ..., M,$$

where the subscripts i and l – number of center vectors and the number of inputs, respectively; y_i and r_i – input vector and the Euclidean distance from the neuron's center; Ce_{ji} – cluster center.

The output of the RBF model [66] as follows, further details regarding this neural network model can be found in references [67-69]:

$$x_c(y) = \sum_{i=1}^{M} cw_i \varphi_{ci}\left(\|y_c - Ce_i\|\right), \quad i = 1, ..., M, \ \ c = 1, ..., N,$$

where cw_i – connection weight; M – number of hidden-layer neurons; Ce_i – center vector; φ – transfer function.

This is an open access article under the CC BY 4.0 license

Multilayer Perceptron (MLP). The MLP is a widely used feedforward ANN [65] composed of an input layer, one or more hidden layers, and an output layer. The input variables are fed into the input layer, while the hidden layers, typically employing nonlinear activation functions such as tansig and logsig, transform these inputs into higher-level representations [70, 71]. The output layer generally utilizes a purelin activation function to generate the final predictions. Training the MLP is performed using the backpropagation algorithm, in which the network weights and biases are iteratively updated to minimize the error between the predicted and target outputs. Although a single hidden layer is often sufficient to capture the relationships between inputs and outputs, additional layers may be required when modeling more complex systems.

Generalized Reduced Gradient (GRG). The GRG method is widely used to solve optimization problems involving multiple variables. This approach is based on the concept of reduced gradients and is capable of handling both linear and nonlinear constraints while ensuring that active constraints are satisfied throughout the solution process. By approximating the gradient at a given point z, the GRG method simultaneously considers the gradients of both the objective function and the constraint equation. As a result, the constraints are incorporated into the gradients of the objective function, restricting the search to feasible directions and effectively reducing the solution space. In this study, $f(z)$ represents the objective function to the constraint $h(z)$ [72].

Minimizes: $f(z) = z$; subjected to: $h_k(z) = 0$. The GRG formulation can be expressed as follows:

$$\frac{df}{dz_k} = \nabla z_k^t f - \nabla z_i^t f \left(\frac{dh}{dz_i} \right) \frac{dh}{dz_k}.$$

A necessary condition for minimizing $f(y)$ is that its first derivative vanishes, i.e., $df(y) = 0$.

Optimization algorithm. The effectiveness of neural network models largely depends on the selection of appropriate training algorithms used to optimize their weights and biases. In this study, three optimization algorithms were employed to train the MLP model. The LM algorithm is widely recognized for its capability to enhance MLP performance by efficiently solving nonlinear least-squares problems [73, 74]. Furthermore, the BR algorithm provides a robust alternative by adjusting the network weights and biases within the LM training framework, while applying Bayes' theorem to update their distributions [75, 76]. The SCG algorithm eliminated the need for computationally expensive line searches, thereby offering a faster and more efficient training process compared with other gradient-based methods.

Results and discussion

In this study, the formation temperature of gas hydrates was modeled over a wide range of operating conditions. The intelligent models used pressure and gas specific gravity as input variables, while the gas hydrates formation temperature served as the output. A comprehensive databank containing 459 experimental data points was randomly divided into two subsets for model development:

• Training Set. This subset was used for model development, optimization, and performance improvement. During training, the model establishes a relationship between input parameters and the output by iteratively adjusting biases and weights to minimize the deviation between the experimental and predicted values.

• Test Set. This subset was reserved to evaluate the predictive capabilities of model and assess their accuracy.

For all models in this research, 80 % of the data were allocated to the training phase, while the remaining 20 % were used for testing. It is important to note that good performance during training

This is an open access article under the CC BY 4.0 license

does not necessarily guarantee the model reliability. Therefore, testing on the reserved data is essential to validate the accuracy and robustness of the developed models.

Advanced machine learning algorithms, including CatBoost, XGBoost, MLP, RBF, and LSSVM, were employed to model the gas hydrate formation temperature. Additionally, three optimization techniques, LM, SCG, and BR, were applied to train the MLP network. Various statistical and graphical error analyses were conducted to evaluate the performance of the developed models and sensitivity analysis was performed to determine the influence of the input parameters on the models' outputs.

Prior to model development, all input and output variables were normalized using min-max scaling to the range of −1 to 1 to improve numerical stability and convergence. The predicted outputs were subsequently transformed back to their original scale. As an initial step, a correlation based on the input parameters was developed to estimate the formation temperature of gas hydrates.

Development of correlation. For the GRG algorithm, a correlation was established, demonstrating its capability to predict the target parameters with high accuracy. As a result, a clear equation was developed, comprising two input parameters and five additional coefficients:

$$T = aSG^{b}\left(\frac{\log(P)}{1.5}\right)^{C} - dSG\sqrt{\frac{\log(P)}{3.25}} + e, \tag{1}$$

where T – temperature, K; P – pressure, kPa; SG – gas specific gravity; a, b, c, d, and e – correlation constants, a = 162.4292; b = 0.244852; c = 0.36583; d = 50.60196; e = 116.777.

The correlation presented in equation (1) can be used to estimate the gas hydrate formation temperature as a function of pressure and gas specific gravity.

Evaluation of models. In this study, the proposed models were evaluated using statistical error analysis. Their performance was assessed using several metrics, including the coefficient of determination R^2, RMSE, and AAPRE:

$$\mathrm{RMSE} = \sqrt{\frac{\sum_{i=1}^{N}\left(T_{exp,i} - T_{\mathrm{pred},i}\right)^2}{N}};$$

$$\mathrm{AAPRE} = \frac{100}{N}\sum_{i=1}^{N}\frac{\left|T_{exp,i} - T_{\mathrm{pred},i}\right|}{T_{exp,i}};$$

$$\mathrm{R}^2 = 1 - \frac{\sum_{i=1}^{N}\left(T_{exp,i} - T_{\mathrm{pred},i}\right)^2}{\sum_{i=1}^{N}\left(T_{exp,i} - \bar{T}\right)^2},$$

where N – total number of data points; $T_{exp,i}$ – experimentally observed temperature; $T_{\mathrm{pred},i}$ – predicted temperature.

Statistical evaluation. To identify the most accurate model, the developed models were systematically evaluated and compared using statistical metrics, including R^2, AAPRE, and RMSE. According to statistical principles, model accuracy and validity improve as the R^2 value approaches 1, while lower values of RMSE and AAPRE indicate greater precision in the modeling process. The parameter values are presented in Table 2.

The results revealed that, among the tested models, the CatBoost model exhibited the highest accuracy, followed by XGBoost, MLP-LM, MLP-BR, MLP-SCG, and LSSVM in terms of predictive performance. As shown in Table 2, the AAPRE values of 0.126 % for the testing set, 0.086 % for the

This is an open access article under the CC BY 4.0 license

training set, and 0.094 % for the entire dataset indicate that the CatBoost approach provides highly accurate predictions of gas hydrate formation temperature. Additionally, this method achieved an outstanding overall R^2 value of 0.996. The results further established the following hierarchy of predictive accuracy for gas hydrate formation temperature: CatBoost outperformed XGBoost, followed by MLP-LM, MLP-BR, MLP-SCG, RBF, and finally LSSVM. Overfitting was assessed by comparing training and testing performance; the minimal difference in R^2 and AAPRE demonstrates that the developed models generalize well across the dataset.

Table 2

Statistical indexes of the developed model for the experimental temperature

Errors	MLP			RBF	LSSVM	CatBoost	XGBoost	Developed correlation
	LM	BR	SCG					
Training								
AAPRE, %	0.187	0.21	0.271	0.308	0.311	0.086	0.103	0.35
RMSE	0.753	0.86	1.037	1.12	1.14	0.414	0.405	1.44
R^2	0.99	0.987	0.981	0.978	0.977	0.997	0.997	0.96
Testing								
AAPRE, %	0.18	0.208	0.277	0.309	0.31	0.126	0.249	0.35
RMSE	0.756	0.837	1.102	1.155	1.13	0.494	1.198	1.44
R^2	0.99	0.987	0.978	0.975	0.978	0.996	0.974	0.96
Total								
AAPRE, %	0.186	0.209	0.272	0.308	0.311	0.094	0.132	0.35
RMSE	0.753	0.855	1.05	1.127	1.138	0.431	0.647	1.43
R^2	0.989	0.987	0.98	0.977	0.977	0.996	0.992	0.96

The hyperparameters of all machine learning models employed in this study were carefully selected to ensure optimal performance:

• MLP: hidden layers – [5.5]; transfer function – tansig, logsig, purelin; training function – LM, BR, SCG;

• RBF: spread – 2.78; max neuron – 100;

• LSSVM: σ^2 – 1.3130; kernel type – RBF kernel; γ – 589.5852;

• CatBoost: colsample bytree – 0.9; gamma – 0.01; learning rate – 0.05; max depth – 5; min child weight – 5; n_estimator – 1000; reg_lambda – 10; subsample – 0.9;

• XGBoost: learning rate – 0.05; l2 leaf reg – 5; iterations – 1500; depth – 6.

In addition to the ML models developed in this study, a correlation was proposed for estimating the formation temperature of gas hydrates. The performance of the proposed correlation, compared with existing models, is presented in Table 3.

Table 3

Statistical analysis of the suggested correlation relative to existing models

Model	AAPRE, %	RMSE	R^2
New correlation	0.3536	1.4287	0.9645
B.Towler, S.Mokhatab [33]	71.4943	203.552	0.9565
M.Safamirzaei et al. [35]	0.4071	1.5506	0.9607
E.Hammerschmidt et al. [20]	66.6774	190.9806	0.8660
S.Chavoshi et al. [77]	0.5292	1.9424	0.9455
M.Motiee et al. [31]	74.2416	211.3726	0.9546

This is an open access article under the CC BY 4.0 license

As shown in Table 3, the correlation developed in the present study demonstrated superior performance compared with existing correlations: AAPRE – 0.3536 %, RMSE – 1.4287, and R^2 – 0.9645.

In addition to the statistical evaluation, a visual assessment was conducted through graphical analysis to examine model performance. Figure 1 presents cross-plots of the predicted versus experimental gas hydrate formation temperatures for both the training and testing datasets, facilitating a visual assessment of the models' accuracy.

A cross-plot is a type of chart that illustrates the relationship between predicted and experimental values. As shown in Fig.1, the tight clustering of predicted data points along the unity line indicates a strong correlation between observed and predicted values, highlighting the remarkable precision of the CatBoost models. Furthermore, the greatest data dispersion is evident in the cross-plot of the LSSVM model, which predicts the gas hydrate formation temperature to be lower than that of the other developed models. This observation is consistent with the error values reported in Table 2.

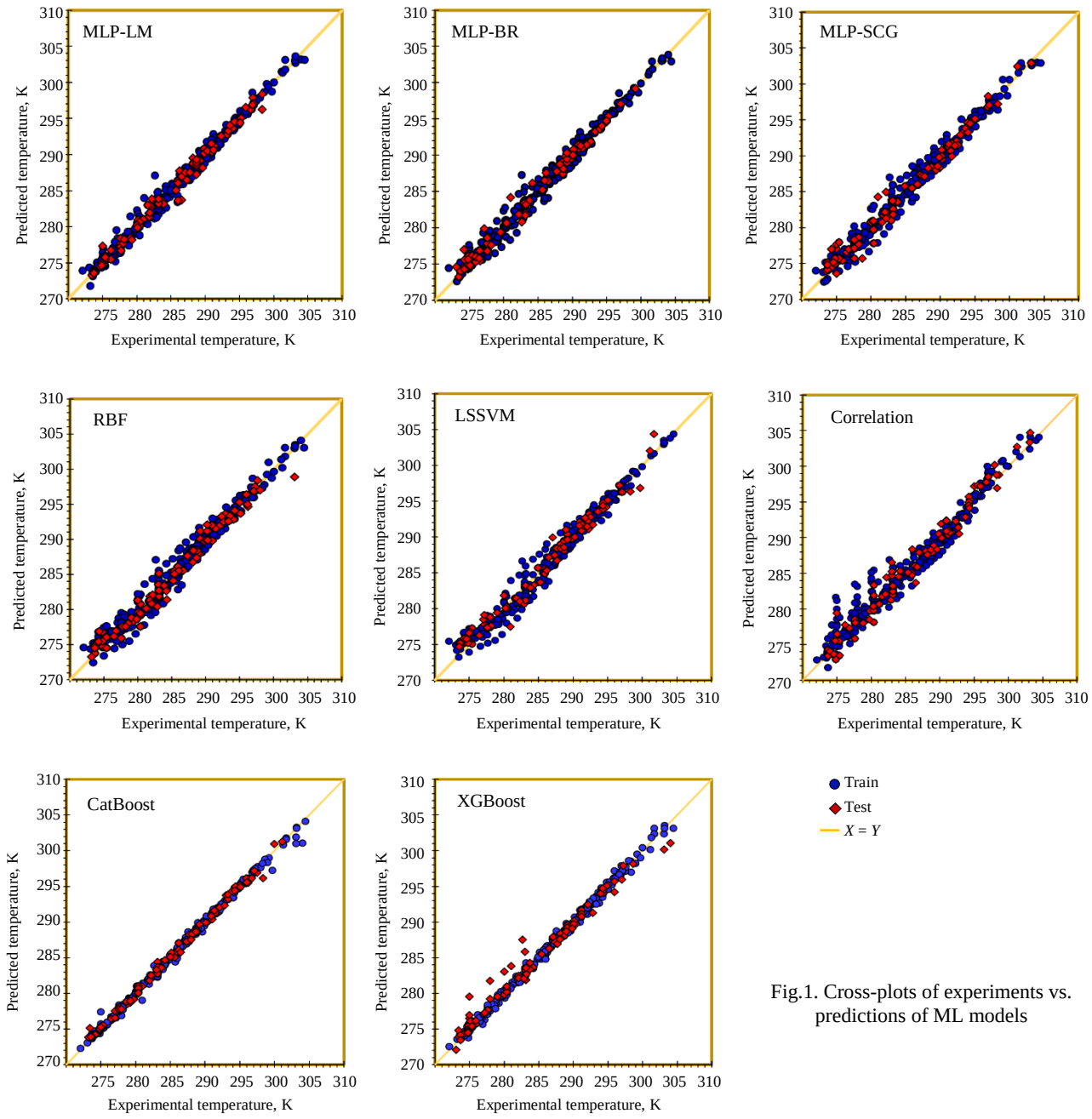


Fig.1. Cross-plots of experiments vs. predictions of ML models

This is an open access article under the CC BY 4.0 license

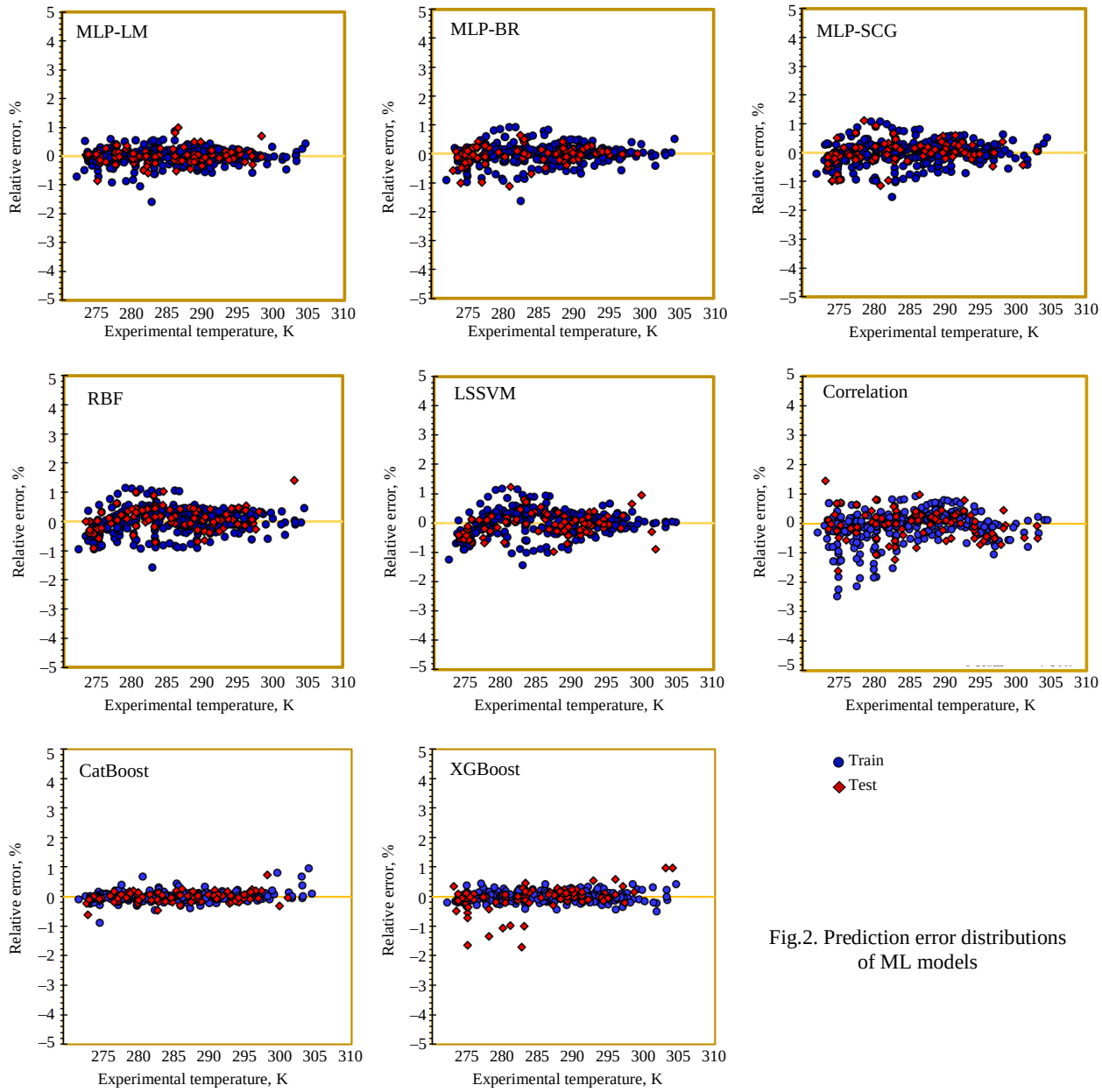


Fig.2. Prediction error distributions of ML models

Figure 2 illustrates the distribution of relative error percentages against the experimentally measured gas hydrate formation temperatures for all models. In this error evaluation, the observed output data are compared with the AAPRE values.

A predictive model demonstrates superior performance in estimating gas hydrate temperature when most data points exhibit errors close to zero. The near-zero errors of the CatBoost model confirmed its precision and reliability. However, other models, particularly XGBoost, can also provide accurate predictions with minimal errors for gas hydrate temperature estimation.

The performance of the developed models, evaluated using R^2 metrics, is shown in Fig.3.

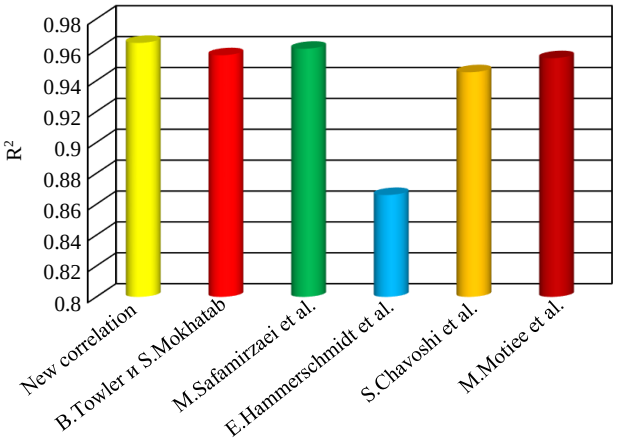


Fig.3. Comparison of R^2 values among the suggested correlation models

This is an open access article under the CC BY 4.0 license

© Mohsen Riazi, Hossein Mehrjoo, Mohammad-Saber Dabiri, Jamilyam Ismailova, Masoud Riazi, 2026

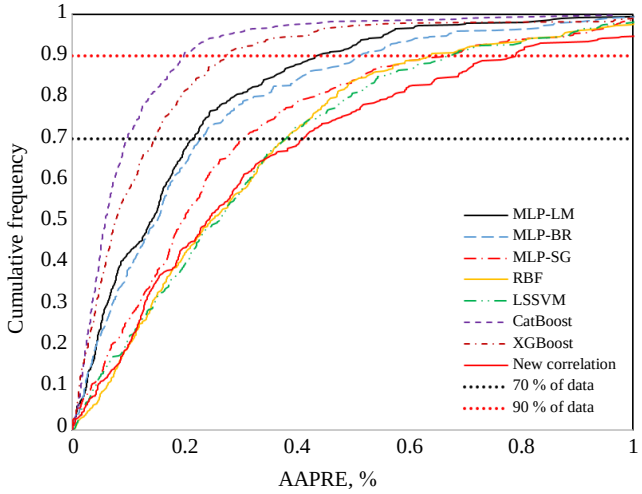


Fig.4. The cumulative frequency diagram of several ML models and the new correlation proposed in this survey

As noted above, the newly developed correlation model exhibited the highest performance among the proposed models, as illustrated in Fig.3.

The next step in visually evaluating the proposed ML models for predicting gas hydrate formation temperature is the analysis of the cumulative error frequency. This analysis allows the prediction of a larger proportion of data points with minimal errors. Figure 4 presents cumulative frequency distributions of AAPRE for various models applied to the entire dataset.

In Fig.4, the dark horizontal dashed line representing 70 % of the data indicates ARE, %: 0.1 – CatBoost, 0.15 – XGBoost, 0.2 – MLP-LM, 0.22 – MLP-BR, 0.29 – MLP-SCG, 0.37 – RBF, 0.38 – LSSVM, and 0.42 – new correlation models. These results demonstrate that 70 % of the dataset achieves prediction errors below the corresponding values. Additionally, approximately 90 % of the CatBoost model's predicted values exhibit absolute relative errors below 0.2 %, whereas the other models exceed this threshold. These findings, corroborated by statistical and graphical analyses, confirm the CatBoost model's superior accuracy in predicting gas hydrate formation temperature.

Trend analysis of the CatBoost and developed correlation. In this section, a trend analysis was conducted to examine whether the optimal models proposed in this study, namely CatBoost, and developed correlation accurately reflects the expected variations in gas hydrate formation temperature with respect to the selected independent variables. Figure 5 illustrate the relationship between gas hydrate formation temperature and pressure, while maintain a constant gas specific gravity.

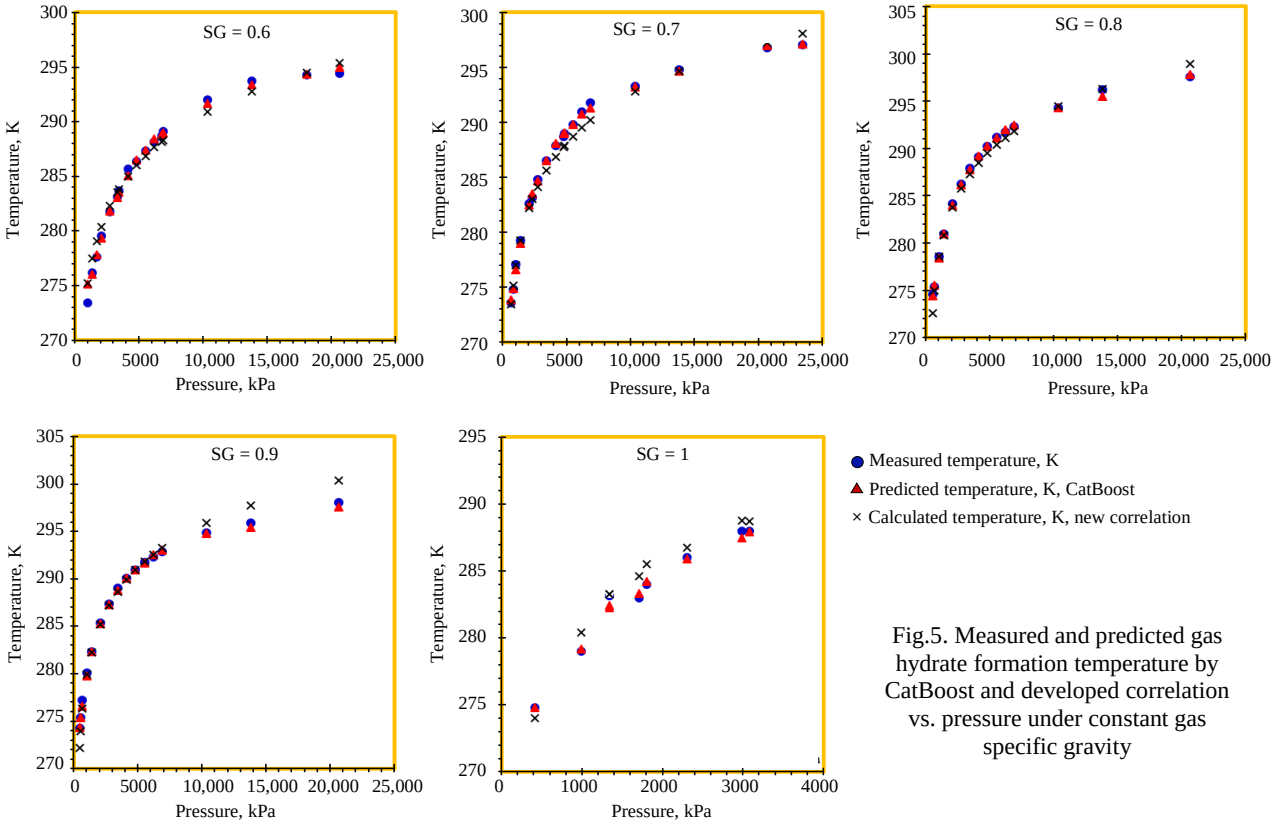


Fig.5. Measured and predicted gas hydrate formation temperature by CatBoost and developed correlation vs. pressure under constant gas specific gravity

This is an open access article under the CC BY 4.0 license

Figure 5 offers further confirmation of the accuracy of the developed models: for gas specific gravity values of 0.6, 0.7, 0.8, and 0.9, both the CatBoost model and the developed correlation closely match the experimental data. However, a slight discrepancy between the prediction models and the experimental data is observed at a gas specific gravity of 1. Furthermore, at high pressures across all gas specific gravities, the prediction accuracy of the models is slightly reduced. The primary reason for these minor deviations is attributed to the limited data available for a gas specific gravity of 1 and for higher pressures within the collected dataset. Additionally, experimental errors may also contribute to the discrepancies observed in the predictions of the developed correlation. Overall, as depicted in Fig.5, the predictions from both the CatBoost model and the developed correlation exhibit excellent agreement with the experimental data under various operational conditions. Additionally, Fig.5 demonstrates that, at a constant gas specific gravity, an increase in pressure leads to a higher gas hydrate formation temperature, a trend accurately captured by both the model and the correlation.

Sensitivity analysis. In this section of the present study, a sensitivity analysis using the absolute relevance factor *r* was performed to assess the influence of input parameters on gas hydrate formation temperature [67, 78, 79]. An input parameter is considered significant if its absolute relevance value is high. This factor is defined as follows:

$$r = \frac{abs\left(\sum_{i=1}^{n}\left(I_{k,i} - \bar{I}_k\right)\left(O_i - \bar{O}\right)\right)}{\sqrt{\sum_{i=1}^{n}\left(I_{k,i} - \bar{I}_k\right)^2 \sum_{i=1}^{n}\left(O_i - \bar{O}\right)^2}},$$

where $I_{k,i}$, $\bar{I}_k$ – *k*-th input parameter and average value of I_k, respectively; *i* refers to either the specific pressure or pressure; O_i, $\bar{O}$ – output and the *i*-th average value of O_i.

The parameter *r*, ranging from –1 to 1, represents the correlation between the dependent and independent variables [80]. A positive value of *r* indicates a direct relationship, meaning that as the independent variable increases, the dependent variable also increases.

The sensitivity analysis of input variables affecting gas hydrate formation temperature, conducted using the Pearson correlation technique: gas specific gravity – 0.067; pressure – 0.752. Input variables such as pressure and gas specific gravity positively influence the target value, indicating that an increase in these parameters leads to an increase in gas hydrate formation temperature. Among them, pressure had the most significant impact, contributing 75.2 %, to the estimate of hydrate temperature. The gas hydrate temperature also increased with pressure.

Leverage approach. To evaluate the robustness of the proposed model and dataset, the Leverage method was applied. The proposed method aims to detect entries showing significant discrepancies across the data [81]. One of the key parameters of this method is the standardized residuals:

$$\mathrm{SR} = \frac{Z_i}{\left[\mathrm{MSE}\left(1 - H_{ii}\right)\right]^{0.5}},$$

where H_{ii} – hat indices; Z_i – error values; MSE – mean square error.

Another key parameter of this approach is the leverage threshold

$$H^* = \frac{3\left(I+1\right)}{N},$$

where *N* – total number of data points.

The last important parameter in this technique is the hat matrix

$$H = X\left(X^t X\right)^{-1} X^t,$$

where *X* – two-dimensional matrix; X^t – transpose [81-83].

This is an open access article under the CC BY 4.0 license

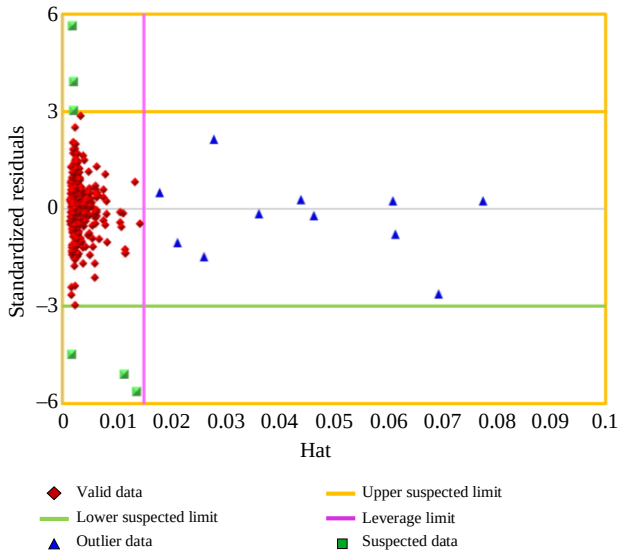


Fig.6. Williams plots for the complete dataset associated with the developed model in this study

William's plot demonstrates the correlation between standardized residuals SR and Hat values, dividing the data into four categories: bad leverage points, valid points, good leverage points, and upper or lower suspected points. A reliable model is characterized by having the majority of its data points fall in a range considered valid, with SR values ranging from –3 to 3 and Hat values staying below the leverage threshold. Data points are considered good leverage points when their Hat values exceed the threshold but their SR values remain within the range of –3 to 3, as they contribute to accurate predictions [71]. Conversely, leverage points that fall outside both domains are considered poor predictors. Suspected values are those with SR values outside the –3 to 3 range but with hat values below the leverage limit. A plot of SR against hat values was created for the CatBoost model to evaluate the formation temperature of gas hydrates (Fig.6).

Williams plot is used to assess the applicability scope of the new correlation and detect potential outliers. As shown in Fig.6, most data points fall within the ranges of $0 \leq H \leq 0.015$ and $-3 \leq \mathrm{SR} \leq 3$, indicating that the experimental data are of high quality and that the new developed model exhibits strong reliability. Data points with $\mathrm{SR} > 3$ or $\mathrm{SR} < -3$ are considered suspicious, because they suggest a high level of uncertainty. Outliers were identified as data points with $H > 0.015$ and $-3 < \mathrm{SR} < 3$, indicating that they fell outside the valid range of the proposed model. A total of 6 data points (1.3 % of the overall dataset) were identified as suspected outliers, with 11 outliers present in the temperature dataset, thereby reinforcing the reliability of the experimental dataset used for modeling.

Model limitations, applicable range, and future work. These models were developed using experimental data covering a pressure range of 330-68,600 kPa, gas specific gravity from 0.552 to 1.03, and laboratory temperatures between 272.04 and 304 K. Therefore, the proposed models are recommended for use within these specific ranges. Outside these boundaries, particularly at pressures lower than 330 kPa or higher than 68,600 kPa, temperatures outside the 272-305 K range, or for gas specific gravities not represented in the training data, prediction accuracy may decrease.

A slight discrepancy between the prediction models and the experimental data is observed at a gas specific gravity of 1 (Fig.5). Furthermore, at high pressures across all gas specific gravities, the prediction accuracy of the models is slightly reduced. The primary reason for these minor deviations is attributed to the limited data available for a gas specific gravity of 1 and for higher pressures within the collected dataset. The correlation is empirical and does not explicitly account for salinity, impurities, or kinetic non-equilibrium effects. These factors may introduce additional uncertainties under such conditions.

Conclusion

In this study, two distinct methodologies were employed to predict gas hydrate formation temperatures. The first approach was data-driven, utilizing several advanced machine learning algorithms: Multilayer Perceptron (MLP) optimized by Levenberg – Marquardt (LM), Bayesian Regularization (BR), and Scaled Conjugate Gradient (SCG); Radial Basis Function (RBF); and Least Squares Support Vector Machine (LSSVM). The second method involved developing a correlation using the

This is an open access article under the CC BY 4.0 license

Generalized Reduced Gradient (GRG) optimization technique, which accounts for variations in pressure and gas specific gravity. These models were developed and validated using a comprehensive dataset of 459 experimental temperature data points compiled from existing studies. Model performance was rigorously evaluated using statistical metrics, including the average absolute percentage relative error (AAPRE), root mean square error (RMSE), coefficient of determination (R^2), and further assessed through visual analyses such as cross-plots, error distribution graphs, and cumulative frequency distributions.

Among all models, the CatBoost algorithm demonstrated the highest predictive accuracy, achieving an AAPRE of 0.094 % and an R^2 value of 0.996. The subsequent models, XGBoost, MLP-LM, MLP-BR, MLP-SCG, RBF, and LSSVM, achieved AAPRE values of 0.103, 0.187, 0.209, 0.272, 0.308, and 0.311 %, respectively, indicating strong performance. The GRG-derived correlation also outperformed existing models in terms of predictive accuracy.

While the developed models exhibit high predictive accuracy within the training data's parameter space, their applicability is inherently limited by the range of input parameters used during development. Predictions made outside these established boundaries may result in reduced accuracy, a crucial consideration for practical implementation. Furthermore, the confidence in predictions can be affected by inherent uncertainties in the input data, particularly for highly relevant parameters. To provide a more critical accuracy assessment beyond standard metrics, we have analyzed outlier predictions, noting that they predominantly occur at the extremes of the input ranges or with less common data points. This offers a more nuanced understanding of the model's performance envelope. The comparative analysis against existing models has also been strengthened, clearly outlining scenarios where our models excel and acknowledging specific contexts where alternative approaches might be more suitable, thereby offering a balanced perspective relative to the state of the art. Sensitivity analysis revealed that pressure has a direct and positive influence on gas hydrate formation temperatures, with pressure being the most significant input variable.

Future research could expand the scope by incorporating influential factors such as salinity, gas composition, and the presence of inhibitors, which were not included in this study due to data limitations. Such an expansion would further enhance the generalizability and robustness of the predictive models.

Access to data

The full dataset used to predict the formation temperature of gas hydrate is available at the link: Supplement, https://pmi.spmi.ru/pmi/article/download/16663/16705.

REFERENCES

1. Safamirzaei M.P. Predict gas hydrate formation temperature with a simple correlation. *Gas Processing Journal*. 2015. July/August, p. 51-54.

2. Esfahani S., Baselizadeh S., Hemmati-Sarapardeh A. On determination of natural gas density: Least square support vector machine modeling approach. *Journal of Natural Gas Science and Engineering*. 2015. Vol. 22, p. 348-358. DOI: 10.1016/j.jngse.2014.12.003

3. Inkong K., Rangsunvigit P., Kulprathipanja S., Linga P. Effects of temperature and pressure on the methane hydrate formation with the presence of tetrahydrofuran (THF) as a promoter in an unstirred tank reactor. *Fuel*. 2019. Vol. 255. N 115705. DOI: 10.1016/j.fuel.2019.115705

4. Tatar A., Barati-Harooni A., Najafi-Marghmaleki A. et al. Prediction of moisture content of natural gases using a GA-RBF model. *Journal of Molecular Liquids*. 2016. Vol. 223, p. 994-999. DOI: 10.1016/j.molliq.2016.08.108

This is an open access article under the CC BY 4.0 license

5. Jingzhou Wang, Lu Zhang, Ran Li et al. A simple generalized viscosity model for natural gas components and their mixtures based on free-volume theory. *Journal of Molecular Liquids*. 2020. Vol. 320. Part B. N 114483. DOI: 10.1016/j.molliq.2020.114483

6. Jianbo Zhang, Zhiyuan Wang, Shun Liu et al. Prediction of hydrate deposition in pipelines to improve gas transportation efficiency and safety. *Applied Energy*. 2019. Vol. 253. N 113521. DOI: 10.1016/j.apenergy.2019.113521

7. Yan Wang, Koh C.A., White J. et al. Hydrate formation management simulations with anti-agglomerants and thermodynamic inhibitors in a subsea tieback. *Fuel*. 2019. Vol. 252, p. 458-468. DOI: 10.1016/j.fuel.2019.04.146

8. Zhiyuan Wang, Shikun Tong, Chao Wang et al. Hydrate deposition prediction model for deep-water gas wells under shut-in conditions. *Fuel*. 2020. Vol. 275. N 117944. DOI: 10.1016/j.fuel.2020.117944

9. Olajire A.A. Flow assurance issues in deep-water gas well testing and mitigation strategies with respect to gas hydrates deposition in flowlines – A review. *Journal of Molecular Liquids*. 2020. Vol. 318. N 114203. DOI: 10.1016/j.molliq.2020.114203

10. Chuanliang Yan, Yang Li, Yuanfang Cheng et al. Sand production evaluation during gas production from natural gas hydrates. *Journal of Natural Gas Science and Engineering*. 2018. Vol. 57, p. 77-88. DOI: 10.1016/j.jngse.2018.07.006

11. Kelland M.A., Iversen J.E. Kinetic Hydrate Inhibition at Pressures up to 760 Bar in Deep Water Drilling Fluids. *Energy & Fuels*. 2010. Vol. 24. Iss. 5, p. 3003-3013. DOI: 10.1021/ef9016152

12. Xin Zhao, Zhengsong Qiu, Zhen Zhang, Yubin Zhang. Relationship between the gas hydrate suppression temperature and water activity in the presence of thermodynamic hydrate inhibitor. *Fuel*. 2020. Vol. 264. N 116776. DOI: 10.1016/j.fuel.2019.116776

13. Yarveicy H., Ghiasi M.M. Modeling of gas hydrate phase equilibria: Extremely randomized trees and LSSVM approaches. *Journal of Molecular Liquids*. 2017. Vol. 243, p. 533-541. DOI: 10.1016/j.molliq.2017.08.053

14. Minwei Sun, Firoozabadi A. Gas hydrate powder formation – Ultimate solution in natural gas flow assurance. *Fuel*. 2015. Vol. 146, p. 1-5. DOI: 10.1016/j.fuel.2014.12.078

15. Sloan Jr. E.D., Koh C.A. Clathrate Hydrates of Natural Gases. CRC press, 2007, p. 752. DOI: 10.1201/9781420008494

16. Koh C.A., Westacott R.E., Zhang W. et al. Mechanisms of gas hydrate formation and inhibition. *Fluid Phase Equilibria*. 2002. Vol. 194-197, p. 143-151. DOI: 10.1016/S0378-3812(01)00660-4

17. Huangjing Zhao, Minwei Sun, Firoozabadi A. Anti-agglomeration of natural gas hydrates in liquid condensate and crude oil at constant pressure conditions. *Fuel*. 2016. Vol. 180, p. 187-193. DOI: 10.1016/j.fuel.2016.03.029

18. Li Wan, Na Zhang, De-Qing Liang. Inhibition effects of polysaccharides for gas hydrate formation in methane–water system. *Journal of Molecular Liquids*. 2019. Vol. 292. N 111435. DOI: 10.1016/j.molliq.2019.111435

19. Liang Yang, Zhenzhen Liu, Daoping Liu et al. Enhanced natural gas hydrates formation in the suspension with metal particles and fibers. *Journal of Molecular Liquids*. 2020. Vol. 301. № 112410. DOI: 10.1016/j.molliq.2019.112410

20. Hammerschmidt E. Formation of Gas Hydrates in Natural Gas Transmission Lines. *Industrial & Engineering Chemistry*. 1934. Vol. 26. Iss. 8, p. 851-855. DOI: 10.1021/ie50296a010

21. Kondori J., Zendehboudi S., James L. New insights into methane hydrate dissociation: Utilization of molecular dynamics strategy. *Fuel*. 2019. Vol. 249, p. 264-276. DOI: 10.1016/j.fuel.2019.02.125

22. Caili Dai, Yong Hu, Yining Wu et al. Effects of structural properties of alcohol molecules on decomposition of natural gas hydrates: A molecular dynamics study. *Fuel*. 2020. Vol. 268. N 117322. DOI: 10.1016/j.fuel.2020.117322

23. Bingbing Chen, Huiru Sun, Kehan Li et al. Experimental investigation of natural gas hydrate production characteristics via novel combination modes of depressurization with water flow erosion. *Fuel*. 2019. Vol. 252, p. 295-303. DOI: 10.1016/j.fuel.2019.04.120

24. Yutaek Seo, Seong-Pil Kang. Inhibition of methane hydrate re-formation in offshore pipelines with a kinetic hydrate inhibitor. *Journal of Petroleum Science and Engineering*. 2012. Vol. 88-89, p. 61-66. DOI: 10.1016/j.petrol.2011.11.001

25. Ju Dong Lee, Englezos P. Unusual kinetic inhibitor effects on gas hydrate formation. *Chemical Engineering Science*. 2006. Vol. 61. Iss. 5, p. 1368-1376. DOI: 10.1016/j.ces.2005.08.009

26. Bo-Hui Shi, Shang-Fei Song, Xiao-Fang Lv et al. Investigation on natural gas hydrate dissociation from a slurry to a water-in-oil emulsion in a high-pressure flow loop. *Fuel*. 2018. Vol. 233, p. 743-758. DOI: 10.1016/j.fuel.2018.06.054

27. Bahadori A. Fluid Phase Behavior for Conventional and Unconventional Oil and Gas Reservoirs. Gulf Professional Publishing, 2017, p. 554.

28. Soroush E., Mesbah M., Shokrollahi A. et al. Evolving a robust modeling tool for prediction of natural gas hydrate formation conditions. *Journal of Unconventional Oil and Gas Resources*. 2015. Vol. 12, p. 45-55. DOI: 10.1016/j.juogr.2015.09.002

29. Mesbah M., Soroush E., Rezakazemi M. Development of a least squares support vector machine model for prediction of natural gas hydrate formation temperature. *Chinese Journal of Chemical Engineering*. 2017. Vol. 25. Iss. 9, p. 1238-1248. DOI: 10.1016/j.cjche.2016.09.007

30. Berge B.K. Hydrate Predictions on a Microcomputer. Petroleum Industry Application of Microcomputers, 18-20 June 1986, Silvercreek, CO, USA. OnePetro, 1986. N SPE-15306-MS. DOI: 10.2118/15306-MS

31. Motiee M. Estimate possibility of hydrates. *Hydrocarbon Processing*. 1991. Vol. 70. N 7, p. 98-99.

32. Sun C.-Y., Chen G.-J., Lin W., Guo T.-M. Hydrate Formation Conditions of Sour Natural Gases. *Journal of Chemical & Engineering Data*. 2003. Vol. 48. Iss. 3, p. 600-602. DOI: 10.1021/je020155h

33. Towler B., Mokhatab S. Quickly estimate hydrate formation conditions in natural gases. *Hydrocarbon Processing*. 2005. Vol. 84. N 4, p. 61-63.

34. Salufu S.O., Nwakwo P. New Empirical Correlation for Predicting Hydrate Formation Conditions. SPE Nigeria Annual International Conference and Exhibition, 5-7 August 2013, Lagos, Nigeria. OnePetro, 2013. N SPE-167571-MS. DOI: 10.2118/167571-MS

35. Safamirzaei M. Predict gas hydrate formation temperature with a simple correlation. URL: https://gasprocessingnews.com/articles/2015/08/predict-gas-hydrate-formation-temperature-with-a-simple-correlation/ (accessed 09.02.2025).

36. Elgibaly A.A., Elkamel A.M. A new correlation for predicting hydrate formation conditions for various gas mixtures and inhibitors. *Fluid Phase Equilibria*. 1998. Vol. 152. Iss. 1, p. 23-42. DOI: 10.1016/S0378-3812(98)00368-9

37. Zahedi G., Karami Z., Yaghoobi H. Prediction of hydrate formation temperature by both statistical models and artificial neural network approaches. *Energy Conversion and Management*. 2009. Vol. 50. Iss. 8, p. 2052-2059. DOI: 10.1016/j.enconman.2009.04.005

38. Riazi S.H., Heydari H., Ahmadpour E. et al. Development of novel correlation for prediction of hydrate formation temperature based on intelligent optimization algorithms. *Journal of Natural Gas Science and Engineering*. 2014. Vol. 18, p. 377-384. DOI: 10.1016/j.jngse.2014.03.012

This is an open access article under the CC BY 4.0 license

39. Hesami S.M., Dehghani M., Kamali Z., Bakyani A.E. Developing a simple-to-use predictive model for prediction of hydrate formation temperature. *International Journal of Ambient Energy*. 2017. Vol. 38. Iss. 4, p. 380-388. DOI: 10.1080/01430750.2015.1100678

40. Amar M.N. Prediction of hydrate formation temperature using gene expression programming. *Journal of Natural Gas Science and Engineering*. 2021. Vol. 89. N 103879. DOI: 10.1016/j.jngse.2021.103879

41. Mesbah M., Habibnia S., Ahmadi S. et al. Developing a robust correlation for prediction of sweet and sour gas hydrate formation temperature. *Petroleum*. 2022. Vol. 8. Iss. 2, p. 204-209. DOI: 10.1016/j.petlm.2020.07.007

42. Hosseini M., Leonenko Y. A reliable model to predict the methane-hydrate equilibrium: An updated database and machine learning approach. *Renewable and Sustainable Energy Reviews*. 2023. Vol. 173. N 113103. DOI: 10.1016/j.rser.2022.113103

43. Karaköse M., Yücel Ö. Predictive Modeling of the Hydrate Formation Temperature in Highly Pressurized Natural Gas Pipelines. *Energies*. 2024. Vol. 17. Iss. 21. N 5306. DOI: 10.3390/en17215306

44. Khan N., Khan Ya., Zhang Lei et al. Investigating a User-Friendly Machine Learning Approach to Predict the Gas Hydrate Formation Temperature Available to Purchase. *Journal of the Geological Society of India*. 2026. Vol. 102 (4), p. 555-565. DOI: 10.17491/jgsi/2026/174383

45. Aleem W., Ahmad S., Qamar S. et al. Exploring Machine Learning Techniques for Accurate Prediction of Methane Hydrate Formation Temperature in Brine: A Comparative Study. *Arabian Journal for Science and Engineering*. 2024. Vol. 49. Iss. 6, p. 8983-8996. DOI: 10.1007/s13369-024-09030-5

46. Khafaie M., Masoumeh M., Azimi A., Mohammadi A. Comparing ANN with PSO-ANN in Prediction of Natural Gas Hydrate Formation Parameters. *Journal of the Japan Petroleum Institute*. 2025. Vol. 68. Iss. 2, p. 53-60. DOI: 10.1627/jpi.68.53

47. Mahmood Riyadh Atta, Akram Fadhl Al-Mahmodi, Bhajan Lal et al. Artificial Intelligence and Machine Learning in Thermodynamic Gas Hydrate Studies: A Review. *Energy & Fuels*. 2025. Vol. 39. Iss. 38, p. 18287-18310. DOI: 10.1021/acs.energyfuels.5c02863

48. Mokwenye P.O. Evaluation Of Gas Hydrate In Gas Pipeline Transportation: A Thesis Submitted to the Graduate Faculty of the University of North Dakota In partial fulfillment of the requirements for the degree of Master of Science. Grand Forks, 2020, p. 107. (N 3383). URL: https://commons.und.edu/theses/3383/ (дата обращения 09.02.2025).

49. Azizi J., Azizi J., Davarnejad R. Prediction of Gas Hydrate Formation using HYSYS Software. *International Journal of Engineering, Transactions C: Aspects*. 2014. Vol. 27. Iss. 9, p. 1325-1330.

50. Bahadori A., Vuthaluru H.B. A novel correlation for estimation of hydrate forming condition of natural gases. *Journal of Natural Gas Chemistry*. 2009. Vol. 18. Iss. 4, p. 453-457. DOI: 10.1016/S1003-9953(08)60143-7

51. Wilcox W.I., Carson D.B., Katz D.L. Natural Gas Hydrates. *Industrial & Engineering Chemistry*. 1941. Vol. 33. Iss. 5, p. 662-665. DOI: 10.1021/ie50377a027

52. Guang-Jin Chen, Tian-Min Guo. Thermodynamic modeling of hydrate formation based on new concepts. *Fluid Phase Equilibria*. 1996. Vol. 122. Iss. 1-2, p. 43-65. DOI: 10.1016/0378-3812(96)03032-4

53. Jøssang A., Stange E. A new predictive activity model for aqueous salt solutions. *Fluid Phase Equilibria*. 2001. Vol. 181. Iss. 1-2, p. 33-46. DOI: 10.1016/S0378-3812(00)00515-X

54. Sloan E.D. Clathrate hydrates of natural gases. Marcel Dekker, New York, 1990, p. 641.

55. Nasrifar K., Moshfeghian M. A model for prediction of gas hydrate formation conditions in aqueous solutions containing electrolytes and/or alcohol. *The Journal of Chemical Thermodynamics*. 2001. Vol. 33. Iss. 9, p. 999-1014. DOI: 10.1006/jcht.2000.0811

56. Deaton W.M., Frost E.M. Gas hydrates and their relation to the operation of natural-gas pipe mines. American Gas Association. United States. Bureau of Mines. Monograph 8, p. 101.

57. Hashemkhani M., Soleimani R., Fazeli H. et al. Prediction of the binary surface tension of mixtures containing ionic liquids using Support Vector Machine algorithms. *Journal of Molecular Liquids*. 2015. Vol. 211, p. 534-552. DOI: 10.1016/j.molliq.2015.07.038

58. Suykens J.A.K., Van Gestel T., De Brabanter J. et al. Least Squares Support Vector Machines. World Scientific, 2002, p. 308. DOI: 10.1142/5089

59. Suykens J.A.K., Vandewalle J. Least Squares Support Vector Machine Classifiers. *Neural Processing Letters*. 1999. Vol. 9. Iss. 3, p. 293-300. DOI: 10.1023/A:1018628609742

60. Suykens J.A.K., De Brabanter J., Lukas L., Vandewalle J. Weighted least squares support vector machines: robustness and sparse approximation. *Neurocomputing*. 2002. Vol. 48. Iss. 1-4, p. 85-105. DOI: 10.1016/S0925-2312(01)00644-0

61. Varamesh A., Hemmati-Sarapardeh A., Keshavarz Moraveji M., Mohammadi A.H. Generalized models for predicting the critical properties of pure chemical compounds. *Journal of Molecular Liquids*. 2017. Vol. 240, p. 777-793. DOI: 10.1016/j.molliq.2017.05.023

62. Varamesh A., Hemmati-Sarapardeh A., Dabir B., Mohammadi A.H. Development of robust generalized models for estimating the normal boiling points of pure chemical compounds. *Journal of Molecular Liquids*. 2017. Vol. 242, p. 59-69. DOI: 10.1016/j.molliq.2017.06.039

63. Ningbo Zhao, Xueyou Wen, Jialong Yang et al. Modeling and prediction of viscosity of water-based nanofluids by radial basis function neural networks. *Powder Technology*. 2015. Vol. 281, p. 173-183. DOI: 10.1016/j.powtec.2015.04.058

64. Faris H., Aljarah I., Mirjalili S. Evolving Radial Basis Function Networks Using Moth–Flame Optimizer. Handbook of Neural Computation. Elsevier, 2017, p. 537-550. DOI: 10.1016/B978-0-12-811318-9.00028-4

65. Hemmati-Sarapardeh A., Varamesh A., Husein M.M., Karan K. On the evaluation of the viscosity of nanofluid systems: Modeling and data assessment. *Renewable and Sustainable Energy Reviews*. 2018. Vol. 81. Part 1, p. 313-329. DOI: 10.1016/j.rser.2017.07.049

66. Turnbull D., Elkan C. Fast recognition of musical genres using RBF networks. *IEEE Transactions on Knowledge and Data Engineering*. 2005. Vol. 17. Iss. 4, p. 580-584. DOI: 10.1109/TKDE.2005.62

67. Mehrjoo H., Riazi M., Nait Amar M., Hemmati-Sarapardeh A. Modeling interfacial tension of methane-brine systems at high pressure and high salinity conditions. *Journal of the Taiwan Institute of Chemical Engineers*. 2020. Vol. 114, p. 125-141. DOI: 10.1016/j.jtice.2020.09.014

68. Riazi M., Mehrjoo H., Nait Amar M. et al. Modeling the density of acid gases at extensive ranges of pressure and temperature conditions. *Journal of Petroleum Science and Engineering*, 2021. Vol. 207. N 109063. DOI: 10.1016/j.petrol.2021.109063

69. Rostami A., Hemmati-Sarapardeh A., Shamshirband S. Rigorous prognostication of natural gas viscosity: Smart modeling and comparative study. *Fuel*. 2018. Vol. 222, p. 766-778. DOI: 10.1016/j.fuel.2018.02.069

70. Zendehboudi A., Tatar A., Xianting Li. A comparative study and prediction of the liquid desiccant dehumidifiers using intelligent models. *Renewable Energy*. 2017. Vol. 114. Part B, p. 1023-1035. DOI: 10.1016/j.renene.2017.07.078

This is an open access article under the CC BY 4.0 license

71. Riazi M., Mehrjoo H., Nakhaei R. et al. Modelling rate of penetration in drilling operations using RBF, MLP, LSSVM, and DT models. *Scientific Reports*. 2022. Vol. 12. N 11650. DOI: 10.1038/s41598-022-14710-z

72. Dabiri M.-S., Hadavimoghaddam F., Ashoorian S. et al. Modeling liquid rate through wellhead chokes using machine learning techniques. *Scientific Reports*. 2024. Vol. 14. N 6945. DOI: 10.1038/s41598-024-54010-2

73. Xinyuan Zou, Yingting Zhu, Jing Lv et al. Toward Estimating CO_2 Solubility in Pure Water and Brine Using Cascade Forward Neural Network and Generalized Regression Neural Network: Application to CO_2 Dissolution Trapping in Saline Aquifers. *ACS Omega*. 2024. Vol. 9. Iss. 4, p. 4705-4720. DOI: 10.1021/acsomega.3c07962

74. Nanda A.K., Neelakandan S., Gupta S. et al. Multi-layer perceptron's neural network with optimization algorithm for greenhouse gas forecasting systems. *Environmental Challenges*. 2023. Vol. 11. N 100708. DOI: 10.1016/j.envc.2023.100708

75. MacKay D.J.C. Bayesian Interpolation. *Neural Computation*. 1992. Vol. 4. Iss. 3, p. 415-447. DOI: 10.1162/neco.1992.4.3.415

76. Makomere R., Rutto H., Koech L., Banza M. The use of artificial neural network (ANN) in dry flue gas desulphurization modelling: Levenberg–Marquardt (LM) and Bayesian regularization (BR) algorithm comparison. *The Canadian Journal of Chemical Engineering*. 2023. Vol. 101. Iss. 6, p. 3273-3286. DOI: 10.1002/cjce.24715

77. Chavoshi S., Safamirzaei M., Pajoum Shariati F. Evaluation of Empirical Correlations for Predicting Gas Hydrate Formation Temperature. *Gas Processing Journal*. 2018. Vol. 6. Iss. 2, p. 15-36. DOI: 10.22108/gpj.2018.112052.1036

78. Shateri M., Ghorbani S., Hemmati-Sarapardeh A., Mohammadi A.H. Application of Wilcoxon generalized radial basis function network for prediction of natural gas compressibility factor. *Journal of the Taiwan Institute of Chemical Engineers*. 2015. Vol. 50, p. 131-141. DOI: 10.1016/j.jtice.2014.12.011

79. Benamara C., Gharbi K., Nait Amar M., Hamada B. Prediction of Wax Appearance Temperature Using Artificial Intelligent Techniques. *Arabian Journal for Science and Engineering*. 2020. Vol. 45. Iss. 2, p. 1319-1330. DOI: 10.1007/s13369-019-04290-y

80. Castillo E., Hadi A.S., Conejo A., Fernández-Canteli A. A General Method for Local Sensitivity Analysis With Application to Regression Models and Other Optimization Problems. *Technometrics.* 2004. Vol. 46. Iss. 4, p. 430-444. DOI: 10.1198/004017004000000509

81. Rousseeuw P.J., Leroy A.M. Robust Regression and Outlier Detection. John Wiley & Sons, 2003, p. 360.

82. Mehrjoo H., Riazi M., Rezaei F. et al. Modeling interfacial tension of methane-brine systems at high pressure high temperature conditions. *Geoenergy Science and Engineering*. 2024. Vol. 242. N 213258. DOI: 10.1016/j.geoen.2024.213258

83. Dabiri M.-S., Haji-Hashemi R., Ashoorian S. et al. Modeling drilling fluid density at high-pressure high-temperature conditions using advanced machine-learning techniques. *Geoenergy Science and Engineering*. 2025. Vol. 244. N 213369. DOI: 10.1016/j.geoen.2024.213369

***Authors*: Mohsen Riazi,** *MSc* (*Shahid Bahonar University of Kerman, Kerman, Iran*), **Hossein Mehrjoo,** *PhD* (*Shahid Bahonar University of Kerman, Kerman, Iran*), **Mohammad-Saber Dabiri,** *MSc* (*Shahid Bahonar University of Kerman, Kerman, Iran*), **Jamilyam Ismailova,** *PhD, Associate Professor* (*Satbayev University, Almaty, Republic of Kazakhstan*), **Masoud Riazi,** *PhD, Associate Professor* (*Nazarbayev University, Astana, Republic of Kazakhstan*), *masoud.riazi@nu.edu.kz*.

The authors declare no conflict of interests.

This is an open access article under the CC BY 4.0 license

ISSN 2411-3336; e-ISSN 2541-9404

JOURNAL OF MINING INSTITUTE

Zapiski Gornogo instituta

Journal homepage: pmi.spmi.ru

Research article

Geology

Insights into field surveying and automated processing of digital outcrop models for fracture analysis

Oksana V. Lunina✉, Aleksei S. Nizovtsev,

Institute of the Earth's Crust SB RAS, Irkutsk, Russia

How to cite this article: Lunina O.V., Nizovtsev A.S. Insights into field surveying and automated processing of digital outcrop models for fracture analysis. Journal of Mining Institute. 2026. Vol. 280, p. 163-175.

Abstract

When automatically extracting fracture attitudes from a dense point cloud, there are challenges that complicate the correct characterization of the outcrop disrupted by certain fracture sets. In this regard, experimental and methodological studies were carried out to analyze fractures and their associated sets, which were extracted using an automated method to identify satisfactory conditions for data collection and processing. Primary data were acquired using a DJI Phantom 4 RTK unmanned aerial vehicle in the Primorsky and North Baikal deep fault zones of the Baikal rift. Structure from Motion photogrammetry was used to create dense point clouds. The obtained results show that the unidirectional camera orientation and the exposure of a single wall of the rock outcrop present a challenge for determining fracture sets. However, selecting a fragment of the digital outcrop model (DOM) facing various cardinal directions helps avoid orientation bias in the stereographic projections of poles to fractures and provides high-precision data on the fracture pattern. A well-chosen fragment of the DOM accurately represents fracture sets of the overall outcrop, saving time and computational resources. When the structural environment changes, the DOM allows for an analysis of the fracture pattern at any outcrop section, thereby improving the quality and productivity of the work. In the case of limited processing power, it is sufficient to use a dense point cloud of medium quality to extract fractures and their sets. The correct automated identification of fracture sets enhances the efficiency of rock deformation analysis in the field of engineering geology and mineral resource development.

Keywords

fractures; dip and strike; sets; digital outcrop model; unmanned aerial photography; software

Funding

This study was funded by Russian Science Foundation grant 25-27-00565, https://rscf.ru/project/25-27-00565/.

Received: 27.02.2026 ***Accepted: 25.06.2026*** ***Online: 10.09.2026*** ***Published: 10.09.2026***

Introduction

Fracture analysis is used to examine rock deformations and the degree of their disruption. It is also applied to mapping fault lines and their associated zones, as well as to studying the kinematic processes of material movement and the dynamic conditions that controlled structure formation (i.e., the direction and nature of the stresses that caused the deformation; a specific aspect is known as tectonophysical analysis). Traditionally, almost all studies of the fracture networks in outcrops are based on measuring the fracture attitude using a geological compass and counting their number per unit length, area, or volume with a manual approach [1]. Mobile phones with specialized applications (e.g., GeoCompass) are used less frequently. Routine fracture surveys are often conducted across a limited area of 10-20 m, regardless of the size of the outcrop. The heterogeneity of the outcrop structure is documented qualitatively in descriptions, sketches, and photography.

This is an open access article under the CC BY 4.0 license

In recent years, advances in unmanned aerial vehicle (UAV) technology and specialized software for building and processing digital outcrop models (DOM) have opened up unique opportunities to acquire and analyze significantly more data on rock mass fracturing. Dense point clouds and photorealistic textured 3D models of the rock masses are created using remote sensing methods implemented in software such as Agisoft Metashape (formerly Agisoft PhotoScan) [2-4], ShapeMetriX [5, 6], 3DM Analyst [7], Sirovision, and others. Subsequently, mathematical algorithms are applied to DOM to identify fractures and their principal sets [8], including through the use of computer programs such as Discontinuity Set Extractor (DSE) [9-11] and CloudCompare with plugins [12-14], as well as machine learning techniques [15]. Using the output data from DSE and CloudCompare, it is possible to calculate the spacing between fractures within each set [16], the stability parameters of the rock mass [17], and the fracture density over the entire outcrop surface, quantified using various parameters in the DICE module for MATLAB [18]. Virtual reality applications have also been proposed for DOM of rock masses [19].

The earliest studies on fracture analysis in a digital environment focused on comparing the results derived from photogrammetric processing of aerial imagery, lidar surveys, and traditional compass measurements [20, 21]. Later research developed approaches for extracting attitude data not only for fractures but also for dikes, slickensides, and other structures [22], as well as for calculating fracture intensity [13, 23]. Digital models can be applied repeatedly to solve various geological-structural and geomechanical problems, and is positioned as a modern method for studying the geological environment [24], particularly in hard-to-reach areas [25], where safety and time constraints are critical [26]. The articles [27, 28] present comprehensive reviews on DOM application and the automated extraction of fracture characteristics from dense point clouds.

Despite the advantages of digital technologies for fracture analysis, most published DOM-based studies rely on a semi-automatic method to extract fracture attitude data, whereby fractures are either digitized or manually picked by clicking on the discontinuity surface in the image. The automated approach often yields only one or, occasionally, two, fracture maxima on stereographic projections of normal vector poles [29-31], which is insufficient for tectonophysical analysis aimed at stress reconstruction using paragenetic methods [32, 33]. In reality, the fracturing of any rock mass is characterized by at least three main fracture sets, which differ in azimuths and/or dip angles.

Other problems associated with digital outcrop analysis are time consumption and compute resources. Even on sufficiently powerful workstations, constructing and processing DOM can exceed 24 h. Thus, an optimal approach is required for remote data acquisition and subsequent automated analysis of fracture networks in outcrops. The aim of this study is to conduct methodological experiments on the analysis of fractures and their sets, extracted automatically in well-known software packages to find satisfactory conditions for data acquisition and processing that will facilitate the use of digital outcrop models for fracture analysis and their more meaningful integration into the practice of mining and geological works.

Methods

The experimental and methodological work was carried out on five rock outcrops located within the zones of the Primorsky and North Baikal deep faults of the Baikal rift system (Fig.1). Aerial photography was done manually using a DJI Phantom 4 RTK UAV, which has a camera with a 1-inch 20 MP CMOS sensor and a mechanical shutter to avoid image distortion. An advanced sensor, the optimized wide-angle lens with a diaphragm of f/2.8-f/11 along with the processing technology make it possible to obtain detailed photos with realistic colors. The survey was carried out from a distance of 1.5 m for the Krasnoyarovskoye outcrop to the first tens of meters for the Sukhoye outcrop.

This is an open access article under the CC BY 4.0 license

The predominant camera tilt angle of 0° relative to the horizontal was gradually varied up to 45° and occasionally up to 90° (when necessary). The flight path was conducted from bottom to top, right to left, right to bottom, and so on, with drone rotations in both directions at appropriate angles determined by the outcrop morphology. The overlap between images was 75-80 %.

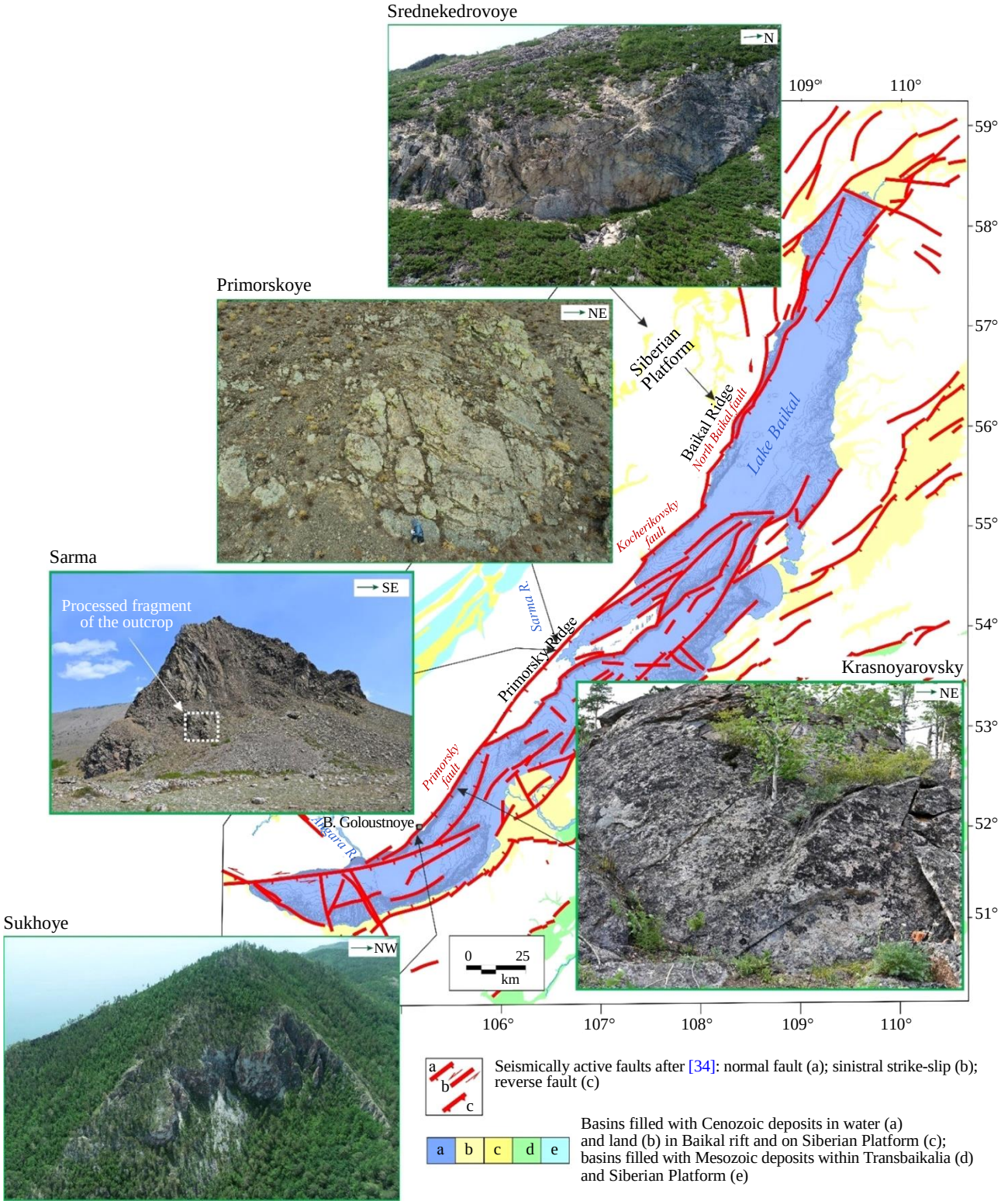


Fig.1. Location of investigated outcrops within the Baikal rift

This is an open access article under the CC BY 4.0 license

Dense point clouds, representing a type of DOM, were generated using the photogrammetric method implemented in Agisoft Metashape. Prior to processing, all defective and out-of-focus images were discarded. The following steps were then carried out automatically: image loading, image alignment, alignment optimization, and reconstruction of dense point cloud, which is similar to those from LIDAR surveys. The points in the resulting dense cloud are colored according to the spectral RGB data of the corresponding images, have spatial coordinates, and accurately describe the topography of the rock outcrop. At medium processing quality, the average point density ranged from 7115 points/m^2 at the Srednekedrovoye outcrop to 65,263 points/m^2 at the Sarma outcrop, while the Sukhoye exposure yielded 449 points/m^2. The dense point cloud, due to its discrete nature, is used for automatic extraction of fracture orientations and their sets. In contrast, the textured DOM is preferred for object visualization and geological interpretation through manual digitization of bedding planes, fractures, and other structural features.

Two well-known open-source software tools – DSE [9] and the FACETS plugin for CloudCompare [12] – were tested for extracting dip azimuths and dip angles. The construction of fracture diagrams and the identification of the main fracture sets were conducted using DSE and Dips v. 7.0 software. The latter made it possible to compare stereographic projections constructed uniformly from fracture datasets obtained by different methods. Before processing, all areas with interferences, such as vegetation, talus, and other obstructions, were removed from the dense point cloud.

In the DSE software, a fracture is defined as a set of points arranged in a plane in 3D space based on certain fitting parameters. Each point from the cloud that is classified to a plane is considered as a fracture with associated dip azimuth and dip angle, which are then used to plot the stereographic projections of poles to fractures. In CloudCompare, these points have already been combined into planes (FACETS).

Geological-structural documentation and statistical compass measurements, each comprising 100 to 103 fractures, were performed at four of the five rock exposures. The measurements were carried out following standard structural geology procedures by systematically measuring all fractures within a randomly selected ~10 m^2 section of the bedrock outcrop. For each fracture, dip azimuth and dip angle were recorded, along with, where identifiable, its genetic type (shear or extension fracture), slip surface condition, and other relevant features. Traditional description was not undertaken for the collapse bedrock scarp, exposed at a relative height of more than 300 m above Sukhoye Lake in the Semyonovka valley, 4.13 km west-southwest of the southern outskirts of the village of Bolshoye Goloustnoye (Fig.1).

Results and discussion

First test digital outcrop models of rock exposures. The results of DOM processing of the first three outcrops – the Srednekedrovoye, Primorskoye and Krasnoyarovskoye – composed of granites, showed strong agreement in the location of the main maximum on the stereographic projections of poles to fractures obtained by automated extraction and manual compass measurements (Fig.2). A major limitation, as in many earlier studies, was the apparent unipolarity of the fracture sets, which is attributed to the orientation of the main outcrop wall facing the camera. The field data also revealed systematic fracturing but the presence of only one maximum is geologically unacceptable. Thus, the authors faced the problem of the influence of the camera angle, highlighting that a certain approach to outcrop surveying and fracture pattern analysis using automated extraction is required for most geological-structural tasks (identification of main fracture sets and conjugate fracture maxima for subsequent stress field reconstruction).

A UAV survey of the fourth outcrop in the Semyonovka valley was performed on July 10, 2021, to test the feasibility of acquiring data on inaccessible rock exposures situated at high elevation and considerable distance from the researcher. According to [35], the rockfall was triggered by an earthquake 3810±100 years ago, when the collapse of a highly fractured rock mass occurred at an absolute elevation of 850 m on the right side of the valley downstream. The resulting debris blocked the drainage, forming Sukhoye Lake, which fills only intermittently in response to groundwater fluctuations (Fig.3, *a*). The headscarp, situated about 630 m on the straight from the lake floor and the operator

This is an open access article under the CC BY 4.0 license

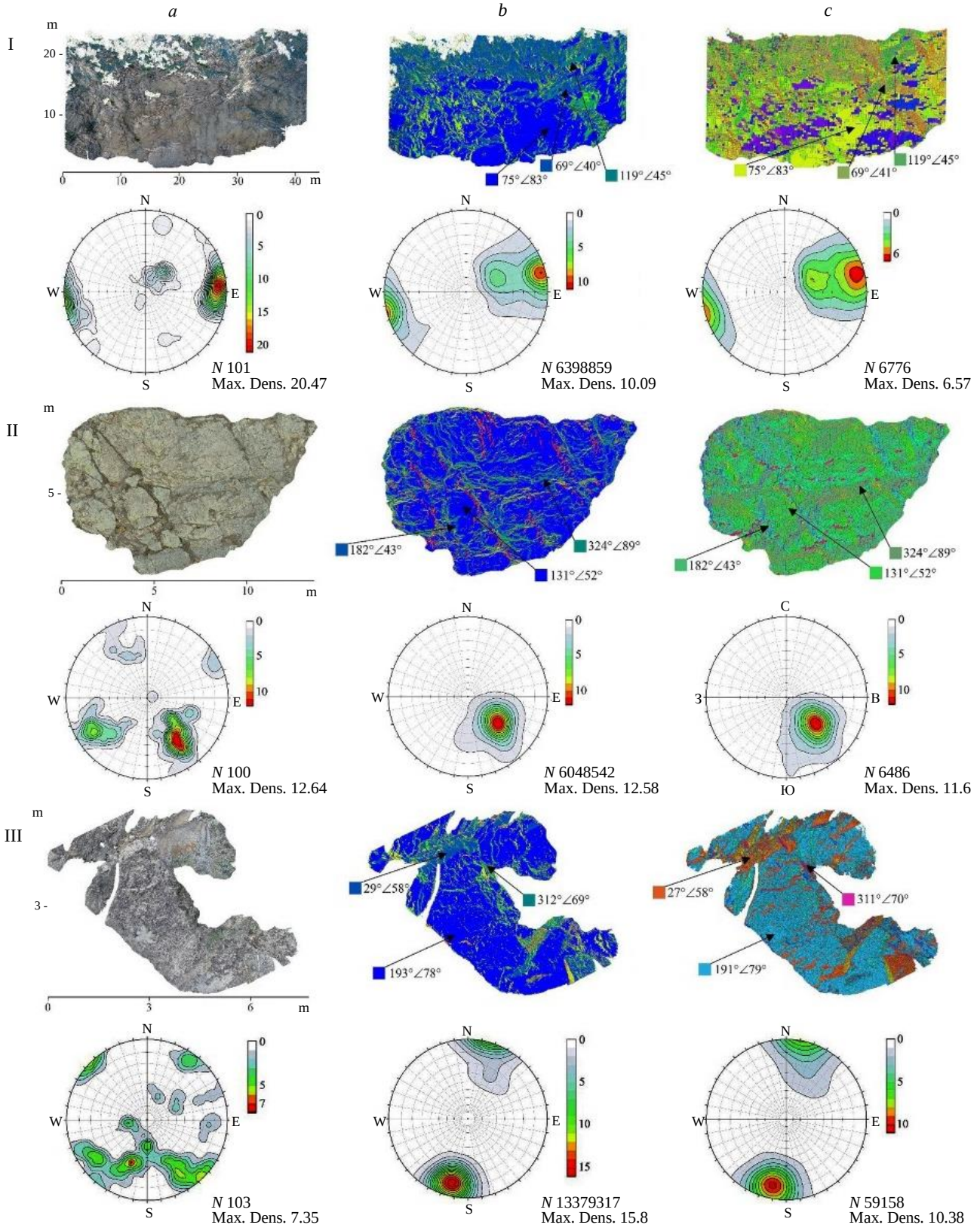


Fig.2. Results of DOM processing for the Srednekedrovoye (I), Primorskoye (II), and Krasnoyarovskoye (III) granite outcrops:
a – dense point clouds and stereographic projections of poles to fractures measured by geological compass;
b – dense point clouds classified using DSE, and stereographic projections of poles to fractures extracted using the same software;
c – dense point clouds classified using CloudCompare, and stereographic projections of poles to fractures extracted using the same software. Contours are shown at 1 % intervals. Colors in the classified dense point clouds represent individual fracture sets, with selected sets labeled; the stereoplots are presented as upper-hemisphere projections
N – number of measurements; Max. Dens. – maximum density

This is an open access article under the CC BY 4.0 license

Journal of Mining Institute. *2026. Vol. 280. P. 163-175*
© Oksana V. Lunina, Aleksei S. Nizovtsev, 2026

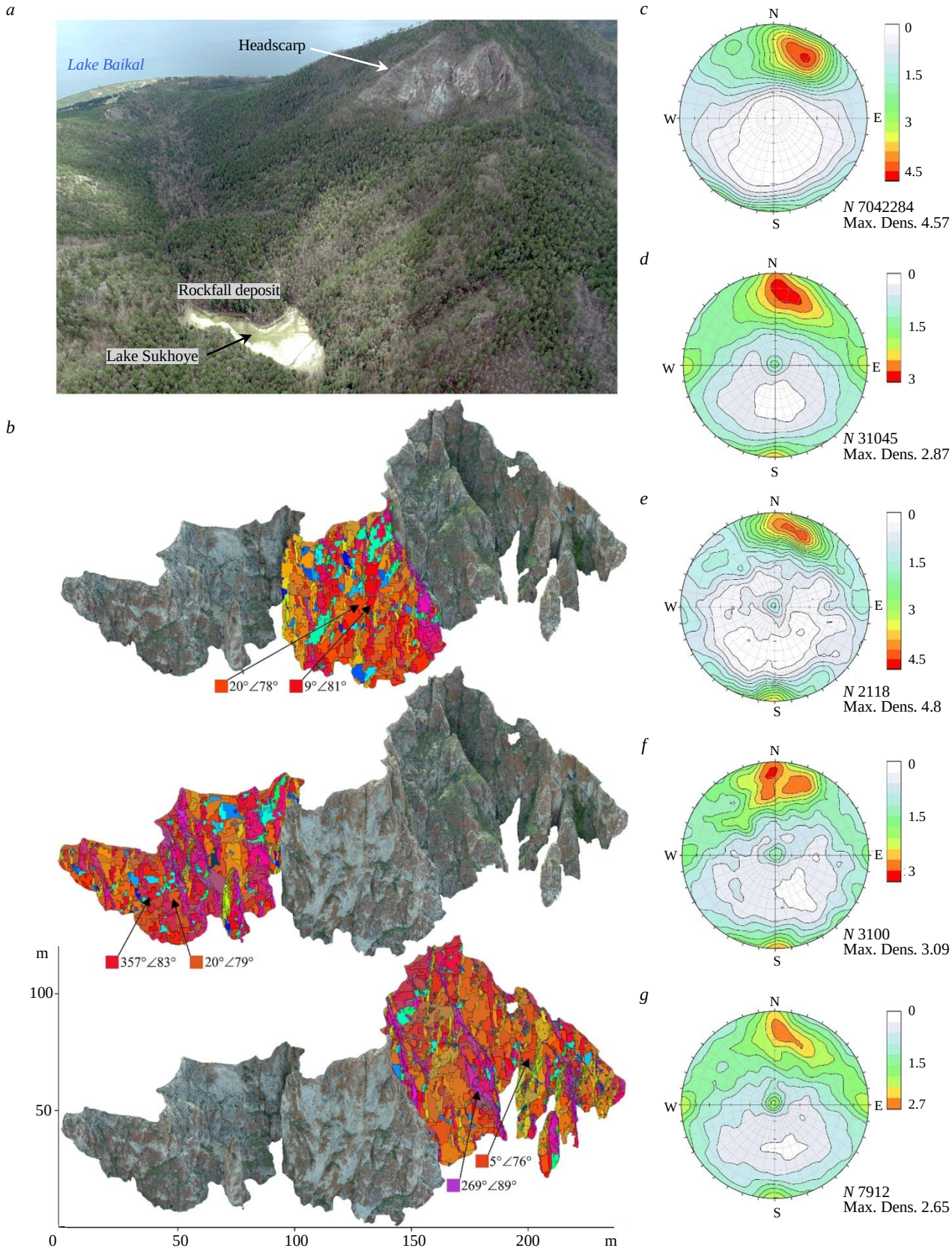


Fig.3. Results of DOM processing for the Sukhoye outcrop: *a* – the location of the rockfall headscarp formed by dolomite bedrock; *b* – the dense point cloud of the outcrop prepared for processing, with its fragments superimposed and classified in CloudCompare based on the spatial orientation of fractures; *c*, *d* – stereographic projections of poles to fractures extracted from the entire outcrop using DSE (*c*) and CloudCompare (*d*); *e-g* – stereographic projections of poles to fractures extracted from the outcrop fragments using CloudCompare. Contours are shown at 0.3 % intervals

This is an open access article under the CC BY 4.0 license

of the aerial survey, is an arcuate feature with irregular edges and a total length of 543 m. Stereographic projections of poles to fractures derived from the entire rock outcrop using DSE and CloudCompare show the dominant dip azimuths, with their maxima exhibiting a belt-like arrangement corresponding to this arc (Fig.3, *c*, *d*). Input of a large number of fractures from DSE (7,042,284 normal projections) and from CloudCompare (31,045 fractures – facets) produces only two maxima on the diagrams due to the significant dominance of fractures with certain dip azimuths and dip angles facing the camera. The principal maximum steeply dips to north-northeast (27°∠72° from DSE and 10°∠75° from CloudCompare). Splitting the outcrop into three segments reduces the dominance of camera-facing surfaces in each subset, thereby increasing the number of distinguishable maxima (Fig.3, *e*-*g*). The role of the transverse fracture sets with a nearly N-S strike is highlighted more clearly. At the same time, similarity is observed between the stereoplots constructed for the left, central, and right parts of the outcrop, as well as the invariance of the position of the main fracture sets within 10°, based on the data processed in CloudCompare.

In contrast to CloudCompare, DSE constructs normal vector poles stereographic projection as density contours and calculates the main fracture sets [21]. The number of maxima to be identified and the allowable angle between them are set as input parameters for the computation and visualization. Thus, even when one fracture set strongly dominates, DSE can still calculate several maxima, some of which – or even most – will not be expressed as contour lines but will be indicated only by a point, because their density (intensity) on the diagram is too low. It follows that for structural tasks, when only a single outcrop wall is exposed without significant protrusions, it is preferable to use either DSE or the manual mode of fracture picking in CloudCompare with the built-in Compass tool for constructing stereographic projections of poles to fractures.

Experimental and methodological studies at the Sarma outcrop. The clear effect of camera angle and azimuth on the results of automated structural analysis necessitated a targeted study of the fifth bedrock exposure of granites and granite-gneisses, located on the left bank of the Sarma River valley (see Fig.1). Classical geological-structural documentation of the outcrop with systematic fracture measurements was carried out simultaneously with aerial photography on May 26, 2022.

Accessible from three main sides, the bedrock exposure in the Sarma Gorge (Fig.4, *a*) represents an ideal object for experimental and methodological work on the investigation of fractures and their sets, identified by an automated approach. A digital twin was constructed for the entire outcrop (Fig.4, *b*), but only a prominent protrusion, which was photographed from multiple directions, was selected for the analysis (Fig.4, *c*), and proved sufficient for obtaining reliable results. Dense point clouds of this subset were classified in DSE and CloudCompare (Fig.4, *d*, *e*). Fracture stereoplots generated from field compass measurements (Fig.4, *f*), from DSE (Fig.4, *g*), and from Dips using DSE-derived data (Fig.4, *h*) demonstrate strong mutual agreement and the absence of unipolar maxima. In contrast, the maxima derived from the FACETS plugin (Fig.4, *i*) show a poorer correlation with the fracture sets revealed from field data. The main fracture set of the Primorsky fault (Fig.4, *a*) with a dip azimuth of 161°∠64° in Fig.4, *f*, 159°∠61° in Fig.4, *g*, and 159°∠59° in Fig.4, *h*, did not appear in Fig.4, *i*. Considering the algorithm underlying the FACETS program, it is reasonable to infer that the imaging process captured a considerable number of minor fractures whose dip direction faces the camera (i.e., to the southwest). If the fracture surfaces were larger, this effect would not have occurred. This finding supports the conclusion that the DSE is better suited for structural analysis in large-scale data contexts, since its point-based methodology accounts for both the number of measurements and the fracture surface area. The work on the digital twin of the Sarma outcrop demonstrates that combining a multi-directional camera angle with the selection of exposure fragments oriented toward various azimuthal directions, while considering the size of fracture surfaces, helps avoid unipolarity in the stereographic projection of poles to fractures.

This is an open access article under the CC BY 4.0 license

Journal of Mining Institute. *2026. Vol. 280. P. 163-175*
© Oksana V. Lunina, Aleksei S. Nizovtsev, 2026

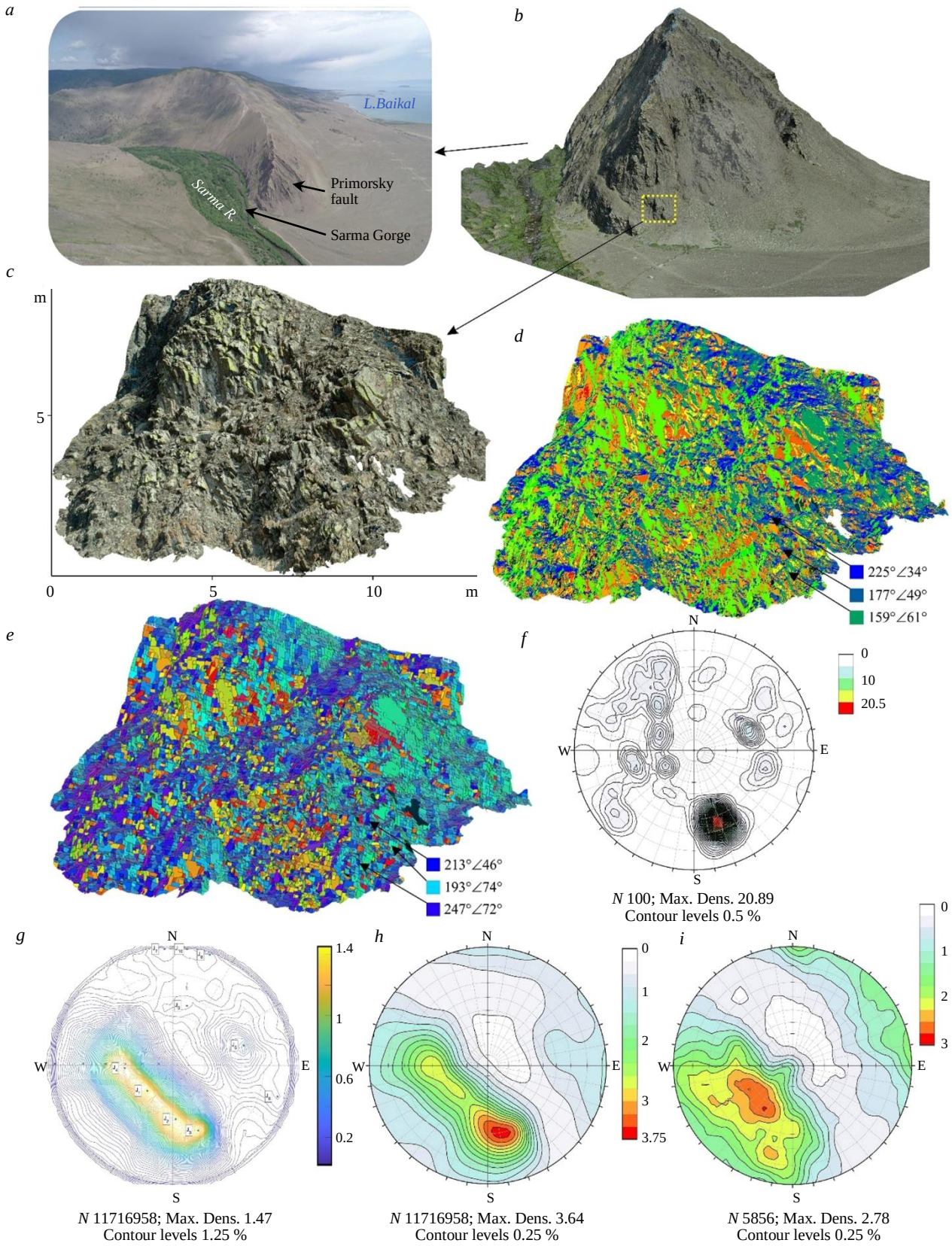


Fig.4. Results of DOM processing for the Sarma outcrop: *a* – the location of the outcrop in the Primorsky fault zone; *b* – digital model; *c* – DOM fragment; *d*, *e* – the dense point clouds classified in DSE (*d*) and CloudCompare (*e*) based on the spatial orientation of fractures; *f-j* – stereographic projections of poles to fractures measured by geological compass (*f*), extracted using DSE and plotted within it (*g*), as well as in Dips software (*h*); extracted using CloudCompare (*i*)

This is an open access article under the CC BY 4.0 license

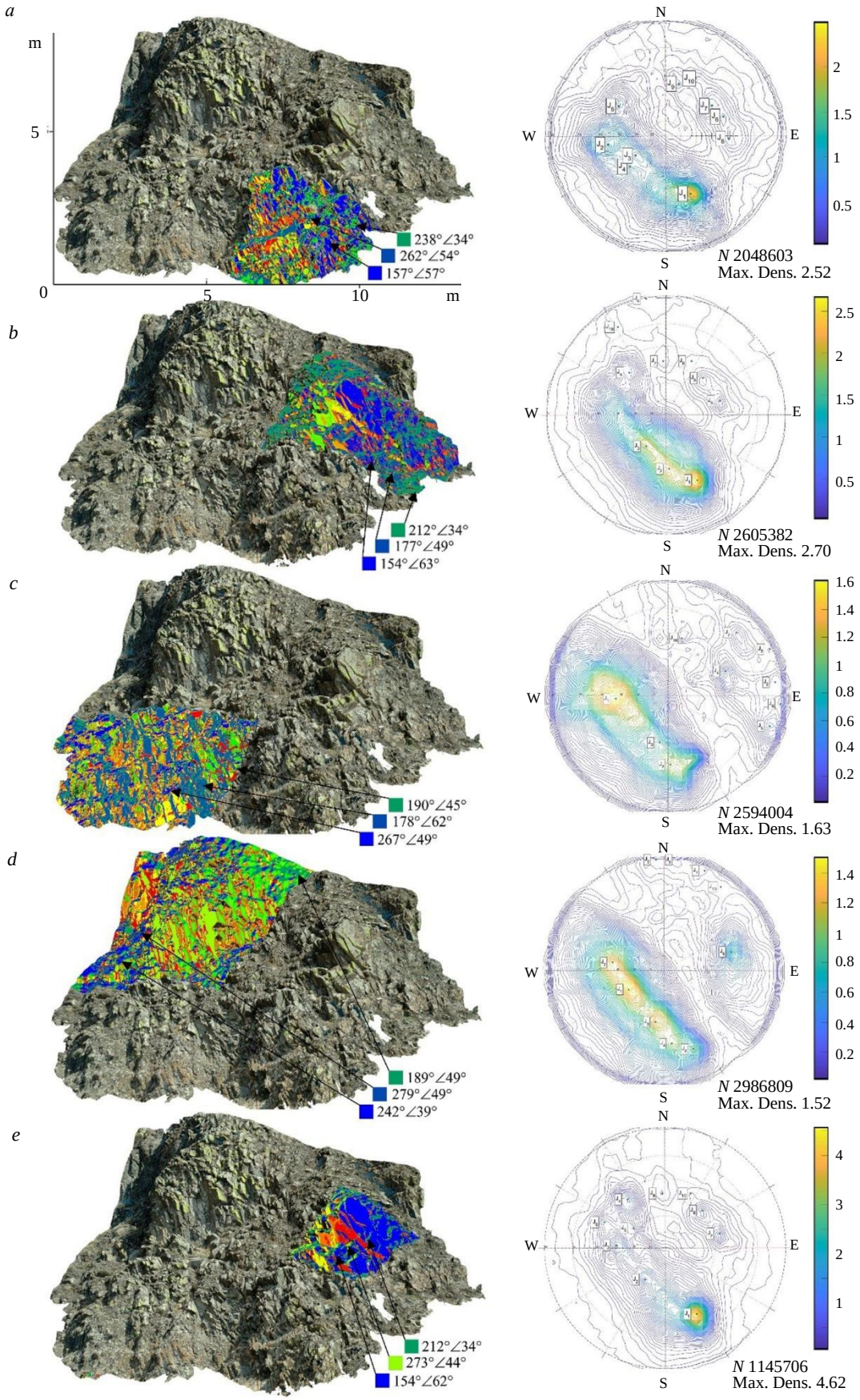


Fig.5. The dense point clouds of the Sarma outcrop classified based on the spatial orientation of fractures and corresponding stereographic projections of poles to fractures with contours shown at 1.25 % intervals: *a-d* – four parts of the tested outcrop fragments; *e* – part of the fragment shown in Fig.5, *b*. Data processing and visualization were carried out using DSE

This is an open access article under the CC BY 4.0 license

At the next stage, the tested bedrock fragment in the Sarma Gorge was subdivided into four parts, each yielding a fracture stereoplot (Fig.5, *a-d*). A smaller subarea was then extracted from the fragment in Fig.5, *b*, and fracture attitudes were analyzed (Fig.5, *e*). Testing of these and other smaller datasets showed that the main fracture maxima persist irrespective of the sampled area, although their density may vary slightly. The principal fracture sets match those on the composite stereoplot for the entire outcrop, whether derived from field measurements (see Fig.4, *f*) or DSE processing (see Fig.4, *g*). Thus, stereographic projections of poles to fractures from a fragment are representative of the overall structural pattern, obviating the need to process the entire dense point cloud. However, the fragment should encompass as wide a range of azimuthal directions as possible.

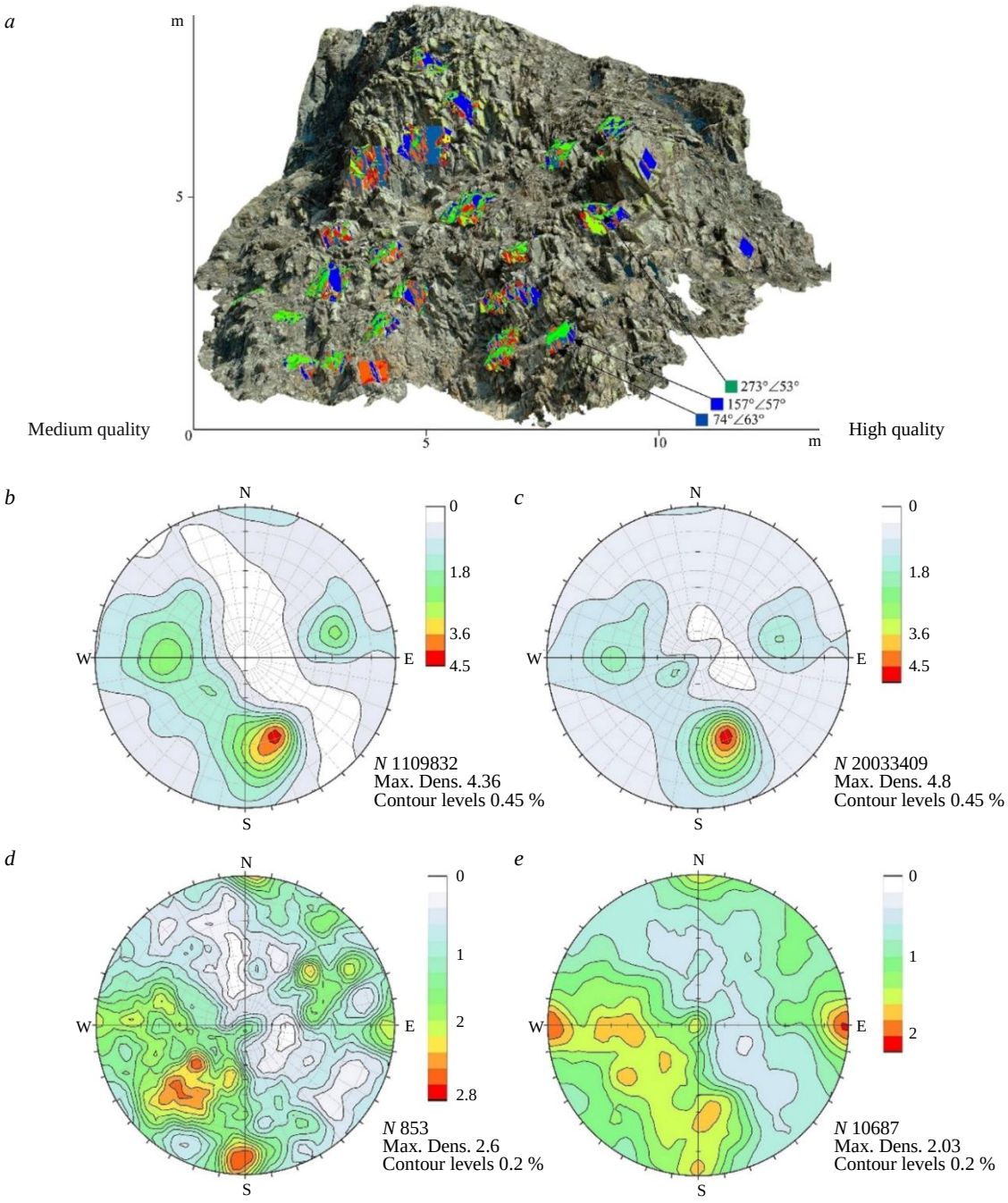


Fig.6. Results of the analysis of dense point clouds from the Sarma outcrop at medium (*b*, *d*) and high (*c*, *e*) resolution:
a – local fragments of the outcrop from which fracture attitudes were extracted and grouped into datasets;
b-e – stereographic projections of poles to fractures extracted using DSE (*b*, *c*) and CloudCompare (*d*, *e*)

This is an open access article under the CC BY 4.0 license

Despite the satisfactory visualization of fracture data in DSE for structural analysis (Fig.5), for solving geomechanical problems, fracture attitudes from DSE are more conveniently visualized in other programs, such as Dips. This is due to the specialized built-in tools for slope stability assessment. However, it should be taken into account that due to the large number of fractures, even with a 1 % contouring window size, Dips performs significant data averaging during construction of the stereoplot, resulting in a reduction in the number of maxima (see Fig.4, *h*) compared to those identified in DSE (see Fig.4, *g*, Fig.5). This issue can be resolved by reducing the number of analyzed fractures through the selection of one or more small fragments of the point cloud model (Fig.6, *a*), following the same approach as used in traditional statistical fracture measurements on a natural outcrop.

A significant challenge in analyzing digital twins is the limited capacity of computers and the time required for data processing. In this regard, an additional experiment was conducted to examine fracture patterns using dense point cloud data of medium and high quality. For this purpose, several small fragments of the digital model of the Sarma outcrop were selected (Fig.6, *a*), from which fractures were extracted and compiled into two datasets. The first dataset consisted of fractures derived from all fragments of the medium-quality dense point cloud, and the second – from the high-quality one. It was found that the stereographic projections of poles to fractures constructed from the DSE data are identical, although the number of fractures in one dataset is 18 times greater than in the other (Fig.6, *b*, *c*). According to the FACETS plugin of CloudCompare, the stereoplots are also generally very similar (Fig.6, *d*, *e*), indicating that for automated fracture extraction and identification of fracture sets, it is sufficient to use a medium-quality dense point cloud generated in Agisoft Metashape.

Conclusion

Modern technical systems and software are evolving rapidly, and their integration into fracture analysis is both inevitable and essential for incorporating the results of structural-geological and tectonophysical studies into the overall technological workflow related to mineral exploration, development, and mining, as well as engineering-geological surveys for the construction of particularly critical facilities. At the same time, their proper application is necessary to obtain reliable results regarding brittle deformations of the Earth's crust, which is facilitated by methodological and experimental studies.

This study has highlighted the main challenges of automated fracture attitude extraction, proposed solutions, and led to the following conclusions:

• The high precision of mathematically extracted fracture dip azimuths and dip angles, combined with their satisfactory correspondence to geological compass-based field measurements, permits the robust use, subject to certain conditions, of the specialized software DSE and the FACETS plugin of CloudCompare for rock fracture analysis. Choosing between these tools because of their distinct algorithms may depend on the outcrop geometry and the size of fracture surfaces oriented toward the camera during data acquisition. Furthermore, when processing large datasets, e.g., exceeding 10,000 extracted fractures, DSE will be a more useful tool for tectonophysical analysis, offering built-in generation of stereographic projections and the ability to resolve a larger number of fracture maxima on them. Along with it, exporting fracture attitude data from both programs to Dips or other software for stereoplot construction will be more appropriate for specific applications.

• An unidirectional survey angle and the exposure of only one wall of the outcrop hinder the identification of diverse fracture sets, since one of them, facing the camera with its dip azimuth, dominates over all others. Although DSE allows determining the main fracture sets with their densities listed in a table, they appear merely as centers of maxima on the stereoplot and are unsuitable for the identification of conjugate fracture sets using some tectonophysical methods (e.g., the Nikolaev method). A multi-directional survey angle and the choice of an outcrop fragment oriented toward different compass directions help avoid unipolarity on the stereographic projections of poles to fractures and enable the acquisition of high-precision data on the structure of the fracture patterns of the rock mass.

This is an open access article under the CC BY 4.0 license

• A properly selected outcrop fragment for calculation reflects its overall structural pattern. This means there is no need to waste time and computer resources analyzing the entire dense cloud. At the same time, if the structural environment changes visually due to a large fault zone, a change in rock type, the need for a detailed study of the quarry walls, or other factors, DOM enable repeated automated analysis of the fracture patterns at any section of the outcrop, including areas that are difficult or even inaccessible to humans, thereby enhancing the quality and productivity of the works.

• Under conditions of limited computing capacity, a dense cloud generated at medium quality in Agisoft Metashape is adequate for extraction of fractures and their associated sets. This approach saves time and computer resources. The high quality of DOM is suitable for visually identification of fractures and other deformation structures.

The potential of using DOM for analyzing the fracture pattern of natural and artificial rock exposures holds great promise for implementation in fundamental research on the Earth's crust structure and in the practice of mining geology. The development of software, including machine learning and neural networks will facilitate this process to identify fractures of various hierarchical levels, calculate their parameters, and construct models of the fault-block environment based on a series of spatially close DOM or on a digital model of an entire quarry. The appropriate use of automated extraction of fracture attitudes and their sets significantly increases the efficiency of studying the deformation characteristics of rocks involved in engineering interventions and mineral deposit development.

REFERENCES

1. Serebryakov E.V., Gladkov A.S. Geological and structural characteristics of deep-level rock mass of the Udachnaya pipe deposit. *Journal of Mining Institute.* 2021. Vol. 250, p. 512-525. DOI: 10.31897/PMI.2021.4.4

2. Chesley J.T., Leier A.L., White S., Torres R. Using unmanned aerial vehicles and structure-from-motion photogrammetry to characterize sedimentary outcrops: An example from the Morrison Formation, Utah, USA. *Sedimentary Geology*. 2017. Vol. 354, p. 1-8. DOI: 10.1016/j.sedgeo.2017.03.013

3. Junjie Zou, Honglin He, Yokoyama Y. et al. A comparative study of bedrock fault scarps by s-UAV and t-LiDAR: Insights into site selection criteria for paleo-seismology studies. *Geomorphology*. 2022. Vol. 414. N 108372. DOI: 10.1016/j.geomorph.2022.108372

4. Koukouvelas I.K., Kyriou A., Nikolakopoulos K.G. et al. Geological and 3D Image Analysis Toward Protecting a Geosite: The Case Study of Falakra, Limnos, Greece. *Minerals*. 2025. Vol. 15. Iss. 2. N 148. DOI: 10.3390/min15020148

5. Na Wu, Zhengzhao Liang, Yan Tao et al. Sensitivity Analysis of Fracture Geometry Parameters on the Mechanical Behavior of Rock Mass with an Embedded Three-Dimensional Fracture Network. *Applied Sciences*. 2022. Vol. 12. Iss. 18. N 9284. DOI: 10.3390/app12189284

6. Tuckey Z. An integrated UAV photogrammetry-discrete element investigation of jointed Triassic sandstone near Sydney, Australia. *Engineering Geology*. 2022. Vol. 297. N 106517. DOI: 10.1016/j.enggeo.2022.106517

7. Birch J.S. Using 3DM Analyst Mine Mapping Suite for Rock Face Characterisation. Laser and Photogrammetric Methods for Rock Face Characterization: Proceedings of the Workshop (Golden, Colorado, June 17-18, 2006. Golden: American Rock Mechanics Association, 2006, p. 13-32.

8. Boos I.Yu., Yunakov Yu.L., Patachakov I.V., Grishin A.A. Structural analysis of pit wall rock mass on 3D slope model constructed using a multicopter. *Mining Informational and Analytical Bulletin*. 2021. N 12, p. 19-30 (in Russian). DOI: 10.25018/0236_1493_2021_12_0_19

9. Riquelme A.J., Abellán A., Tomás R., Jaboyedoff M. A new approach for semi-automatic rock mass joints recognition from 3D point clouds. *Computers & Geosciences*. 2014. Vol. 68, p. 38-52. DOI: 10.1016/j.cageo.2014.03.014

10. García-Luna R., Senent S., Jurado-Piña R., Jimenez R. Structure from Motion photogrammetry to characterize underground rock masses: Experiences from two real tunnels. *Tunnelling and Underground Space Technology*. 2019. Vol. 83, p. 262-273. DOI: 10.1016/j.tust.2018.09.026

11. Monsalve J.J., Pfreundschuh A., Soni A., Ripepi N. Automated Discontinuity Extraction Software Versus Manual Virtual Discontinuity Mapping: Performance Evaluation in Rock Mass Characterization and Rockfall Hazard Identification. *Mining, Metallurgy & Exploration*. 2021. Vol. 38. Iss. 3, p. 1383-1394. DOI: 10.1007/s42461-021-00416-9

12. Dewez T.J.B., Girardeau-Montaut D., Allanic C., Rohmer J. Facets: A CloudCompare plugin to extract geological planes from unstructured 3D point clouds. The International Archives of the Photogrammetry, Remote Sensing and Spatial Information Sciences. ISPRS, 2016. Vol. XLI-B5, p. 799-804. DOI: 10.5194/isprs-archives-XL-B5-799-2016

13. Panara Y., Menegoni N., Carboni F., Inama R. 3D digital outcrop model-based analysis of fracture network along the seismogenic Mt. Vettore Fault System (Central Italy): the importance of inherited fractures. *Journal of Structural Geology*. 2022. Vol. 161. N 104654. DOI: 10.1016/j.jsg.2022.104654

14. Perozzo M., Menegoni N., Crispini L. et al. Quantitative characterization of fracture network in large sheath-fold: field and UAV-based digital outcrop model analysis (Ligurian Alps, Italy). *Journal of Structural Geology*. 2025. Vol. 201. N 105551. DOI: 10.1016/j.jsg.2025.105551

This is an open access article under the CC BY 4.0 license

15. Battulwar R., Emami E., Zare M. et al. Utilizing Deep Learning for the Automated Extraction of Rock Mass Features from Point Clouds. *Geotechnical and Geological Engineering*. 2024. Vol. 42. Iss. 7, p. 6179-6194. DOI: 10.1007/s10706-024-02886-2

16. Buyer A., Schubert W. Calculation the Spacing of Discontinuities from 3D Point Clouds. *Procedia Engineering*. 2017. Vol. 191, p. 270-278. DOI: 10.1016/j.proeng.2017.05.181

17. Riquelme A.J., Tomás R., Abellán A. Characterization of rock slopes through slope mass rating using 3D point clouds. *International Journal of Rock Mechanics and Mining Sciences*. 2016. Vol. 84, p. 165-176. DOI: 10.1016/j.ijrmms.2015.12.008

18. Menegoni N., Giordan D., Inama R., Perotti C. DICE: An open-source MATLAB application for quantification and parametrization of digital outcrop model-based fracture datasets. *Journal of Rock Mechanics and Geotechnical Engineering*. 2023. Vol. 15. Iss. 5, p. 1090-1110. DOI: 10.1016/j.jrmge.2022.09.011

19. Seers T.D., Sheharyar A., Tavani S., Corradetti A. Virtual outcrop geology comes of age: The application of consumer-grade virtual reality hardware and software to digital outcrop data analysis. *Computers & Geosciences*. 2022. Vol. 159. № 105006. DOI: 10.1016/j.cageo.2021.105006

20. Cawood A.J., Bond C.E., Howell J.A. et al. LiDAR, UAV or compass-clinometer? Accuracy, coverage and the effects on structural models. *Journal of Structural Geology*. 2017. Vol. 98, p. 67-82. DOI: 10.1016/j.jsg.2017.04.004

21. Villarreal J. C.A., Rojas D. J.D., Ríos R. C.A. 3D digital outcrop modelling of the Lower Cretaceous Los Santos formation sandstones, Mesa de Los Santos region (Colombia): Implications for structural analysis. *Journal of Structural Geology*. 2020. Vol. 141. N 104214. DOI: 10.1016/j.jsg.2020.104214

22. Triantafyllou A., Watlet A., Le Mouélic S. et al. 3-D digital outcrop model for analysis of brittle deformation and lithological mapping (Lorette cave, Belgium). *Journal of Structural Geology*. 2019. Vol. 120, p. 55-66. DOI: 10.1016/j.jsg.2019.01.001

23. Panara Y., Chandra V., Finkbeiner T. et al. Fracture intensity and associated variability: A new methodology for 3D digital outcrop model analysis of carbonate reservoirs. *Marine and Petroleum Geology*. Vol. 158. Part B. N 106532. DOI: 10.1016/j.marpetgeo.2023.106532

24. Shekov V.A., Ivanov A.A., Krylova S.A. Digital outcrop model as a modern method of geological environment research: the example of Precambrian complexes in Lahdenpohsky district. *Transactions of the Karelian Research Centre of the Russian Academy of Sciences*. 2020. N 10, p. 84-98 (in Russian). DOI: 10.17076/geo1238

25. Nizovtsev A.S., Lunina O.V. Towards new approaches to fracture studies based on UAV aerial photography (examples from Baikal Rift). Continental Rifting, Accompanied Processes: Proceedings of the 5th All-Russian Conference with Participation of Foreign Scientists, Dedicated to the Memory of Academician Nikolay Logatchev on the Occasion of the 95th Anniversary of His Birth, 16-19 April 2024, Irkutsk, Russia. Irkutsk: Izd-vo Irkutskogo gosudarstvennogo universiteta, 2024, p. 96-99 (in Russian).

26. Serebriakov E.V., Gladkov A.S., Gapfarov T.D. Modern methods of data collection for structural damage assessment in rock mass: Review. *Mining Informational and Analytical Bulletin.* 2023. N 9, p. 160-177 (in Russian). DOI: 10.25018/0236_1493_2023_9_0_160

27. Marques Jr. A., Horota R.K., de Souza E.M. et al. Virtual and digital outcrops in the petroleum industry: A systematic review. *Earth-Science Reviews*. 2020. Vol. 208. N 103260. DOI: 10.1016/j.earscirev.2020.103260

28. Battulwar R., Zare-Naghadehi M., Emami E., Sattarvand J. A state-of-the-art review of automated extraction of rock mass discontinuity characteristics using three-dimensional surface models. *Journal of Rock Mechanics and Geotechnical Engineering*. 2021. Vol. 13. Iss. 4, p. 920-936. DOI: 10.1016/j.jrmge.2021.01.008

29. Nurshal M.E.M., Sadewo M.S., Hidayat A. et al. Automatic and Manual Fracture-Lineament Identification on Digital Surface Models as Methods for Collecting Fracture Data on Outcrops: Case Study on Fractured Granite Outcrops, Bangka. *Frontiers in Earth Science*. 2020. Vol. 8. N 560596. DOI: 10.3389/feart.2020.560596

30. Riquelme A., Cano M., Tomás R., Abellán A. Identification of Rock Slope Discontinuity Sets from Laser Scanner and Photogrammetric Point Clouds: A Comparative Analysis. *Procedia Engineering*. 2017. Vol. 191, p. 838-845. DOI: 10.1016/j.proeng.2017.05.251

31. Wen Yan Tung, Nagendran S.K., Ismail M.A.M. 3D rock slope data acquisition by photogrammetry approach and extraction of geological planes using FACET plugin in CloudCompare. *IOP Conference Series: Earth and Environmental Science*. 2018. Vol. 169. № 012051. DOI: 10.1088/1755-1315/169/1/012051

32. Seminsky K.Zh. Specialized mapping of crustal fault zones. Part 1: Basic theoretical concepts and principles. *Geodynamics & Tectonophysics*. 2014. Vol. 5. Iss. 2, p. 445-467 (in Russian). DOI: 10.5800/GT-2014-5-2-0136

33. Sherman S.I., Dneprovskii Yu.I. Stress fields in the Earth's Crust and geological-structural methods of their study. Novosibirsk: Nauka, 1989, p.154 (in Russian).

34. Lunina O.V. The digital map of the Pliocene-Quaternary crustal faults in the southern East Siberia and the adjacent Northern Mongolia. *Geodynamics & Tectonophysics*. 2016. Vol. 7. Iss. 3, p. 407-434 (in Russian). DOI: 10.5800/GT-2016-7-3-0215

35. Makarov S.A. The development history of the Ozerko Valley on the western coast of Lake Baikal. *Geografiya i prirodnye resursy*. 1999. N 4, p. 36-43 (in Russian).

Authors: **Oksana V. Lunina,** *Doctor of Geological and Mineralogical Sciences, Chief Researcher* (*Institute of the Earth's Crust SB RAS, Irkutsk, Russia*), *lounina@crust.irk.ru, https://orcid.org/0000-0001-7743-8877*, **Aleksei S. Nizovtsev,** *Postgraduate Student, Senior Laboratory Assistant* (*Institute of the Earth's Crust SB RAS, Irkutsk, Russia*), *https://orcid.org/0009-0008-1047-0846*.

The authors declare no conflict of interests.

This is an open access article under the CC BY 4.0 license

ISSN 2411-3336; e-ISSN 2541-9404

JOURNAL OF MINING INSTITUTE
Zapiski Gornogo instituta
Journal homepage: pmi.spmi.ru

Review article
Geotechnical Engineering and Engineering Geology

Analysis of technologies and equipment for Antarctic subglacial lake research

Ilya V. Rakitin✉, Dmitrii A. Vasilev, Aleksei V. Bolshunov, Anatolii Yu. Ozhigin
Empress Catherine II Saint Petersburg Mining University, Saint Petersburg, Russia

***How to cite this article*:** Rakitin I.V., Vasilev D.A., Bolshunov A.V., Ozhigin A.Yu. Analysis of technologies and equipment for Antarctic subglacial lake research. Journal of Mining Institute. 2026, Vol. 280, p. 176-188.

Abstract
Antarctica's subglacial hydrological system is a unique and still largely unexplored source of geological, paleoclimatic, and biological information that can be accessed only through direct investigation involving the sampling of water, suspended particulate matter, and bottom sediments. Of greatest scientific value are sites that have remained isolated for hundreds of thousands of years and preserve continuous sedimentary sequences containing thick deposits of ancient bottom sediments unaffected by basal glacial erosion. Such sites occur in subglacial lakes, which are key components of Antarctica's subglacial hydrological system. The planning and implementation of direct investigations of Antarctic subglacial lakes beneath both relatively thin ice and more than 2500 m of ice remain subjects of debate because experience with such operations is limited and there is no consensus on how compliance with environmental requirements should be ensured and monitored when subglacial environments are accessed. This article synthesizes the results of interdisciplinary studies of Antarctic subglacial lakes, including their locations, depths below the ice surface, morphometric and hydrodynamic parameters, and bottom-sediment composition. Particular attention is given to the technologies and equipment used to investigate subglacial lakes, including geophysical surveys, access-borehole drilling, lake access, measurement of the water body's physical and chemical parameters, and sampling of water, bottom sediments, and suspended particulate matter. The challenges and constraints associated with investigating "stable" subglacial lakes are analyzed and discussed, and key priorities for advancing the relevant technologies and equipment are identified.

Keywords
Antarctica; subglacial lakes; geophysical surveys; ice-drilling technologies; sampling technologies

Funding
This study was conducted under the 2024 State assignment for scientific research N FSRW-2024-0003.

Received: 09.12.2025 ***Accepted: 25.06.2026*** ***Online: 02.09.2026*** ***Published: 10.09.2026***

Introduction

Research into Antarctic subglacial hydrological systems remains a major priority in the Earth sciences (geophysics, hydrology, geology, and paleoclimatology) and biological sciences (microbiology, molecular biology, ecology, and exobiology). Antarctica's subglacial hydrological system comprises marine environments beneath ice shelves, subglacial watercourses, and lakes, all overlain by ice that impedes direct investigation. Subglacial lakes are among the principal objects of study and are classified as "stable" or "active" according to the constancy of their water volume and the presence of hydraulic connections to other components of the subglacial hydrological system. Antarctica currently contains 766 known subglacial lakes [1], 70 % of which have remained isolated from the external environment for hundreds of thousands of years. Their scientific value stems from the considerable age of their bottom sediments [2] and the possible presence of unknown forms of life [3, 4].

This is an open access article under the CC BY 4.0 license

Current understanding of subglacial lakes has been advanced substantially by geophysical methods (airborne and ground-based radar sounding, reflection seismic surveys, satellite radar altimetry [5-7], gravimetry and magnetometry [8], and transient electromagnetic sounding [9]), predictive computational methods (models of basal ice-sheet melting [10, 11]), and geostatistical modeling [12]. Despite the advantages of these methods, the extensive experience gained in their application, and the importance of the resulting data, they provide only indirect information about the subglacial environment and cannot fully characterize its structure, the mineralogical and biological composition of its water and bottom sediments, or the lake's hydrological regime. Such information is central to future subglacial lake research [13] and can be obtained only by direct sampling, primarily through the recovery of sediment cores and the collection of water, and suspended mineral and biological particles.

Direct investigations of subglacial lakes now span more than two decades, during which numerous technologies and items of equipment have been developed and tested. The diversity of lake morphometry and hydrodynamics, the lithological characteristics of bottom sediments, the broad range of overlying ice thicknesses, and the remoteness of study sites from research stations require a tailored approach to each lake.

No comprehensive account has yet been published of the most mature technologies and equipment developed by different research teams and used at successive stages of lake investigation. This article analyzes the principal parameters of Antarctic subglacial lakes and reviews both established and emerging technologies and equipment used in preliminary geophysical surveys, access-borehole drilling, lake access, and the collection of water, bottom-sediment, and suspended-particulate-matter samples. It also examines the limitations of research into “stable” subglacial lakes – the least studied and scientifically most valuable components of Antarctica's subglacial hydrological system, and identifies the main priorities for further research.

Characteristics of Antarctic subglacial lakes

Shielded from the atmosphere by thick ice, Antarctic subglacial lakes differ markedly from lakes on other continents in their formation conditions, hydrological regimes, biodiversity, water chemistry, and the mineralogical composition and age of their bottom sediments.

Antarctic subglacial lakes are thought to form primarily through basal melting of the ice sheet caused by geothermal heat or frictional heating associated with ice flow. Most “active” lakes lie beneath fast-flowing ice streams in coastal Antarctica. Consequently, they are relatively shallow and small, and their bottom sediments are comparatively young (about several hundred thousand years) and often structurally disturbed [14].

“Stable” lakes occur where basal melting is slow or absent [15] and the overlying ice flows slowly. Compared with “active” lakes, they are larger and deeper and contain areas of undisturbed natural sediment accumulation. Some “stable” lakes are unique features formed by tectonic [16-18] and hydrological processes before Antarctic glaciation; they may therefore preserve relict biological material and geological and hydrological records from an extended preglacial period [19]. In the basin of some of these lakes, the water column may be strongly stratified by density, salinity, and temperature, while hot, highly mineralized geothermal water may occupy the deepest layers [20].

Morphometric and hydrodynamic parameters of subglacial lakes. The principal morphometric parameters of subglacial lakes are water volume and depth, both of which depend on basin geomorphology. Subglacial lake depths range from a few meters for coastal “active” lakes to

This is an open access article under the CC BY 4.0 license

1300 m for "stable" lakes (e.g., Lake Vostok [5, 21]), while water volumes range from 0.2 km^3 to 5400 km^3 (Table 1). Other parameters include current velocity and direction, which govern the mixing of water and suspended particulate matter and, together with bottom topography, affect sedimentation rates and hence the age and structure of bottom sediments [22].

Table 1

Morphometric and hydrological parameters of the best-studied Antarctic subglacial lakes and their bottom sediments

Name	Average ice thickness, m [15]	Depth, m [15]	Volume, km^3 [15]	Lakes type	Sediments type	Sediments thickness, m	Velocity of water circulation, mm/s [23]
Whillans* [24]	798	6	0.155	Active	Silty diamicton comprising 8 % granules and pebbles, 33 % sand, 26 % silt, and 33 % clay (D50 ≈ 0.078 μm)	N/A	N/A
South Pole [25]	2857	32	N/A***	Stable	Density 1800 kg/m^3	150	0.1
Concordia [15]	4055	126	31	Stable	N/A	N/A	0.83
Ellsworth [2]	3400	156	1.37	Active	Fine-grained silts (< 0.6 mm) with a porosity of 77 % (clay-silt-sand 80-18-1.6 %)	6	0.69
Vostok** [26-28]	3945	Average 400 m; max 1200 m	6100	Stable	Fine-grained (clay-silt) fraction of clay-mica minerals and micrometer-sized quartz grains, with siltstone and sandstone inclusions measuring 0.3 to 8 mm. Mean inclusion size 0.5-2.0 mm	300	3.8
90E [29]	4074	900	1800	Stable	N/A	N/A	N/A
Mercer** [30]	1149	15	0.43	Active	Fine-grained silts or clays, D60 < 0.063 mm (porosity 77 %; clay-silt-sand 80-18-1.6 %)	N/A	N/A
CECs [22]	2653	310	2.5	Active	Fine-grained sediments dominated by silt and clay, with a porosity of 77 % (clay 80 %; silt 18 %)	15	0.97
Snow Eagle (LSE, PEL) [31]	3600	115	21	Active	Unconsolidated water-saturated sediments with a density of 1700 kg/m^3	200	N/A
Hodgson* [32]	4	90	N/A	Former subglacial	Gray sandy silt with numerous interbeds of coarser sediment ranging from sand to gravel	3.8	N/A
Untersee* [33]	3	64	0.7	Surface lake	Organic-rich terrigenous black silts (silty clay, clayey silt, and sandy silty clay)	N/A	N/A

* The lake was accessed and bottom sediments were subsequently sampled; for all other lakes, the inferred bottom-sediment structure is shown.
** The lake was accessed, but bottom sediments were not sampled.
*** Not available.

This is an open access article under the CC BY 4.0 license

© Ilya V. Rakitin, Dmitrii A. Vasilev, Aleksei V. Bolshunov, Anatolii Yu. Ozhigin, 2026

Locations and overlying ice thicknesses of subglacial lakes. Subglacial lake research is complicated by the extreme isolation of the study sites (Fig.1, *a*), particularly the considerable thickness of the overlying ice and the lakes' distance from polar stations. The thickness of ice overlying the lakes varies widely, from several tens of meters near the coast to 4661 m above LVS-12 [15] in the Antarctic interior, while distances from polar stations range from 0 km for Lake Vostok to 791 km for Recovery9 [15].

As a rule, "stable" lakes have thicker overlying ice than "active" lakes: 90 % are covered by more than 2500 m of ice, compared with 26 % of "active" lakes (Fig.1, *b*).

"Active" lakes tend to be farther from polar stations: 73 % are located more than 200 km away, compared with 44 % of "stable" lakes (Fig.1, *c*).

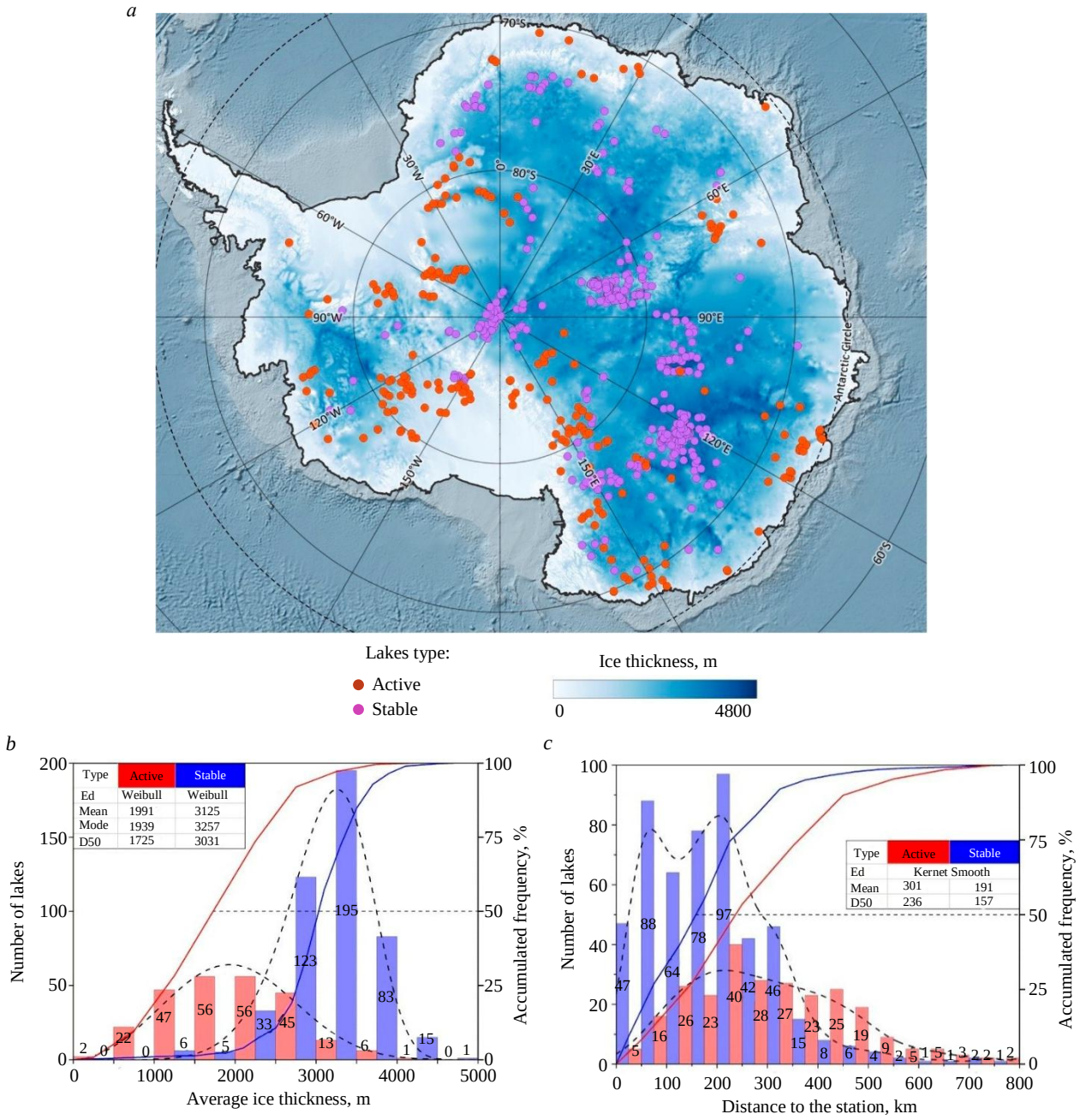


Fig.1. Location and accessibility parameters of Antarctic subglacial lakes: *a* – Antarctic ice-thickness map showing the locations of subglacial lakes (based on data from [34]); *b* – distribution of ice thickness above subglacial lakes (based on data from [15]); *c* – distribution of distances from lakes to the nearest polar stations (based on data from [15])

This is an open access article under the CC BY 4.0 license

Lithological characteristics of bottom sediments. Because direct sampling of Antarctic subglacial lakes remains limited, current understanding of their bottom sediments is based on geophysical surveys and interpretation of the resulting data, together with analyses of sediment cores recovered from beneath ice shelves, from subglacial streams, from two "active" lakes, and from lakes formerly covered by ice. Subglacial lake sediments may be either strongly stratified, with interbeds that differ in their physical and mechanical properties, or homogeneous. Sediment structure depends on the origin and evolution of the lake and on the dynamics of the overlying ice. Analyses of cores from subglacial water bodies, including two "active" subglacial lakes, indicate that Antarctic subglacial sediments are less homogeneous than sediments in ice-free temperate lakes and may have high shear strength (more than 70 kPa at a depth of 2 m [35]), and comprise unconsolidated water-saturated diamictons, silts, or sands containing interbedded coarse clastic layers (4-64 mm) of inorganic terrigenous origin [36] (Table 1). The occurrence of coarse clastic interbeds depends on the distance from the depositional site to the glacier outlet at the coast. With increasing distance from the outlet, the sediment becomes finer grained and the sedimentation rate decreases [37]. Steep basin slopes and vigorous circulation promote gravity-driven downslope transport and the formation of sediment accumulations near the lake bed; these processes disrupt the natural depositional sequence and must therefore be considered when selecting sampling sites.

Thus, lake location, overlying ice thickness, morphometric and hydrodynamic parameters, and sediment lithology not only determine the scope and scale of the scientific questions that can be addressed but also dictate the technologies and equipment required for a project.

Technologies and equipment for subglacial lake research

A comprehensive investigation of a subglacial lake includes:

• Characterization of the water column by vertical profiling, scanning, depth-discrete water sampling, and filtration of water to collect suspended particulate matter from the "ice – water" interface to the lake bed, providing information on the physical, chemical, and biological characteristics of subglacial lakes [15, 19].

• Analysis of bottom-sediment cores and mineral inclusions in congelation ice, providing essential information on geological, tectonic, hydrological, and paleoclimatic processes in Antarctica and on organisms that may have inhabited the lakes' water columns before continental glaciation began [4, 35]. For example, studies of ice cores recovered from the ice sheet overlying Lake Vostok led to the hypothesis that geothermal springs occur within its basin, as they do in lakes of tectonic origin [26].

A direct investigation of a subglacial lake consists of several main stages:

• Geophysical surveys.

• Access-borehole drilling.

• Subglacial lake access.

• Sampling of water, bottom sediments, and suspended particulate matter, and measurement of subglacial lake parameters.

Geophysical surveys. Before a subglacial lake is investigated directly, its physical characteristics and topographic setting must be determined [38-40]. Predictive models of basal ice-sheet melting [41], combined with satellite altimetry and surface-based geophysical surveys (Fig.2, *c*), provide the only practical means of identifying subglacial water bodies. Together, these methods can determine lake location and size, track volume changes, and, in some cases, estimate water salinity [38]. Seismic surveys provide the most detailed information on sediment structure and thickness and can also constrain lake depth [5, 20, 22]. Acoustic impedance inferred from the seismic data is used to estimate sediment consolidation, grain-size distribution, and stratigraphy (Table 1).

This is an open access article under the CC BY 4.0 license

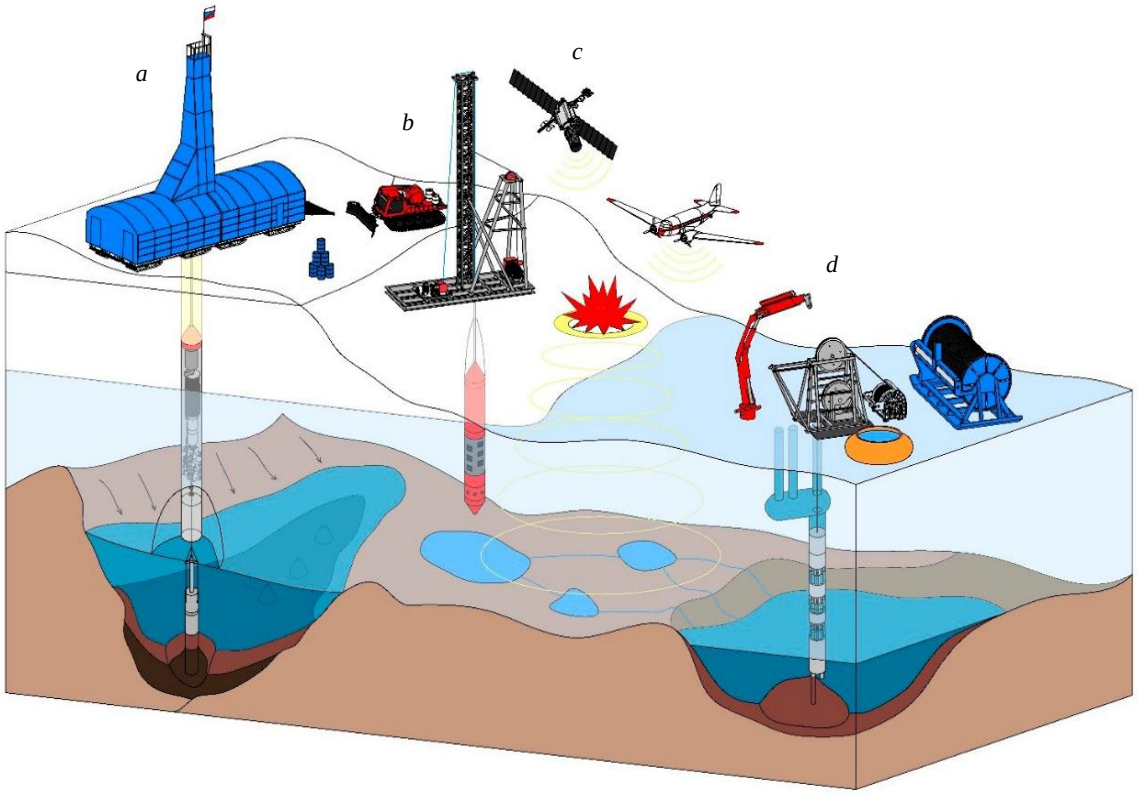


Fig.2. Technologies and equipment for Antarctic subglacial lake research:
a – bottom-sediment sampling with a modular device through a borehole drilled using an electromechanical drill and filled with an environmentally safe borehole fluid; *b* – thermal-probe drilling; *c* – geophysical identification of lakes and determination of their parameters; *d* – bottom-sediment and water sampling with a single-unit device through a hot-water-drilled borehole

Geophysical data and mathematical modeling can be used to estimate sediment age, construct depositional models, and thereby provide a sound basis for selecting both the lake bed sampling site and the drilling location on the ice surface [22].

Access-borehole drilling. Access-borehole drilling is the most labor- and energy-intensive stage of the work. Because the operating conditions are unique, every ice-drilling technology currently in use incorporates purpose-built engineering solutions, each with its own advantages and disadvantages. The key parameters are maximum drilling depth, drilling time, borehole diameter, borehole lifetime, equipment mass, total fuel consumption during drilling, and compliance with environmental requirements. The following ice-drilling technologies are currently the most mature:

Cable-suspended electromechanical drilling (Fig.2, *a*) has low energy consumption and can create a long-lived research borehole when a nonfreezing borehole fluid is used. Its principal disadvantage is a low overall drilling rate because tripping operations are time-consuming. A long-lived borehole permits periodic sampling over an extended period, yielding information on hydrological-system dynamics, the stability of microbial communities, and rates of ecosystem change [15].

Hot-water drilling (Fig.2, *d*) provides high penetration and overall drilling rates and is environmentally safe, but it has high energy demand and a short borehole lifetime. At an ice temperature of –25 °C and an initial borehole diameter of 100-240 mm, the borehole refreezes within 4-23 h [13]. Completing the investigation within several days substantially reduces the cost of supplying a temporary station.

This is an open access article under the CC BY 4.0 license

Thermal-probe drilling (Fig.2, *b*) offers autonomous drilling, portable equipment, and extended in-lake operating time. Its limitations include technical difficulties at great drilling depths and sensitivity to the mineral-particle content of the ice.

The main parameters of existing access-borehole drilling systems are presented in Table 2.

Table 2

Key parameters of existing and emerging access-borehole drilling technologies for subglacial lakes*

Technology	System	Borehole diameter, mm	Reached/ expected drilling depth, m	Drilling speed, m/day	Equipment weight (fuel weight), t	Drilling power[1], kW	Lake access technology
Cable-suspended electromechanical drilling	IBED	136	541/1400	20	25 (N/A)	3 + 11	Closed, staged, isolated
	KEMS-135	138	3765/4500	30	35 (N/A)	2.2 + 18.2	
	Foro 3000	129.6	– /2800	17	18 (31,93)	1.79 + 8.7	
Hot-water drilling	EHWD	600	2500/ –	2160	566 (N/A)	4700 + 300	Direct
	WISSARD	300	1092/ –	720-1480	230 (40)	1000	
	SLCEC CHWD [42]	300	2154/2700	max 2880	88 (N/A)	1000 + 120	
	Ellsworth	360	– /3400	N/A	111 (51)	1500	
	DeepRAD[2]	N/A	3413/3800	480	N/A	N/A	
Thermal-probe drilling	RECAS [43]	180	200/3800	36	330 kg (N/A)	9.7	Isolated
	TRIPLE [44]	200	52/4000	84	320 kg (N/A)	25	

Notes:
[1] For hot-water drilling systems, thermal and electrical power are reported; for electromechanical drills, the power ratings of the drill motor and drilling winch are reported.
[2] Based on the presentation by Wu Xiong, "Progress in polar scientific drilling research of CUGB" (09.04.2026).

Subglacial lake access. The access-borehole drilling method and the borehole fluid determine which lake-access methods can be used (Fig.3):

• Closed access, in which the pressure in the access borehole is maintained below the lake pressure so that lake water rises into part of the borehole and subsequently freezes. This method yielded the first frozen water samples from Lake Vostok [45]. A variant uses a thermal drill with a pilot bit to penetrate the subglacial lake [46].

• Direct access, providing immediate access to the lake when the borehole is filled with meltwater or another environmentally safe fluid [47, 48].

• Staged access, using a buffer of environmentally safe nonfreezing fluid or meltwater while the remainder of the borehole contains a toxic borehole fluid [46, 49].

• Isolated access, in which a layer of ice isolates the lake environment from the borehole environment [43].

The parameters of this stage directly affect the choice of methods for sampling water, bottom sediments, and suspended particulate matter, as well as for measuring subglacial lake parameters.

Sampling water, bottom sediments, and suspended particulate matter and measuring subglacial lake parameters. The following sampling configurations are used in subglacial lakes (Fig.3):

• a single-unit device, in which the research equipment is lowered directly through the borehole into the lake [50];

* Boeckmann G., Kuhl T., Moravec E. Basal Access and Sampling Feasibility Study. White Paper. 2022, p. 26.

This is an open access article under the CC BY 4.0 license

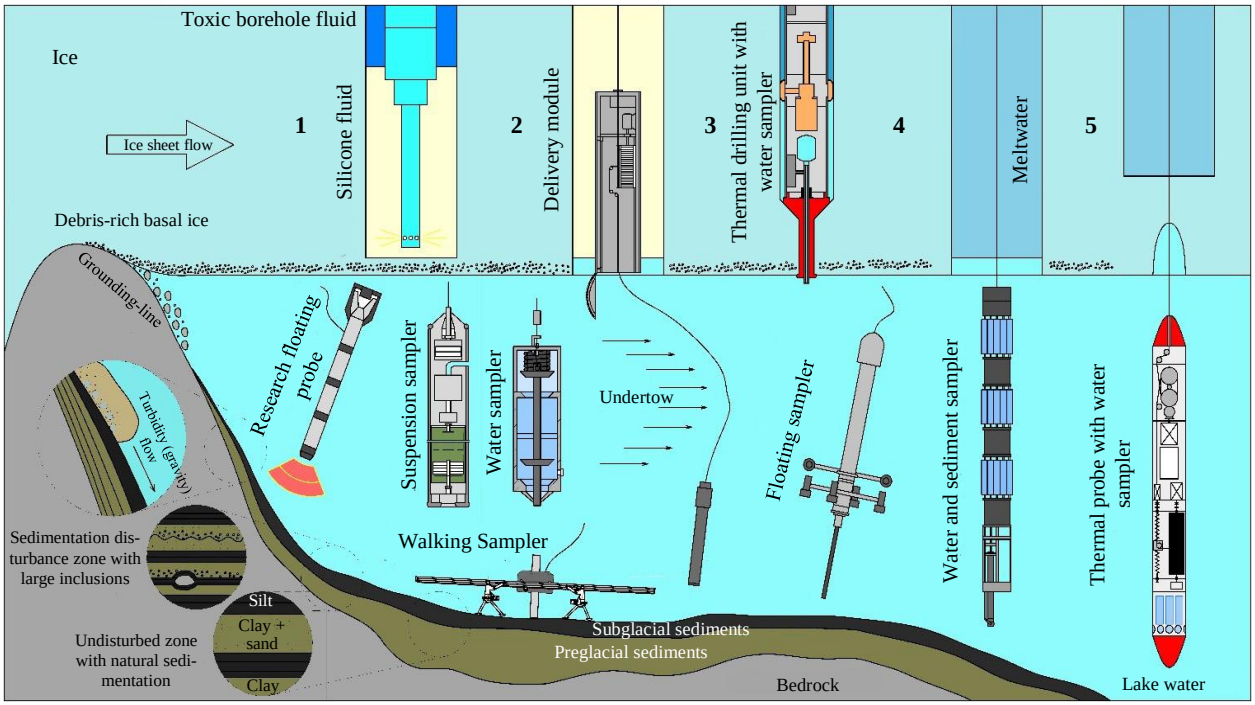


Fig.3. Equipment for direct investigation of Antarctic subglacial lakes and subglacial lake-access methods: 1 – staged; 2 – direct, followed by use of a modular research device; 3 – closed; 4 – direct, followed by use of a single-unit research device; 5 – isolated

• a modular device incorporating an intermediate component – a delivery module [51, 52] that isolates the research equipment from the borehole environment.

Water can be sampled from subglacial lakes using either a standard suite of hydrological instruments adapted to borehole conditions or purpose-built systems such as RECAS [43] and the Lake Ellsworth exploration system [53].

In studies of aquatic systems, sediment coring is generally used to characterize the sedimentary succession and thereby reconstruct the evolution of the water body. The principal sampler parameters are selected based on seismic surveys of the subglacial lake bed that provide a preliminary identification of sediment type.

Sediment samplers are classified by sampling method as follows:

• gravity corers (for soft sediments) [54];
• piston corers (for soft sediments) [55];
• percussion corers (from soft sediment to sand) [56];
• vibratory corers (from soft sediment to sand) [57];
• push corers (for soft sediments) [53];
• reciprocating rotary corers (for all sediment types, including bedrock) [26].

Mesh filters [58] are used to collect biological and mineral particles suspended in lake water; their operating principle involves pumping water through mesh cartridges with different aperture sizes. One such device, originally developed for oceanographic research and subsequently adapted for use in subglacial lakes, was deployed during the investigation of Mercer Subglacial Lake [30].

To maximize the information obtained from direct investigations and guide sampling-site selection, instruments are used to measure the following lake parameters in real time: hydrostatic pressure, temperature, dissolved-gas concentrations, pH, redox potential, electrical conductivity, and subglacial-water-body geometry using acoustic and laser ranging.

This is an open access article under the CC BY 4.0 license

During an investigation, equipment operation should be monitored using both analog readings transmitted to the surface and video recordings. Compact video systems can be integrated into a multifunctional research platform with limited maneuverability [59] or mounted on a separate remotely operated floating vehicle [44, 60].

Challenges and limitations of Antarctic subglacial lake research

Technologies and equipment for lake research have continued to advance since the first access to Lake Vostok. Nevertheless, despite numerous studies that yielded important results at Lake Vostok, Mercer Subglacial Lake, Subglacial Lake Whillans, and Lake Ellsworth, bottom sediments have yet to be sampled directly from deep "stable" subglacial lakes. This is attributable to the following distinguishing characteristics of "stable" subglacial lakes.

The ice thickness covering 90 % of this type of lakes is more than 2500 m. Increasing the target drilling depth substantially complicates drilling-system design, increases total equipment mass, and consequently raises logistical costs.

Relatively large lake depths – more than 50 m, together with underwater currents increase the area over which a suspended sampler may drift. Overlying ice thickness and water-column depth determine the hydrostatic pressure and therefore the design of pressure housings for electronic and propulsion components that cannot operate unprotected in water. Hydrostatic pressure also compresses gas inclusions in the sediment; their expansion during decompression may disrupt the core structure [61]. In deep lakes, the sampler cable or load-bearing tether may deviate from the vertical, hindering penetration into the bottom sediments.

A wide range of temperature differences, from –57 to 0 °C, from the surface of the glacier to the surface of the lake, determines the power of the hot water heating system during drilling, as well as additional heaters to prevent the well from freezing during lake exploration.

Geological uncertainty and variations in the physical and mechanical properties of stratigraphically diverse sediment layers present further challenges. Sediment consolidation, porosity, water saturation, and grain-size distribution strongly influence resistance to penetration by the sampler's core barrel and therefore affect the size of the recovered sample [62]. Together, these parameters also determine the rheological properties of the sediment mass, which affect the force required to detach the core, the performance of dynamic sampler systems, and the likelihood of disturbing the core structure during sampling.

Logistical difficulties in conducting research on lakes that are remote from polar stations, which leads to higher transportation costs per kilogram of cargo and, as a result, increased requirements for the weight and size of the equipment used and the amount of fuel.

Technological difficulties in complying with the mass and size restrictions of the equipment that is lowered into the lake, which is caused by the cramped conditions of the access well, which narrows over time.

Environmental requirements for preserving the relic ecological system of subglacial lakes, which significantly complicate the research technology and design of the devices used, and increase the cost of the work.

Some phenomena and conditions may remain unidentified because few subglacial lakes have been investigated directly and experience remains limited. For example, analyses of bottom-sediment cores from the "active" Mercer Subglacial Lake (1087 m of overlying ice) and Subglacial Lake Whillans (800 m of overlying ice) showed that their sediments did not preserve a record of natural lacustrine sedimentation but consisted instead of particles transported by subglacial flows. Their composition therefore did not differ from that of cores collected beneath ice streams and on the continental shelf in the same region of Antarctica [22].

This is an open access article under the CC BY 4.0 license

Future priorities for technological development

Given these distinguishing characteristics of "stable" subglacial lakes, the following priorities can be identified for developing and improving the technologies and equipment used to investigate them:

• Ensuring environmentally safe access to subglacial lakes during cable-suspended electromechanical drilling by using a silicone borehole fluid (e.g., polymethylsiloxane fluid PMS-3), a composite polymer cable, and systems for cleaning the borehole walls [47].

• Increasing borehole diameter and both penetration and overall drilling rates during deep cable-suspended electromechanical drilling by using improved cleaning systems, cutting tools, and tripping equipment.

• Increasing hot-water drilling depths and borehole lifetime, particularly in East Antarctica, where ice thickness commonly exceeds 3000 m.

• Increasing thermal-probe drilling depths by upgrading the built-in winch and overcoming constraints imposed by mineral inclusions in the ice using directional-drilling systems [13, 43].

• Increasing the length of recovered bottom-sediment cores while reducing the sampler's power demand [56].

• Expanding the area accessible for bottom-sediment sampling by fitting the sampler with propulsion units.

• Preserving the integrity of recovered bottom-sediment cores during drilling, recovery, and transport, as disturbance at these stages biases analyses of the sample's physical, geochemical, and biological properties [61].

• Ensuring reliable operation of electronic devices under high pressure and at low temperatures.

Conclusion

The investigation of Antarctic subglacial lakes is a complex interdisciplinary undertaking that requires advanced geophysical methods, drilling technologies, environmentally safe lake-access techniques, integrated characterization of water bodies, and methods for analyzing the resulting data. This article has examined the distinctive geographic and geotechnical settings of subglacial lakes and the established and emerging technologies and equipment used to investigate them.

Over decades of remote and direct subglacial lake research, the technologies and equipment employed have steadily advanced through the efforts of engineers and scientists worldwide. Despite substantial progress, particularly in identifying subglacial lakes by geophysical methods, many questions remain unresolved. Foremost among them is the challenge of obtaining samples from "stable" subglacial lakes while meeting environmental-protection requirements. Addressing this challenge requires integrated planning that explicitly aligns scientific objectives, logistical and infrastructure capabilities, access-borehole drilling, lake-access procedures, and sampling technologies. Before field deployment, experimental studies should be conducted under conditions representative of actual operations to assess the reliability, energy efficiency, and environmental safety of the proposed technologies. At the current level of scientific and technological development, direct investigations of subglacial lakes present a set of formidable challenges. Successful implementation of such projects, however, could produce discoveries that fundamentally reshape our understanding of Earth's climate history, past and present biogeochemical processes in isolated ecosystems, and the future dynamics of Earth's cryosphere.

This is an open access article under the CC BY 4.0 license

REFERENCES

1. Wilson S.F., Hogg A.E., Rigby R. et al. Detection of 85 new active subglacial lakes in Antarctica from a decade of CryoSat-2 data. *Nature Communications*. 2025. Vol. 16. N 8311. DOI: 10.1038/s41467-025-63773-9

2. Smith A.M., Woodward J., Ross N. et al. Evidence for the long-term sedimentary environment in an Antarctic subglacial lake. *Earth and Planetary Science Letters*. 2018. Vol. 504, p. 139-151. DOI: 10.1016/j.epsl.2018.10.011

3. Siegert M.J., Priscu J.C., Alekhina I.A. et al. Antarctic subglacial lake exploration: first results and future plans. *Philosophical Transactions of the Royal Society A. Mathematical, physical and engineering sciences*. 2016. Vol. 374. Iss. 2059. N 20140466. DOI: 10.1098/rsta.2014.0466

4. Bulat S., Petit J.-R. Vostok, Subglacial Lake. Encyclopedia of Astrobiology. Springer, 2023, p. 3206-3212. DOI: 10.1007/978-3-662-65093-6_1765

5. Masolov V.N., Popov S.V., Lukin V.V., Popkov A.M. The Bottom Topography and Subglacial Lake Vostok Water Body, East Antarctica. *Doklady Earth Sciences.* 2010. Vol. 433. Part 2, p. 1092-1097. DOI: 10.1134/S1028334X10080222

6. Siegert M. A 60-year international history of Antarctic subglacial lake exploration. *Geological Society, London, Special Publications*. 2018. Vol. 461, p. 7-21. DOI: 10.1144/SP461.5

7. Gorelik G.D., Egorov A.S., Shuklin I.A., Ushakov D.E. Substantiation of optimal range of geophysical surveys to study deep structure of the Lake Vostok area. *Gornyi zhurnal.* 2024. N 9, p. 56-61 (in Russian). DOI: 10.17580/gzh.2024.09.09

8. Studinger M, Bell R.E., Karner G.D. et al. Ice cover, landscape setting, and geological framework of Lake Vostok, East Antarctica. *Earth and Planetary Science Letters*. 2003. Vol. 205. Iss. 3-4, p. 195-210. DOI: 10.1016/S0012-821X(02)01041-5

9. Killingbeck S.F., Dow C.F., Unsworth M.J. A quantitative method for deriving salinity of subglacial water using ground-based transient electromagnetics. *Journal of Glaciology*. 2022. Vol. 68. Iss. 268, p. 319-336. DOI: 10.1017/jog.2021.94

10. Pattyn F. Antarctic subglacial conditions inferred from a hybrid ice sheet/ice stream model. *Earth and Planetary Science Letters*. 2010. Vol. 295. Iss. 3-4, p. 451-461. DOI: 10.1016/j.epsl.2010.04.025

11. Zotikov I.A. Bottom melting in the central zone of the ice shield on the Antarctic continent and its influence upon the present balance of the ice mass. *International Association of Scientific Hydrology. Bulletin*. 1963. Vol. 8. Iss. 1, p. 36-44. DOI: 10.1080/02626666309493295

12. MacKie E.J., Schroeder D.M., Caers J. et al. Antarctic Topographic Realizations and Geostatistical Modeling Used to Map Subglacial Lakes. *Journal of Geophysical Research: Earth Surface*. 2020. Vol. 125. Iss. 3. N e2019JF005420. DOI: 10.1029/2019JF005420

13. Talalay P.G., Xiaopeng Fan. Alternative clean approaches to accessing subglacial Lake Vostok. *Arctic and Antarctic Research.* 2024. Vol. 70. N 4, p. 499-513. DOI: 10.30758/0555-2648-2024-70-4-499-513

14. Siegfried M.R., Venturelli R.A., Patterson M.O. et al. The life and death of a subglacial lake in West Antarctica. *Geology*. 2023. Vol. 51. N 5, p. 434-438. DOI: 10.1130/G50995.1

15. Livingstone S.J., Yan Li, Rutishauser A. et al. Subglacial lakes and their changing role in a warming climate. *Nature Reviews Earth & Environment*. 2022. Vol. 3. Iss. 2, p. 106-124. DOI: 10.1038/s43017-021-00246-9

16. Egorov A.S., Ageev A.S., Shuklin I.A. et al. On the similarity of deep structure of the basement and genesis of depressions on the eastern flank of East Antarctic and in Lake Baikal area. *Journal of Mining Institute.* 2025. Vol. 273, p. 26-41.

17. Studinger M., Karner G.D., Bell R.E. Geophysical models for the tectonic framework of the Lake Vostok region, East Antarctica. *Earth and Planetary Science Letters*. 2003. Vol. 216. Iss. 4, p. 663-677. DOI: 10.1016/S0012-821X(03)00548-X

18. Tabacco I.E., Cianfarra P., Forieri A. et al. Physiography and tectonic setting of the subglacial lake district between Vostok and Belgica subglacial highlands (Antarctica). *Geophysical Journal International*. 2006. Vol. 165. Iss. 3, p. 1029-1040. DOI: 10.1111/j.1365-246X.2006.02954.x

19. Lukin V.V., Markov A.N. Hypothesis of Tectonic Preglacial Genesis of the Basin and Water Body of Antarctica's Lake Vostok. *Geography and Natural Resources.* 2024. Vol. 45. N 2, p. 192-201. DOI: 10.1134/S1875372824700264

20. Popov S.V., Boronina A.S., Ekaykin A.A. et al. Remote sensing and mathematical modelling of Lake Vostok, East Antarctica: past, present and future research. *Arctic and Antarctic Research.* 2024. Vol. 70. N 4, p. 460-476. DOI: 10.30758/0555-2648-2024-70-4-460-476

21. Litvinenko V. Foreword: Sixty-year Russian history of Antarctic sub-glacial lake exploration and Arctic natural resource development. *Geochemistry*. 2020. Vol. 80. Iss. 3. N 125652. DOI: 10.1016/j.chemer.2020.125652

22. Brisbourne A.M., Smith A.M., Rivera A. et al. Bathymetry and bed conditions of Lago Subglacial CECs, West Antarctica. *Journal of Glaciology*. 2023. Vol. 69. Iss. 278, p. 1546-1555. DOI: 10.1017/jog.2023.38

23. Couston L.-A., Siegert M. Dynamic flows create potentially habitable conditions in Antarctic subglacial lakes. *Science Advances*. 2021. Vol. 7. Iss. 8. N eabc3972. DOI: 10.1126/sciadv.abc3972

24. Hodson T.O., Powell R.D., Brachfeld S.A. et al. Physical processes in Subglacial Lake Whillans, West Antarctica: Inferences from sediment cores. *Earth and Planetary Science Letters*. 2016. Vol. 444, p. 56-63. DOI: 10.1016/j.epsl.2016.03.036

25. Peters L.E., Anandakrishnan S., Holland C.W. et al. Seismic detection of a subglacial lake near the South Pole, Antarctica. *Geophysical Research Letters*. 2008. Vol. 35. Iss. 23. N L23501. DOI: 10.1029/2008GL035704

26. Vasilyev N.I., Leychenkov G.L., Zagrivny E.A. Prospects of Obtaining Samples of Bottom Sediments from Subglacial Lake Vostok. *Journal of Mining Institute.* 2017. Vol. 224, p. 199-208. DOI: 10.18454/PMI.2017.2.199

27. Popov S.V. Six decades of radar and seismic research in Antarctica. *Ice and Snow.* 2021. Vol. 61. N 4, p. 587-619 (in Russian). DOI: 10.31857/S2076673421040110

28. Leitchenkov G.L., Antonov A.V., Luneov P.I., Lipenkov V.Ya. Geology and environments of subglacial Lake Vostok. *Philosophical Transactions of the Royal Society A. Mathematical, physical and engineering sciences*. 2016. Vol. 374. Iss. 2059. N 20140302. DOI: 10.1098/rsta.2014.0302

29. Bell R.E., Studinger M., Fahnestock M.A., Shuman C.A. Tectonically controlled subglacial lakes on the flanks of the Gamburtsev Subglacial Mountains, East Antarctica. *Geophysical Research Letters*. 2006. Vol. 33. Iss. 2. N L02504. DOI: 10.1029/2005GL025207

This is an open access article under the CC BY 4.0 license

30. Priscu J.C., Kalin J., Winans J. et al. Scientific access into Mercer Subglacial Lake: scientific objectives, drilling operations and initial observations. *Annals of Glaciology*. 2021. Vol. 62. Iss. 85-86, p. 340-352. DOI: 10.1017/aog.2021.10

31. Shuai Yan, Blankenship D.D., Greenbaum J.S. et al. A newly discovered subglacial lake in East Antarctica likely hosts a valuable sedimentary record of ice and climate change. *Geology*. 2022. Vol. 50. N 8, p. 949-953. DOI: 10.1130/G50009.1

32. Hodgson D.A., Roberts S.J., Bentley M.J. et al. Exploring former subglacial Hodgson Lake, Antarctica. Paper II: palaeolimnology. *Quaternary Science Reviews*. 2009. Vol. 28. Iss. 23-24, p. 2310-2325. DOI: 10.1016/j.quascirev.2009.04.014

33. Levitan M.A., Girin Yu.P., Luksha V.L. et al. Modern Sedimentation System of Lake Untersee, East Antarctica. *Geochemistry International*. 2011. Vol. 49. Iss. 5. P. 459-481. DOI: 10.1134/S0016702911050077

34. Pritchard H.D., Fretwell P.T., Fremand A.C. et al. Bedmap3 updated ice bed, surface and thickness gridded datasets for Antarctica. *Scientific Data*. 2025. Vol. 12. N 414. DOI: 10.1038/s41597-025-04672-y

35. Dunbar G., Niessen F., Vogel S. Late Pleistocene to Holocene Strata from Soft-Sediment Coring at the AND-1B Site, ANDRILL McMurdo Ice Shelf Project, Antarctica. *Terra Antartica*. 2007. Vol. 14. N 3, p. 141-154.

36. Bentley M.J., Christoffersen P., Hodgson D. A. et al. Subglacial Lake Sediments and Sedimentary Processes: Potential Archives of Ice Sheet Evolution, Past Environmental Change, and the Presence of Life. Antarctic Subglacial Aquatic Environments. American Geophysical Union, 2011. Vol. 192, p. 83-110.

37. Campbell T.D., Skidmore M.L., Patterson M.O. et al. Dynamic subglacial meltwater history archived in Antarctic subglacial lake sediments. *Geological Society of America Bulletin*. 2025. Vol. 137. N 7-8, p. 3055-3068. DOI: 10.1130/B37731.1

38. Yan Zhou, Xiangbin Cui, Zhenxue Dai et al. The Antarctic Subglacial Hydrological Environment and International Drilling Projects: A Review. *Water*. 2024. Vol. 16. Iss. 7. N 1111. DOI: 10.3390/w16081111

39. Talovina I.V., Babenko I.A., Ilalova R.K., Duryagina A.M. Olivine-spinel geothermometry – Indicator of formation identity of rocks and a basis for geodynamic reconstructions in Antarctica. *Gornyi zhurnal*. 2024. N 9, p. 77-82 (in Russian). DOI: 10.17580/gzh.2024.09.12

40. Abdrakhmanov I.A., Gulbin Y.L., Skublov S.G., Galankina O.L. Mineralogical Constraints on the Pressure–Temperature Evolution of Granulites in the Bunger Hills, East Antarctica. *Minerals*. 2024. Vol. 14. Iss. 5. N 488. DOI: 10.3390/min14050488

41. Litvinenko V., Trushko V. Modelling of geomechanical processes of interaction of the ice cover with subglacial Lake Vostok in Antarctica. *Antarctic Science*. 2025. Vol. 37. Iss. 1, p. 39-48. DOI: 10.1017/S0954102024000506

42. Makinson K., Anker P.G.D., Garcés J. et al. Development of a clean hot water drill to access Subglacial Lake CECs, West Antarctica. *Annals of Glaciology*. 2021. Vol. 62. Iss. 85-86, p. 250-262. DOI: 10.1017/aog.2020.88

43. Youhong Sun, Bing Li, Xiaopeng Fan et al. Brief communication: New sonde to unravel the mystery of polar subglacial lakes. *The Cryosphere*. 2023. Vol. 17. Iss. 3, p. 1089-1095. DOI: 10.5194/tc-17-1089-2023

44. Audehm J., Bachmayer R., Bande M. et al. TRIPLE – Technologies for Rapid Ice Penetration and Subglacial Lake Exploration: Whitepaper by the TRIPLE Project within the German Space Agency Explorer Initiative at DLR. German Space Agency at DLR, 2025, p. 36. DOI: 10.22541/essoar.175371779.92742499/v2

45. Lipenkov V.Ya., Turkeev A.V., Ekaykin A.A. et al. Unsealing Subglacial Lake Vostok: Lessons and implications for future full-scale exploration. *Arctic and Antarctic Research*. 2024. Vol. 70. N 4, p. 477-498. DOI: 10.30758/0555-2648-2024-70-4-477-498

46. Vasiliev N.I., Talalay P.G., Bobin N.E. et al. Deep drilling at Vostok station, Antarctica: history and recent events. *Annals of Glaciology*. 2007. Vol. 47, p. 10-23. DOI: 10.3189/172756407786857776

47. Serbin D.V., Buslaev G.V., Lavrik A.Yu. et al. Study of the interaction between the drilling fluid and lake water during the opening of the subglacial Lake Vostok in Antarctica. *Journal of Mining Institute*. 2025. Vol. 273, p. 136-146.

48. Alemany O., Talalay P., Boissonneau P. et al. The SUBGLACIOR drilling probe: hydraulic considerations. *Annals of Glaciology*. 2021. Vol. 62. Iss. 84, p. 131-142. DOI: 10.1017/aog.2020.79

49. Serbin D.V. Prevention of emulsion formation during opening subglasial reservoirs. *News of the Ural State Mining University*. 2021. Iss. 3 (63), p. 80-88 (in Russian). DOI: 10.21440/2307-2091-2021-3-80-88

50. Da Gong, Xiaopeng Fan, Yazhou Li et al. Coring of Antarctic Subglacial Sediments. *Journal of Marine Science and Engineering*. 2019. Vol. 7. Iss. 6. N 194. DOI: 10.3390/jmse7060194

51. Litvinenko V.S., Leitchenkov G.L., Vasiliev N.I. Anticipated sub-bottom geology of Lake Vostok and technological approaches considered for sampling. *Geochemistry*. 2020. Vol. 80. Iss. 3. N 125556. DOI: 10.1016/j.chemer.2019.125556

52. Vasilev N.I., Bolshunov A.V., Dmitriev A.N., Podoliak A.V. Round-trip assembly for investigations of subglacial lake Vostok. *International Journal of Applied Engineering Research*. 2016. Vol. 11. N 9, p. 6376-6380.

53. Keen P., Saw K., Rundle N. et al. A mini-corer for precision sampling of the water-sediment interface in subglacial lakes and other remote aqueous environments. *Limnology and Oceanography: Methods*. 2018. Vol. 16. Iss. 12, p. 856-867. DOI: 10.1002/lom3.10288

54. Rosenheim B.E., Michaud A.B., Broda J. et al. A method for successful collection of multicores and gravity cores from Antarctic subglacial lakes. *Limnology and Oceanography: Methods*. 2023. Vol. 21. Iss. 5, p. 279-294. DOI: 10.1002/lom3.10545

55. Hodgson D.A., Bentley M.J., Smith J.A. et al. Technologies for retrieving sediment cores in Antarctic subglacial settings. *Philosophical Transactions of the Royal Society A. Mathematical, physical and engineering sciences*. 2016. Vol. 374. Iss. 2059. N 20150056. DOI: 10.1098/rsta.2015.0056

56. Makinson K., Ashurst D., Anker P.G.D. et al. A new percussion hammer mechanism for a borehole deployable subglacial sediment corer. *Annals of Glaciology*. 2020. Vol. 62. Iss. 85-86, p. 385-389. DOI: 10.1017/aog.2020.83

57. Da Gong, Nan Zhang, Yunchen Liu et al. Small-diameter vibrocorer for sediment coring beneath Antarctic ice shelves: General concept and testing. *Ocean Engineering*. 2016. Vol. 126, p. 232-239. DOI: 10.1016/j.oceaneng.2016.09.023

58. Bobin N.E., Talatai P.G., Yankilevich S.V. Technical means for the study of subglacial reservoirs in the example of Lake Vostok in Antarctica. *Journal of Mining Institute*. 2004. Vol. 157, p. 147-149 (in Russian).

59. Mowlem M., Saw K., Brown R. et al. Probe technologies for clean sampling and measurement of subglacial lakes. *Philosophical Transactions of the Royal Society A. Mathematical, physical and engineering sciences*. 2016. Vol. 374. Iss. 2059. N 20150267. DOI: 10.1098/rsta.2015.0267

This is an open access article under the CC BY 4.0 license

60. Behar A.E., Chen D.D., Ho C. et al. MSLED: The Micro Subglacial Lake Exploration Device. *Underwater Technology*. 2015. Vol. 33. N 1, p. 3-17. DOI: 10.3723/ut.33.003

61. Dück Y., Lorke A., Jokiel C., Gierse J. Laboratory and field investigations on freeze and gravity core sampling and assessment of coring disturbances with implications on gas bubble characterization. *Limnology and Oceanography: Methods*. 2019. Vol. 17. Iss. 11, p. 585-606. DOI: 10.1002/lom3.10335

62. Jun Han Bae, Wonse Jo, Jee Hwan Park et al. Evaluation of Sampling Methods for Robotic Sediment Sampling Systems. *IEEE Journal of Oceanic Engineering*. 2020. Vol. 46. Iss. 2, p. 542-554. DOI: 10.1109/JOE.2020.3005576

***Authors*: Ilya V. Rakitin,** *Postgraduate Student* (*Empress Catherine II Saint Petersburg Mining University*, *Saint Petersburg*, *Russia*), *ilja.rakitin@mail.ru*, *https://orcid.org/0000-0002-7874-1859*, **Dmitrii A. Vasilev,** *Candidate of Engineering Sciences, Assistant Lecturer* (*Empress Catherine II Saint Petersburg Mining University*, *Saint Petersburg*, *Russia*), *https://orcid.org/0000-0001-8132-8881*, **Aleksei V. Bolshunov,** *Candidate of Engineering Sciences, Scientific Supervisor of the Laboratory* (*Empress Catherine II Saint Petersburg Mining University*, *Saint Petersburg*, *Russia*), *https://orcid.org/0000-0002-3879-7380*, **Anatolii Yu. Ozhigin,** *Design Engineer* (*Empress Catherine II Saint Petersburg Mining University*, *Saint Petersburg*, *Russia*), *https://orcid.org/0000-0002-8279-8866*.

The authors declare no conflict of interests.

This is an open access article under the CC BY 4.0 license